Université Côte d'Azur

Habilitation à Diriger des Recherches

présentée par

Dario Vincenzi

Dynamique Lagrangienne en Turbulence et Turbulence Élastique

le 14 décembre 2018

Jury

Philippe Peyla	Rapporteur
Alain Pumir	Rapporteur
Emmanuel Villermaux	Rapporteur
Mireille Bossy	Examinatrice
Uriel Frisch	Examinateur
Hamid Kellay	Examinateur

Table des matières

Avant-propos

Ce mémoire est dédié à mes travaux sur la dynamique d'objets microscopiques en turbulence hydrodynamique et sur la turbulence élastique dans les solutions de polymères. Ces travaux ont été effectués entre 2005 et 2018. Certains d'entre eux ont été réalisés dans le cadre d'une thèse (Emmanuel L.C. VI M. Plan, actuellement post-doc à Oxford) et le suivi de post-docs (Aamir Ali et Adeel Ahmad, actuellement professeurs assistants à COMSATS University Islamabad).

La première partie du document résume mes principaux résultats sur les deux thématiques. Pour une lecture plus approfondie le lecteur peut consulter les articles en annexe.

Les nombres en exposant dans le texte renvoient à la bibliographie de la page 39 ; quant aux lettres entre crochets elles renvoient à mes articles en annexe.

Chapitre 1

Introduction

1.1 Approche lagrangienne à l'étude de la turbulence

Les écoulements fluides que l'on retrouve en géophysique, en astrophysique ou dans l'industrie présentent souvent un caractère turbulent. Au cours des vingt dernières années, l'étude de la turbulence hydrodynamique a reçu une impulsion nouvelle grâce au développement de techniques expérimentales, théoriques et numériques dans le référentiel lagrangien[1–3]. L'approche lagrangienne se propose de décrire le mouvement et la déformation d'un élément de volume fluide et est alternative à l'approche eulérienne, qui fournit une description de l'écoulement en termes de champs spatio-temporels.

Les études expérimentales lagrangiennes ont connu un développement important grâce à l'utilisation de caméras ultra-rapides et à la mise au point de techniques optiques permettant de suivre des particules microscopiques dans des écoulements turbulents[2] (figure 1.1). Les expériences de laboratoire, de turbulence isotrope ou en soufflerie, ont ainsi mesuré les statistiques de la vitesse et de l'accélération à la fois de traceurs et de particules inertielles (c'est-à-dire ayant une densité différente de celle du fluide).

Les simulations numériques ont bénéficié de nouveaux algorithmes de suivi de particules et de moyens de calcul plus puissants, qui ont rendu possible l'analyse d'un grand nombre de trajectoires fluides (typiquement de l'ordre d'un million) dans des écoulements à un nombre de Reynolds élevé. Ceci a permis, d'une part, de comparer avec les données expérimentales les prédictions obtenues pour des écoulements modèles (voir à titre d'exemple la référence 4) et, d'autre part, d'analyser des quantités physiques difficilement accessibles expérimentalement, comme certaines propriétés lagrangiennes du gradient de vitesse[5].

Les études théoriques, quant à elles, se sont concentrées sur des modèles stochastiques de transport turbulent. On est en effet encore loin de savoir résoudre analytiquement les équations de Navier–Stokes dans le régime turbulent. Une stratégie possible pour l'étude analytique du transport turbulent consiste donc à remplacer la solution des équations de Navier–Stokes par un champ de vitesse aléatoire qui reproduit au moins quelques unes des propriétés statistiques des champs turbulents réels. L'un des modèles de transport turbulent les plus connus est celui proposé par R.H. Kraichnan[6,7]. Dans ce modèle le champ de vitesse, gaussien et décorrélé en temps, présente des corrélations spatiales non lisses, qui simulent le comportement d'un écoulement turbulent dans l'intervalle d'échelles spatiales plus grandes que les échelles dominées par la viscosité et plus petites que l'échelle du forçage qui génère l'écoulement. Les propriétés du modèle de Kraichnan ont permis de développer une approche analytique à l'étude du trans-

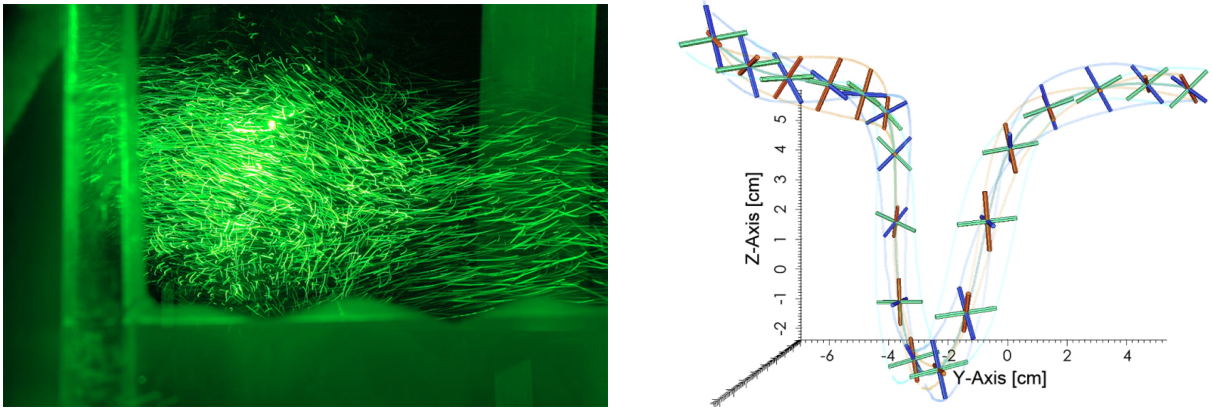

FIGURE 1.1 – ***A gauche :*** *visualisation de traceurs dans un écoulement de Von Kármán turbulent au Max Planck Institute for Dynamics and Self-Organization de Goettingen © MPIDS.* ***A droite :*** *trajectoire d'une particule en forme de croix à trois bras dans un écoulement turbulent entre deux grilles en oscillation [d'après Marcus et al.* New J. Phys. **16**, *102001 (2014)].*

port turbulent, qui exploite la relation mathématique entre équations aux dérivées partielles paraboliques et équations ordinaires stochastiques. Cette approche a conduit à une interprétation lagrangienne des propriétés statistiques du transport turbulent et a, par exemple, permis de démontrer l'intermittence de champs scalaires passifs tels que la température dans un fluide faiblement chauffé ou la concentration d'un colorant dans un liquide[1].

La description lagrangienne est celle qui est naturelle non seulement pour décrire le mouvement des particules fluides, mais aussi pour comprendre la dynamique d'objets microscopiques possédant des degrés de liberté supplémentaires et passivement transportés par un écoulement turbulent. Ce problème a attiré beaucoup d'attention dans les années récentes et on peut compter plusieurs études sur la dynamique lagrangienne de bâtonnets[8], de croix[9] (avec deux ou trois bras), d'hélicoïdes isotropes[10], de dipôles chiraux[11], de fibres[12] en turbulence (figure 1.1). Chacun de ces objets réagit en effet de façon distinctive à l'action du gradient de vitesse et permet d'explorer des propriétés différentes d'un écoulement turbulent.

C'est dans ce contexte que se situe une partie essentielle de mes recherches. Les travaux présentés au chapitre 2 portent sur la rotation et l'orientation de particules solides anisotropes, l'étirement de polymères élastiques et la déformation de gouttelettes ou de particules semi-flexibles. L'approche que j'ai adoptée consiste à utiliser des modèles de particules simplifiés qui permettent de se concentrer sur un seul degré de liberté dynamique (translation, rotation, étirement, flexion) et à décrire la turbulence par des champs de vitesse stochastiques. Le but est d'obtenir des résultats analytiques sur les propriétés statistiques de la dynamique lagrangienne. Les techniques utilisées ont été pour l'essentiel empruntées à la théorie des processus stochastiques. Dans la plupart des travaux présentés dans ce mémoire, les résultats analytiques sont comparés avec des simulations numériques de turbulence. Celles-ci ont pour l'essentiel été effectuées dans le cadre de collaborations, notamment au sein des programmes européens COST « Particles in Turbulence » (MP0806) et « Flowing Matter » (MP1305) et de la collaboration franco–indienne IFCAM (Indo–French Centre for Applied Mathematics).

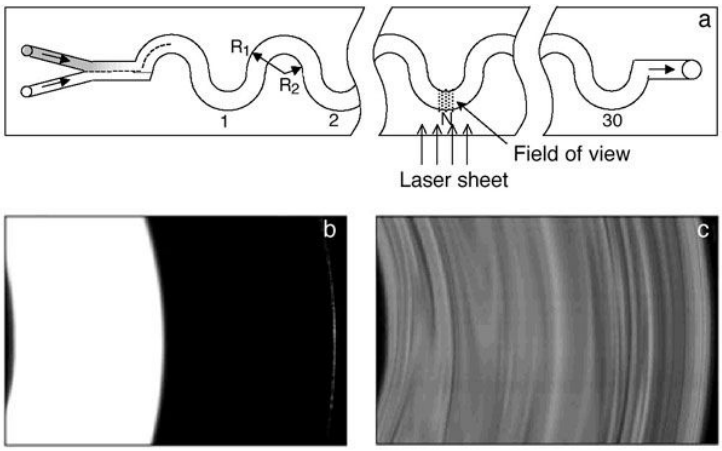

FIGURE 1.2 – *Turbulence élastique dans un microcanal en forme de serpentin [d'après Groisman & Steinberg,* Nature **410***, 905 (2001)].* (a) *Le canal a deux entrées séparées. Le même liquide est injecté dans les deux entrées, mais dans l'une des deux le liquide est mélangé avec un colorant fluorescent. Le nombre de Reynolds est* Re = 0.16*. Le canal est ensuite visualisé par l'intermédiaire d'un faisceau laser à une distance de 29 demi-anneaux des entrées :* (b) *le liquide pur et celui fluorescent sont encore parfaitement séparés, puisque* Re *est très petit et le mélange est entièrement confié à la la diffusion moléculaire, qui agit sur des échelles de temps très longues ;* (c) *on ajoute une petite concentration de polyacrylamide (80 parts par million) au liquide et, après le même nombre de demi-anneaux, le liquide pur et celui fluorescent sont bien mélangés grâce à l'écoulement chaotique engendré par les instabilités élastiques.*

1.2 Dynamique chaotique à petits nombres de Reynolds : la turbulence élastique dans les solutions de polymères

Un autre sujet de recherche auquel je m'intéresse depuis quelques années est la turbulence élastique. Si un fluide est newtonien ‡ et le nombre de Reynolds *Re* (rapport entre l'inertie et la dissipation visqueuse) est petit, le comportement du fluide est laminaire ; il ne devient turbulent que lorsque le nombre de Reynolds dépasse une valeur critique. Ceci n'est pas nécessairement vrai pour les fluides non-newtoniens. En particulier, les solutions de polymères présentent des instabilités même pour *Re* petit[13] et, si les polymères sont suffisamment élastiques, ces instabilités donnent lieu à un régime chaotique connu sous le nom de *turbulence élastique*.

La turbulence élastique, découverte il y a une vingtaine d'année par Groisman et Steinberg[14], est maintenant très utilisée en microfluidique, où *Re* est typiquement très petit. Elle permet notamment d'accélérer le mélange dans les dispositifs microfluidiques[15] ainsi que de favoriser les transferts de chaleur[16] et l'émulsification[17]. La figure 1.2 illustre le régime de turbulence élastique dans un microcanal en forme de serpentin.

Récemment une nouvelle application de la turbulence élastique a été proposée dans le cadre de l'extraction du pétrole. L'une des techniques les plus utilisées afin d'extraire le pétrole consiste en effet à inonder les roches-réservoirs par de l'eau. Des solutions aqueuses de polymères sont ensuite employées pour extraire les résidus de pétrole qui restent piégés dans les pores les plus fins. La performance de cette technique est bien plus haute qu'attendu, et la

‡. Nous rappelons qu'un fluide est dit newtonien si le tenseur des contraintes est proportionnel au tenseur des déformations.

turbulence élastique a été proposée comme explication possible de cet effet[18].

Le propriétés principales de la turbulence élastique peuvent être résumées comme il suit. Dans le régime de turbulence élastique, l'exposant de Lyapunov de l'écoulement croît rapidement en fonction de l'élasticité de la solution[19] et la vitesse présente des fluctuations fortement intermittentes[20]. La transition vers la turbulence élastique se fait par une succession d'états périodiques ou quasi-périodiques[21]. La puissance nécessaire pour maintenir l'écoulement augmente considérablement par rapport à sa valeur dans le régime laminaire[22], ce qui indique une augmentation de la dissipation d'énergie cinétique. De plus, les spectres spatial et temporel de la vitesse montrent un comportement en loi de puissance[14,22]. Un grand nombre de modes de Fourier sont donc activés dans le système ; toutefois le spectre spatial décroît avec le nombre d'onde k plus rapidement que k^{-3}, c'est-à-dire l'énergie cinétique est essentiellement concentrée aux grandes échelles et les fluctuations décroissent rapidement aux échelles plus petites. Cette propriété distingue la turbulence élastique de la turbulence hydrodynamique, où la théorie de Kolmogorov prévoit que le spectre de la vitesse se comporte comme $k^{-5/3}$ aux nombres d'onde plus grands que celui du forçage[23]. En fait, contrairement à ce que l'on observe pour la turbulence hydrodynamique, en turbulence élastique l'exposant d'échelle du spectre n'est pas universel et dépend de la géométrie de l'écoulement, de la concentration des polymères et de la façon dans laquelle l'écoulement est généré[20,24–27] (voir aussi [F2] et [F5]).

Les résultats présentés au chapitre 3 portent sur le rôle de la géométrie de l'écoulement et sur celui de l'extensibilité des polymères dans l'apparition du régime de turbulence élastique. Le chapitre 3 contient également une étude des propriétés mathématiques de l'un des modèles de turbulence élastique les plus connus. Il se termine par une discussion des méthodes numériques habituellement employées dans la simulation des écoulements de solutions de polymères.

Chapitre 2

Dynamique lagrangienne en turbulence

2.1 Introduction

2.1.1 Le modèle de Kraichnan

Dans ce chapitre nous nous intéressons à la dynamique d'objets microscopiques transportés par un écoulements turbulent. Chaque objet décrit un degré de liberté différent : translation, rotation, étirement, flexion. L'étude comporte des simulations numériques et des calculs analytiques obtenus dans le contexte du modèle de transport turbulent de Kraichnan[6,7]. Avant de passer à la présentation des résultats sur la dynamique lagrangienne, il convient donc d'introduire brièvement le modèle de Kraichnan et plus particulièrement son régime lisse en espace.

Dans le modèle de Kraichnan le champ de vitesse $\boldsymbol{u}(\boldsymbol{x}, t)$ est un processus stochastique vectoriel gaussien. La moyenne du champ de vitesse est nulle, $\langle \boldsymbol{u}(\boldsymbol{x}, t) \rangle = 0$, et sa corrélation est de la forme :

$$\langle u_i(\boldsymbol{x}, t)\, u_j(\boldsymbol{y}, t') \rangle = \mathsf{D}_{ij}(\boldsymbol{x}, \boldsymbol{y})\, \delta(t - t'), \qquad i, j = 1, \ldots, d, \tag{2.1}$$

où d est la dimension de l'espace et $\delta(t - t')$ est la distribution de Dirac. De ce fait, le champ de vitesse se comporte en temps comme un bruit blanc. La forme du tenseur D_{ij} est fixée par l'incompressibilité du champ de vitesse ($\nabla \cdot \boldsymbol{u} = 0$) et par ses symétries statistiques. Si en effet on suppose que $\boldsymbol{u}(\boldsymbol{x}, t)$ est statistiquement invariant par translations, rotations et réflexions et que les corrélations spatiales ont un comportement en loi de puissance, D_{ij} ne dépend que de $\boldsymbol{r} = |\boldsymbol{x} - \boldsymbol{y}|$ et s'écrit :

$$\mathsf{D}_{ij}(\boldsymbol{r}) = D_0 \delta_{ij} - D_1 |\boldsymbol{r}|^{\xi} [(d - 1 + \xi)\delta_{ij} - \xi \hat{r}_i \hat{r}_j], \tag{2.2}$$

où $\hat{r}_i = r_i / |\boldsymbol{r}|$. Les coefficients D_0 et D_1 déterminent respectivement l'amplitude des fluctuations de la vitesse et celle des différences de vitesse. Le paramètre ξ est lié à l'exposant de Lipschitz du champ de vitesse, puisque l'équation (2.2) implique essentiellement que dans une réalisation typique du champ de vitesse : $|\boldsymbol{u}(\boldsymbol{x}, t) - \boldsymbol{u}(\boldsymbol{y}, t)| \propto |\boldsymbol{r}|^{\xi/2}$. En faisant varier ξ entre 0 et 2, on peut donc passer d'un champ de vitesse complètement décorrélé en espace à un champ de vitesse lisse. L'hypothèse d'isotropie (invariance par rotations) implique, en particulier, que l'on s'intéresse au comportement du fluide loin des parois qui le contiennent et de toute autre obstacle qui pourrait en contraindre l'écoulement.

Le modèle de Kraichnan peut être généralisé de façon à décrire un champ de vitesse compressible. Pour cela il suffit de modifier la corrélation (2.2) comme il suit[1] :

$$\mathsf{D}_{ij}(\boldsymbol{r}) = D_0 \delta_{ij} - D_1 |\boldsymbol{r}|^{\xi} [(d - 1 + \xi - \mathscr{C}\xi)\delta_{ij} + \xi(\mathscr{C} d - 1)\hat{r}_i \hat{r}_j], \tag{2.3}$$

où

$$\mathscr{C} = \langle (\nabla \cdot \boldsymbol{u})^2 / \langle \|\nabla \boldsymbol{u}\|^2 \rangle \tag{2.4}$$

représente le degré de compressibilité du champ de vitesse.

Malgré les hypothèses très fortes sur lesquelles il repose et certaines propriétés peu réalistes (avant tout la δ-corrélation en temps), le modèle de Kraichnan a joué un rôle important dans l'étude du transport turbulent et a été appliqué à des problèmes tels que la dispersion de particules, le mélange, l'effet dynamo et la transition *coil–stretch* des polymères[1]. Il a en effet permis d'obtenir des résultats exacts, qui, même si non directement comparables aux expériences ou aux simulations numériques, ont permis d'améliorer considérablement notre compréhension du transport turbulent. C'est dans cet esprit que le modèle de Kraichan sera utilisé dans la suite.

Nous nous concentrerons surtout sur la dynamique d'objets plus petits que l'échelle visqueuse d'un écoulement turbulent. A ces échelles la viscosité atténue les fluctuations spatiales de la vitesse et le champ $\boldsymbol{u}(\boldsymbol{x}, t)$ est lisse en espace. Dans le modèle de Kraichnan ce régime correspond au cas $\xi = 2$, pour lequel le gradient de $\boldsymbol{u}(\boldsymbol{x}, t)$ est bien défini et sa corrélation temporelle peut être déduite de la corrélation de la vitesse[1] :

$$\langle \partial_j u_i(t)\, \partial_l u_k(t') \rangle = 2D_1[(d + 1 - 2\mathscr{C})\delta_{ik}\delta_{jl} + (d\mathscr{C} - 1)(\delta_{ij}\delta_{kl} + \delta_{il}\delta_{jk})]\, \delta(t - t'). \tag{2.5}$$

Pour $\xi = 2$ les exposant de Lyapounov de l'écoulement, $\lambda_1 \geqslant \lambda_2 \geqslant \cdots \geqslant \lambda_d$, peuvent être calculés de façon exacte[1] :

$$\lambda_i = D_1\{d(d - 2i + 1) - 2\mathscr{C}[d + (d - 2)i]\}, \qquad i = 1, \ldots, d. \tag{2.6}$$

Nous rappelons que l'exposant de Lyapounov le plus grand, λ_1, représente le taux d'étirement d'un élément de ligne fluide. Dans la suite λ_1 sera directement appelé « l'exposant de Lyapunov de l'écoulement ».

Le cas $\xi = 2$ est souvent appelé « régime de Batchelor du modèle de Kraichnan » ou, plus simplement, « modèle de Batchelor–Kraichnan » en hommage à G.K. Batchelor, qui a donné une contribution fondamentale au problème du transport dans un champ de vitesse lisse.

2.1.2 Simulations numériques lagrangiennes

Les résultats analytiques obtenus en utilisant le champ de vitesse de Batchelor–Kraichnan ou d'autres écoulements aléatoires seront dans la plupart des cas comparés avec des simulations numériques. Ces simulations ont été effectuées en collaboration avec les co-auteurs des articles mentionnés et permettent de s'assurer que la validité des prédictions analytiques n'est pas limitée aux modèles théoriques considérés. Pour un certain nombre de problèmes, la comparaison est faite avec des simulations numériques de turbulence isotrope, en deux ou en trois dimensions selon le système considéré. Même si les paramètres de ces simulations sont choisis à chaque fois de façon adaptée au problème étudié, les techniques sont les mêmes pour toutes les simulations lagrangiennes de turbulence considérées dans ce chapitre. Il est donc plus simple de les introduire avant la présentation des résultats.

Dans les simulations de turbulence incompressible en trois dimensions, le champ de vitesse $\boldsymbol{u}(\boldsymbol{x}, t)$ est la solution des équations de Navier–Stokes :

$$\partial_t \boldsymbol{u} + \boldsymbol{u} \cdot \nabla \boldsymbol{u} = -\nabla p + \nu \Delta \boldsymbol{u} + \boldsymbol{f}, \qquad \nabla \cdot \boldsymbol{u} = 0, \tag{2.7}$$

où p est la pression, ν est la viscosité cinématique du fluide et $\boldsymbol{f}$ est le forçage qui engendre l'écoulement. Le domaine de définition de la solution est le cube $[0, 2\pi]^3$ et les conditions aux bords sont périodiques. Le forçage est localisé autour d'un nombre d'onde fixé.

En deux dimensions, il est plus pratique de résoudre l'équation pour la vorticité $\omega = |\nabla \times \boldsymbol{u}|$,

$$\partial_t \omega + \boldsymbol{u} \cdot \nabla \omega = \nu \Delta \omega + F, \qquad F = |\nabla \times \boldsymbol{f}|, \tag{2.8}$$

et de reconstruire le champ de vitesse à partir de la relation $\boldsymbol{u} = \nabla^\perp \Delta^{-1} \omega$, où $\nabla^\perp = (-\partial_y, \partial_x)$. Dans ce cas le domaine est le carré $[0, 2\pi]^2$ avec des conditions aux bords périodiques. Un terme de friction, $-\mu\Delta\omega$, est ajouté au membre de droite de l'équation (2.8) afin d'arrêter la cascade d'énergie cinétique vers les grandes échelles[28] et obtenir un régime stationnaire.

La méthode utilisée pour la solution numérique est la méthode pseudo-spectrale avec une résolution de 1024^2 ou 2048^2 en deux dimensions et de 512^3 en trois dimensions. L'intégration temporelle est effectuée soit par un schéma de Runge–Kutta soit par un schéma d'Adam–Bashforth.

La position d'une particule fluide, $\boldsymbol{x}(t)$, évolue selon l'équation :

$$\frac{\mathrm{d}\boldsymbol{x}}{\mathrm{d}t} = \boldsymbol{u}(\boldsymbol{x}(t), t), \tag{2.9}$$

pour laquelle des algorithmes d'intégration standards sont utilisés selon la situation : Euler, Adam–Bashforth, Runge–Kutta. Il est toutefois important de remarquer que le champ de vitesse eulérien $\boldsymbol{u}(\boldsymbol{x}, t)$ est défini sur une grille spatiale uniforme, mais en général la position d'une particule ne coïncide pas avec un point grille. Un schéma d'interpolation, bilinéaire ou trilinéaire, est alors utilisé pour reconstruire le champ de vitesse à la position de la particule à partir du champ de vitesse eulérien et pour évaluer ainsi le membre de droite de l'équation (2.9).

Lorsque l'écoulement transporte un objet (une particule non sphérique, un polymère, une gouttelette) de taille plus petite que l'échelle visqueuse de la turbulence et de même densité que celle du fluide, le mouvement du centre de masse d'un tel objet satisfait l'équation (2.9). La dynamique interne de l'objet est déterminée par un système d'équations différentielles ordinaires dont la forme dépend évidemment de l'objet considéré. Ces équations peuvent être stochastiques si l'on prend en compte les collisions des molécules du fluide avec l'objet, dont l'effet est habituellement modélisé par un bruit blanc. Les schémas utilisés pour intégrer la dynamique interne sont à nouveau ceux d'Euler, d'Adam–Bashforth, de Runge–Kutta et, dans le cas stochastique, celui de Euler–Maruyama.

Après ces courtes sections introductives, nous passons maintenant à l'étude de la dynamique lagrangienne en turbulence. Les sections qui suivent portent chacune sur la statistique d'un degré de liberté différent.

2.2 Translation : traceurs dans des écoulements compressibles

Le cas le plus simple de dynamique lagrangienne est celui d'une particule ponctuelle de même densité que celle du fluide qui la transporte. Une telle particule est appelée un « traceur », puisqu'elle se comporte comme un élément de volume fluide et se déplace le long d'une trajectoire lagrangienne. Sa position évolue selon l'équation (2.9).

L'étude de traceurs dans des écoulements turbulents a d'importantes applications physiques allant de la dispersion de polluants atmosphériques[29] au transport du plancton dans les océans[30].

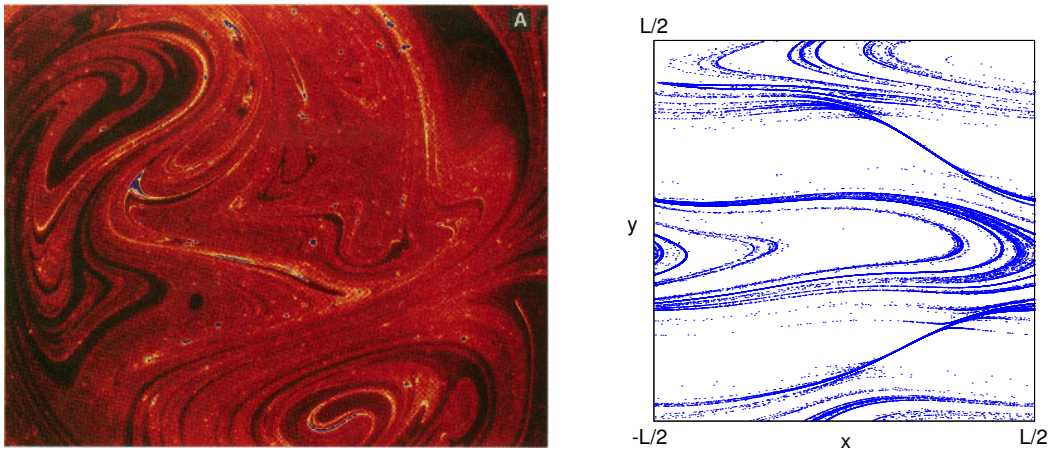

FIGURE 2.1 – **A gauche :** *Visualisation de particules flottantes à la surface d'un fluide chaotique. La couleur est proportionnelle à la densité de particules (les régions plus claires correspondent à une densité plus élevée) [d'après Sommerer & Ott,* Science **259***, 335 (1993)].* **A droite :** *Distribution de traceurs dans l'écoulement renewing [voir les équations* (2.12)*] pour* $\mathscr{C} = 1/4$ *et* $Ku = 10$ (d'après [A1]).

De plus, comme il a été rappelé au chapitre 1, la dynamique des traceurs est étroitement liée au propriétés de mélange des écoulements turbulents.

Dans un champ de vitesse, turbulent ou aléatoire, incompressible les traceurs ont un comportement chaotique et se distribuent uniformément à l'intérieur du fluide suite à la conservation des volumes de fluide. En revanche, si l'écoulement est compressible et donc les volumes de fluide se contractent, les traceurs s'agglomèrent sur un ensemble fractal de dimension inférieure à celle de l'espace occupé par le fluide. Les écoulements qui ont mieux permis d'étudier ce phénomène, à la fois expérimentalement et numériquement, sont les écoulements de surface[31] (figure 2.1). Le champ de vitesse bidimensionnel ressenti par des particules qui flottent à la surface libre d'un écoulement incompressible a en effet une divergence non nulle : $\partial_x u_x + \partial_y u_y = -\partial_z u_z \neq 0$. Les écoulements de surface ont donc permis d'étudier les effets de la compressibilité sur la dynamique des traceurs même pour des nombres de Mach petits.

Afin de quantifier l'agglomération des traceurs, on peut considérer les exposants de Lyapounov de l'écoulement, $\lambda_1 \geqslant \lambda_2 \cdots \geqslant \lambda_d$, et calculer la dimension de Lyapounov de l'attracteur des positions,

$$D_L = N + \frac{\sum_{i=1}^{N} \lambda_i}{|\lambda_{N+1}|}, \tag{2.10}$$

où N est le nombre entier le plus grand tel que $\sum_{i=1}^{N} \lambda_i \geqslant 0$ et d est la dimension de l'espace. Pour un système dynamique d-dimensionnel, la dimension de Lyapounov est telle que, si $N \leqslant D_L < N+1 \leqslant d$, les volumes $(N+1)$-dimensionnels se contractent et les volumes N-dimensionnels se dilatent. Elle exprime donc l'équilibre entre contraction et dilatation des volumes qui se produit sur l'attracteur.

Dans le cas d'un écoulement turbulent ou chaotique on peut identifier trois régimes :

i. si l'écoulement est incompressible ($\sum_{i=1}^{d} \lambda_i = 0$), $D_L = d$ et les traceurs se distribuent uniformément dans l'espace ;

ii. si l'écoulement est faiblement compressible ($\sum_{i=1}^{d} \lambda_i < 0$, mais $\lambda_1 > 0$), $0 < D_L < d$ et les traceurs s'agglomèrent sur un ensemble fractale ;

iii. si l'écoulement est fortement compressible ($\sum_{i=1}^{d} \lambda_i < 0$ et $\lambda_1 < 0$), la dynamique des traceurs n'est plus chaotique et l'attracteur devient ponctiforme ($D_L = 0$).

Pour l'écoulement stochastique de Batchelor–Kraichnan les exposants des Lyapounov, donc D_L, peuvent être calculés exactement [voir l'équation (2.6)]. En deux dimensions

$$D_L = \begin{cases} 2 & \mathscr{C} = 0 \\ 2/(1+2\mathscr{C}) & 0 < \mathscr{C} < 1/2 \\ 0 & \mathscr{C} > 1/2, \end{cases} \tag{2.11}$$

$\mathscr{C}$ étant le degré de compressibilité [voir l'équation (2.3)]. On peut remarquer que D_L décroît en fonction de $\mathscr{C}$ et la transition vers le régime de forte compressibilité (régime iii.) a lieu pour $\mathscr{C} = 1/2$.

L'écoulement de Batchelor–Kraichnan est décorrélé en temps. Afin d'étudier l'effet d'un temps de corrélation non nul, Boffetta *et al.*[32], Ducasse et Pumir[33], Gustavsson et Mehlig[34] ont considéré la dynamique de traceurs dans des écoulements compressibles turbulents ou plus simplement aléatoires, mais ayant un temps de corrélation non nul. Les résultats obtenus diffèrent entre eux en ce qui concerne la dépendance de D_L de $\mathscr{C}$ et du temps de corrélation de la vitesse. Ils soulèvent donc la question de l'interaction entre la compressibilité et la corrélation temporelle dans un écoulement turbulent.

Pour répondre à cette question, dans [A1] nous utilisons une version compressible de l'écoulement dit *renewing*, qui consiste en une succession aléatoire de profils de vitesse sinusoïdaux avec origine et orientation variables. Chaque profil reste gelé pendant un temps T fixé ; en variant la durée de la phase gelée, il est possible de varier le temps de corrélation de la vitesse et étudier comment les propriétés d'agglomération des traceurs changent. Plus précisément le champ de vitesse que nous considérons est

$$\begin{cases} u_x = U\sqrt{2(1-\mathscr{C})}\cos(ky+\varphi_y) + U\sqrt{2\mathscr{C}}\cos(kx+\varphi_x), \\ u_y = 0, \end{cases} \qquad 2nT \leqslant t < (2n+1)T \tag{2.12a}$$

et

$$\begin{cases} u_x = 0, \\ u_y = U\sqrt{2(1-\mathscr{C})}\cos(kx+\varphi_x) + U\sqrt{2\mathscr{C}}\cos(ky+\varphi_y), \end{cases} \qquad (2n+1)T \leqslant t < 2(n+1)T, \tag{2.12b}$$

où $(x, y) \in [-L/2, L/2]^2$, $n \in \mathbb{N}$, $k = 2\pi/L$ et les angles φ_x, φ_y sont des nombres aléatoires indépendants et uniformément distribués sur l'intervalle $[0, 2\pi]$; φ_x et φ_y changent de façon aléatoire à chaque période T. Le degré de compressibilité $\mathscr{C}$ est défini comme dans l'équation (2.4).

En plus du degré de compressibilité, la dynamique dépend d'un deuxième nombre sans dimension, c'est-à-dire le nombre de Kubo $Ku \equiv TUk$, qui est proportionnel au rapport entre le temps de corrélation de l'écoulement et le temps de retournement typique des tourbillons, $(Uk)^{-1}$. Dans la limite $Ku \to 0$, on retrouve l'écoulement de Batchelor–Kraichnan ; pour $Ku \to \infty$ on obtient un champ de vitesse gelé. Dans sa version incompressible, l'écoulement *renewing* a été appliqué à l'étude de plusieurs phénomènes de transport chaotique, tels que la dynamo cinématique[35,36], le mélange turbulent[37–41], la dynamique des particules inertielles[42] et la déformation des polymères (voir la section 2.4.1).

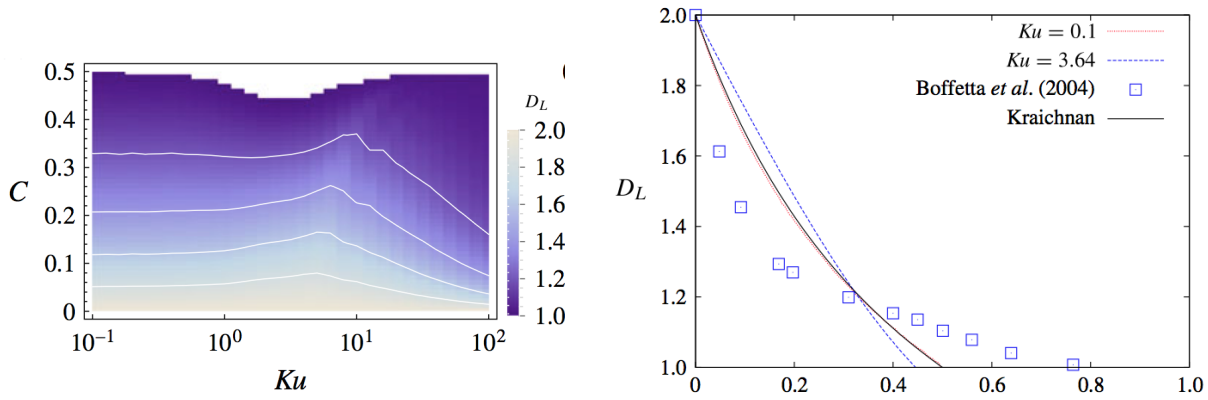

FIGURE 2.2 – **A gauche** *: Dimension de Lyapounov en fonction du nombre de Kubo* Ku *et du degré de compressibilité* $\mathscr{C}$ *pour l'écoulement renewing. La région en blanc est celle où* $D_L = 0$. **A droite** *: dépendence de* D_L *de Ku pour l'écoulement renewing (courbes rouges et bleues), pour l'écoulement turbulent de Boffetta et al. (carrés)*[32] *et pour le modèle de Kraichnan (courbe noire ; voir aussi l'équation* (2.10)*).* (D'après [A1])

Les propriétés de cet écoulement modèle nous permettent d'examiner la statistique lagrangienne des traceurs en fonction du degré de compressibilité $0 \leqslant \mathscr{C} \leqslant 1$ et sur un très grand intervalle de valeurs de Ku ($10^{-1} \leqslant Ku \leqslant 10^2$). Nous nous concentrons ici sur les résultats concernant l'agglomération des traceurs.

Dans un écoulement incompressible ($\mathscr{C} = 0$), la statistique à un point de la vitesse eulérienne coïncide avec la statistique de la vitesse lagrangienne, parce que les traceurs échantillonnent l'espace des phases de manière uniforme. On observe le même comportement si le temps de corrélation de l'écoulement est nul ($Ku = 0$)[1]. En revanche, si $\mathscr{C} > 0$ et $Ku > 0$, nous montrons que cela n'est plus vrai, la raison étant que les traceurs tendent à s'agglomérer aux alentours des points où la vitesse s'annule, appelés *points de stagnation* (figure 2.1, à droite). Dans l'écoulement considéré, ces points forment carrément des « lignes de stagnation », qui peuvent représenter des barrières pour le mouvement des traceurs dans le fluide. La présence et la forme spécifique des lignes de stagnation de l'écoulement renewing ont les conséquences suivantes sur l'agglomération des traceurs :

a. pour $Ku \ll 1$ et $Ku \gg 1$, tous les exposants de Lyapounov deviennent négatifs pour $\mathscr{C} \simeq 1/2$. Donc le seuil de compressibilité pour la transition du régime de faible agglomération à celui de forte agglomération est le même que pour le modèle de Batchelor–Kraichnan. En revanche, pour $Ku \approx 1$, le degré de compressibilité critique est inférieur à 1/2, c'est-à-dire une compressibilité eulérienne plus petite est suffisante pour que la transition ait lieu.

b. Pour $\mathscr{C}$ fixé, la dimension de Lyapounov D_L n'est pas une fonction monotone de Ku et est minimum pour $Ku \simeq 1$ (figure 2.2, à gauche).

Le comportement décrit ci-dessus est encore différent par rapport à ceux observés par Boffetta *et al.*[32] (voire la figure 2.2, à droite) et par Gustavsson et Mehlig[34]. Cela n'est toutefois pas surprenant. En reliant les propriétés d'agglomération des traceurs à la structure de l'ensemble des points de stagnation, nous n'avons fait rien d'autre que de montrer la forte non universalité de la dynamique lagrangienne dans les écoulements compressibles et corrélés en temps. Le comportement non universel est la conséquence du fait que le phénomène d'agglomération dépend

des détails des structures vers lesquelles les traceurs sont attirés. Ce résultat sur la non universalité du phénomène d'agglomération permet ainsi de réconcilier certaines études précédentes qui paraissaient contradictoires.

2.3 Rotation : particules solides non sphériques

L'étude de la dynamique lagrangienne de particules non sphériques revêt un intérêt à la fois fondamental et appliqué. D'une part, elle permet de mieux comprendre les propriétés lagrangiennes du gradient de vitesse dans un écoulement turbulent[43]. D'autre part, des particules anisotropes interviennent dans plusieurs phénomènes physiques. Par exemple, les cristaux de glace dans les nuages ont une forme approximativement sphéroïdale et leur orientation influence le transfert radiatif[44]. La nage de certains micro-organismes biologiques est souvent modélisée par la dynamique de bâtonnets autopropulsées[45]. L'orientation et la distribution des fibres de cellulose dans une feuille de papier en détermine les propriétés : la formation d'agglomérats de fibres, phénomène connu sous le nom de floculation, réduit par exemple la qualité du papier et une façon pour éviter la floculation consiste à porter la suspension de fibres dans un état turbulent avant de la traiter[46].

Nous nous intéressons à la dynamique d'une particule de densité homogène ayant la forme d'un solide de révolution et symétrique par rapport au plan perpendiculaire à son axe de révolution (un sphéroïde est un exemple d'une telle particule). La particule est plongée dans un fluide newtonien de même densité et son inertie est négligeable. L'orientation de la particule est déterminée par un vecteur unitaire $\boldsymbol{N}$ parallèle à son axe de révolution. Si l'écoulement du fluide est incompressible et linéaire en espace, l'evolution de la position du centre de masse $\boldsymbol{x}_c$ et de l'orientation $\boldsymbol{N}$ est alors donnée par les équations suivantes

$$\frac{\mathrm{d}\boldsymbol{x}_c}{\mathrm{d}t} = \boldsymbol{u}(\boldsymbol{x}_c(t), t), \tag{2.13a}$$

$$\frac{\mathrm{d}\boldsymbol{N}}{\mathrm{d}t} = \mathbf{G}(t)\,\boldsymbol{N} - [\boldsymbol{N}^\top \mathbf{G}(t)\,\boldsymbol{N}]\,\boldsymbol{N}, \tag{2.13b}$$

où $\mathbf{G}(t) = \mathbf{\Omega}(t) + \gamma\,\mathbf{S}(t)$. Les tenseurs $\mathbf{\Omega}(t) = [\nabla \boldsymbol{u}(t) - \nabla \boldsymbol{u}(t)^\top]/2$ et $\mathbf{\Omega}(t) = [\nabla \boldsymbol{u}(t) + \nabla \boldsymbol{u}(t)^\top]/2$ sont respectivement la partie antisymétrique et la partie symétrique du gradient de vitesse calculé à la position du centre de masse de la particule. Le coefficient γ décrit la capacité du gradient d'orienter la particule et dépend de la forme géométrique de la particule même. Si $|\gamma| < 1$, l'évolution de la particule est équivalente à celle d'un sphéroïde avec rapport d'aspect

$$\alpha = \sqrt{\frac{1+\gamma}{1-\gamma}}. \tag{2.14}$$

Quelques cas particuliers sont : la sphère ($\gamma = 0$), le disque ($\gamma = -1$) et le bâtonnet ($\gamma = 1$). L'équation (2.13b) a été dérivée par Jeffery[47] pour des sphéroïdes et a été étendue au cas de corps de révolution plus généraux par Bretherton[48].

Lorsque l'écoulement est turbulent, l'équation de Jeffery reste valable pourvu que la taille de la particule soit plus petite que l'échelle visqueuse. Dans ce cas, le nombre de Reynolds à l'échelle de la particule est inférieur à 1 et la dynamique est entièrement contrôlée par le gradient de vitesse.

Les deux sous-sections qui suivent décrivent des simulations numériques de particules non sphériques en turbulence bidimensionnelle et des résultats analytiques concernant la statistique de l'orientation dans un champ de vitesse axisymétrique.

2.3.1 Statistique de l'orientation et de la rotation en turbulence bidimensionnelle

Plusieurs études expérimentales et numériques[49] ont considéré des particules microscopiques sphéroïdales dans un écoulement turbulent tridimensionnel (figure 2.3, à gauche). En trois dimensions, $\boldsymbol{N}$ a une forte tendence à s'aligner avec la vorticité[43], le taux de rotation quadratique moyen de $\boldsymbol{N}$ décroît en fonction du rapport d'aspect de la particule[8] et l'autocorrélation de $\boldsymbol{N}$ est exponentielle, le temps de corrélation étant une fonction croissante de Re (voir la référence 43).

En deux dimensions, seuls des écoulements à petit Re avaient été considérés[50,51]. Dans [B2] nous étudions la dynamique lagrangienne de particules elliptiques dans un écoulement turbulent bidimensionnel, incompressible et isotrope. Les particules sont passivement transportées et n'interagissent pas entre elles. Dans un écoulement bidimensionnel, $\boldsymbol{N} = (\cos\theta, \sin\theta)$, où θ est l'angle que l'axe majeur de la particule elliptique forme avec un axe fixe. L'équation de Jeffery se simplifie alors de la façon suivante[51] :

$$\frac{\mathrm{d}\theta}{\mathrm{d}t} = \frac{1}{2}\omega + \gamma[\sin(2\theta)\mathsf{S}_{11}(t) - \cos(2\theta)\mathsf{S}_{12}(t)], \tag{2.15}$$

où ω est la vorticité. Le champ de vitesse est obtenu par des simulations numériques directes des équations de Navier–Stokes dans un carré périodique. L'écoulement est maintenu dans un état stationnaire par un forçage aléatoire gaussien localisé sur les nombres d'onde $\boldsymbol{k}$ tels que $|\boldsymbol{k}| = k_{\mathrm{inj}}$; deux séries de simulations ont été effectuées, l'une forcée à grande échelle ($k_{\mathrm{inj}} = 2$, cas A) et l'autre à une échelle spatiale intermédiaire ($k_{\mathrm{inj}} = 50$, cas B). Pour chacun des deux cas nous considérons trois valeurs de Re différentes, de façon à pouvoir examiner la dépendence de la statistique de l'orientation des particules de Re. L'équation (2.15) est résolue pour 10^4 particules simultanément.

La figure 2.3 (à droite) montre que la dynamique des particules dépend sensiblement de k_{inj} et est qualitativement différente dans les cas (A) et (B). Cette différence peut être attribuée à une différente statistique lagrangienne du gradient de vitesse dans les deux cas. Afin de quantifier les différences entre les cas (A) et (B), nous avons étudié, en fonction de γ et de Re :

- la statistique de l'alignement entre $\boldsymbol{N}$ et $\nabla \times \boldsymbol{\omega}$;
- la statistique de l'alignement entre $\boldsymbol{N}$ et les vecteurs propres de S ;
- la corrélation lagrangienne du paramètre d'ordre $M(\boldsymbol{r}, t) = 2\cos^2\theta(\boldsymbol{r}, t) - 1$;
- l'autocorrélation de $\boldsymbol{N}$: $\langle \boldsymbol{N}(t) \cdot \boldsymbol{N}(0) \rangle$;
- la statistique du taux de rotation $\dot{\theta}$.

Cette analyse nous permet également de mettre en évidence des différences importantes entre la dynamique en deux dimensions et celle en trois dimensions. Nous montrons, par exemple, que le taux de rotation d'une particule croît en fonction du rapport d'aspect en deux dimensions, alors qu'il décroît en trois dimensions[8].

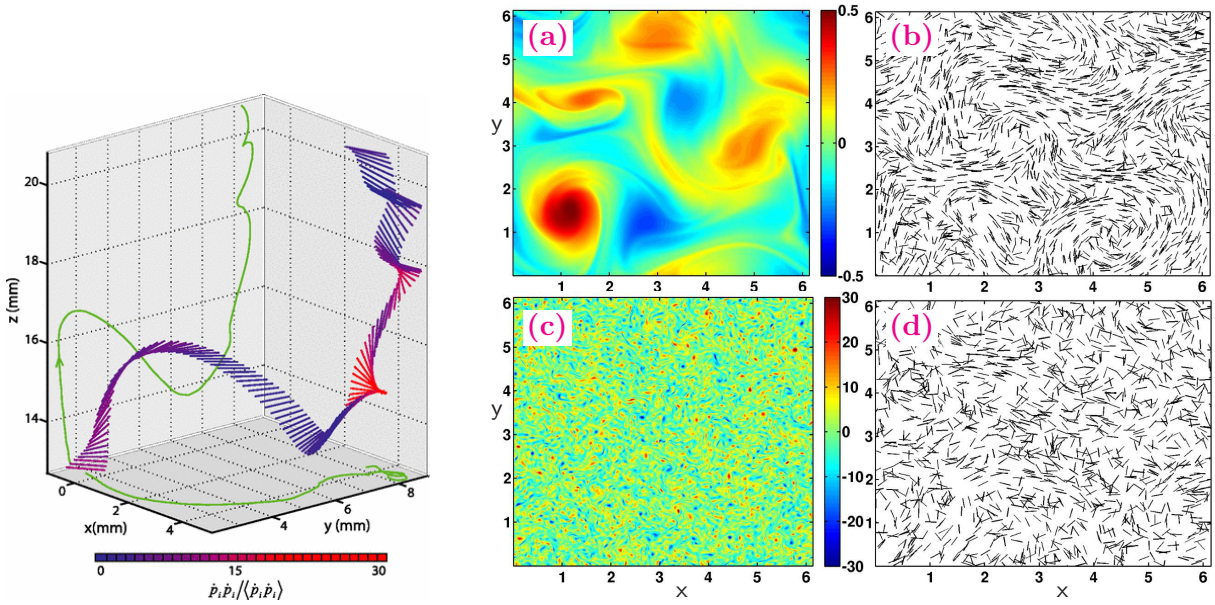

FIGURE 2.3 – **A gauche :** *Visualisation de la dynamique rotationnelle d'un bâtonnet dans une expérience de turbulence homogène et isotrope. La couleur du bâtonnet représente le taux de rotation ; les courbes vertes sont les projections de la trajectoire du centre du bâtonnet sur les plans y-z et x-y [d'après Parsa* et al., Phys. Rev. Lett. ***109****, 134501 (2012)].* **A droite :** (a) *Champ de vorticité dans le cas A ($k_{\mathrm{inj}} = 2$) ;* (b) *positions et orientations de bâtonnets ($\gamma = 1$) dans l'écoulement décrit dans la figure (a) ;* (c) *champ de vorticité dans le cas B ($k_{\mathrm{inj}} = 50$) ;* (d) *positions et orientations de bâtonnets ($\gamma = 1$) dans l'écoulement décrit dans la figure (c)* (d'après [B2]).

2.3.2 Dynamique d'une particule sphéroïdale dans un écoulement aléatoire axisymétrique

Contrairement au cas laminaire, il existe peu de résultats analytiques sur la dynamique de particules non sphériques dans des écoulements turbulents ou aléatoires. Turitsyn[52] a considéré un bâtonnet ($\gamma = 1$) dans un écoulement cisaillé laminaire perturbé par des fluctuations gaussiennes, isotropes et décorrélées en temps. Wilkinson et Kennard[53] ont étudié l'alignement de bâtonnets avec la vorticité dans un écoulement aléatoire isotrope. Gustavsson *et al.*[54] ont calculé le taux de rotation de particules sphéroïdales dans un écoulement gaussien et isotrope. J'ai contribué à ce sujet en étudiant la statistique de l'orientation d'une particule sphéroïdale dans un écoulement aléatoire statistiquement axisymétrique (voir [B1]).

Un champ aléatoire est statistiquement axisymétrique[55,56] s'il existe une direction $\boldsymbol{\lambda}$ telle que le champ est statistiquement invariant par rapport aux rotations autour de la direction $\boldsymbol{\lambda}$ et par rapport aux réflexions selon tout plan perpendiculaire à $\boldsymbol{\lambda}$ ou contenant $\boldsymbol{\lambda}$. L'axisymétrie est la forme la plus simple d'anisotropie ; on la retrouve par exemple dans la turbulence stratifiée, dans la turbulence en rotation ou à l'intérieur d'une soufflerie[57].

Si le champ de vitesse axisymétrique est en plus gaussien, lisse en espace et δ-corrélé en temps, un tel champ de vitesse représente une généralisation anisotrope de l'écoulement de Batchelor–Kraichnan isotrope. Dans ce cas, la corrélation du gradient de vitesse s'écrit comme il suit :

$$\langle \partial_j u_i(t+\tau)\partial_q u_p(t)\rangle = \Gamma_{ijpq}\delta(\tau) \tag{2.16}$$

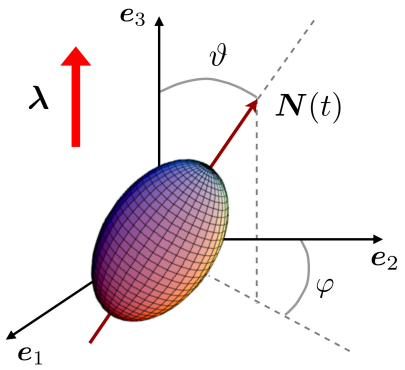

FIGURE 2.4 – *Orientation d'une particule sphéroïdale dans l'espace ; $\boldsymbol{\lambda}$ est la direction de symétrie du champ de vitesse axisymétrique.*

où

$$\Gamma_{ijpq} = (d+4a)\delta_{jq}\delta_{ip} - a(\delta_{pq}\delta_{ij} + \delta_{iq}\delta_{pj}) + (b+c+5d)\delta_{jq}\lambda_i\lambda_p - b\delta_{ip}\lambda_j\lambda_q \\ - d[(\delta_{pq}\lambda_i + \delta_{iq}\lambda_p)\lambda_j + (\delta_{pj}\lambda_i + \delta_{ij}\lambda_p)\lambda_q] - c\lambda_i\lambda_j\lambda_q. \quad (2.17)$$

Le paramètre a fixe l'amplitude de la composante isotrope du gradient [voir l'équation (2.1)] et les rapports b/a, c/a, d/a déterminent l'anisotropie du gradient. Ces paramètres ne sont pas libres, mais doivent respecter des inégalités afin de préserver le caractère semi-défini positif de $\boldsymbol{\Gamma}$ ($\boldsymbol{\Gamma}$ est la covariance d'un tenseur Gaussien et est donc semi-défini positif).

L'orientation d'une particule sphéroïdale dans le champ axisymétrique défini ci-dessus satisfait l'équation de Jeffery (2.13b), où le gradient de vitesse joue maintenant le rôle d'une bruit multiplicatif. En utilisant les symétries statistiques du problème, j'ai pu calculer de manière exacte la densité de probabilité stationnaire de l'angle ϑ compris entre l'axe de révolution de la particule et la direction $\boldsymbol{\lambda}$ (figure 2.4). Cette distribution est en effet la solution d'une équation de Fokker–Planck en une variable avec conditions de bord périodiques. Selon les valeurs des paramètres a, b, c et d, quatre régimes dynamiques différents peuvent être identifiés :

i. rotation de la particule dans un plan perpendiculaire à $\boldsymbol{\lambda}$;
ii. oscillation entre la configuration alignée avec $\boldsymbol{\lambda}$ et celle alignée avec $-\boldsymbol{\lambda}$. Ce mouvement est parfois appelé *tumbling* ;
iii. alignement préférentiel avec une direction oblique par rapport à $\boldsymbol{\lambda}$;
iv. combinaison des mouvements de rotation et d'oscillation décrits aux points i. et ii.

Dans chacun de ces régimes, le niveau d'alignement dépend de l'anisotropie de la particule (déterminée par le rapport d'aspect γ) et de la géométrie particulière du champ de vitesse (fixée par b/a, c/a et d/a).

2.4 Etirement : polymères élastiques

2.4.1 Transition *coil–stretch*

La transition *coil–stretch* est l'un des principaux phénomènes qui caractérisent la dynamique d'un polymère élastique dans un écoulement fluide. Elle a été prédite par de Gennes[58]

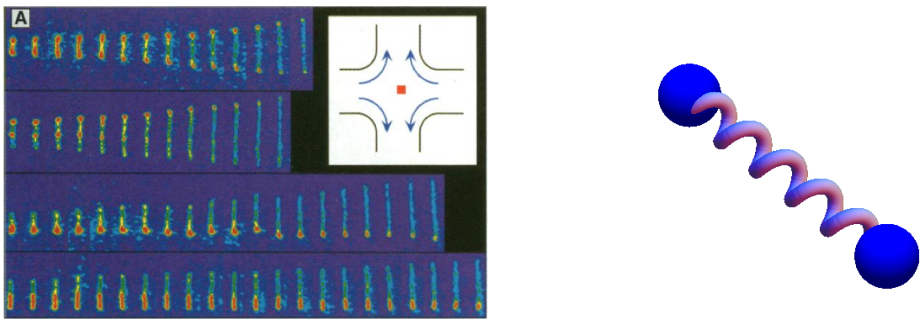

FIGURE 2.5 – **A gauche :** *Visualisation de l'étirement d'une molécule d'ADN dans un écoulement hyperbolique planaire [d'après Perkins, Smith & Chu,* Science ***276****, 2016 (1997)].* **A droite :** *Le modèle en haltère élastique (le modèle dumbbell).*

pour un champ de vitesse hyperbolique planaire et consiste en une croissance abrupte de l'extension R du polymère lorsque l'amplitude du gradient de vitesse dépasse une valeur critique. Le nombre sans dimensions qui contrôle la transition est le nombre de Weissenberg $Wi = \sigma\tau$, où σ est l'amplitude du gradient de vitesse et τ est le temps de relaxation du polymère vers sa configuration d'équilibre. Dans un champ de vitesse hyperbolique, un polymère est dans la configuration enroulée (*coiled*) tant que Wi est inférieur à la valeur critique $Wi_c = 1/2$ et se défait complètement (configuration *stretched*) dès que Wi dépasse Wi_c. En termes de densité de probabilité stationnaire de l'extension, $p(R)$, la transition coil–stretch peut-être décrite comme il suit. Dénotons par R_0 l'extension d'équilibre du polymère en l'absence d'écoulement et par $R_{\max}$ son extension maximum. La densité $p(R)$ est caractérisée par un pic très prononcé qui se déplace rapidement de R_0 vers $R_{\max}$ dès que Wi dépasse Wi_c. Perkins *et al.* [59] ont été les premiers à observer la transition coil–stretch en examinant la déformation d'une macromolécule d'ADN dans un écoulement hyperbolique planaire (figure 2.5, à gauche).

L'étude de de Gennes se fonde sur le modèle en haltère élastique[60] (le modèle *dumbbell*), qui se focalise sur le mode de relaxation le plus lent et décrit le polymère comme deux billes liées par un ressort linéaire (figure 2.5, à droite). Les forces qui agissent sur chaque bille sont : la force de traînée du fluide (décrite par la loi de Stokes), la force élastique exercée par le ressort et les forces dues aux collisions avec les molécules du fluide (modélisées par un bruit blanc). Par contre l'inertie des billes est négligée en raison de la petite taille d'un polymère. La configuration de l'haltère est définie par la position de son centre de masse $\boldsymbol{x}_c(t)$, qui se comporte comme un traceur [$\dot{\boldsymbol{x}}_c = \boldsymbol{u}(\boldsymbol{x}_c(t), t)$], et par le vecteur de séparation entre les billes, $\boldsymbol{R}(t) = \boldsymbol{x}_2(t) - \boldsymbol{x}_1(t)$, où $\boldsymbol{x}_1(t)$ et $\boldsymbol{x}_2(t)$ sont les positions des deux billes qui constituent l'haltère. Le vecteur $\boldsymbol{R}(t)$ satisfait l'équation stochastique :

$$\frac{\mathrm{d}\boldsymbol{R}}{\mathrm{d}t} = \nabla\boldsymbol{u}(t)\cdot\boldsymbol{R} - \frac{\boldsymbol{R}}{2\tau} + \sqrt{\frac{R_0^2}{\tau}}\,\boldsymbol{\xi}(t), \tag{2.18}$$

où $\nabla\boldsymbol{u}(t)$ est évalué à la position du centre de masse et $\boldsymbol{\xi}(t)$ est un bruit blanc. La longueur de $\boldsymbol{R}(t)$ représente l'extension du polymère.

Le modèle en haltère élastique a été employé par Lumley[61], et successivement par Balkovsky *et al.*[62], pour montrer que la transition coil–stretch existe aussi dans les champs de vitesse chaotiques ou aléatoires (cette prédiction s'applique également à un polymère plus petit que l'échelle visqueuse dans un écoulement turbulent). Steinberg et ses co-auteurs[63] ont

confirmé la théorie de Lumley et de Balkovsky *et al.* à travers l'observation directe de la dynamique d'un polymère dans un écoulement microfluidique chaotique généré par des instabilités élastiques. Dans le cas chaotique on définit $Wi = \lambda\tau$, où λ est l'exposant de Lyapunov de l'écoulement, et le seuil pour la transition reste $Wi_c = 1/2$ (voir la référence 62). La statistique de l'extension a toutefois des propriétés différentes par rapport au cas laminaire. Pour des extensions intermédiaires ($R_0 \ll R \ll R_{\max}$), la densité de probabilité de R se comporte en effet comme une loi de puissance $R^{-1-\alpha}$ et est donc bien plus large que pour un champ de vitesse hyperbolique. En conséquence, pour tout Wi, des polymères enroulés et des polymères étirés coexistent dans le fluide et la valeur de Wi ne détermine que la configuration dominante.

Les paragraphes qui suivent détaillent mes résultats sur la transition coil–stretch obtenus dans le cadre du modèle en haltère elastique.

Statistique de l'extension dans un écoulement aléatoire : élasticité non linéaire

Les prédictions de Balkovsky *et al.*[62] pour un écoulement aléatoire reposent en fait sur l'hypothèse que la force élastique qui détermine la relaxation de l'haltère vers son extension d'équilibre est linéaire. En d'autre terms, elles sont valables y compris pour des polymères infiniment étirés (limite $R_{\max} \to \infty$). Dans ce cas l'exposant α est une fonction décroissante de Wi : il est positif pour $Wi < Wi_c$, s'annule pour $Wi = Wi_c$ et devient négatif pour des valeurs de Wi plus grandes que Wi_c. La transition coil–stretch est alors associée au fait que la densité de probabilité de R n'est plus normalisable lorsque $Wi > Wi_c$.

Dans [C1] nous généralisons les prédictions de Balkovsky *et al.* au cas plus réaliste où la force élastique est non-linéaire et diverge lorsque R approche $R_{\max} < \infty$. Plus précisément, le terme de relaxation dans l'équation (2.18), $-\boldsymbol{R}/\tau$, est multipliée par la fonction

$$h(R) = \frac{1}{1 - R^2/R_{\max}^2}. \tag{2.19}$$

Ceci garantit que l'extension du polymère est tout le temps finie et inférieure à $R_{\max}$. Le modèle en haltère élastique avec une force non linéaire est appelé « modèle FENE » (Finitely Extensible Nonlinear Elastic)[60].

Si le gradient de vitesse dans l'équation (2.18) est décrit par le modèle de Batchelor–Kraichnan [§], la densité de probabilité de l'extension satisfait une équation de Fokker–Planck, dont la solution stationnaire peut être calculée exactement. Cela nous permet de proposer le mécanisme suivant pour la transition coil–stretch : lorsque Wi dépasse Wi_c, la pente de la densité stationnaire $p(R)$ pour $R_0 \ll R \ll R_{\max}$ change rapidement de négative à positive et par conséquent le maximum de probabilité se déplace brusquement de R_0 vers $R_{\max}$ (figure 2.6, gauche).

Nos résultats sont confirmés par les expériences de Steinberg et ses co-auteurs (voir par exemple la référence 63) et par les simulations numériques de chaînes élastiques en turbulence isotrope effectuées par Watanabe et Gotoh[64].

§. Etant donné que dans la plupart des applications les polymères ont une taille bien plus petite que l'échelle de dissipation visqueuse, il est approprié d'utiliser le régime lisse du modèle de Kraichnan pour en étudier la dynamique.

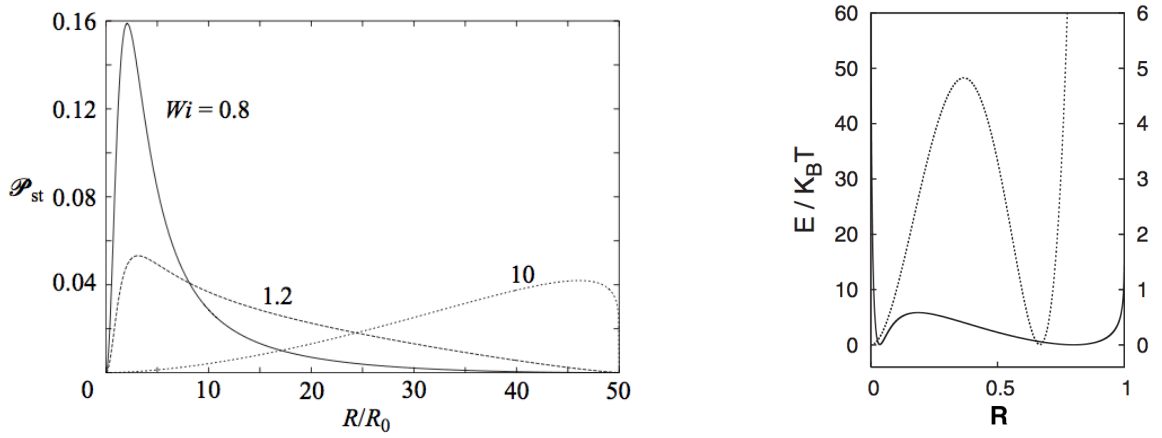

FIGURE 2.6 – **A gauche :** *densité de probabilité stationnaire de l'extension d'un polymère dans l'écoulement de Batchelor–Kraichnan pour des valeurs de Wi différentes* (d'après [C1]). **A droite :** *potentiel efficace décrivant la densité de probabilité stationnaire de l'extension dans un écoulement hyperbolique (courbe en pointillés) et dans l'écoulement aléatoire de Batchelor–Kraichnan (courbe en trait plein). La valeur de Wi correspond à la transition coil–stretch ; les autres paramètres du modèle en haltère élastique reproduisent une molécule de polyacrylamide* (d'après [C3]).

Ralentissement de la relaxation vers l'équilibre

Les résultats présentés ci-dessus concernent la densité de probabilité stationnaire de l'extension des polymères. Nous nous intéressons maintenant à la relaxation temporelle de la densité de probabilité de l'extension vers sa forme stationnaire.

Si un ensemble de polymères est introduit dans un écoulement laminaire indépendant du temps ou bien dans un écoulement aléatoire mais stationnaire, au bout d'un certain temps la densité de probabilité de l'extension atteint une forme indépendante du temps. Dans [C2] et [C3] nous montrons que le temps nécessaire pour atteindre l'état stationnaire est beaucoup plus long pour $Wi \approx Wi_c$ que pour Wi loin du seuil critique.

Pour un écoulement laminaire hyperbolique (voir [C2]), ce ralentissement de la relaxation vers l'état stationnaire est très important et donne lieu à un phénomène d'hystérésis observé lorsque l'extension moyenne des polymères est mesurée en fonction de Wi (voir la référence 65). Un tel comportement peut être expliqué dans le cadre du modèle en haltère élastique en considérant que la dynamique du polymère est équivalente à celle d'une particule dans un potentiel unidimensionnel $E(R)$ (voir la référence 66). Près de la transition coil–stretch, le potentiel est caractérisé par deux puits séparés par une barrière beaucoup plus haute que l'énergie thermique (figure 2.6, à droite). En conséquence, le polymère reste pendant longtemps dans sa configuration initiale (enroulée ou étirée) et le temps nécessaire pour atteindre l'équilibre est extrêmement long.

Dans le cas d'un écoulement aléatoire ou turbulent isotrope (voir [C3]), la forme du potentiel est différente, mais le résultat final est similaire. En correspondance de la transition coil–stretch la barrière de potentiel est de l'ordre de l'énergie thermique, mais le puits de potentiel correspondant à l'état étiré est très plat (figure 2.6, à droite). On n'observe donc pas l'hystérésis, mais le temps nécessaire pour atteindre l'équilibre reste long, parce que le polymère doit explorer un grand nombre de configurations ayant une probabilité comparable.

Pour un écoulement hyperbolique et pour l'écoulement aléatoire de Batchelor–Kraichnan,

nous obtenons les résultats ci-dessus en calculant (par une méthode variationnelle–itérative) la première valeur propre de l'opérateur de Fokker–Planck qui détermine l'évolution de la densité de probabilité de R. Dans [C3] nous effectuons également des simulations numériques pour un écoulement aléatoire isotrope ayant un temps de corrélation non nul, afin de confirmer que les résultats obtenus pour l'écoulement de Batchelor–Kraichnan ne dépendent pas de la forme particulière de cet écoulement modèle.

Il est important de remarquer que le ralentissement de la dynamique que nous avons prédit a été observé expérimentalement par Gerashchenko et Steinberg[67]. Il a aussi été confirmé par Watanabe et Gotoh[64] à travers des simulations numériques d'une chaîne élastique de billes en turbulence homogène et isotrope.

Effet du temps de corrélation de l'écoulement

Pour un écoulement aléatoire, la phénoménologie de la transition coil–stretch que nous avons décrite jusqu'ici est valable lorsque le temps de corrélation du gradient de la vitesse est court devant λ^{-1} ou du même ordre que λ^{-1}, où λ est l'exposant de Lyapounov du champ de vitesse. Dans [C5] nous montrons que, si le temps de corrélation de $\nabla \boldsymbol{u}$ dans l'équation (2.18) est plus long que λ^{-1}, la phénoménologie de la transition coil–stretch est différente. La densité de probabilité stationnaire de R est en effet bimodale et l'on passe de l'état enroulé à l'état étiré à travers la descente du pic correspondant à R_0 et l'apparition simultanée d'un deuxième pic près de $R_{\max}$, tandis que les extensions intermédiaires restent peu probables ($p(R) \sim R^{-1}$ pour $R_0 \ll R \ll R_{\max}$ et Wi grand). La figure 2.7 (gauche) illustre le comportement de la statistique de R.

Cette dynamique peut-être expliquée de la façon suivante. L'écoulement ressenti par le polymère le long de son évolution dans le fluide peut-être imaginé comme une succession de champs hyperboliques à nombre de Weissenberg variable. Si le temps de corrélation de l'écoulement est suffisamment long devant le temps typique d'étirement (c'est-à-dire si le nombre de Kubo est tel que $Ku \gg 1$), le polymère a le temps de s'aligner avec la direction d'étirement de l'écoulement. Comme on vient de le remarquer, cet écoulement est approximativement hyperbolique. Donc l'extension du polymère est proche soit de R_0 soit de $R_{\max}$ selon la valeur locale du gradient de vitesse, d'où la forme bimodale de la distribution de l'extension.

Dans [C5] nous obtenons ces résultats par des simulations numériques du modèle en haltère élastique dans un champ de vitesse aléatoire du type *renewing* (ce type d'écoulement a déjà été utilisé à la section 2.2). Ce dernier consiste en une succession de profils de vitesse aléatoires, chacun restant « gelé » pendant un temps de corrélation fixé. L'avantage d'un tel écoulement est que l'on peut facilement faire varier le temps de corrélation tout en gardant l'exposant de Lyapunov, et donc Wi, constants.

Etirement dans l'intervalle inertiel de la turbulence

Les études mentionnées jusque là considèrent un champ de vitesse régulier en espace à l'échelle du polymère. Pour Re suffisamment élevé, la longueur maximum des polymères peut toutefois être plus grande que l'échelle de dissipation visqueuse η_ν et peut atteindre l'intervalle inertiel de la turbulence, où le champ de vitesse est irrégulier en espace[68]. Certaines fibres peuvent même avoir une extension proche de la longueur de corrélation du champ de vitesse[69]. Dans [C7] nous nous intéressons à la dynamique de polymères de taille plus longue que η_ν

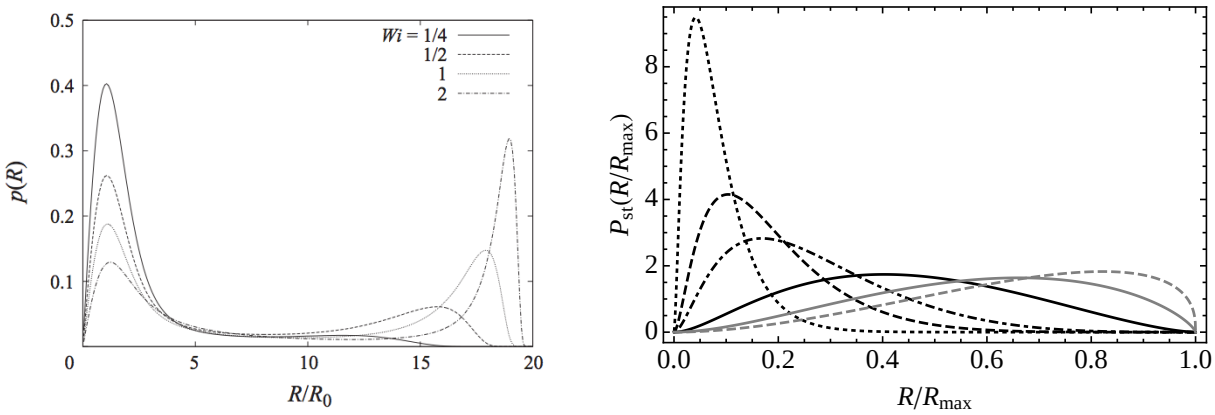

FIGURE 2.7 – **A droite :** *densité de probabilité stationnaire de l'extension des polymères dans un écoulement* renewing *incompressible pour Ku = 10 et des valeurs différentes de Wi* (d'après [C5]). **A gauche :** *densité de probabilité stationnaire de l'extension des polymères dans l'écoulement de Kraichnan non lisse ($\xi = 4/3$) pour $R_{\max} > \eta_\nu$ et Wi = 2.75 (courbe noire en pointillés) Wi = 5 (courbe noire en tirets), Wi = 7 (courbe noire $- \cdot -$), Wi = 14.5 (courbe noire en trait plein), Wi = 30 (courbe grise en trait plein), Wi = 60 (courbe grise en tirets). Les autres paramètres sont : $R_0 = 0.1$, $\eta_\nu = 1$, $R_{\max} = 10^3$ [voir l'équation* (2.20)*]* (d'après [C8]).

(c'est-à-dire $R_{\max} > \eta_\nu$). Dans ce cas, l'équation (2.18) prend la forme[70,71] :

$$\frac{\mathrm{d}\boldsymbol{R}}{\mathrm{d}t} = \boldsymbol{u}(\boldsymbol{x}_1, t) - \boldsymbol{u}(\boldsymbol{x}_2, t) - \frac{\boldsymbol{R}}{2\tau} + \sqrt{\frac{R_0^2}{\tau}}\,\boldsymbol{\xi}(t), \tag{2.20}$$

où le terme $\nabla \boldsymbol{u}(t) \cdot \boldsymbol{R}$ a été remplacé par la différence entre les vitesses des deux billes.

En utilisant le modèle en haltère élastique et l'écoulement aléatoire de Kraichnan[6] (ici nous considérons la version originaire, non lisse de l'écoulement de Kraichnan, puisque nous nous intéressons à l'intervalle inertiel de la turbulence), dans [C7] nous calculons analytiquement la densité de probabilité stationnaire de l'extension des polymères pour une dimension spatiale d quelconque et en fonction de Wi et de l'exposant d'échelle ξ [voir l'équation (2.1)]. Nous rappelons que ξ varie entre 0 et 2 et le champ de vitesse devient de plus en plus régulier au fur et à mesure que ξ s'approche de 2, le cas limite $\xi = 2$ correspondant à l'écoulement de Batchelor–Kraichnan, déjà mentionné plusieurs fois dans ce chapitre.

La densité de probabilité stationnaire de R se comporte comme une loi de puissance pour les extensions inférieures à l'échelle de dissipation visqueuse, $p(R) \propto R^{-1-\alpha}$ pour $R_0 \ll R \ll \eta_\nu$, et prend la forme $p(R) \propto R^{d-1} \exp(-b_\xi Wi^{-1} R^{2-\xi}/\eta_\nu^{2-\xi})$ au-delà ($\eta_\nu \ll R \ll R_{\max}$), où b_ξ est une constante positive. Pour des valeurs de Wi suffisamment grandes, la densité de probabilité présente donc deux queues. Celle de gauche est une loi de puissance avec un exposant α qui tend vers $-d$ pour Wi $\gg Wi_c$, tandis que celle de droite est une fonction exponentielle étirée et décroît rapidement vers zéro en correspondance de $R_{\max}$. La densité de probabilité est ainsi très large et des polymères d'extensions très différentes coexistent dans l'écoulement. Cela montre que même un champ de vitesse non lisse en espace est capable d'étirer considérablement les polymères. Le mécanisme qui conduit à l'état étiré est cependant très différent par rapport à ceux connus pour les écoulements laminaires ou pour des écoulements chaotiques lisses en espace et décrits plus haut. Dans le cas présent, au fur et à mesure que Wi croît, le maximum de la densité de probabilité se déplace progressivement de R_0 vers $R_\star \propto \eta_\nu Wi^{1/(2-\xi)}$, jusqu'à ce que

les effets élastiques non-linéaires deviennent importants (figure 2.7, à droite). L'apparition de l'état étiré n'est donc pas abrupte et on ne peut pas parler de transition coil–stretch. De plus, des valeurs de *Wi* beaucoup plus grandes sont nécessaires pour obtenir des extensions comparables à celle du cas $R_{\max} < \eta_\nu$ et la capacité de l'écoulement d'étirer les polymères diminue au fur et à mesure que son irrégularité spatiale croît (c'est-à-dire au fur et à mesure que ξ s'approche de zéro).

L'échelle $R_\star$ correspond à l'échelle de Lumley que l'on retrouve dans les écoulements turbulents de solutions de polymères[72]. En dessous de cette échelle, l'effet de l'écoulement sur les polymères est plus fort que la relaxation élastique, alors que pour $R > R_\star$ c'est la relaxation élastique qui domine.

Pour terminer, les résultats ci-dessus peuvent être généralisés au cas où l'extension des polymères est plus grande que l'échelle de corrélation du champ turbulent, L_u. Cette situation correspond en effet au cas où l'exposant d'échelle ξ est nul, car au-delà de L_u les corrélations spatiales de la vitesse sont négligeables. Pour $L_u \ll R \ll R_{\max}$, la forme de la densité de probabilité de R est alors $P(R) \propto R^{d-1} \exp[-b_0 R^2/L_u^2 \mathrm{Wi}]$ (avec $b_0 > 0$) et la probabilité décroît très rapidement pour $R \gtrsim L_u \mathrm{Wi}^{1/2}$.

Lorsque l'extension maximum d'un polymère se trouve dans l'intervalle inertiel de la turbulence, les résultats ci-dessus pour le modèle en haltère élastique donnent une idée approximative de la capacité de l'écoulement à déformer le polymère. Un polymère ou un filament élastique de taille plus grande que l'échelle visqueuse est cependant exposé à la structure spatiale très complexe d'un champ de vitesse turbulent. Il faut donc reconnaître que, dans ce régime, le modèle en haltère élastique ne permet pas de décrire des aspects essentiels de la dynamique d'un filament élastique. Des modes de déformation d'ordre plus élevé doivent en effet être pris en compte. Dans [C9] nous étudions la dynamique d'une chaîne de billes de masse négligeable reliées par des ressorts et transportées par un écoulement turbulent incompressible. Les modèles en chaîne ont été beaucoup employés en physique statistique, notamment pour l'étude des polymères (voir par exemple la référence 73) ; nous les généralisons au cas où la différence entre les vitesses calculées aux positions de deux billes ne peut pas être remplacée par une approximation linéaire. Cette généralisation est en effet indispensable pour modéliser une chaîne où la distance entre deux billes peut devenir plus grande que l'échelle visqueuse η_ν. Nous nous concentrons sur le cas bidimensionnel ($d = 2$) car l'interaction entre la chaîne et les structures de l'écoulement est mieux illustrée en deux dimensions.

Nous montrons que, contrairement au cas des traceurs, le centre de masse d'une chaîne élastique n'explore pas l'écoulement de façon uniforme, mais sélectionne les régions tourbillonnaires (figure 2.8). Le mécanisme qui conduit à ce phénomène peut être décrit comme il suit. Dans les régions de l'écoulement où l'étirement est important, une chaîne élastique est fortement étirée et sa taille devient tellement grande que la chaîne cesse de suivre l'écoulement, jusqu'à ce qu'elle rencontre un vortex. Dans le vortex, l'étirement est faible ; la chaîne donc s'enroule, reste piégée dans le vortex et en suit l'évolution jusqu'à sa dissipation (figure 2.8, à droite). Nous quantifions ce phénomène de concentration préférentielle en calculant la statistique du paramètre d'Okubo–Weiss Λ . Ceci est défini comme la différence entre le carré de la vorticité et le carré du taux d'étirement et est donc positif dans les régions tourbillonnaires et négatif dans les régions dominées par l'étirement. Les simulations montrent une préférence pour les valeurs positives de Λ bien plus marquée que dans le cas des traceurs et confirment donc le scénario décrit ci-dessus. Nous étudions également la dépendance de la statistique de Λ

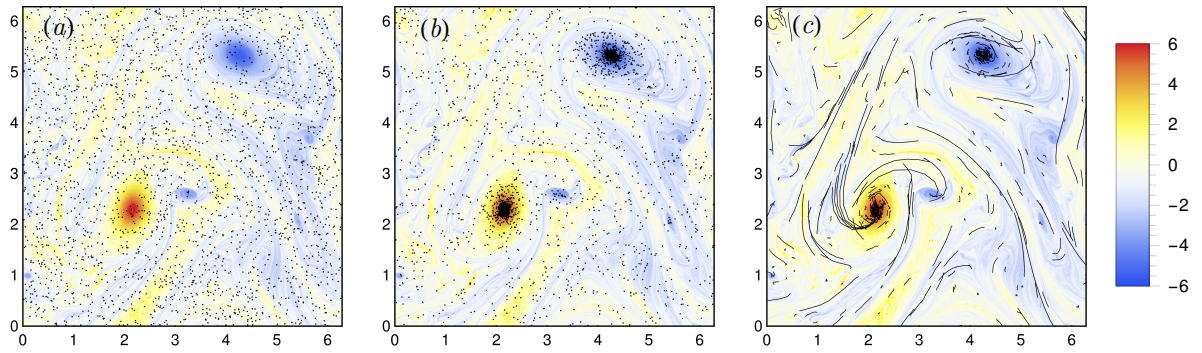

FIGURE 2.8 – (a) *et* (b) *: positions des centres de masse d'un ensemble de chaînes élastiques superposées au champ de vorticité d'un écoulement turbulent bidimensionnel incompressible. La barre couleurs représente les valeurs de la vorticité. Le nombre de billes qui composent chaque chaîne est* $N_L = 9$ *et la longueur maximale de la chaîne est deux fois l'échelle typique du forçage qui engendre l'écoulement. Dans* (a) Wi *est petit et les chaînes se distribuent uniformément dans le fluide ; dans* (b) Wi *est grand et on observe une préférence marquée pour les régions de forte vorticité. La figure* (c) *montre la déformation d'un ensemble de chaînes, et notamment leur enroulement dans les vortex, pour les mêmes paramètres que dans la figure* (b)*.* (D'après [C9])

de l'élasticité de la chaîne et de sa « résistance à la flexion », qui est définie par le rapport entre la longueur maximum de la chaîne et la distance maximum entre deux billes.

2.4.2 Effet de l'approximation de Peterlin

L'injection de polymères dans un fluide newtonien modifie les propriétés rhéologiques du fluide et donc son comportement. Dans le régime turbulent, la nature non-newtonienne d'une solution de polymères se manifeste par une réduction considérable de la traînée turbulente par rapport à celle du solvant[72]. Ce phénomène est systématiquement utilisée dans les oléoducs pour réduire les pertes d'énergie et donc les coûts associés au transport du pétrole.

Les simulations numériques des écoulements turbulents de solutions de polymères utilisent généralement une approche continue, c'est-à-dire les polymères sont décrits par un champ tensoriel $\mathbf{C}(\boldsymbol{x}, t)$ représentant le tenseur d'inertie des polymères à un instant donné et à une position donnée[60]. Ce champ tensoriel est appelé *tenseur de conformation*. L'équation qui régit l'évolution du tenseur de conformation est dérivée à partir du modèle en haltère élastique présenté plus haut [voir l'équation (2.18)]. Dans le cas où l'élasticité des polymères est non-linéaire (modèle FENE-P), la dérivation utilise toutefois une fermeture de type champ moyen connue comme *approximation de Peterlin*[74,75]. L'équation pour le tenseur de conformation avec la fermeture de Peterlin est ensuite couplée avec les équations de Navier–Stokes par le biais d'un terme modélisant les contraintes élastiques. Les équations qui décrivent l'évolution de la vitesse et du tenseur de conformation dans le modèle FENE-P sont :

$$\partial_t \boldsymbol{u} + \boldsymbol{u}\cdot\nabla\boldsymbol{u} = -\nabla p + \nu\Delta\boldsymbol{u} + \frac{\beta}{\tau}\nabla\cdot[h(\operatorname{tr}\mathbf{C})\,\mathbf{C}] + \boldsymbol{f}, \tag{2.21a}$$

$$\partial_t \mathbf{C} + \boldsymbol{u}\cdot\nabla\mathbf{C} = (\nabla\boldsymbol{u})\,\mathbf{C} + \mathbf{C}\,(\nabla\boldsymbol{u})^{\top} - \frac{1}{\tau}[h(\operatorname{tr}\mathbf{C})\,\mathbf{C} - \mathbf{I}], \tag{2.21b}$$

où $\mathbf{I}$ est la matrice identité, le coefficient β est proportionnel à la concentration des polymères et la fonction h est définie dans l'équation (2.19). De nombreuses simulations numériques

montrent que le modèle FENE-P reproduit les principales propriétés qualitatives de la réduction de traînée[76–79], mais il n'y a pas d'accord quantitatif avec les donnée expérimentales. Il est donc important d'analyser les hypothèses sur lesquelles se fonde l'approximation de Peterlin.

La validité de l'approximation de Peterlin a été étudiée auparavant pour des écoulements turbulents et ses limites potentielles ont été mises en évidence par d'autres études[80–83]. Cependant, soit ces études ont utilisé des ensembles de polymères trop petits pour une analyse statistique détaillée soit elles ont considéré des écoulements inhomogènes et les conclusions dépendaient de la position dans le fluide. Dans [C6] nous effectuons une analyse systématique de l'approximation de Peterlin dans un écoulement turbulent homogène et isotrope tridimensionnel. Pour cela, nous utilisons une simulation lagrangienne d'un grand nombre de polymères *passifs* (128×10^3 polymères et 2×10^3 réalisations du bruit moléculaire par polymère), ce qui nous permet d'examiner dans le détail l'effet de la approximation de Peterlin sur les propriétés statistiques de l'extension et de l'orientation des polymères. Nous montrons notamment que la probabilité des grandes extensions est surestimée par l'approximation de Peterlin, tandis que le niveau d'alignement des polymères avec les vecteurs propres de la partie symétrique du gradient de vitesse et avec la vorticité est réduit. De plus, pour Wi grand la fermeture de Peterlin sous-estime les temps de corrélation à la fois de l'extension et de l'orientation des polymères. Ces résultats donnent des indications importantes pour la modélisation des écoulements turbulents de solutions de polymères.

Pour terminer cette section sur le polymères, je mentionne un travail sur le modèle FENE-P (voir [C4]) où nous utilisons les outils stochastiques employés pour l'étude de la dynamique lagrangienne des polymères afin de dériver une fermeture de type RANS (Reynolds Averaged Navier–Stokes) du modèle. La comparaison avec des simulations numériques directes du même modèle confirment la justesse de l'approximation proposée.

2.5 Flexion : le modèle trumbbell

Un degré de liberté lagrangien peu étudié en turbulence est la flexion. Afin d'obtenir des résultats analytiques, nous considérons l'exemple le plus simple d'objet qui peut se plier sous l'action du gradient de vitesse : le *trumbbell*[84]. Un trumbbell est composé de trois billes reliées par deux barres rigides de masse négligeable et de la même longueur (figure 2.9). Il représente l'extension à trois billes du modèle en haltère (*dumbbell* en anglais). La configuration d'équilibre est celle dans laquelle les deux barres sont antiparallèles ($\chi = \pi$), un potentiel harmonique s'opposant à la flexion du trumbbell. L'action de l'écoulement sur chaque bille est décrite par la loi de Stokes. L'inertie des billes ainsi que les interactions hydrodynamiques entre elles sont négligées. De plus, le trumbbell est suffisamment petit pour que sa dynamique soit influencée par le bruit moléculaire et pour que le gradient de vitesse puisse être considéré uniforme sur toute la taille du trumbbell.

La position du centre de masse, $\boldsymbol{x}_c(t)$, évolue une fois de plus comme celle d'un traceur : $\dot{\boldsymbol{x}}_c = \boldsymbol{u}(\boldsymbol{x}_c(t), t)$. Dans le référentiel du centre de masse, la configuration du trumbbell est décrite par un ensemble de coordonnées angulaires $\boldsymbol{q}$, où $\boldsymbol{q} = (\theta, \chi)$ en deux dimensions et $\boldsymbol{q} = (\alpha, \beta, \gamma, \chi)$ en trois dimensions. L'angle χ est l'angle interne entre les deux barres (figure 2.9) et les autres angles décrivent l'orientation du trumbbell dans l'espace : en deux dimensions θ est l'angle entre l'une des barres et un axe fixe (figure 2.10, à gauche), tandis qu'en trois dimensions α, β, γ sont les angles d'Euler. La dynamique est contrôlée une fois de plus par le nombre de

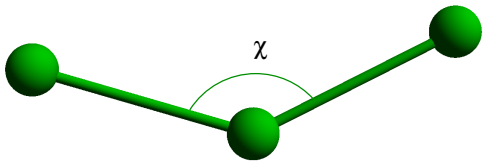

FIGURE 2.9 – *Le modèle trumbbell.*

Weissenberg *Wi*, défini dans ce contexte comme le rapport entre le temps de relaxation associé à la force élastique qui ramène le trumbbell à sa configuration d'équilibre ($\chi = \pi$) et le temps typique de déformation associé au gradient de vitesse.

Malgré sa simplicité, le modèle trumbbell a été très utilisé en chimie physique et en rhéologie car il reproduit qualitativement certaines des propriétés visco-élastiques des suspensions de macromolécules semi-flexibles[85]. Ce modèle joue aussi un rôle important en mécanique statistique, puisqu'il est le modèle de macromolécule le plus simple permettant de montrer que la limite de liens infiniment forts est singulière[86]. De plus, une version active du modèle trumbbell décrit la nage de certains micro-organismes biologiques[87].

2.5.1 Tumbling dans un écoulement hyperbolique

Nous nous intéressons d'abord à la dynamique d'un trumbbell transporté par un champ de vitesse laminaire.

Dans un écoulement cisaillé linéaire, la dynamique de plusieurs objets microscopiques est caractérisée par des retournements, périodiques ou chaotiques, dans le plan du cisaillement. Ce mouvement est appelé *tumbling* et a été observé pour des objets aussi variés que les particules solides anisotropes[88], les polymères flexibles[89,90] ou semi-flexibles[91], les vésicules[92], les bactéries[93], les globules rouges[94]. Le phénomène du tumbling est ainsi communément associé aux écoulements cisaillés linéaires.

Dans [D1] nous nous proposons de comprendre si le tumbling peut être observé aussi pour les écoulements hyperboliques et éventuellement pour quel type de particules. Des objets tels que les bâtonnets ou les haltères élastiques ne peuvent clairement pas effectuer un mouvement de tumbling dans un écoulement hyperbolique : ils s'alignent tout simplement avec la direction d'étirement et ils restent dans cette configuration. Par contre, en étudiant un trumbbell dans un champ de vitesse de la forme $\boldsymbol{u} = \sigma(x, -y, 0)$, $\sigma > 0$, nous montrons que pour un objet flexible le tumbling est possible même dans un écoulement hyperbolique. Dans un tel écoulement, un trumbbell passe la plupart du temps aligné avec la direction d'étirement du champ de vitesse. De temps en temps une succession favorable de fluctuations thermiques fait en sorte que le trumbbell se plie, inverse son orientation et se déplie à nouveau le long de la direction d'étirement (figure 2.10, à droite). Cette dynamique, que nous appelons *tumbling through folding*, peut être comprise en étudiant les configurations stables du trumbbell et la structure de leurs bassins d'attraction.

Dans [D1] nous étudions également la statistique des intervalles de temps entre deux retournements. La distribution est exponentielle et le temps moyen qui sépare deux retournements croît exponentiellement avec *Wi*. Il est intéressant de noter que ces propriétés, que nous expliquons en utilisant la théorie des grandes déviations, sont très différentes par rapport à celles du tumbling dans un cisaillement linéaire. Dans ce dernier cas, en effet, la distribution des temps de tumbling se comporte comme une loi de puissance avec un exposant qui décroît avec *Wi*

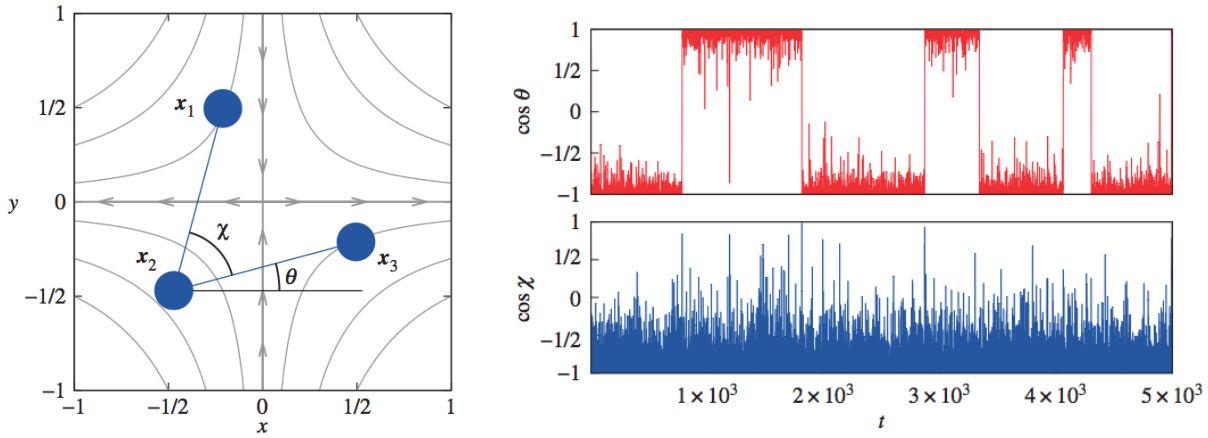

FIGURE 2.10 – **A gauche** *: trumbell dans un écoulement hyperbolique planaire.* **A droite** *: évolution temporelle de l'orientation du trumbbell (angle θ) et de son angle interne χ pour Wi* = 6. (D'après [D1])

(voir les références 90, 95). Un telle différence s'explique par le fait que dans un écoulement hyperbolique la configuration alignée avec la direction d'étirement est stable, alors que dans un écoulement cisaillé la configuration alignée avec la direction de cisaillement n'est que marginalement stable.

La dynamique tumbling-through-folding a été récemment confirmée, avec des propriétés analogues à celles prédites pour le trumbbell, par une étude numérique de la dynamique d'une chaîne de billes de masse non négligeable et avec liens rigides dans un écoulement hyperbolique[96].

2.5.2 Statistique lagrangienne de la flexion

Comme il a été mentionné plus haut, le trumbbell est un modèle simple de particule qui permet d'étudier la statistique lagrangienne de la flexion en turbulence. Des résultats analytiques sur la statistique de l'angle interne χ sont obtenus dans [D2] en considérant le modèle de Batchelor–Kraichnan, où le gradient de vitesse est un processus stochastique $d\times d$-dimensionnel gaussien, isotrope, de moyenne nulle et avec temps de corrélation très court [voir la section 2.1.1 et plus particulièrement l'équation (2.5)]).

Dénotons par $p(\boldsymbol{q};t)$ la densité de probabilité de la configuration du trumbbell par rapport aux réalisations à la fois du bruit thermique et du gradient de vitesse. En d dimensions, la densité $p(\boldsymbol{q};t)$ satisfait une équation de Fokker–Planck en $2(d-1)$ variables angulaires. ‡ Malgré la complexité de cette équation, la symétrie isotrope permet de simplifier considérablement le problème et de le reformuler comme la solution d'une équation de Fokker–Planck en une seule variable (l'angle interne χ). Il est donc possible de calculer analytiquement la densité de probabilité stationnaire de χ, $p_{\mathrm{st}}(\chi)$, à la fois en deux et en trois dimensions. La figure 2.11 montre $p_{\mathrm{st}}(\chi)$ pour $d=2$ et $d=3$ et indique que les deux cas sont qualitativement très différents.

‡. L'équation de Fokker–Planck pour la configuration du trumbbell est en fait un cas particulier d'une équation beaucoup plus générale que nous dérivons dans [C8] pour des chaînes de billes avec des liens élastiques et/ou rigides. Dans [C8] nous utilisons cette équation pour calculer, par exemple, la configuration stationnaire d'un polymère en forme de losange transporté par le champ de vitesse de Batchelor–Kraichnan.

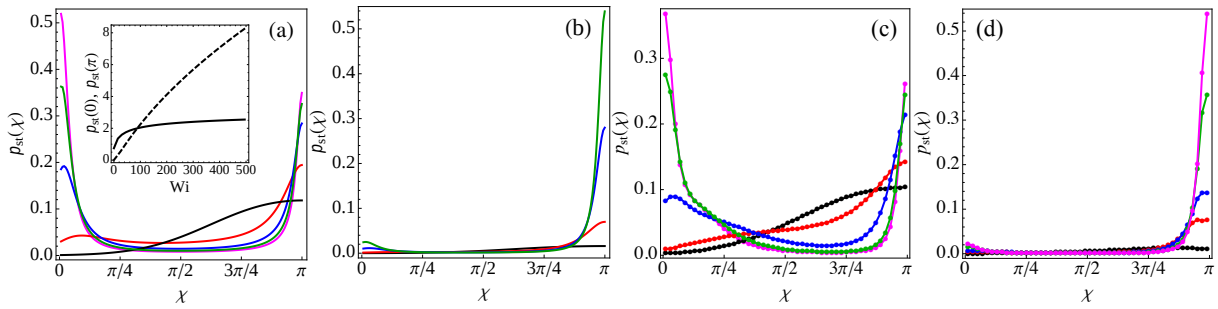

FIGURE 2.11 – *Densité de probabilité stationnaire de l'angle χ pour l'écoulement aléatoire de Batchelor–Kraichnan avec $Wi = 0$ (noir), $Wi = 10$ (rouge), $Wi = 50$ (bleu), $Wi = 100$ (vert), and $Wi = 150$ (magenta)* (a) *en deux et* (b) *en trois dimensions. Les figures* (c) *et* (d) *montrent la densité de probabilité stationnaire de χ pour des simulations numériques de turbulence homogène et isotrope* (c) *en deux et* (d) *en trois dimensions. Les valeurs de Wi sont comparables à celles utilisés pour les densités de probabilité théoriques.*

En deux dimensions et pour *Wi* petit, la configuration la plus probable est celle allongée ($\chi = \pi$). Cependant, lorsque *Wi* croît, un deuxième pic apparaît près de la configuration repliée ($\chi = 0$), tandis que les valeurs intermédiaires de χ deviennent de moins en moins probables. Pour des valeurs de *Wi* très grandes, $p_{st}(\chi)$ montre deux pics très prononcés, l'un à $\chi = \pi$ et l'autre de plus en plus proche de $\chi = 0$. Finalement, ce dernier pic prévaut.

En revanche, en trois dimensions la configuration antiparallèle ($\chi = \pi$) est la plus probable pour toute valeur de *Wi* ; un pic très modeste près de $\chi = 0$ n'apparaît que pour des valeurs de *Wi* très élevées. La différence de comportement en deux et en trois dimensions a une origine géométrique et peut être expliquée en étudiant le temps moyen de sortie des configurations $\chi = 0$ et $\chi = \pi$ dans les deux dimensions (voir [D2]).

Dans [D2] nous comparons également les prédictions théoriques ci-dessus avec des simulations numériques directes de turbulence isotrope en deux et en trois dimensions. Les simulations numériques sont en accord avec les résultats obtenus pour l'écoulement aléatoire de Batchelor–Kraichnan (figure 2.11).

Cette étude montre que la dynamique lagrangienne de particules semi-flexibles dépend fortement de la géométrie du champ de vitesse et de son caractère laminaire ou turbulent. Ce comportement est très différent par rapport au comportement des polymères élastiques dans un écoulement turbulent, qui est qualitativement indépendant de la dimension de l'écoulement et peut être essentiellement déduit du cas laminaire hyperbolique. Ces résultats pourraient avoir des conséquences intéressantes pour la rhéologie des suspensions turbulentes de particules semi-flexibles. Les propriétés rhéologiques pourraient en effet être très différentes selon la dimension de l'écoulement.

2.6 Rupture : gouttelettes en turbulence isotrope

L'approche développée à la section 2.4 pour l'étude des polymères permet aussi d'analyser la déformation et la rupture d'une gouttelette dans un écoulement turbulent.

L'une des premières études sur la distribution des tailles des gouttes dans une émulsion turbulente a été effectuée par Clay[98]. D'après la théorie de Kolmogorov[99] et de Hinze[100], on distingue deux régimes dynamiques différents selon que la taille d'une goutte soit plus grande

ou plus petite que l'échelle de dissipation visqueuse de l'écoulement turbulent. Dans le premier cas, la déformation de la goutte est déterminée par l'équilibre entre les contraintes inertielles et la tension de surface. Dans le deuxième cas, c'est l'équilibre entre la tension de surface et les forces visqueuses qui régit la déformation de la goutte. Ce dernier régime est difficile à examiner expérimentalement à cause de la petite taille des gouttelettes ; les plus petits objets que l'on peut suivre à l'heure actuelle par des caméras rapides ont en effet une taille de l'ordre de l'échelle visqueuse. L'étude numérique présente aussi des difficultés. Pour *Re* élevé, la simulation *directe* de gouttelettes plus petites que l'échelle visqueuse est pour l'instant irréalisable, surtout si un grand nombre de gouttelettes doit être considéré dans le but d'obtenir une statistique adéquate.

Une stratégie possible pour la simulation numérique consiste à utiliser un modèle simplifié de goutte et à l'intégrer le long des trajectoires lagrangiennes. Le modèle de Maffettone et Minale[101] décrit la dynamique d'une goutte ellipsoïdale de la même densité que celle du fluide dans lequel elle est immergée. La goutte est transportée passivement par un écoulement incompressible linéaire en espace et son volume est préservé. A la fois le fluide à l'intérieur de la goutte et celui à l'extérieur sont newtoniens. La forme et l'orientation de la goutte sont décrites par un tenseur $\mathbf{M}$ de deuxième rang et semi-défini positif qui représente le tenseur d'inerti de la goutte. Les vecteurs propres de $\mathbf{M}$ sont les demi-axes de la goutte et ses valeurs propres donnent les longueurs au carré des mêmes demi-axes. Le centre de masse de la goutte évolue comme un traceur [$\dot{\boldsymbol{x}}_c = \boldsymbol{u}(\boldsymbol{x}_c, t)$], tandis que l'évolution lagrangienne de $\mathbf{M}$ est déterminée par l'équation suivante :

$$\frac{\mathrm{d}\mathbf{M}}{\mathrm{d}t} = \mathbf{G}\mathbf{M} + \mathbf{M}\mathbf{G}^{\top} - \frac{f_1(\mu)}{\tau}[\mathbf{M} - g(\mathbf{M})\mathbf{I}], \qquad \mathbf{M}(0) = \mathbf{I}, \tag{2.22}$$

où $\mathbf{I}$ est la matrice identité et $\mathbf{G} = f_2(\mu)\,\mathbf{S} + \mathbf{\Omega}$ est un gradient de vitesse efficace : $\mathbf{S}$ et $\mathbf{\Omega}$ sont à nouveau les parties symétrique et antisymétrique du gradient de vitesse évaluées à la position du centre de masse de la goutte. Les coefficients $f_1(\mu)$ et $f_2(\mu)$ dépendent du rapport μ entre la viscosité du fluide à l'intérieur de la goutte et la viscosité du fluide à l'extérieur. La fonction $g(\mathbf{M})$ est choisie de manière à préserver le produit des valeurs propres de $\mathbf{M}$ et donc le volume de la goutte. Outre le rapport de viscosités μ, la dynamique de la gouttelette dépend du nombre capillaire $Ca = \lambda\tau$, où λ est l'exposant de Lyapounov de l'écoulement et τ est l'échelle de temps associée à la relaxation capillaire vers la forme sphérique. Le nombre capillaire joue dans ce contexte le même rôle que le nombre de Weissenberg jouait dans la dynamique des polymères.

Bien que dérivé pour un champ de vitesse linéaire en espace, le modèle de Maffettone et Minale peut tout aussi bien être utilisé dans des écoulements turbulents si la taille de la goutte est plus petite que l'échelle visqueuse. Dans ce cas la déformation de la goutte est contrôlée par le gradient de vitesse. Biferale *et al.*[102] ont justement appliqué cette approche à des simulations lagrangiennes de turbulence isotrope. La rupture d'une goutte due aux fluctuations du gradient de vitesse est modélisée en introduisant un rapport d'aspect critique au delà duquel la goutte se casse. Dans cette approche on se focalise sur la première rupture d'une goutte et on ne prend pas en compte les gouttes filles issues de sa rupture.

Dans [E1] nous utilisons la stratégie ci-dessus pour étudier la statistique de la déformation et de la rupture de gouttelettes plus petites que l'échelle visqueuse en turbulence homogène et isotrope. Nous abordons ce problème par des calculs analytiques pour l'écoulement aléatoire de Batchelor–Kraichnan, que nous confirmons par des simulations numériques de turbulence isotrope.

Dans les simulations nous considérons le champ de vitesse obtenu par la solution numérique des équations de Navier–Stokes dans un cube périodique. L'équation (2.22) est intégrée en

utilisant l'algorithme d'Adam–Bashforth ; une décomposition de type Cholesky est appliquée au tenseur $\mathbf{M}$ afin d'en préserver le caractère semi-défini positif. Le nombre initial de gouttelettes est de 10^6.

Pour l'étude analytique, nous considérons une approximation vectorielle de l'équation (2.22) (si la goutte est suffisamment déformée, l'une des valeurs propres de $\mathbf{M}$ est bien plus grande que les autres deux et $\mathbf{M} \approx \boldsymbol{r} \otimes \boldsymbol{r}$, où $\boldsymbol{r}$ est le vecteur propre associé à la valeur propre la plus grande. Dans cette approximation, $|\boldsymbol{r}|$ représente la taille de la goutte). Le modèle de Batchelor–Kraichnan nous permet de reformuler le problème de la rupture des gouttelettes en termes d'une équation de Fokker–Planck pour la densité de probabilité de la taille avec une condition de bord absorbante en correspondance de la taille critique de rupture.

Les principaux résultats analytiques et numériques sont résumés ci-dessous :

i. Dénotons par ℓ la taille critique de rupture et supposons qu'à l'instant initial les gouttelettes soient plus petites qu'une taille donnée r_0. La distribution de la taille des gouttelettes intégrée en temps présente alors deux queues en loi de puissance, une pour $r \ll r_0$ et l'autre pour $r_0 \ll r \ll \ell$. L'exposant de la première queue croît au fur et à mesure que le nombre capillaire augmente et il passe de négatif à positif pour les grandes valeurs de Ca. L'exposant de la deuxième queue est toujours négatif et il existe une valeur critique du nombre capillaire, $Ca_c = f_1(\mu)/2f_2(\mu)$, au-delà de laquelle l'exposant sature à la valeur -1.

ii. Le temps moyen de vie d'une gouttelettes croît comme une puissance de ℓ/r_0 pour $Ca < Ca_c$ et se comporte comme le logarithme de ℓ/r_0 dans le cas opposé.

iii. Suite à la rupture des gouttelettes, leur nombre diminue exponentiellement en temps. Le déclin du nombre de gouttelettes accélère rapidement lorsque Ca dépasse sa valeur critique Ca_c, mais il ralentit au fur et à mesure que le rapport μ entre les viscosités croît.

Ces résultats étendent significativement ceux de Biferale *et al.*[102] et fournissent une explication analytique des observations numériques. Plusieurs questions restent cependant ouvertes. Le modèle de goutte que nous avons considéré est assez élémentaire et néglige des effets importants, tels que les déviations de la forme ellipsoïdale, la non linéarité de la déformation près de la rupture, des différences de densité entre les fluides à l'intérieur et à l'extérieure de la goutte, les ruptures successives des gouttes filles. Des progrès importants dans la modélisation et la simulation de la rupture d'une goutte dans un écoulement turbulent sont donc indispensables pour pouvoir avancer dans ce domaine.

Chapitre 3

Turbulence élastique

3.1 Modèle en couche de turbulence élastique

Les travaux présentés à la section 2.4 portent sur la dynamique lagrangienne d'un polymère individuel. Nous avons déjà remarqué que, lorsque l'on considère une solution (même diluée) de polymères, les effets collectifs de ces derniers sur le solvant en modifient les propriétés rhéologiques et donnent lieu à des phénomènes nouveaux. C'est par exemple le cas de la turbulence élastique, un régime chaotique qui apparaît dans les solutions de polymères à *Re* petit suite à des instabilités purement élastiques (voir le chapitre 1 pour une courte introduction au sujet).

Les premières expériences de turbulence élastique ont utilisé des écoulements ayant des lignes de courant courbées[103]. Il a toutefois été montré que des instabilités purement élastiques se développent aussi dans une version visco-élastique de l'écoulement de Kolmogorov, pour lequel le forçage est périodique et parallèle[104,105]. D'ailleurs, les simulations numériques de turbulence élastique dans l'écoulement de Kolmogorov montrent des propriétés similaires à celles observées dans les expériences[24]. Des instabilités purement élastiques ont été aussi prédites pour les écoulements de Poiseuille et de Couette visco-élastiques[106,107]. Plus récemment, le régime de turbulence élastique a été observée dans un microcanal droit[108]. Ces résultats indiquent donc que la turbulence élastique se développe aussi dans des configurations géométriques simples et que la courbure des lignes de courant n'est pas indispensable pour les instabilités élastiques.

Afin d'explorer ultérieurement cet aspect, nous étudions dans [F1] un modèle « en couche » de solution de polymères. A l'origine les modèles en couche ont été introduits comme versions à basse dimension des équations aux dérivées partielles (EDPs) de l'hydrodynamique. Même s'ils ne sont pas obtenus de façon rigoureuse, ils imitent la structure de ces équations dans l'espace de Fourier et ont joué un rôle essentiel au moment où les simulations numériques directes de turbulence développée représentaient encore un défi[23,109].

La version « en couche» du modèle FENE-P introduit à la section 2.4.1 s'exprime en terme de deux ensembles de variables scalaires complexes, u_n et b_n, qui représentent les amplitudes de Fourier du champ de vitesse et du champ de conformation des polymères, respectivement [§].

§. Pour être précis, les variables b_n sont à interpréter comme les amplitudes de Fourier de la racine carrée du tenseur de conformation.

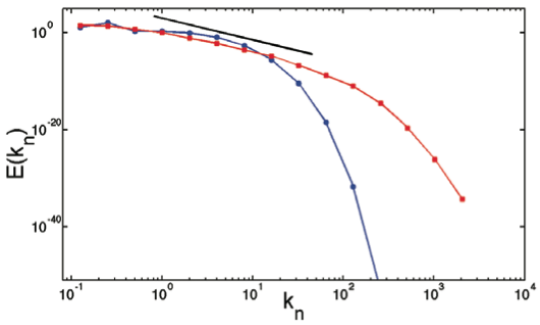

FIGURE 3.1 – *Spectre de l'énergie cinétique du modèle en couche sans (courbe bleue) et avec (courbe rouge) polymères. La droite en noire est proportionnelle à* k_n^{-4}. (D'après [F1])

Ces variables satisfont le système d'équations différentielles couplées :

$$\frac{\mathrm{d}u_n}{\mathrm{d}t} = \Phi_{n,uu} - \nu_s k_n^2 u_n + \frac{\nu_p}{\tau} P(b)\Phi_{n,bb} + f_n, \tag{3.1a}$$

$$\frac{\mathrm{d}b_n}{\mathrm{d}t} = \Phi_{n,ub} + \Phi_{n,bu} - \frac{1}{\tau} P(b) b_n - \nu_b k_n^2 b_n \tag{3.1b}$$

avec

$$\Phi_{n,uu} = i(k_n u_{n+1}u_{n+2} - \epsilon k_{n-1}u_{n+1}u_{n-1} - (1-\epsilon)k_{n-2}u_{n-1}u_{n-2})^* \tag{3.2a}$$

$$\Phi_{n,bb} = -i(k_n b_{n+1}b_{n+2} - \epsilon k_{n-1}b_{n+1}b_{n-1} - (1-\epsilon)k_{n-2}b_{n-1}b_{n-2})^* \tag{3.2b}$$

$$\Phi_{n,ub} = i(k_n u_{n+1}b_{n+2}/6 + k_{n-1}u_{n-1}b_{n+1}/3 - 2k_{n-2}u_{n-1}b_{n-2}/3)^* \tag{3.2c}$$

$$\Phi_{n,bu} = -i(k_n b_{n+1}u_{n+2}/6 + k_{n-1}b_{n-1}u_{n+1}/3 - 2k_{n-2}b_{n-1}u_{n-2}/3)^*, \tag{3.2d}$$

où $n = 1, \ldots, N$, $k_n \propto 2^n$, ν_s est la viscosité du solvant, ν_p est proportionnel à la concentration des polymères et τ est le temps de relaxation des polymères. Le terme $P(b) = 1/(1 - \sum_n |b_n|^2)$ représente la force élastique non linéaire dans le modèle FENE-P et ν_b est une (petite) diffusivité polymérique artificielle nécessaire à stabiliser le système. Le paramètre ϵ est libre et, dans la version hydrodynamique originaire du modèle en couche, est habituellement choisi égal à $1/2$, de manière à conserver à la fois l'énergie cinétique et l'hélicité. Le nombre de Weissenberg *Wi* est défini ici comme le rapport entre τ et un temps de grand échelle associé aux variables u_n.

Le modèle en couche de solution de polymères ci-dessus a été introduit pour l'étude de la réduction de la traînée turbulente aux nombres de Reynolds élevés[110]. Nous l'étudions pour la première fois dans le régime de turbulence élastique, où les effets inertiels sont négligeables (*Re* est petit). Nous choisissons ainsi les paramètres du système de façon que, sans rétroaction des variables polymèriques sur les variables u_n ($\nu_p = 0$), le système n'est pas chaotique. Nous activons ensuite le couplage ($\nu_p \neq 0$) et étudions l'effet des polymères sur la vitesse lorsque *Re* reste petit, mais *Wi* est grand. Nous considérons à la fois $\epsilon = 1/2$ comme dans les études de turbulence hydrodynamique et $\epsilon = 0.3$, valeur pour laquelle on sait à priori que le modèle en couche hydrodynamique ($\nu_p = 0$) n'est pas chaotique[109]. Les deux valeurs de ϵ génèrent la même phénoménologie.

La simplicité du modèle nous permet d'examiner un intervalle de valeurs du nombre de Weissenberg et de la concentration assez ample. Nous montrons que, lorsque les non-linéarités inertielles sont négligeables et *Wi* est élevé, même ce simple modèle en couche reproduit les propriétés qualitatives de la turbulence élastique, comme par exemple :

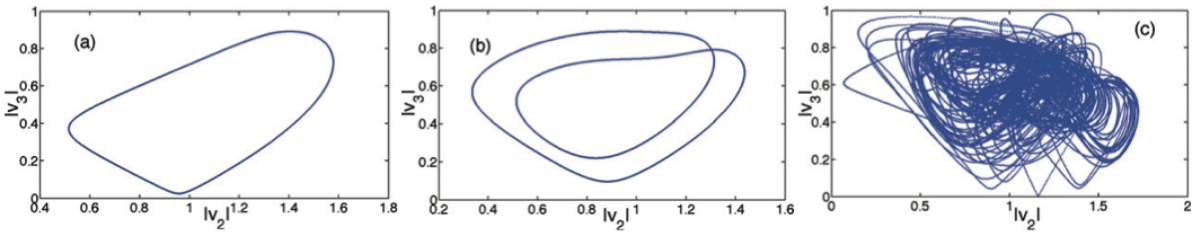

FIGURE 3.2 – $|u_3|$ *en fonction de* $|u_2|$ *pour* $Wi = 25$ *et pour une concentration croissante de polymères (de gauche à droite). La figure illustre la transition vers le régime chaotique de turbulence élastique à travers des états périodiques.* (D'après [F1])

a. le comportement en loi de puissance du spectre d'énergie cinétique (figure 3.1) ;

b. la croissance de l'exposant de Lyapounov en fonction de Wi ;

c. la transition vers la turbulence élastique par une phénomène de *doubling period* (figure 3.2).

Comme le modèle en couche n'a pas une dépendance spatiale explicite, cette étude confirme que les mécanismes physiques à l'origine de la turbulence élastique ne reposent pas sur les propriétés géométriques du champ de vitesse ou du forçage. Celle-ci est en effet la conclusion principale que l'on peut tirer de l'étude de ce modèle.

Nous montrons également que la transition vers la turbulence élastique présente des propriétés similaires lorsque l'on fait varier la concentration ou le nombre de Weissenberg. Un autre résultat intéressant concerne le transfert d'énergie entre le champ de vitesse et la phase polymérique : en turbulence élastique le transfert d'énergie n'a pas une direction privilégiée (vers la vitesse ou vers les polymères), alors que pour Re élevé il est en moyenne en faveur du champ de vitesse[111].

3.2 Dimension de Lyapounov de la turbulence élastique

Nous rappelons que la description mathématique des solutions de polymères se fonde sur des modèles constitutifs qui couplent l'évolution du champ de vitesse de la solution avec l'évolution d'un deuxième champ spatial décrivant la déformation des polymères. Nous avons plusieurs fois évoqué le modèle FENE-P. Un modèle constitutif plus simple est celui d'Oldroyd-B[112]. La phase polymérique y est encore décrite par un champ tensoriel symétrique $\mathbf{C}(\boldsymbol{x}, t)$ (appelé le tenseur de conformation), qui représente le tenseur d'inertie des polymères moyenné sur les fluctuations thermiques. Cependant, dans le modèle Oldroyd-B, l'élasticité des polymères est linéaire. Les équations qui régissent l'évolution de la vitesse de la solution, $\boldsymbol{u}(\boldsymbol{x}, t)$, et du tenseur de conformation sont :

$$\partial_t \boldsymbol{u} + \boldsymbol{u} \cdot \nabla \boldsymbol{u} = -\nabla p + \nu \Delta \boldsymbol{u} + \frac{\beta \nu}{\tau} \nabla \cdot \mathbf{C} + \boldsymbol{f}, \tag{3.3a}$$

$$\partial_t \mathbf{C} + \boldsymbol{u} \cdot \nabla \mathbf{C} = (\nabla \boldsymbol{u})\,\mathbf{C} + \mathbf{C}\,(\nabla \boldsymbol{u})^{\top} - \frac{1}{\tau}(\mathbf{C} - \boldsymbol{I}) \tag{3.3b}$$

où le coefficient β est proportionnel à la concentration des polymères et $\boldsymbol{f}$ est un forçage indépendant du temps.

L'élasticité linéaire est une limitation du modèle, puisque sous certaines conditions elle peut conduire à des extensions infinies. Malgré cette simplification, les simulations numériques du modèle d'Oldroyd-B reproduisent bien les propriétés principales de la turbulence élastique[24,25,113–115], même dans des configurations géométriques idéalisées (deux dimensions, conditions de bords périodiques, etc.). Ce modèle a aussi attiré beaucoup d'attention dans la communauté d'analyse mathématique et plusieurs résultats rigoureux sur l'existence, l'unicité et la régularité de ses solutions ont été obtenus (voir, à titre d'exemple, les références 116–120). Cependant il existe peu de résultats théoriques dans le régime de turbulence élastique. Dans [E2] nous nous intéressons à la dimension fractale de l'attracteur dans l'espace des solutions du modèle, qui fournit une estimation de la complexité de la solution dans le régime de turbulence élastique.

Considérons un système d'EDPs et supposons que dans l'espace fonctionnel des solutions il existe un attracteur global, $\mathscr{A}$, vers lequel toutes les solutions convergent asymptotiquement en temps. La dimension de Lyapounov de l'attracteur, $d_{\mathrm{L}}(\mathscr{A})$, fournit une estimation du nombres d'harmoniques nécessaires à représenter la solution sur une base de l'espace fonctionnel ; elle quantifie donc le nombre de degrés de liberté du système et la complexité de ses solutions[121]. Pour le modèle d'Oldroyd-B, les résultats mathématiques actuellement disponibles ne permettent pas de prouver l'existence d'un attracteur global[118], mais les simulations numériques montrent que la solution du modèle converge vers un état stationnaire en temps. Dans [F2] nous abordons l'estimation de $d_{\mathrm{L}}(\mathscr{A})$ en combinant des techniques d'analyse mathématique précédemment appliquées aux équations de Navier–Stokes bidimensionnelles[122] et des simulations numériques directes de turbulence élastique. Nous montrons que pour le modèle d'Oldroyd-B en deux dimensions :

$$d_{\mathrm{L}}(\mathscr{A}) \leqslant c_1 \langle \|\nabla \mathbf{C}\|_2^2 \rangle \sim c_2 \, Wi^{\alpha},$$

où les constantes c_1 et c_2 dépendent de Re, $\langle\cdot\rangle$ dénote une moyenne temporelle sur l'état stationnaire et $\alpha \approx 0.7$ pour un ensemble de forçages différents. Ce résultat indique que la complexité de la solution du modèle d'Oldroyd-B augmente comme une puissance du nombre de Weissenberg et est liée à l'apparition de forts gradients dans le champ de conformation des polymères (des régions du fluide où les polymères sont faiblement étirés bordent des régions de très fort étirement).

3.3 L'extensibilité des polymères est-elle indispensable pour la turbulence élastique ?

Les expériences et les simulations numériques de turbulence élastique effectuées jusqu'à présent ont utilisé des polymères extensibles. On peut cependant se demander si un régime chaotique comparable à la turbulence élastique peut aussi apparaître dans une solution de polymères *rigides*. Cette question est suggérée par le comportement des solutions de polymères dans le régime de Re élevés. Comme rappelé dans la section 2.4.2, dans ce régime la dissolution de polymères dans un écoulement turbulent d'un fluide newtonien réduit considérablement les pertes d'énergie cinétique dues à la dissipation visqueuse. Ce phénomène, connu sous le nom de *réduction de la traînée turbulente*[72], est observé à la fois pour des polymères élastiques et pour des polymères rigides[123].

Afin de comprendre si une telle analogie de comportement subsiste pour Re petit, nous menons dans [F3] et [F4] une étude numérique de la dynamique d'une solution de polymères ri-

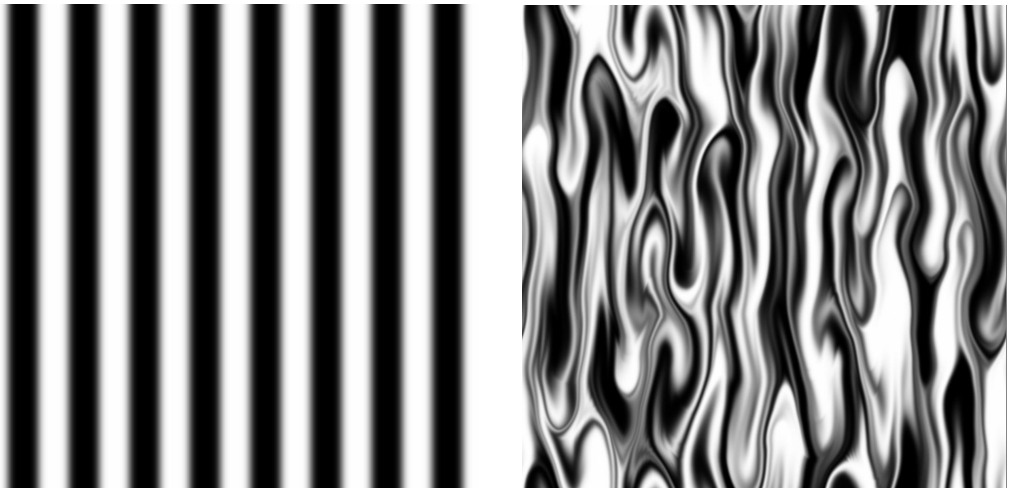

FIGURE 3.3 – *Accélération du mélange dans une solution de polymères* rigides *à un petit nombre de Reynolds.* **A gauche** *: champ scalaire $\theta(\boldsymbol{x}, t)$ dans un écoulement de Kolmogorov en l'absence de polymères. La condition initiale est $\theta_0(x) = \cos 8x$.* **A droite** *: la figure montre le même champ scalaire que dans la figure de gauche et au même instant temporel, mais cette fois-ci des polymères rigides sont dilués dans le fluide.* (D'après [F4])

gides. Nous considérons un modèle de solution proposé par Doi et Edwards[73] et très étudié dans le régime de réduction de traînée turbulente[124]. La phase polymérique est décrite par le champ tensoriel $\mathbf{R}(\boldsymbol{x}, t) = \overline{\boldsymbol{n} \otimes \boldsymbol{n}}$, où $\boldsymbol{n}$ est un vecteur unitaire qui définit l'orientation d'un polymère rigide et la moyenne est prise sur tous les polymères contenus dans un élément de volume au point $\boldsymbol{x}$ au temps t. Le tenseur $\mathbf{R}$, symétrique et de trace unitaire, satisfait une équation de transport, qui peut être obtenue à partir de l'équation de Jeffery pour un bâtonnet dans un champs de vitesse linéaire. Le champ de vitesse est donné par les équations de Navier–Stokes avec une contribution supplémentaire au tenseur des contraintes venant de la présence des polymères (et donc fonction des composantes de $\mathbf{R}$) :

$$\partial_t \boldsymbol{u} + \boldsymbol{u} \cdot \nabla \boldsymbol{u} = -\nabla p + \nu \Delta \boldsymbol{u} + \nabla \cdot \boldsymbol{\tau}_\mathrm{p} + \boldsymbol{f}, \tag{3.4a}$$

$$\partial_t \mathbf{R} + \boldsymbol{u} \cdot \nabla \mathbf{R} = (\nabla \boldsymbol{u})\,\mathbf{R} + \mathbf{R}\,(\nabla \boldsymbol{u})^\top - 2\,(\nabla \boldsymbol{u} : \mathbf{R})\,\mathbf{R}, \tag{3.4b}$$

où $\boldsymbol{\tau}_\mathrm{p} = 6\nu\eta_p(\nabla \boldsymbol{u} : \mathbf{R})\,\mathbf{R}$ est la composante polymérique du tenseur des contraintes et le coefficient de couplage η_p est une fonction croissante de la concentration des polymères rigides. La forme du tenseur $\boldsymbol{\tau}_\mathrm{p}$ est obtenue à partir de la dynamique microscopique des polymères ; une approximation gaussienne (*decoupling approximation*) est utilisée afin d'exprimer le moment d'ordre 4 de l'orientation $\boldsymbol{n}$ en termes de composantes de $\mathbf{R}$ et fermer ainsi les équations (voir la référence 73).

Dans [F3] et [F4] nous considérons une solution bidimensionnelle et utilisons le forçage de Kolmogorov (forçage sinusoïdal et parallèle), déjà employé auparavant pour la simulation de la turbulence élastique dans les solutions de polymères extensibles[24,25]. L'amplitude du forçage est fixée à une valeur plus petite que l'amplitude critique pour l'apparition d'instabilités inertielles ; de cette manière, l'inertie de la solution est négligeable et la dynamique observée n'est le résultat que du couplage entre les polymères rigides et le champ de vitesse. Les équations (3.4) sont résolues numériquement par une méthode pseudo-spectrale avec résolution 1024^2 ; l'intégration temporelle est effectuée en utilisant un schéma de type Runge–Kutta du quatrième

ordre.

Les résultats numériques montrent une phénoménologie tout à fait comparable à celle de la turbulence élastique (voir le chapitre 1) : comportement chaotique de l'énergie cinétique, augmentation de la puissance nécessaire à maintenir l'écoulement en fonction de la concentration des polymères, spectre d'énergie cinétique en loi de puissance avec un exposant inférieur à -3, accélération considérable du mélange d'un champ scalaire passif (figure 3.3). Nos simulations indiquent donc que l'extensibilité des polymères n'est pas indispensable pour générer un régime chaotique à *Re* petit, leur dynamique rotationnelle étant suffisante.

Ce résultat a également des implications pratiques. Les polymères extensibles sont en effet cassés par les fluctuations du gradients de vitesse et cela limite sensiblement la durée temporelle du régime de turbulence élastique[103] (une fois cassés, les polymères ne sont plus en mesure de soutenir le régime chaotique). Or les polymères rigides se dégradent plus difficilement et il pourrait donc être plus avantageux de générer le régime chaotique en utilisant des polymères rigides. Il reste néanmoins à comprendre quelles concentrations de polymères rigides sont nécessaires pour obtenir le même niveau de mélange chaotique que dans les solutions de polymères extensibles. Vues les nombreuses approximations derrière les modèles constitutifs disponibles à l'heure actuelle, la réponse à une telle question ne peut venir que d'une étude expérimentale du problème.

3.4 Effet de la diffusivité polymérique dans la simulation de la turbulence élastique

Nous avons déjà rappelé que les modèles constitutifs de solutions de polymères comme le modèle Oldroyd-B et le modèle FENE-P consistent en un système d'EDPs pour le champ de vitesse de la solution et pour le tenseur de conformation des polymères. Ce dernier est par définition défini positif, mais les erreurs numériques peuvent conduire à la perte de cette propriété et finalement à des instabilités numériques[125]. Une façon standard de remédier à cela est d'introduire de la *diffusivité artificielle* dans le système[126], c'est-à-dire d'ajouter un laplacien avec coefficient constant, $\kappa\Delta\mathbf{C}$, dans le terme de gauche de l'équation pour le tenseur de conformation [équation (2.21b) ou équation (3.3b)]. Un tel terme a en fait une origine physique, puisqu'il décrit la diffusion du centre de masse des polymères, mais les valeurs du coefficient de diffusion κ habituellement utilisées pour stabiliser les simulations numériques sont plusieurs ordres de grandeur plus grandes que les valeurs réelles[127]. Ainsi des méthodes d'intégration alternatifs ont été développées. Certaines de ces méthodes n'utilisent de la diffusivité que localement aux points où $\nabla\mathbf{C}$ devient trop grand[128], d'autres sont des adaptations de méthodes habituellement utilisées pour les EDPs hyperboliques[127] et d'autres encore se fondent sur des décompositions du tenseur $\mathbf{C}$ qui en préservent le caractère défini positif[129,130].

Aux *Re* élevés l'effet de la diffusivité artificielle est assez bien caractérisé (voir par exemple les références 127, 128, 131). Les simulations numériques qui font recours à la diffusivité artificielle reproduisent les propriétés qualitatives de la réduction de la traînée turbulente, mais, si on les compare avec les méthodes d'intégration alternatives mentionnées ci-dessus, on observe des différences quantitatives. Par exemple, le niveau de réduction de traînée est réduit par la diffusivité artificielle, à la fois le champ de vitesse et le tenseur de conformation sont étalés de façon significative et une diffusivité artificielle trop élevée peut conduire à une relaminarisation de la solution.

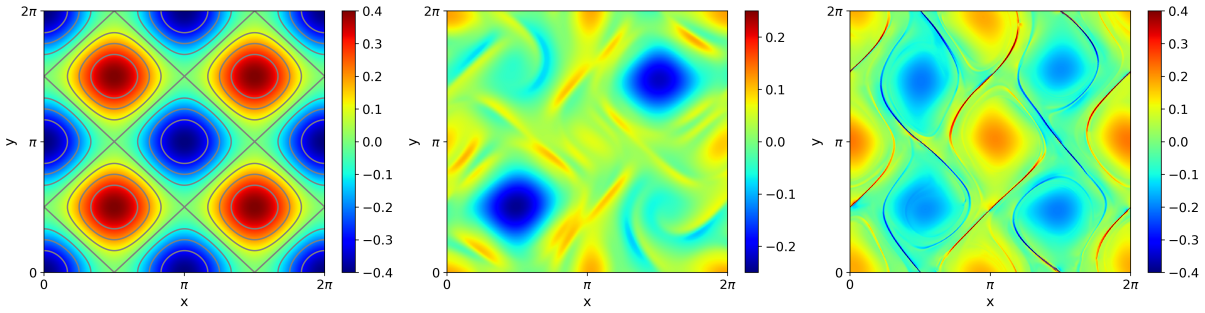

FIGURE 3.4 – **A gauche :** *Champ de vorticité engendré par le forçage cellulaire* $\boldsymbol{f} = f_0(-\sin 2y, \sin 2x)$ *(*$f_0 = 0.002$*). En l'absence de polymères l'écoulement est laminaire. La barre couleurs représente les valeurs de la vorticité.* **Au centre :** *Champ de vorticité dans le régime de turbulence élastique (*$\mathrm{Wi} = 10$*) d'après une simulation numérique utilisant la diffusivité artificielle (la valeur du nombre de Schmidt* $Sc \equiv \nu/\kappa$ *est comparable à celle utilisée dans d'autres simulations de turbulence élastique*[114, 132, 133]*).* **A droite :** *Champ de vorticité dans le régime de turbulence élastique (*$\mathrm{Wi} = 10$*) d'après une simulation numérique utilisant le schéma d'intégration de Kurganov–Tadmor pour les EDPs hyperboliques (voir par exemple la référence 127).* (D'après [F5])

Aux *Re* petits, dans le régime de turbulence élastique, plusieurs simulations numériques ont utilisé la diffusivité artificielle[24, 25, 114, 132–134], mais son effet n'a pas encore été étudié de façon systématique. Dans [F5] nous comparons des simulations numériques de turbulence élastique avec et sans diffusivité artificielle. Nous considérons comme cas test le modèle Oldroyd-B [équations (3.3)] dans un carré périodique ; le mouvement de la solution polymérique est soutenu par un forçage cellulaire, qui en l'absence de polymères engendrerait une série de vortex de signe alterné et séparés par des lignes d'étirement (figure 3.4, à gauche). Nous montrons que la diffusivité artificielle a un effet très important sur les propriétés de l'écoulement, à tel point que même l'écoulement moyen est faussé. En présence de diffusivité artificielle, on observe en effet une brisure de la symétrie cellulaire qui serait imposée par le forçage : certains vortex restent intacts, alors que d'autres sont cassés (figure 3.4, au centre). Ce comportement est cohérent avec les simulations de Thomases et Shelley[132, 133], qui utilisent la diffusivité artificielle. En revanche, lorsque nous employons une méthode d'intégration adaptée aux EDPs hyperbolyques et qui ne fait donc pas recours à la diffusivité artificielle, l'écoulement moyen reproduit la structure cellulaire du forçage, même si des fluctuations chaotiques sont bien évidemment présentes (figure 3.4, à droite). Cette différence dans les résultats s'explique de la façon suivante. Pour pouvoir affecter l'écoulement, les polymères doivent être très étirés. Dans le cas du forçage cellulaire, les perturbations de l'écoulement dues aux polymères sont donc concentrées aux alentours des lignes d'étirement. A l'intérieur des vortex les polymères sont en revanche peu étirés et donc le forçage cellulaire domine et restaure la symétrie cellulaire. Or, si l'on ajoute une diffusivité polymérique trop importante, des polymères très étirés peuvent rejoindre l'intérieur des vortex, modifier l'écoulement et par conséquent déstabiliser la structure imposée par le forçage.

D'autres effets importants de la diffusivité artificielle sur le comportement temporel de l'énergie cinétique et sur le spectre de la vitesse sont discutés dans [F5].

Cette étude montre donc que, dans le régime de turbulence élastique, l'utilisation de la diffusivité artificielle pour stabiliser l'intégration numérique des modèles constitutifs de solutions de polymères peut conduire à des résultats erronés et doit donc être évitée.

3.5 Perspectives

La turbulence élastique et ses applications en microfluidique ont fait l'objet de plusieurs études expérimentales. Les propriétés statistiques et de mélange de l'écoulement ont été caractérisées en fonction du nombre de Weissenberg et de la concentration des polymères dans des configurations géométriques différentes (voir par exemple la référence[135] pour une étude détaillé des propriétés statistiques de la vitesse et de la pression). En revanche, la compréhension théorique des propriétés de la turbulence élastique est encore limitée et les travaux numériques sur ce phénomène sont peu nombreux.

Depuis la découverte de la turbulence élastique en 2000 on peut compter une quinzaine de travaux numériques, qui pour la plupart se cantonnent à des configurations très simplifiées : en deux dimensions et/ou dans des domaines périodiques. Les simulations effectuées jusqu'ici ont donc permis de reproduire certains aspects qualitatifs de la turbulence élastique, mais ont rarement conduit à des prédictions quantitatives. La simulation numérique du régime de turbulence élastique est en effet difficile pour au moins deux raisons. D'une part, nous avons vu que le tenseur de conformation développe des gradients spatiaux très forts et donc des méthodes d'intégration avancées doivent être employées pour résoudre l'évolution de la solution avec précision. D'autre part, il est indispensable d'utiliser un pas temporel très petit, parce que dans ce régime la viscosité est très élevée. Toutefois, les techniques numériques que nous avons évoquées dans la section 3.4 (auxquelles on peut ajouter les méthodes Lattice–Boltzmann, très utilisées en microfluidique) et des moyens de calcul maintenant plus puissants devraient permettre d'effectuer des simulations numériques de turbulence élastique dans des configurations plus proches des conditions expérimentales. La simulation numérique peut en effet apporter une contribution complémentaire à l'étude expérimentale, dans le sens où elle représente un moyen pour améliorer la conception de dispositifs microfluidiques et au même temps elle permet de calculer des quantités physiques difficilement accessibles aux expériences, notamment les propriétés de la composante polymérique du tenseur des contraintes ou des statistiques fines du champ de vitesse.

Des questions importantes qui demandent une étude théorique et numérique sont listées dans ce qui suit.

Nous avons mentionné le fait que les propriétés de la turbulence élastique sont dans une certaine mesure non universelles. Par exemple, le spectre des fluctuations de la vitesse est bien plus raide qu'en turbulence hydrodynamique, mais des expériences et des simulations effectuées dans des conditions différentes ont montré une certaine variabilité de la pente du spectre[20,24–27] (voir aussi [F1], [F2], [F5]) : si celui-ci se comporte comme $k^{-\alpha}$, les valeurs de α que l'on trouve dans la littérature varient entre 2.5 et 4.7. Il est donc important de comprendre comment les propriétés statistiques de l'écoulement sont influencées par la concentration des polymères, par le forçage qui soutient l'écoulement ou encore par la géométrie du dispositif.

La turbulence élastique est un régime chaotique se développant à partir d'instabilités qui n'ont pas une origine inertielle. Pour l'instant ce type de mécanisme, qui permet de générer un écoulement chaotique malgré des nombres de Reynolds très petits, n'a été exploré que pour des fluides viscoélastiques. Il existe toutefois d'autres fluides non-newtoniens pour lesquelles des instabilités à petits nombres de Reynolds ont été prédites, notamment les fluides rhéopectiques[136]. Une accélération importante du mélange est également observée dans les suspensions de particules sphériques soumises à un cisaillement linéaire[137]. Il serait intéressant de comprendre si un phénomène analogue à la turbulence élastique peut être observé dans d'autres

fluides non-newtoniens et éventuellement quelles sont les propriétés du régime chaotique pour ces fluides.

La plupart des simulations de turbulence élastique utilisent les équations de Navier–Stokes (couplées bien évidemment avec des équations qui décrivent l'évolution de la phase polymérique). Certains travaux[130, 132, 133] ont directement utilisé les équations de Stokes en raison de la faible inertie de l'écoulement. Les propriétés macroscopiques de la turbulence élastique semblent être reproduites correctement par cette approche, mais une comparaison systématique avec l'approche qui utilise les équations de Navier–Stokes n'a pas encore été faite. D'une part, la possibilité d'utiliser les équations de Stokes à la place de celles de Navier–Stokes permettrait d'accélérer considérablement les simulations numériques. D'autre part, si en turbulence élastique le terme non linéaire $(\boldsymbol{u} \cdot \nabla \boldsymbol{u})$ est clairement négligeable, il n'est pas évident qu'il en est de même pour le terme $\partial_t \boldsymbol{u}$, vu que le comportement du champ de vitesse est chaotique. Par exemple la présence d'ondes élastiques[25] dans l'écoulement pourraient ne pas être reproduite correctement si la dérivée temporelle du champ de vitesse est négligée. Une question importante pour la simulation numérique de la turbulence élastique consiste donc à comprendre la validité de l'approximation de Stokes dans ce régime.

La turbulence élastique est observée dans les solutions de polymères lorsque le nombre de Reynolds est petit et le nombre de Weissenberg est grand. Si le nombre de Reynolds est lui aussi grand, le mouvement du solvant est déjà turbulent et nous avons vu que l'ajout des polymères provoque une réduction importante de la traînée. La même solution de polymères montre donc deux comportements très différents suivant que le nombre de Reynolds est petit ou grand. Il serait donc intéressant de comprendre la transition entre le régime de turbulence élastique et celui de réduction de traînée ainsi que les mécanismes qui conduisent à un tel changement de comportement lorsque l'on varie le nombre de Reynolds.

Pour terminer, une question majeure concerne la modélisation des solutions des polymères. Les études numériques de la turbulence élastique, mais aussi de la réduction de traînée, se fondent en effet sur des modèles constitutifs tels que les modèles Oldroyd-B et FENE-P. Or ces modèles sont obtenus de façon empirique à partir d'hypothèses très fortes ; ils ne sont finalement que des versions continues du modèle en haltère. Des phénomènes très importants sont par conséquent négligés, par exemple :

a. seul le mode de déformation le plus lent du polymère est pris en compte et la configuration complexe de la macromolécule n'est pas représentée ;

b. le coefficient de traînée du polymère est indépendant de sa forme et la force de traînée est concentrée sur les billes qui composent l'haltère ;

c. Les modèles constitutifs habituellement utilisés ne prennent pas en compte le fait que, dans un régime chaotique, le gradient de la vitesse présente de fortes fluctuations et celles-ci peuvent casser les polymères et réduire ainsi leur action sur le solvant[103]. Cet effet peut cependant jouer un rôle important, puisqu'il introduit une dépendance temporelle supplémentaire dans les propriétés non newtoniennes d'une solution de polymères.

Pour avancer dans la simulation numérique des fluides viscoélastiques et pouvoir obtenir des prédictions quantitatives sur des phénomènes comme la turbulence élastique, il est donc indispensable d'améliorer la modélisation des équations qui régissent l'évolution de ces fluides.

Bibliographie

[1] G. Falkovich, K. Gawędzki & M. Vergassola, *Rev. Mod. Phys.* **73**, 913 (2001)

[2] F. Toschi & E. Bodenschatz, *Annu. Rev. Fluid Mech.* **41**, 375 (2009)

[3] R. Pandit, P. Perlekar & S.S. Ray, *Pramana – J. Phys.* **73**, 157 (2009)

[4] Arnèodo et al., *Phys. Rev. Lett.* **100**, 254504 (2008)

[5] C. Meneveau, *Annu. Rev. Fluid Mech.* **43**, 219 (2011)

[6] R.H. Kraichnan, *Phys. Fluids* **11**, 945 (1968)

[7] R.H. Kraichnan, *Phys. Rev. Lett.* **72**, 1016 (1994)

[8] S. Parsa, E. Calzavarini, F. Toschi & G. A. Voth, *Phys. Rev. Lett.* **109**, 134501 (2012)

[9] G.G. Marcus, S. Parsa, S. Kramel, R. Ni & G.A. Voth, *New J. Phys.* **16**, 102001 (2014)

[10] K. Gustavsson & L. Biferale, *Phys. Rev. Fluids* **1**, 054201 (2016)

[11] S. Kramel, G.A. Voth, S. Tympel & F. Toschi, *Phys. Rev. Lett.* **117**, 154501 (2016)

[12] S. Allende, C. Henry & J. Bec, *Phys. Rev. Lett.* **121**, 154501 (2018)

[13] E.S.G. Shaqfeh, *Annu. Rev. Fluid Mech.* **28**, 129 (1996)

[14] A Groisman & V Steinberg, *Nature* **405**, 53 (2000)

[15] Y. Jun & V. Steinberg, *Phys. Rev.* E **84**, 056325 (2011)

[16] B. Traore, C. Castelain & T. Burghelea, *J. Non-Newtonian Fluid Mech.* **223**, 62 (2015)

[17] R.J. Poole, B. Budhiraja, A.R. Cain & P.A. Scott, *J. Non-Newtonian Fluid Mech.* **177-178**, 15 (2012)

[18] J. Mitchell, K. Lyons, A.M. Howe & A. Clarke, *Soft Matter* **12**, 460 (2016)

[19] T Burghelea, E Segre & V Steinberg, *Europhys. Lett.* **68**, 529 (2004)

[20] Y. Jun & V. Steinberg, *Phys. Rev. Lett.* **102**, 124503 (2009)

[21] B.A. Schiamberg, L.T. Shereda, H. Hu & R.G. Larson, *J. Fluid Mech.* **554**, 191 (2006)

[22] T. Burghelea, E. Segre & V. Steinberg, *Phys. Fluids* **19**, 053104 (2007)

[23] U. Frisch, *Turbulence : The Legacy of Kolmogorov*, Cambridge University Press (1995)

[24] S. Berti, A. Bistagnino, G. Boffetta, A. Celani & S. Musacchio, *Phys. Rev.* E **77**, 055306(R) (2008)

[25] S. Berti & G. Boffetta, *Phys. Rev.* E **82**, 036314 (2010)

[26] T. Watanabe & T. Gotoh, *Phys. Fluids* **26**, 035110 (2014)

[27] A. Gupta & R. Pandit, *Phys. Rev.* E **95**, 033119 (2017)

[28] G. Boffetta & R.E. Ecke, *Annu. Rev. Fluid Mech.* **44**, 427 (2012)

[29] G.T. Csanady, *Turbulent diffusion in the environment* (Springer, 1973)

[30] E.R. Abraham, Nature **391**, 577 (1998)

[31] J.C. Sommerer & E. Ott, *Science* **259**, 335 (1993)

[32] G. Boffetta, J. Davoudi, B. Eckhardt & J. Schumacher, *Phys. Rev. Lett.* **93**, 134501 (2004)

[33] L. Ducasse & A. Pumir, *Phys. Rev.* E **77**, 066304 (2008)

[34] K. Gustavsson & B. Mehlig *J. Stat. Phys.* **153**, 813 (2013)

[35] Ya.B. Zel'dovich, A.A. Ruzmaikin, S.A. Molchanov & D.D. Sokoloff, *J. Fluid Mech.* **144**, 1 (1984)

[36] A.D. Gilbert & B.G. Bayly, J. Fluid Mech. **241**, 199 (1992)

[37] R.T. Pierrehumbert, Chaos, Solitons Fractals **4**, 1091 (1994)

[38] T.M. Jr. Antonsen, Z. Fan, E. Ott & E. Garcia-Lopez, Phys. Fluids **8**, 3094 (1996)

[39] W.R. Young, *Stirring and Mixing : Proc. 1999 Summer Program in Geophysical Fluid Dynamics* (ed. J.-L. Thiffeault & C. Pasquero). Woods Hole Oceanographic Institution, Woods Hole, MA, USA (1999)

[40] J.-L. Thiffeault, C.R. Doering & J.D. Gibbon, J. Fluid Mech. **521**, 105 (2004)

[41] A. Alexakis & A. Tzella, J. Fluid Mech. **688**, 443 (2011)

[42] T. Elperin, N. Kleeorin, V.S. L'vov, I. Rogachevskii, & D. Sokoloff, Phys. Rev. E **66**, 036302 (2002)

[43] A. Pumir & M. Wilkinson, *New J. Phys.* **13** 093030 (2011)

[44] J.P. Chen & D. Lamb, *J. Atmos. Sci.* **51**, 1206 (1994)

[45] D.L. Koch & G. Subramanian, *Annu. Rev. Fluid Mech.* **43**, 637 (2011)

[46] F. Lundell, L.D. Söderberg, & P.H. Alfredsson, *Annu. Rev. Fluid Mech.* **43**, 195 (2011)

[47] G.B. Jeffery, *Proc. R. Soc. Lond.* A **102**, 161 (1922)

[48] F.P. Bretherton, *J. Fluid Mech.* **14**, 284 (1962)

[49] G. Voth & A. Soldati, *Annu. Rev. Fluid Mech.* **49**, 249 (2017)

[50] M. Wilkinson, V. Bezuglyy & B. Mehlig, *Phys. Fluids* **21**, 043304 (2009)

[51] S. Parsa, J.S. Guasto, M. Kishore, N.T. Ouellette, J.P. Gollub & G.A. Voth, *Phys. Fluids* **23**, 043302 (2011)

[52] K.S. Turitsyn, *J. Expl Theor. Phys.* **105**, 655 (2007)

[53] M. Wilkinson and H.R. Kennard, *J. Phys.* A : *Math. Theor.* **45**, 455502 (2012)

[54] K. Gustavsson, J. Einarsson & B. Mehlig, *Phys. Rev. Lett.* **112**, 014501 (2014)

[55] G.K. Batchelor, *Proc. R. Soc. Lond.* A **186**, 480 (1946)

[56] S. Chandrasekhar, *Phil. Trans. R. Soc. Lond.* A **242**, 557 (1950)

[57] E. Lindborg, *J. Fluid Mech.* **302**, 179–201 (1995).

[58] P.G. de Gennes, *J. Chem. Phys.* **60** 5030, (1974)

[59] T.T. Perkins, D.E. Smith & S. Chu, *Science* **276**, 2016 (1997)

[60] R.B. Bird, O. Hassager, R.C. Armstrong, and C.F.C. Curtiss, *Dynamics of Polymeric Liquids* (Wiley, New York, 1977), Vol. 2.

[61] J.L. Lumley, *Symp. Math.* **9**, 315 (1972)

[62] E. Balkovsky, A. Fouxon & V. Lebedev, *Phys. Rev. Lett.* **84**, 4765 (2000)

[63] Y. Liu & V. Steinberg, *Macromol. Symp.* **337** 34, (2014)

[64] T. Watanabe & T. Gotoh, *Phys. Rev.* E **81**, 066301 (2010)

[65] C.M. Schroeder *et al.*, *Science* **301**, 1515 (2003)

[66] C.M. Schroeder, E.S.G. Shaqfeh & S. Chu, *Macromolecules* **37**, 9242 (2004)

[67] S. Gerashchenko & V. Steinberg, *Phys. Rev.* E **78**, 040801(R) (2008)

[68] A.M. Crawford, N. Mordant, H. Xu & E. Bodenschatz, *New J. Phys.* **10**, 123015 (2008)

[69] C. Brouzet, G. Verhille & P.L. Gal, *Phys. Rev. Lett.* **112**, 074501 (2014)

[70] J. Davoudi & J. Schumacher, *Phys. Fluids* **18**, 025103 (2006)

[71] M. De Lucia, A. Mazzino, and A. Vulpiani, Europhys.*Lett.* **60**, 181 (2002)

[72] C.M. White & M.G. Mungal, *Annu. Rev. Fluid Mech.* **40**, 235 (2008)

[73] M. Doi & S.F. Edwards, *The Theory of Polymer Dynamics*, Oxford University Press (1988)

[74] A. Peterlin, *J. Polym. Sci. Pt. B–Polym. Lett.* **4**, 287 (1966)

[75] R.B. Bird, P.J. Dotson & N.L. Johnson, *J. Non-Newtonian Fluid Mech.* **7**, 213 (1980)

[76] R. Sureshkumar, A.N. Beris & R.A. Handler, *Phys. Fluids* **9**, 743 (1997)

[77] E. De Angelis, C.M. Casciola & R. Piva, *Comput. Fluids* **31**, 495 (2002)

[78] P.K. Ptasinski, B.J. Boersma, F.T. Nieuwstadt, M.A. Hulsen, B.H.A.A. Van den Brule & J.C.R. Hunt, *J. Fluid Mech.* **490**, 251 (2003)

[79] Y. Dubief, C.M. White, V.E. Terrapon, E.S.G. Shaqfeh, P. Moin & S.K. Lele, *J. Fluid Mech.* **514**, 271 (2004)

[80] V.E. Terrapon, Y. Dubief, P. Moin & E.S.G. Shaqfeh, in *Proceedings of ASME, ASME/JSME 4th Joint Fluids Engineering Conference (FEDSM2003)* (Honolulu, Hawaii, USA, July 6–10, 2003), pp. 773–780

[81] P. Ilg, E. De Angelis, I.V. Karlin, C.M. Casciola & S. Succi, *Europhys. Lett.* **58**, 616 (2002)

[82] Q. Zhou & R. Akhavan, *J. Non-Newtonian Fluid Mech.* **109**, 115 (2003)

[83] V.K. Gupta, R. Sureshkumar & B. Khomami, *Phys. Fluids* **16**, 1546 (2004)

[84] O. Hassager, *J. Chem. Phys.* **60**, 2111 (1974) ; *ibid.* **60**, 4001 (1974).

[85] J. Garcia de la Torre, *Eur. Biophys. J.* **23**, 307 (1994).

[86] E.J. Hinch, *J. Fluid Mech.* **271**, 219 (1994)

[87] A. Ajdari and R. Golestanian, *Phys. Rev.* E **69**, 062901 (2004).

[88] J. Einarsson, B.M. Mihiretie, A. Laas, S. Ankardal, J.R. Angilella, D. Hanstorp, B. Mehlig, *Phys. Fluids* **28**, 013302 (2016)

[89] C.M. Schroeder, R.E. Teixeira, E.S.G. Shaqfeh, S. Chu, *Phys. Rev. Lett.* **95**, 018301 (2005)

[90] S. Gerashchenko & V. Steinberg, *Phys. Rev. Lett.* **96**, 038304 (2006)

[91] M. Harasim, B. Wunderlich, O. Peleg, M. Kröger, A.R. Bausch, *Phys. Rev. Lett.* **110**, 108302 (2013)

[92] C. Kantsler & V. Steinberg, *Phys. Rev. Lett.* **96**, 036001 (2006)

[93] T. Kaya & H. Koser, *Phys. Rev. Lett.* **103**, 138103 (2009)

[94] J. Dupire, M. Socol, A. Viallat, *Proc. Natl Acad. Sci. USA* **109**, 20808 (2012)

[95] A. Celani, A. Puliafito, K. Turitsyn, *Europhys. Lett.* **70**, 464 (2005)

[96] C. Henry, G. Krstulovic & J. Bec, *Phys. Rev.* E **98**, 023107 (2018)

[97] E.L.C. VI M. Plan, A. Ali & D. Vincenzi, *Phys. Rev.* E **94**, 020501(R) (2016)

[98] P.H. Clay, em Proc. Roy. Acad. Sci. (Amsterdan) **43**, 852 (1940).

[99] A.N. Kolmogorov, *Dokl. Akad. Nauk. SSSR* **66**, 825 (1949)

[100] J.O. Hinze, *AIChE J.* **1**, 289 (1955)

[101] P.L. Maffettone & M. Minale, *J. Non-Newton. Fluid Mech.* **78**, 227 (1998)

[102] L. Biferale, C. Meneveau & R. Verzicco, *J. Fluid Mech.* **754**, 184 (2014)

[103] A. Groisman & V. Steinberg, *New J. Phys.* **6**, 29 (2004)

[104] G. Boffetta, A. Celani, A. Mazzino, A. Puliafito & M. Vergassola, *J. Fluid Mech.* **523**, 61 (2005)

[105] A. Bistagnino, G. Boffetta, A. Celani, A. Mazzino, A. Puliafito & M. Vergassola, *J. Fluid Mech.* **590**, 61 (2007)

[106] B. Meulenbroek et al., *J. Non-Newtonian Fluid Mech.* **116**, 235 (2004)

[107] A.N. Morozov & W. Van Saarloos, *Phys. Rev. Lett.* **95**, 024501 (2005)

[108] L. Pan et al., *Phys. Rev. Lett.* **110**, 174501 (2013)

[109] L. Biferale, *Annu. Rev. Fluid Mech.* **35**, 441 (2003).

[110] C. Kalelkar, R. Govindarajan & R. Pandit, *Phys. Rev.* E, **72** (2005) 017301 ; *ibidem* **83** (2011) 039903(E)

[111] R. Benzi et al., *Phys. Rev.* E **68**, 016308 (2003)

[112] J.G. Oldroyd, *Proc. R. Soc. Lond.* A **200**, 523 (1950)

[113] M. Grilli, A. Vázquez–Quesad & M. Elloro, *Phys. Rev. Lett.* **110** 174501 (2013)

[114] H. Garg, E. Calzavarini, G. Mompean & S. Berti, *Eur. Phys. J.* E **41**, 155 (2018)

[115] R. van Buel, C. Schaaf, & H. Stark, `arXiv:1806.02715` (2018)

[116] Z. Lei, N. Masmoudi & Y. Zhou, *J. Differ. Equ.* **248**, 328 (2010)

[117] J.W. Barrett & E. Süli, *Math. Models Meth. Appl. Sci.* **21**, 1211 (2011)

[118] P. Constantin & M. Kliegel, *Arch. Rat. Mech. Anal.* **206**, 725 (2012)

[119] T.M. Elgindi & F. Rousset, *Commun. Pure Appl. Math.* **68**, 2005 (2015)

[120] X. Hu & F. Lin, *Commun. Pure Appl. Math.* **69**, 372 (2016)

[121] C.R. Doering & J.D. Gibbon, *Applied Analysis of the Navier–Stokes Equations*, Cambridge University Press (1995)

[122] C.R. Doering & J.D. Gibbon, *Physica* D **48**, 471 (1991)

[123] P.S. Virk, D.C. Sherman & D.L. Wagger, *AIChE J.* **43**, 3257 (1997)

[124] I. Procaccia, V.S. L'vov & R. Benzi, *Rev. Mod. Phys.* **80**, 225 (2008)

[125] D.D. Joseph, *Fluid dynamics of viscoelastic liquids* (Springer, 1990).

[126] R. Sureshkumar & A.N. Beris, *J. Non-Newtonian Fluid Mech.* **60**, 53 (1995)

[127] T. Vaithianathan, A. Robert, J.G. Brasseur & L.R. Collins, *J. Non-Newtonian Fluid Mech.* **140**, 3 (2006)

[128] T. Min, J.Y. Yoo & H. Choi, *J. Non-Newtonian Fluid Mech.* **100**, 27 (2001)

[129] T. Vaithianathan & L.R. Collins, *J. Comp. Phys.* **187**, 1 (2003)

[130] N. Balci, B. Thomases, M. Renardy & C.R. Doering, *J. Non-Newtonian Fluid Mech.* **166**, 546 (2011)

[131] S. Sid, V.E. Terrapon & Y. Dubief, *Phys. Rev. Fluids* **3**, 011301(R) (2018)

[132] B. Thomases & M. Shelley, *Phys. Rev. Lett.* **103**, 094501 (2009)

[133] B. Thomases, M. Shelley & J.-L. Thiffeault, *Physica* D **240**, 1602 (2011)

[134] N. Liu & B. Khomami, *J. Fluid Mech.* **737**, R4 (2013)

[135] Y. Jun & V. Steinberg, *Phys. Rev. Fluids* **2**, 103301 (2017)

[136] S. Boi, A. Mazzino & J.O. Pralits, *Phys. Rev.* E **88**, 033007 (2013)

[137] M. Souzy, H. Lhuissier, E. Villermaux & B. Metzger, *J. Fluid Mech.* **812**, 611 (2017)

Annexes

Annexe A

Translation

A1. A. Dhanagare, S. Musacchio & D. Vincenzi
"Weak–strong clustering transition in time-correlated compressible flows"
J. Fluid Mech. **761**, 431–442 (2014)

J. Fluid Mech. (2014), *vol.* 761, *pp.* 431–442.
doi:10.1017/jfm.2014.634

Weak–strong clustering transition in renewing compressible flows

Ajinkya Dhanagare[1], Stefano Musacchio[1] and Dario Vincenzi[1,†]

[1]Laboratoire J. A. Dieudonné, CNRS, Université Nice Sophia Antipolis, 06100 Nice, France

(Received 24 July 2014; revised 1 October 2014; accepted 28 October 2014)

We investigate the statistical properties of Lagrangian tracers transported by a time-correlated compressible renewing flow. We show that the preferential sampling of the phase space performed by tracers yields significant differences between the Lagrangian statistics and its Eulerian counterpart. In particular, the effective compressibility experienced by tracers has a non-trivial dependence on the time correlation of the flow. We examine the consequence of this phenomenon on the clustering of tracers, focusing on the transition from the weak- to the strong-clustering regime. We find that the critical compressibility at which the transition occurs is minimum when the time correlation of the flow is of the order of the typical eddy turnover time. Further, we demonstrate that the clustering properties in time-correlated compressible flows are non-universal and are strongly influenced by the spatio-temporal structure of the velocity field.

Key words: chaotic advection, mixing

1. Introduction

The dynamics of tracers in turbulent flows has important applications in a variety of physical phenomena, ranging from the dispersion of atmospheric pollutants (Csanady 1973) to the transport of plankton in the oceans (Abraham 1998). Moreover, the motion of tracers is intimately related to the mixing properties of turbulent flows, and therefore determines the statistics of passive fields such as temperature in a weakly heated fluid or the concentration of a dye in a liquid (Falkovich, Gawędzki & Vergassola 2001). The last fifteen years have seen a renewed interest in the Lagrangian study of turbulence thanks to the development of new experimental and numerical particle-tracking techniques (Pandit, Perlekar & Ray 2009; Toschi & Bodenschatz 2009).

Several of the qualitative properties of tracer dynamics in turbulent flows have been understood by means of the Kraichnan (1968) model, in which the velocity is a homogeneous and isotropic Gaussian field with zero correlation time and power-law spatial correlations. Under these assumptions, the separations between tracers form a multi-dimensional diffusion process with space-dependent diffusivity, the properties of which have been studied analytically (Falkovich *et al.* 2001; Cardy, Falkovich & Gawędzki 2008). In particular, in the smooth and incompressible regime of the

†Email address for correspondence: dario.vincenzi@unice.fr

Kraichnan model, tracers behave chaotically and spread out evenly in the fluid. If the velocity field is weakly compressible, the Lagrangian dynamics remains chaotic, but tracers cluster over a fractal set with Lyapunov dimension $1 < D_L < d$, where d is the spatial dimension of the fluid (Le Jan 1984, 1985; Chertkov, Kolokolov & Vergassola 1998). The Lyapunov dimension decreases as the degree of compressibility increases; furthermore, the density of tracers exhibits a multifractal behaviour in space, which indicates the presence of strong fluctuations in the distribution of tracers within the fluid (Bec, Gawędzki & Horvai 2004). Finally, if the degree of compressibility of the Kraichnan model exceeds a critical value, all the Lyapunov exponents of the flow become negative and tracers collapse onto a point-like fractal with $D_L = 0$. This latter regime only exists if $d \leqslant 4$ (Chertkov *et al.* 1998) and is known as the regime of strong compressibility.

In nature, compressible flows are not only found for large values of the Mach number. An example of a low-Mach-number compressible flow is given by the velocity field on the free surface of a three-dimensional incompressible flow (Sommerer & Ott 1993; Cressman *et al.* 2004). Furthermore, at small Stokes numbers, the dynamics of inertial particles in an incompressible flow can be assimilated to that of tracers in an effective compressible velocity field (Maxey 1987; Boffetta *et al.* 2007). Compressible flows like those mentioned above have a non-zero correlation time. In this respect, the Kraichnan model is not realistic, and quantitative discrepancies may be expected between the theoretical predictions and the experimental and numerical observations. In a numerical simulation of a turbulent surface flow, Boffetta *et al.* (2004) have found that D_L does decrease as a function of the degree of compressibility, in accordance with the prediction of the Kraichnan model. However, the transition from the weak- to the strong-clustering regime occurs at a larger degree of compressibility compared to the Kraichnan model. This phenomenon is counter-intuitive, because the level of clustering would be expected to increase when the correlation of the flow is non-zero. Thus, the study by Boffetta *et al.* (2004) raises the questions of the interplay between compressibility and temporal correlation in turbulent flows and of the degree of universality of the weak–strong clustering transition – for further studies on clustering in turbulent surface flows, see Schumacher & Eckhardt (2002), Boffetta, Davoudi & De Lillo (2006), Vucelja, Falkovich & Fouxon (2007), Ducasse & Pumir (2008), Larkin & Goldburg (2010), Larkin, Goldburg & Bandi (2010), Lovecchio, Marchioli & Soldati (2013) and Perez-Munuzuri (2014). The investigation of the universality of this phenomenon is particularly interesting in the light of previous findings of non-universal transport properties in random compressible flows for passive scalar fields (Elperin *et al.* 2000).

For inertial particles, the effect of the temporal correlation of the flow on the Lagrangian dynamics has been studied analytically in the following one-dimensional cases: for a velocity gradient described by the telegraph noise (Falkovich *et al.* 2007) or by the Ornstein–Uhlenbeck process (Wilkinson 2011) and for a velocity field given by a Gaussian potential with exponential correlations (Gustavsson & Mehlig 2013*a*). In the case of tracers in compressible flows, Chaves *et al.* (2003) have studied two-particle dispersion in Gaussian self-similar random fields. Falkovich & Martins Afonso (2007) have calculated the Lyapunov exponent and the statistics of the stretching rates for a one-dimensional strain described by the telegraph noise. Gustavsson & Mehlig (2013*b*) have obtained the Lyapunov exponents of a two-dimensional random flow in the limits of short and long correlation times; the solenoidal and potential components of the velocity were assumed to be Gaussian random functions with exponential spatio-temporal correlations.

In this paper, we undertake a thorough study of the effects of temporal correlations on tracer dynamics in a compressible random flow. We consider a compressible version of the two-dimensional renewing flow, which consists of a random sequence of sinusoidal velocity profiles with variable origin and orientation. Each profile remains frozen for a fixed time; by changing the duration of the frozen phase, we can vary the correlation time of the flow and examine the effect on clustering. The renewing flow, in its original incompressible version, has been successfully applied to the study of the kinematic dynamo (Zel'dovich *et al.* 1984; Gilbert & Bayly 1992), chaotic mixing (Pierrehumbert 1994; Antonsen *et al.* 1996; Young 1999; Elperin *et al.* 2000; Thiffeault, Doering & Gibbon 2004; Alexakis & Tzella 2011), inertial-particle dynamics (Elperin *et al.* 2002; Pergolizzi 2012) and polymer stretching (Musacchio & Vincenzi 2011). The properties of this model flow allow us to fully characterise the Lagrangian statistics of tracers as a function of the degree of compressibility and for a wide range of correlation times. We show that, in a time-correlated compressible flow, even single-time Lagrangian averages can differ considerably from their Eulerian counterparts. Furthermore, we demonstrate that the properties of clustering depend not only on universal parameters such as the degree of compressibility and the Kubo number, but also on the specific spatial and temporal properties of the velocity field. In particular, we show that a crucial role is played by the spatial distribution of the stagnation points.

The rest of the paper is organised as follows. In § 2, we introduce the compressible renewing flow and describe its Eulerian properties. In § 3, we compare the Lagrangian and Eulerian statistics of tracer dynamics as a function of the degree of compressibility and of the correlation time of the flow. Section 4 describes the fractal clustering of tracers in the weakly compressible regime and the weak–strong clustering transition. Section 5 concludes the paper by discussing the non-universal character of the weak–strong clustering transition.

2. Compressible renewing flow

We consider the following velocity field $\boldsymbol{u} = (u_x, u_y)$ on a periodic square box $\Omega = [-L/2, L/2]^2$:

$$\begin{cases} u_x = U\sqrt{2(1-C)}\cos(ky+\phi_y) + U\sqrt{2C}\cos(kx+\phi_x), \\ u_y = 0, \end{cases} \qquad 2nT \leqslant t < (2n+1)T \quad (2.1)$$

and

$$\begin{cases} u_x = 0, \\ u_y = U\sqrt{2(1-C)}\cos(kx+\phi_x) + U\sqrt{2C}\cos(ky+\phi_y), \end{cases} \qquad (2n+1)T \leqslant t < 2(n+1)T. \quad (2.2)$$

Here $n \in \mathbb{N}$, $k = 2\pi/L$, $U = \sqrt{\langle u^2 \rangle}$ is the root-mean-square (r.m.s.) velocity and $C = \langle (\boldsymbol{\nabla} \cdot \boldsymbol{u})^2 \rangle / \langle \|\boldsymbol{\nabla u}\|_F^2 \rangle$ is the degree of compressibility of the flow. Here, $\|\cdot\|_F$ is the Frobenius norm and $\langle \cdot \rangle$ denotes a spatial average over the domain Ω. Note that $0 \leqslant C \leqslant 1$; $C = 0$ corresponds to an incompressible flow, and $C = 1$ to a gradient flow. The angles ϕ_x and ϕ_y are independent random numbers uniformly distributed over $[0, 2\pi]$ and change randomly at each time period T.

The velocity field defined in (2.1) and (2.2) is a sequence of randomly translated sinusoidal profiles, each of which persists for a time T; the velocity is alternately

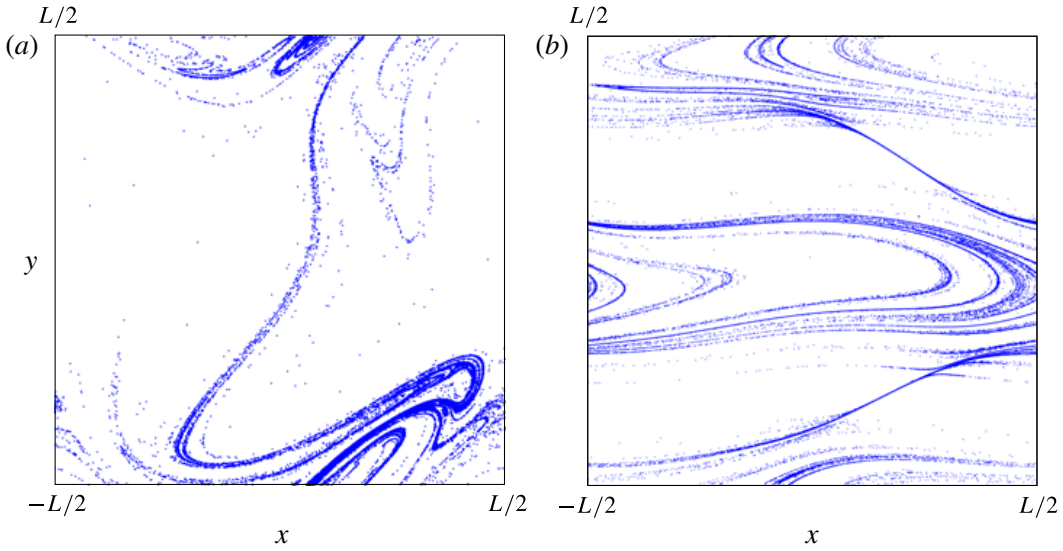

FIGURE 1. (Colour online) Spatial distribution of tracers in the compressible renewing flow for $C = 1/4$ and (*a*) $Ku = 0.1$ and (*b*) $Ku = 10$. Each plot shows the positions of 10^5 tracers. For $Ku = 10$, the distribution of tracers mirrors the structure of the flow, which consists of periodic channels and of regions where transport is inhibited by the stagnation lines.

oriented in the x and y directions. The renewing flow is in principle non-stationary, because the values of the velocity at two different times are either correlated or independent depending on whether or not the two times belong to the same frozen phase. However, it can be regarded as stationary for times much longer than T (Zel'dovich *et al.* 1984). The temporal statistics of the flow is characterised by the correlation function:

$$F_{\mathscr{E}}(t) \equiv \frac{\langle \boldsymbol{u}(\boldsymbol{x}, s+t) \cdot \boldsymbol{u}(\boldsymbol{x}, s) \rangle_{\mathscr{E}}}{U^2} = \begin{cases} 1 - \dfrac{t}{T}, & t \leqslant T, \\ 0, & t > T. \end{cases} \tag{2.3}$$

Here $\langle \cdot \rangle_{\mathscr{E}}$ denotes a space–time Eulerian average: $\langle \cdot \rangle_{\mathscr{E}} \equiv T^{-1} L^{-2} \int_0^T \int_\Omega \cdot \, \mathrm{d}s \, \mathrm{d}\boldsymbol{x}$. The correlation time of the flow is: $T_{\mathscr{E}} \equiv \int_0^T F_{\mathscr{E}}(t) \, \mathrm{d}t = T/2$. A dimensionless measure of the correlation time is given by the Kubo number $Ku \equiv TUk$; Ku is proportional to the ratio of $T_{\mathscr{E}}$ and the eddy turnover time of the flow.

The position of a tracer evolves according to the following equation:

$$\dot{\boldsymbol{X}}(t) = \boldsymbol{u}(\boldsymbol{X}(t), t). \tag{2.4}$$

Figure 1 shows the distribution of tracers in the weakly compressible regime. The transition from the regime of weak compressibility to that of strong compressibility occurs when the maximum Lyapunov exponent of the flow becomes negative. In this case, the flow is no longer chaotic and tracers are attracted to a point-like set. To study this transition, it is useful to consider the set of stagnation points of the flow, in which $\boldsymbol{u} = (0, 0)$. Tracers indeed tend to accumulate in the neighbourhood of these points. From (2.1) and (2.2), we deduce that the set of stagnation points of the renewing flow consists of the two lines

$$y = \pm \frac{1}{k} \arccos\left(\sqrt{\frac{C}{1-C}} \cos(kx + \phi_x) \right) - \frac{\phi_y}{k} + 2\pi m, \tag{2.5}$$

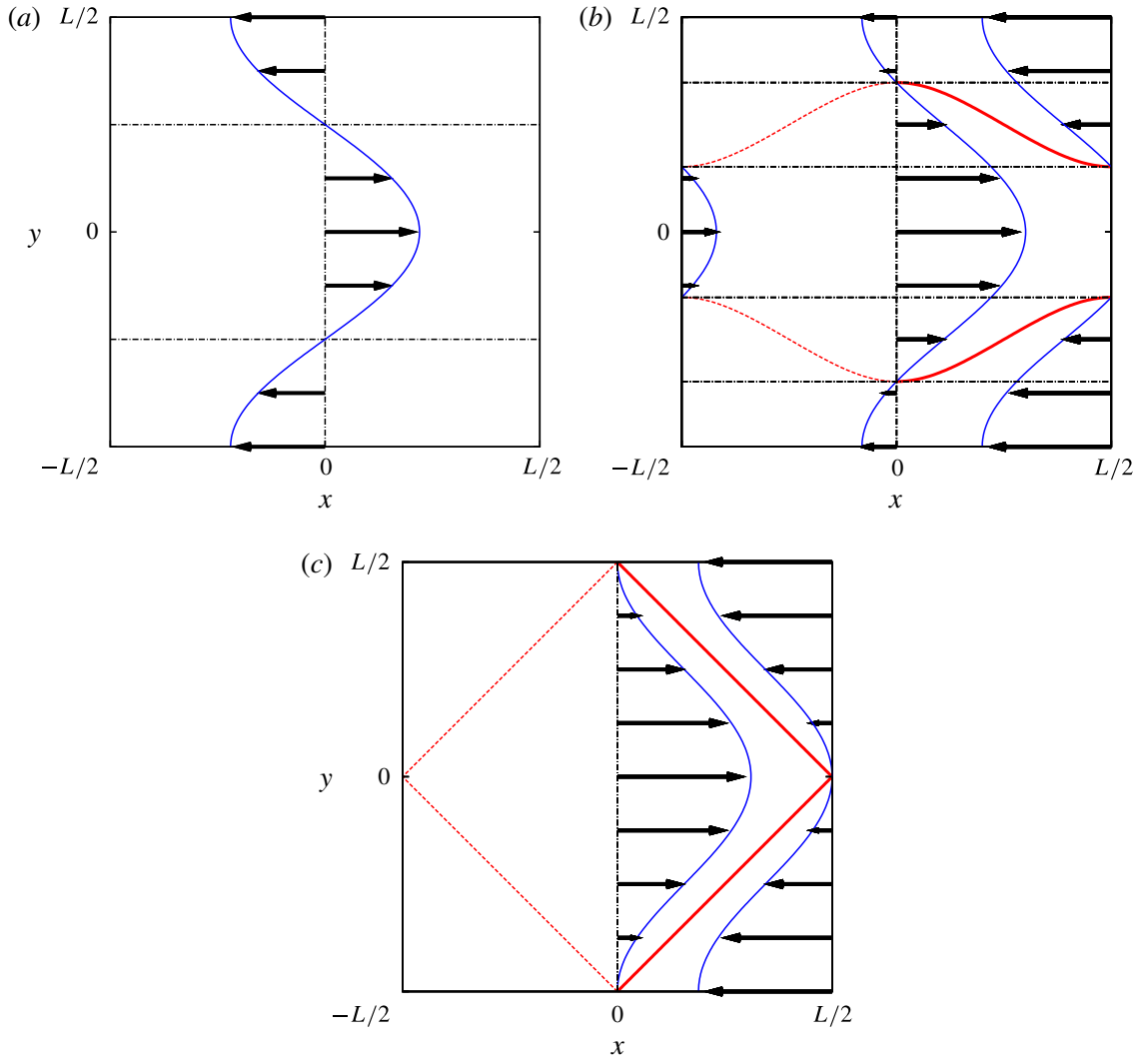

FIGURE 2. (Colour online) Velocity profile of the renewing flow for (*a*) $C=0$, (*b*) $C=1/4$ and (*c*) $C=1/2$. The thick solid grey lines (red online) are the portions of the stagnation lines where $\boldsymbol{\nabla}\cdot\boldsymbol{u}<0$.

if the velocity is given by (2.1), or

$$y=\pm\frac{1}{k}\arccos\left(\sqrt{\frac{1-C}{C}}\cos(kx+\phi_x)\right)-\frac{\phi_y}{k}+2\pi m, \tag{2.6}$$

if the velocity is given by (2.2). In (2.5) and (2.6), $m\in\mathbb{Z}$ is such that $(x,y)\in\Omega$. The stagnation lines are shown in figure 2 for some representative values of the degree of compressibility. If $C=0$, the flow consists of parallel periodic 'channels' of width $L/2$. If $0<C<1/2$, the stagnation lines form barriers that block the motion of tracers over a portion of the domain whose size increases as C approaches $1/2$; the width of the periodic channels shrinks accordingly. Finally, if $1/2\leqslant C\leqslant 1$, the stagnation lines divide the domain into regions that are not linked by any streamline. For these values of C, there are no periodic trajectories, and if Ku is sufficiently large, all tracers collapse onto the stagnation lines. We conclude that the transition from the regime of

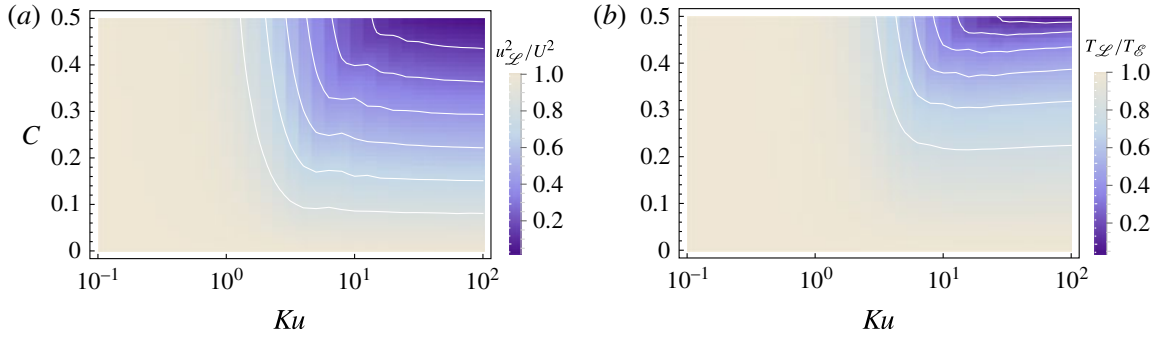

FIGURE 3. (Colour online) (*a*) Ratio of the r.m.s. Lagrangian and Eulerian velocities as a function of the Kubo number Ku and of the degree of compressibility C of the flow. (*b*) Ratio of the Lagrangian and Eulerian correlation times of the velocity as a function of C and Ku.

weak clustering to that of strong clustering must occur for $C \leqslant 1/2$. However, the critical value of the degree of compressibility depends on Ku.

3. Lagrangian versus Eulerian statistics

The properties of the flow introduced in § 2, namely the r.m.s. velocity, the degree of compressibility and the correlation function, are of an Eulerian nature. If the flow is compressible and has a non-zero correlation time, the Lagrangian counterparts of the aforementioned quantities may be different. Indeed, tracers are attracted towards the stagnation points and hence do not sample the phase space uniformly.

We define the r.m.s. Lagrangian velocity as $u_{\mathscr{L}} \equiv \sqrt{\langle u^2(\boldsymbol{X}(s), s)\rangle_{\mathscr{L}}}$, where $u = |\boldsymbol{u}|$ and $\langle\cdot\rangle_{\mathscr{L}}$ is a Lagrangian average over both the random trajectory $\boldsymbol{X}(s)$ and time. Figure 3(*a*) compares $u^2_{\mathscr{L}}$ and its Eulerian counterpart U^2 for different values of Ku and C. The plot includes 51 values of C between 0 and 1/2, and 31 values of Ku ranging from 10^{-1} to 10^2. For each pair (Ku, C), we have computed $u^2_{\mathscr{L}}$ by solving (2.4) for 10^2 tracers and for an integration time $t = 2 \times 10^3\, T$ (to integrate (2.4), we have used a fourth-order Runge–Kutta method). At $C = 0$, $u_{\mathscr{L}}$ is the same as U for all values of Ku, because tracers explore the phase space uniformly. Likewise, at $Ku = 0$ the Eulerian and the Lagrangian statistics coincide independently of the value of C. By contrast, for $C \neq 0$ and $Ku \neq 0$, $u_{\mathscr{L}} < U$ because tracers are attracted towards the stagnation lines, where $u = 0$. The ability of the stagnation points to trap tracers strengthens with increasing C and Ku; hence $u_{\mathscr{L}}$ eventually approaches zero.

The Lagrangian correlation function of the velocity is defined as

$$F_{\mathscr{L}}(t) \equiv \frac{\langle \boldsymbol{u}(\boldsymbol{X}(s+t), s+t) \cdot \boldsymbol{u}(\boldsymbol{X}(s), s)\rangle_{\mathscr{L}}}{u^2_{\mathscr{L}}}. \tag{3.1}$$

The associated Lagrangian correlation time is $T_{\mathscr{L}} \equiv \int_0^T F_{\mathscr{L}}(t)\,\mathrm{d}t$. If the flow is incompressible ($C = 0$) or if it is decorrelated in time ($Ku = 0$), then $T_{\mathscr{L}} = T_{\mathscr{E}}$ (figure 3*b*). If both C and Ku are non-zero, $T_{\mathscr{L}}$ is smaller than $T_{\mathscr{E}}$, and the ratio $T_{\mathscr{L}}/T_{\mathscr{E}}$ decreases as Ku or C increase (figure 3*b*). Again, this behaviour can be explained by considering that a tracer is attracted towards the stagnation points, where $u = 0$, and hence its velocity decorrelates from the velocity it had at the beginning of the period. As Ku and C increase, a larger fraction of tracers get

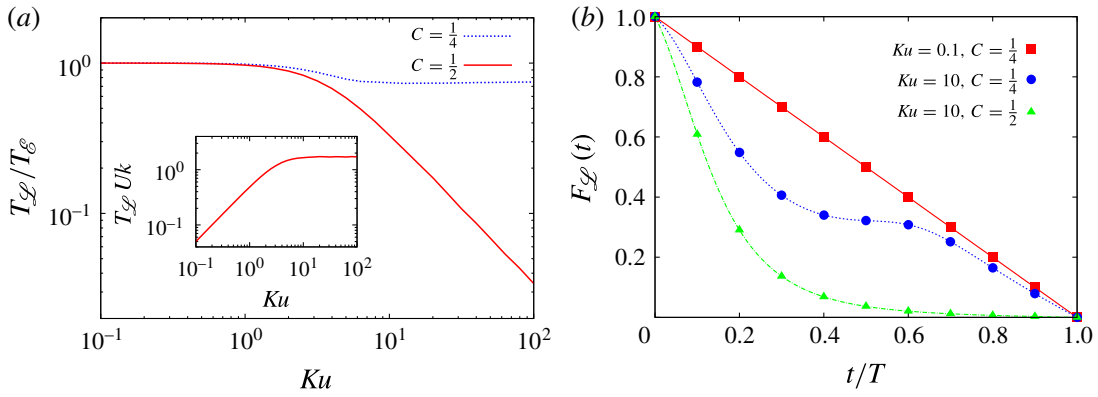

FIGURE 4. (Colour online) (*a*) Ratio of the Lagrangian and Eulerian correlation times of the velocity as a function of Ku for $C = 1/4$ and $C = 1/2$. The inset shows the Lagrangian correlation time rescaled by $(Uk)^{-1}$ as a function of Ku for $C = 1/2$. (*b*) Lagrangian correlation function of the velocity for $Ku = 0.1$, $C = 1/4$, $Ku = 10$, $C = 1/4$ and $Ku = 10$, $C = 1/2$.

close to the stagnation points, and therefore the decorrelation is faster. The inset of figure 4(*a*) also shows that, for C close to $1/2$, $T_{\mathscr{L}}$ is proportional to T for small values of Ku, whereas it saturates to a value proportional to the eddy turnover time for large values of Ku. Indeed, after that time most of the tracers have reached a stagnation point, and their velocities have completely decorrelated.

Figure 4(*b*) shows that, for small values of Ku, $F_{\mathscr{L}}(t)$ is the same as $F_{\mathscr{E}}(t)$ irrespective of the value of C. However, at large Ku, not only the Lagrangian correlation time of the velocity but also the functional form of $F_{\mathscr{L}}(t)$ varies with C.

The degree of compressibility experienced by tracers also depends on Ku and C and differs from its Eulerian value if $Ku \neq 0$ and $C \neq 0$. Let us define the Lagrangian degree of compressibility as $C_{\mathscr{L}} \equiv \langle(\boldsymbol{\nabla}\cdot\boldsymbol{u})^2\rangle_{\mathscr{L}}/\langle\|\boldsymbol{\nabla u}\|_F^2\rangle_{\mathscr{L}}$. Then, $C_{\mathscr{L}} > C$ for all non-zero values of Ku and C, because tracers spend more time in high-compressibility regions. For fixed Ku, the increase in compressibility is an increasing function of C, whereas for fixed C it is maximum when Ku is near to unity and vanishes in both the small- and the large-Ku limits (figure 5*a*). The non-monotonic behaviour of the Lagrangian compressibility as a function of Ku is due to a peculiar feature of the model flow considered here. The stagnation lines (2.5) and (2.6) towards which the tracers are attracted do not coincide with the regions where the local compressibility of the flow is maximum, i.e. the lines $ky + \phi_y = m\pi$ for $2nT \leqslant t < (2n+1)T$ and $kx + \phi_x = m\pi$ for $(2n+1)T \leqslant t < 2(n+1)T$. Therefore, in the long-correlated limit the preferential sampling of the regions of strong compressibility is reduced.

4. Fractal clustering

The spatial distribution of tracers within a fluid can be characterised in terms of the Lyapunov dimension (e.g. Sommerer & Ott 1993),

$$D_L = N + \frac{\sum_{i=1}^{N}\lambda_i}{|\lambda_{N+1}|}, \tag{4.1}$$

where $\lambda_1 \geqslant \lambda_2 \geqslant \cdots \geqslant \lambda_d$ are the Lyapunov exponents of the flow and N is the maximum integer such that $\sum_{i=1}^{N}\lambda_i \geqslant 0$ (d denotes the dimension of the flow). Three

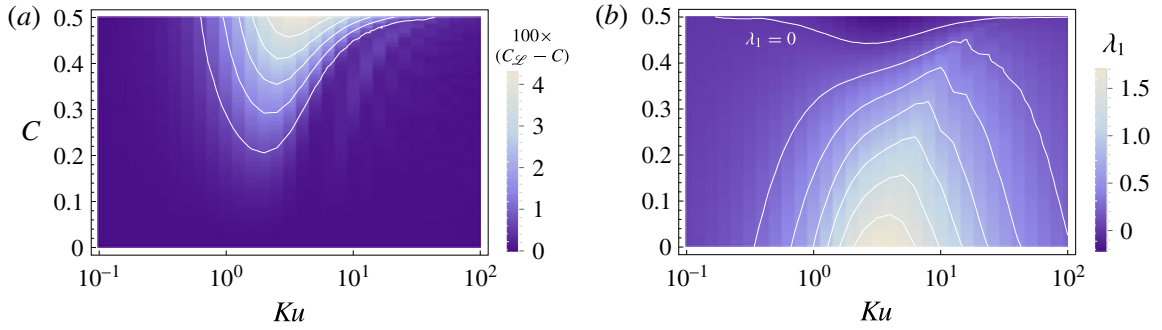

FIGURE 5. (Colour online) (*a*) Increase in compressibility multiplied by 100, $(C_{\mathscr{L}} - C) \times 100$, as a function of Ku and C. (*b*) Maximum Lyapunov exponent of the compressible renewing flow as a function of Ku and C.

different regimes can be identified. If the flow is incompressible ($\sum_{i=1}^{d} \lambda_i = 0$), tracers spread out evenly within the fluid ($D_L = d$). In the weakly compressible regime ($\sum_{i=1}^{d} \lambda_i < 0$ and $\lambda_1 > 0$), tracers cluster over a fractal set ($1 < D_L < d$). In the strongly compressible regime ($\sum_{i=1}^{d} \lambda_i < 0$ and $\lambda_1 < 0$), tracers are attracted to a point-like set ($D_L = 0$). The transition from the regime of weak compressibility to that of strong compressibility occurs when λ_1 changes sign.

For the smooth d-dimensional Kraichnan (1968) flow, the Lyapunov exponents can be calculated exactly (we remind the reader that in the Kraichnan model the velocity field is Gaussian, delta-correlated in time, and statistically homogenous and isotropic). The Lyapunov exponents are $\lambda_i = \mathscr{D}\{d(d - 2i + 1) - 2C[d + (d - 2)i]\}$, where $i = 1, \ldots, d$, C is defined as in § 2, and $\mathscr{D} > 0$ determines the amplitude of the fluctuations of the velocity gradient (Le Jan 1984, 1985). Thus, for $d = 2$, the Lyapunov dimension of the smooth Kraichnan model is $D_L^0 = 2/(1 + 2C)$ and the weak–strong clustering transition occurs at $C = 1/2$. In time-correlated flows, the prediction of the Kraichnan model is recovered in the small-Ku limit (Boffetta *et al.* 2004; Gustavsson & Mehlig 2013*b*).

In this section, we study how the weak–strong clustering transition depends on Ku in the compressible renewing flow. To compute the Lyapunov exponents, we have used the method proposed by Benettin *et al.* (1980). We have set the integration time to $t = 10^6$ for all values of Ku and C in order to ensure the convergence of the stretching rates to their asymptotic values.

The maximum Lyapunov exponent decreases with increasing C (figure 5*b*). Its behaviour as a function of Ku is different in the weakly compressible and strongly compressible regimes. For small values of C, λ_1 is maximum for Ku near to unity, which signals an increase in chaoticity when the correlation time of the flow is comparable to the eddy turnover time. By contrast, for values of C near to $1/2$, λ_1 is minimum at $Ku \approx 1$, in accordance with the fact that the Lagrangian compressibility is maximum for these values of the parameters (figure 5). We also note that if Ku is near to unity, λ_1 becomes negative for $C < 1/2$; hence the weak–strong clustering transition occurs at a lower degree of compressibility compared to the short-correlated case.

Analogous conclusions can be reached by studying the behaviour of $D_L = 1 - \lambda_1/\lambda_2$ (figure 6). For fixed Ku, an increase in the Eulerian compressibility yields an increased level of clustering. The behaviour as a function of Ku is not monotonic and depends on the value of C. When Ku is near to unity, the level of clustering is minimum if C

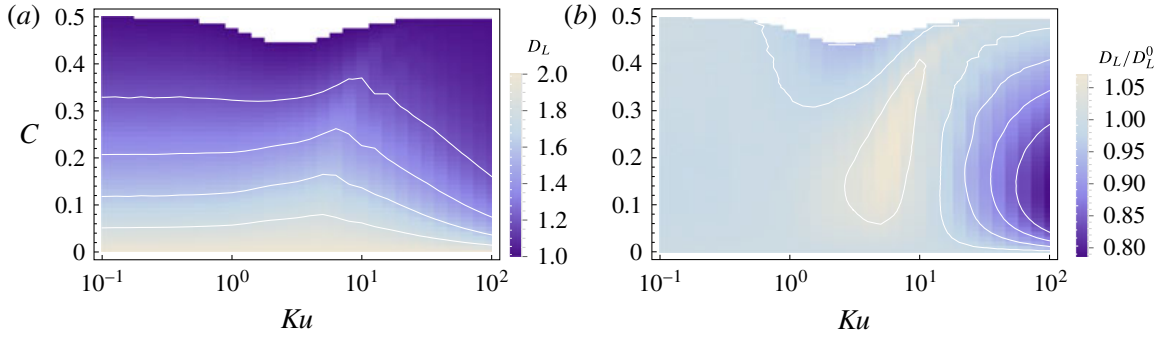

FIGURE 6. (Colour online) (*a*) Lyapunov dimension D_L as a function of Ku and C. The region in which $D_L = 0$ is coloured in white in the plot. (*b*) Lyapunov dimension D_L rescaled by its value at $Ku = 0$, D_L^0, as a function of Ku and C.

is small and is maximum if C is near to $1/2$. Furthermore, D_L vanishes for values of C smaller than the critical value of the short-correlated case. The most important deviations of D_L from the $Ku = 0$ prediction are observed for values of Ku greater than unity (figure 6*b*).

5. Conclusions

We have studied the Lagrangian dynamics of tracers in a time-correlated compressible random flow as a function of the degree of compressibility and the Kubo number. The use of the compressible renewing flow has allowed us to examine a wide area of the parameter space (Ku, C). We have shown that, in compressible random flows with non-zero correlation time, Lagrangian correlations differ significantly from their Eulerian counterparts, because tracers are attracted towards the stagnation points and therefore do not sample the phase space uniformly. This fact influences the spatial distribution of tracers within the fluid. In particular, in both the small- and large-Ku limits, the critical degree of compressibility for the weak–strong clustering transition is the same as for a short-correlated flow. By contrast, when the correlation time of the flow is comparable to the eddy turnover time, a smaller degree of compressibility is required for the transition to occur. The non-monotonic behaviour of the critical degree of compressibility is a consequence of the fact that the stagnation points do not coincide with the points in which the compressibility is maximum. This behaviour is very different from that observed by Gustavsson & Mehlig (2013*b*) in a Gaussian velocity field with exponential spatio-temporal correlations. In that flow, the critical degree of compressibility indeed decreases monotonically as a function of Ku and tends to zero in the large-Ku limit, i.e. the weak–strong clustering transition is more and more favoured as Ku increases.

The comparison of our results for intermediate values of Ku with those by Boffetta *et al.* (2004) reveals yet another difference. In the compressible renewing flow, the clustering is reduced compared to the small-Ku case if the compressibility is small, but it is enhanced if the compressibility is large. This behaviour is the opposite of that found in the turbulent surface flow (figure 7). Moreover, in the renewing flow, the critical degree of compressibility is less than or equal to $1/2$ for all values of Ku; in the surface flow, it is significantly greater (figure 7). In the light of our findings, it would be interesting to examine the distribution of the stagnation points of the surface flow considered by Boffetta *et al.* (2004) and understand how it influences the statistics of clustering.

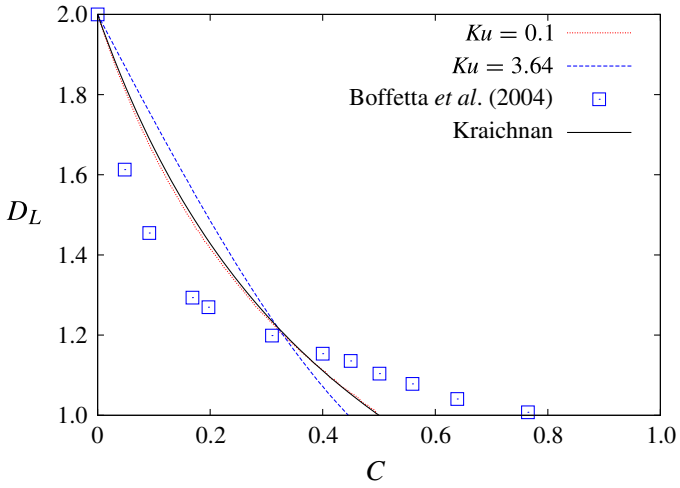

FIGURE 7. (Colour online) Lyapunov dimension D_L as a function of C for the Kraichnan model (solid curve; black) and for the compressible renewing flow with $Ku = 0.1$ (dotted curve; red online) and $Ku = 3.64$ (dashed curve; blue online). The square symbols are from the direct numerical simulation of a turbulent surface flow by Boffetta *et al.* (2004).

In conclusion, the differences between our findings and those obtained in different flows demonstrate that the properties of tracer dynamics in time-correlated compressible flows are strongly non-universal, to the extent that flows with comparable C and Ku can have an opposite effect on clustering. In particular, the level of clustering depends dramatically on the peculiar structures of the velocity field towards which tracers are attracted.

Acknowledgements

The authors are grateful to B. Mehlig and K. Gustavsson for useful discussions.

REFERENCES

ABRAHAM, E. R. 1998 The generation of plankton patchiness by turbulent stirring. *Nature* **391**, 577–580.

ALEXAKIS, A. & TZELLA, A. 2011 Bounding the scalar dissipation scale for mixing flows in the presence of sources. *J. Fluid Mech.* **688**, 443–460.

ANTONSEN, T. M. JR, FAN, Z., OTT, E. & GARCIA-LOPEZ, E. 1996 The role of chaotic orbits in the determination of power spectra of passive scalars. *Phys. Fluids* **8**, 3094–3104.

BEC, J., GAWĘDZKI, K. & HORVAI, P. 2004 Multifractal clustering in compressible flows. *Phys. Rev. Lett.* **92**, 224501.

BENETTIN, G., GALGANI, L., GIORGILLI, A. & STRELCYN, J.-M. 1980 Lyapunov characteristic exponents for smooth dynamical systems and for Hamiltonian systems. A method for computing all of them. Part 2: Numerical application. *Meccanica* **15**, 21–30.

BOFFETTA, G., DAVOUDI, J., ECKHARDT, B. & SCHUMACHER, J. 2004 Lagrangian tracers on a surface flow: the role of time correlations. *Phys. Rev. Lett.* **93**, 134501.

BOFFETTA, G., DAVOUDI, J. & DE LILLO, F. 2006 Multifractal clustering of passive tracers on a surface flow. *Europhys. Lett.* **74**, 62–68.

BOFFETTA, G., CELANI, A., DE LILLO, F. & MUSACCHIO, S. 2007 The Eulerian description of dilute collisionless suspension. *Europhys. Lett.* **78**, 140001.

CARDY, J., GAWĘDZKI, K. & FALKOVICH, G. 2008 *Non-equilibrium statistical mechanics and turbulence* (ed. S. Nazarenko & O. V. Zaboronski), London Mathematical Society Lecture Note Series, vol. 355. Cambridge University Press.

CHAVES, M., GAWĘDZKI, K., HORVAI, P., KUPIAINEN, A. & VERGASSOLA, M. 2003 Lagrangian dispersion in Gaussian self-similar velocity ensembles. *J. Stat. Phys.* **113**, 643–692.

CHERTKOV, M., KOLOKOLOV, I. & VERGASSOLA, M. 1998 Inverse versus direct cascades in turbulent advection. *Phys. Rev. Lett.* **80**, 512–515.

CRESSMAN, J. R., DAVOUDI, J., GOLDBURG, W. I. & SCHUMACHER, J. 2004 Eulerian and Lagrangian studies in surface flow turbulence. *New J. Phys.* **6**, 53.

CSANADY, G. T. 1973 *Turbulent Diffusion in the Environment*. Springer.

DUCASSE, L. & PUMIR, A. 2008 Intermittent particle distribution in synthetic free-surface turbulent flows. *Phys. Rev.* E **77**, 066304.

ELPERIN, T., KLEEORIN, N., ROGACHEVSKII, I. & SOKOLOFF, D. 2000 Passive scalar transport in a random flow with a finite renewal time: mean-field equations. *Phys. Rev.* E **61**, 2617–2625.

ELPERIN, T., KLEEORIN, N., L'VOV, V. S., ROGACHEVSKII, I. & SOKOLOFF, D. 2002 Clustering instability of the spatial distribution of inertial particles in turbulent flows. *Phys. Rev.* E **66**, 036302.

FALKOVICH, G., GAWĘDZKI, K. & VERGASSOLA, M. 2001 Particles and fields in fluid turbulence. *Rev. Mod. Phys.* **73**, 913–975.

FALKOVICH, G. & MARTINS AFONSO, M. 2007 Fluid–particle separation in a random flow described by the telegraph model. *Phys. Rev.* E **76**, 026312.

FALKOVICH, G., MUSACCHIO, S., PITERBARG, L. & VUCELJA, M. 2007 Inertial particles driven by a telegraph noise. *Phys. Rev.* E **76**, 026313.

GILBERT, A. D. & BAYLY, B. G. 1992 Magnetic field intermittency and fast dynamo action in random helical flows. *J. Fluid Mech.* **241**, 199–214.

GUSTAVSSON, K. & MEHLIG, B. 2013*a* Distribution of velocity gradients and rate of caustic formation in turbulent aerosols at finite Kubo numbers. *Phys. Rev.* E **87**, 023016.

GUSTAVSSON, K. & MEHLIG, B. 2013*b* Lyapunov exponents for particles advected in compressible random velocity fields at small and large Kubo numbers. *J. Stat. Phys.* **153**, 813–827.

KRAICHNAN, R. H. 1968 Small-scale structure of a scalar field convected by turbulence. *Phys. Fluids* **11**, 945–953.

LARKIN, J. & GOLDBURG, W. I. 2010 Decorrelating a compressible turbulent flow: an experiment. *Phys. Rev.* E **82**, 016301.

LARKIN, J., GOLDBURG, W. & BANDI, M. M. 2010 Time evolution of a fractal distribution: particle concentrations in free-surface turbulence. *Physica* D **239**, 1264–1268.

LE JAN, Y. 1984 Exposants de Lyapunov pour les mouvements browniens isotropes. *C. R. Acad. Sci. Paris Ser.* I **299**, 947–949.

LE JAN, Y. 1985 On isotropic Brownian motions. *Z. Wahrscheinlichkeitstheor. verw. Gebiete* **70**, 609–620.

LOVECCHIO, S., MARCHIOLI, C. & SOLDATI, A. 2013 Time persistence of floating-particle clusters in free-surface turbulence. *Phys. Rev.* E **88**, 033003.

MAXEY, M. R. 1987 The gravitational settling of aerosol particles in homogeneous turbulence and random flow fields. *J. Fluid Mech.* **174**, 441–465.

MUSACCHIO, S. & VINCENZI, D. 2011 Deformation of a flexible polymer in a random flow with long correlation time. *J. Fluid Mech.* **670**, 326–336.

PANDIT, R., PERLEKAR, P. & RAY, S. S. 2009 Statistical properties of turbulence: an overview. *Pramana – J. Phys.* **73**, 157–191.

PEREZ-MUNUZURI, V. 2014 Mixing and clustering in compressible chaotic stirred flows. *Phys. Rev.* E **89**, 022917.

PERGOLIZZI, B. 2012 Étude de la dynamique des particules inertielles dans des écoulements aléatoires. PhD thesis, Université Nice Sophia Antipolis.

PIERREHUMBERT, R. T. 1994 Tracer microstructure in the large-eddy dominated regime. *Chaos, Solitons Fractals* **4**, 1091–1110.

SCHUMACHER, J. & ECKHARDT, B. 2002 Clustering dynamics of Lagrangian tracers in free-surface flows. *Phys. Rev.* E **66**, 017303.

SOMMERER, J. C. & OTT, E. 1993 Particles floating on a moving fluid: a dynamically comprehensible physical fractal. *Science* **259**, 335–339.

THIFFEAULT, J.-L., DOERING, C. R. & GIBBON, J. D. 2004 A bound on mixing efficiency for the advection–diffusion equation. *J. Fluid Mech.* **521**, 105–114.

TOSCHI, F. & BODENSCHATZ, E. 2009 Lagrangian properties of particles in turbulence. *Annu. Rev. Fluid Mech.* **41**, 375–404.

VUCELJA, M., FALKOVICH, G. & FOUXON, I. 2007 Clustering of matter in waves and currents. *Phys. Rev.* E **75**, 065301.

WILKINSON, M. 2011 Lyapunov exponent for small particles in smooth one-dimensional flows. *J. Phys.* A **44**, 045502.

YOUNG, W. R. 1999 *Stirring and Mixing: Proceedings of the 1999 Summer Program in Geophysical Fluid Dynamics* (ed. J.-L. Thiffeault & C. Pasquero), Woods Hole Oceanographic Institution.

ZEL'DOVICH, YA. B., RUZMAIKIN, A. A., MOLCHANOV, S. A. & SOKOLOFF, D. D. 1984 Kinematic dynamo problem in a linear velocity field. *J. Fluid Mech.* **144**, 1–11.

Annexe B

Rotation

B1. D. Vincenzi
Orientation of non-spherical particles in an axisymmetric random flow
J. Fluid Mech. **719**, 465–487 (2013)

B2. A. Gupta, D. Vincenzi & R. Pandit
Elliptical tracers in two-dimensional, homogeneous, isotropic fluid turbulence : the statistics of alignment, rotation, and nematic order
Phys. Rev. E **89**, 021001(R) (2014)

J. Fluid Mech. (2013), *vol.* 719, *pp.* 465–487.
doi:10.1017/jfm.2013.8

Orientation of non-spherical particles in an axisymmetric random flow

Dario Vincenzi†

CNRS UMR 7351, Laboratoire J.-A. Dieudonné, Université de Nice Sophia Antipolis, Parc Valrose, 06108 Nice, France

(Received 3 June 2012; revised 16 October 2012; accepted 25 December 2012)

The dynamics of non-spherical rigid particles immersed in an axisymmetric random flow is studied analytically. The motion of the particles is described by Jeffery's equation; the random flow is Gaussian and has short correlation time. The stationary probability density function of orientations is calculated exactly. Four regimes are identified depending on the statistical anisotropy of the flow and on the geometrical shape of the particle. If $\boldsymbol{\lambda}$ is the axis of symmetry of the flow, the four regimes are: rotation about $\boldsymbol{\lambda}$, tumbling motion between $\boldsymbol{\lambda}$ and $-\boldsymbol{\lambda}$, combination of rotation and tumbling, and preferential alignment with a direction oblique to $\boldsymbol{\lambda}$.

Key words: multiphase and particle-laden flows, suspensions

1. Introduction

Non-spherical solid particles suspended in a moving fluid rotate and orient themselves under the action of the velocity gradient. Even at low concentrations, the orientational dynamics of non-spherical particles can influence the rheological properties of a suspension, namely the intrinsic viscosity and the normal stress coefficients (Bird *et al.* 1977; Larson 1999). This phenomenon has diverse practical applications. In the turbulent regime, for instance, the injection of rod-like polymers in a Newtonian fluid can produce a considerable reduction of the turbulent drag, with this effect being routinely exploited to reduce energy losses in pipelines (Gyr & Bewersdorff 1995). The study of the orientation of non-spherical particles in a fluid flow also has numerous applications in the natural sciences. Amongst them it is worth mentioning the swimming motion of certain biological micro-organisms (Saintillan & Shelley 2008; Koch & Subramanian 2011) and the formation of ice crystals in clouds (Chen & Lamb 1994). This latter phenomenon plays a crucial role in processes such as rain initiation and radiative transfer.

The starting point for understanding the properties of a dilute suspension is the motion of an isolated particle in a given flow field. Analytical results on the dynamics of a non-spherical particle have been obtained for various laminar flows, both steady and unsteady. Jeffery (1922) derived the equations of motion for an inertialess ellipsoid in a steady uniform shear flow at low Reynolds number. For a spheroid (i.e. an ellipsoid of revolution), Jeffery showed that the axis of symmetry of the particle performs a periodic motion on a closed orbit. Bretherton (1962) subsequently extended

† Email address for correspondence: dario.vincenzi@unice.fr

Jeffery's analysis to particles of a more general shape: he demonstrated that, except for certain very long particles, the dynamics of any body of revolution transported by a low-Reynolds-number shear is equivalent to that of a spheroid with an effective aspect ratio. Amongst bodies of revolution, rigid dumbbells and rods have been systematically investigated as prototypes of elongated particles (Bird, Warner & Evans 1971; Doi & Edwards 1986).

In Jeffery's (1922) and Bretherton's (1962) derivations, not only are fluid and particle inertia disregarded, but also Brownian fluctuations due to the collisions of the molecules of the fluid with the particles. Nevertheless, if a particle is sufficiently small, molecular diffusion does influence its orientational dynamics, as was shown by Leal & Hinch (1971) and Hinch & Leal (1972). The review article by Brenner (1974) collects analytical results on the motion of rigid neutrally buoyant bodies of revolution subject to a uniform velocity gradient and to Brownian fluctuations – a more recent review on this problem can be found in Petrie (1999). Finally, even in simple laminar flows, the orientation of particles can form complex patterns; this behaviour was studied by Szeri (1993) in the context of the theory of dynamical systems.

In turbulent flows and in some chaotic flows, the velocity gradient exhibits small-scale fluctuations. Thus, if a particle is larger than the Kolmogorov scale ℓ_K, the velocity gradient can vary appreciably over the size of the particle and Jeffery's assumption of a spatially uniform velocity gradient does not apply. The probability of orientations of particles larger than ℓ_K has been measured experimentally by Parsheh, Brown & Aidun (2005), Parsa *et al.* (2011), Zimmermann *et al.* (2011*a*,*b*) and Parsa *et al.* (2012) (in these experiments, the size of the particles ranged from a few ℓ_K to two orders of magnitude greater than ℓ_K). Jeffery's approach, however, remains applicable to turbulent flows if the particles are much smaller than ℓ_K, since below this scale viscosity smooths out the velocity fluctuations and hence the velocity gradient can be assumed as spatially uniform. The orientation dynamics of such small particles has been studied experimentally in atmospheric flows (Krushkal & Gallily 1988; Newsom & Bruce 1998) and in water-tunnel flows (Bernstein & Shapiro 1994), as well as numerically in turbulent channel flows (Zhang *et al.* 2001; Mortensen *et al.* 2008*a*,*b*), in isotropic turbulence (Shin & Koch 2005; Pumir & Wilkinson 2011; Parsa *et al.* 2012), and in chaotic velocity fields (Wilkinson, Bezuglyy & Mehlig 2009). Theoretical studies were mainly concerned with the derivation of model equations for the probability of orientations, in which turbulent fluctuations were described by an effective isotropic diffusion term (e.g. Krushkal & Gallily 1988; Olson & Kerekes 1998; Shin & Koch 2005). In contrast with the case of laminar flows, few analytical results seem to exist for the probability distribution of orientations in turbulent or chaotic flows. Turitsyn (2007) examined the tumbling motion of rod-like polymers in a random flow resulting from the superposition of a mean shear and of short-correlated isotropic fluctuations. Wilkinson & Kennard (2012) recently studied the alignment of rods with vorticity in an isotropic random flow.

Here, the probability density function (p.d.f.) of orientations is derived exactly for non-spherical particles transported by a homogeneous random flow with axisymmetric statistics. The particles are general bodies of revolution possessing fore–aft symmetry. The axisymmetry of the flow means that the velocity field is statistically invariant under arbitrary rotations of the axes about a given direction as well as under reflections in planes containing that direction or normal to it (Batchelor 1946; Chandrasekhar 1950). Axisymmetry is the simplest form of statistical anisotropy (Biferale & Procaccia 2005; Chang, Bewley & Bodenschatz 2012), and is found in rotating, stratified, or wind-tunnel turbulence (Lindborg 1995). Furthermore, the

random flow is assumed to be Gaussian and to have zero correlation time. The assumption of temporal decorrelation is adequate when the correlation time of the flow is short compared to the characteristic time scale of material-line-element stretching. This assumption, albeit restrictive, allows a fully analytical solution of the problem.

The evolution equation for the orientation vector of a non-spherical rigid particle is introduced in § 2. Section 3 is devoted to the derivation of the convection–diffusion equation for the p.d.f. of the orientation angle. The steady-state orientation dynamics is studied in § 4. Some conclusions are drawn in § 5.

2. Orientation dynamics

The particles considered here are rigid bodies of revolution possessing fore–aft symmetry (although in the literature such particles are commonly referred to as 'axisymmetric', this terminology will be avoided here so as not to generate confusion; the term 'axisymmetry' will be reserved for the statistical invariance of the velocity field). The particles are of uniform composition and are suspended in a Newtonian fluid of the same density. Furthermore, the inertia of the particles as well as hydrodynamic particle–particle interactions are disregarded, and no externally imposed force or couple influences the dynamics. In particular, it is appropriate to disregard hydrodynamic interactions when the suspension is sufficiently dilute.

The undisturbed motion of the fluid is described by the velocity field $\boldsymbol{v}(\boldsymbol{x}, t)$. The size of the particles is assumed to be small compared to the typical length over which the velocity gradient $\boldsymbol{\nabla v} = (\partial_j v_i)_{1\leqslant i,j\leqslant 3}$ changes ($\partial_j \equiv \partial/\partial x_j$). For turbulent flows, this means that the particles are smaller than the Kolmogorov scale, and thus the Reynolds number at the scale of a particle is less than 1. Given their small size, the particles also experience Brownian collisions with the molecules of the fluid.

In a sufficiently dilute suspension, attention can be restricted to the dynamics of a single isolated particle. The configuration of a body of revolution is determined by the position of its centre of mass, $\boldsymbol{r}_c(t)$, and by the orientation of its axis of revolution, which is specified by a unit vector $\boldsymbol{N}(t)$ parallel to the axis itself. As the particles are subject to Brownian fluctuations, their dynamics is random even in a laminar flow. Consider first a deterministic velocity field or a given realization of a random velocity field. On the above assumptions, the centre of mass moves according to the following equation (e.g. Doi & Edwards 1986):

$$\dot{\boldsymbol{r}}_c(t) = \boldsymbol{v}(\boldsymbol{r}_c(t), t) + \sqrt{D_T}\,\boldsymbol{\zeta}(t), \tag{2.1}$$

where $D_T > 0$ is the translational diffusion coefficient and $\boldsymbol{\zeta}(t)$ is three-dimensional white noise, i.e. a Gaussian stochastic process with

$$\langle \boldsymbol{\zeta}(t) \rangle = 0 \quad \text{and} \quad \langle \zeta_i(t+\tau)\zeta_j(t) \rangle = \delta_{ij}\delta(\tau) \tag{2.2}$$

for all $t, \tau > 0$ and $i, j = 1, 2, 3$. The orientation vector satisfies the following stochastic differential equation (summation over repeated indexes is implied):

$$\dot{N}_i = \kappa_{ij}(t)N_j - \kappa_{pq}(t)\frac{N_p N_q}{|\boldsymbol{N}|^2}N_i + \sqrt{D_R}\,\Sigma_{ij}(\boldsymbol{N}) \circ \xi_j(t), \quad |\boldsymbol{N}(0)| = 1, \tag{2.3}$$

where

$$\boldsymbol{\kappa}(t) = \boldsymbol{\Omega}(t) + \gamma \boldsymbol{E}(t) \tag{2.4}$$

with

$$\boldsymbol{\Omega}(t) = \frac{\boldsymbol{G}(t) - \boldsymbol{G}^{\mathrm{T}}(t)}{2}, \quad \boldsymbol{E}(t) = \frac{\boldsymbol{G}(t) + \boldsymbol{G}^{\mathrm{T}}(t)}{2}, \tag{2.5}$$

and $\boldsymbol{G}(t) = \nabla \boldsymbol{v}(\boldsymbol{r}_c(t), t)$. Thus, $\boldsymbol{\Omega}(t)$ and $\boldsymbol{E}(t)$ are the vorticity tensor and the rate-of-strain tensor evaluated at $\boldsymbol{r}_c(t)$, and $\boldsymbol{\kappa}(t)$ is an effective Lagrangian velocity gradient. The scalar constant γ describes the strain efficiency in orienting the particle and depends on the geometrical shape of the particle itself. For $|\gamma| < 1$, the evolution equation can be mapped into that of a spheroid with aspect ratio equal to $\sqrt{(1+\gamma)/(1-\gamma)}$ (Bretherton 1962). Prolate spheroids are obtained for $0 < \gamma < 1$, oblate spheroids for $-1 < \gamma < 0$. Special cases are: spheres ($\gamma = 0$), rigid dumbbells ($\gamma = 1$), rods ($\gamma = 1$), and disks ($\gamma = -1$). Moreover, Bretherton (1962) demonstrated the existence of geometrical shapes for which $|\gamma| > 1$; he provided an example consisting of two non-spherical bodies of revolution connected by a long and thin rigid rod (see figure 5 in Bretherton 1962), even though he observed that the required length and thickness may be unrealistic for a rigid particle.

In (2.3), the random vector $\boldsymbol{\xi}(t)$ is three-dimensional white noise and hence has the same properties as $\boldsymbol{\zeta}(t)$, but is statistically independent of it. The matrix $\boldsymbol{\Sigma}(\boldsymbol{n})$ has the following form:

$$\boldsymbol{\Sigma}(\boldsymbol{n}) = \boldsymbol{I} - \boldsymbol{n}\boldsymbol{n}/|\boldsymbol{n}|^2 \tag{2.6}$$

and $D_R > 0$ is the rotary diffusion coefficient. By using the Cauchy–Schwarz inequality, it is easy to check that $\boldsymbol{\Sigma}(\boldsymbol{n})$ is positive semi-definite. Finally, the symbol $\circ$ indicates that the stochastic term in (2.3) is understood in the Stratonovich sense.

Equation (2.3) is Jeffery's equation for the orientation vector of a body of revolution with the addition of a stochastic term modelling Brownian fluctuations. The stochastic term is chosen in such a way as to produce isotropic diffusion of $\boldsymbol{N}(t)$ on the unit sphere, so that $|\boldsymbol{N}(t)|$ is preserved in time (see appendix A for more details). It is worth remarking that a Brownian term of the same form has been used to model the turbulent fluctuations of the velocity gradient (Krushkal & Gallily 1988; Olson & Kerekes 1998; Shin & Koch 2005) or to describe particle–particle interactions both in semi-dilute suspensions (Doi & Edwards 1986) and in concentrated suspensions (Doi & Edwards 1978; Kuzuu & Doi 1980).

Equation (2.3) can be generalized to the case of a homogeneous axisymmetric random flow. The velocity field transporting the particle is Gaussian and has zero mean and correlation:

$$\langle v_i(\boldsymbol{x} + \boldsymbol{r}, t + \tau) v_j(\boldsymbol{x}, t) \rangle = Q_{ij}(\boldsymbol{r}) \delta(\tau), \quad i, j = 1, 2, 3. \tag{2.7}$$

The form of the correlation guarantees that $\boldsymbol{v}(\boldsymbol{x}, t)$ is statistically homogeneous in space. Additionally, the velocity field is assumed to be incompressible ($\nabla \cdot \boldsymbol{v} = 0$) and statistically axisymmetric with respect to the direction specified by the unit vector $\boldsymbol{\lambda}$. The tensor $\boldsymbol{Q}(\boldsymbol{r})$ must then take the form:

$$Q_{ij}(\boldsymbol{r}) = A r_i r_j + B \delta_{ij} + C \lambda_i \lambda_j + D(r_i \lambda_j + \lambda_i r_j), \tag{2.8}$$

where A, B and C are smooth functions of r^2 and $\mu^2 r^2$ with $r = |\boldsymbol{r}|$ and $\mu = (\boldsymbol{r} \cdot \boldsymbol{\lambda})/r$, while D is a function of r^2 and μr, being odd in μr (Batchelor 1946; Chandrasekhar 1950). As a consequence of incompressibility, the functions A, B, C, D are not

independent and satisfy certain differential relations (Batchelor 1946; Chandrasekhar 1950). Moreover, the expansion of these functions for small values of r is (Batchelor 1946, p. 486):

$$A = a + O\left(r^2\right), \tag{2.9a}$$

$$B = B_0 - \tfrac{1}{2}\left(4a + d - b\mu^2\right) r^2 + O\left(r^4\right), \tag{2.9b}$$

$$C = C_0 - \tfrac{1}{2}(b + c + 5d - c\mu^2)r^2 + O\left(r^4\right), \tag{2.9c}$$

$$D = \mu r\left[d + O\left(r^2\right)\right], \tag{2.9d}$$

where a, b, c, d and B_0, C_0 are real constants. The velocity field defined above is an axisymmetric generalization of the isotropic random flow introduced by Kraichnan (1968) in the context of passive turbulent transport. The same axisymmetric velocity field was used by Shaqfeh & Koch (1992) to study polymer stretching in flows through random beds of fibres.

The velocity gradient is also Gaussian and zero-mean. The single-point two-time correlation of the components of $\boldsymbol{\nabla v}$ can be derived from (2.7) by using the statistical homogeneity of the velocity field:

$$\langle \partial_j v_i(\boldsymbol{x}, t+\tau)\partial_q v_p(\boldsymbol{x}, t)\rangle = \Gamma_{ijpq}\delta(\tau), \quad i, j, p, q = 1, 2, 3, \tag{2.10}$$

where

$$\Gamma_{ijpq} \equiv 2\int_0^\infty \langle \partial_j v_i(\boldsymbol{x}, t+\tau)\partial_q v_p(\boldsymbol{x}, t)\rangle \,\mathrm{d}\tau \tag{2.11}$$

is the time integral of the correlation of the components of $\boldsymbol{\nabla v}$ and satisfies:

$$\Gamma_{ijpq} = -\frac{\partial^2 Q_{ip}}{\partial r_j \partial r_q}\bigg|_{\boldsymbol{r}=0}. \tag{2.12}$$

Thus, $\boldsymbol{\nabla v}$ is a tensorial white noise with diffusion tensor $\boldsymbol{\Gamma}$. In particular, Γ_{ijij} (no summation) gives the amplitude of the fluctuations of $\partial_j v_i$. Substituting (2.8) and (2.9) into (2.12) yields (see (5.12) in Batchelor 1946):

$$\begin{aligned}\Gamma_{ijpq} = {} & (d + 4a)\delta_{jq}\delta_{ip} - a(\delta_{pq}\delta_{ij} + \delta_{iq}\delta_{pj}) + (b + c + 5d)\delta_{jq}\lambda_i\lambda_p - b\delta_{ip}\lambda_j\lambda_q \\ & - d[(\delta_{pq}\lambda_i + \delta_{iq}\lambda_p)\lambda_j + (\delta_{pj}\lambda_i + \delta_{ij}\lambda_p)\lambda_q] - c\lambda_i\lambda_p\lambda_j\lambda_q.\end{aligned} \tag{2.13}$$

For the sake of simplicity, $\boldsymbol{\lambda}$ is taken in the direction of the third axis, i.e. $\boldsymbol{\lambda} = (0, 0, 1)$. Then, the coefficients a, b, c, d are related to the time integrals of the correlations of the components of $\boldsymbol{\nabla v}$ (see (2.11)) as follows:

$$a = \tfrac{1}{2}\left(\Gamma_{1212} - \Gamma_{1111}\right), \quad d = \Gamma_{3333} - \Gamma_{1111}, \tag{2.14a}$$

$$b = \Gamma_{1212} - \Gamma_{1313}, \quad 2a + b + c + 4d = \Gamma_{3131} - \Gamma_{3333}. \tag{2.14b}$$

Note that the two-time correlation of the components of the vorticity $\boldsymbol{\omega} = \boldsymbol{\nabla} \times \boldsymbol{v}$ can be expressed in terms of a, c and d (Batchelor 1946, p. 490):

$$\langle \omega_1(\boldsymbol{x}, t+\tau)\omega_1(\boldsymbol{x}, t)\rangle = \langle \omega_2(\boldsymbol{x}, t+\tau)\omega_2(\boldsymbol{x}, t)\rangle = (10a + c + 9d)\delta(\tau) \tag{2.15}$$

and

$$\langle \omega_3(\boldsymbol{x}, t+\tau)\omega_3(\boldsymbol{x}, t)\rangle = (10a + 2d)\delta(\tau). \tag{2.16}$$

Moreover, the coefficients a, b, c, d in (2.13) are not free; they are constrained by the following inequalities (see appendix C):

$$\left.\begin{array}{ll} a+d>0 & \text{if } a \geqslant 0, \\ 5a+d>0 & \text{if } a<0, \end{array}\right\} \tag{2.17a}$$

$$4a-b+d>0, \quad 4a+b+c+6d>0, \tag{2.17b}$$

$$15a^2-b^2-(b-d)(c+5d)+2a(2c+13d)>0. \tag{2.17c}$$

If $a>0$ and $b=c=d=0$, then Γ_{ijpq} gives the single-point correlation of the gradient of an isotropic velocity field (Robertson 1940). Thus, a determines the intensity of the isotropic part of $\boldsymbol{\nabla v}$, while b, c, d control the statistical anisotropy of the flow.

Note that an alternative representation of the tensor $\boldsymbol{Q}$ was proposed by Lindborg (1995). The relation between (2.13) and Lindborg's representation is given in appendix B.

The orientation dynamics of the particle depends on the velocity gradient evaluated at $\boldsymbol{r}_c(t)$, which was denoted as $\boldsymbol{G}(t)$ in § 2. By virtue of the δ-correlation in time and the statistical homogeneity of the flow, $\boldsymbol{G}(t)$ has the same temporal statistics as $\boldsymbol{\nabla v}(\boldsymbol{x}, t)$ for any given $\boldsymbol{x}$ (Falkovich, Gawędzki & Vergassola 2001) (the presence of white noise in (2.1) does not modify the statistics of $\boldsymbol{G}(t)$). The components of $\boldsymbol{\kappa}(t)$, defined in (2.4), are a linear combination of the components of $\boldsymbol{G}(t)$, and consequently $\boldsymbol{\kappa}(t)$ is a Gaussian process with zero mean and correlation:

$$\langle \kappa_{ij}(t+\tau)\kappa_{pq}(t)\rangle = K_{ijpq}\delta(\tau) \tag{2.18}$$

with

$$\begin{aligned} K_{ijpq} = \tfrac{1}{4}[&\Gamma_{ijpq}-\Gamma_{ijqp}-\Gamma_{jipq}+\Gamma_{jiqp}+2\gamma(\Gamma_{ijpq}-\Gamma_{jiqp}) \\ &+\gamma^2(\Gamma_{ijpq}+\Gamma_{ijqp}+\Gamma_{jipq}+\Gamma_{jiqp})]. \end{aligned} \tag{2.19}$$

The form of K_{ijpq} can be derived by substituting (2.4) and (2.5) into the left-hand side of (2.18) and by using (2.10). The tensor K_{ijpq} is positive semi-definite, for it is the covariance of a second-order Gaussian tensor. Thus, in the evolution equation for the orientation vector, $\boldsymbol{\kappa}(t)$ plays the role of a multiplicative tensorial white noise. As $\boldsymbol{\kappa}(t)$ can be thought of as an approximation of a real noise process in the limit of zero correlation time, the corresponding terms in (2.3) must be interpreted in the Stratonovich sense (e.g. Kloeden & Platen 1992, p. 227). The stochastic differential equation for $\boldsymbol{N}(t)$ can then be rewritten as follows:

$$\dot{N}_i = M_{ipq}(\boldsymbol{N}) \circ \kappa_{pq}(t) + \sqrt{D_R}\,\Sigma_{ij}(\boldsymbol{N}) \circ \xi_j(t), \tag{2.20}$$

where $M_{ipq}(\boldsymbol{n}) = (\delta_{ip}\delta_{jk}-\delta_{ik}\delta_{jp})n_j n_k n_q/|\boldsymbol{n}|^2$ and the initial condition $\boldsymbol{N}(0)$ is such that $|\boldsymbol{N}(0)|=1$.

3. Convection–diffusion equation for the probability density function of the orientation angle

As $\boldsymbol{v}(\boldsymbol{x}, t)$ is statistically invariant under spatial translations, the p.d.f. of $\boldsymbol{N}(t)$ taking the value $\boldsymbol{n}=(n_1, n_2, n_3)$ at time t is independent of $\boldsymbol{r}_c$ and is thus denoted by $f(\boldsymbol{n}; t)$. The Itô equation equivalent to (2.20) is

$$\dot{N}_i = \beta_i(\boldsymbol{N}) + M_{ipq}(\boldsymbol{N})\kappa_{pq}(t) + \sqrt{D_R}\,\Sigma_{ij}(\boldsymbol{N})\xi_j(t) \tag{3.1}$$

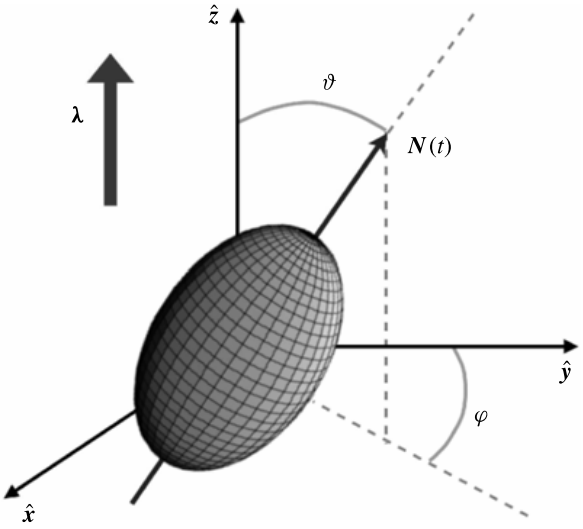

FIGURE 1. Orientation of a non-spherical particle.

with

$$\beta_i(\boldsymbol{n}) = \frac{1}{2} K_{mnpq} M_{jpq}(\boldsymbol{n}) \frac{\partial}{\partial n_j} M_{imn}(\boldsymbol{n}) + \frac{D_R}{2} \Sigma_{jk}(\boldsymbol{n}) \frac{\partial}{\partial n_j} \Sigma_{ik}(\boldsymbol{n}). \tag{3.2}$$

Consequently, $f(\boldsymbol{n}; t)$ satisfies the Fokker–Planck equation:

$$\frac{\partial f}{\partial t} = -\frac{\partial}{\partial n_i} [\beta_i(\boldsymbol{n}) f] + \frac{1}{2} \frac{\partial^2}{\partial n_i \partial n_j} [\alpha_{ij}(\boldsymbol{n}) f] \tag{3.3}$$

with

$$\begin{aligned} \alpha_{ij}(\boldsymbol{n}) &= K_{mnpq} M_{imn}(\boldsymbol{n}) M_{jpq}(\boldsymbol{n}) + D_R \Sigma_{ik}(\boldsymbol{n}) \Sigma_{jk}(\boldsymbol{n}) \\ &= K_{mnpq} M_{imn}(\boldsymbol{n}) M_{jpq}(\boldsymbol{n}) + D_R \Sigma_{ij}(\boldsymbol{n}), \end{aligned} \tag{3.4}$$

where the last equality follows from (A 3) in appendix A. Equations (3.1) and (3.3) can be derived from (2.20) by using the formal rules $\kappa_{ij}(t)\,\mathrm{d}t = O(\sqrt{\mathrm{d}t})$ and $\kappa_{ij}(t)\,\mathrm{d}t\,\kappa_{pq}(t)\,\mathrm{d}t = K_{ijpq}\,\mathrm{d}t$ and by proceeding as in the case of a vectorial white noise (see Gardiner 1983 and the appendix in Falkovich *et al.* 2001). The diffusion tensor $\boldsymbol{\alpha}$ is positive semi-definite as a consequence of the positive semi-definiteness of $\boldsymbol{K}$ and $\boldsymbol{\Sigma}$.

To study the orientation dynamics of a non-spherical particle, it is convenient to move from Cartesian coordinates (n_1, n_2, n_3) to spherical coordinates (n, ϑ, φ) according to the usual transformations:

$$n = \sqrt{n_1^2 + n_2^2 + n_3^2}, \quad \vartheta = \arctan\left(\sqrt{n_1^2 + n_2^2}/n_3\right), \quad \varphi = \arctan(n_2/n_1) \tag{3.5}$$

with $0 \leqslant n$, $0 \leqslant \vartheta \leqslant \pi$, and $0 \leqslant \varphi < 2\pi$ (figure 1). On account of the fixed length of the orientation vector, the probability density function of orientations must take the form $f(n, \vartheta, \varphi; t) = \psi(\vartheta, \varphi; t)\delta(n - L)$ with $L = 1$. Thus, $\psi(\vartheta, \varphi; t) \sin\vartheta\,\mathrm{d}\vartheta\,\mathrm{d}\varphi$ is the probability of the particle being oriented at time t within an elementary solid

angle $\sin\vartheta\,\mathrm{d}\vartheta\,\mathrm{d}\varphi$ of (ϑ,φ). In addition, the following normalization holds:

$$\int_0^{\pi}\int_0^{2\pi}\psi(\vartheta,\varphi;t)\sin\vartheta\,\mathrm{d}\vartheta\,\mathrm{d}\varphi=1\quad\forall\,t\geqslant 0. \tag{3.6}$$

The function $\psi(\vartheta,\varphi;t)$ satisfies the convection–diffusion equation (see appendix D for the derivation):

$$\frac{\partial\psi}{\partial t}=\frac{1}{\sin\vartheta}\frac{\partial}{\partial\vartheta}\left\{\sin\vartheta\left[-\mathscr{W}_{\vartheta}(\vartheta)\psi+\frac{1}{2}\mathscr{D}_{\vartheta\vartheta}(\vartheta)\frac{\partial\psi}{\partial\vartheta}\right]\right\}+\frac{\mathscr{D}_{\varphi\varphi}(\vartheta)}{2\sin^2(\vartheta)}\frac{\partial^2\psi}{\partial\varphi^2}, \tag{3.7}$$

where

$$\mathscr{W}_{\vartheta}(\vartheta)=\tfrac{1}{4}\sin(2\vartheta)[2\nu_2-3\nu_4-3\nu_3\sin^2(\vartheta)] \tag{3.8}$$

and

$$\mathscr{D}_{\vartheta\vartheta}(\vartheta)=2\nu_1+\nu_4\sin^2(\vartheta)+\nu_3\sin^4(\vartheta), \tag{3.9a}$$

$$\mathscr{D}_{\varphi\varphi}(\vartheta)=2\nu_1+\nu_5\sin^2(\vartheta) \tag{3.9b}$$

with

$$\nu_1=\tfrac{1}{8}\left[2(5+3\gamma^2)a-4\gamma b+(1-\gamma)^2c+(9-10\gamma+5\gamma^2)d+4D_R'\right], \tag{3.10a}$$

$$\nu_2=\tfrac{3}{4}\gamma\left[2b+(1-\gamma)c+(5-\gamma)d\right], \tag{3.10b}$$

$$\nu_3=c\gamma^2, \tag{3.10c}$$

$$\nu_4=\gamma[2b+(1-\gamma)c+5d], \tag{3.10d}$$

$$\nu_5=\tfrac{1}{4}\left[4b\gamma-(1-\gamma)^2c-(1-\gamma)(7-3\gamma)d\right], \tag{3.10e}$$

and $D_R'=D_R/L^2$ with $L=1$ (the numerical values of D_R' and D_R coincide, but their physical dimensions are different).

Inequalities (2.17) guarantee that $\mathscr{D}_{\vartheta\vartheta}(\vartheta)$ and $\mathscr{D}_{\varphi\varphi}(\vartheta)$ are strictly positive (appendix C). The contribution to (3.7) due to the isotropic part of $\boldsymbol{\Gamma}$ is a diffusion term with diffusion coefficient proportional to a; this contribution is of the same form as that coming from $\boldsymbol{\xi}(t)$. The isotropic component of the flow and the Brownian fluctuations therefore have the same effect on the orientation statistics of the particle. Note that $\mathscr{W}_{\vartheta}(\vartheta)$ plays the role of an apparent drift velocity; its explicit expression is:

$$\mathscr{W}_{\vartheta}(\vartheta)=\tfrac{3}{8}\gamma\sin(2\vartheta)[c\gamma\cos(2\vartheta)-2b-c-(5+\gamma)d]. \tag{3.11}$$

Also observe that $\mathscr{W}_{\vartheta}(\vartheta)$ does not depend on a, and hence the convective term in (3.7) vanishes for an isotropic flow.

As ϑ and φ are angular variables, the boundary conditions for $\psi(\vartheta,\varphi;t)$ are periodic:

$$\psi(\vartheta,\varphi;t)=\psi(\vartheta+2\pi,\varphi;t)\quad\text{and}\quad\psi(\vartheta,\varphi;t)=\psi(\vartheta,\varphi+2\pi;t) \tag{3.12}$$

for all ϑ, φ, and t. The long-time properties of $\psi(\vartheta,\varphi;t)$ can be deduced from (3.7). If the partial derivative with respect to time is dropped, then (3.7) is invariant under the transformations $\vartheta\leftrightarrow 2\pi-\vartheta$ (reflections with respect to planes containing $\boldsymbol{\lambda}$) and $\vartheta\leftrightarrow\pi-\vartheta$ (reflections with respect to planes orthogonal to $\boldsymbol{\lambda}$). Furthermore, the coefficients $\mathscr{W}_{\vartheta}$, $\mathscr{D}_{\vartheta\vartheta}$ and $\mathscr{D}_{\varphi\varphi}$ do not depend on φ (invariance under rotations about $\boldsymbol{\lambda}$). These properties of (3.7) are a natural consequence of the statistical axisymmetry of the velocity field and translate into analogous properties of the stationary p.d.f. of orientations.

The invariance of (3.7) under rotations about $\boldsymbol{\lambda}$ can be used to derive a one-dimensional convection–diffusion equation for the marginal p.d.f.: $\widehat{\psi}(\vartheta; t) \equiv \int_0^{2\pi} \psi(\vartheta, \varphi; t)\, \mathrm{d}\varphi$. Indeed, integrating (3.7) with respect to φ from 0 to 2π and making use of (3.12) yields:

$$\frac{\partial \widehat{\psi}}{\partial t} = \frac{1}{\sin\vartheta}\frac{\partial}{\partial \vartheta}\left\{\sin\vartheta\left[-\mathscr{W}_\vartheta(\vartheta)\widehat{\psi} + \frac{1}{2}\mathscr{D}_{\vartheta\vartheta}(\vartheta)\frac{\partial \widehat{\psi}}{\partial \vartheta}\right]\right\}. \tag{3.13}$$

The solution of the above equation must be normalized and periodic: $\widehat{\psi}(\vartheta; t) = \widehat{\psi}(\vartheta + 2\pi; t)$ for all ϑ, t. A direct consequence of (3.13) is that, along the trajectory of the particle, the time evolution of $\vartheta(t)$ is decoupled from that of $\varphi(t)$ and is described by the Itô stochastic ordinary differential equation (see appendix D):

$$\dot{\vartheta}(t) = \mathscr{B}_\vartheta(\vartheta(t)) + \sqrt{\mathscr{D}_{\vartheta\vartheta}(\vartheta(t))}\,\eta(t), \quad 0 \leqslant \vartheta(t) \leqslant \pi, \tag{3.14}$$

where $\eta(t)$ is white noise and

$$\mathscr{B}_\vartheta(\vartheta) = \mathscr{W}_\vartheta(\vartheta) + \frac{1}{2\sin\vartheta}\frac{\partial}{\partial\vartheta}[\mathscr{D}_{\vartheta\vartheta}(\vartheta)\sin\vartheta]. \tag{3.15}$$

4. Stationary statistics of the orientation angle

It was argued in § 3 that the stationary solution of (3.7), ψ_{st}, does not depend on φ. Therefore, ψ_{st} solves the equation:

$$\frac{\mathrm{d}}{\mathrm{d}\vartheta}\left\{\sin\vartheta\left[-\mathscr{W}_\vartheta(\vartheta)\psi_{st} + \frac{1}{2}\mathscr{D}_{\vartheta\vartheta}(\vartheta)\frac{\mathrm{d}\psi_{st}}{\mathrm{d}\vartheta}\right]\right\} = 0. \tag{4.1}$$

Thanks to the periodic boundary conditions (3.12), $\psi_{st}(\vartheta)$ can be calculated by equating the term in square brackets in (4.1) to zero (see appendix D), whence:

$$\psi_{st}(\vartheta) = \mathscr{N}\exp\left[2\int_{\vartheta_0}^{\vartheta}\frac{\mathscr{W}_\vartheta(s)}{\mathscr{D}_{\vartheta\vartheta}(s)}\,\mathrm{d}s\right], \tag{4.2}$$

where $0 \leqslant \vartheta_0 \leqslant \pi$ and $\mathscr{N}$ is a positive normalization constant such that

$$2\pi\int_0^\pi \psi_{st}(\vartheta)\sin\vartheta\,\mathrm{d}\vartheta = 1. \tag{4.3}$$

In (4.2), the choice of ϑ_0 is in fact unimportant, since it only modifies the value of $\mathscr{N}$.

Only the case $\nu_3 \neq 0$ is considered here; the case $\nu_3 = 0$ is examined in appendix E, even though no new physical regimes emerge when ν_3 is equal to zero. For $\nu_3 \neq 0$, the integral on the right-hand side of (4.2) can be calculated explicitly (see appendix D). The final result is:

$$\psi_{st}(\vartheta) = \frac{\mathscr{N}\chi(\vartheta)}{[\mathscr{D}_{\vartheta\vartheta}(\vartheta)]^{3/4}}, \tag{4.4}$$

where

$$\chi(\vartheta)=\begin{cases}\exp\left\{\dfrac{2}{\sqrt{\Delta}}\left(\nu_2-\dfrac{3}{4}\nu_4\right)\arctan\left[\dfrac{\nu_4+2\nu_3\sin^2(\vartheta)}{\sqrt{\Delta}}\right]\right\} & (\Delta>0)\\ \exp\left\{\left(\dfrac{3}{4}\nu_4-\nu_2\right)\dfrac{2}{\nu_4+2\nu_3\sin^2(\vartheta)}\right\} & (\Delta=0)\\ \left|\dfrac{\sqrt{-\Delta}+\nu_4+2\nu_3\sin^2(\vartheta)}{\sqrt{-\Delta}-\nu_4-2\nu_3\sin^2(\vartheta)}\right|^{(3\nu_4/4-\nu_2)/\sqrt{-\Delta}} & (\Delta<0)\end{cases}\tag{4.5}$$

with $\Delta=8\nu_1\nu_3-\nu_4^2$. It is shown in appendix C that $\psi_{st}(\vartheta)$ is bounded for all values of a, b, c, d and γ. The stationary p.d.f. of orientations satisfies $\psi_{st}(2\pi-\vartheta)=\psi_{st}(\vartheta)$ and $\psi_{st}(\pi-\vartheta)=\psi_{st}(\vartheta)$. These properties are a consequence of the statistical symmetries of the carrier flow, as was noted after (3.12).

Since Δ can be written as $\Delta=a^2F(\gamma,b/a,c/a,d/a,D'_R/a)$, $\psi_{st}(\vartheta)$ only depends on the ratios b/a, c/a, d/a, D'_R/a (and on γ). The same conclusion could have been reached by rescaling t by a^{-1} in (3.7).

For a spherical particle (i.e. $\gamma=0$), ν_2 and ν_4 vanish. Consequently, $\chi(\vartheta)=1$, $\mathscr{D}_{\vartheta\vartheta}(\vartheta)=\text{const.}$, and hence $\psi_{st}(\vartheta)=(4\pi)^{-1}$, in accordance with the fact that all orientations are equally probable for a sphere. Similarly, if a or D'_R is much greater than b, c, d, i.e. if the isotropic component of the velocity field or the Brownian fluctuations prevail over the anisotropic component of the flow, then $\nu_1\gg\nu_i$, $i=2,\dots,5$ and hence $\psi_{st}(\vartheta)$ weakly depends on ϑ regardless of the shape of the particle. In the following, therefore, γ is assumed to be non-zero and b, c, d are of the same order of magnitude as a and D'_R or greater.

The behaviour of $\psi_{st}(\vartheta)$ can be deduced from that of its first derivative. By using (3.11), (4.1) and (4.2), it is easy to see that, for all values of Δ,

$$\frac{\mathrm{d}}{\mathrm{d}\vartheta}\psi_{st}(\vartheta)=\mathscr{W}_\vartheta(\vartheta)h(\vartheta)=\frac{3}{8}\gamma\sin(2\vartheta)[c\gamma\cos(2\vartheta)-\sigma]h(\vartheta),\tag{4.6}$$

where $h(\vartheta)\equiv 2\psi_{st}(\vartheta)/\mathscr{D}_{\vartheta\vartheta}(\vartheta)$ is strictly positive for all $0\leqslant\vartheta\leqslant\pi$ (see (C 7*a*) and (C 8*a*)) and

$$\sigma\equiv 2b+c+(5+\gamma)d.\tag{4.7}$$

Thus, the extrema of ψ_{st} are the zeros of the function $\mathscr{W}_\vartheta$ determining the apparent drift velocity in the convection–diffusion equation (3.7). Note that σ can be rewritten as $\sigma=(\Gamma_{3131}-\Gamma_{1313})+\gamma(\Gamma_{3333}-\Gamma_{1111})$, where the term in the first parentheses describes the anisotropy of the vorticity tensor and that in the second is related to the anisotropy of the strain tensor, with the ratio of the two terms being given by γ.

Four regimes are identified depending on the properties of the axisymmetric flow and on the geometrical shape of the particle.

(i) *Rotation about the axis of symmetry of the flow*. For the following values of the parameters:

$$|\sigma|>|c\gamma|\quad\text{and}\quad\gamma\sigma<0,\tag{4.8}$$

the function ψ_{st} only has three extrema at $\vartheta=0,\pi/2,\pi$ (indeed the equation $c\gamma\cos(2\vartheta)=\sigma$ has no solution). More precisely, $\psi_{st}(\vartheta)$ has a maximum at $\pi/2$ and two minima at 0 and π (figure 2). Thus, in this regime a non-spherical particles rotates about the direction $\mathbf{\lambda}$; the level of alignment with the plane

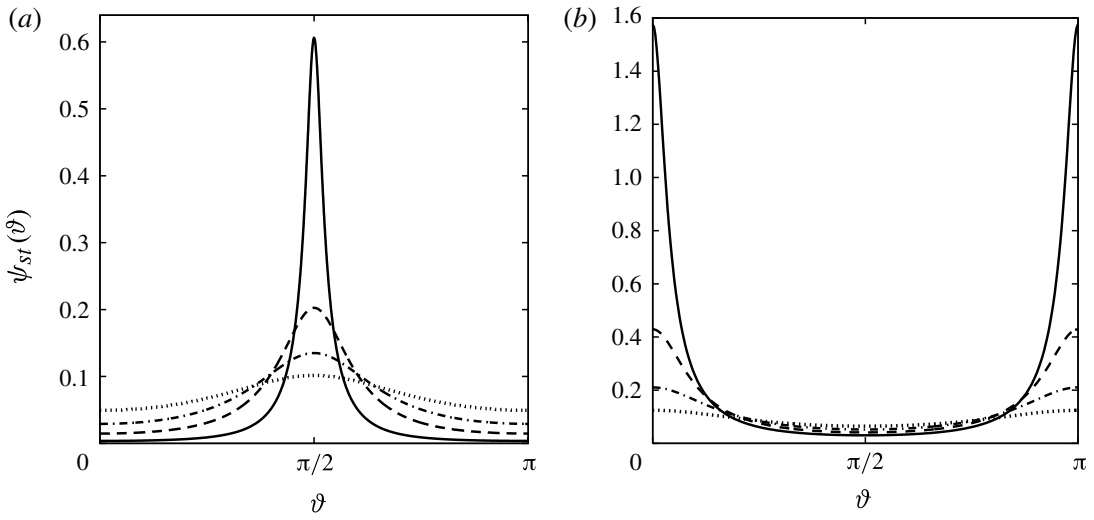

FIGURE 2. Stationary p.d.f. of the orientation angle ϑ. The normalization coefficient $\mathcal{N}$ has been computed numerically according to (4.3). (*a*) Rotation about $\mathbf{\lambda}$: $b/a = 4.8$, $c/a = 55$, $d/a = 0.85$, $D_R'/a = 10^{-2}$ and $\gamma = -1$ (solid line), $\gamma = -0.75$ (dashed line), $\gamma = -0.5$ (dot-dashed line), $\gamma = -0.25$ (dotted line). (*b*) Tumbling motion between $\mathbf{\lambda}$ and $-\mathbf{\lambda}$: $b/a = 4.75$, $c/a = 10$, $d/a = 0.9$, $D_R'/a = 10^{-2}$ and $\gamma = 1$ (solid line), $\gamma = 0.75$ (dashed line), $\gamma = 0.5$ (dot-dashed line), $\gamma = 0.25$ (dotted line).

perpendicular to $\mathbf{\lambda}$ decreases as the degree of anisotropy of the flow vanishes or the shape of the particle approaches a spherical one (figure 2).

(ii) *Tumbling motion*. In the following regime:

$$|\sigma| > |c\gamma| \quad \text{and} \quad \gamma\sigma > 0, \tag{4.9}$$

ψ_{st} has three extrema: a minimum at $\pi/2$ and two maxima at 0 and at π (figure 2). The particle tumbles between the direction parallel to $\mathbf{\lambda}$ and that antiparallel to $\mathbf{\lambda}$. The probability of the orientation angle ϑ being in the neighbourhood of 0 or π depends on the anisotropy degree of the flow and on the shape of the particle (figure 2).

(iii) *Preferential alignment with a direction oblique to the axis of symmetry of the flow*. If

$$|\sigma| < |c\gamma| \quad \text{and} \quad c > 0, \tag{4.10}$$

then ψ_{st} has three minima at $0, \pi/2, \pi$ and two maxima at $\vartheta_\star$ and $\pi - \vartheta_\star$, where $0 < \vartheta_\star < \pi/2$ is such that

$$\sin\vartheta_\star = \sqrt{\frac{1}{2}\left(1 - \frac{\sigma}{c\gamma}\right)}. \tag{4.11}$$

The particle, therefore, spends most of the time at an angle $\vartheta_\star$ (or $\pi - \vartheta_\star$) with respect to $\mathbf{\lambda}$ (figure 3).

(iv) *Combination of rotation and tumbling*. For

$$|\sigma| < |c\gamma| \quad \text{and} \quad c < 0, \tag{4.12}$$

the function ψ_{st} has three maxima at $0, \pi/2, \pi$ and two minima at $\vartheta_\star$ and $\pi - \vartheta_\star$ with $\vartheta_\star$ defined in (4.11) (see figure 3). In this regime, the particle preferentially

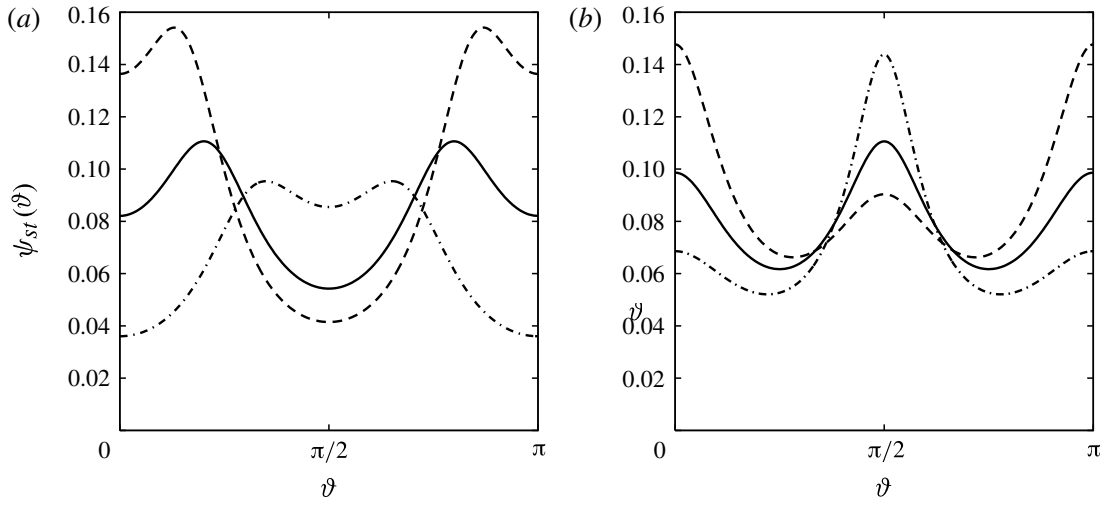

FIGURE 3. Stationary p.d.f. of the orientation angle ϑ. The p.d.f. has been normalized numerically according to (4.3). (*a*) Preferential alignment with a direction oblique to $\boldsymbol{\lambda}$: $\gamma = 1$, $D_R'/a = 10^{-2}$, $b/a = -6$, $d/a = -0.9$ and $c/a = 55$ (dashed line), $c/a = 25$ (solid line), $c/a = 11$ (dot-dashed line). (*b*) Combination of rotation and tumbling: $\gamma = 1$, $D_R'/a = 10^{-2}$, $c/a = -10$, $d/a = 1$ and $b/a = 1.1$ (dot-dashed line), $b/a = 2$ (solid line), $b/a = 3$ (dashed line).

lies either in the plane perpendicular to $\boldsymbol{\lambda}$, in the direction parallel to $\boldsymbol{\lambda}$, or in the direction antiparallel to it.

Note that whereas sufficiently elongated or flattened spheroids can be strongly aligned in regimes (i) and (ii), the ability of the flow to orient particles is weaker in regimes (iii) and (iv) (figure 3). In these regimes, strong alignment can be obtained only for $|\gamma| > 1$ (figure 4). However, Bretherton (1962) observed that particles with $|\gamma| > 1$ may be unrealistic, albeit conceivable from a purely geometrical point of view.

The above classification holds for all $\gamma \neq 0$ and for all a, b, c, d satisfying inequalities (2.17) (with $c \neq 0$). Naturally, the coefficient a controlling the intensity of the isotropic component of the flow does not play any role in the classification; the dynamical regime is selected by b, c, d, and by the shape coefficient γ. The way the anisotropy parameters and the shape coefficient enter conditions (4.8), (4.9), (4.10) and (4.12) is rather involved. There are cases, however, which can be easily interpreted from a physical point of view.

Consider for example the case $b = d = 0$, $c \neq 0$, $a > 0$, and $|\gamma| \leqslant 1$. Then, the condition $|\sigma| > |c\gamma|$ is trivially satisfied and the sign of γc determines whether a particle rotates around $\boldsymbol{\lambda}$ ($\gamma c < 0$) or tumbles ($\gamma c > 0$). This behaviour can be easily understood by noting that if $c > 0$, the flow differs from an isotropic flow only in that $\Gamma_{3131} - \Gamma_{3333}$ is greater in value, i.e. the difference between the amplitude of the fluctuations of $\partial_1 v_3$ and that of the fluctuations of $\partial_3 v_3$ is greater than it would be in the isotropic case (recall that v_3 is the component of the velocity in the direction of $\boldsymbol{\lambda}$, while v_1 and v_2 are the components orthogonal to $\boldsymbol{\lambda}$). Therefore, the orientation vector of an elongated particle ($0 < \gamma \leqslant 1$ and hence $\gamma c > 0$) is attracted towards the direction parallel to $\boldsymbol{\lambda}$ or towards that antiparallel to $\boldsymbol{\lambda}$ and thus performs a tumbling motion between the two directions; the orientation vector of a flattened particle ($-1 \leqslant \gamma < 0$ and hence $\gamma c < 0$) is attracted to the plane orthogonal to $\boldsymbol{\lambda}$ and thus predominantly rotates in that plane. The situation is reversed for $c < 0$, since

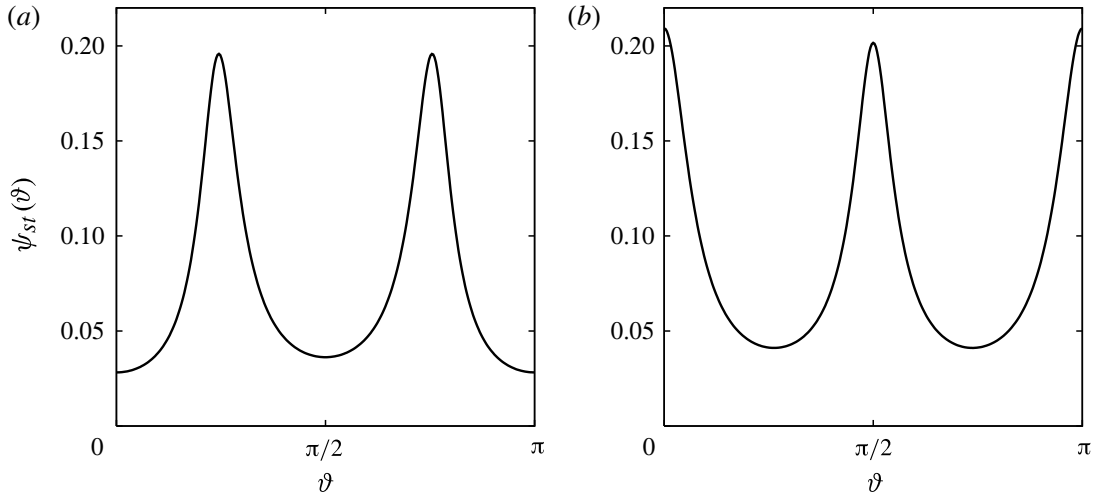

FIGURE 4. Stationary p.d.f. of the orientation angle ϑ for $|\gamma| > 1$. (*a*) Preferential alignment with a direction oblique to $\boldsymbol{\lambda}$: $\gamma = 5$, $D'_R/a = 10^{-2}$, $b/a = -6$, $c/a = 25$, $d/a = -0.9$. (*b*) Combination of rotation and tumbling: $\gamma = 5$, $D'_R/a = 10^{-2}$, $b/a = 2$, $c/a = -10$, $d/a = 1$.

in this case the difference between the amplitude of the fluctuations of $\partial_1 v_3$ and the amplitude of the fluctuations of $\partial_3 v_3$ is less than in an isotropic flow. Other examples can be examined in a similar way, but the analysis may be less intuitive when b, c, d are all non-zero.

For $d = 0$ (i.e. when the fluctuations of $\partial_1 v_1$, $\partial_2 v_2$, and $\partial_3 v_3$ have the same amplitude), the study of the dependence of $\psi_{st}(\vartheta)$ upon the shape of the particles can be developed further. This case is examined below.

4.1. *The case* $d = 0$

If $d = 0$, then $\nu_2 = 3\nu_4/4$ and the form of $\psi_{st}(\vartheta)$ simplifies considerably (see (4.4) and (4.5)):

$$\psi_{st}(\vartheta) = \mathscr{N}\,[\mathscr{D}_{\vartheta\vartheta}(\vartheta)]^{-3/4}. \tag{4.13}$$

Furthermore, σ does not depend on γ; the conditions $|\sigma| \gtrless |c\gamma|$ are thus independent of the sign of γ, i.e. of whether a particle is elongated or flattened. This property of the $d = 0$ case has the following implications (which once again hold for any $\gamma \neq 0$).

(*a*) If for a given σ the particles with shape coefficient $\widehat{\gamma}$ are in regime (i) (i.e. they rotate in the plane orthogonal to $\boldsymbol{\lambda}$), then for the same σ the particles with shape coefficient $-\widehat{\gamma}$ are in regime (ii) (i.e. they tumble). Similarly, if the particles with shape coefficient $\widehat{\gamma}$ are in regime (ii), then the particles with shape coefficient $-\widehat{\gamma}$ are in regime (i). Thus, for $d = 0$, elongated and flattened particles behave in an opposite way if $|\sigma| > |c\gamma|$.

(*b*) If for a given flow the particles with shape coefficient $\widehat{\gamma}$ are in regime (i) (i.e. they rotate about $\boldsymbol{\lambda}$), then in such a flow all particles with $|\gamma| < |\widehat{\gamma}|$ and $\mathrm{sgn}(\gamma) = \mathrm{sgn}(\widehat{\gamma})$ are in the same regime. In other words, if a prolate spheroid rotates about $\boldsymbol{\lambda}$, then all prolate spheroids having smaller aspect ratio rotate around $\boldsymbol{\lambda}$. Oblate spheroids behave analogously. Moreover, if the particles with shape coefficient $\widehat{\gamma}$ are in regime (ii) (i.e. they tumble), then all particles with $|\gamma| < |\widehat{\gamma}|$ and $\mathrm{sgn}(\gamma) = \mathrm{sgn}(\widehat{\gamma})$ also tumble.

(*c*) In contrast with regimes (i) and (ii), regimes (iii) and (iv) are independent of the sign of γ, i.e. of whether a particle is elongated or flattened; nevertheless, $\vartheta_\star$ changes if the sign of γ changes.

(*d*) If the particles with shape coefficient $\widehat{\gamma}$ are in regime (iii) (respectively in regime (iv)), then all particles with $|\gamma| > |\widehat{\gamma}|$ are in regime (iii) (respectively in regime (iv)). This means, for instance, that if a prolate spheroid preferentially orients itself in a direction oblique $\boldsymbol{\lambda}$, the same holds for all prolate spheroids with greater aspect ratio.

The above properties hold for $d = 0$, but in general do not extend to the case $d \neq 0$. For example, if $b/a = -4.4$, $c/a = 0.5$, $d/a = 1.5$, then particles tumble for $1 \geqslant \gamma > 0.8$, they have a preferential orientation for $0.8 > \gamma > 0.4$, they rotate for $0.4 > \gamma > 0$, and they tumble again for $0 > \gamma \geqslant -1$.

5. Conclusions

Axisymmetric turbulence arises as one of the simplest frameworks in which to study the orientation dynamics of non-spherical particles. On the assumptions of Gaussianity and short correlation in time, it has been shown analytically that the dynamics of a non-spherical particle immersed in a random axisymmetric flow exhibits four regimes: rotation around the axis of symmetry of the flow, tumbling, a combination of rotation and tumbling, and preferential alignment with a direction oblique to the axis of symmetry of the flow. The regime is selected by the form of the anisotropic component of the flow and by the geometrical shape of the particle. If the flow is weakly anisotropic or if the particle is almost spherical, the mathematical description of $\psi_{st}(\vartheta)$ in terms of minima and maxima remains formally valid, but the above physical classification loses its meaning, since $\psi_{st}(\vartheta)$ does not deviate appreciably from the uniform distribution.

The orientational dynamics of a rigid rod in the flow resulting from the superposition of a uniform shear and of an isotropic short-correlated random noise is characterized by a tumbling motion in the plane of the shear (Puliafito & Turistyn 2005; Turitsyn 2007). Such tumbling motion, however, differs from that experienced by non-spherical particles in the axisymmetric random flow (see regime (ii) in § 4). In the presence of a strong mean shear, the tumbling dynamics of a rod consists of aperiodic transitions between two unstable states: the one aligned with the direction of the shear and that anti-aligned with it. When a fluctuation takes the rod away from the aligned or anti-aligned state and moves it into the unstable region of the flow the mean shear makes the rod flip. By contrast, in the axisymmetric case, large deviations of the orientation of the particle from the axis of symmetry of the flow do not necessarily result into sudden flips of the particle (figure 5). Simply, the orientation vector of the particle fluctuates randomly, but the orientations aligned and anti-aligned with the axis of symmetry of the flow are much more probable than the other orientations. Thus, there can be excursions of $\vartheta(t)$ from $\vartheta \approx 0$ to $\vartheta \approx \pi/2$ followed by a return to $\vartheta \approx 0$ (figure 5). The probability of such events would be extremely small in the presence of a strong mean shear.

The orientational dynamics in the laminar uniform shear (Jeffery 1922; Bretherton 1962) and that in the axisymmetric random flow depend on the geometrical shape of particles in a different way. In the former case, the motion of a rod or of a disk represents a degenerate case of the dynamics (Jeffery 1922); furthermore, the orientational dynamics is qualitatively different for $|\gamma| < 1$ and $|\gamma| > 1$

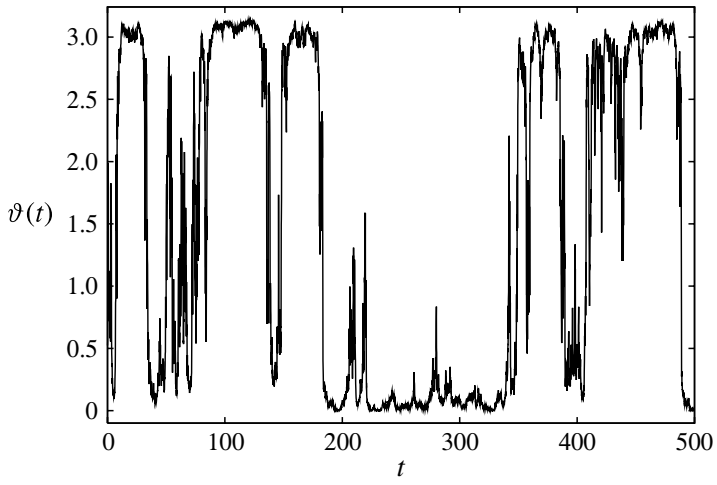

FIGURE 5. A typical time evolution of $\vartheta(t)$ in the tumbling regime ($\gamma = 1$, $b/a = 4.75$, $c/a = 10$, $d/a = 0.9$, $D'_R/a = 10^{-2}$); $\vartheta(t)$ has been computed by numerically integrating (3.14).

(Bretherton 1962). In the latter case, the dynamics of particles changes smoothly as a function of the shape coefficient.

It is moreover worth remarking that the function χ defined in (4.5) also determines the probability distribution of Jeffery's orbits in the presence of weak Brownian fluctuations (Leal & Hinch 1971). There does not seem to be, however, a simple relation between the orientation dynamics in the uniform shear and that in the axisymmetric random flow.

Finally, the results presented here also hold for elastic dumbbells or for slightly deformable spheroids, since for such particles the dynamics of the size and that of the orientation are decoupled (Olbricht, Rallison & Leal 1982). The study of highly deformable particles requires more detailed models that also account for the shape dynamics (e.g. Minale 2010) and is the topic of future work.

Acknowledgements

The author is grateful to J. Bec, A. Celani, F. Delarue, P. Perlekar, R. Shaw and M. Wilkinson for useful suggestions. The author also wishes to thank two anonymous referees for their helpful comments. This work was supported in part by the French National Research Agency (ANR) under grant BLAN07-1_192604 'Dynamique et statistique des particules en turbulence' and by the EU COST Action MP0806 'Particles in turbulence'.

Appendix A. Rotary diffusion

Rotary diffusion is introduced in the dynamics of $\boldsymbol{N}(t)$ by assuming that it produces isotropic Brownian fluctuations of the direction of $\boldsymbol{N}(t)$, but not of its length. Mathematically, this is obtained by adding a Laplacian term to the equation for $f(\boldsymbol{n}; t)$ which acts only on the orientation of $\boldsymbol{n}$. For a deterministic flow, $f(\boldsymbol{n}; t)$ thus satisfies the following equation (e.g. Leal & Hinch 1971; Hinch & Leal 1972; Brenner 1974; Bird *et al.* 1977; Doi & Edwards 1986):

$$\partial_t f = -\widetilde{\boldsymbol{\nabla}} \cdot [\boldsymbol{w}(\boldsymbol{n}, t) f] + \frac{D_R}{2} \widetilde{\nabla}^2 f, \tag{A 1}$$

where

$$\widetilde{\boldsymbol{\nabla}} \equiv \boldsymbol{\Sigma}(\boldsymbol{n}) \cdot \boldsymbol{\nabla}_{\boldsymbol{n}} \tag{A 2}$$

with $\boldsymbol{\Sigma}(\boldsymbol{n}) = \boldsymbol{I} - \boldsymbol{nn}/|\boldsymbol{n}|^2$ and $\boldsymbol{\nabla}_{\boldsymbol{n}} = (\partial/\partial n_1, \partial/\partial n_2, \partial/\partial n_3)$. The differential operator $\widetilde{\boldsymbol{\nabla}}$ is the angular part of the gradient or, in other words, the restriction of the gradient to the sphere of radius $|\boldsymbol{n}|$. In (A 1), $\widetilde{\nabla}^2 \equiv \widetilde{\boldsymbol{\nabla}} \cdot \widetilde{\boldsymbol{\nabla}}$ and $\boldsymbol{w}(\boldsymbol{n}, t) = \boldsymbol{\kappa}(t) \cdot \boldsymbol{n} - [\boldsymbol{\kappa}(t){:}\boldsymbol{nn}]\boldsymbol{n}/|\boldsymbol{n}|^2$.

The matrix $\boldsymbol{\Sigma}$ satisfies:

$$\boldsymbol{\Sigma} = \boldsymbol{\Sigma}^{\mathrm{T}} = \boldsymbol{\Sigma}^2, \quad \boldsymbol{n} \times [\boldsymbol{\nabla}_{\boldsymbol{n}} \cdot \boldsymbol{\Sigma}(\boldsymbol{n})] = \boldsymbol{0}, \quad \boldsymbol{\Sigma}(\boldsymbol{n}) \cdot \boldsymbol{n} = \boldsymbol{0}. \tag{A 3}$$

By using properties (A 3) and $\boldsymbol{w}(\boldsymbol{n}, t) \cdot \boldsymbol{n} = 0$, it is possible to rewrite (A 1) as follows:

$$\frac{\partial f}{\partial t} = -\frac{\partial}{\partial n_i}[w_i(\boldsymbol{n}, t) f] + \frac{D_R}{2} \frac{\partial}{\partial n_i} \Sigma_{ik}(\boldsymbol{n}) \frac{\partial}{\partial n_j} \Sigma_{jk}(\boldsymbol{n}) f. \tag{A 4}$$

Equation (2.3) is the Stratonovich stochastic differential equation associated with (A 4).

It is worth noting that given that the orientation vector has unit length, $f(\boldsymbol{n}; t)$ must take the form $f(\boldsymbol{n}; t) = F(\boldsymbol{n}; t)\delta(|\boldsymbol{n}| - 1)$ with $\partial F/\partial n = 0$. It would therefore be more natural to consider the evolution equation for $F(\boldsymbol{n}; t)$ instead of that for $f(\boldsymbol{n}; t)$; this is indeed the usual approach in the literature (Leal & Hinch 1971; Hinch & Leal 1972; Brenner 1974; Bird *et al.* 1977; Doi & Edwards 1986). In the present context, however, it is more convenient to formulate the problem in Cartesian coordinates and to move to angular variables afterwards.

Appendix B. Representation of the velocity correlation tensor of a homogeneous axisymmetric random flow

Consider the scalar variable $z = \mu r$ and the orthogonal unit vectors $\boldsymbol{\mathfrak{e}}^{(1)} = (\boldsymbol{\lambda} \times \boldsymbol{r})/\rho$, $\boldsymbol{\mathfrak{e}}^{(2)} = \boldsymbol{\mathfrak{e}}^{(1)} \times \boldsymbol{\lambda}$ with $\rho = |\boldsymbol{\lambda} \times \boldsymbol{r}|$. Then, an alternative representation of the tensor $\boldsymbol{Q}$ defined in (2.7) is (Lindborg 1995):

$$\begin{aligned} Q_{ij}(\boldsymbol{r}) = {} & R_1(\rho, z)\lambda_i\lambda_j + R_2(\rho, z)\mathfrak{e}_i^{(2)}\mathfrak{e}_j^{(2)} + R_3(\rho, z)\mathfrak{e}_i^{(1)}\mathfrak{e}_j^{(1)} \\ & + R_4(\rho, z)(\lambda_i\mathfrak{e}_j^{(2)} + \lambda_j\mathfrak{e}_i^{(2)}), \end{aligned} \tag{B 1}$$

where up to second-order in ρ and z (see Lindborg 1995, p. 189):

$$R_1(\rho, z) = R_1(0, 0) - \mathfrak{a}_1\rho^2 - \mathfrak{b}_1 z^2 + \cdots, \tag{B 2a}$$

$$R_2(\rho, z) = R_2(0, 0) - \mathfrak{a}_2\rho^2 - \mathfrak{b}_2 z^2 + \cdots, \tag{B 2b}$$

$$R_3(\rho, z) = R_2(0, 0) - (3\mathfrak{a}_2 - \mathfrak{b}_1)\rho^2 - \mathfrak{b}_2 z^2 + \cdots, \tag{B 2c}$$

$$R_4(\rho, z) = \mathfrak{b}_1\rho z + \cdots. \tag{B 2d}$$

In the above equations, $\mathfrak{a}_1$, $\mathfrak{a}_2$, $\mathfrak{b}_1$ and $\mathfrak{b}_2$ are real constants. The functions R_1, R_2, R_3, R_4 are related to the functions A, B, C, D in (2.8) through the following identities (Lindborg 1995, p. 185):

$$R_1 = \mu^2 r^2 A + B + C + 2r\mu D, \quad R_2 = r^2(1 - \mu^2)A + B, \tag{B 3a}$$

$$R_3 = B, \quad R_4 = \mu r^2\sqrt{1 - \mu^2}\,A + r\sqrt{1 - \mu^2}\,D. \tag{B 3b}$$

The relations between the parameters $\mathfrak{a}_1$, $\mathfrak{a}_2$, $\mathfrak{b}_1$, $\mathfrak{b}_2$ and the parameters a, b, c, d used in the text are obtained by substituting (2.9) into (B3), by making the change of variables $r = (\rho^2 + z^2)^{1/2}$ and $\mu = z\,(\rho^2 + z^2)^{-1/2}$, and by comparing the resulting

expressions for R_1, R_2, R_3, R_4 with the expansions given in (B2). It follows that

$$a = 2\mathfrak{a}_2 - \mathfrak{b}_1, \qquad b = 2(3\mathfrak{a}_2 - \mathfrak{b}_1) - 2\mathfrak{b}_2, \tag{B 4a}$$

$$c = 2(\mathfrak{a}_1 - \mathfrak{a}_2 - 3\mathfrak{b}_1 + \mathfrak{b}_2), \quad d = 2(\mathfrak{b}_1 - \mathfrak{a}_2). \tag{B 4b}$$

In particular, the parameter σ defined in (4.7) is written:

$$\sigma = 2[(\mathfrak{a}_1 - \mathfrak{b}_2) + \gamma(\mathfrak{b}_1 - \mathfrak{a}_2]. \tag{B 5}$$

Moreover, by inverting (B4) and using inequalities (2.17), it is possible to show that $\mathfrak{a}_1$, $\mathfrak{a}_2$, $\mathfrak{b}_1$ and $\mathfrak{b}_2$ are strictly positive.

Appendix C. Positive semi-definiteness of the covariance tensor

The fourth-order tensor $\boldsymbol{\Gamma}$ is the covariance of a Gaussian second-order tensor, and must therefore be positive semi-definite, i.e.

$$\sum_{1\leqslant i,j,p,q\leqslant 3} U_{ij}\Gamma_{ijpq}U_{pq} \geqslant 0 \tag{C 1}$$

for all second-order tensors $\boldsymbol{U}$. Inequality (C 1) can be reinterpreted within the theory of positive semi-definite second-order tensors (e.g. Moakher 2008). Consider an invertible map ℓ which assigns to each pair of indices (i, j), $1 \leqslant i, j \leqslant 3$, a single index $\ell(i, j)$ ranging from 1 to 9. By means of the map ℓ, $\boldsymbol{U}$ can be regarded as a nine-dimensional vector; likewise, $\boldsymbol{\Gamma}$ can be regarded as a symmetric 9×9 second-order tensor, whose symmetry follows from $\Gamma_{ijpq} = \Gamma_{pqij}$. Accordingly, (C 1) can be rewritten in the following form:

$$\sum_{1\leqslant \ell(i,j),\ell(p,q)\leqslant 9} U_{\ell(i,j)}\Gamma_{\ell(i,j)\ell(p,q)}U_{\ell(p,q)} \geqslant 0. \tag{C 2}$$

Inequality (C 2) is the definition of positive semi-definiteness for second-order tensors. The theory of such tensors says that a necessary and sufficient condition for an Hermitian second-order tensor to be positive semi-definite is that all the principal minors of the tensor are non-negative (Gantmacher 1959, p. 307). When this condition is applied to $\Gamma_{\ell(i,j)\ell(p,q)}$ it yields the following inequalities:

$$\left.\begin{array}{ll} a + d \geqslant 0 & \text{if } a \geqslant 0, \\ 5a + d \geqslant 0 & \text{if } a < 0, \end{array}\right\} \tag{C 3}$$

and

$$\varpi_1 \equiv 4a - b + d \geqslant 0, \quad \varpi_2 \equiv 4a + b + c + 6d \geqslant 0, \tag{C 4}$$

$$\varpi_3 \equiv 15a^2 - b^2 - (b - d)(c + 5d) + 2a(2c + 13d) \geqslant 0. \tag{C 5}$$

In this paper, the above inequalities are assumed to hold strictly; (2.17) follows from this assumption.

Some useful inequalities can be derived from (2.17). Here, $\gamma \neq 0$ (the case of a spherical particle is indeed trivial), $D'_R = 0$ (it is easily seen that a positive D'_R does not alter the inequalities below), and $\nu_3 \neq 0$ (the case $\nu_3 = 0$ is treated separately in appendix E).

First, $\mathscr{D}_{\vartheta\vartheta}(\vartheta)$ and $\mathscr{D}_{\varphi\varphi}(\vartheta)$ are positive for all $\gamma \neq 0$ and for all values of a, b, c, d satisfying (2.17). Indeed, the quantities $2\nu_1$ and $2\nu_1 + \nu_3 + \nu_4$ are quadratic polynomials in γ, their discriminant is equal to $-\varpi_3 < 0$, and for $\gamma = 1$ they are equal to $\varpi_1 > 0$

and to $\varpi_2 > 0$, respectively. Moreover, $2\nu_1 + \nu_5$ is a quadratic polynomial in γ with discriminant equal to $-(3a+d)(5a+d) < 0$ and takes the value $4a + d > 0$ for $\gamma = 1$. Hence

$$\nu_1 > 0, \quad 2\nu_1 + \nu_5 > 0, \quad 2\nu_1 + \nu_3 + \nu_4 > 0 \tag{C 6}$$

for all a, b, c, d and γ, and consequently

$$\mathscr{D}_{\vartheta\vartheta}(0) = \mathscr{D}_{\vartheta\vartheta}(\pi) = 2\nu_1 > 0, \tag{C 7a}$$

$$\mathscr{D}_{\varphi\varphi}(0) = \mathscr{D}_{\varphi\varphi}(\pi) = 2\nu_1 > 0, \tag{C 7b}$$

and

$$\mathscr{D}_{\vartheta\vartheta}(\vartheta) \geqslant \nu_4 \sin^2(\vartheta) + (2\nu_1 + \nu_3)\sin^4(\vartheta) \geqslant (2\nu_1 + \nu_3 + \nu_4)\sin^4(\vartheta) > 0, \tag{C 8a}$$

$$\mathscr{D}_{\varphi\varphi}(\vartheta) \geqslant (2\nu_1 + \nu_5)\sin^2(\vartheta) > 0 \tag{C 8b}$$

for all $0 < \vartheta < \pi$.

Secondly, $\psi_{st}(\vartheta)$ is bounded for all a, b, c, d and γ and for all $0 \leqslant \vartheta \leqslant \pi$. For $\Delta > 0$, this property is obvious. For $\Delta < 0$, note that

$$\left(\sqrt{-\Delta} + \nu_4\right)\left(\sqrt{-\Delta} - \nu_4\right) = -\nu_3 P_1(\gamma), \tag{C 9}$$

and

$$\left(\sqrt{-\Delta} + \nu_4 + 2\nu_3\right)\left(\sqrt{-\Delta} - \nu_4 - 2\nu_3\right) = -\nu_3 P_2(\gamma), \tag{C 10}$$

where $P_1(\gamma)$ and $P_2(\gamma)$ are quadratic polynomials in γ such that $P_1(1) = 4\varpi_1 > 0$ and $P_2(1) = 4\varpi_2 > 0$. Furthermore, the discriminants of $P_1(\gamma)$ and $P_2(\gamma)$ are equal to $-16\varpi_3 < 0$. Therefore $P_1(\gamma)$ and $P_2(\gamma)$ are positive for all γ, and the products on the left-hand sides of (C 9) and (C 10) have the same sign as $-\nu_3$.

Also observe that

$$\left(\sqrt{-\Delta} + \nu_4 + 2\nu_3\right)\left(\sqrt{-\Delta} - \nu_4\right) = -\nu_3\left[P_3(\gamma) - 2\sqrt{-\Delta}\right], \tag{C 11}$$

where $P_3(\gamma)$ is a quadratic polynomial satisfying: $P_3^2(\gamma) + 4\Delta = P_1(\gamma)P_2(\gamma) > 0$. Hence $P_3(\gamma) - 2\sqrt{-\Delta} \neq 0$ for all γ. Moreover, for $\gamma = 0$, $P_3(0) - 2\sqrt{-\Delta} = P_3(0) = \varpi_1 + \varpi_2 + 2(a+d) > 0$. As a result $P_3(\gamma) - 2\sqrt{-\Delta} > 0$ for all γ. The left-hand side of (C 11) therefore has the same sign as $-\nu_3$.

Three cases should now be distinguished.

(a) $\nu_3 < 0$: in this case, $\sqrt{-\Delta} \pm \nu_4 > 0$ and $\sqrt{-\Delta} - \nu_4 - 2\nu_3 > 0$ (recall that $\Delta = 8\nu_1\nu_3 - \nu_4^2$ with $\nu_1 > 0$), whence $\sqrt{-\Delta} + \nu_4 + 2\nu_3 > 0$ (see (C 10)). Therefore

$$\sqrt{-\Delta} + \nu_4 + 2\nu_3\sin^2(\vartheta) \geqslant \sqrt{-\Delta} + \nu_4 + 2\nu_3 > 0, \tag{C 12a}$$

$$\sqrt{-\Delta} - \nu_4 - 2\nu_3\sin^2(\vartheta) \geqslant \sqrt{-\Delta} - \nu_4 > 0. \tag{C 12b}$$

(b) $\nu_3 > 0$ and $\nu_4 > 0$: then $\sqrt{-\Delta} + \nu_4 > 0$ and consequently $\sqrt{-\Delta} - \nu_4 < 0$ (see (C 9)). Hence

$$\sqrt{-\Delta} + \nu_4 + 2\nu_3\sin^2(\vartheta) \geqslant \sqrt{-\Delta} + \nu_4 > 0, \tag{C 13a}$$

$$\sqrt{-\Delta} - \nu_4 - 2\nu_3\sin^2(\vartheta) \leqslant \sqrt{-\Delta} - \nu_4 < 0. \tag{C 13b}$$

(c) $\nu_3 > 0$ and $\nu_4 < 0$: for these values of the parameters, (C 10) and (C 11) yield the following relations:

$$\sqrt{-\Delta} + \nu_4 + 2\nu_3\sin^2(\vartheta) \leqslant \sqrt{-\Delta} + \nu_4 + 2\nu_3 < 0, \tag{C 14a}$$

$$\sqrt{-\Delta} - \nu_4 - 2\nu_3 \sin^2(\vartheta) \geqslant \sqrt{-\Delta} - \nu_4 - 2\nu_3 > 0. \qquad \text{(C 14}b\text{)}$$

Inequalities (C12)–(C14) guarantee that if $\Delta < 0$, the function $\chi(\vartheta)$ is bounded for all a, b, c, d, and γ.

For $\Delta = 8\nu_1\nu_3 - \nu_4^2 = 0$, ν_4 cannot be zero since $\nu_1 > 0$ and $\nu_3 \neq 0$. Moreover, ν_3 and hence c must be positive given that $\nu_1 > 0$. Therefore, for $\nu_4 > 0$ the function $\chi(\vartheta)$ is bounded. The case $\nu_4 < 0$ requires a more detailed analysis. Δ can be rewritten thus: $\Delta = c(6a + 5d)\gamma^2(\gamma^2 - \varrho)$ with

$$\varrho = \frac{(2b + c + 5d)^2 - c(10a + c + 9d)}{c(6a + 5d)}. \qquad \text{(C 15)}$$

(Note that, for $\gamma = 0$, $\nu_1 = (10a + c + 9d)/8$ and hence $10a + c + 9d > 0$ for all a, c, d as a consequence of (C 6); this is consistent with the positivity of the variance of the components of the vorticity – see (2.15).) Provided that $\varrho > 0$, Δ vanishes for $\gamma = \pm\gamma_\star$ with $\gamma_\star = \sqrt{\varrho}$ (the case $\gamma = 0$ is not considered here). Now note that both ν_4 and $2\nu_3 + \nu_4$ are quadratic polynomials in γ. If $\gamma_{\star\star} \equiv 1 + (2b + 5d)/c$ is positive, then

$$\left.\begin{array}{ll} \nu_4 > 0 & \text{if } \gamma \in (0, \gamma_{\star\star}) \\ \nu_4 < 0 & \text{if } \gamma \notin [0, \gamma_{\star\star}] \end{array}\right\} \quad \text{and} \quad \left.\begin{array}{ll} 2\nu_3 + \nu_4 < 0 & \text{if } \gamma \in (-\gamma_{\star\star}, 0) \\ 2\nu_3 + \nu_4 > 0 & \text{if } \gamma \notin [-\gamma_{\star\star}, 0]. \end{array}\right\} \qquad \text{(C 16)}$$

If $\gamma_{\star\star} < 0$, then

$$\left.\begin{array}{ll} \nu_4 > 0 & \text{if } \gamma \in (-\gamma_{\star\star}, 0) \\ \nu_4 < 0 & \text{if } \gamma \notin [-\gamma_{\star\star}, 0] \end{array}\right\} \quad \text{and} \quad \left.\begin{array}{ll} 2\nu_3 + \nu_4 < 0 & \text{if } \gamma \in (0, \gamma_{\star\star}) \\ 2\nu_3 + \nu_4 > 0 & \text{if } \gamma \notin [0, \gamma_{\star\star}]. \end{array}\right\} \qquad \text{(C 17)}$$

Hence

$$\nu_4(2\nu_3 + \nu_4) > 0 \quad \forall\, |\gamma| < |\gamma_{\star\star}|. \qquad \text{(C 18)}$$

Let us now show that $|\gamma_\star| < |\gamma_{\star\star}|$. The quantity $\gamma_{\star\star}^2 - \gamma_\star^2$ is written:

$$\gamma_{\star\star}^2 - \gamma_\star^2 = \frac{P_4(c)}{(6a + 5d)c^2}, \qquad \text{(C 19)}$$

where $P_4(c)$ is a quadratic polynomial in c whose coefficients depend on a, b, d and such that $P_4(0) = (6a + 5d)\,(2b + 5d)^2 > 0$ and $\lim_{c\to\infty} P_4(c)/c^2 = 4\varpi_1 > 0$. Moreover, $P_4'(c) = 0$ if and only if $c = \widehat{c} \equiv -(2b + 5d)(12a - 2b + 5d)/(8\varpi_1)$, and:

$$P_4(\widehat{c}) = \frac{(2b + 5d)^2[16\varpi_3 + (2b + 5d)^2]}{16\varpi_1} > 0. \qquad \text{(C 20)}$$

Therefore, $P_4(c) > 0$ for all $c > 0$ and hence $\gamma_{\star\star}^2 > \gamma_\star^2$ for all $c > 0$. As a conclusion, if $\Delta = 0$, inequality (C 18) holds, and for $\nu_4 < 0$:

$$\nu_4 + 2\nu_3 \sin^2\vartheta \leqslant \nu_4 + 2\nu_3 < 0 \quad \forall\, 0 \leqslant \vartheta \leqslant \pi. \qquad \text{(C 21)}$$

This result proves that $\chi(\vartheta)$ is bounded also for $\Delta = 0$ and $\nu_4 < 0$.

Appendix D. Stationary probability density function of the orientation angle

The convection–diffusion equation (3.7) and its stationary solution can be obtained by using the general properties of the Fokker–Planck equation (Risken 1989). The starting point is the Fokker–Planck equation (3.3) for $f(\boldsymbol{n}; t)$. Consider the p.d.f. of the

angles ϑ and φ:

$$\Psi(\vartheta,\varphi;t)\equiv\psi(\vartheta,\varphi;t)\sin\vartheta, \tag{D 1}$$

which is normalized thus: $\int_0^\pi\int_0^{2\pi}\Psi(\vartheta,\varphi;t)\,\mathrm{d}\vartheta\,\mathrm{d}\varphi=1$ for all $t\geqslant 0$. The p.d.f. $\Psi(\vartheta,\varphi;t)$ satisfies a new Fokker–Planck equation, whose form is derived from (3.3) by using the transformation formulae for the drift and diffusion coefficients under a change of variables (Risken 1989, p. 88), by writing $f(n,\vartheta,\varphi;t)=\psi(\vartheta,\varphi;t)\delta(n-L)$ with $L=1$, and by integrating the resulting equation with respect to n. The final result is:

$$\frac{\partial\Psi}{\partial t}=-\frac{\partial}{\partial\vartheta}[\mathscr{B}_\vartheta(\vartheta)\Psi]+\frac{1}{2}\frac{\partial^2}{\partial\vartheta^2}[\mathscr{A}_{\vartheta\vartheta}(\vartheta)\Psi]+\frac{1}{2}\mathscr{A}_{\varphi\varphi}(\vartheta)\frac{\partial^2\Psi}{\partial\varphi^2}, \tag{D 2}$$

where

$$\mathscr{B}_\vartheta(\vartheta)=\beta_i(\boldsymbol{n})\frac{\partial\vartheta}{\partial n_i}+\frac{\alpha_{ij}(\boldsymbol{n})}{2}\frac{\partial^2\vartheta}{\partial n_i\partial n_j}=\left[\nu_1+\nu_2\sin^2(\vartheta)+\nu_3\sin^4(\vartheta)\right]\cot\vartheta, \tag{D 3a}$$

$$\mathscr{A}_{\vartheta\vartheta}(\vartheta)=\alpha_{ij}(\boldsymbol{n})\frac{\partial\vartheta}{\partial n_i}\frac{\partial\vartheta}{\partial n_j}=2\nu_1+\nu_4\sin^2(\vartheta)+\nu_3\sin^4(\vartheta), \tag{D 3b}$$

$$\mathscr{A}_{\varphi\varphi}(\vartheta)=\alpha_{ij}(\boldsymbol{n})\frac{\partial\varphi}{\partial n_i}\frac{\partial\varphi}{\partial n_j}=\nu_5+2\nu_1\mathrm{cosec}^2(\vartheta) \tag{D 3c}$$

with ν_k, $k=1,\ldots,5$ defined in (3.10). Equations (D3) involve the Jacobian and the Hessian of the transformation from Cartesian to spherical coordinates, which can be calculated from (3.5). The convection–diffusion equation (3.7) follows from (D 1) and (D 2) with:

$$\mathscr{W}_\vartheta(\vartheta)=\mathscr{B}_\vartheta(\vartheta)-\frac{1}{2\sin\vartheta}\frac{\partial}{\partial\vartheta}[\mathscr{A}_{\vartheta\vartheta}(\vartheta)\sin\vartheta], \tag{D 4a}$$

$$\mathscr{D}_{\vartheta\vartheta}(\vartheta)=\mathscr{A}_{\vartheta\vartheta}(\vartheta), \tag{D 4b}$$

$$\mathscr{D}_{\varphi\varphi}(\vartheta)=\mathscr{A}_{\varphi\varphi}(\vartheta)\sin^2(\vartheta). \tag{D 4c}$$

The coefficients $\mathscr{A}_{\vartheta\vartheta}(\vartheta)$ and $\mathscr{A}_{\varphi\varphi}(\vartheta)$ are strictly positive as a consequence of (C7) and (C8). The boundary conditions for $\Psi(\vartheta,\varphi;t)$ are periodic, given that ϑ and φ are angular variables:

$$\Psi(\vartheta,\varphi;t)=\Psi(\vartheta+2\pi,\varphi;t)\quad\text{and}\quad\Psi(\vartheta,\varphi;t)=\Psi(\vartheta,\varphi+2\pi;t) \tag{D 5}$$

for all ϑ, φ and t. Moreover, at long times, $\Psi(\vartheta,\varphi;t)$ enjoys the same symmetries as $\psi(\vartheta,\varphi;t)$ as a consequence of the analogous symmetries of (D 2). In particular, the invariance of (D 2) under rotations about $\boldsymbol{\lambda}$ yields a one-dimensional Fokker–Planck equation for $\widehat{\Psi}(\vartheta;t)=\widehat{\psi}(\vartheta;t)\sin\vartheta$ with $\widehat{\psi}(\vartheta;t)=\int_0^{2\pi}\psi(\vartheta,\varphi;t)\,\mathrm{d}\varphi$. This equation is derived by integrating (D 2) with respect to φ from 0 to 2π and by using (D 5):

$$\frac{\partial\widehat{\Psi}}{\partial t}=-\frac{\partial}{\partial\vartheta}[\mathscr{B}_\vartheta(\vartheta)\widehat{\Psi}]+\frac{1}{2}\frac{\partial^2}{\partial\vartheta^2}[\mathscr{A}_{\vartheta\vartheta}(\vartheta)\widehat{\Psi}]. \tag{D 6}$$

The Itô stochastic differential equation associated with (D 6) is:

$$\dot{\vartheta}(t)=\mathscr{B}_\vartheta(\vartheta(t))+\sqrt{\mathscr{A}_{\vartheta\vartheta}(\vartheta(t))}\,\eta(t),\quad 0\leqslant\vartheta(t)\leqslant\pi, \tag{D 7}$$

where $\eta(t)$ is white noise. Equations (3.14) and (3.15) follow from (D 4*a*), (D 4*b*) and (D 7).

Consider now the functions:

$$\Phi(\vartheta) = \ln\left[\frac{\mathscr{A}_{\vartheta\vartheta}(\vartheta)}{2}\right] - 2\int_{\vartheta_0}^{\vartheta} \frac{\mathscr{B}_{\vartheta}(s)}{\mathscr{A}_{\vartheta\vartheta}(s)}\,\mathrm{d}s \tag{D 8}$$

and

$$g(\vartheta) = 2\int_{\vartheta_0}^{\vartheta} \frac{\mathrm{e}^{\Phi(s)}}{\mathscr{A}_{\vartheta\vartheta}(s)}\,\mathrm{d}s. \tag{D 9}$$

The stationary solution of (D 2) is written (see Risken 1989, p. 98):

$$\Psi_{st}(\vartheta) = \mathscr{N}\mathrm{e}^{-\Phi(\vartheta)} - \mathscr{S}g(\vartheta)\mathrm{e}^{-\Phi(\vartheta)}, \tag{D 10}$$

where $\mathscr{N}$ and $\mathscr{S}$ are constants. Consequently:

$$\psi_{st}(\vartheta) = \mathscr{N}\frac{\mathrm{e}^{-\Phi(\vartheta)}}{\sin\vartheta} - \mathscr{S}g(\vartheta)\frac{\mathrm{e}^{-\Phi(\vartheta)}}{\sin\vartheta}. \tag{D 11}$$

As $\mathscr{A}_{\vartheta\vartheta}(\vartheta)$ and $\mathscr{B}_{\vartheta}(\vartheta)$ are periodic, $\mathrm{e}^{-\Phi(\vartheta)}$ is also periodic. By contrast, $g(\vartheta)$ cannot be periodic given that $\mathscr{A}_{\vartheta\vartheta}(\vartheta) > 0$ for all $0 \leqslant \vartheta \leqslant \pi$ (see (D 4*b*), (C 7*a*), (C 8*a*)) and as a result $g'(\vartheta) > 0$ for all $0 \leqslant \vartheta \leqslant \pi$. Therefore, $\psi_{st}(\vartheta)$ satisfies (3.12) if and only if $\mathscr{S} = 0$, whence

$$\psi_{st}(\vartheta) = \frac{\mathscr{N}}{\mathscr{A}_{\vartheta\vartheta}(\vartheta)\sin\vartheta}\exp\left[2\int_{\vartheta_0}^{\vartheta}\frac{\mathscr{B}_{\vartheta}(s)}{\mathscr{A}_{\vartheta\vartheta}(s)}\,\mathrm{d}s\right]. \tag{D 12}$$

Equation (4.2) follows from (D 4*a*), (D 4*b*) and (D 12). For $\nu_3 \neq 0$, the integral on the right-hand side of (D 12) can be calculated by using the change of variable $y = \sin^2(z)$ and formulae 2.172, 2.175(1), and 2.177(1) in Gradshteyn & Ryzhik (1965). The final result is given in (4.4) and (4.5).

Appendix E. The case $\nu_3 = 0$

If $\nu_3 = 0$ and $\gamma \neq 0$ (i.e. $c = 0$), three cases should be distinguished.

For $\nu_3 = 0$, $\nu_4 \neq 0$, and $\nu_2 \neq 3\nu_4/2$, the integral in (4.2) can be easily calculated by means of the transformation $y = \sin^2(z)$ to yield:

$$\psi_{st}(\vartheta) = \mathscr{N}\left(2\nu_1 + \nu_4\sin^2\vartheta\right)^{(\nu_2/\nu_4)-(3/2)}. \tag{E 1}$$

The stationary p.d.f. is bounded as a consequence of (C 6) with $\nu_3 = 0$. By examining the first derivative of the above function, it can be shown that, depending on the value of the parameters, ψ_{st} has either three or five extrema in the interval $0 \leqslant \vartheta \leqslant \pi$. Therefore, the four regimes identified for $\nu_3 \neq 0$ also describe the dynamics of a non-spherical particle for $\nu_3 = 0$.

For $\nu_3 = \nu_4 = 0$ (i.e. $c = 2b + 5d = 0$), the stationary solution is:

$$\psi_{st}(\vartheta) = \mathscr{N}\exp\left[\frac{\nu_2}{2\nu_1}\sin^2(\vartheta)\right]. \tag{E 2}$$

For $\nu_2/\nu_1 > 0$, ψ_{st} has two minima at 0 and π and one maximum at $\pi/2$, and hence the particle rotates in the plane orthogonal to $\boldsymbol{\lambda}$. For $\nu_2/\nu_1 < 0$, ψ_{st} has two maxima at 0 and π and one minimum at $\pi/2$; therefore the particle tumbles between the direction parallel to $\boldsymbol{\lambda}$ and that antiparallel to $\boldsymbol{\lambda}$.

Finally, for $\nu_3 = 0$ and $\nu_2 = 3\nu_4/2$ (i.e. $c = 2b + (5+\gamma)d = 0$), (E 1) implies that the stationary statistics of orientations is isotropic: $\psi_{st}(\vartheta) = (4\pi)^{-1}$.

REFERENCES

BATCHELOR, G. K. 1946 The theory of axisymmetric turbulence. *Proc. R. Soc. Lond.* A **186**, 480–502.

BERNSTEIN, O. & SHAPIRO, M. 1994 Direct determination of the orientation distribution function of cylindrical particles immersed in laminar and turbulent shear flows. *J. Aerosol Sci.* **25**, 113–136.

BIFERALE, L. & PROCACCIA, I. 2005 Anisotropy in turbulent flows and in turbulent transport. *Phys. Rep.* **414**, 43–164.

BIRD, R. B., HASSAGER, O, ARMSTRONG, R. C. & CURTISS, C. F. 1977 *Dynamics of Polymeric Liquids*, vol. II. Wiley.

BIRD, R. B., WARNER, H. R. Jr & EVANS, D. C. 1971 Kinetic theory and rheology of dumbbell suspensions with Brownian motion. *Fortschr. Hochpolym.-Forsch.* **8**, 1–90.

BRENNER, H. 1974 Rheology of a dilute suspension of axisymmetric Brownian particles. *Intl J. Multiphase Flow* **1**, 195–341.

BRETHERTON, F. P. 1962 The motion of rigid particles in a shear flow at low Reynolds number. *J. Fluid Mech.* **14**, 284–304.

CHANDRASEKHAR, S. 1950 The theory of axisymmetric turbulence. *Phil. Trans. R. Soc. Lond.* A **242**, 557–577.

CHANG, K., BEWLEY, G. P. & BODENSCHATZ, E. 2012 Experimental study of the influence of anisotropy on the inertial scales of turbulence. *J. Fluid Mech.* **692**, 464–481.

CHEN, J.-P. & LAMB, D. 1994 The theoretical basis for the parametrization of ice crystal habits: growth by vapour deposition. *J. Atmos. Sci.* **51**, 1206–1221.

DOI, M. & EDWARDS, S. F. 1978 Dynamics of rod-like macromolecules in concentrated solution. 2. *J. Chem. Soc. Faraday Trans.* II **74**, 918–932.

DOI, M. & EDWARDS, S. F. 1986 *The Theory of Polymer Dynamics*. Oxford University Press.

FALKOVICH, G., GAWĘDZKI, K. & VERGASSOLA, M. 2001 Particles and fields in fluid turbulence. *Rev. Mod. Phys.* **73**, 913–975.

GANTMACHER, F. R. 1959 *The Theory of Matrices*, vol. 1. Chelsea Publishing Company.

GARDINER, C. W. 1983 *Handbook of Stochastic Methods*. Springer.

GRADSHTEYN, I. S. & RYZHIK, I. M. 1965 *Table of Integrals, Series, and Products*. Academic.

GYR, A. & BEWERSDORFF, W. 1995 *Drag Reduction of Turbulent Flows by Additives*. Kluwer.

HINCH, E. J. & LEAL, L. G. 1972 The effect of Brownian motion on the rheological properties of a suspension of non-spherical particles. *J. Fluid Mech.* **52**, 683–712.

JEFFERY, G. B. 1922 The motion of ellipsoidal particles immersed in a viscous fluid. *Proc. R. Soc. Lond.* A **102**, 161–179.

KLOEDEN, P. E. & PLATEN, E. 1992 *Numerical Solution of Stochastic Differential Equations*. Springer.

KOCH, D. L. & SUBRAMANIAN, G. 2011 Collective hydrodynamics of swimming microorganisms: living fluids. *Annu. Rev. Fluid Mech.* **43**, 637–659.

KRAICHNAN, R. H. 1968 Small-scale structure of a scalar field convected by turbulence. *Phys. Fluids* **11**, 945–953.

KRUSHKAL, E. M. & GALLILY, I. 1988 On the orientation distribution function of nonspherical aerosol particles in a general shear flow–II. The turbulent case. *J. Aerosol Sci.* **19**, 197–211.

KUZUU, N. Y. & DOI, M. 1980 Nonlinear viscoelasticity of concentrated solution of rod-like polymers. *Polym. J.* **12**, 883–890.

LARSON, R. G. 1999 *The Structure and Rheology of Complex Fluids*. Oxford University Press.

LEAL, L. G. & HINCH, E. J. 1971 The effect of weak Brownian rotations on particles in shear flow. *J. Fluid Mech.* **46**, 685–703.

LINDBORG, E. 1995 Kinematics of homogeneous axisymmetric turbulence. *J. Fluid Mech.* **302**, 179–201.

MINALE, M. 2010 Models for the deformation of a single ellipsoidal drop: a review. *Rheol. Acta* **49**, 789–806.

MOAKHER, M. 2008 Fourth-order Cartesian tensors: old and new facts, notions and applications. *Q. J. Mech. Appl. Maths* **61**, 181–203.

MORTENSEN, P. H., ANDERSON, H. I., GILLISSEN, J. J. J. & BOERSMA, B. J. 2008*a* Dynamics of prolate ellipsoidal particles in a turbulent channel flow. *Phys. Fluids* **20**, 093302.

MORTENSEN, P. H., ANDERSON, H. I., GILLISSEN, J. J. J. & BOERSMA, B. J. 2008*b* On the orientation of ellipsoidal particles in a turbulent shear flow. *Intl J. Multiphase Flow* **34**, 678–683.

NEWSOM, R. K. & BRUCE, C. W. 1998 Orientational properties of fibrous aerosols in atmospheric turbulence. *J. Aerosol Sci.* **29**, 773–797.

OLBRICHT, W. L., RALLISON, J. M. & LEAL, L. G. 1982 Strong flow criteria based on microstructure deformation. *J. Non-Newtonian Fluid Mech.* **10**, 291–318.

OLSON, J. A. & KEREKES, R. J. 1998 The motion of fibres in turbulent flow. *J. Fluid Mech.* **377**, 47–64.

PARSA, S., CALZAVARINI, E., TOSCHI, F. & VOTH, G. A. 2012 Rotation rate of rods in turbulent fluid flow. *Phys. Rev. Lett.* **109**, 134501.

PARSA, S., GUASTO, J. S., KISHORE, M., OUELLETTE, N. T., GOLLUB, J. P. & VOTH, G. A. 2011 Rotation and alignment of rods in two-dimensional chaotic flow. *Phys. Fluids* **23**, 043302.

PARSHEH, M., BROWN, M. L. & AIDUN, C. K. 2005 On the orientation of stiff fibres suspended in turbulent flow in a planar contraction. *J. Fluid Mech.* **545**, 245–269.

PETRIE, J. S. P. 1999 The rheology of fibre suspensions. *J. Non-Newtonian Fluid Mech.* **87**, 369–402.

PULIAFITO, A. & TURISTYN, K. 2005 Numerical study of polymer tumbling in linear shear flows. *Physica* D **211**, 9–22.

PUMIR, A. & WILKINSON, M. 2011 Orientation statistics of small particles in turbulence. *New J. Phys.* **13**, 093030.

RISKEN, H. 1989 *The Fokker–Planck Equation*. Springer.

ROBERTSON, H. P. 1940 The invariant theory of isotropic turbulence. *Proc. Camb. Phil. Soc.* **36**, 209–223.

SAINTILLAN, D. & SHELLEY, M. J. 2008 Instabilities and pattern formation in active particle suspensions: kinetic theory and continuum simulations. *Phys. Rev. Lett.* **100**, 178103.

SHAQFEH, E. S. G. & KOCH, D. L. 1992 Polymer stretch in dilute fixed beds of fibres or spheres. *J. Fluid Mech.* **244**, 17–54.

SHIN, M. & KOCH, D. L. 2005 Rotational and translational dispersion of fibres in isotropic turbulent flows. *J. Fluid Mech.* **540**, 143–173.

SZERI, A. J. 1993 Pattern formation in recirculating flows of suspensions of orientable particles. *Phil. Trans. R. Soc. Lond.* A **345**, 477–506.

TURITSYN, K. S. 2007 Polymer dynamics in chaotic flows with a strong shear component. *J. Expl Theor. Phys.* **105**, 655–664.

WILKINSON, M., BEZUGLYY, V. & MEHLIG, B. 2009 Fingerprints of random flows. *Phys. Fluids* **21**, 043304.

WILKINSON, M. & KENNARD, H. R. 2012 A model for alignment between microscopic rods and vorticity. *J. Phys.* A: *Math. Theor.* **45**, 455502.

ZHANG, H., AHMADI, G., FAN, F. G. & MCLAUGHLIN, J. B. 2001 Ellipsoidal particles transport and deposition in turbulent channel flows. *Intl J. Multiphase Flow* **27**, 971–1009.

ZIMMERMANN, R., GASTEUIL, Y., BOURGOIN, M., VOLK, R., PUMIR, A. & PINTON, J.-F. 2011*a* Rotational intermittency and turbulence induced lift experienced by large particles in a turbulent flow. *Phys. Rev. Lett.* **106**, 154501.

ZIMMERMANN, R., GASTEUIL, Y., BOURGOIN, M., VOLK, R., PUMIR, A. & PINTON, J.-F. 2011*b* Tracking the dynamics of translation and absolute orientation of a sphere in a turbulent flow. *Rev. Sci. Instrum.* **82**, 033906.

PHYSICAL REVIEW E **89**, 021001(R) (2014)

Elliptical tracers in two-dimensional, homogeneous, isotropic fluid turbulence: The statistics of alignment, rotation, and nematic order

Anupam Gupta,[1] Dario Vincenzi,[2] and Rahul Pandit[1,*]

[1]*Center for Condensed Matter Theory, Department of Physics, Indian Institute of Science, Bangalore 560012, India*

[2]*Université Nice Sophia Antipolis, CNRS, Laboratoire J. A. Dieudonné, UMR 7351, 06100 Nice, France*

(Received 28 August 2013; published 19 February 2014)

We study the statistical properties of orientation and rotation dynamics of elliptical tracer particles in two-dimensional, homogeneous, and isotropic turbulence by direct numerical simulations. We consider both the cases in which the turbulent flow is generated by forcing at large and intermediate length scales. We show that the two cases are qualitatively different. For large-scale forcing, the spatial distribution of particle orientations forms large-scale structures, which are absent for intermediate-scale forcing. The alignment with the local directions of the flow is much weaker in the latter case than in the former. For intermediate-scale forcing, the statistics of rotation rates depends weakly on the Reynolds number and on the aspect ratio of particles. In contrast with what is observed in three-dimensional turbulence, in two dimensions the mean-square rotation rate increases as the aspect ratio increases.

DOI: 10.1103/PhysRevE.89.021001 PACS number(s): 47.27.Gs, 47.27.Jv, 47.27.T−, 47.55.Kf

The elucidation of the statistical properties of fluid turbulence is a problem of central importance in a variety of areas that include fluid dynamics, nonlinear dynamics, and nonequilibrium statistical mechanics [1–4]. Over the last decade or so, important advances have been made in developing an understanding of the statistical properties of homogeneous, isotropic turbulence in the Lagrangian framework [5–7]. Most of the studies in this framework, whether experimental, theoretical, or numerical, have used spherical or circular tracer particles in three and two dimensions. The study of the dynamics of nonspherical particles in turbulent flows has applications in the simplest models for swimming microorganisms [8], ice crystals in clouds [9], and fibers in the paper industry [10]. Recent work in three-dimensional (3D) turbulent flows [11–17] and in two-dimensional (2D) low-Reynolds-number flows [18,19] has renewed interest in Lagrangian studies with anisotropic particles. We extend these studies to 2D, homogeneous, and isotropic turbulence with elliptical tracer particles. Our study yields several interesting results, which have neither been obtained nor anticipated hitherto. We show that the dynamics of elliptical particles depends significantly on whether the fluid is forced at (A) large or (B) small length scales; the alignment of $\boldsymbol{p}$, the unit vector along the semimajor axis of an elliptical particle, and $\nabla \times \boldsymbol{\omega}$, where $\boldsymbol{\omega}$ is the vorticity, is more pronounced in case (A) than in case (B); and the statistics of the particle-rotation rate depends appreciably on the Reynolds number of the flow and the aspect ratio of the particles in case (A) but not in case (B). Moreover, we find important differences between the statistical properties of elliptical tracers in 2D turbulence and their counterparts for ellipsoidal particles in 3D turbulence. In three dimensions, $\boldsymbol{p}$ exhibits a strong alignment with $\boldsymbol{\omega}$ [12], the mean-square-rotation rate of $\boldsymbol{p}$ decreases as the aspect ratio of particles increases [13], and the autocorrelation function of $\boldsymbol{p}$ decays exponentially, with a correlation time increasing as a function of the Reynolds number [12]. By contrast, in two dimensions, we show that the alignment of $\boldsymbol{p}$ and $\nabla \times \boldsymbol{\omega}$ is much weaker than its analog in three dimensions, namely, the alignment of $\boldsymbol{p}$ and $\boldsymbol{\omega}$; in addition, the mean-square-rotation rate of $\boldsymbol{p}$ increases as the aspect ratio of particles increases. We thus extend significantly what is known about the differences between 2D and 3D turbulence [2,4,20,21].

The 2D, incompressible Navier-Stokes equations can be written in terms of the stream function ψ and the vorticity $\boldsymbol{\omega} = \nabla \times \boldsymbol{u}(\boldsymbol{x},t) \equiv \omega \hat{\boldsymbol{z}}$, where $\boldsymbol{u} \equiv (-\partial_y \psi, \partial_x \psi)$ is the fluid velocity at the point $\boldsymbol{x}$ and time t, and $\hat{\boldsymbol{z}}$ is the unit normal to the fluid film:

$$D_t \omega = \nu \nabla^2 \omega - \mu \omega + f_\omega; \quad \nabla^2 \psi = \omega. \tag{1}$$

Here $D_t \equiv \partial_t + \boldsymbol{u} \cdot \nabla$, the uniform solvent density $\rho = 1$, μ is the coefficient of friction (which is always present in experimental fluid films [22]), and ν is the kinematic viscosity of the fluid. We use a zero-mean, Gaussian stochastic forcing with $\langle \tilde{f}_\omega(\boldsymbol{k}) \tilde{f}_\omega(\boldsymbol{k}') \rangle = A(\boldsymbol{k}) \delta(\boldsymbol{k} + \boldsymbol{k}')$, where $A(\boldsymbol{k}) = f_{\rm inj}$ if $|\boldsymbol{k}| = k_{\rm inj}$ and zero otherwise, the tilde denotes a spatial Fourier transform, and $k_{\rm inj}$ is the length of the energy-injection wave vector. The configuration of an elliptical particle is given by the position of its center of mass, $\boldsymbol{x}_c$, and by the axial unit vector $\boldsymbol{p} = (\cos\theta, \sin\theta)$ that specifies the orientation of the semimajor axis with respect to a fixed direction. The elliptical particles we consider are neutrally buoyant, of uniform composition, and much smaller than the viscous dissipation scale, so the velocity gradient is uniform over the size of a particle. In addition, we study suspensions that are sufficiently dilute for hydrodynamic particle-particle interactions to be disregarded. Under the above assumptions, $\boldsymbol{x}_c$ satisfies

$$\dot{\boldsymbol{x}}_c = \boldsymbol{u}(\boldsymbol{x}_c(t),t); \tag{2}$$

and the time evolution of the orientation is given by the Jeffery equation [23], which reduces in a 2D, incompressible flow to the following one for the angle θ:

$$\dot{\theta} = \tfrac{1}{2}\omega + \gamma(\alpha)[\sin(2\theta) S_{11} - \cos(2\theta) S_{12}], \tag{3}$$

[*] Also at Jawaharlal Nehru Centre for Advanced Scientific Research, Jakkur, Bangalore, India.

TABLE I. The parameters for our DNS runs. Here, $\eta \equiv (\nu^3/\varepsilon)^{1/4}$ is the dissipation scale, $\lambda \equiv \sqrt{\nu\mathcal{E}/\varepsilon}$ is the Taylor-microscale, $\mathrm{Re}_\lambda = u_{\rm rms}\lambda/\nu$ is the Taylor-microscale Reynolds number, $T_{\rm eddy} \equiv \Sigma_k \frac{(E(k)/k)}{E(k)}/u_{\rm rms}$ is the eddy-turnover time, and $\tau_\eta \equiv \sqrt{\nu/\varepsilon}$ is the Kolmogorov time scale, where $\mathcal{E} \equiv \langle \frac{1}{2}|u(x,t)|^2\rangle_{x,t}$, where $\langle\cdot\rangle_{x,t}$ denotes a space-time average, is the total kinetic energy of the flow, $u_{\rm rms}$ is the root-mean-square velocity, ε is the kinetic-energy dissipation rate, and $E(k) \equiv \sum_{k-1/2<k'\leqslant k+1/2} k'^2\langle|\widetilde{\psi}(k',t)|^2\rangle_t$, where $\langle\cdot\rangle_t$ indicates a time average over the statistically steady state, is the fluid-energy spectrum. The Lagrangian correlation times of S_{11}, S_{12}, and ω are defined as $\tau_{S_{11}} \equiv \langle S_{11}^2\rangle^{-1}\int_0^\infty \langle S_{11}(t)S_{11}(0)\rangle\, dt$, $\tau_{S_{12}} \equiv \langle S_{12}^2\rangle^{-1}\int_0^\infty \langle S_{12}(t)S_{12}(0)\rangle\, dt$, and $\tau_\omega \equiv \langle\omega^2\rangle^{-1}\int_0^\infty \langle\omega(t)\omega(0)\rangle\, dt$, respectively.

Run	N	ν	μ	$f_{\rm inj}$	$k_{\rm inj}$	δt	η	λ	Re_λ	$T_{\rm eddy}$	τ_η	$\tau_{S_{11}}$	$\tau_{S_{12}}$	τ_ω	N_p
A1	2048	5×10^{-5}	0.01	1.9×10^{-6}	2	4.0×10^{-3}	3.3×10^{-2}	0.460	199	23.5	21.3	92.2	94.4	46.6	10^4
B1	2048	5×10^{-5}	0.01	7.8×10^{-3}	50	1.0×10^{-3}	3.8×10^{-3}	0.053	202	1.34	0.28	1.59×10^{-2}	1.61×10^{-2}	8.01×10^{-3}	10^4
A2	2048	5×10^{-5}	0.01	8×10^{-6}	2	2.0×10^{-3}	2.6×10^{-2}	0.470	382	14.7	12.0	24.7	24.1	12.2	10^4
B2	2048	5×10^{-5}	0.01	1.65×10^{-2}	50	5.0×10^{-4}	3.2×10^{-3}	0.063	385	1.37	0.21	8.66×10^{-3}	8.73×10^{-3}	4.35×10^{-3}	10^4
A3	2048	5×10^{-5}	0.01	1.5×10^{-5}	2	2.0×10^{-3}	2.0×10^{-2}	0.474	536	11.1	8.38	12.6	9.98	5.55	10^4
B3	2048	5×10^{-5}	0.01	2.5×10^{-2}	50	5.0×10^{-4}	3.0×10^{-3}	0.069	539	1.17	0.17	1.55×10^{-3}	1.56×10^{-3}	7.79×10^{-4}	10^4

where $S_{ij} = (\partial_i u_j + \partial_j u_i)/2$ are the components of the rate-of-strain tensor evaluated at $\boldsymbol{x}_c$, $\gamma(\alpha) \equiv (\alpha^2-1)/(\alpha^2+1)$, and α is the ratio of the lengths of the semimajor and semiminor axes of the elliptical particle; γ varies from 0 (circular disks) to 1 (thin rods).

Our direct numerical simulation (DNS) of Eqs. (1)–(3) uses periodic boundary conditions over a square domain with side $L = 2\pi$, a pseudospectral method [24] with $N^2 = 2048^2$ collocation points, the 2/3 dealiasing rule, and, for the time evolution, a second-order, exponential-time-differencing Runge-Kutta method [25,26]. For the integration of Eq. (2), we use an Euler scheme, because, in one time step δt, a tracer particle crosses roughly one-tenth of a grid spacing. At off-lattice points, we evaluate the particle velocity from the Eulerian velocity field by using a bilinear-interpolation scheme [27]. Finally, we integrate Eq. (3) by using an Euler scheme, with the same time step as for Eq. (2); and, at $t = 0$, the orientation angles are uniformly distributed over $[0,2\pi]$. We track $N_p = 10^4$ particles over time to obtain the statistics of particle alignment and rotation for 12 different values of $0 < \gamma \leqslant 1$. We collect data for averages only when our system has reached a nonequilibrium statistically steady state, i.e., for $t > 20T_{\rm eddy}$, where $T_{\rm eddy}$ is the integral-scale eddy-turnover time of the flow. The parameters used in our simulations are given in Table I. Our study consists of two sets of simulations (A) and (B) at comparable values of Re_λ, the Taylor-microscale Reynolds numbers. In (A), the flow is forced at small $k_{\rm inj}$ (i.e., a large length scale); in (B), it is forced at an intermediate value of $k_{\rm inj}$ (i.e., an intermediate length scale); even in case (B) $k_{\rm inj}$ is small enough that the energy spectrum displays both a part with an inverse-energy cascade and a part with a forward cascade of enstrophy. We have also performed simulations at a lower resolution ($N = 1024$) and obtained similar results, so our study does not suffer from finite-resolution effects.

In Fig. 1(a), we show a pseudocolor plot of ω for case (A) at a representative time in the statistically steady state; Fig. 1(b) shows the positions and the orientations of particles at the same time; an elliptical particle is represented here by a black line whose center indicates $\boldsymbol{x}_c$ and whose orientation is that of $\boldsymbol{p}$. Analogous plots for case (B) are given in Figs. 1(c) and 1(d). Figure 1 suggests that the particle dynamics is qualitatively different in cases (A) and (B). In particular, in the former case, the orientation of particles is such that we see large-scale structures, which are absent in the latter case. To quantify this behavior, we study the statistics of the alignment of particles with the local directions of the flow.

The curl of the vorticity is tangent to the isolines of ω; a strong alignment between $\boldsymbol{p}$ and $\nabla\times\boldsymbol{\omega}$ would thus indicate a significant correlation between the spatial distribution of particle orientations and the vorticity field. Figure 2 shows the probability density function (PDF) of the angle χ between $\boldsymbol{p}$ and $\nabla\times\boldsymbol{\omega}$. In case (A), $\boldsymbol{p}$ tends to align with $\nabla\times\boldsymbol{\omega}$, but the alignment is not very strong. A careful inspection of Fig. 1 shows indeed that the spatial distribution of particle orientations does not closely reproduce the isolines of vorticity. Moreover, the alignment weakens as γ decreases and Re_λ increases (Fig. 2). In case (B), the PDF of χ depends very weakly on χ; i.e., the elliptical tracers do not exhibit a definite preferential orientation with respect to $\nabla\times\boldsymbol{\omega}$. We observe this behavior for all the values of Re_λ considered in Fig. 2.

An examination of the statistics of χ shows the first, remarkable difference between the dynamics of nonspherical

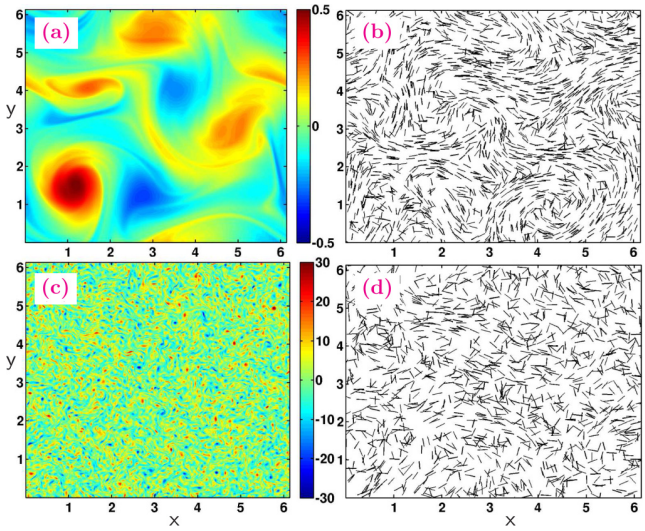

FIG. 1. (Color online) (a) Pseudocolor plot of ω at $t = 17.5$ for run A3; (b) particle positions and orientations at $t = 17.5$ for run A3 and $\gamma = 1$; (c) pseudocolor plot of ω at $t = 17.5$ for run B3; (d) particle positions and orientations at $t = 17.5$ for run B3 and $\gamma = 1$. The number of particles shown in (b) and (d) is 2×10^3. For the spatiotemporal evolution of these plots see Ref. [29].

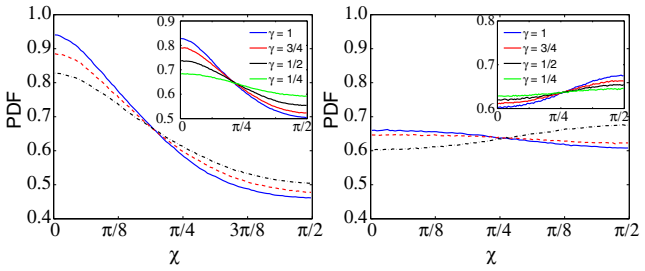

FIG. 2. (Color online) PDFs of the angle between $\boldsymbol{p}$ and $\nabla \times \boldsymbol{\omega}$. Left: Run A1 (solid, blue curve), run A2 (dashed, red curve), and run A3 (dot-dashed, black curve) for $\gamma = 1$. The inset shows the same PDF for run A3 and different values of γ (from top to bottom, $\gamma = 1, 3/4, 1/2$, and $1/4$). Right: Run B1 (solid, blue curve), run B2 (dashed, red curve), and run B3 (dot-dashed, black curve) for $\gamma = 1$. The inset shows the same PDF for run B3 and different values of γ (from top to bottom, $\gamma = 1,\ 3/4,\ 1/2$,and $1/4$).

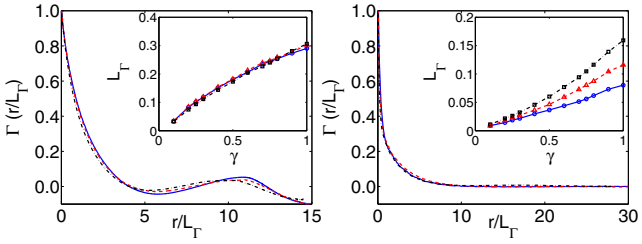

FIG. 4. (Color online) Single-time two-point correlation function of M as a function of the space separation rescaled by the correlation length. Left: Run A1 (solid, blue curve), run A2 (dashed, red curve), and run A3 (dot-dashed, black curve) for $\gamma = 1$. Right: Run B1 (solid, blue curve), run B2 (dashed, red curve), run B3 (dot-dashed, black curve) for $\gamma = 1$. The insets show the correlation length as a function of γ; the color code is the same as in the main plots.

tracers in three dimensions and that of elliptical particles in two dimensions. In three dimensions, the tracer particles align strongly with $\boldsymbol{\omega}$ [12]. This behavior has been explained in Ref. [12] by arguing that, if viscosity is disregarded, the equation describing the Lagrangian evolution of $\boldsymbol{\omega}/|\boldsymbol{\omega}|$ is equivalent to the evolution equation for the axial unit vector of a thin rod. In two dimensions, an analogous equivalence exists, because $(\nabla \times \boldsymbol{\omega})/|\nabla \times \boldsymbol{\omega}|$ satisfies the Jeffery equation with $\gamma = 1$ (provided that $\nu = 0$). In two dimensions, this formal equivalence does not yield a strong alignment between $\boldsymbol{p}$ and $\nabla \times \boldsymbol{\omega}$ because the effect of the viscosity on $\nabla \times \boldsymbol{\omega}$ in two dimensions is more important than its effect on $\boldsymbol{\omega}$ in three dimensions. The aforementioned equivalence also explains why the alignment of particles with $\nabla \times \boldsymbol{\omega}$ becomes weaker as their aspect ratio decreases; and indeed the evolution equation for $\boldsymbol{p}$ increasingly deviates from that for $(\nabla \times \boldsymbol{\omega})/|\nabla \times \boldsymbol{\omega}|$. The decrease of the probability of alignment with increasing Re_λ is, on the contrary, attributable to the increase of the fluctuations of the components of $\nabla \boldsymbol{u}$.

The eigenvectors of S form a Lagrangian orthogonal frame of reference. In Fig. 3, we show the PDF of the angle β between $\boldsymbol{p}$ and the eigenvector $\boldsymbol{e}_1$, associated with the positive eigenvalue of S. Particles tend to align with $\boldsymbol{e}_1$, but the alignment is weaker in case (B) than in case (A). The alignment becomes weaker as γ decreases, because the contribution of

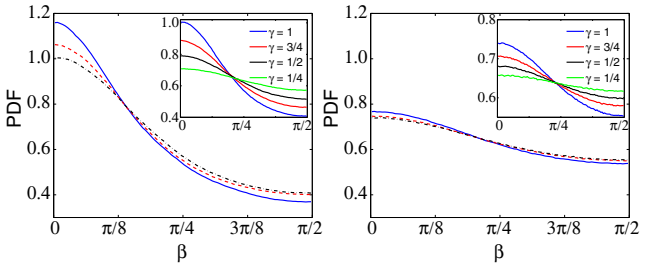

FIG. 3. (Color online) PDFs of the angle β between $\boldsymbol{p}$ and $\boldsymbol{e}_1$ for $\gamma = 1$ and different Re_λ in case (A) (left) and in case (B) (right). The insets show the PDF of β for different values of γ for runs A3 (left) and B3 (right). The color code is the same as in Fig. 2.

S to the evolution of $\boldsymbol{p}$ diminishes [see Eq. (3)]. The tendency of particles to align with $\boldsymbol{e}_1$ diminishes as Re_λ increases, i.e., as turbulent fluctuations are enhanced. The moderate degree of alignment, shown in Fig. 3, is comparable with that found for rods in 2D, low-Reynolds-number flows [18] and in 3D, homogeneous, isotropic turbulence [12].

We have calculated the conditional PDFs of the alignment of particles conditioned on the sign of the Okubo-Weiss parameter [26,28], which distinguishes between vortical and extensional regions of the flow; the conditional PDFs do not deviate from their unconditional counterparts [29].

To quantify the spatial distribution of particle orientations, we define the correlation function $\Gamma(r) = [\langle M(\boldsymbol{r},t)M(\boldsymbol{0},t)\rangle - \langle M(\boldsymbol{r},t)\rangle\langle M(\boldsymbol{0},t)\rangle]/\langle M^2\rangle$, where $M(\boldsymbol{r},t) \equiv [2\cos^2\theta(\boldsymbol{r},t) - 1]$ is the local nematic order parameter in two dimensions [30] and $\langle\cdot\rangle$ denotes an average over time and over the tracer particles. The function $\Gamma(r)$ is shown in Fig. 4 for different values of Re_λ. In both cases (A) and (B), the shape of $\Gamma(r)$ depends only weakly on Re_λ. However, in case (A), the order parameter of rods is correlated up to distances of the order of 5% of L and is anticorrelated at large r; in case (B), $\Gamma(r)$ decays exponentially to zero. These behaviors are in accordance with the spatial distributions of orientations shown in Fig. 1. Furthermore, in case (A), the correlation length $L_\Gamma = [\int_0^\pi \Gamma(r)dr]/\Gamma(0)$ depends weakly on Re_λ, because the value of L_Γ is determined principally by k_{inj}; in case (B), the size of large-scale flow structures increases with increasing Re_λ [31]; hence, L_Γ increases accordingly. In both cases, L_Γ is obviously an increasing function of γ.

Let us now examine the temporal autocorrelation function of $\boldsymbol{p}$. In both cases (A) and (B), $C(t) = \langle \boldsymbol{p}(t)\cdot\boldsymbol{p}(0)\rangle$ decays exponentially to zero (Fig. 5), but the correlation time $\tau_c = \int_0^\infty C(t)dt$ is much shorter in the former case. The ratio τ_c/τ_η increases as a function of both Re_λ and γ; this behavior is similar to that observed in 3D turbulence, where the orientational dynamics of spheres decorrelates faster than that of rods [12].

Figure 6 shows the PDFs of the rotation rate $\dot{\theta}$ of particles for different values of Re_λ (for the analogous PDFs at fixed Re_λ and different γ; see [29]). Very large fluctuations characterize the statistics of $\dot{\theta}$, as has been observed in 3D turbulence [13]. However, the probability of large fluctuations increases with

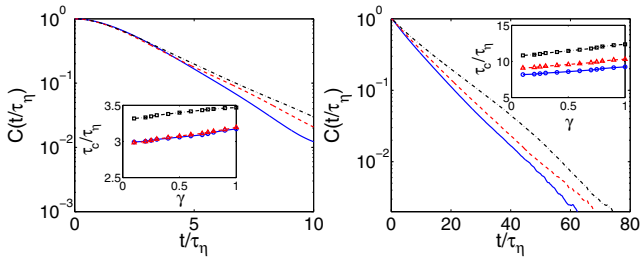

FIG. 5. (Color online) Autocorrelation function of $\boldsymbol{p}$ as a function of the time separation rescaled by τ_η for different Re_λ in case (A) (left) and in case (B) (right). The insets show the correlation time rescaled by τ_η as a function of γ for different Re_λ. The color codes are the same as in Fig. 4.

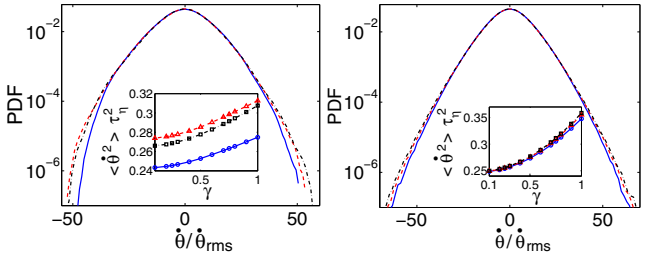

FIG. 6. (Color online) PDFs of $\dot{\theta}$ rescaled by $\dot{\theta}_{\mathrm{rms}} = \sqrt{\langle \dot{\theta}^2 \rangle}$ for $\gamma = 1$ and different Re_λ in case (A) (left) and in case (B) (right). The insets show the mean-square rotation rate multiplied by τ_η^2 as a function of γ. The color codes are the same as in Fig. 4.

increasing γ and Re_λ in case (A), whereas it depends weakly on γ and Re_λ in case (B). The main difference between 2D and 3D cases is the dependence of the mean-squared-rotation rate $\langle \dot{\theta}^2 \rangle$ upon γ. In three dimensions, $\langle \dot{\theta}^2 \rangle$ decreases as γ increases and is thus smaller for rods than for spheres [13]. The reason for this behavior is that the tendency to align with $\boldsymbol{\omega}$ is stronger for elongated particles [12,13] than for spheres. In two dimensions, such an alignment cannot take place and $\langle \dot{\theta}^2 \rangle$ increases as γ increases.

We have examined the statistics of the orientational and rotational dynamics of elliptical tracers in 2D, homogeneous, and isotropic turbulence. By considering two sets of simulations with different k_{inj}, we have shown that these properties depend on the scale at which the turbulent flow is generated. In the small-k_{inj} case, the spatial correlation of the nematic order parameter indicates the existence of large-scale structures in the spatial distribution of $\boldsymbol{p}$, which are absent in the intermediate-k_{inj} case. Moreover, the probability of $\boldsymbol{p}$ being aligned with $\nabla \times \boldsymbol{\omega}$ or $\boldsymbol{e}_1$ is much lower for intermediate k_{inj} than for small k_{inj}. These differences can be explained by noting that the dynamics of fluid particles is different in the direct- and inverse-cascade regimes [32,33], and hence the Lagrangian statistics of $\nabla \boldsymbol{u}$ depends on k_{inj} (see, e.g., $\tau_{S_{11}}$, $\tau_{S_{12}}$, and τ_ω given in Table I, as well as the Lagrangian autocorrelation functions of the components of $\nabla \boldsymbol{u}$ reported in [29]). Our study sheds new light on the qualitative differences between 2D and 3D homogeneous, isotropic fluid turbulence. These differences lead to a weaker alignment between $\boldsymbol{p}$ and $\nabla \times \boldsymbol{\omega}$ in two dimensions as compared to the alignment between $\boldsymbol{p}$ and $\boldsymbol{\omega}$ in three dimensions and to a different dependence of $\langle \dot{\theta}^2 \rangle$ upon γ (as γ increases, $\langle \dot{\theta}^2 \rangle$ *increases* in two dimensions but *decreases* in three dimensions). We hope our comprehensive study of the statistical properties of elliptical tracer particles in 2D, homogeneous, and isotropic turbulent fluid flows will stimulate experimental studies of such particles.

We are grateful to G. Boffetta, D. Mitra, S. Musacchio, P. Perlekar, and S. S. Ray for useful discussions. We acknowledge support from the EU COST Action MP0806 "Particles in Turbulence" and the Indo-French Centre for Applied Mathematics (IFCAM). AG and RP thank UGC, CSIR, DST (India) for support and SERC (IISc) for computational resources.

[1] A. S. Monin and A. M. Yaglom, *Statistical Fluid Mechanics* (Dover, Mineola, NY, 1975).
[2] U. Frisch, *Turbulence: The Legacy of A. N. Kolmogorov* (Cambridge University Press, Cambridge, England, 1995).
[3] T. Bohr, M. H. Jensen, G. Paladin, and A. Vulpiani, *Dynamical Systems Approach to Turbulence* (Cambridge University Press, Cambridge, England, 1998).
[4] R. Pandit, P. Perlekar, and S. S. Ray, Pramana **73**, 157 (2009).
[5] G. Falkovich, K. Gawędzki, and M. Vergassola, Rev. Mod. Phys. **73**, 913 (2001).
[6] F. Toschi and E. Bodenschatz, Annu. Rev. Fluid Mech. **41**, 375 (2009).
[7] J. P. L. C. Salazar and L. R. Collins, Annu. Rev. Fluid Mech. **41**, 405 (2009).
[8] D. L. Koch and G. Subramanian, Annu. Rev. Fluid Mech. **43**, 637 (2011).
[9] J. P. Chen and D. Lamb, J. Atmos. Sci. **51**, 1206 (1994).
[10] F. Lundell, L. D. Söderberg, and P. H. Alfredsson, Annu. Rev. Fluid Mech. **43**, 195 (2011).
[11] E. S. G. Shin and D. L. Koch, J. Fluid Mech. **540**, 143 (2005).
[12] A. Pumir and M. Wilkinson, New J. Phys. **13**, 093030 (2011).
[13] S. Parsa, E. Calzavarini, F. Toschi, and G. A. Voth, Phys. Rev. Lett. **109**, 134501 (2012).
[14] M. Wilkinson and H. R. Kennard, J. Phys. A: Math. Theor. **45**, 455502 (2012).
[15] D. Vincenzi, J. Fluid Mech. **719**, 465 (2013).
[16] L. Chevillard and C. Meneveau, J. Fluid Mech. **737**, 571 (2013).
[17] K. Gustavsson, J. Einarsson, and B. Mehlig, Phys. Rev. Lett. **112**, 014501 (2014).
[18] S. Parsa, J. S. Guasto, M. Kishore, N. T. Ouellette, J. P. Gollub, and G. A. Voth, Phys. Fluids **23**, 043302 (2011).
[19] M. Wilkinson, V. Bezuglyy, and B. Mehlig, Phys. Fluids **21**, 043304 (2009); V. Bezuglyy, B. Mehlig, and M. Wilkinson, Europhys. Lett. **89**, 34003 (2010).
[20] M. Lesieur, *Turbulence in Fluids* (Springer, Dordrecht, 2008).
[21] G. Boffetta and R. E. Ecke, Annu. Rev. Fluid Mech. **44**, 427 (2012).

[22] P. Perlekar and R. Pandit, New J. Phys. **12**, 023033 (2010), and references therein.
[23] G. B. Jeffery, Proc. R. Soc. London, Ser. A **102**, 161 (1922).
[24] C. Canuto, M. Y. Hussaini, A. Quarteroni, and T. A. Zang, *Spectral Methods in Fluid Dynamics* (Springer-Verlag, Berlin, 1988).
[25] S. M. Cox and P. C. Matthews, J. Comput. Phys. **176**, 430 (2002).
[26] P. Perlekar, S. S. Ray, D. Mitra, and R. Pandit, Phys. Rev. Lett. **106**, 054501 (2011).
[27] W. Press, B. Flannery, S. Teukolsky, and W. Vetterling, *Numerical Recipes in Fortran* (Cambridge University Press, Cambridge, 1992).
[28] A. Okubo, Deep-Sea Res. Oceanogr. Abstr. **17**, 445 (1970); J. Weiss, Physica D **48**, 273 (1991).
[29] See Supplemental Material at http://link.aps.org/supplemental/10.1103/PhysRevE.89.021001 for the spatiotemporal evolution of the plots shown in Fig. 1, the PDFs of the alignment conditioned on the sign of the Okubo-Weiss parameter, the PDFs of $\dot{\theta}$ for different values of γ, and the Lagrangian statistics of $\boldsymbol{\nabla u}$.
[30] P. M. Chaikin and T. C. Lubensky, *Principles of Condensed Matter Physics* (Cambridge University Press, Cambridge, England, 1995).
[31] G. Boffetta and S. Musacchio, Phys. Rev. E **82**, 016307 (2010).
[32] G. Boffetta and A. Celani, Physica A **280**, 1 (2000).
[33] G. Boffetta and I. M. Sokolov, Phys. Fluids **14**, 3224 (2002).

Annexe C

Etirement

C1. M. Martins Afonso & D. Vincenzi
Nonlinear elastic polymers in random flow
J. Fluid Mech. **540**, 99–108 (2005)

C2. D. Vincenzi & E. Bodenschatz
Single polymer dynamics in elongational flow and the confluent Heun equation
J. Phys. A : *Math. Gen.* **39**,10691–10701 (2006)

C3. A. Celani, A. Puliafito & D. Vincenzi
Dynamical slowdown of polymers in laminar and random flows
Phys. Rev. Lett. **97**, 118301 (2006)

C4. D. Vincenzi, S. Jin, E. Bodenschatz & L. R. Collins
Stretching of polymers in isotropic turbulence : A statistical closure
Phys. Rev. Lett. **98**, 024503 (2007)

C5. S. Musacchio & D. Vincenzi
Deformation of a flexible polymer in a random flow with long correlation time
J. Fluid Mech. **670**, 326–336 (2011)

C6. D. Vincenzi, P. Perlekar, L. Biferale & F. Toschi
Impact of the Peterlin approximation on polymer dynamics in turbulent flows
Phys. Rev. E **92**, 053004 (2015)

C7. A. Ahmad & D. Vincenzi
Polymer stretching in the inertial range of turbulence
Phys. Rev. E *93*, 052605 (2016)

C8. E.L.C. VI M. Plan, A. Ali & D. Vincenzi
Bead-rod-spring models in random flows
Phys. Rev. E **94**, 020501(R) (2016)

C9. J.R. Picardo, D. Vincenzi, N. Pal & S.S. Ray
Preferential sampling of elastic chains in turbulent flows
Phys. Rev. Lett., sous presse, `arXiv:1809.00333` (2018)

J. Fluid Mech. (2005), *vol.* 540, *pp.* 99–108.
doi:10.1017/S0022112005005951 Printed in the United Kingdom

Nonlinear elastic polymers in random flow

By M. MARTINS AFONSO[1] AND D. VINCENZI[2,3,4]

[1]INFM-Dipartimento di Fisica, Università di Genova and INFN, Sezione di Genova, Via Dodecaneso 33, 16146 Genova, Italy

[2]Dipartimento di Fisica, Università di Genova, Via Dodecaneso 33, 16146 Genova, Italy

[3]Max-Planck-Institut für Dynamik und Selbstorganisation, Göttingen, Germany

[4]LASSP, Clark Hall, Cornell University, Ithaca, NY 14853, USA

(Received 17 January 2005 and in revised form 4 May 2005)

Polymer stretching in random smooth flows is investigated within the framework of the FENE dumbbell model. The advecting flow is Gaussian and short-correlated in time. The stationary probability density function of polymer extension is derived exactly. The characteristic time needed for the system to attain the stationary regime is computed as a function of the Weissenberg number and the maximum length of polymers. The transient relaxation to the stationary regime is predicted to be exceptionally slow in the proximity of the coil–stretch transition.

1. Introduction

The ability of polymers to considerably change the large-scale statistics of the advecting flow has important practical applications, drag reduction being one of the most relevant ones (see Gyr & Bewersdorff 1995). Polymers affect the dynamics of the advecting velocity field only if they are highly elongated. Understanding how a single polymer chain is stretched by a random flow is thus the first issue to address in the study of hydrodynamical properties of polymer solutions.

At equilibrium, the radial shape of coiled polymers is spherical due to their entropy. When placed in a non-homogeneous flow, polymers are deformed and stretched by the gradients of the velocity. The product of the longest relaxation time of polymers and the characteristic rate of deformation is called the Weissenberg number *Wi*. For small *Wi* the entropic force prevails and polymers are in the coiled state. When *Wi* exceeds a critical value the molecules become highly elongated and their extension increases sharply. This phenomenon is called coil–stretch transition and the critical Weissenberg number is known to be approximately one.

We investigate the statistics of polymer extension in the FENE (finite extensible nonlinear elastic) dumbbell model (see e.g. Bird *et al.* 1977, for a review). A polymer is described as two beads joined by an elastic spring. The elastic force diverges as the elongation of polymers attains its maximum value, R_m, and this gives a large-extension cutoff. Consequently the stationary regime exists however strong the velocity gradients are. Since attention is directed only to the dynamics of a single molecule, the feedback on the advecting flow is disregarded. To allow analytical progress, the random flow is chosen to have Batchelor–Kraichnan statistics. This means that the considered flow is Gaussian, white in time and linear in space. The Batchelor–Kraichnan model is a fully-solvable model for passive turbulent transport which can provide useful connections between theory and real behaviours (see Falkovich, Gawędzki & Vergassola 2001,

for a review on the applications to scalar and magnetic fields). The results should be intended as a qualitative description of real polymer dynamics. We derive the complete form of the stationary probability density function (p.d.f.) of polymer extension and describe how the statistics of polymer stretching changes with increasing velocity gradients. Concerning the statistics at finite times, we compute the typical time needed for the system to reach the steady state and predict how it depends on the maximum length of polymers and the stretching by the flow. Our analysis shows that the coil–stretch transition of polymers is characterized by an anomalous dynamics in time.

The coil–stretch transition was predicted in 1974 for shear and hyperbolic flows (De Gennes 1974) and has been widely studied experimentally for such flows (Perkins, Smith & Chu 1997; Smith, Babcock & Chu 1999; Hur *et al.* 2002; Babcock *et al.* 2003). In contrast, the experimental study of polymer dynamics in random flows is a very recent achievement. This is due to the difficulty in generating a flow that is random at scales comparable with the size of polymers (about 100 μm). This difficulty can be overcome thanks to the elastic turbulence discovered by Groisman & Steinberg (2000); the flow of a highly elastic polymer solution at low Reynolds numbers but large Wi has all the main properties of fully developed turbulence. Therefore, in solutions of sufficiently elastic polymers it is possible to excite turbulent motion in exceedingly small volumes. Exploiting elastic turbulence in polymer solutions, Gerashchenko, Chevallard & Steinberg (2005) thus investigated the stretching and the deformation of a single DNA molecule in a three-dimensional random flow.

Theoretical studies concerning the coil–stretch transition in random flows have focused mainly on the Hookean dumbbell model (Chertkov 2000; Balkovsky, Fouxon & Lebedev 2000; Celani, Musacchio & Vincenzi 2005*a*). This model is suitable only for the coiled state ($Wi < 1$) since the linear force in principle allows infinite extensions and for large Wi polymers can become more and more elongated under the action of velocity gradients. For $Wi \geqslant 1$ a stationary p.d.f. of the extension no longer exists and this behaviour was conjectured to coincide with the coil–stretch transition. To overcome this oversimplification, the maximum length of polymers must be taken into account. One possibility is to replace the Hookean force by a nonlinear elastic force. Chertkov (2000) obtained the large-value tail of the stationary p.d.f. of the extension for a general anharmonic force; this approximate analysis was subsequently applied by Thiffeault (2003) to the FENE model. Here we exactly derive the complete statistics of polymer stretching within the context of the FENE dumbbell model at general Wi.

Concerning the statistics at finite times, preliminary results were obtained for the Hookean model by Celani *et al.* (2005*a*). There, the relaxation time to the stationary regime could be defined only in the coiled state. Celani *et al.* (2005*a*) thus derived the behaviour of the relaxation time for very small Wi and observed a divergence for $Wi = 1$; this suggested a critical behaviour close to the coil–stretch transition. We present the first prediction of the complete dependence of the transient relaxation time on Wi and R_m with the more realistic FENE model.

The rest of this paper is organized as follows. In § 2 we introduce the model and present the main results. The stationary p.d.f. of the elongation and the transient relaxation time are computed in § 3 and in § 4 respectively. In § 5 we discuss the relevance of our results for experiments and numerical simulations.

2. Coil–stretch transition

In elastic dumbbell models a polymer is described as two beads connected by a spring. The beads represent the ends of the molecule and their separation is a measure

of the extension. The beads experience: (*a*) a hydrodynamic drag force modelled by the Stokes law; (*b*) a Brownian force due to thermal fluctuations of the fluid; (*c*) an elastic force due to the spring connecting one bead to the other. We consider both two-dimensional and three-dimensional flows in the same way, the dimension of the flow being denoted by d. Since in physical applications the elongation of polymers is always smaller than the viscous scale of the flow, the dumbbell is assumed to move in a linear velocity field $\boldsymbol{v}(\boldsymbol{r}, t) = \boldsymbol{v}_0(t) + \boldsymbol{r} \cdot \nabla \boldsymbol{v}(t)$. Inertial effects and hydrodynamic interactions between the beads are neglected. Consequently, the separation vector between the beads, $\boldsymbol{R}$, evolves according to the stochastic differential equation (see Bird *et al.* 1977)

$$\mathrm{d}\boldsymbol{R} = (\boldsymbol{R} \cdot \nabla \boldsymbol{v})\,\mathrm{d}t - \frac{\boldsymbol{F}(\boldsymbol{R})}{\tau}\,\mathrm{d}t + \sqrt{\frac{2R_0^2}{\tau}}\,\mathrm{d}\boldsymbol{W}, \tag{2.1}$$

where R_0 is the equilibrium length of the polymer, τ is its relaxation time in the absence of flow, and $\boldsymbol{W}$ is a d-dimensional Brownian motion which accounts for thermal noise. In the FENE dumbbell model, the elastic force $\boldsymbol{F}(\boldsymbol{R})$ takes the form $\boldsymbol{F}(\boldsymbol{R}) = \boldsymbol{R}/(1 - R^2/R_m^2)$, where R_m denotes the maximum extension of the molecule. In physical applications the ratio R_m/R_0 usually lies between 10 and 100 (Bird *et al.* 1977). The length of the vector $\boldsymbol{R}$ is a measure of the extension of the polymer.

Within the Kraichnan model $\boldsymbol{v}(\boldsymbol{x}, t)$ is a statistically homogeneous Gaussian field with zero mean and second-order correlation (Kraichnan 1968):

$$\langle v_i(\boldsymbol{x}, t) v_j(\boldsymbol{x} + \boldsymbol{r}, t') \rangle = \boldsymbol{D}_{ij}(\boldsymbol{r}) \delta(t - t').$$

In the so-called Batchelor regime the flow is assumed to be smooth in space. If we further impose incompressibility and statistical invariance with respect to reflections and rotations, the tensor $\boldsymbol{D}_{ij}(\boldsymbol{r})$ must take the form (Monin & Yaglom 1975)

$$\boldsymbol{D}_{ij}(\boldsymbol{r}) = D_0 \delta_{ij} - D_1[(d+1)\delta_{ij} r^2 - 2 r_i r_j],$$

where D_0 represents the eddy diffusivity of the flow and D_1 determines the intensity of turbulent fluctuations. In random flows the Weissenberg number can be defined as $Wi = \lambda\tau$, where λ is the maximum Lyapunov exponent of the flow, that is the average logarithmic growth rate of nearby fluid particle separations. The maximum Lyapunov exponent of the Batchelor–Kraichnan flow has asymptotically a Gaussian p.d.f. with mean value $\lambda = D_1 d(d-1)$ and variance $\Delta = 2\lambda/d$ (Kraichnan 1974).

2.1. *Stationary regime*

The statistics of polymer elongation is described by the p.d.f. of the norm of $\boldsymbol{R}$ averaged over velocity realizations†: $\mathscr{P}(R, t) = \int \langle P(\boldsymbol{R}, t) \rangle R^{d-1}\,\mathrm{d}\Omega$, where $\mathrm{d}\Omega$ denotes integration over angular variables. When the flow $\boldsymbol{v}$ has Batchelor–Kraichnan statistics $\mathscr{P}(R, t)$ obeys a one-dimensional Fokker–Planck equation with non-trivial drift and diffusion coefficients (see § 3). Under reflecting boundary conditions (the probability does not flow outside the domain of definition) the system reaches a steady state for all Wi‡. The stationary p.d.f. of the elongation, $\mathscr{P}_{\mathrm{st}}(R) = \lim_{t \to \infty} \mathscr{P}(R, t)$, has the form

† Because of the statistical homogeneity of $\boldsymbol{v}$, the average p.d.f. of the elongation does not depend on the point of application of the vector $\boldsymbol{R}$.

‡ This should be contrasted with the Hookean model where the stationary regime does not exist for $Wi \geqslant 1$ (see Chertkov 2000; Balkovsky *et al.* 2000; Thiffeault 2003; Celani *et al.* 2005*a*).

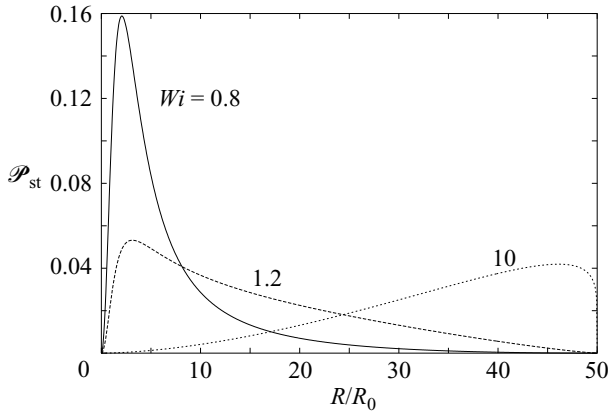

FIGURE 1. Stationary p.d.f. of polymer elongation for the three-dimensional FENE model at different Weissenberg numbers Wi ($R_m/R_0 = 50$).

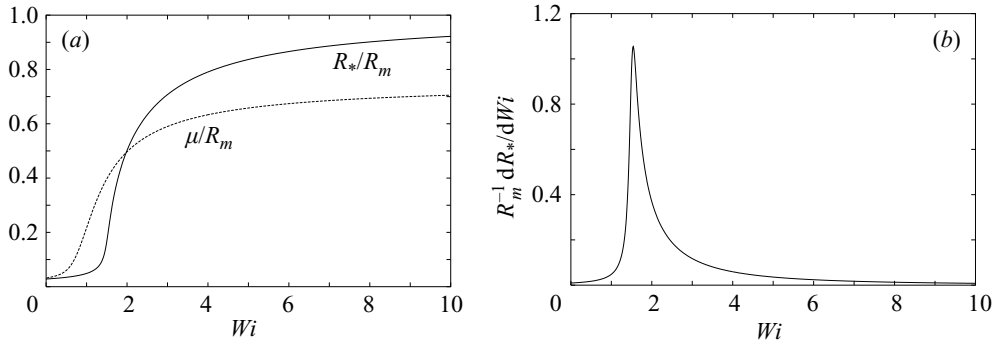

FIGURE 2. (a) Most probable rescaled elongation $R_\star/R_m$ and average rescaled extension μ/R_m as functions of the Weissenberg number Wi ($d = 3$, $R_m = 50$, $R_0 = 1$). (b) First derivative of $R_\star/R_m$ with respect to Wi.

(see § 3)

$$\mathscr{P}_{\rm st}(R) = N\,R^{d-1}\left(1 + \frac{Wi}{d}\frac{R^2}{R_0^2}\right)^{-h}\left(1 - \frac{R^2}{R_m^2}\right)^{h}, \qquad 0 \leqslant R \leqslant R_m, \tag{2.2}$$

where $h = [2(R_0^2/R_m^2 + Wi/d)]^{-1}$ and N is the normalization coefficient (see (3.5) below). The stationary p.d.f. is shown in figure 1 for different Wi. For small elongations compared to the equilibrium length, $\mathscr{P}_{\rm st}(R)$ scales as R^{d-1}; this result holds for a general elastic force since the left tail of $\mathscr{P}_{\rm st}$ comes from the events where the elastic force dominates and equation (2.1) reduces to a d-dimensional Langevin equation (for physically meaningful elastic interactions $\boldsymbol{F}(\boldsymbol{R})$ should scale as $\boldsymbol{R}$ for $R \to 0$). For intermediate extensions, $R_0 \ll R \ll R_m$, the stationary p.d.f. is proportional to the power law R^{d-1-2h} in accordance with the prediction of Balkovsky *et al.* (2000). For large elongations $\mathscr{P}_{\rm st}(R)$ scales as $(R_m^2 - R^2)^h$ and vanishes for $R = R_m$. In practical applications, $R_0/R_m \ll 1$, the exponent h is approximatively $d/(2Wi)$, as predicted by Thiffeault (2003). Obviously, when $R_m \to \infty$ and $Wi < 1$, $\mathscr{P}_{\rm st}(R)$ tends to the stationary solution of the Hookean model (see Celani *et al.* 2005*a*).

The maximum of the p.d.f., $R_\star$, determines the fraction of polymers which are highly stretched. The graph of $R_\star$ as a function of Wi is shown in figure 2(a). When Wi is smaller than one, $R_\star$ is of the order of R_0 and most of polymers have the coiled equilibrium configuration. With increasing Wi the most probable elongation $R_\star$ grows slowly

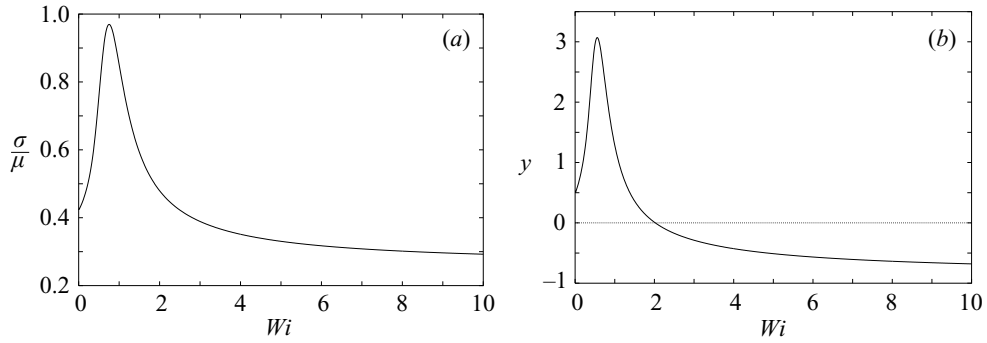

FIGURE 3. (*a*) Normalized root mean square σ/μ as a function of the Weissenberg number Wi ($d=3$, $R_m=50$, $R_0=1$). (*b*) Skewness y *vs* Wi for the same values of the parameters.

until Wi exceeds $d/(d-1)$. Then, a sharp transition occurs to a strongly elongated state. This can be appreciated from the behaviour of the first-order derivative of $R_\star$ as a function of Wi (figure 2*b*). As Wi becomes very large, $R_\star$ approaches R_m. The same analysis holds for the average extension μ, apart from the fact that it starts increasing for a smaller Wi and its limiting value is $\frac{3}{4}R_m$ (see figure 2). It is worth noticing that the coil–stretch transition becomes sharper and sharper with increasing R_m (not plotted).

The normalized r.m.s. value of the extension, σ/μ, $\sigma^2=\int(R-\mu)^2\mathscr{P}_{\rm st}(R)\,\mathrm{d}R$, is represented in figure 3(*a*). It increases at low Wi until it reaches a maximum value; then σ is compensated by the sharp increase in μ and at large Wi the rescaled r.m.s. eventually relaxes to the constant value $1/\sqrt{15}$.

The skewness $y=[\int(R-\mu)^3\mathscr{P}_{\rm st}(R)\,\mathrm{d}R]/\sigma^3$ is positive for small Wi and becomes negative at large Wi (figure 3*b*), corresponding to the qualitative behaviour of the stationary p.d.f. (figure 1). The maximum of skewness in the neighbourhood of the coil–stretch transition can be easily understood as follows. At low Wi the p.d.f. is peaked at R_0 and the skewness is positive. With increasing Wi the right tail starts increasing, but μ is still of the order of R_0: the skewness, therefore, increases and achieves is maximum value. Beyond the coil–stretch transition μ starts moving towards the maximum extension and the skewness decreases until it becomes negative at large Wi, that is when the p.d.f. has a long left tail. The limiting value of y for $Wi\to\infty$ is $-\frac{2}{3}\sqrt{5/3}$.

2.2. *Relaxation to the stationary regime*

We now turn to the time dependence of the p.d.f. of the elongation. Starting from an initial condition peaked at R_0, the system relaxes to the stationary regime described by (2.2). The time needed to reach the stationary regime, T, is the solution of a transcendental equation which involves continued fractions (see § 4).

For small Weissenberg numbers, $0\leqslant Wi\lesssim d/(d+4)$, the transient relaxation time T behaves according to the prediction of the linear model (Celani *et al.* 2005*a*):

$$T/\tau=\tfrac{1}{2}[1-Wi\,(d+2)/d]^{-1} \tag{2.3}$$

independently of R_m (see inset in figure 4).

In the proximity of the coil–stretch transition T displays a maximum as a function of Wi. The relaxation is exceptionally slow in this range of Wi because the stationary regime results from the competition between the coiled state and the highly stretched state. The position and the value of the maximum relaxation time $T_{\max}$ depend on the cutoff R_m (figure 4*b*). As the maximum allowed extension of polymers increases, $T_{\max}$ is closer and closer to $Wi=1$ and grows; at large R_m the FENE model should

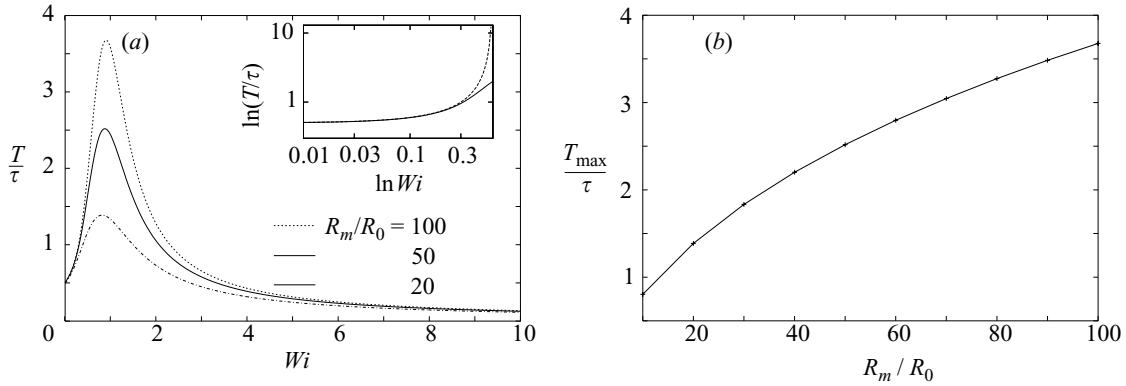

FIGURE 4. (*a*) Rescaled time of relaxation to the stationary regime, T/τ, as a function of the Weissenberg number Wi for three different values of R_m/R_0 ($d = 3$). The inset shows the linear-model approximation given by equation (2.3) (dashed line) for $R_m/R_0 = 50$: the agreement is good up to $d/(d+4) \simeq 0.4$. (*b*) Dependence of the maximum rescaled relaxation time $T_{\max}/\tau$ on the maximum relative extension of polymers R_m/R_0.

indeed match the Hookean model, where T diverges as Wi tends to one (Celani *et al.* 2005*a*).

For very large Weissenberg numbers the stretching time is small compared to τ and the molecules are expected to rapidly reach the highly stretched configuration. Hence, T vanishes as Wi tends to infinity. A numerical fit shows that T scales as Wi^{-1} at large Wi.

In the next sections we explicitly derive (2.2) and the equation for T.

3. Fokker–Planck equation

For a fixed realization of the velocity field the p.d.f. of the end-to-end vector, $P(\boldsymbol{R}, t)$, satisfies the Fokker–Planck equation associated with (2.1) (see e.g. Risken 1989):

$$\partial_t P + \mathrm{div}_{\boldsymbol{R}}\left[\left(\boldsymbol{R}\cdot\boldsymbol{\nabla v} - \frac{\boldsymbol{F}(\boldsymbol{R})}{\tau}\right)P\right] = \frac{R_0^2}{\tau}\nabla^2_{\boldsymbol{R}} P. \tag{3.1}$$

To obtain an equation for $\mathscr{P}(R, t)$, we average the above equation over the velocity realizations and integrate the result over angular variables. The terms of the type $\langle v_i P\rangle$ in general do not lead to a closed form for the mean p.d.f. and a closed equation cannot be deduced from (3.1). The Gaussianity and the δ-correlation in time of the Batchelor–Kraichnan model provide an exact closure. Exploiting the Novikov–Furutsu formula (see e.g. Klyatskin, Woyczynski & Gurarie 1996), we obtain: $\langle(\nabla_i v_j)P\rangle = -C_{ijk\ell}\partial_{R_\ell}[R_k\langle P\rangle]$ with $C_{ijk\ell} = D_1[(d+1)\delta_{ik}\delta_{j\ell} - \delta_{ij}\delta_{k\ell} - \delta_{i\ell}\delta_{jk}]$. We can thus derive from (3.1) a one-dimensional Fokker–Planck equation for $\mathscr{P}(R, t)$:

$$\partial_s \mathscr{P}(R, s) = -\partial_R[A(R)\mathscr{P}(R, s)] + \partial^2_R[B(R)\mathscr{P}(R, s)], \tag{3.2}$$

where the time has been rescaled with τ, $s = t/\tau$, and the drift and diffusion coefficients have the form

$$A(R) = \frac{(d+1)}{d} Wi\, R - F(R) + (d-1)\frac{R_0^2}{R} \qquad \text{and} \qquad B(R) = \frac{Wi}{d}R^2 + R_0^2. \tag{3.3}$$

The coefficients A and B are time independent due to the stationarity of the advecting flow. If R_0 is set to zero, then equation (3.2) reduces to the approximate equation for the large-value tail of the p.d.f. derived by Chertkov (2000).

To solve (3.2) we impose reflecting boundary conditions, that is the probability current associated with the solution, $J(R,s)=A(R)\mathscr{P}(R,s)-\partial_R\,[B(R)\mathscr{P}(R,s)]$, vanishes in $R=0$ and $R=R_m$ for all $s\geqslant 0$. This means that there is no flow of probability through the boundaries of the domain. Under these conditions the stationary p.d.f. of the elongation takes the form (Risken 1989)

$$\mathscr{P}_{\rm st}(R)=\frac{C}{B(R)}\exp\left[\int_{R_1}^{R}A(x)/B(x)\,\mathrm{d}x\right] \tag{3.4}$$

where the constant C and the lower integration limit R_1 are fixed by the normalization condition. The above formula holds for a general elastic force of the form $\boldsymbol{F}(\boldsymbol{R})=f(R)\boldsymbol{R}$. Placing the force of the FENE model into (3.4), we thus obtain (2.2) with

$$N=\frac{2\Gamma(d/2+h+1)}{R_m^d\,\Gamma(d/2)\Gamma(h+1)\,{}_2F_1(d/2,h;d/2+h+1;-Wi\,R_m^2/dR_0^2)}. \tag{3.5}$$

The function ${}_2F_1$ in the normalization coefficient denotes the hypergeometric function.

4. Relaxation time

The time-dependent solution of equation (3.2) can be obtained by separation of variables (Risken 1989). In other words, $\mathscr{P}(R,s)$ can be sought in the form

$$\mathscr{P}(R,s)=\mathscr{P}_{\rm st}(R)+\sum_{k=1}^{\infty}c_k\,\mathrm{e}^{-\mu_k s}\,p_k(R) \tag{4.1}$$

where the coefficients c_k are fixed by the initial condition $\mathscr{P}(R,0)$, and μ_k, $p_k(R)$ are respectively the eigenvalues and the eigenfunctions of the ordinary differential equation

$$\frac{\mathrm{d}^2}{\mathrm{d}R^2}[B(R)p_k(R)]-\frac{\mathrm{d}}{\mathrm{d}R}[A(R)p_k(R)]+\mu_k p_k(R)=0. \tag{4.2}$$

The above equation should be solved with reflecting boundary conditions: $J_k(0)=\lim_{R\to R_m}J_k(R)=0$, J_k being the probability current associated with the eigenfunction p_k. It can be shown that the eigenvalues μ_k are real and non-negative, $\mathscr{P}_{\rm st}(R)$ belonging to the eigenvalue $\mu_0=0$ (Risken 1989). As we will see, the eigenvalues form a countable set and may be arranged in ascending order: $0<\mu_1<\mu_2<\ldots$. The reciprocal of μ_1, therefore, is the time of relaxation to the stationary regime rescaled by τ.

Equation (4.2) is a second-order linear differential equation with four regular singularities in the complex plane. By a change of dependent and independent variables $z=(R/R_m)^2$, $p_k(z)=z^{(d-1)/2}\,(1-z)^h w_k(z)$, this equation can be transformed into a standard Heun equation for the function $w_k(z)$ (see Ronveaux 1995, for a review):

$$\frac{\mathrm{d}^2 w_k}{\mathrm{d}z^2}+\left(\frac{\gamma}{z}+\frac{\delta}{z-1}+\frac{\epsilon}{z-a}\right)\frac{\mathrm{d}w_k}{\mathrm{d}z}+\frac{\alpha\beta z-q}{z(z-1)(z-a)}w_k=0, \tag{4.3}$$

where

$$a=-\frac{d}{Wi}\,\frac{R_0^2}{R_m^2},\qquad q=\frac{d}{2}\left(h+\frac{\mu_k}{2Wi}\right),$$

$$\alpha=h+\frac{d}{4}-\frac{1}{4}\sqrt{d\left(d-\frac{4\mu_k}{Wi}\right)},\qquad \beta=h+\frac{d}{4}+\frac{1}{4}\sqrt{d\left(d-\frac{4\mu_k}{Wi}\right)},$$

$$\gamma=d/2,\qquad \delta=h,\qquad \epsilon=1+h,$$

with $h = [2(R_0^2/R_m^2 + Wi/d)]^{-1}$. Reflecting boundary conditions for p_k map into the following limiting conditions for w_k:

$$\lim_{z\to 0} z^{\gamma-1} w_k(z) = 0 \qquad \text{and} \qquad \lim_{z\to 1}(1-z)^{\delta-1} w_k(z) = 0. \tag{4.4}$$

The Heun equation is the general Fuchsian equation with four singularities. In the standard form (4.3) the singular points are 0, 1, a, ∞. Let z_0 be a generic singularity of (4.3). From the theory of Fuchsian equations, the local behaviour of $w_k(z)$ near z_0 is specified by the characteristic exponents ρ_1, ρ_2 associated with z_0 (see e.g. Whittaker & Watson 1996). If $\rho_1 - \rho_2$ is not integer, in a neighbourhood of z_0 which excludes the nearest other singularity, $w_k(z)$ can be written in the form $b_1(z-z_0)^{\rho_1}\varphi(z-z_0) + b_2(z-z_0)^{\rho_2}\psi(z-z_0)$, where b_1, b_2 are constant and φ, ψ are analytic functions such that $\varphi(z_0) \neq 0$, $\psi(z_0) \neq 0$. If $\rho_1 - \rho_2$ is integer and $\rho_1 \geqslant \rho_2$, the function ψ can be no longer analytic in z_0 and involve the function $\log(z - z_0)$.

The singularity $z = 0$ has characteristic exponents 0 and $1-\gamma$; the singularity $z = 1$ has characteristic exponents 0 and $1-\delta$. In physical applications we can exclude the situation where δ is integer. On the contrary, $1-\gamma$ is zero when $d = 2$.

Consider first the case $d = 3$, where there are not logarithmic singularities in $z = 0$. To fulfil conditions (4.4), w_k must be simultaneously a local solution about $z = 0$ and $z = 1$, in both cases belonging to the exponent 0. Such a solution is called a Heun function of class I relative to the points 0 and 1, and exists only for a countable set of values of q and hence of μ_k (see Ronveaux 1995). The condition for the aforementioned Heun function to exist leads to a transcendental equation for the eigenvalues μ_k (Erdélyi 1944):

$$L_0 - \cfrac{M_0 K_1}{L_1 - \cfrac{M_1 K_2}{L_2 - \dots}} = 0, \tag{4.5}$$

where

$$K_i = \frac{(i+\alpha-1)(i+\beta-1)(i+\gamma-1)(i+\omega-1)}{(2i+\omega-1)(2i+\omega-2)},$$

$$L_i = q + ai(i+\omega) - \frac{\epsilon\, i(i+\omega)(\gamma-\delta) + [i(i+\omega)+\alpha\beta][2i(i+\omega)+\gamma(\omega-1)]}{(2i+\omega-1)(2i+\omega+1)},$$

$$M_i = \frac{(i+1)(i+\omega-\alpha+1)(i+\omega-\beta+1)(i+\delta)}{(2i+\omega+1)(2i+\omega+2)},$$

with $\omega = \gamma + \delta - 1$. The rescaled relaxation time T/τ is then the reciprocal of the lowest non-zero solution of (4.5). In the case $d = 2$ the conclusions are unchanged since the solution involving a logarithm in the neighbourhood of $z = 0$ should be discarded.

We solved (4.5) numerically: the continued fraction was computed by the modified Lentz method and the first non-zero solution was evaluated by the root false position method (see e.g. Press *et al.* 1993).

5. Summary and discussion

The goal of the paper was to investigate polymer stretching in a turbulent flow within the context of a fully solvable model. The statistical features of the Batchelor–Kraichnan flow allow us to derive the complete form of the stationary p.d.f. of polymer elongation for a general elastic force. When specializing to finitely extensible polymers

we recover the main properties of polymer dynamics in real turbulent flows and compute the time of relaxation to the stationary regime.

It should be noted that the velocity field we consider is statistically isotropic. Together with the δ-correlation in time, this is a key assumption in order to derive a fully analytical solution of the problem. In the experimental setup of Gerashchenko *et al.* (2004) the elastic turbulent flow is superimposed on a mean shear flow. The long-time statistics of polymer extension in the presence of a mean shear has been recently considered by Chertkov *et al.* (2005); Celani, Puliafito & Turitsyn (2005*b*); Puliafito & Turitsyn (2005); Turitsyn (2005).

The main result of our study is the behaviour of the time of relaxation to the steady state as a function of *Wi*. At low *Wi* the transient relaxation time is an increasing function of *Wi*, it is maximum close to the coil–stretch transition, and eventually tends to zero with increasing *Wi*. Knowing the dependence of the transient time on *Wi* is relevant both for numerical simulations and experiments. For example, in the former case, the time required for uncorrelated polymer chains that are suddenly exposed to the same flow to correlate is (implicitly) related to the sharpness of stress gradients one can expect in the flow. Hence, the prediction of the transient time in our study is useful to estimate the required grid spacing to fully resolve those gradients (L. Collins 2005, private communication). In the latter case, the fact that the transient relaxation time is especially long just below the coil–stretch transition implies that within such range of *Wi* experimental measures are more sensitive to statistical fluctuations.

Experiments concerning the transient relaxation to the stationary regime can investigate the time dependence of the conditional p.d.f. $\mathscr{P}(R, t|R_0, 0)$, which corresponds to the initial condition peaked at the equilibrium size: $\mathscr{P}(R, 0|R_0, 0) = \delta(R - R_0)$. Such an initial condition can be fixed experimentally as follows (A. Celani 2005, private communication). The p.d.f. of the extension is constructed by following the motion of different polymer molecules and collecting $R(t)$ for each molecule: one should then start counting time only when the length of the corresponding polymer is approximatively R_0. This is equivalent to selecting the initial state where all molecules have the equilibrium extension, $R(0) = R_0$.

The transient relaxation time can be measured directly from the time behaviour of the conditional moments of the extension: $\overline{R^n}(t) = \int R^n \mathscr{P}(R, t|R_0, 0)\,\mathrm{d}R$, where n is a positive integer. The conditional p.d.f. can indeed be expanded as in (4.1) and the order of series and integral can be interchanged in the definition of $\overline{R^n}$ due to the integrability of $R^n p_k(R)$ and the uniform convergence of series (4.1) (see e.g. Smirnov 1984). Therefore, all the moments of the extension converge to their stationary value with the same rate as the p.d.f. of the extension.

To conclude, we believe that the results obtained for the nonlinear dumbbell model are relevant for the comprehension of polymer dynamics in turbulent flows at any Weissenberg number. Moreover, we hope that our study may stimulate new experiments directed to investigate the transient relaxation to the stationary regime.

We are deeply grateful to E. Bodenschatz, A. Celani, and L. Collins for very useful suggestions. We wish to thank C. M. Casciola, M. Chertkov, J. Davoudi, E. De Angelis, B. Eckhardt, A. Mazzino, S. Musacchio, J. Schumacher, and V. Steinberg for illuminating discussions. This research has been supported in part by the European Union under contract No. HPRN-CT-2000-00162, by the French-German program PAI "Procope" 07574NM, and by the Italian Ministry of Education, University and Research under contract Cofin. 2003 (prot. 020302002038).

REFERENCES

Babcock, H. P., Teixeira, R. E., Hur, J. S., Shaqfeh, E. S. & Chu, S. 2003 Visualization of molecular fluctuations near the critical point of the coil–stretch transition in polymer elongation. *Macromolecules* **36**, 4544–4548.

Balkovsky, E., Fouxon, A. & Lebedev, V. 2000 Turbulent dynamics of polymer solutions. *Phys. Rev. Lett.* **84**, 4765–4768.

Bird, R. B., Hassager, O., Armstrong, R. C. & Curtiss, C. F. 1977 *Dynamics of Polymeric Liquids, Kinetic Theory*, vol. II. Wiley.

Celani, A., Musacchio, S. & Vincenzi, D. 2005*a* Polymer transport in random flow. *J. Statist. Phys.* **118**, 531–554.

Celani, A., Puliafito, A. & Turitsyn, K. 2005*b* Polymers in linear shear flow: a numerical study. *Europhys. Lett.* **70**, 464–470.

Chertkov, M. 2000 Polymer stretching by turbulence. *Phys. Rev. Lett.* **84**, 4761–4764.

Chertkov, M., Kolokolov, I., Lebedev, V. & Turitsyn, K. 2005 Statistics of polymer extension in a random flow with mean shear. *J. Fluid Mech.* **531**, 251–260.

De Gennes, P. G. 1974 Coil–stretch transition of dilute flexible polymer under ultra-high velocity gradients. *J. Chem. Phys.* **60**, 5030–5042.

Erdélyi, A. 1944 Certain expansions of solutions of the Heun equation. *Q. J. Maths* (*Oxford Series*) **15**, 62–69.

Falkovich, G., Gawędzki, K. & Vergassola, M. 2001 Particles and fields in fluid turbulence. *Rev. Mod. Phys.* **73**, 913–975.

Gerashchenko, S., Chevallard, C. & Steinberg, V. 2005 Single polymer dynamics: coil–stretch transition in a random flow. *Europhys. Lett.* **71**, 221–227.

Groisman, A. & Steinberg, V. 2000 Elastic turbulence in a polymer solution flow. *Nature* **405**, 53–55.

Gyr, A. & Bewersdorff, H. W. 1995 *Drag Reduction of Turbulent Flows by Additives*. Kluwer.

Hur, J. S., Shaqfeh, E. S., Babcock, H. P. & Chu, S. 2002 Dynamics and configurational fluctuations of single DNA molecules in linear mixed flows. *Phys. Rev.* E **66**, 011915.

Klyatskin, V. I., Woyczynski, W. A. & Gurarie, D. 1996 Short-time correlation approximations for diffusing tracers in random velocity fields: A functional approach. In *Stochastic Modeling in Physical Oceanography* (ed. R. J. Ader). Progress in Probability, pp. 221–270, Birkhauser.

Kraichnan, R. H. 1968 Small-scale structure of a scalar field convected by turbulence. *Phys. Fluids* **11**, 945–963.

Kraichnan, R. H. 1974 Convection of a passive scalar by a quasi-uniform random straining field. *J. Fluid Mech.* **64**, 737–762.

Monin, A. A. & Yaglom, A. M. 1975 *Statistical Fluid Mechanics*. MIT Press.

Perkins, T. T., Smith, D. E. & Chu, S. 1997 Single polymer dynamics in an elongational flow. *Science* **276**, 2016–2021.

Press, W. H., Flannery, B. P., Teukolsky, S. A. & Vetterling, W. T. 1993 *Numerical Recipes*. Cambridge University Press.

Puliafito, A. & Turitsyn, K. 2005 Single polymer dynamics in shear flow. *Physica* D (in press).

Risken, H. 1989 *The Fokker-Planck Equation, Methods of Solution and Applications* (ed. H. Haken). Springer Series in Synergetics, Springer.

Ronveaux, A. (Ed.) 1995 *Heun's Differential Equations*. Oxford University Press.

Smirnov, V. 1984 *Cours de Mathématiques Supérieures*, Vol. IV, 2nd part. MIR.

Smith, D. E., Babcock, H. P. & Chu, S. 1999 Single-Polymer Dynamics in Steady Shear Flow. *Science* **283**, 1724–1727.

Thiffeault, J.-L. 2003 Finite extension of polymers in turbulent flow. *Phys. Lett.* A **308**, 445–450.

Turitsyn, K. S. 2005 Polymer dynamics in chaotic flows with strong shear component. *Phys. Rev.* E (submitted).

Whittaker, E. T. & Watson, G. N. 1996 *A Course of Modern Analysis*, 4th edn. Cambridge University Press.

INSTITUTE OF PHYSICS PUBLISHING JOURNAL OF PHYSICS A: MATHEMATICAL AND GENERAL

J. Phys. A: Math. Gen. **39** (2006) 10691–10701 doi:10.1088/0305-4470/39/34/007

Single polymer dynamics in elongational flow and the confluent Heun equation

D Vincenzi[1,2,3] **and E Bodenschatz**[1,2,3]

[1] Max-Planck-Institut für Dynamik und Selbstorganisation, 37077 Göttingen, Germany
[2] School of Mechanical & Aerospace Engineering, Cornell University, Ithaca, NY 14853, USA
[3] LASSP, Cornell University, Ithaca, NY 14853, USA

E-mail: dv47@cornell.edu

Received 13 March 2006, in final form 5 July 2006
Published 9 August 2006
Online at stacks.iop.org/JPhysA/39/10691

Abstract

We investigate the non-equilibrium dynamics of an isolated polymer in a stationary elongational flow. We compute the relaxation time to the steady-state configuration as a function of the Weissenberg number. A strong increase of the relaxation time is found around the coil–stretch transition, which is attributed to the large number of polymer configurations. The relaxation dynamics of the polymer is solved analytically in terms of a central two-point connection problem for the singly confluent Heun equation.

PACS numbers: 05.10.Gg, 47.57.Ng, 02.30.Hq

1. Introduction

Dilute polymer solutions exhibit physical behaviours that distinguish them from ordinary Newtonian fluids. Even a small polymer concentration can considerably change the large-scale behaviour of the flow by enhancing viscosity and reducing the turbulent drag. A comprehensive understanding of hydrodynamical properties of polymer solutions is still lacking despite the large number of industrial applications (e.g. Sreenivasan and White (2000)). A starting point for the theoretical description of dilute polymer solutions is the dynamics of isolated polymer molecules. The knowledge of how a single molecule is deformed by the velocity gradient allows the development of constitutive models that in turn can be used to calculate the large scale flow. The stationary dynamics of a single, isolated polymer has received much attention to date (see Larson (2005), Shaqfeh (2005), for a review). In contrast, less is known about non-equilibrium dynamics of isolated polymers in flow. Since Rouse (1953) and Zimm's (1956) seminal works, experimental, numerical and theoretical studies focused on the internal relaxation dynamics of a polymer floating in a solvent under the influence of Brownian fluctuations. The two model situations considered were (a) a polymer suspended in solution and pulled at the ends (Quake *et al* 1997, Hatfield and Quake 1999); (b) a tethered polymer

0305-4470/06/3410691+11$30.00

submitted to a uniform flow and freely relaxing after cessation of the flow (Perkins *et al* 1994, Brochard-Wyart 1995, Manneville *et al* 1996, Rzehak and Zimmermann 2002). The above studies did not take into account the interaction between the polymer and an external flow. Hernández Cifre and García de la Torre (1999) note that Rouse and Zimm's theories may not provide the adequate time scale for coil–stretch processes in flow on the basis of Brownian dynamics simulations. Here, we investigate how an elongational flow influences polymer relaxation dynamics. We determine the time scale associated with polymer deformation *in the flow* and show a significant deviation from Rouse and Zimm's predictions in the vicinity of the coil–stretch transition. Our analysis is based on an eigenvalue problem for the confluent Heun equation, and constitutes a new physical application of this latter equation.

Polymer dynamics is extremely rich already in simple deterministic flows, such as elongational flows (Perkins *et al* 1997, Smith and Chu 1998), shear flows (Smith *et al* 1999, Celani *et al* 2005b, Puliafito and Turitsyn 2005, Gerashchenko and Steinberg 2006) or combinations of the two (Hur *et al* 2002, Babcock *et al* 2003). The velocity gradient of a non-uniform flow stretches the polymer, while entropic forces attempt to restore the polymer into the coiled equilibrium shape. In other words, the configuration of the polymer results from the counterbalance between the entropic forces and the hydrodynamic drag. Here we consider an elongational flow, which is defined by a constant velocity gradient λ. This flow is particularly effective in stretching polymers far from their equilibrium configuration. A transition to the stretched state of the polymer occurs as the velocity gradient exceeds the critical value $\lambda_c = 1/(2\tau)$, where τ is the time associated with the slowest relaxation mode of the polymer in thermal equilibrium with the surrounding medium. For $\lambda < \lambda_c$ polymers stay in the coiled equilibrium configuration; for $\lambda > \lambda_c$ they become fully extended. This phenomenon is known as the coil–stretch transition (de Gennes 1974). Rouse (1953) computed τ as a function of the number of monomers in the polymer assuming the polymer could be described as a beads-and-springs chain with Hookean interactions. Zimm (1956) refined Rouse's prediction by taking into account hydrodynamic interactions between segments of the chain.

The study of polymer dynamics has benefited from a class of mesoscopic models that are based on a coarse-grained treatment of the polymer molecule. One of the simplest is the elastic dumbbell model, which only takes into account the slowest oscillation mode of the molecule (Bird *et al* 1987). Notwithstanding this crude simplification, the dumbbell model captures the main aspects of polymer dynamics in elongational flows, such as the coil–stretch transition (Perkins *et al* 1997) and finite-time conformation hysteresis (Schroeder *et al* 2003, 2004). We examine how the probability density function (PDF) of the extension of a dumbbell-like molecule approaches its stationary form. We compute the typical time it takes for the initial PDF to attain its steady-state form and show that, in the proximity of the coil–stretch transition, this time is exceedingly long compared to τ. A similar behaviour is encountered in white-in-time isotropic random flows (Celani *et al* 2005a, Martins Afonso and Vincenzi 2005); however, for an elongational flow the amplification of the transient relaxation time is much stronger.

The problem is solved within the framework of the Fokker–Planck equation for the PDF of the extension of the polymer. The computation of the transient relaxation time is recast as a central two-point connection problem (CTCP) for a singly confluent Heun equation. The Heun equation is the general Fuchsian differential equation with four regular singularities. Its singly confluent form, also known as the generalized spheroidal wave equation, results from the merging of two regular singularities into one irregular singularity of Poincaré rank 1 (see Slavyanov (1995) for a review). A CTCP is an eigenvalue problem for an ordinary differential equation where (a) at both endpoints of the interval of definition is located a

singularity of the equation; (b) the solutions are required to have a specified asymptotic behaviour while approaching the two singularities from inside. Contrary to the hypergeometric equation, an explicit formula for the CTCP is not known for the Heun family of equations. The eigenvalues can be determined only as solutions of transcendental equations involving continued fractions. Well-known applications of the confluent Heun equation are the electronic spectra of the hydrogen-molecule ion in the Born–Oppenheimer approximation (Jaffé 1933) and the Teukolsky equation describing small perturbations to the Kerr geometry in black hole theory (Leaver 1985). For a comprehensive introduction to physical applications of the Heun equations we refer the reader to the book by Slavyanov and Lay (2000).

The rest of this paper is organized as follows. The dumbbell model is introduced in section 2. The computation of the transient relaxation time and the related CTCP for the confluent Heun equation are presented in section 3. Section 4 is devoted to conclusions.

2. Elastic dumbbell model

When one is interested in the statistics of polymer extension the dynamics of a polymer molecule can be described, to a first approximation, in terms of its slowest oscillation mode. In this case, the molecule can be modelled as an elastic dumbbell, i.e. as two beads connected by a spring. The beads represent the ends of the molecule and the spring models entropic forces. The separation between the beads measures the extension of the polymer. When introduced into a non-uniform flow the molecule experiences collisions with fluid particles and becomes stretched under the action of the velocity gradient. In the simplest case, the drag force is assumed to be proportional to the velocity of the polymer relative to the fluid and thermal agitation is modelled by Brownian motion. In most applications the extension of the polymer remains smaller than the dissipative scale of the carrier flow, and therefore the velocity field can be assumed to be linear[4]. The separation vector of the ends of the polymer, $\boldsymbol{Q}$, is then a stochastic process evolving according to the three-dimensional stochastic ordinary differential equation[5] (e.g. Bird *et al* (1987))

$$\mathrm{d}\boldsymbol{Q} = \boldsymbol{Q}\cdot\nabla\boldsymbol{v}(s)\,\mathrm{d}s - f(Q)\,\frac{\boldsymbol{Q}}{2\tau}\,\mathrm{d}s + \sqrt{\frac{Q_0^2}{\tau}}\,\mathrm{d}\boldsymbol{B}(s), \tag{1}$$

where $Q = |\boldsymbol{Q}|$, Q_0^2 is the equilibrium mean-square separation of the ends of the molecule, and $\boldsymbol{B}(s)$ denotes the three-dimensional standard Brownian motion. The function f determines the entropic force. We consider the finitely extensible nonlinear elastic (FENE) dumbbell model with

$$f(Q) = \frac{1}{1 - Q^2/L^2}, \qquad 0 \leqslant Q < L,$$

where L is the maximum extension of the molecule. The force diverges as the molecular extension approaches L; thus the extension of the molecule will be finite and smaller than L. The FENE model is appropriate for synthetic polymers such as polyacrylamide and polyethyleneoxide; biological macromolecules such as DNA and polypeptides are better described by the worm-like chain model (e.g. Larson (2005)). In elongational-flow experiments, the flexibility parameter $b = L^2/Q_0^2$ usually ranges from 10^2 to 10^4 (Larson 2005, Shaqfeh 2005).

[4] Davoudi and Schumacher (2006) recently investigated the situation where the extension of the polymer can reach the inertial range of turbulence.

[5] There is no Ito–Stratonovich ambiguity in this case because the coefficient of Brownian motion does not depend on $\boldsymbol{Q}$.

The FENE model (1) neglects hydrodynamic interactions between the segments of the polymer. Inclusion of hydrodynamic interactions makes the coil–stretch transition sharper, but do not change the transition qualitatively (e.g. Wiest *et al* (1989), Hernández Cifre and García de la Torre (1998, 1999)). Furthermore, the dumbbell model without hydrodynamic interactions accurately reproduces the extension–strain curve observed in experiments (Perkins *et al* 1997). The accuracy of the model can be ascribed to the cancellation between the effect of the distribution of drag forces along the chain and the effect of the increase in effective drag coefficient with polymer extension (Larson *et al* 1997). Neglecting hydrodynamic interactions has the benefits of providing analytical results.

3. Relaxation dynamics

A steady planar elongational flow is characterized by one direction of stretch, one direction of compression and one neutral direction. The velocity gradient is constant along the directions of both the extensional and compressional axes: $\nabla_j v_i = \lambda(\delta_{i1}\delta_{j1} - \delta_{i2}\delta_{j2})$, $\lambda > 0$. When a polymer is immersed in that flow the first component of the separation vector rapidly becomes much greater than the other components: $Q_1 \gg Q_2$ and $Q_1 \gg Q_3$. The extension of the molecule, therefore, is approximatively $Q \simeq Q_1$, and $f(Q)$ can be replaced by $f(Q_1)$.[6] According to this approximation, the first component of (1) gives a one-dimensional stochastic differential equation for the extension of the dumbbell:

$$\mathrm{d}Q = \lambda Q\,\mathrm{d}s - f(Q)\,\frac{Q}{2\tau}\,\mathrm{d}s + \sqrt{\frac{Q_0^2}{\tau}}\,\mathrm{d}B(s), \tag{2}$$

where $B(s)$ is the one-dimensional Brownian motion. For the sake of notational simplicity, we introduce the rescaled separation vector $\boldsymbol{q} = \boldsymbol{Q}/L$. The PDF of $q = |\boldsymbol{q}|$, $\psi(q;t)$ with $q \in [0,1]$, satisfies the one-dimensional Fokker–Planck equation associated with (2) (e.g. Stratonovich (1963))

$$\begin{aligned} &\partial_t \psi = \mathscr{L}\psi, \\ &\mathscr{L}\psi := -\frac{\partial}{\partial q}\left[\left(Wi - \frac{\hat{f}(q)}{2}\right) q\psi\right] + \frac{1}{2b}\,\frac{\partial^2 \psi}{\partial q^2}, \end{aligned} \tag{3}$$

where $t = s/\tau$, $\hat{f}(q) = f(Lq)$ and $Wi = \lambda\tau$. The dimensionless number Wi is known as the Weissenberg number and measures the level of polymer stretching. For $Wi < 1/2$ polymers are in the coiled state; for $Wi > 1/2$ polymers are fully extended. The critical value $Wi_c = \lambda_c\tau = 1/2$ marks the coil–stretch transition in elongational flows (de Gennes 1974). Strictly speaking, the approximation leading to (2) and (3) holds true when the polymer is sufficiently stretched, i.e. only for $Wi \gtrsim Wi_c$. Equation (3), indeed, does not yield a good approximation of $\psi(q;t)$ at low Wi. However, as we shall see at the end of this section, it is appropriate to investigate polymer relaxation dynamics in terms of (2) and (3) also below the coil–stretch transition.

The Fokker–Planck equation (3) is solved with reflecting boundary conditions, that is the probability current

$$j(q;t) = Wi\,q\psi(q;t) - \frac{\hat{f}(q)}{2} q\psi(q;t) - \frac{1}{2b}\,\frac{\partial \psi}{\partial q}\bigg|_{q,t}$$

is assumed to vanish at the endpoints of the interval of definition: $j(0;t) = j(1;t) = 0\,\forall\, t > 0$

[6] The above approximation holds true for a steady uniaxial extensional flow as well: $\nabla_j v_i = \lambda(\delta_{i1}\delta_{j1} - \delta_{i2}\delta_{j2}/2 - \delta_{i3}\delta_{j3}/2)$. Therefore, the results henceforth presented are unchanged for this flow.

(Stratonovich 1963). Under these conditions, the stationary distribution of the extension, $\psi_0(q) = \lim_{t\to\infty} \psi(q;t)$, can be derived by simple integration (Bird *et al* 1987):

$$\psi_0(q) = N\,\mathrm{e}^{bWi\,q^2}(1-q^2)^{\frac{b}{2}}, \qquad 0 \leqslant q \leqslant 1, \tag{4}$$

where

$$N = 2\Gamma((b+3)/2)/[\sqrt{\pi}\Gamma(b/2+1) \times {}_1F_1(1/2;(b+3)/2;bWi)]$$

and Γ and ${}_1F_1$ denote the Euler Gamma function and the confluent hypergeometric function, respectively (e.g. Erdélyi *et al* (1953)). Large extensions become more and more probable with increasing *Wi* in accordance with experiments (Perkins *et al* 1997). Note however that, at low *Wi*, equation (4) does not constitute a good description of the PDF of small extensions due to the approximation behind (3).

The time behaviour of the system depends on the form of the spectrum of the operator $\mathscr{L}$ with reflecting boundary conditions:

$$\mathscr{L}\psi_\mu = -\mu\psi_\mu, \tag{5}$$

$$j_\mu(0) = j_\mu(1) = 0, \tag{6}$$

where j_μ denotes the probability current associated with the eigenfunction ψ_μ. Under conditions (6), $\mathscr{L}$ is non-positive defined and symmetric with respect to the scalar product with weighting function $1/\psi_0$. Its eigenvalues μ are therefore real and non-negative, $\mu = 0$ being associated with the long-time solution ψ_0 (Stratonovich 1963). If $\mathscr{L}$ has a countable spectrum $\{0, \mu_1, \mu_2, \ldots\}$ with $\mu_i < \mu_{i+1}$, then $T_{\mathrm{rel}} = \tau/\mu_1$ is the characteristic time needed for $\psi(q;t)$ to attain its long-time form $\psi_0(q)$ when the initial condition $\psi(q;0)$ is taken far from equilibrium (Schenzle and Brand 1979). We note that while τ is the relaxation time of the polymer *in the absence of flow*, T_{rel} characterizes polymer relaxation dynamics *in the flow*.

To compute T_{rel}, we need to solve the eigenvalue problem (5), (6). By making the substitutions $z = q^2$, $\psi_\mu(z) = (1-z)^{\frac{b}{2}} w_\mu(z)$, we can rewrite (5) in the form

$$w_\mu'' + \left(\beta + \frac{\gamma}{z} + \frac{\delta}{z-1}\right) w_\mu' + \frac{\alpha\beta z - \nu}{z(z-1)}\, w_\mu = 0, \tag{7}$$

where $w_\mu' := \mathrm{d}w_\mu/\mathrm{d}z$, $\gamma = 1/2$, $\delta = b/2$, $\alpha = (1+b-\mu/Wi)/2$, $\beta = -bWi$ and $\nu = b(\mu - Wi)/2$. The above equation is a singly confluent Heun equation in the non-symmetrical canonical form (Decarreau *et al* 1978a, 1978b, Slavyanov 1995)[7].

Equation (7) has two regular singularities at $z = 0$ and $z = 1$ and an irregular singularity of Poincaré rank 1 at $z = \infty$. The characteristic exponents at $z = 0$ are 0 and $1-\gamma$; at $z = 1$, they are 0 and $1-\delta$. We neglect the case of b integer and odd since it does not have physical relevance. Consequently, there are no logarithmic solutions and, for $|z| < 1$, $w_\mu(z)$ can be written as $w_\mu(z) = a_0\varphi_0(z) + d_0 z^{1/2}\chi_0(z)$ with a_0, d_0 complex constants and φ_0, χ_0 analytic functions of z (equivalently of q^2) such that $\varphi_0(0) \neq 0$ and $\chi_0(0) \neq 0$. Similarly, for $|z-1| < 1$, $w_\mu(z)$ takes the form $w_\mu(z) = a_1\varphi_1(z-1) + d_1(1-z)^{1-b/2}\chi_1(z-1)$ with a_1, d_1 complex constants and φ_1, χ_1 analytic functions of z such that $\varphi_1(0) \neq 0$ and $\chi_1(0) \neq 0$.

It is easily seen that boundary conditions (6) can be matched only by those solutions of (7) that belong to the exponent 0 both in $z = 0$ and $z = 1$ (that is both d_0 and d_1 have to be zero)[8]. The eigenvalue problem defined by (5) and (6) is therefore mapped into a CTCP on $[0, 1]$

[7] The worm-like chain model, $\hat{f}(q) = 2/3 - 1/(6q) + 1/[6q(1-q)^2]$, would lead to a second-order linear differential equation with two irregular singularities of Poincaré rank 1 and 3, respectively. The FENE model in a δ-correlated random flow can be solved in terms of a general Heun equation (Martins Afonso and Vincenzi 2005).

[8] We leave aside the case $b = 2$ since it does not have physical relevance.

for the confluent Heun equation (7). To compute the eigenvalues μ, we adapt the procedure exploited by Svartholm (1939) and Erdélyi (1942, 1944) to (7) (see also Slavyanov (1995), Slavyanov and Lay (2000)). We then expand w_μ in series of Jacobi polynomials having the required characteristic exponent at $z = 0$ and $z = 1$:

$$w_\mu(z) = \sum_{n=0}^{\infty} c_n(\mu) u_n(z), \tag{8}$$

with

$$u_n(z) = {}_2F_1(-n, \omega + n; \gamma; z) = (-1)^n \frac{n!\sqrt{\pi}}{\Gamma(n+\gamma)} P_n^{(\omega-\gamma,\gamma-1)}(2z-1)$$

and $\omega = \gamma + \delta - 1$. The function ${}_2F_1$ denotes the Gauss hypergeometric function; $P_n^{(\omega-\gamma,\gamma-1)}$ are the Jacobi polynomials of parameters $\omega - \gamma$ and $\gamma - 1$ and degree n (e.g. Erdélyi *et al* (1953)). The conditions for the convergence of (8) will determine the spectrum of $\mathscr{L}$.

By defining the operators

$$\mathscr{D}_1 w_\mu := z(z-1)\left[w_\mu'' + \left(\frac{\gamma}{z} + \frac{\delta}{z-1}\right) w_\mu'\right],$$
$$\mathscr{D}_2 w_\mu := -z(z-1) w_\mu',$$

we can rewrite (7) in the form

$$\mathscr{D}_1 w_\mu + \varepsilon \mathscr{D}_2 w_\mu + (\rho z + \sigma) w_\mu = 0, \tag{9}$$

where $\varepsilon = bWi$, $\rho = b[\mu - (1+b)Wi]/2$, $\sigma = b(Wi - \mu)/2$. The polynomials u_n satisfy the differential relations (Erdélyi *et al* 1953)

$$\mathscr{D}_1 u_n = n(\omega + n) u_n \tag{10}$$

and

$$\mathscr{D}_2 u_n = \widetilde{A}_n u_{n+1} + \widetilde{B}_n u_n + \widetilde{C}_n u_{n-1}, \tag{11}$$

with

$$\widetilde{A}_n = \frac{n(n+\omega)(n+\gamma)}{(2n+\omega)(2n+\omega+1)}, \qquad \widetilde{B}_n = \frac{n(n+\omega)(\delta-\gamma)}{(2n+\omega-1)(2n+\omega+1)},$$
$$\widetilde{C}_n = -\frac{n(n+\omega)(n+\delta-1)}{(2n+\omega)(2n+\omega-1)}.$$

In addition, the following recurrence relation holds (Erdélyi *et al* 1953):

$$z u_n = \widehat{A}_n u_{n+1} + \widehat{B}_n u_n + \widehat{C}_n u_{n-1}, \tag{12}$$

with coefficients

$$\widehat{A}_n = -\frac{(n+\gamma)(n+\omega)}{(2n+\omega)(2n+\omega+1)}, \qquad \widehat{B}_n = \frac{2n(n+\omega)+\gamma(\omega-1)}{(2n+\omega-1)(2n+\omega+1)},$$
$$\widehat{C}_n = -\frac{n(n+\delta-1)}{(2n+\omega-1)(2n+\omega)}.$$

Inserting expansion (8) in (9) and exploiting relations (10), (11), (12) yield the following three-term recurrence relation for $c_n(\mu)$:

$$g_{-1} c_0 = 0 \tag{13}$$

$$g_0 c_1 + h_0 c_0 = 0 \tag{14}$$

$$g_n c_{n+1} + h_n c_n + k_n c_{n-1} = 0 \qquad \text{for} \quad n \geqslant 2, \tag{15}$$

where the coefficients

$$g_n = \varepsilon\widetilde{C}_{n+1} + \rho\widehat{C}_{n+1}, \qquad h_n = n(\omega+n) + \varepsilon\widetilde{B}_n + \rho\widehat{B}_n + \sigma,$$
$$k_n = \varepsilon\widetilde{A}_{n-1} + \rho\widehat{A}_{n-1}$$

depend on μ through ρ and σ. The asymptotic behaviour of h_n/g_n and k_n/g_n is given by

$$\frac{h_n}{g_n} \sim -\frac{4n}{\varepsilon} \qquad \text{and} \qquad \frac{k_n}{g_n} \sim -1 \qquad (n \to \infty). \tag{16}$$

According to the Perron–Kreuser theorem (e.g. Gautschi (1967), Wimp (1984)), (16) implies that the recurrence relation (15) has two linearly independent solutions $\left(c_n^+\right)_n$ and $(c_n^-)_n$ such that

$$\frac{c_{n+1}^+}{c_n^+} \sim \frac{4n}{\varepsilon} \qquad \text{and} \qquad \frac{c_{n+1}^-}{c_n^-} \sim -\frac{\varepsilon}{4n} \qquad (n \to \infty). \tag{17}$$

The above sequences have the property $\lim_{n\to\infty} c_n^- \big/ c_n^+ = 0$; hence $(c_n^-)_n$ is what is called a minimal solution of (15). Every other solution non-proportional to $(c_n^-)_n$ is asymptotically proportional to $\left(c_n^+\right)_n$, and therefore diverges with increasing n. Therefore, we can already say that (8) can converge only if the sequence $(c_n)_n$ is a minimal solution of (15).

The second limit in (17) implies that $\lim_{n\to\infty} \sqrt[n]{|c_n^-|} = 0$. This condition ensures that, if the coefficients c_n form a minimal solution of (15), then expansion (8) converges absolutely to an analytic function in the whole complex plane (Szegö 1939, p 252).

Nonetheless, it is also required that $c_n = 0$ for $n < 0$, that is the sequence $(c_n)_n$ is subject to initial conditions (13) and (14). Equation (13) is trivially satisfied since $g_{-1} = 0$, and so does (14) for $\mu = 0$. (This is in accordance with the fact that ψ_0 exists for all Wi and b.) However, for $\mu \neq 0$, equation (14) fixes the ratio $c_1/c_0 = -(b+3)/2$. This latter requirement is not satisfied by whatever μ and therefore selects the spectrum of $\mathscr{L}$.

To summarize, the spectrum of $\mathscr{L}$ is the set of those μ such that $(c_n(\mu))_{n\geqslant 0}$ is a minimal solution of (15) satisfying $c_1(\mu)/c_0(\mu) = -(b+3)/2$. From Pincherle's theorem (e.g. Gautschi (1967), p 31), this conclusion is equivalent to stating that the eigenvalues μ are the solutions of

$$\cfrac{k_1/g_1}{h_1/g_1 - \cfrac{k_2/g_2}{h_2/g_2 - \cfrac{k_3/g_3}{h_3/g_3 - \cdots}}} = \frac{b+3}{2}.$$

The latter represents a transcendental equation for the relaxation spectrum associated with the Fokker–Planck equation (3). The reciprocal of the smallest nonzero solution is T_{rel}/τ.

We calculated T_{rel} numerically by means of the modified Miller algorithm (Wimp 1984, pp 82–85). The behaviour of T_{rel} as a function of Wi is reported in figure 1. For very small Wi the influence of the external flow is negligible and T_{rel} is approximately equal to τ. With increasing Wi the ratio T_{rel}/τ starts growing as $1/(1-2Wi)$. This behaviour can be deduced by replacing the spring force with a Hookean force, $\hat{f}(q) = 1$, and computing the relaxation of the moments of q. For a fixed b, the rescaled relaxation time reaches a sharp maximum $T_{\max}$ in the neighbourhood of the coil–stretch transition ($Wi_c = 1/2$); the value of $T_{\max}$ increases linearly with $\sqrt{b}$ (figure 2). With increasing b, T_{rel} attains its maximum value $T_{\max}$ closer and closer to Wi_c and the width of the peak decreases (figure 2). For large Wi the relaxation time is fixed by the time scale of the flow λ^{-1}, and therefore T_{rel}/τ decreases as Wi^{-1}.

The computation of T_{rel} shows that, near the coil–stretch transition, the typical time scale involved in polymer relaxation dynamics is strongly different from τ. The time associated with the fundamental oscillation mode is not representative of polymer temporal dynamics

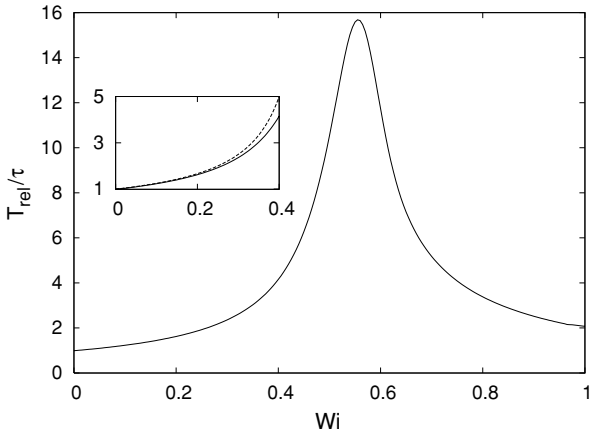

Figure 1. Rescaled relaxation time $T_{\rm rel}/\tau$ as a function of the Weissenberg number Wi for $b = 600.25$; the inset shows the comparison with the small Wi behaviour $1/(1 - 2Wi)$ (dashed line).

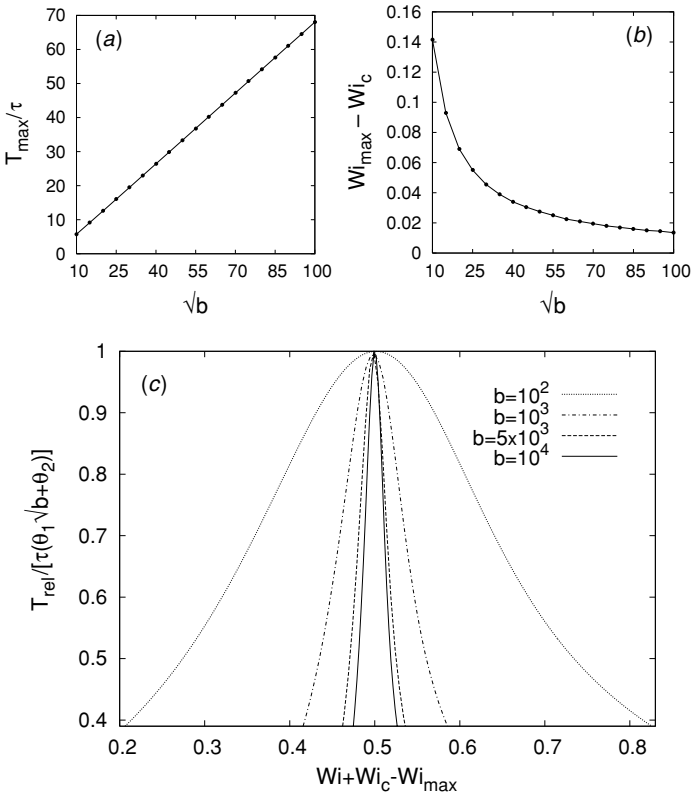

Figure 2. (*a*) Maximum rescaled relaxation time $T_{\rm max}/\tau$ versus the square root of the flexibility parameter $b = L^2/Q_0^2$: $T_{\rm max}/\tau$ increases as $\theta_1\sqrt{b} + \theta_2$ with $\theta_1 \approx 0.69$ and $\theta_2 \approx -1.18$; (*b*) behaviour of $Wi_{\rm max}$ as a function of $\sqrt{b}$, where $Wi_{\rm max}$ is the Weissenberg number at which the relaxation time attains its maximum value $T_{\rm max}$; (*c*) relaxation time versus Wi for different b, rescaled to make the maximum values coincide.

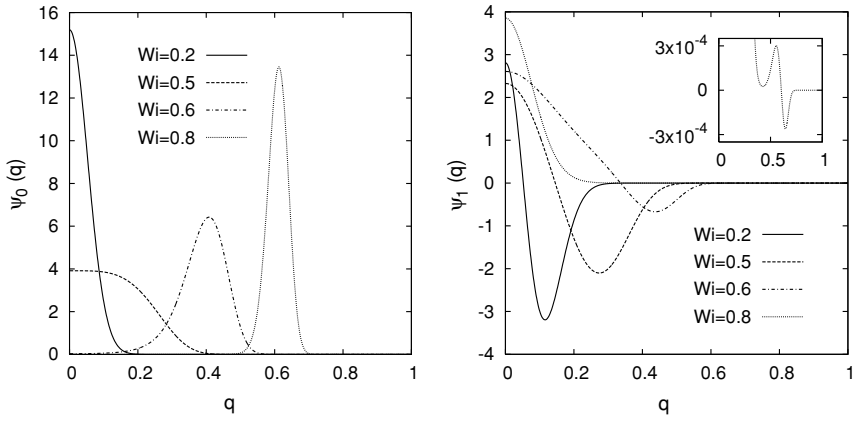

Figure 3. Stationary PDF of the extension and eigenfunction of the Fokker–Planck operator $\mathscr{L}$ associated with the smallest nonzero eigenvalue μ_1. The eigenfunctions have been computed numerically by means of the iteration-variation method (Morse and Feshbach 1953).

in flow. These results confirm the behaviour encountered in isotropic δ-correlated Gaussian flows (Celani *et al* 2005a, Martins Afonso and Vincenzi 2005), but here the enhancement of $T_{\rm rel}$ is stronger since the elongational flow is more efficient in deforming polymers.

In Brownian dynamics simulations and experiments the relaxation time of $\psi(q;t)$ can be measured from the decay of the moments of the extension to their steady-state value. To observe $T_{\rm rel}$, one has to make sure that the initial condition $\psi(q;0)$ is not orthogonal to the first eigenfunction of $\mathscr{L}$, that is $\psi_1(q)$ in (5), with respect to the scalar product with weighting function $\psi_0(q)$. Figure 3 shows the shape of $\psi_1(q)$ for different Wi. An initial PDF concentrated either at a coiled or a stretched extension $\bar{q}$ (formally $\psi(q;0)=\delta(q-\bar{q})$) has projection onto $\psi_1(q)$ equal to $\psi_1(\bar{q})/\psi_0(\bar{q})$ by construction (e.g. Stratonovich (1963)). The initial condition with all the polymers having the same extension $\bar{q}$ is therefore not orthogonal to $\psi_1(q)$ if $\psi_1(\bar{q})\neq 0$; all the moments will thus tend to their stationary value with a typical time scale $T_{\rm rel}$.

We now show that it is accurate to compute $T_{\rm rel}$ by means of (3) also for $Wi < Wi_c$. At low Wi, the entropic force can be modelled as a Hookean force, i.e. $f(Q)=1$ in (1). The vector equation (1) therefore reduces to a set of three decoupled stochastic differential equations for Q_1, Q_2, Q_3. Hence we have $\Psi(\boldsymbol{q};t)=\psi^{(1)}(q_1;t)\psi^{(2)}(q_2;t)\psi^{(3)}(q_3;t)$, where $\Psi(\boldsymbol{q};t)$ is the PDF of the vector $\boldsymbol{q}$ and $\psi^{(i)}(q_i;t)$ is the PDF of the ith component of $\boldsymbol{q}$. The relaxation time of $\Psi(\boldsymbol{q};t)$ is thus the longest of the relaxation times of $\psi^{(1)}(q_1;t)$, $\psi^{(2)}(q_2;t)$ and $\psi^{(3)}(q_3;t)$ given that all $\psi^{(i)}(q_i;t)$ have a non-trivial long-time limit. It is easy to check that at low Wi the relaxation time of $\psi^{(1)}(q_1;t)$ is $T^{(1)}_{\rm rel}=\tau/(1-2Wi)$, while $T^{(2)}_{\rm rel}=\tau/(1+2Wi)$ and $T^{(3)}_{\rm rel}=\tau$ (with obvious notation). The function $\Psi(\boldsymbol{q};t)$ therefore has the same relaxation time as $\psi^{(1)}(q_1;t)$. Now we note that $\psi(q;t)$ and $\Psi(\boldsymbol{q};t)$ have the same long-time behaviour since $\psi(q;t)=q^2\int_0^{\pi}\int_0^{2\pi}\Psi(\boldsymbol{q}(q,\vartheta,\phi);t)\sin\vartheta\,{\rm d}\vartheta\,{\rm d}\phi$. We thus come to the following conclusion: the relaxation times of $\psi(q;t)$ and $\psi^{(1)}(q_1;t)$ coincide at low Wi and $\psi^{(1)}(q_1;t)$ satisfies (3). This fact explains why (3) yields an accurate computation of $T_{\rm rel}$ also below the coil–stretch transition.

4. Summary and conclusions

We have investigated the relaxation dynamics of an isolated polymer in an external flow. Previous studies focused on the relaxation of a polymer in a solvent driven only by Brownian

motion. Those studies determined the time τ associated with the slowest oscillation mode of the molecule in the absence of external flow. We have considered an elongational flow and derived a transcendental equation for the relaxation spectrum associated with the time evolution of the PDF of polymer extension. The problem of computing this spectrum has been recast as a central two-point connection problem for a confluent Heun equation. The Heun equation results from the separation of the time variable in the Fokker–Planck equation for the PDF of the extension.

Our analysis shows that an external elongational flow strongly influences polymer relaxation dynamics. The longest relaxation time associated with the evolution of the PDF of the extension provides an estimation of the time scale of polymer deformation. Near the coil–stretch transition, this time is significantly greater than τ (already one order of magnitude greater for short molecules). The physical reason is the large number of polymer configurations close to the coil–stretch transition. At intermediate Weissenberg numbers polymer conformation results from a critical competition between the entropic force and the velocity gradient. Therefore, around the transition, coiled and stretched polymer coexist in the flow, and this makes the relaxation to the equilibrium PDF particularly long. It is worth noting that the amplification of the relaxation time is stronger when hydrodynamic interactions are taken into account; this behaviour is intimately related to the finite-time conformation hysteresis observed in elongational flows (Celani *et al* 2006).

Acknowledgments

The authors are grateful to A Celani, C Doering, M Martins Afonso, A Puliafito and B Rajaratnam for useful suggestions. This work has been partially supported by the European Union under the contract HPRN-CT-2002-0030 'Fluid Mechanical Stirring and Mixing: the Lagrangian Approach'.

References

Babcock H P, Teixeira R E, Hur J S, Shaqfeh E S and Chu S 2003 *Macromolecules* **36** 4544–8
Bird R B, Hassager O, Armstrong R C and Curtiss C F 1987 *Dynamics of Polymeric Liquids, Fluid Mechanics* vol 2 (New York: Wiley)
Brochard-Wyart F 1995 *Europhys. Lett.* **30** 387–92
Celani A, Musacchio S and Vincenzi D 2005a *J. Stat. Phys.* **118** 531–54
Celani A, Puliafito A and Turitsyn K 2005b *Europhys. Lett.* **70** 464–70
Celani A, Puliafito A and Vincenzi D 2006 *Phys. Rev. Lett.* (submitted)
Davoudi J and Schumacher J 2006 *Phys. Fluids* **18** 025103
Decarreau A, Dumont-Lepage M-Cl, Maroni P, Robert A and Ronveaux A 1978a *Ann. Soc. Sci. Brux.* **92** 53–78
Decarreau A, Maroni P and Robert A 1978b *Ann. Soc. Sci. Brux.* **92** 151–89
Erdélyi A 1942 *Duke Math. J.* **9** 48–58
Erdélyi A 1944 *Q. J. Math.* **15** 62–9
Erdélyi, Magnus W, Oberhettinger F and Tricomi F G 1953 *Higher Transcendental Functions* (New York: McGraw-Hill)
Gautschi W 1967 *SIAM Rev.* **9** 24–82
de Gennes P G 1974 *J. Chem. Phys.* **60** 5030–42
Gerashchenko S and Steinberg V 2006 *Phys. Rev. Lett.* **96** 038304
Hatfield J W and Quake S R 1999 *Phys. Rev. Lett.* **82** 3548–51
Hernández Cifre J G and García de la Torre J 1998 *J. Non-Cryst. Solids* **235–237** 717–22
Hernández Cifre J G and García de la Torre J 1999 *J. Rheol.* **43** 339–58
Hur J S, Shaqfeh E S, Babcock H P and Chu S 2002 *Phys. Rev.* E **66** 011915
Jaffé G 1933 *Z. Phys.* **87** 535–44
Larson R G, Perkins T T, Smith D E and Chu S 1997 *Phys. Rev.* E **55** 1794–7

Larson R G 2005 *J. Rheol.* **49** 1–70
Leaver E W 1985 *Proc. R. Soc.* A **402** 285–98
Manneville S, Cluzel Ph, Viovy J-L, Chatenay D and Caron F 1996 *Europhys. Lett.* **36** 413–8
Martins Afonso M and Vincenzi D 2005 *J. Fluid Mech.* **540** 99–108
Morse P M and Feshbach H 1953 *Methods of Theoretical Physics* (New York: McGraw-Hill)
Perkins T T, Quake S R, Smith D E and Chu S 1994 *Science* **264** 822
Perkins T T, Smith D E and Chu S 1997 *Science* **276** 2016–21
Puliafito A and Turitsyn K 2005 *Physica* D **211** 9–22
Quake S R, Babcock H and Chu S 1997 *Nature* **388** 151–4
Rouse P E 1953 *J. Chem. Phys.* **21** 1272–80
Rzehak R and Zimmermann W 2002 *Europhys. Lett.* **59** 779–85
Schenzle A and Brand H 1979 *Phys. Rev.* A **20** 1628–47
Schroeder C M, Babcock H P, Shaqfeh E S G and Chu S 2003 *Science* **301** 1515–9
Schroeder C M, Shaqfeh E S G and Chu S 2004 *Macromolecules* **37** 9242–56
Shaqfeh E S G 2005 *J. Non-Newtonian Fluid Mech.* **130** 1–28
Slavyanov S Yu 1995 *Confluent Heun Equation, Heun's Differential Equations* ed A Ronveaux (New York: Oxford University Press)
Slavyanov S Yu and Lay W 2000 *Special Functions. A Unified Theory Based on Singularities* (New York: Oxford University Press)
Smith D E, Babcock H P and Chu S 1999 *Science* **283** 1724–7
Smith D E and Chu S 1998 *Science* **281** 1335–40
Sreenivasan K R and White C M 2000 *J. Fluid Mech.* **409** 149–64
Stratonovich R L 1963 *Topics in the Theory of Random Noise* (New York: Gordon and Breach)
Svartholm N 1939 *Math. Ann.* **116** 413–21
Szegö G 1939 *Orthogonal Polynomials* (Providence, RI: American Mathematical Society)
Wiest J L, Wedgewood L and Bird R B 1989 *J. Chem. Phys.* **90** 587–94
Wimp J 1984 *Computation with Recurrence Relations* (Boston, MA: Pitman)
Zimm B H 1956 *J. Chem. Phys.* **24** 269–78

Dynamical Slowdown of Polymers in Laminar and Random Flows

A. Celani,[1] A. Puliafito,[1] and D. Vincenzi[2,3]

[1]*CNRS-INLN, 1361 Route des Lucioles, 06560 Valbonne, France*

[2]*Max-Planck-Institut für Dynamik und Selbstorganisation, Bunsenstrasse 10, 37073 Göttingen, Germany*

[3]*Sibley School of Mechanical and Aerospace Engineering and LASSP, Cornell University, Ithaca, New York 14853, USA*

(Received 23 March 2006; published 15 September 2006)

The influence of an external flow on the relaxation dynamics of a single polymer is investigated theoretically and numerically. We show that a pronounced dynamical slowdown occurs in the vicinity of the coil-stretch transition, especially when the dependence on polymer conformation of the drag is accounted for. For the elongational flow, relaxation times are exceedingly larger than the Zimm relaxation time, resulting in the observation of conformation hysteresis. For random smooth flows, hysteresis is not present. Yet, relaxation dynamics is significantly slowed down because of the large variety of accessible polymer configurations. The implications of these results for the modeling of dilute polymer solutions in turbulent flows are addressed.

DOI: 10.1103/PhysRevLett.97.118301 PACS numbers: 47.57.Ng, 47.27.−i

The dynamics of an isolated polymer in a flow field forms the basis of constitutive models for dilute polymer solutions [1–3]. The modeling of drag-reducing flows, for instance, requires an appropriate description of single polymer deformation in turbulent velocity fields [4]. In the last decade, major advances in fluorescence microscopy offered the possibility of tracking isolated polymers both in laminar [3] and random flows [5]. The dynamics of a polymer in thermal equilibrium with the surrounding solvent is commonly described in terms of normal modes and the relaxation times associated with them. The analytical form of the relaxation spectrum was first obtained by Rouse under the assumption that the polymer could be described as a series of beads connected by Hookean springs [6]. The Rouse model was subsequently improved by Zimm to include hydrodynamical interactions between segments of the polymer [7]. In Zimm's formulation, the equations of motion are decoupled into a normal mode structure by preaveraging the distances between the beads over the distribution of polymer configurations. The relaxation time associated with the fundamental mode, τ, determines the typical time that it takes for a deformed polymer to recover the equilibrium configuration in a solvent. The normal mode theory was confirmed by the analysis of the oscillatory motion of a DNA molecule immersed in a solvent and held in a partially extended state by means of optical tweezers [8]. An alternative approach to examine polymer relaxation consists in stretching a tethered DNA molecule in a flow and measuring its relaxation after cessation of the flow [9,10]. The theoretical predictions for these experimental conditions are provided by the scaling theory [11] and the static dynamics formalism [12].

The aforementioned studies all consider the internal dynamics of a polymer floating in a solvent under the influence of thermal noise only—the interaction of the polymer with an external flow is not taken into account. One of the aspects highlighted by experiments is that polymer dynamics in a moving fluid is strongly influenced by the carrier velocity field. The coil-stretch transition is the most noticeable example: as the strain rate exceeds a threshold value, the polymer undergoes a transition from the coiled, equilibrium configuration to an almost fully extended one [13]. Therefore, when a polymer is freely transported by a nonuniform flow, we expect that the time scales describing its dynamics may be significantly different from the Zimm time τ. Simple models for polymer stretching indeed suggest deviations from Zimm's theory near the coil-stretch transition [14–16]. Discrepancies in the definition of the correct relaxation time are also encountered in drop formation experiments [17].

In this Letter we investigate polymer relaxation dynamics both in elongational and random smooth flows. Our analysis brings to evidence an important slowdown of dynamics with respect to the Zimm time scales, in the vicinity of the coil-stretch transition. For the elongational flow, this is related to conformation hysteresis [18–20]. For random flows, we show that hysteresis is not present. Nonetheless, the amplification of the relaxation time persists, albeit to a lesser extent, due to the large heterogeneity of polymer configurations. In both cases, the dependence of the drag force on the polymer configuration plays a prominent role. This suggests the necessity of improving current models of polymer solutions in turbulent flows to account for such an effect.

The dumbbell approximation is the basis of the most common models of single polymer dynamics and viscoelastic models of dilute polymer solutions [21]. Its validity relies on the fact that the slowest deformational mode of the polymer is the most influential in producing viscoelasticity [4]. However, when attention is directed to nonequilibrium dynamics it is often too crude to assume that τ is independent of the conformation of the molecule [22]. Therefore, following the approach of de Gennes [13], Hinch [23], and Tanner [24], we consider a model where the polymer is described as two beads connected by an

elastic spring and the probability density function of the end-to-end vector, $\Psi(\boldsymbol{R}, t)$, satisfies the diffusion equation:

$$\frac{\partial \Psi}{\partial t} = -\frac{\partial}{\partial \boldsymbol{R}} \cdot \left[\boldsymbol{\kappa}(t) \cdot \boldsymbol{R}\Psi - \frac{f(R)\boldsymbol{R}}{2\tau\nu(R)}\Psi - \frac{R_0^2}{2\tau\nu(R)}\frac{\partial \Psi}{\partial \boldsymbol{R}} \right], \tag{1}$$

where $\kappa_{ij}(t) = \partial_j v_i(t)$ is the velocity gradient, R_0 is the mean extension at thermal equilibrium, and $R = |\boldsymbol{R}|$. The function $f(R)$ defines the entropic force restoring stretched molecules into the coiled configuration. Synthetic polymers are properly described by the Warner law, $f(R) = 1/(1 - R^2/L^2)$, where L is the contour length of the polymer; biological macromolecules are better characterized by the Marko-Siggia law, $f(R) = 2/3 - L/(6R) + L/[6R(1 - R/L)^2]$ [2]. The flow strength relative to the polymer tendency to recoil is expressed by the Weissenberg number Wi, defined as the product of the Zimm time τ by a characteristic extension rate of the flow. The function $\nu(R)$ encodes for the dependence on the polymer conformation of the drag exerted by the fluid: a spherical coil offers a smaller resistance with respect to a long rodlike configuration. We utilize the expression $\nu(R) = 1 + (\zeta_s/\zeta_c - 1)R/L$ that interpolates linearly between these extremes (see Refs. [25,26]). Here, $\zeta_c = 3\sqrt{6\pi^3}R_0\eta/8$ and $\zeta_s = 2\pi L\eta/\ln(L/\ell)$ are the friction coefficients for the coiled and the stretched configuration, respectively, η is the solvent viscosity, and ℓ is the diameter of the molecule. Strictly speaking, the above form of $\nu(R)$ was deduced from experiments and microscopic simulations of laminar flows. To our knowledge, measures of $\nu(R)$ in random flows are not available yet, and the study of its functional dependence lies beyond the scope of the present work. Assuming that the polymer is aligned with the local stretching direction of the flow for the most part of its evolution, we shall use a linear $\nu(R)$ for a random flow as well.

To define the relaxation time in the presence of an arbitrary external flow, we consider the probability density function of the rescaled extension, $P(r, t)$ with $r = R/L$, and identify the dynamical relaxation time, $t_{\rm rel}$, as the characteristic time needed for $P(r, t)$ to attain its stationary form $P_{\rm st}(r)$. In the cases examined in this Letter, as we shall see, the probability density function of r satisfies the Fokker-Planck equation

$$\partial_{t'}P = -\partial_r(D_1(r)P) + \partial_r D_2(r)\partial_r P, \tag{2}$$

where the form of $D_1(r)$ and $D_2(r)$ depends on the flow and $t' = t/\tau$. The stationary solution to Eq. (2) takes the potential form $P_{\rm st}(r) = N\exp[-E(r)/K_BT]$, where N is the normalization constant and $E(r) = -K_BT\int^r D_1(\rho)/D_2(\rho)d\rho$. The finite-time solution admits the expansion

$$P(r, t') = P_{\rm st}(r) + \sum_{n=1}^{\infty} a_n p_n(r) e^{-t'/\sigma_n}, \tag{3}$$

where the coefficients a_n are fixed by $P(r, 0)$, $p_n(r)$ are the eigenfunctions of the Fokker-Planck operator, and σ_n are the reciprocals of its (strictly positive) eigenvalues, arranged in descending order ($\sigma_n > \sigma_{n+1}$). The relaxation time is thus defined as $t_{\rm rel} \equiv \sigma_1\tau$.

As a first example, we examine the steady planar elongational flow $\boldsymbol{v} = \gamma(x, -y)$. By assuming that the polymer extension in the x direction is much greater than in the y direction, it is easy to derive from Eq. (1) an equation of the form (2) with $D_1(r) = {\rm Wi}r - \hat{f}(r)r/[2\hat{\nu}(r)]$, $D_2(r) = [2b\hat{\nu}(r)]^{-1}$, $\hat{f}(r) = f(rL)$, $\hat{\nu}(r) = \nu(rL)$, $b = L^2/R_0^2$, and ${\rm Wi} = \gamma\tau$ [27]. For $\zeta_s = \zeta_c$, $t_{\rm rel}$ can be computed from (3) by solving a central two-point connection problem for a generalized spheroidal wave equation [16]. In the general case, $\zeta_s > \zeta_c$, we resorted to a numerical computation based on the variation-iteration method of quantum mechanics [28]. In the vicinity of the coil-stretch transition (${\rm Wi} = 1/2$) $t_{\rm rel}$ shows a sharp peak (Fig. 1). In this range of Wi there is a critical competition between the entropic force and the velocity gradient that makes the convergence time to the steady state extremely long. This effect is strongly enhanced by the conformation-dependent drag; the peak $t_{\rm max}$ indeed increases with ζ_s/ζ_c (Fig. 1). Those extremely long relaxation times are intimately connected with the observation of finite-time conformation hysteresis [18–20]. For large enough ζ_s/ζ_c, there is a narrow range of Wi around the critical value for the coil-stretch transition where $E(r)$ has a double well structure [18–20]. The barrier height separating the coiled and the stretched state is much greater than the thermal energy K_BT, and therefore the polymer remains trapped in its initial configuration for an exceptionally long time (Fig. 2).

The discovery of elastic turbulence has recently allowed the examination of single polymer dynamics in a random smooth flow generated by viscoelastic instabilities [5,29]. The velocity gradient fluctuates along fluid trajectories; the average local deformation rates define the three Lyapunov exponents of the flow. Experimental observa-

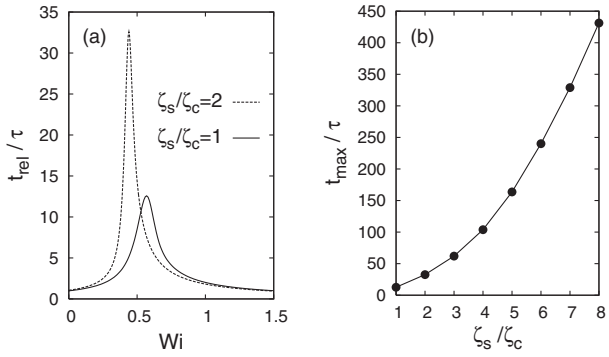

FIG. 1. Elongational flow: (a) rescaled relaxation time vs Wi for $b = 400$. The entropic force is given by the Warner law. For small Wi, $t_{\rm rel}/\tau$ grows as $1/(1–2{\rm Wi})$, as can be seen by replacing $\hat{f}(r)$ with 1 in Eq. (2). For ${\rm Wi} \gg {\rm Wi}_{\rm crit}$, the time needed to reach the asymptotic regime is set by the time scale of the flow, γ^{-1}, and $t_{\rm rel}/\tau$ decreases as ${\rm Wi}^{-1}$. (b) Rescaled maximum relaxation time $t_{\rm max}/\tau$ vs ζ_s/ζ_c ($b = 400$).

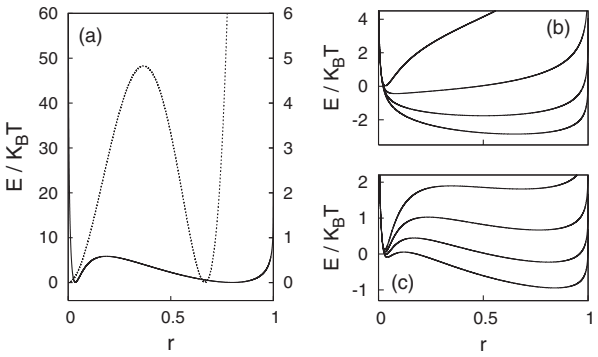

FIG. 2. (a) Effective energy at the coil-stretch transition for a polyacrylamide (PAM) molecule ($b = 3953$, $\zeta_s/\zeta_c = 6.87$) in the elongational flow (dashed line) and the 3D Batchelor-Kraichnan flow (solid line). The left vertical axis refers to the dashed line; the right vertical axis refers to the solid line. (b) Effective energy in the random flow for a PAM molecule with constant drag ($\zeta_s = \zeta_c$) (from top to bottom Wi = 0.4, 0.7, 1.0, and 1.3); (c) the same as (b), but with $\zeta_s = 6.87\zeta_c$ (from top to bottom Wi = 0.28, 0.33, 0.38, and 0.43). When $\zeta_s > \zeta_c$ the transition occurs in a much narrower range of Wi.

tions have been accompanied by theoretical and numerical studies based on the dumbbell model (see, e.g., Refs. [14,15,30]). To analytically investigate polymer relaxation dynamics in random flows, we initially assume that the velocity field obeys the Batchelor-Kraichnan statistics [31]. The velocity gradient is then a statistically isotropic and parity invariant Gaussian process with zero mean and correlation: $\langle \kappa_{ij}(t)\kappa_{kl}(s)\rangle = 2\lambda\delta(t-s)\times[(d+1)\delta_{ik}\delta_{jl} - \delta_{ij}\delta_{kl} - \delta_{il}\delta_{jk}]/[d(d-1)]$, where d is the dimension of the flow and λ denotes the largest Lyapunov exponent. In this context, we indicate by $P(r,t')$ the probability density function of the extension both with respect to thermal noise and the realizations of the velocity field. For the elongational flow Eq. (2) was obtained under the uniaxial approximation. On the contrary, for the isotropic random flow Eq. (2) holds exactly and can be obtained by a Gaussian integration by parts followed by integration over angular variables. The drift and diffusion coefficients take the form $D_1(r) = (d-1)/d\mathrm{Wi}r - \hat{f}(r)r/[2\hat{\nu}(r)] + (d-1)/[2b\hat{\nu}(r)r]$ and $D_2(r) = \mathrm{Wi}r^2/d + [2b\hat{\nu}(r)]^{-1}$ with $\mathrm{Wi} = \lambda\tau$. The stationary distribution admits once more a potential form. For $d = 3$ and $\zeta_s > \zeta_c$, the potential displays a very wide well, the effect of the conformation-dependent drag being to increase the probability of large extensions. There is no evidence of pronounced double wells (Fig. 2). Near the coil-stretch transition, the effective barrier heights separating the coiled and stretched states are indeed at most comparable to thermal energy. For realistic ζ_s/ζ_c no conformation hysteresis is therefore expected to be observed in random flows. The behavior of t_{rel} vs Wi is, however, analogous to the one encountered in the elongational flow: t_{rel}/τ increases as $[1 - \mathrm{Wi}(d+2)/d]^{-1}$ at small Wi and decreases as Wi^{-1} at large Wi. A peak near the transition is present, which becomes more and more pronounced with increasing ζ_s/ζ_c, attaining values as large as about 30 times τ (Fig. 3). The reason for this behavior is the breadth of $P_{\mathrm{st}}(r)$ and the consequent large heterogeneity of accessible polymer configurations.

To corroborate the results obtained in the context of the short-correlated flow, we performed Brownian dynamics simulations of dumbbell molecules [32] in the random flow introduced by Brunk *et al.* [34]. This model reproduces the small-scale structure of a turbulent flow by means of a statistically isotropic Gaussian velocity gradient. The autocorrelation times of components of the strain and rotation tensors are set to be a multiple of the Kolmogorov time τ_η by comparison with direct numerical simulations of 3D isotropic turbulence ($\tau_S = 2.3\tau_\eta$, $\tau_R = 7.2\tau_\eta$). The Lyapunov exponent of this flow is $\lambda \simeq 10\tau_\eta^{-1}$. We computed t_{rel} as the time of convergence of the moments $\langle r^n(t)\rangle$ to their stationary value $\langle r^n\rangle_{\mathrm{st}}$: $t_{\mathrm{rel}}^{-1} = -\lim_{t\to\infty}\ln[\langle r^n(t)\rangle - \langle r^n\rangle_{\mathrm{st}}]/t$, where the averages were taken over an ensemble of realizations of the flow, all with the same initial extension $r(0)$. The numerical difficulty arising from the singularity of the entropic force at $R = L$ has been overcome by exploiting the algorithm introduced in [35]. The results shown in Fig. 4 confirm the scenario depicted in the context of the short-correlated flow. It is worth noting that the above definition provides an operational method to measure t_{rel} that can be implemented in experiments.

In summary, we have shown that the equilibrium configuration of a polymer in a flow as well as the time a deformed molecule takes on average to recover that configuration depend sensitively on the properties of the flow. In the vicinity of the coil-stretch transition the characteristic relaxation time is much longer than the Zimm time,

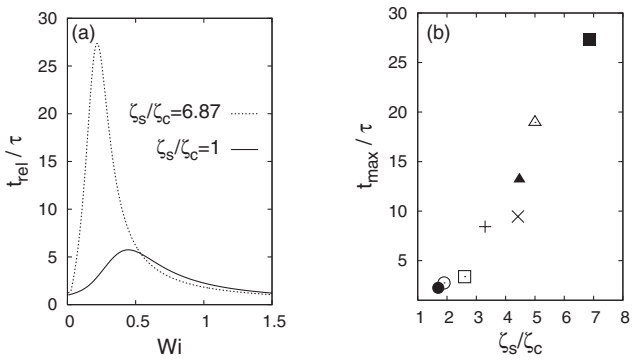

FIG. 3. Three-dimensional Batchelor-Kraichnan flow: (a) t_{rel}/τ vs Wi for a PAM molecule ($b = 3953$); (b) t_{max}/τ for the following polymers: DNA (●, $b = 191.5$; ○, $b = 260$; □, $b = 565$; +, $b = 2250$), polystyrene (×, $b = 673$), polyethyleneoxide (PEO) (▲, $b = 1666$), *Escherichia Coli* DNA (△, $b = 9250$), and PAM (■). Measures of b and ζ_s/ζ_c can be found in [18–20,25]. Synthetic polymers are modeled by the Warner law, whereas biological molecules are described by the Marko-Siggia law. Relaxation times were computed by means of the variation-iteration method [28]. For $\zeta_s = \zeta_c$ they can be obtained by solving an eigenvalue problem for a Heun equation [15].

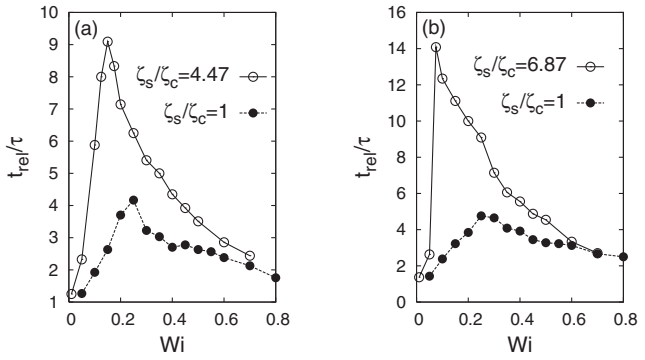

FIG. 4. Brunk-Koch-Lion flow: t_{rel}/τ vs $\mathrm{Wi} = \lambda\tau$ from Brownian dynamics simulations; (a) PEO; (b) PAM.

both in elongational and random flows. In other words, the effective Wi differs considerably from the "bare" one [36]. This effect is strongly amplified when the drag coefficient depends on the conformation of the polymer and may play an important role in drag-reducing turbulent flows, where the strain rate often fluctuates around values typical of the coil-stretch transition [38]. Our conclusions thus suggest that the conformation-dependent drag should be included as a basic ingredient of continuum models of polymer solutions, calling for further theoretical, experimental, and numerical study.

The authors gratefully acknowledge inspiring discussions with M. Chertkov, S. Gerashchenko, M. Martins Afonso, and V. Steinberg. This work has been partially supported by the EU (Contract No. HPRN-CT-2002-00300).

[1] S. Chu, Phil. Trans. R. Soc. A **361**, 689 (2003).
[2] R. G. Larson, J. Rheol. (N.Y.) **49**, 1 (2005).
[3] E. S. G. Shaqfeh, J. Non-Newton. Fluid Mech. **130**, 1 (2005).
[4] A. Gyr and H. W. Bewersdorff, *Drag Reduction of Turbulent Flows by Additives* (Kluwer Academic, Dordrecht, 1995).
[5] S. Gerashchenko, C. Chevallard, and V. Steinberg, Europhys. Lett. **71**, 221 (2005).
[6] P. E. Rouse, Jr., J. Chem. Phys. **21**, 1272 (1953).
[7] B. H. Zimm, J. Chem. Phys. **24**, 269 (1956).
[8] S. R. Quake, H. Babcock, and S. Chu, Nature (London) **388**, 151 (1997).
[9] T. T. Perkins *et al.*, Science **264**, 822 (1994).
[10] S. Manneville *et al.*, Europhys. Lett. **36**, 413 (1996).
[11] Y. Marciano and F. Brochard-Wyart, Macromolecules **28**, 985 (1995).
[12] R. Rzehak and W. Zimmermann, Europhys. Lett. **59**, 779 (2002).
[13] P. G. de Gennes, J. Chem. Phys. **60**, 5030 (1974).
[14] A. Celani, S. Musacchio, and D. Vincenzi, J. Stat. Phys. **118**, 531 (2005).
[15] M. Martins Afonso and D. Vincenzi, J. Fluid Mech. **540**, 99 (2005).
[16] D. Vincenzi and E. Bodenschatz, J. Phys. A **39**, 10 691 (2006).
[17] V. Tirtaatmadja, G. H. McKinley, and J. J. Cooper-White, Phys. Fluids **18**, 043101 (2006).
[18] C. M. Schroeder *et al.*, Science **301**, 1515 (2003).
[19] C. M. Schroeder, E. S. G. Shaqfeh, and S. Chu, Macromolecules **37**, 9242 (2004).
[20] C.-C. Hsieh and R. G. Larson, J. Rheol. (N.Y.) **49**, 1081 (2005).
[21] R. B. Bird *et al.*, *Dynamics of Polymeric Liquids* (Wiley, New York, 1987), 2nd ed., Vol. 2.
[22] J. W. Hatfield and S. R. Quake, Phys. Rev. Lett. **82**, 3548 (1999).
[23] E. J. Hinch, in *Proceedings of Colloques Internationaux du CNRS No. 233* (CNRS Editions, Paris, 1974), p. 241.
[24] R. I. Tanner, Trans. Soc. Rheol. **19**, 557 (1975).
[25] R. G. Larson *et al.*, Phys. Rev. E **55**, 1794 (1997).
[26] P. S. Doyle *et al.*, J. Non-Newton. Fluid Mech. **76**, 79 (1998).
[27] Our definition of Wi follows the literature on elongational flows and therefore is half the one commonly adopted in the context of random flows.
[28] P. M. Morse and H. Feshbach, *Methods of Theoretical Physics* (McGraw-Hill, New York, 1953).
[29] A. Groisman and V. Steinberg, Nature (London) **405**, 53 (2000); New J. Phys. **6**, 29 (2004); T. Burghelea, E. Segre, and V. Steinberg, Phys. Fluids **17**, 103101 (2005).
[30] M. Chertkov, Phys. Rev. Lett. **84**, 4761 (2000); E. Balkovsky, A. Fouxon, and V. Lebedev, Phys. Rev. Lett. **84**, 4765 (2000); J.-L. Thiffeault, Phys. Lett. A **308**, 445 (2003); M. Chertkov *et al.*, J. Fluid Mech. **531**, 251 (2005); A. Puliafito and K. Turitsyn, Physica (Amsterdam) **211D**, 9 (2005); J. Davoudi and J. Schumacher, Phys. Fluids **18**, 025103 (2006).
[31] R. H. Kraichnan, Phys. Fluids **11**, 945 (1968).
[32] The integration algorithm is based on the Itô stochastic differential equation equivalent to Eq. (1), $d\boldsymbol{R} = \{\boldsymbol{\kappa}(t)\cdot\boldsymbol{R} - f(R)\boldsymbol{R}/[2\tau\nu(R)] - R_0^2\nu'(R)\boldsymbol{R}/[2\tau\nu^2(R)R]\}dt + \sqrt{R_0^2/[\tau\nu(R)]}d\boldsymbol{W}(t)$ [33]; $\boldsymbol{W}(t)$ is the Brownian motion.
[33] H. C. Öttinger, *Stochastic Processes in Polymeric Fluids* (Springer-Verlag, Berlin, 1996).
[34] B. K. Brunk, D. L. Koch, and L. W. Lion, Phys. Fluids **9**, 2670 (1997); J. Fluid Mech. **364**, 81 (1998).
[35] A. Celani, A. Puliafito, and K. Turitsyn, Europhys. Lett. **70**, 464 (2005).
[36] This fact is related to the overestimation of the drag-reducing Wi encountered in numerical simulations [37].
[37] Y. Dubief *et al.*, J. Fluid Mech. **514**, 271 (2004).
[38] K. R. Sreenivasan and C. M. White, J. Fluid Mech. **409**, 149 (2000); E. Balkovsky, A. Fouxon, and V. Lebedev, Phys. Rev. E **64**, 056301 (2001); G. Boffetta, A. Celani, and S. Musacchio, Phys. Rev. Lett. **91**, 034501 (2003); V. S. L'vov *et al.*, *ibid.* **92**, 244503 (2004).

Stretching of Polymers in Isotropic Turbulence: A Statistical Closure

Dario Vincenzi,[1,2,3] Shi Jin,[2] Eberhard Bodenschatz,[1,2,3] and Lance R. Collins[2,*]

[1]*Max Planck Institute for Dynamics and Self Organization, Bunsenstraße 10, 37073 Göttingen, Germany*
[2]*Sibley School of Mechanical & Aerospace Engineering, Cornell University, Ithaca, New York 14853, USA*
[3]*Laboratory for Atomic and Solid State Physics, Cornell University, Ithaca, New York 14853, USA*

(Received 22 April 2006; published 12 January 2007)

We present a new closure for the mean rate of stretching of a dissolved polymer by homogeneous isotropic turbulence. The polymer is modeled by a bead-spring-type model (e.g., Oldroyd B, FENE-P, Giesekus) and the analytical closure is obtained assuming the Lagrangian velocity gradient can be modeled as a Gaussian, white-noise stochastic process. The resulting closure for the mean stretching depends upon the ratio of the correlation time for strain and rotation. Additionally, we derived a second-order expression for circumstances when strain and rotation have a finite correlation time. Finally, the base level closure is shown to reproduce results from direct numerical simulations by simply modifying the coefficients.

DOI: 10.1103/PhysRevLett.98.024503 PACS numbers: 47.50.−d, 47.27.E−, 47.57.Ng, 47.85.lb

The dynamics of an isolated polymer molecule in a turbulent flow field is of both fundamental and practical significance. Turbulence provides a mixture of flow types (from rotation to strain) and the response of the polymer is very sensitive to the nature of the underlying flow. Moreover, turbulent flows vary rapidly in space and time, and this, combined with the elasticity of the polymer, produces very complex memory effects. The prime motivation to understand polymer-turbulence interactions is their potential use as drag reducing agents. Since the pioneering work of Toms [1], this technology is routinely used in oil pipelines to reduce pumping costs [2]. The notion of using polymer additives to reduce the drag around ships and submarines has been around for decades, but has yet to be demonstrated on a full-scale system. Early approaches based on trial and error were not successful. Prediction of drag reduction on a complex surface moving at high Reynolds number requires generalized turbulence models (e.g., k-ϵ, Reynolds stress) capable of describing non-Newtonian fluids. Of course, the reliability of these models will depend strongly on the assumptions used to model the higher-order terms.

Direct numerical simulation (DNS) has recently emerged as an important tool for analyzing drag reduction in channel flows [3–6], boundary layers [7,8], and homogeneous turbulence [9–11]. The advantage DNS has over laboratory experiments is that it yields information about the polymer orientation and the flow simultaneously, making it easier to understand the mechanism(s) of turbulent drag reduction and how they depend upon the polymer parameters. However, despite the successes of DNS, it is clear that it will not be a useful tool for designing large-scale systems at realistic Reynolds numbers.

In this Letter, we present a systematic closure approximation for the stretching term in the equation for the mean polymer conformation. This term plays an important role in non-Newtonian turbulence by establishing the mean stretch of the polymer due to turbulent fluctuations. The closure is obtained by assuming the velocity gradient in the Lagrangian frame of reference (i.e., frame of reference moving with the polymer molecule) is Gaussian and short correlated. In that limit, the stretching term takes on an analytic form. We compare the result to stochastic simulations of the velocity gradient and find agreement in the limit as the correlation time approaches zero, as would be expected. For finite correlation times, the form of the closure approximation still appears to hold, but the coefficients must be adjusted. From simple fits, we obtain expressions for the coefficients as functions of the correlation time. Furthermore, we make comparisons with DNS of Newtonian turbulence with polymer and obtain optimized coefficients for this case.

We consider a dilute solution of polymers described by the finite extensible nonlinear elastic model with the Peterline closure (FENE-P). Conservation of mass and momentum take the form

$$\boldsymbol{\nabla}\cdot\mathbf{u}=0, \tag{1}$$

$$\frac{D\mathbf{u}}{Dt}\equiv\frac{\partial\mathbf{u}}{\partial t}+\mathbf{u}\cdot\boldsymbol{\nabla}\mathbf{u}=-\frac{1}{\rho}\boldsymbol{\nabla}p+\frac{1}{\rho}\boldsymbol{\nabla}\cdot\mathbf{T}^{[s]}+\frac{1}{\rho}\boldsymbol{\nabla}\cdot\mathbf{T}^{[p]}, \tag{2}$$

where $\mathbf{u}(\mathbf{x},t)$ is the velocity vector, ρ is the constant fluid density, $p(\mathbf{x},t)$ is the local pressure, $\mathbf{T}^{[s]}(\mathbf{x},t)$ is the Newtonian stress due to the solvent, and $\mathbf{T}^{[p]}(\mathbf{x},t)$ is the polymer stress. Note that vectors are designated by bold, lower case letters and rank 2 tensors are designated by bold, upper case letters. The Newtonian and polymer stresses, respectively, are given by $\mathbf{T}^{[s]}=2\mu^{[s]}\mathbf{S}$ and $\mathbf{T}^{[p]}=(1-\beta)\mu[f(r)\mathbf{C}-\mathbf{I}]/\tau_p$, where $\mathbf{S}\equiv\frac{1}{2}(\boldsymbol{\Delta}+\boldsymbol{\Delta}^T)$ is the rate-of-strain tensor, $\boldsymbol{\Delta}\equiv\boldsymbol{\nabla}\mathbf{u}$, $\mu^{[s]}$ is the solvent molecular viscosity, $\beta\equiv\mu^{[s]}/\mu$ is the ratio of the solvent viscosity to the solution viscosity at zero shear, τ_p is the polymer relaxation time, $\mathbf{C}$ is the conformation tensor, $r\equiv\sqrt{\mathrm{Tr}(\mathbf{C})}$ is the end-to-end distance of the polymer chain,

and $f(r) = L^2/(L^2 - r^2)$ is a nonlinear entropic force. Note that the function $f(r)$ diverges as $r \to L$, preventing the polymer from extending beyond L. To complete the model, a transport equation for the conformation tensor $\mathbf{C}$ is required

$$\frac{D\mathbf{C}}{Dt} = \mathbf{C}\cdot\mathbf{\Delta} + \mathbf{\Delta}^T\cdot\mathbf{C} - \frac{1}{\tau_p}[f(r)\mathbf{C} - \mathbf{I}]. \quad (3)$$

If we apply a Reynolds average to Eq. (3), we obtain the following exact equation

$$\frac{\bar{D}\,\bar{\mathbf{C}}}{Dt} - \bar{\mathbf{C}}\cdot\bar{\mathbf{\Delta}} - \bar{\mathbf{\Delta}}^T\cdot\bar{\mathbf{C}} = \underbrace{\overline{\mathbf{C}\cdot\mathbf{\Delta}' + \mathbf{\Delta}'^T\cdot\mathbf{C}}}_{\mathbf{\Lambda}/\tau_p} - \frac{1}{\tau_p}\underbrace{\left[\overline{f(r)\mathbf{C}} - \mathbf{I}\right]}_{\boldsymbol{P}}, \quad (4)$$

where the overbar denotes the average over the statistics of the flow and the prime indicates the zero-mean, fluctuating part of the concerned tensor. The terms on the right-hand side of Eq. (4) are not closed. The focus of this Letter is to derive a closed expression for $\mathbf{\Lambda}$, the dimensionless stretching term.

The appropriate reference frame to consider deformation of a dissolved polymer molecule is the Lagrangian frame [12]. Under the assumption that the molecular extension of the polymer chain is small compared to the Kolmogorov length, the velocity increment between the two beads of the chain is given by the local velocity gradient dotted into the separation vector. Hence, polymer dynamics are controlled exclusively by the time history of the velocity gradient in the Lagrangian frame, $\mathbf{\Delta}'(t)$. We adopt the model for $\mathbf{\Delta}'(t)$ introduced by Brunk *et al.* [13]. The gradient is decomposed into the sum of the rate of strain, $\mathbf{S}' \equiv \frac{1}{2}(\mathbf{\Delta}' + \mathbf{\Delta}'^T)$, and rate of rotation, $\mathbf{R}' \equiv \frac{1}{2}\times(\mathbf{\Delta}' - \mathbf{\Delta}'^T)$, tensors that each satisfy a Langevin equation of the form

$$d\mathbf{S}' + \frac{\mathbf{S}'}{\tau_S}dt = \mathbf{A}d\mathbf{W}, \quad (5)$$

$$d\mathbf{R}' + \frac{\mathbf{S}'}{\tau_R}dt = \mathbf{B}d\tilde{\mathbf{W}}, \quad (6)$$

where τ_S and τ_R are the correlation times for the strain and rotation components, respectively, and $\mathbf{W}$ and $\tilde{\mathbf{W}}$ are independent, tensor Wiener processes. The fourth-order, constant matrices $\mathbf{A}$ and $\mathbf{B}$ are defined to satisfy the symmetries of the two tensors, incompressibility, and to be consistent with $\overline{\mathbf{S}'(t):\mathbf{S}'(t)} = \overline{\mathbf{R}'(t):\mathbf{R}'(t)} = \tau_\eta^{-2}$, where $\tau_\eta \equiv (\nu/\epsilon)^{1/2}$ is the Kolmogorov time scale, ϵ is the turbulent energy dissipation rate, and ν is the kinematic viscosity of the solution.

It is useful to introduce the parameters $\Omega \equiv \tau_S/\tau_\eta$ and $a \equiv \tau_R/\tau_S$. From DNS [14] we know that $\Omega \approx 2.3$ and $a \approx 3.1$ [14] at $R_\lambda = 90$, where R_λ is the Reynolds number based on the Taylor microscale. In order to make analytical progress, though, we first consider the limit $\Omega \to 0$ while keeping fixed the ratio a and the Weissenberg number defined in this limit as $\mathrm{We}_\Omega = \tau_p\tau_S/\tau_\eta^2$. This latter condition ensures that the level of polymer stretching remains constant as $\Omega \to 0$. To compute the limit of small Ω, we extend Dekker's perturbation method to tensorial stochastic differential equations [15]. An expansion of $\mathbf{\Lambda}$ in powers of Ω can be derived by exploiting the formula for Gaussian integration by parts, expanding the response function of $\mathbf{C}(t)$ under variations of $\mathbf{\Delta}'(s)$ around the point $t = s$, collecting the terms of the same order in Ω, and resuming the coefficients of these latter as convergent infinite series. The first term in the expansion for $\mathbf{\Lambda}$, corresponding to the white-noise limit, reads (summation over repeated indexes is understood)

$$\Lambda_{ij} = \frac{\tau_p}{2}(M_{ikjl}\bar{C}_{kl} + M_{ikkl}\bar{C}_{jl} + M_{jkil}\bar{C}_{kl} + M_{jkkl}\bar{C}_{il}), \quad (7)$$

where $M_{ijkl} = 2\tau_S S_{ijkl} + 2\tau_R R_{ijkl}$ and the fourth-order matrices S_{ijkl} and R_{ijkl} are defined such that: $\overline{S'_{ij}(s)S'_{kl}(s+t)} = S_{ijkl}\exp(-t/\tau_S)$ and $\overline{R'_{ij}(s)R'_{kl}(s+t)} = R_{ijkl}\exp(-t/\tau_R)$. Equation (7) holds for a general stationary, Gaussian velocity gradient. If we now impose isotropy on the model, the above expression simplifies to

$$\mathbf{\Lambda} = \alpha_1\mathrm{We}_\Omega\,\mathrm{Tr}(\bar{\mathbf{C}})\mathbf{I} + \beta_1\mathrm{We}_\Omega\bar{\mathbf{C}}, \quad (8)$$

where $\alpha_1 = (3 + 5a)/30$ and $\beta_1 = (11 - 15a)/30$. Note that when $\tau_R = \tau_S$ (i.e., $a = 1$), Eq. (8) reduces to the expression derived in Ref. [16]. However, with this restriction, the model does not capture some key aspects of the phenomenology. For example, when $a = 1$, $\Lambda_{11} > 0$ for all We_Ω, which is not consistent with DNS [11]. The discrepancy arises from the fact that the rate-of-strain and rate-of-rotation tensors have distinct correlation times in the Lagrangian frame of reference. Equation (8) is also similar to the expression derived in Ref. [17], although we do not predict an explicit dependence of $\mathbf{\Lambda}$ on the kinetic energy. Comparisons with DNS (not shown) do not support the inclusion of this term.

The second-order expression for $\mathbf{\Lambda}$ is given by

$$\begin{aligned}\mathbf{\Lambda} = {} & \alpha_2\mathrm{We}_\Omega\,\mathrm{Tr}(\bar{\mathbf{C}})\mathbf{I} + \beta_2\mathrm{We}_\Omega\bar{\mathbf{C}} \\ & - \gamma\mathrm{We}_\Omega\tau_\eta[2(\bar{\mathbf{C}}:\bar{\mathbf{S}})\mathbf{I} - \mathrm{Tr}(\bar{\mathbf{C}})\bar{\mathbf{S}} - \bar{\mathbf{\Delta}}^T\cdot\bar{\mathbf{C}} - \bar{\mathbf{C}}\cdot\bar{\mathbf{\Delta}}] \\ & + \delta\mathrm{We}_\Omega\tau_\eta(\bar{\mathbf{C}}\cdot\bar{\mathbf{\Delta}}^T + \bar{\mathbf{\Delta}}\cdot\bar{\mathbf{C}}) \\ & - \phi\mathbf{I} - \chi\overline{[3\mathbf{C}\cdot\mathbf{C} - \mathrm{Tr}(\mathbf{C})\mathbf{C}]f'(r)}, \end{aligned} \quad (9)$$

where

$$\alpha_2 = \alpha_1 - \Omega^2\frac{243 - a[25a(a-3)(a+4) - 723]}{3600(a+1)},$$

$$\beta_2 = \beta_1 - \Omega^2\frac{a[25a(a-3)(a+4) - 83] - 3}{1200(a+1)},$$

$$\gamma = \Omega(3 + 5a^2)/60, \qquad \delta = \Omega(12 - 10a^2)/60,$$

$$\phi = 2\Omega^2/3, \qquad \chi = 2\Omega^2/15,$$

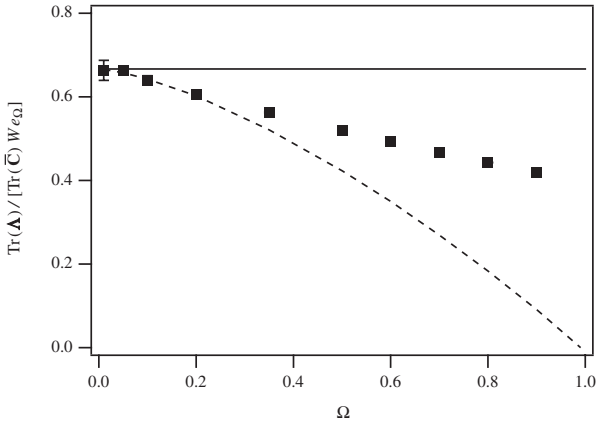

FIG. 1. Plot of $\mathrm{Tr}\,(\mathbf{\Lambda})/[\mathrm{Tr}\,(\bar{\mathbf{C}})\mathrm{We}_\Omega]$ vs Ω at fixed $\mathrm{We}_\Omega = 10$. Straight horizontal line is white-noise prediction: $3\alpha_1 + \beta_1 = 2/3$, and the dashed line corresponds to Eq. (9). Symbols are Brownian dynamics simulations; error bars indicate 1 standard deviation, except where they are smaller than the symbol.

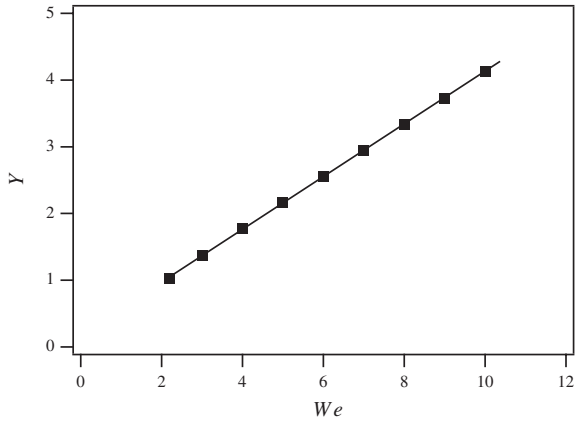

FIG. 2. Plot of $Y \equiv \mathrm{Tr}\,(\mathbf{\Lambda})/[\mathrm{Tr}\,(\bar{\mathbf{C}})]$ vs We from direct numerical simulations. The solid line is a fit through the data ($Y = 0.1822 + 0.3952\mathrm{We}$).

and $f'(r) \equiv df/dr$. Even though Eq. (9) is closed only for the Oldroyd-B model [i.e., $f(r) = 1$], it suggests the form of the terms that arise from the finite correlation time for strain and rotation, including terms that involve all available combinations of $\bar{\mathbf{C}}$ and $\bar{\mathbf{\Delta}}$ with proper symmetry.

We first compare the model predictions to stochastic simulations with $\bar{\mathbf{\Delta}} = 0$. Numerical simulations of Eqs. (5) and (6) were repeated to create an ensemble of trajectories that were used to obtain average polymer properties. Figure 1 shows a normalized plot of the trace of $\mathbf{\Lambda}$ as a function of Ω. The horizontal line at $3\alpha_1 + \beta_1 = 2/3$ corresponds to the white-noise prediction (8). Notice the simulations agree well with the theory in the limit $\Omega \to 0$. The prediction of the second-order theory is accurate for $\Omega < 0.2$; however, at larger values of Ω, it diverges from the simulations. This is most likely due to the truncation of the perturbation expansion. Given the complexity of the series, it is not practical to extend the expansion to higher order.

An alternative approach is to use the form given by Eq. (8), but tune the coefficients to match DNS. The adjusted coefficients will account for higher-order and nonclosed terms in the Ω expansion for $\mathbf{\Lambda}$. We performed decaying isotropic DNS of Eqs. (1)–(3) using the algorithm described in Ref. [18] with $L^2 = 3000$ and initial Weissenberg number $\mathrm{We} \equiv \tau_p/\tau_\eta = 10$ for Cases 1 and 2, and 20 for Case 3. In Navier-Stokes turbulence $\mathrm{We}_\Omega \approx 2.3\mathrm{We}$, where We is the Weissenberg number definition commonly adopted in DNS. The polymer was initially unstretched in Case 1, while Cases 2 and 3 were forced until the polymer equilibrated with the fluid before the decay study was begun. We focus our comparisons on decaying turbulence so as to avoid any unphysical stretching of the polymer by the forcing term. Figure 2 shows $Y \equiv \mathrm{Tr}\,(\mathbf{\Lambda})/[\mathrm{Tr}\,(\bar{\mathbf{C}})]$ for Case 1 that Eq. (8) predicts to be a linear function of We. The behavior is quadratic at low values of We; however, for $\mathrm{We} > 2$, the behavior is very nearly linear. Finite-time correlation effects are expected to be negligible at large We, as polymer relaxation is very slow compared to the decorrelation rate of turbulence. A least squares fit of the linear portion of the curve yields $Y = 0.1822 + 0.3952\mathrm{We}$. Introducing general coefficients into Eq. (8) yields

$$\mathbf{\Lambda} = \tilde{\alpha}_1 \mathrm{We}\,\mathrm{Tr}(\bar{\mathbf{C}})\mathbf{I} + \tilde{\beta}_1 \mathrm{We}\bar{\mathbf{C}}. \tag{10}$$

Figure 3 compares Eq. (10) with $3\tilde{\alpha}_1 + \tilde{\beta}_1 = 0.3952$ (symbols) to the DNS (lines) for the three cases we performed. Overall the model predictions and DNS are in very good agreement.

In summary, we have developed a theoretical expression for the stretching tensor $\mathbf{\Lambda}$ by considering the dynamics of a polymer chain in a stochastic model of the velocity gradient. By considering the limit of small correlation time for the rate-of-strain and rate-of-rotation tensors, it was possible to derive an analytical closure for $\mathbf{\Lambda}$. The result was found to be in excellent agreement with stochas-

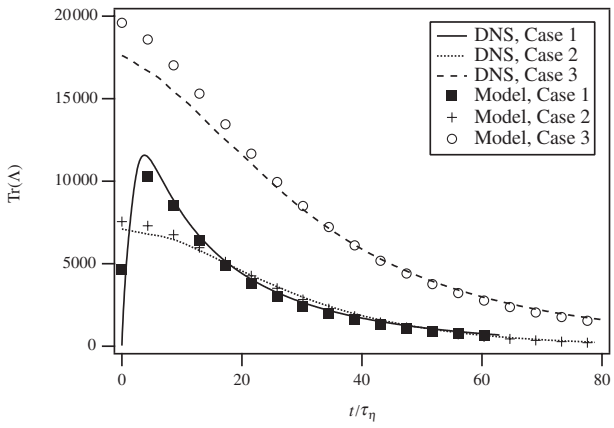

FIG. 3. Plot of $\mathrm{Tr}\,(\mathbf{\Lambda})$ vs t/τ_η, where τ_η is the Kolmogorov time scale. The lines are from direct numerical simulations and the points are Eq. (10) with the tuned coefficients.

tic simulations of the same model in the limit $\Omega \to 0$. However, Navier–Stokes turbulence has a correlation time $\Omega \approx 2.3$. Extending the perturbation expansion to higher order is very difficult. Instead, we were able to modify the white-noise expression to match DNS by adjusting the coefficients. Thus, the analytical work mainly provided the form for $\mathbf{\Lambda}$ and DNS was used to tune the coefficients.

We are extending the model to homogeneous turbulent shear flow. Recent DNS [11,18,19] can be used for comparisons. The second-order theory (9) may suggest the form of the contributions coming from the mean shear. Additionally, we are seeking a closure for the mean restoration term. In this case, knowledge of the distribution of polymer stretch [20] can be used to obtain an approximate closure.

This work has been executed under the auspices of the International Collaboration for Turbulence Research (ICTR). D .V. gratefully acknowledges fruitful discussions with A. Celani. We acknowledge financial support from the National Science Foundation (NSF) Grant No. PHY-0216406. Partial support for S. J. and L. R. C. was obtained from the Defense Advanced Research Projects Agency (DARPA) through the Friction Drag Reduction program under Contract No. MDA972-01-C-0032 and the American Chemical Society (ACS) Petroleum Research Fund Grant No. 36392-AC9.

*Author to whom correspondence should be addressed. Email address: LC246@cornell.edu

[1] B. A. Toms, *Proceedings of the 1st International Congress on Rheology* (North-Holland, Amsterdam, 1949), Vol. 2, pp. 135–141.
[2] http://www.alyeska-pipe.com/default.asp.
[3] R. Sureshkumar, A. N. Beris, and R. A. Handler, Phys. Fluids **9**, 743 (1997).
[4] T. Min, J. Y. Yoo, H. Choi, and D. D. Joseph, J. Fluid Mech. **486**, 213 (2003).
[5] P. K. Ptasinski, B. J. Boersma, F. T. M. Nieuwstadt, M. A. Hulsen, B. H. A. A. Van den Brule, and J. C. R. Hunt, J. Fluid Mech. **490**, 251 (2003).
[6] Y. Dubief, C. M. White, V. E. Terrapon, E. S. G. Shaqfeh, P. Moin, and S. K. Lele, J. Fluid Mech. **514**, 271 (2004).
[7] C. D. Dimitropoulos, Y. Dubief, E. S. G. Shaqfeh, P. Moin, and S. K. Lele, Phys. Fluids **17**, 011705 (2005).
[8] J. S. Paschkewitz, C. D. Dimitropoulos, Y. X. Hou, V. S. R. Somandepalli, M. G. Mungal, E. S. G. Shaqfeh, and P. Moin, Phys. Fluids **17**, 085101 (2005).
[9] T. Vaithianathan and L. R. Collins, J. Comput. Phys. **187**, 1 (2003).
[10] E. De Angelis, C. M. Casciola, R. Benzi, and R. Piva, J. Fluid Mech. **531**, 1 (2005).
[11] A. Robert, T. Vaithianathan, L. R. Collins, and J. G. Brasseur, J. Fluid Mech. (to be published).
[12] V. E. Terrapon, Y. Dubief, P. Moin, E. S. G. Shaqfeh, and S. K. Lele, J. Fluid Mech. **504**, 61 (2004).
[13] B. K. Brunk, D. L. Koch, and L. W. Lion, Phys. Fluids **9**, 2670 (1997).
[14] S. S. Girimaji and S. B. Pope, Phys. Fluids A **2**, 242 (1990).
[15] H. Dekker, Phys. Lett. **90A**, 26 (1982).
[16] V. S. L'vov, A. Pomyalov, I. Procaccia, and V. Tiberkevich, Phys. Rev. E **71**, 016305 (2005).
[17] R. Leighton, D. T. Walker, T. Stephens, and G. Garwood, in *Proceedings of the 4th ASME/JSME Joint Fluid Engineering Conference FEDSM, Honolulu, Hawaii, July 2003* (ASME, New York, 2003), Article 45655, pp. 735—743.
[18] T. Vaithianathan, A. Robert, J. G. Brasseur, and L. R. Collins, J. Non-Newtonian Fluid Mech. **140**, 3 (2006).
[19] T. Vaithianathan, A. Robert, J. G. Brasseur, and L. R. Collins, J. Fluid Mech. (to be published).
[20] M. Martins Afonso and D. Vincenzi, J. Fluid Mech. **540**, 99 (2005).

J. Fluid Mech. (2011), *vol.* 670, *pp.* 326–336. © Cambridge University Press 2011
doi:10.1017/S0022112010006385

Deformation of a flexible polymer in a random flow with long correlation time

STEFANO MUSACCHIO AND DARIO VINCENZI†

CNRS UMR 6621, Laboratoire J.-A. Dieudonné, Université de Nice Sophia Antipolis, Parc Valrose, 06108 Nice, France

(Received 27 October 2010; revised 26 November 2010; accepted 9 December 2010; first published online 7 February 2011)

The effects induced by long temporal correlations of the velocity gradients on the dynamics of a flexible polymer are investigated by means of theoretical and numerical analysis of the Hookean and finitely extensible nonlinear elastic (FENE) dumbbell models in a random renewing flow. For Hookean dumbbells, we show that long temporal correlations strongly suppress the Weissenberg-number dependence of the power-law tail characterising the probability density function (PDF) of the elongation. For the FENE model, the PDF becomes bimodal, and the coil–stretch transition occurs through the simultaneous drop and rise of the two peaks associated with the coiled and stretched configurations, respectively.

Key words: polymers

1. Introduction

The dynamics of a flexible polymer in a moving fluid depends strongly on the properties of the velocity gradients. A remarkable example is given by the coil–stretch transition in a planar extensional flow $\boldsymbol{v} = (\epsilon x, -\epsilon y)$ (de Gennes 1974; Perkins, Smith & Chu 1997). This flow is characterised by a direction of pure compression and a direction of pure stretching with constant strain rate ϵ. The elongation of the polymer is controlled by the Weissenberg number $Wi = \epsilon\tau_p$, where τ_p is the longest relaxation time of the polymer. The value $Wi = 1/2$ marks the coil–stretch transition: for $Wi < 1/2$, the polymer remains coiled under the action of the entropic elastic force, whereas for $Wi > 1/2$ the drag force exerted by the flow overcomes the entropic force and the polymer unravels almost completely. As a consequence, the probability density of the extension, $p(R)$, has a single pronounced peak, whose position depends on Wi. For $Wi < 1/2$, the peak is in the neighbourhood of the equilibrium size of the polymer, R_0; for $Wi > 1/2$, the peak approaches the maximum length R_{max}.

The ability of a (non-uniform) laminar flow to deform an isolated polymer has now been demonstrated for various flow configurations (see, e.g. the reviews by Larson 2005 and Shaqfeh 2005). The corresponding problem for random flows was first studied by Lumley (1972, 1973), who observed that the strain tensor of an incompressible random flow always has a direction of stretching, although such direction fluctuates in time and in space. Lumley further remarked that the vorticity penalises polymer stretching, for it prevents the polymer from remaining aligned with the principal axes of the strain tensor. He then concluded that random flows can

† Email address for correspondence: dario.vincenzi@unice.fr

stretch polymers if the product of the Lagrangian correlation time of the strain tensor and the modulus of the maximum eigenvalue of the deformation tensor exceeds a critical value proportional to τ_p^{-1}. Groisman & Steinberg (2001) confirmed these conclusions by showing evidences of a significant amount of polymer stretching in a low-Reynolds-number random flow generated by viscoelastic instabilities.

In random flows, the time scale describing the stretching of line elements is the reciprocal of the maximum Lyapunov exponent λ. Hence, the appropriate definition of the Weissenberg number is $Wi = \lambda\tau_p$. Balkovsky, Fouxon & Lebedev (2000) and Chertkov (2000) related the deformation of a polymer in a random flow to the statistics of the stretching rate or, more precisely, to the entropy function associated with its probability density function (e.g. Crisanti, Paladin & Vulpiani 1993). Based on this analysis, Balkovsky *et al.* (2000) predicted the existence of the coil–stretch transition for any random flow with positive λ, and proposed the following explanation. For an infinitely extensible polymer ($R_{max} \to \infty$), the stationary probability density function (PDF) of the extension has a power-law tail: $p(R) \propto R^{-1-\alpha}$ for $R \gg R_0$, where α depends on the form of the entropy function. The exponent α is positive for $Wi < 1/2$, it decreases with increasing Wi and becomes negative as Wi exceeds $1/2$. Consequently, $p(R)$ is normalisable only for $Wi < 1/2$, whereas for $Wi \geqslant 1/2$, there is unbounded growth of the extension and the assumption of infinite extensibility becomes inadequate. This abrupt change in the statistics of the extension is interpreted as indicating the coil–stretch transition in random flows. The threshold $Wi = 1/2$ reproduces (to within a numerical factor) Lumley's criterion. (Balkovsky *et al.* (2000) defined the Weissenberg number as $Wi = 2\lambda\tau_p$ so that the coil–stretch transition occurs at $Wi = 1$.)

If the random flow is isotropic and has zero correlation time, $p(R)$ can be written explicitly and the behaviour predicted by Balkovsky *et al.* (2000) can be obtained by direct computation (Chertkov 2000; Thiffeault 2003; Celani, Musacchio & Vincenzi 2005; Martins Afonso & Vincenzi 2005). In this particular case, $\alpha = d(Wi^{-1} - 2)/2$, where d is the spatial dimension of the flow.

A polymer having finite maximum extension ($R_{max} < \infty$) reaches a stationary configuration at any Wi since the entropic force forbids extensions greater than R_{max}. According to the analysis of the infinitely extensible case, $p(R)$ is now expected to display a power-law behaviour $R^{-1-\alpha}$ for $R_0 \ll R \ll R_{max}$. In a short-correlated flow, the coil–stretch transition results from the combination of this power law and the cutoff at $R = R_{max}$: as Wi increases, the intermediate power law rises and the peak of $p(R)$ moves from R_0 to extensions near R_{max} (Martins Afonso & Vincenzi 2005). An important qualitative difference between extensional and random flows must nevertheless be emphasised. In the former case, $p(R)$ has a pronounced peak at an extension near either R_0 or R_{max} depending on whether Wi is less or greater than $1/2$. In the latter case, $p(R)$ has broad tails signalling the coexistence of coiled and stretched configurations with predominance of either configuration according to the value of Wi. In random flows, the coil–stretch transition is not as sharp as in the extensional case because of the random nature of the velocity gradient and the presence of vorticity.

The coil–stretch transition and the relation between the exponent α and the maximum Lyapunov exponent λ were investigated experimentally by Gerashchenko, Chevallard & Steinberg (2005) and Liu & Steinberg (2010). In these experiments, the statistics of the extension was measured by following a fluorescently labelled polymer in a random velocity field generated by elastic turbulence. The PDF of polymer extension was also investigated by means of direct numerical simulations of

the continuum equation for the polymer conformation tensor (Eckhardt, Kronjäger & Schumacher 2002; Boffetta, Celani & Musacchio 2003) and by means of Brownian dynamics simulations for elastic dumbbells (Celani *et al.* 2005; Davoudi & Schumacher 2006; Bagheri *et al.* 2010) or multi-bead chains (Watanabe & Gotoh 2010). The results of the simulations support the picture of polymer dynamics presented above.

The Weissenberg number suffices to determine the elongation of a polymer in laminar flows. By contrast, in random flows, an additional dimensionless number may influence the deformation of the polymer, namely the Kubo number $Ku = \lambda\tau_c$, where τ_c is the Lagrangian correlation time of the velocity gradient. The case $Ku = 0$ has been briefly reviewed above. In this paper, we examine the effect of a non-zero Ku and show that the dynamics at $Ku > 1$ differs significantly from the one predicted for short-correlated flows. To emphasise the basic physical mechanisms, we consider a simplified situation. The polymer molecule is modelled as an elastic dumbbell (Bird *et al.* 1977). This approximation is appropriate when attention is restricted to the extension of the polymer (Watanabe & Gotoh 2010). As for the random advection, we consider a two-dimensional linear renewing flow. In renewing flows, time is split into intervals of length τ_c and the velocities in different intervals are independent and identically distributed (e.g. Childress & Gilbert 1995, p. 320). Linear renewing flows were used by Zel'dovich *et al.* (1984) to study the kinematic dynamo effect; the magnetic field is actually stretched by the velocity gradient in the same way as an infinitely extensible polymer. The use of a linear renewing flow enables us to obtain semi-analytical results and to accurately compute the statistics of polymer extension with moderate numerical effort.

The remainder of the paper is divided as follows. In § 2, we briefly review the elastic dumbbell model. In § 3, we introduce the renewing random flow. The results are presented in § 4. Finally, some conclusions are drawn in § 5.

2. Elastic dumbbell model

An elastic dumbbell is composed of two beads joined by a spring. The beads represent the two ends of the polymer; the spring models the entropic force. For the sake of simplicity, we assume that the flow transporting the dumbbell is two-dimensional.

The vector separating the ends of the polymer, $\boldsymbol{R}$, satisfies the stochastic ordinary differential equation (e.g. Bird *et al.* 1977):

$$\dot{\boldsymbol{R}} = \sigma(t)\boldsymbol{R} - \frac{1}{2\tau_p} f(R)\boldsymbol{R} + \sqrt{\frac{R_0^2}{\tau_p}}\,\boldsymbol{\xi}(t), \tag{2.1}$$

where $R = |\boldsymbol{R}|$ and $\boldsymbol{\xi}(t)$ is white noise, i.e. a Gaussian process with zero mean and two-time correlation $\langle \xi_i(t)\xi_j(t')\rangle = \delta_{ij}\delta(t - t')$. The three terms on the right-hand-side of (2.1) result from the drag force, the entropic elastic force and thermal noise, respectively. The 2×2 matrix $\sigma(t)$ is the velocity gradient evaluated along the trajectory of the centre of mass of the dumbbell: $\sigma_{ij}(t) = \partial_j v_i(t)$. The function $f(R)$ is identically equal to 1 for an infinitely extensible polymer (Hookean model) and has the form $f(R) = 1/(1 - R^2/R_{max}^2)$ for a finitely extensible polymer with nonlinear elasticity (FENE model). In the former case, $\boldsymbol{R}$ is defined on $\mathbb{R}^2$; in the latter case, $\boldsymbol{R}$ belongs to $[0, R_{max}) \times [0, R_{max})$.

Equation (2.1) holds under some assumptions on the dynamics of the beads. The velocity field is assumed to be linear at the size of the dumbbell. The drag on a bead is given by the Stokes law. Furthermore, hydrodynamic interactions between the beads and inertial effects are disregarded.

3. Linear renewing flow

According to the assumptions of the dumbbell model, in the reference frame of the centre of mass of the polymer, the velocity field is of the form: $v_i(\boldsymbol{r}, t) = \sigma_{ij}(t) r_j$. The velocity gradient $\sigma(t)$ is constant in each of the time intervals $I_n = [n\tau_c, (n+1)\tau_c)$, $n \in \mathbb{N}$. We denote by σ_n the (random) value taken by $\sigma(t)$ in I_n: $\sigma(t) = \sigma_n$ for all $t \in I_n$. The random matrices σ_n are identically distributed and statistically independent. We assume that, for a fixed n, σ_n is Gaussian, zero mean, statistically isotropic and traceless (so that the velocity field is incompressible). As a result, $\sigma(t)$ takes the form:

$$\sigma(t) = \frac{S}{2}\begin{pmatrix} \zeta_1(t) & \zeta_2(t) \\ \zeta_2(t) & -\zeta_1(t) \end{pmatrix} + \frac{\Omega}{\sqrt{2}}\begin{pmatrix} 0 & \zeta_3(t) \\ -\zeta_3(t) & 0 \end{pmatrix} \tag{3.1}$$

with S and Ω being positive constants. The elements $\zeta_i(t)$ satisfy: $\zeta_i(t) = \zeta_{i,n}$ for all $t \in I_n$, where the $\zeta_{i,n}$ are Gaussian random variables such that $\langle \zeta_{i,n} \rangle = 0$ for all i and n and $\langle \zeta_{i,n} \zeta_{j,m} \rangle = \delta_{ij}\delta_{nm}$ for all $i, j = 1, 2, 3$ and $n, m \in \mathbb{N}$. The mean-squared strain and rotation rates are S^2 and Ω^2, respectively. We set $\Omega = S$ to reproduce the relation holding for the solution of the Navier–Stokes equation (e.g. Frisch 1995, p. 20).

Strictly speaking, the flow considered is not statistically stationary in time. Nevertheless, over time ranges longer than τ_c, it can be considered as a good approximation to a stationary flow with correlation time τ_c owing to the invariance with respect to the transformation $t \to t + \tau_c$ and thanks to the independence of the matrices $\sigma(t)$ in different time intervals I_n (Zel'dovich *et al.* 1984). The δ-correlated flow (i.e. white-in-time noise) is recovered by letting τ_c tend to zero while holding $S^2\tau_c$ constant.

As mentioned in the Introduction, the elongation of a polymer is related to the statistics of the stretching rate of the flow. For a review on the entropy function and the generalised Lyapunov exponents in statistical physics, we refer the reader to the book by Crisanti *et al.* (1993). Here, we briefly recall some basic elements of the theory. If $\boldsymbol{\ell}(t)$ denotes a fluid-line element, the stretching rate at time t is defined as $\gamma(t) = t^{-1} \ln[\ell(t)/\ell(0)]$. The maximum Lyapunov exponent is the long-time limit of the average stretching rate: $\lambda = \lim_{t\to\infty} \langle \gamma(t) \rangle$, where the average is taken over the realisations of $\sigma(t)$. The PDF of γ for long t takes the large-deviation form (Crisanti *et al.* 1993):

$$P(\gamma, t) \propto \mathrm{e}^{-G(\gamma)t}, \tag{3.2}$$

where $G(\gamma)$ is the entropy function. $G(\gamma)$ is non-negative and attains its minimum value at the point λ. Equivalently, the stretching properties of the flow can be characterised by the generalised Lyapunov exponents, defined as the rate of growth of the moments of $\ell(t)$:

$$L(q) = \lim_{t\to\infty} \frac{1}{t} \ln \left\langle \left(\frac{\ell(t)}{\ell(0)} \right)^q \right\rangle. \tag{3.3}$$

The function $L(q)$ is the Legendre transform of $G(\gamma)$, $L(q) = \max_\gamma [\gamma q - G(\gamma)]$, and satisfies $L'(0) = \lambda$. For small q, $L(q)$ can be obtained by using the quadratic approximation $G(\gamma) \approx (\gamma - \lambda)^2/(2\Delta)$ so that $L(q) \approx \lambda q + \Delta q^2/2$.

For the linear renewing flow, we can compute $L(q)$ by adapting to the present problem the method described by Gilbert & Bayly (1992) (see also Childress & Gilbert 1995, pp. 322–326). A line element satisfies the equation:

$$\dot{\boldsymbol{\ell}}(t) = \sigma(t)\boldsymbol{\ell}(t). \tag{3.4}$$

Since $\sigma(t)$ is constant in I_n, the solution of (3.4) for $t \in I_n$ is: $\boldsymbol{\ell}(t) = \mathrm{e}^{\sigma_n t}\boldsymbol{\ell}(n\tau_c)$. Hence

$$\boldsymbol{\ell}((n+1)\tau_c) = J_n\boldsymbol{\ell}(n\tau_c), \tag{3.5}$$

where $J_n = \mathrm{e}^{\sigma_n\tau_c}$ is written

$$J_n = \frac{1}{2\omega_n}\begin{pmatrix} 2\omega_n c_n^+ + S\zeta_{1,n}c_n^- & (S\zeta_{2,n} + \sqrt{2}\Omega\zeta_{3,n})c_n^- \\ (S\zeta_{2,n} - \sqrt{2}\Omega\zeta_{3,n})c_n^- & 2\omega_n c_n^+ - S\zeta_{1,n}c_n^- \end{pmatrix} \tag{3.6}$$

with $\omega_n = \frac{1}{2}\sqrt{S^2(\zeta_{1,n}^2 + \zeta_{2,n}^2) - 2\Omega^2\zeta_{3,n}^2}$, $c_n^+ = (\mathrm{e}^{\omega_n\tau_c} + \mathrm{e}^{-\omega_n\tau_c})/2$, and $c_n^- = (\mathrm{e}^{\omega_n\tau_c} - \mathrm{e}^{-\omega_n\tau_c})/2$ (we remind the reader that $\zeta_{i,n}$ is the constant value taken by the random function $\zeta_i(t)$ in I_n). If ω_n is real, then J_n can be written in terms of hyperbolic functions; for a non-real complex ω_n, J_n involves trigonometric functions. By using the statistical isotropy of the flow and the fact that the matrices σ_n are identically distributed and independent for different n, it is possible to show the following relation (Gilbert & Bayly 1992; Childress & Gilbert 1995):

$$\frac{\langle \ell^q((n+1)\tau_c)\rangle}{\langle \ell^q(n\tau_c)\rangle} = \langle |J_n\boldsymbol{e}|^q\rangle_{I_n}, \tag{3.7}$$

where $\boldsymbol{e}$ is any constant unit vector and the average $\langle\cdot\rangle_{I_n}$ is taken over the statistics of the gradient in the interval I_n only. Iterating (3.7) yields: $\langle \ell^q(n\tau)\rangle = \langle\rho^q\rangle_{I_n}^n \ell^q(0)$ with $\rho^2 \equiv |J_n\boldsymbol{e}|^2 = \boldsymbol{e}^{\mathrm{T}}J_n^{\mathrm{T}}J_n\boldsymbol{e}$. It follows that $L(q)$ and λ can be written as

$$L(q) = \tau_c^{-1}\,\ln\langle\rho^q\rangle_{I_n} \qquad \text{and} \qquad \lambda = \tau_c^{-1}\,\langle\ln\rho\rangle_{I_n}. \tag{3.8}$$

Given that the σ_n are identically distributed, the average can be taken over any interval I_n. Equations (3.8) provide a simple way to compute the function $L(q)$ and the Lyapunov exponent. The behaviour of λ as a function of τ_c is reported in figure 1. The following asymptotic behaviours hold (Chertkov *et al.* 1996):

$$\lambda \sim \frac{S^2\tau_c}{4} \quad (\tau_c \to 0) \qquad \text{and} \qquad \lambda \sim \mathrm{Re}\langle\omega_n\rangle_{I_n} = \sqrt{\frac{\pi}{2}}\,\frac{S}{2}\sqrt{\frac{S^2}{S^2+2\Omega^2}} \quad (\tau_c \to \infty). \tag{3.9}$$

For $\Omega = S$, one obtains $\lambda \sim \sqrt{\pi/6}\,S/2$ as $\tau_c \to \infty$. Thus, the Lyapunov exponent becomes independent of τ_c for large τ_c, and the convergence to the asymptotic value is exponential. By contrast, the variance Δ monotonically increases like $\Delta \sim S^2\tau_c/4$ both for small and large τ_c (Chertkov *et al.* 1996), and therefore the generalised Lyapunov exponents do not saturate to a constant value (figure 1). We stress the fact that the above asymptotic behaviours hold for any two-dimensional random flow that is incompressible and statistically isotropic and not only for the renewing flow.

4. Statistics of polymer extension

In order to investigate the influence of temporal correlations of the velocity gradients on the dynamics of polymers, we numerically integrated (2.1) for the elastic dumbbell model, where the velocity gradients were determined by (3.1). We computed the

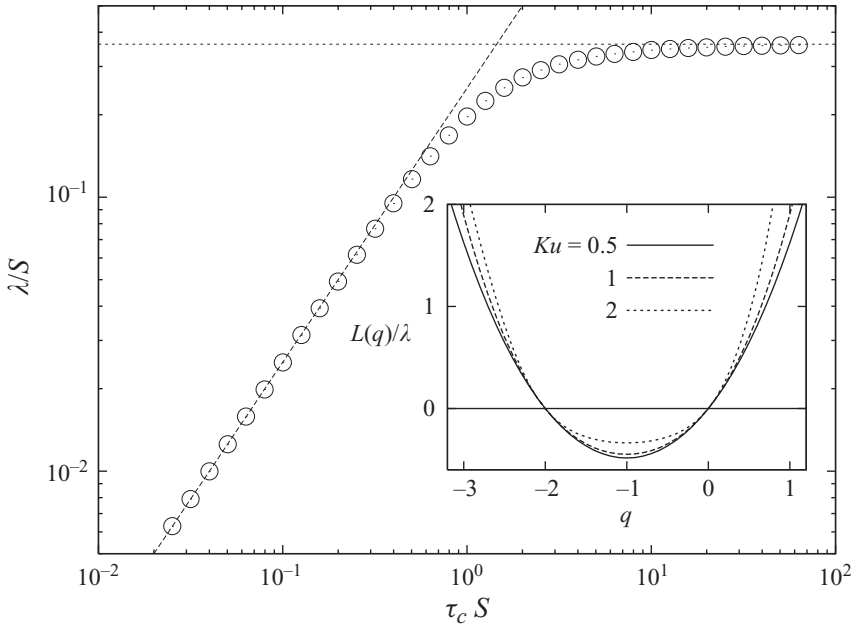

FIGURE 1. Lyapunov exponent as a function of τ_c (circles). Dashed and dotted lines represent the asymptotic behaviours (3.9) for $\tau_c \to 0$ and $\tau_c \to \infty$, respectively. Inset, generalised Lyapunov exponents $L(q)$ for three values of Ku. Note that $L(-d) = L(0) = 0$ in agreement with the properties of the generalised Lyapunov exponents proved by Zel'dovich *et al.* (1984).

PDF of the polymer elongation R for various values of Ku and Wi. The numerical integration has been performed using the predictor–corrector scheme proposed by Öttinger (1996) for the FENE model and the stochastic Runge–Kutta algorithm introduced by Honeycutt (1992) for the Hookean model. The statistics of polymer elongation has been computed by following the dynamics of a single dumbbell for 10^7 time intervals I_n.

Within the Hookean model, the PDF of the extension behaves like $p(R) \propto R^{-1-\alpha}$ for $R \gg R_0$ (Balkovsky *et al.* 2000). The coil–stretch transition is identified by the change of sign of α, which occurs at $Wi = 1/2$. The effects of the temporal correlation of the velocity gradients can be quantified through the dependence of α on the Kubo number. The numerical simulations of the Hookean model show that for small values of Ku the tail of $p(R)$ is almost independent of Ku; conversely, for $Ku \gtrsim 1$, the tail rises as Ku increases and approaches the slope -1 (figure 2). Because of long temporal correlations, even polymers with a short relaxation time occasionally experience significant stretching events, and this effect produces a power-law tail close to the coil–stretch transition also for small values of Wi.

This intuitive idea can be rationalised by the following argument. The exponent α determines the lowest order such that $\langle R^\alpha \rangle$ diverges and satisfies $\alpha = 2\tau_p L(\alpha)$ (Boffetta *et al.* 2003). For Wi near $1/2$, α is not far from zero and it is appropriate to use the quadratic approximation for $L(q)$. $\alpha = 2\tau_p L(\alpha)$ then yields (Balkovsky *et al.* 2000):

$$\alpha = \frac{\lambda}{\Delta}\left(\frac{1}{Wi} - 2\right). \tag{4.1}$$

While the dependence of α on the Weissenberg number is contained entirely in the second factor, the Kubo number enters the expression for α through the ratio λ/Δ.

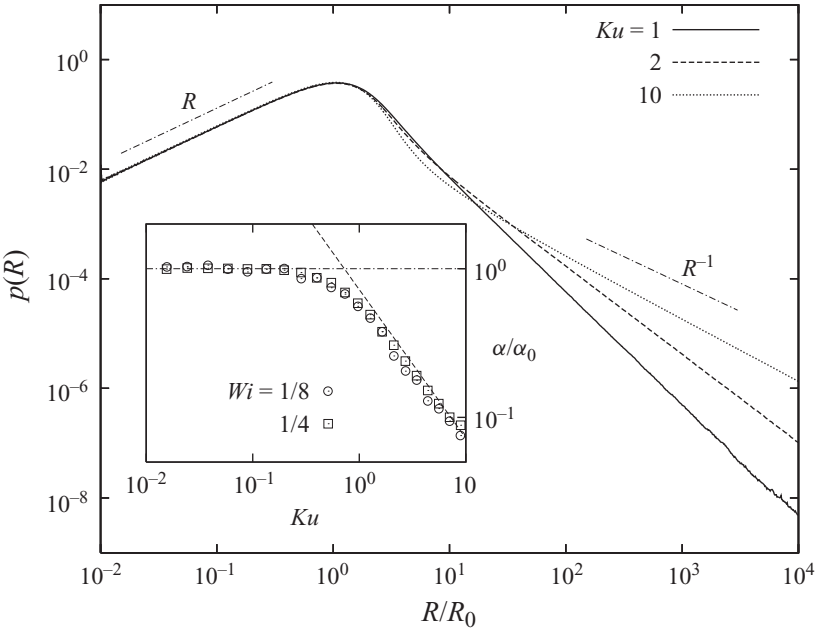

FIGURE 2. PDFs of polymer elongation, $p(R)$, for the Hookean model at $Wi = 1/4$. Note the power-law behaviours $p(R) \propto R^{d-1}$ for $R \ll R_0$ and $p(R) \propto R^{-1-\alpha}$ for $R \gg R_0$. Inset, exponent α as a function of Ku. Here $\alpha_0 = \lim_{Ku \to 0} \alpha$. Dash-dotted and dashed lines are the asymptotic behaviours (4.1) and (4.2) for $Ku \to 0$ and $Ku \to \infty$, respectively.

For the linear renewing flow, the asymptotic behaviours discussed in § 3 give:

$$\lambda/\Delta \sim 1 \quad (Ku \to 0) \qquad \text{and} \qquad \lambda/\Delta = O(Ku^{-1}) \quad (Ku \to \infty). \tag{4.2}$$

One obtains that for small values of Ku the tail of $p(R)$ is independent of Ku, whereas $\alpha = O(Ku^{-1})$ as Ku is increased, in agreement with our numerical findings.

Although for an infinitely extensible polymer, $p(R)$ is normalisable only for $\alpha > 0$ (equivalently for $Wi > 1/2$), the calculation leading to the power-law behaviour remains formally valid also if $\alpha < 0$ ($Wi > 1/2$). In this case, the stationary PDF of the extension exists only if the nonlinearity of the elastic force is taken into account, and the power-law prediction is expected to hold for intermediate extensions $R_0 \ll R \ll R_{max}$. To allow the development of the intermediate power law, we performed numerical simulations of the FENE model at artificially high R_{max}/R_0. For $Wi < 1/2$, the results agree with those obtained for the Hookean model (figure 3*a*). For $Wi > 1/2$, an increase of Ku produces a decrease of the intermediate slope of $p(R)$, which can be negative even for very large Wi (figure 3*b*). According to (4.2), near $Wi = 1/2$, the range of variation of α as a function of Wi can be made arbitrarily small by increasing Ku, to the extent that the intermediate slope of $p(R)$ becomes almost independent of Wi (figure 4). Our findings show that the picture of a coil–stretch transition associated with the increase of the intermediate slope of $p(R)$ does not hold in a long-correlated flow. At large Ku, the appearance of the stretched state occurs through the drop of the maximum at $R \approx R_0$ and the simultaneous rise of a second maximum near R_{max} (figure 4).

For realistic values of R_{max}/R_0, it is difficult to detect a clean power law at intermediate extensions and the above scenario becomes even more relevant. The numerical simulations of the FENE model for $R_{max}/R_0 = 20$ show that, for short-correlated flows ($Ku \ll 1$), the coil–stretch transition manifests through the gradual widening of $p(R)$ and the displacement of its maximum from values close to R_0

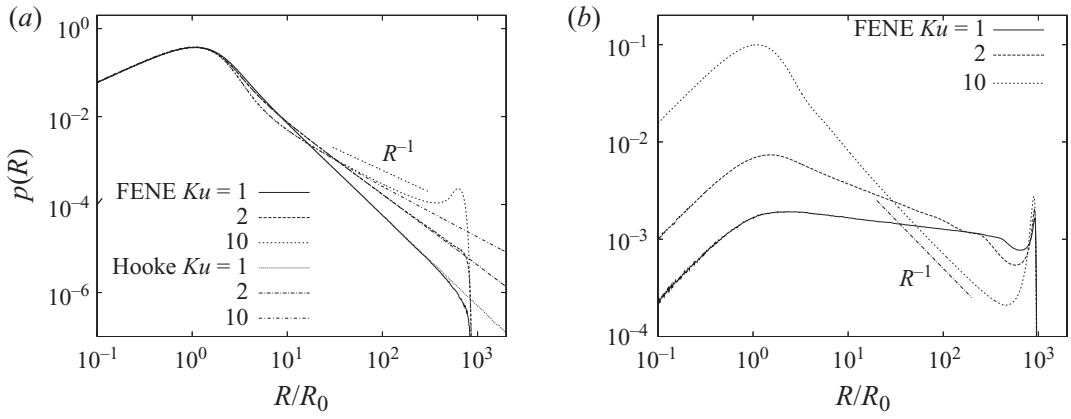

FIGURE 3. PDFs of polymer elongation for the FENE model at various values of Ku for $Wi = 1/4$ (a) and $Wi = 1$ (b). The maximum extension is set to $R_{max} = 10^3 R_0$.

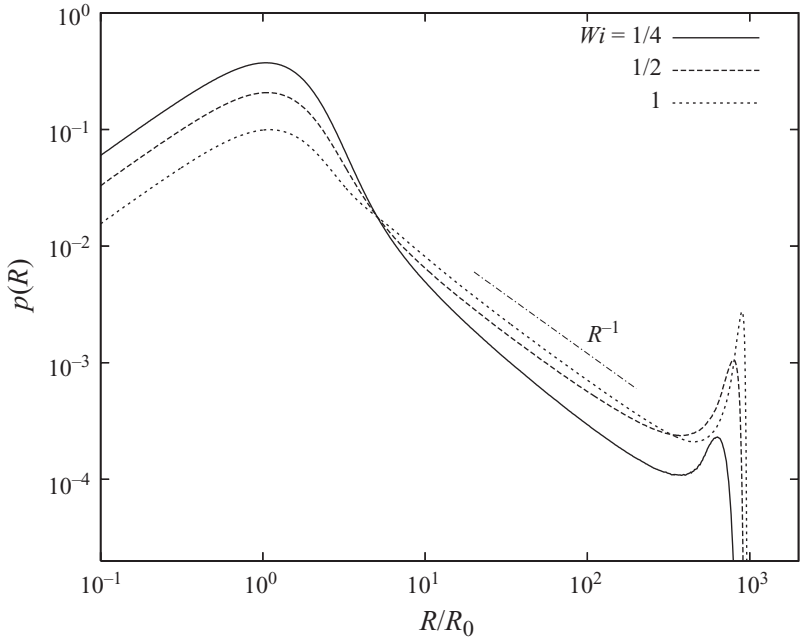

FIGURE 4. PDFs of polymer elongation for the FENE model at various values of Wi in a long-correlated flow ($Ku = 10$). The maximum extension is set to $R_{max} = 10^3 R_0$.

towards values close to R_{max} (see figure 5a). This behaviour is in agreement with the theoretical prediction for the δ-correlated isotropic flow (Martins Afonso & Vincenzi 2005) and with recent experimental measurements of polymer elongation in a random shear flow (Liu & Steinberg 2010). For long-correlated flows ($Ku \gtrsim 1$), the dependence of $p(R)$ on Wi is very different. In this case, increasing Wi at fixed Ku rather produces the drop of the peak at R_0 and the simultaneous formation of a second peak near R_{max} (see figure 5b). The PDF of the extension is bimodal and the two maxima are clearly distinct: intermediate extensions are much less likely than in the small-Ku case.

The shape of $p(R)$ for large Ku can be explained intuitively as follows. If the Lagrangian correlation time of the velocity gradient is long, a typical trajectory of a polymer is composed of long portions where the gradient can be thought of as frozen with a fixed direction of stretching. Some of those portions will be characterised by

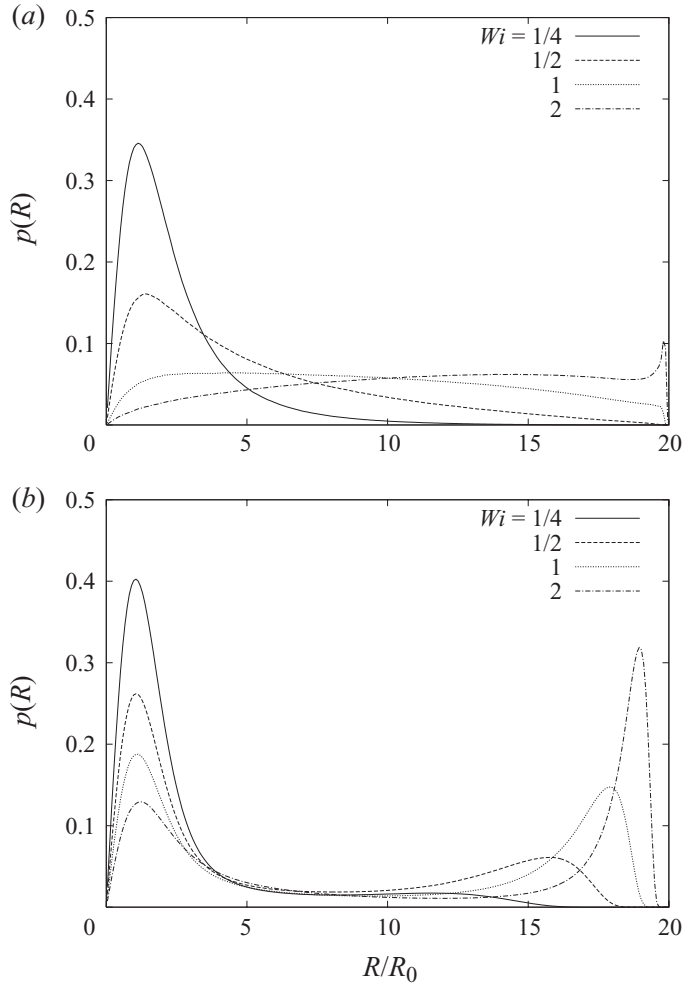

FIGURE 5. PDFs of polymer elongation for the FENE model, at various Wi numbers, in a short-correlated flow ($Ku = 10^{-2}$) (a) and in a long-correlated flow ($Ku = 10$) (b). The maximum extension is set to $R_{max} = 20R_0$.

a weak stretching rate, some by a strong one. The response of the polymer to the velocity gradient along one of those portions of the trajectory will be similar to the response that a polymer would have in an extensional flow with strain rate comparable to the stretching rate. As mentioned earlier, the PDF of R in an extensional flow has a sharp peak either at small extensions or at long extensions depending on the strain rate, and intermediate extensions are very unlikely. Therefore, the evolution of an isolated polymer at large Ku consists of a sequence of long deformation events, whose intensity can produce either a coiled or a highly stretched extension, whence the bimodal shape of $p(R)$.

5. Conclusions

We have studied the influence of long temporal correlations on the dynamics of a Hookean dumbbell and of a FENE dumbbell in a two-dimensional random renewing flow. The time correlation of this simple model flow can be changed arbitrarily, and this property enabled us to obtain semi-analytic predictions for the Kubo-number dependence of the statistics of polymer elongations. It is known that the PDF of the elongation of Hookean dumbbells is characterised by a power-law tail and that

this power law also describes the behaviour of the PDF of FENE dumbbells at intermediate elongations. We have shown that in the long-correlated limit ($Ku \to \infty$), the power-law tail becomes almost insensitive to Wi and its slope is not an effective indicator for the coil–stretch transition. In the case of the FENE model, the long temporal correlations strongly affect the shape of the PDF, which shows two distinct maxima corresponding to the coiled and stretched configurations. For $Ku \gg 1$, we have found a new scenario for the coil–stretch transition, which occurs through the drop of the peak at R_0 and the simultaneous rise of the second peak near R_{max}.

Our findings can be understood in terms of basic properties of long-correlated flows, and the underlying mechanism does not rely on the peculiar choice of the model flow used in our study. It is therefore arguable that the phenomena discussed here could be observed also in realistic flows. In particular, it would be interesting to investigate by means of numerical simulations or experimental measurements whether the presence of long-lived structures in high-Reynolds-number flows could result in the appearance of the two-peak coil–stretch transition scenario depicted here.

We are grateful to A. Celani and P. Perlekar for fruitful discussions.

REFERENCES

Bagheri, F., Mitra, D., Perlekar, P. & Brandt, L. 2010 Statistics of polymer extensions in turbulent channel flow. arXiv:1011.3766v1 [physics.flu-dyn]

Balkovsky, E., Fouxon, A. & Lebedev, V. 2000 Turbulent dynamics of polymer solutions. *Phys. Rev. Lett.* **84**, 4765–4768.

Bird, R. B., Hassager, O., Armstrong, R. C. & Curtiss, C. F. 1977 *Dynamics of Polymeric Liquids*, vol. II. Wiley.

Boffetta, G., Celani, A. & Musacchio, S. 2003 Two-dimensional turbulence of dilute polymer solutions. *Phys. Rev. Lett.* **91**, 034501.

Celani, A., Musacchio, S. & Vincenzi, D. 2005 Polymer transport in random flow. *J. Stat. Phys.* **118**, 531–554.

Chertkov, M. 2000 Polymer stretching by turbulence. *Phys. Rev. Lett.* **84**, 4761–4764.

Chertkov, M., Falkovich, G., Kolokolov, I. & Lebedev, V. 1996 Theory of random advection in two dimensions. *Intl J. Mod. Phys.* B **10**, 2273–2309.

Childress S. & Gilbert A. D. 1995 *Stretch, Twist, Fold: The Fast Dynamo*. Springer.

Crisanti, A., Paladin, G. & Vulpiani, A. 1993 *Products of Random Matrices in Statistical Physics*. Springer.

Davoudi, J. & Schumacher, J. 2006 Stretching of polymers around the Kolmogorov scale in a turbulent shear flow. *Phys. Fluids* **18**, 025103.

Eckhardt, B., Kronjäger, J. & Schumacher, J. 2002 Stretching of polymers in a turbulent environment. *Comput. Phys. Commun.* **147**, 538–543.

Frisch, U. 1995 *Turbulence: The Legacy of A.N. Kolmogorov*. Cambridge University Press.

de Gennes, P. G. 1974 Coil–stretch transition of dilute flexible polymer under ultra-high velocity gradients. *J. Chem. Phys.* **60**, 5030–5042.

Gerashchenko, S., Chevallard, C. & Steinberg, V. 2005 Single polymer dynamics: coil–stretch transition in a random flow. *Europhys. Lett.* **71**, 221–227

Gilbert, A. D. & Bayly B. G. 1992 Magnetic field intermittency and fast dynamo action in random helical flows. *J. Fluid Mech.* **241**, 199–214.

Groisman, A. & Steinberg, V. 2001 Stretching of polymers in a random three-dimensional flow. *Phys. Rev. Lett.* **86**, 934–937.

Honeycutt, R. L. 1992 Stochastic Runge–Kutta algorithms. Part I. White noise. *Phys. Rev.* A **45**, 600–603.

Larson, R. G. 2005 The rheology of dilute solutions of flexible polymers: progress and problems. *J. Rheol.* **49**, 1–70.

Liu, Y. & Steinberg, V. 2010 Stretching of polymer in a random flow: effect of a shear rate. *Europhys. Lett*. **90**, 44005.

Lumley, J. L. 1972 On the solution of equations describing small scale deformation. *Symp. Math.* **9**, 315–334.

Lumley, J. L. 1973 Drag reduction in turbulent flow by polymer additives. *J. Polym. Sci.: Macromol. Rev.* **7**, 263–290.

Martins Afonso, M. & Vincenzi, D. 2005 Nonlinear elastic polymers in random flow. *J. Fluid Mech.* **540**, 99–108.

Öttinger, H. C. 1996 *Stochastic Processes in Polymeric Fluids*. Springer.

Perkins, T. T., Smith, D. E. & Chu, S. 1997 Single polymer dynamics in an elongational flow. *Science* **276**, 2016–2021.

Shaqfeh, E. S. G. 2005 The dynamics of a single-molecule DNA in flow. *J. Non-Newtonian Fluid Mech.* **130**, 1–28.

Thiffeault, J. L. 2003 Finite extension of polymers in turbulent flow. *Phys. Lett*. A **308**, 445–450.

Watanabe, T. & Gotoh, T. 2010 Coil–stretch transition in an ensemble of polymers in isotropic turbulence. *Phys. Rev.* E **81**, 066301.

Zel'dovich, Ya. B., Ruzmaikin, A. A., Molchanov, S. A. & Sokoloff, D. D. 1984 Kinematic dynamo problem in a linear velocity field. *J. Fluid Mech.* **144**, 1–11.

Impact of the Peterlin approximation on polymer dynamics in turbulent flows

Dario Vincenzi,[1] Prasad Perlekar,[2] Luca Biferale,[3] and Federico Toschi[4,5]

[1]*Laboratoire Jean Alexandre Dieudonné, Université Nice Sophia Antipolis, CNRS, UMR 7351, 06100 Nice, France*

[2]*TIFR Center for Interdisciplinary Sciences, Tata Institute of Fundamental Research, Narsingi, Hyderabad 500075, India*

[3]*Department of Physics and INFN, University of Rome "Tor Vergata," Via della Ricerca Scientifica 1, 00133 Roma, Italy*

[4]*Department of Applied Physics, and Department of Mathematics and Computer Science, Eindhoven University of Technology, 5600 MB Eindhoven, The Netherlands*

[5]*IAC, CNR, Via dei Taurini 19, I-00185 Roma, Italy*

(Received 3 June 2015; revised manuscript received 31 August 2015; published 5 November 2015)

We study the impact of the Peterlin approximation on the statistics of the end-to-end separation of polymers in a turbulent flow. The finitely extensible nonlinear elastic (FENE) model and the FENE model with the Peterlin approximation (FENE-P) are numerically integrated along a large number of Lagrangian trajectories resulting from a direct numerical simulation of three-dimensional homogeneous isotropic turbulence. Although the FENE-P model yields results in qualitative agreement with those of the FENE model, quantitative differences emerge. The steady-state probability of large extensions is overestimated by the FENE-P model. The alignment of polymers with the eigenvectors of the rate-of-strain tensor and with the direction of vorticity is weaker when the Peterlin approximation is used. At large Weissenberg numbers, the correlation times of both the extension and of the orientation of polymers are underestimated by the FENE-P model.

DOI: 10.1103/PhysRevE.92.053004 PACS number(s): 47.27.Gs, 47.57.Ng

I. INTRODUCTION

The addition of elastic polymers to a Newtonian solvent introduces a history dependence in the response of the fluid to a deformation and hence modifies the rheological properties of the solvent [1]. In turbulent flows, the non-Newtonian nature of polymer solutions manifests itself through a considerable reduction of the turbulent drag compared to that of the solvent alone [2–6]. What renders this phenomenon even more remarkable is that an appreciable drag reduction can already be observed at very small polymer concentrations (of the order of a few parts per million). Turbulent drag reduction was discovered by Toms [7] more than 60 years ago and is now routinely used to reduce energy losses in crude-oil pipelines [8]. A full understanding of turbulent drag reduction remains nonetheless a difficult challenge, because in the turbulent flow of a polymer solution the dynamics of a large number of polymers is coupled with strongly nonlinear transfers of kinetic energy.

The study of turbulent flows of polymer solutions is essentially based on two approaches: the molecular approach and the continuum one. In the molecular (or Brownian dynamics) approach, a polymer is modeled as a sequence of N beads connected by elastic springs. The deformation of the bead-spring chain is then followed along the trajectory of its center of mass. In homogeneous and isotropic turbulence, Watanabe and Gotoh [9] have shown that $N = 2$ beads are in fact sufficient to describe the stationary statistics of both the extension and the orientation of polymers, i.e., the deformation of a polymeric chain is dominated by its slowest oscillation mode. An analogous conclusion has been reached by Terrapon *et al.* [10] in a study of polymer dynamics in a turbulent channel flow. The model consisting of only $N = 2$ beads is known as the finitely extensible nonlinear elastic (FENE) dumbbell model [1]. The molecular approach is suitable for studying the deformation of passively transported polymers [9–21]. Molecular dynamics has also been employed in combination with standard Eulerian techniques to simulate viscoelastic flows (see the CONNFFESSIT [22,23] and BCF [24] approaches). Peters and Schumacher [25] and Watanabe and Gotoh [26,27] have recently performed two-way coupling simulations of turbulent drag reduction in which the polymer feedback is given by the forces exerted on the fluid by a large number of individual dumbbells.

In practical applications, numerical simulations of turbulent flows of polymer solutions commonly use the continuum approach. The conformation of polymers is then described by means of a space- and time-dependent tensor field, which represents the average inertia tensor of polymers at a given time and position in the fluid. Such a tensor is termed the polymer conformation tensor. An evolution equation for the conformation tensor may be derived in principle from the FENE dumbbell model. Such an equation, however, involves the average over thermal fluctuations of a nonlinear function of the polymer end-to-end vector; a closure approximation is therefore required. Peterlin [28] proposed a mean-field closure according to which the average of the elastic force over thermal fluctuations is replaced by the value of the force at the mean-squared polymer extension. The resulting model was subsequently dubbed the FENE-P model [29]. Within the FENE-P model, the backreaction of polymers on the flow is described by a stress tensor field, which depends on the polymer conformation tensor. This continuum model is thus suitable for simulating turbulent flows of polymer solutions; it indeed amounts to simultaneously solving the evolution equation for the polymer conformation tensor and the Navier-Stokes equation with an additional elastic-stress term. The FENE-P model is widely employed in numerical simulations of turbulent drag reduction and has been successfully applied to channel flows [30–33], shear flows [34,35], and two- and three-dimensional homogeneous and isotropic turbulence [36–39]. Nevertheless, although it qualitatively reproduces the main features of turbulent drag reduction, the FENE-P model

generally does not yield results in quantitative agreement with experimental data (e.g., Ref. [33]). It is therefore essential to assess the validity of the assumptions upon which the model is based.

For laminar flows, the Peterlin approximation has been examined in detail (see Refs. [40,41] and references therein). In particular, the FENE-P model is a good approximation of the FENE model in steady flows, whereas appreciable differences appear in time-dependent flows. This observation suggests that in turbulent flows, important differences between the two models should be expected. Several studies have subsequently investigated the validity of the Peterlin approximation in turbulent flows by comparing one-way coupling simulations of the FENE and FENE-P models [10,12,13,15,19]. These studies have clearly shown potential differences between the FENE and FENE-P models together with high sensitivity on the statistical ensemble and dependency on the degree of homogeneity of the underlying velocity fluctuations. We undertake a systematic analysis of the Peterlin approximation in three-dimensional homogeneous and isotropic turbulence by means of one-way coupling Lagrangian simulations of the FENE and FENE-P models. The size of our statistical ensemble (128×10^3 fluid trajectories and 2×10^3 realizations of thermal noise per trajectory) allows us to fully characterize the statistics of polymer extension and orientation and to investigate certain properties of the polymer conformation tensor that, to the best of our knowledge, had not been studied before. When the flow is turbulent, two independent effects are at the origin of the discrepancies between the FENE and FENE-P models: one is directly related to the closure approximation for the elastic force, while the other is of a statistical nature and is a consequence of deriving the statistics of the end-to-end vector from that of the conformation tensor. By isolating these two effects, we compare the steady-state statistics and the temporal correlation of the extension and of the orientation of polymers in the FENE and FENE-P models.

The rest of the paper is organized as follows. In Sec. II we briefly review the FENE and FENE-P models. The Lagrangian simulations are described in Sec. III. The results of the simulations are presented in Sec. IV. Finally, conclusions are drawn in Sec. V.

II. FENE AND FENE-P MODELS

In the FENE model, a polymer is described as two beads connected by an elastic spring, i.e., as an elastic dumbbell [1]. If the fluid is at rest, the polymer is in a coiled configuration because of entropic forces, and its equilibrium extension is determined by the intensity of thermal fluctuations. If the polymer is introduced in a moving fluid and the velocity field changes over the size of the polymer, then the polymer can stretch and deform. The dynamics of the polymer thus results from the interplay between the stretching action of the velocity gradient and the elastic force, which tends to take the polymer back to its equilibrium configuration.

The maximum extension of the dumbbell is assumed to be smaller than the Kolmogorov scale, so that the velocity field changes linearly in space at the scale of the dumbbell. The drag force on the beads is given by the Stokes law. Moreover, inertial effects and hydrodynamical interactions between the beads are disregarded. Polymer-polymer hydrodynamical interactions are also disregarded under the assumption that the polymer concentration is very low. Thus, the separation vector between the beads, $\boldsymbol{R}(t)$, satisfies the following stochastic ordinary differential equation (the FENE equation) [1,42]:

$$\frac{d\boldsymbol{R}}{dt} = \sigma(t)\boldsymbol{R} - \frac{\phi(R^2)}{2\tau_p}\boldsymbol{R} + \sqrt{\frac{R_0^2}{\tau_p}}\,\boldsymbol{\xi}(t), \tag{1}$$

where $R = |\boldsymbol{R}|$, $\sigma_{ij}(t) = \partial_j u_i(t)$ is the velocity gradient at the position of the center of mass of the dumbbell, $\boldsymbol{\xi}(t)$ is three-dimensional white noise, R_0 is the polymer root-mean-square equilibrium extension, and τ_p is the polymer relaxation time [τ_p is the time scale that describes the exponential relaxation of $\langle R^2(t)\rangle$ to its equilibrium value in the absence of flow]. The three terms on the right-hand side of Eq. (1) represent the stretching by the velocity gradient, the restoring elastic force, and thermal noise, respectively. The function ϕ determines the elastic force, and, in the FENE model, it has the following form:

$$\phi(\zeta) = \frac{1}{1-\zeta/L^2}, \tag{2}$$

where L is the maximum extension of the polymer. The elastic force diverges as R approaches L, hence extensions greater than L are forbidden. Note that $\boldsymbol{R}(t)$ is a random vector and that, when $\boldsymbol{u}$ is turbulent, two independent sources of randomness influence its evolution: thermal noise and the velocity gradient itself.

The polymer conformation tensor is defined as $\mathcal{C}_{ij} \equiv \langle R_i R_j\rangle_\xi$, where $\langle\cdot\rangle_\xi$ denotes an average over thermal fluctuations. To derive the evolution equation for $\mathcal{C}$, we apply the Itô formula to $R_i R_j$ and use Eq. (1):

$$\begin{aligned}\frac{d}{dt}(R_iR_j) &= \frac{dR_i}{dt}R_j + R_i\frac{dR_j}{dt} + \frac{R_0^2}{\tau_p}\delta_{ij}\\ &= \sigma_{ik}(t)R_kR_j + \sigma_{jk}(t)R_kR_i - \frac{1}{\tau_p}\phi(R^2)R_iR_j\\ &\quad + \frac{R_0^2}{\tau_p}\delta_{ij} + \sqrt{\frac{R_0^2}{\tau_p}}[R_j\xi_i(t) + R_i\xi_j(t)].\end{aligned} \tag{3}$$

Whereas there is no Itô-Stratonovich ambiguity for Eq. (1), Eq. (3) should be understood in the Itô sense. We now average Eq. (3) with respect to the realizations of $\boldsymbol{\xi}(t)$ and make use of the following property of the Itô integral: $\langle R_i\xi_j(t)\rangle_\xi = 0$. We thus obtain

$$\begin{aligned}\frac{d}{dt}\langle R_iR_j\rangle_\xi &= \sigma_{ik}(t)\langle R_kR_j\rangle_\xi + \sigma_{jk}(t)\langle R_kR_i\rangle_\xi\\ &\quad - \frac{1}{\tau_p}\big[\langle\phi(R^2)R_iR_j\rangle_\xi - R_0^2\delta_{ij}\big].\end{aligned} \tag{4}$$

Equation (4) is not closed with respect to $\mathcal{C}$ because of the term

$$\mathcal{A}_{ij} \equiv \langle\phi(R^2)R_iR_j\rangle_\xi. \tag{5}$$

To obtain a closed equation, Peterlin [28] proposed the following approximation:

$$\mathcal{A}_{ij} \approx \phi(\langle R^2\rangle_\xi)\langle R_iR_j\rangle_\xi = \phi(\mathrm{tr}\,\mathcal{C})\mathcal{C}_{ij}. \tag{6}$$

In the following, we shall denote

$$\mathcal{T} \equiv \phi(\mathrm{tr}\,\mathcal{C})\mathcal{C}. \tag{7}$$

The resulting evolution equation for the polymer conformation tensor (the FENE-P equation) is

$$\frac{d\mathcal{C}^{\mathrm{P}}}{dt} = \sigma(t)\,\mathcal{C}^{\mathrm{P}} + \mathcal{C}^{\mathrm{P}}\,\sigma^{\mathrm{t}}(t) - \frac{1}{\tau_p}\left[\phi(\mathrm{tr}\,\mathcal{C}^{\mathrm{P}})\mathcal{C}^{\mathrm{P}} - R_0^2\mathcal{I}\right], \tag{8}$$

where $\mathcal{I}$ is the identity matrix and $\mathcal{C}^{\mathrm{P}}$ denotes the polymer conformation tensor calculated according to the Peterlin approximation. If the flow is turbulent, both $\mathcal{C}$ and $\mathcal{C}^{\mathrm{P}}$ have a random behavior. Equation (8) describes the evolution of the conformation tensor of a polymer along the Lagrangian trajectory of its center of mass. Numerical simulations of drag reduction use the Eulerian counterpart of Eq. (8), which is obtained by replacing $d\mathcal{C}^{\mathrm{P}}/dt$ with $\partial_t\mathcal{C}^{\mathrm{P}} + \boldsymbol{u}\cdot\nabla\mathcal{C}^{\mathrm{P}}$ and $\sigma(t)$ with the Eulerian velocity gradient. In principle, the evolution equation for the conformation tensor should be coupled with the Navier-Stokes equations through an additional stress term proportional to $\phi(\mathrm{tr}\,\mathcal{C}^{\mathrm{P}})\mathcal{C}^{\mathrm{P}}$ [1]. Here, however, we focus on the impact of the Peterlin approximation upon the statistics of polymer deformation and consider passive polymers only (one-way coupling). In the rest of the paper, we thus study the relation between Eq. (8) and Eq. (1) when $\sigma(t)$ is given by the incompressible Navier-Stokes equations in the turbulent regime. We expect the Peterlin approximation to be inaccurate when the velocity gradient is much larger than the polymer relaxation time, because in this case the distribution of polymer extensions is broad [43] and hence the factor $\phi(R^2)$ exhibits large fluctuations.

We end this section with some considerations that will be useful to guide our study:

(i) $\boldsymbol{R}(t)$ cannot be calculated from the solution of the FENE-P equation [Eq. (8)]. By contrast, $\mathcal{C}(t)$ can be constructed from the solution of the FENE equation [Eq. (1)] by averaging the dyadic $R_i(t)R_j(t)$ over the realizations of the noise $\boldsymbol{\xi}(t)$. The tensor $\mathcal{C}(t)$ can then be compared with $\mathcal{C}^{\mathrm{P}}(t)$.

(ii) Because of the Peterlin approximation [Eq. (6)], the FENE and FENE-P equations yield a different evolution for the conformation tensor. This holds for both laminar and turbulent flows.

(iii) If the flow is turbulent, the statistics of $\boldsymbol{R}(t)$ differs from that of $\mathcal{C}(t)$, even if $\mathcal{C}(t)$ is calculated from Eq. (1) (and hence no closure approximation is required). Consider, for example, the random variables $R(t)$ and $\rho(t) \equiv \sqrt{\langle R^2(t)\rangle_\xi} = \sqrt{\mathrm{tr}\,\mathcal{C}(t)}$. In general, the probability density function (PDF) of $R(t)$ is different from that of $\rho(t)$, as can be seen from $\langle\langle R^\alpha\rangle_\xi\rangle_\sigma \neq \langle\langle R^2\rangle_\xi^{\frac{\alpha}{2}}\rangle_\sigma$ ($\alpha \neq 2$), where $\langle\cdot\rangle_\sigma$ denotes an average over the statistics of the turbulent velocity gradient.

In conclusion, the FENE and FENE-P models differ for two reasons, namely the Peterlin approximation and the statistical effect due to the fact that the statistics of $\boldsymbol{R}(t)$ cannot be deduced from that of $\mathcal{C}(t)$. Hence, in the turbulent regime, the proper way to examine the Peterlin approximation is to first construct $\mathcal{C}(t)$ from the FENE equation and then compare its statistics with that of the solution of the FENE-P equation. If the statistics of $\boldsymbol{R}(t)$ is directly compared with that of $\mathcal{C}^{\mathrm{P}}(t)$, the error due to the Peterlin approximation is combined with the statistical effect discussed at point (iii) above. This fact seems to have been overlooked in some of the previous studies. We also remark that for the above reasons, our study differs from that presented in Ref. [15]. In that latter study, the statistics of $\boldsymbol{R}$ was indeed compared with that of the end-to-end separation vector of the FENE-P dumbbell model.

III. LAGRANGIAN SIMULATIONS

The dynamics of polymers is studied by using a database of Lagrangian trajectories that was previously generated to examine the dynamics of both tracers and inertial particles in turbulent flows [44,45]. The turbulent velocity field is obtained by direct numerical simulation of the three-dimensional incompressible Navier-Stokes equations:

$$\partial_t\boldsymbol{u} + \boldsymbol{u}\cdot\nabla\boldsymbol{u} = -\nabla p + \nu\nabla^2\boldsymbol{u} + \boldsymbol{f}, \qquad \nabla\cdot\boldsymbol{u} = 0, \tag{9}$$

where p is the pressure field and $\nu = 2\times10^{-3}$ is the kinematic viscosity. The forcing $\boldsymbol{f}$ is such that the spectral content of the first low-wave-number shells remains constant in time. The domain is a three-dimensional periodic box of linear size 2π. Equation (9) are solved by means of a fully dealiased pseudospectral algorithm with second-order Adams-Bashforth time stepping. The number of grid points is 512^3, while the integration time step is $dt = 4\times10^{-4}$. In this simulation, the Kolmogorov time is $\tau_\eta = 4.7\times10^{-2}$ and the Taylor-microscale Reynolds number is $R_\lambda = 185$ (for more details on the numerical simulation, see Refs. [44,45]). We expect our results not to depend significantly on the value of R_λ except for some residual effects induced by intermittency in the statistics of the velocity gradients [46].

As mentioned in Sec. II, the inertia of polymers is negligible. Furthermore, their thermal diffusivity is very small compared to the turbulent diffusivity. Hence the center of mass of a polymer moves like a tracer and its position $\boldsymbol{x}_c(t)$ satisfies the following equation:

$$\frac{d\boldsymbol{x}_c}{dt} = \boldsymbol{u}(\boldsymbol{x}_c(t),t). \tag{10}$$

Equation (10) is once again solved by using a second-order Adams-Bashforth scheme; a trilinear interpolation algorithm is used to determine the value of the velocity field at the position of the polymer [44,45]. After the statistically stationary state is reached for both the fluid motion and the translational dynamics of polymers, the positions of the center of mass of 128×10^3 polymers are recorded every $\Delta t = 10dt = 4\times10^{-3} \approx \tau_\eta/10$. The total integration time after steady state is $T = 13.2$, which corresponds to six eddy turnover times approximately.

The velocity gradient $\sigma(t)$ is recorded every Δt along the trajectory of the center of mass of each polymer and is inserted into Eqs. (1) and (8) in order to determine the dynamics of the separation vector and of the conformation tensor. Equation (1) is solved by using the semi-implicit predictor-corrector method introduced by Öttinger [42]; the integration time step is equal to Δt for all values of the parameters. The initial condition for Eq. (1) is such that $R_i(0) = R_0/\sqrt{3}$, $i = 1,2,3$. Equation (8) for $\mathcal{C}^{\mathrm{P}}$ is integrated by means of the semi-implicit algorithm proposed in Ref. [10], which ensures that $\mathrm{tr}\,\mathcal{C}^{\mathrm{P}} \leq L^2$.

The Weissenberg number is defined as $\mathrm{Wi} \equiv \tau_p/\tau_\eta$ and is the ratio of the time scales associated with the elastic

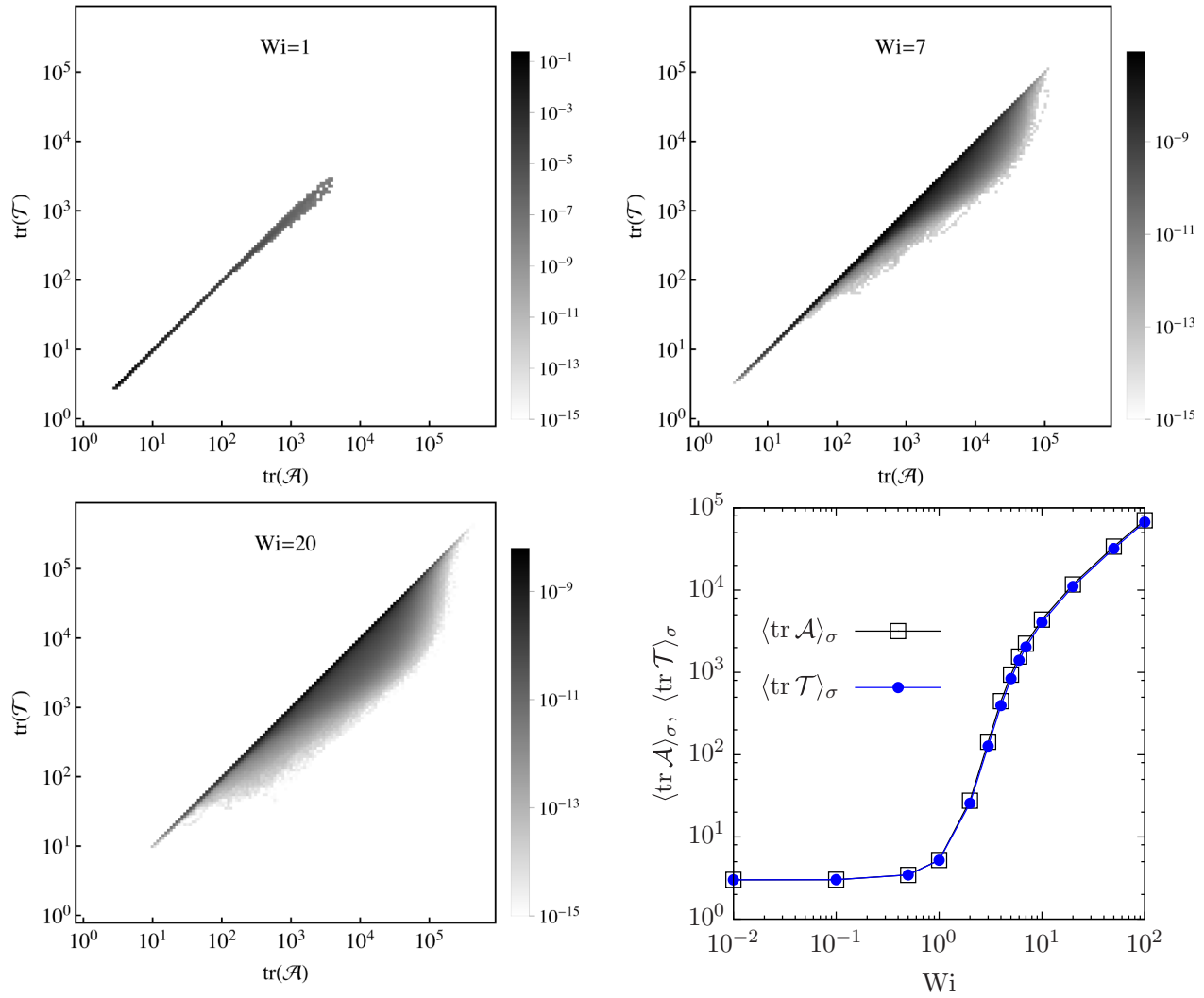

FIG. 1. (Color online) Contour plot of $P_\sigma(\mathrm{tr}\,\mathcal{A}, \mathrm{tr}\,\mathcal{T})$ for Wi = 1 (top left panel), Wi = 7 (top right panel), and Wi = 20 (bottom left panel). The bottom right panel shows the averages of $\mathrm{tr}\,\mathcal{A}$ (black squares) and $\mathrm{tr}\,\mathcal{T}$ (blue circles) as a function of the Weissenberg number.

force and with the velocity gradient. In our simulations, Wi varies between 10^{-2} and 10^2. (An alternative definition of the Weissenberg number uses the maximum Lyapunov exponent of the flow, λ, to estimate the reciprocal of the stretching time associated with the velocity gradient. In our simulations, $\lambda \approx 0.14\tau_\eta^{-1}$ [47]. Thus, the Weissenberg number based on the Lyapunov exponent is $\mathrm{Wi}_\lambda = \lambda\tau_p \approx 0.14\mathrm{Wi}$.) The squares of the equilibrium and maximum extensions of the polymer are $R_0^2 = 1$ and $L^2 = 3 \times 10^3$, as in Refs. [9,19]. The number of realizations of thermal noise per Lagrangian trajectory is 2×10^3.

Finally, the statistics of polymer deformation is collected over the Lagrangian trajectories, over the realizations of thermal noise, and over time [only for times greater than the time required for $\boldsymbol{R}(t)$ to reach the statistically steady state].

We note that the statistics of the separation vector $\boldsymbol{R}$ in isotropic turbulence has been studied thoroughly by Watanabe and Gotoh [9]. The results on the statistics of $\boldsymbol{R}$ given below agree with those presented in Ref. [9]. Here, we compare the statistics of $\mathcal{C}$ with that of $\mathcal{C}^{\mathrm{P}}$ in order to determine the effect of the Peterlin closure on the dynamics of polymers.

IV. RESULTS

In this section, we examine the statistics of polymer extension and orientation in the FENE and FENE-P models. Before presenting the results, it is useful to define some notations. If the statistics of a random variable depends both on thermal noise and on the velocity gradient (such as, for instance, in the case of R), its PDF is denoted as $P_{\xi,\sigma}$. If the statistics of a random variable (e.g., $\mathrm{tr}\,\mathcal{C}$) only depends on the velocity gradient, then its PDF is denoted as P_σ. The autocorrelation function of a scalar random variable $X(t)$ is denoted as $F_X(t)$ and the correlation time of $X(t)$ is $T_X = \int_0^\infty F_X(t)dt$. The autocorrelation function of a statistically isotropic unit random vector $\boldsymbol{X}(t)$ is defined as

$$F_X(t) = 2\langle|\boldsymbol{X}(t+t_0)\cdot\boldsymbol{X}(t_0)|\rangle - 1 \qquad (11)$$

and the associated correlation time is $T_X = \int_0^\infty F_X(t)dt$. We denote by $\hat{\boldsymbol{e}}_i$ $(i = 1,2,3)$ the unit eigenvectors of the rate-of-strain tensor $\mathcal{S} \equiv (\boldsymbol{\nabla u} + \boldsymbol{\nabla u}^{\mathrm{T}})/2$; the eigenvectors $\hat{\boldsymbol{e}}_i$ are ordered by descending eigenvalue, i.e., $\hat{\boldsymbol{e}}_1$ is associated with the largest eigenvalue of $\mathcal{S}$ and $\hat{\boldsymbol{e}}_3$ with the smallest one. The

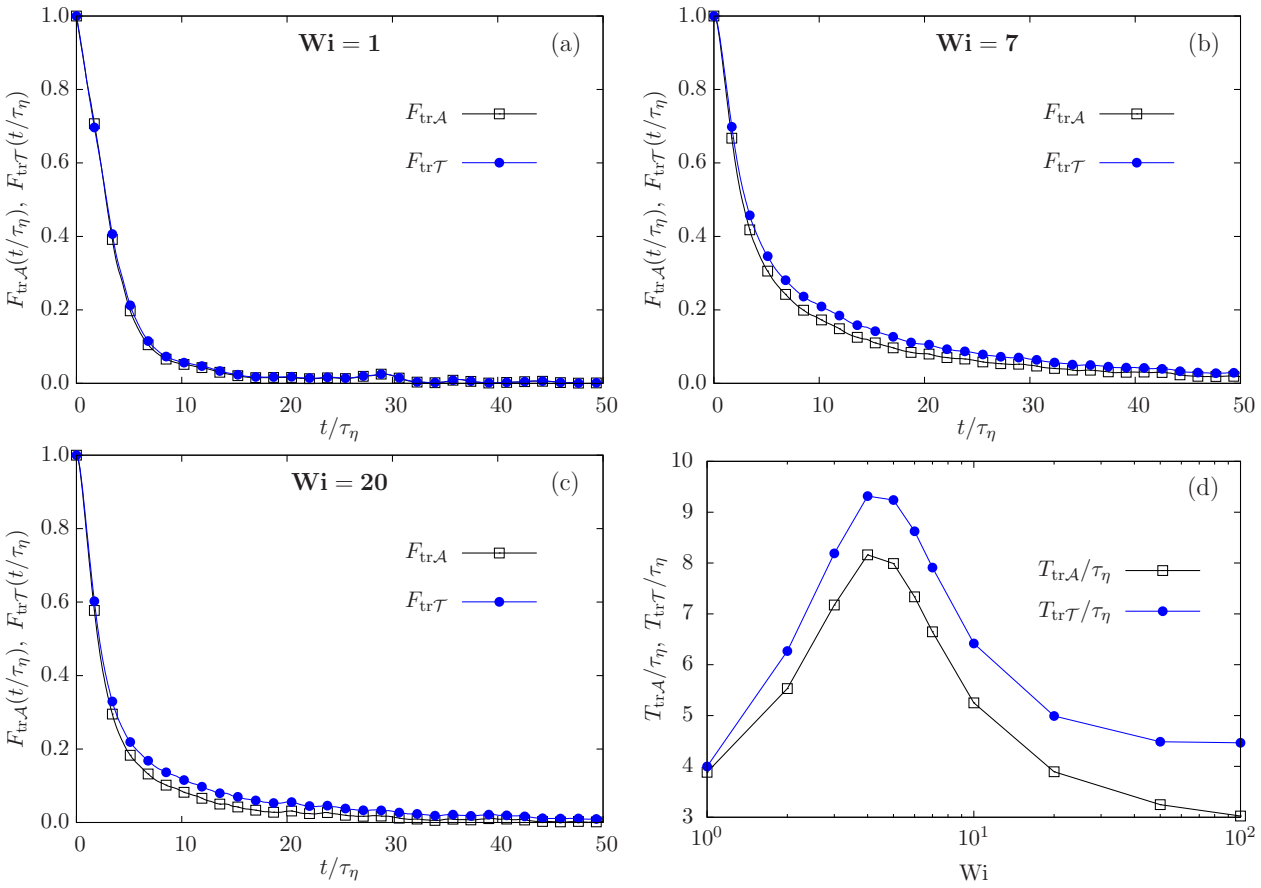

FIG. 2. (Color online) Autocorrelation function of $\mathrm{tr}\,\mathcal{A}$ (black squares) and $\mathrm{tr}\,\mathcal{T}$ (blue circles) for (a) Wi = 1, (b) Wi = 7, and (c) Wi = 20. Panel (d) shows the correlation times $T_{\mathrm{tr}\mathcal{A}}$ (black squares) and $T_{\mathrm{tr}\mathcal{T}}$ (blue circles) rescaled by τ_η as a function of Wi.

direction of vorticity is $\hat{\boldsymbol{\omega}}$. Finally, we denote by $\hat{\boldsymbol{z}}_1$ and $\hat{\boldsymbol{z}}_1^{\mathrm{P}}$ the first unit eigenvector of $\mathcal{C}$ and $\mathcal{C}^{\mathrm{P}}$, respectively.

A. The Peterlin approximation

As mentioned in Sec. II, the Peterlin approximation consists in replacing $\mathcal{A}$ with $\mathcal{T}$ in the evolution equation for the polymer conformation tensor [$\mathcal{A}$ and $\mathcal{T}$ have been defined in Eqs. (5) and (7)]. The eigenvectors of $\mathcal{A}$ and $\mathcal{T}$ are the same, but their eigenvalues may differ. Indeed, Jensen's inequality yields $\mathrm{tr}\,\mathcal{A} \geq \mathrm{tr}\,\mathcal{T}$. A first indication of the effect of the Peterlin approximation is thus given by the joint PDF $P_\sigma(\mathrm{tr}\,\mathcal{A}, \mathrm{tr}\,\mathcal{T})$ (see Fig. 1). For small polymer extensions or for small values of Wi, $\mathrm{tr}\,\mathcal{A}$ and $\mathrm{tr}\,\mathcal{T}$ are approximately the same, i.e., the Peterlin approximation holds very well. This fact can be explained by noting that, for small Wi, polymers are weakly stretched and hence $1 - R^2/L^2 \approx 1$. By contrast, for large extensions or for large values of Wi, the deviations of $\mathrm{tr}\,\mathcal{T}$ from $\mathrm{tr}\,\mathcal{A}$ are appreciable, i.e., the Peterlin approximation is inaccurate. As mentioned earlier, these deviations are due to the broad distribution of polymer extensions in a turbulent flow at large Wi (see Sec. IV B for more details). Nevertheless, $\langle \mathrm{tr}\,\mathcal{T}\rangle_\sigma$ and $\langle \mathrm{tr}\,\mathcal{A}\rangle_\sigma$ do not differ appreciably (see the bottom-right panel in Fig. 1). This fact demonstrates that the study of average values may not suffice to investigate the validity of the Peterlin approximation and that the fluctuations of the restoring term should also be analyzed, as they may influence the statistics of polymer deformation in a nontrivial way.

In addition, the qualitative behavior of the temporal autocorrelations of $\mathrm{tr}\,\mathcal{A}$ and $\mathrm{tr}\,\mathcal{T}$ are similar [Figs. 2(a)–2(c)], but for large Wi the correlation time of $\mathrm{tr}\,\mathcal{A}$ is shorter than that of $\mathrm{tr}\,\mathcal{T}$ [Fig. 2(d)]. The peak in the graph of the correlation time versus Wi can be attributed to the critical slowing down of polymer stretching near the coil-stretch transition [17,48,49] (see also Sec. IV B).

B. Statistics of polymer extension

The statistical properties of the separation R are well understood; we briefly review the theory of the coil-stretch transition, which will be useful to interpret the numerical simulations. For small values of Wi, most of the polymers are in the coiled state, i.e., their extension is close to the equilibrium one. Accordingly, the PDF of R has a pronounced peak at R_0. As Wi increases, polymers unravel and become more and more extended. The transition from the coiled to the stretched state occurs when the Lyapunov exponent of the flow exceeds $1/2\tau_p$, i.e., at $\mathrm{Wi}_\lambda = 1/2$ [43]. [Note that some authors define the Weissenberg number in terms of the time scale associated with the exponential relaxation of $\sqrt{\langle R^2(t)\rangle}$ instead of $\langle R^2(t)\rangle$ and hence obtain a critical Weissenberg number equal to unity.] At intermediate extensions, the PDF

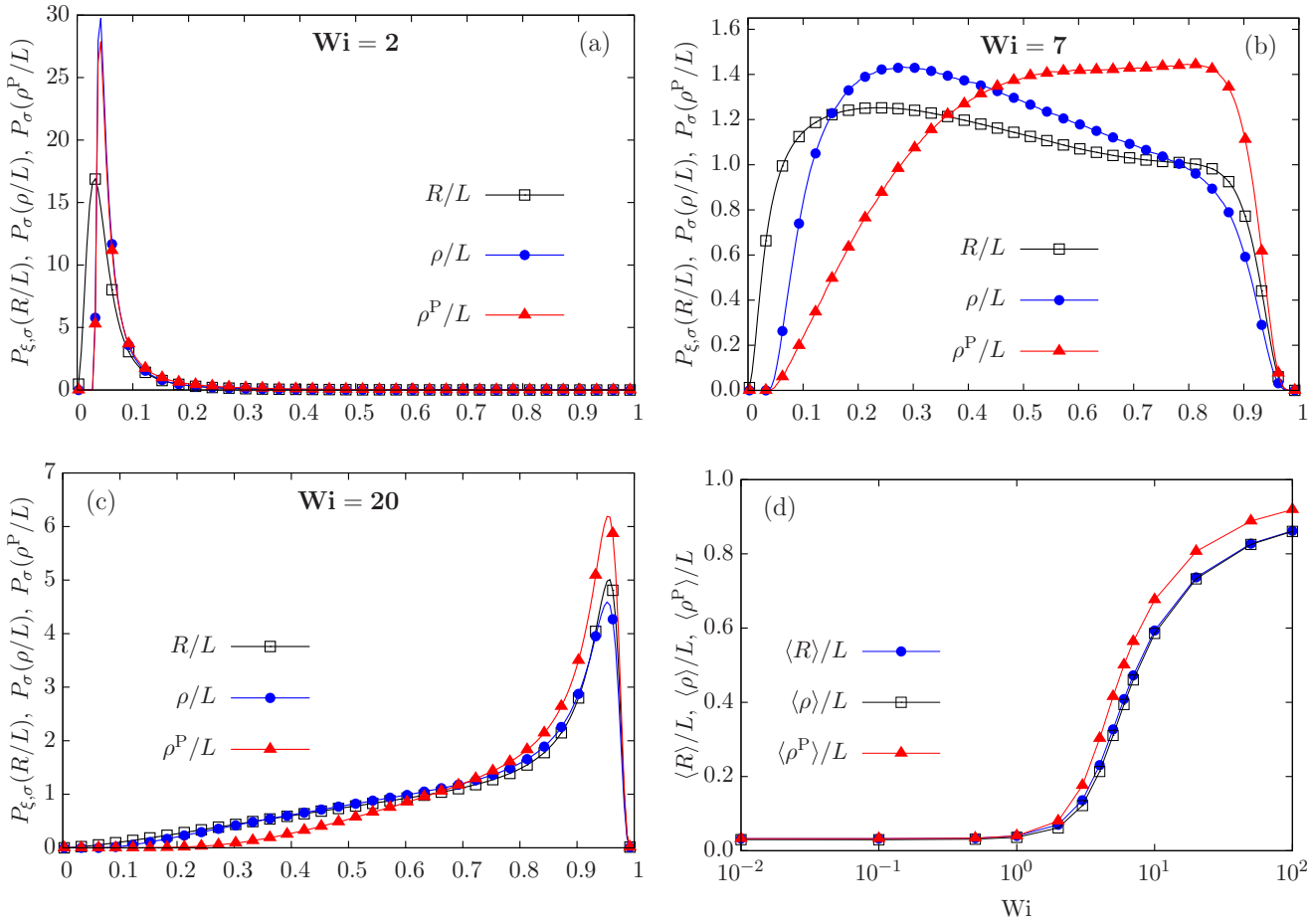

FIG. 3. (Color online) PDF of R/L (black squares), ρ/L (blue circles), and ρ^{P}/L (red triangles) for (a) Wi = 2, (b) Wi = 7, and (c) Wi = 20. Panel (d) shows $\langle R\rangle_{\xi,\sigma}/L$ (black squares), $\langle\rho\rangle_\sigma/L$ (blue circles), and $\langle\rho^{\mathrm{P}}\rangle_\sigma/L$ (red triangles) as a function of the Weissenberg number.

of R has a power-law behavior, i.e., $P_{\xi,\sigma}(R) \sim R^{-1-\alpha}$ for $R_0 \ll R \ll L$ [43]. This property of $P_{\xi,\sigma}(R)$ indicates that polymers with very different extensions coexist in the fluid; whether the coiled or the stretched state dominates depends on the value of Wi. The exponent α is positive in the coiled state and decreases as a function of Wi [9,20,43,50]. As long as $\alpha > 0$, the FENE dumbbell model reaches a steady state even as L tends to infinity (the $L \to \infty$ limit of the FENE model is known as the Hookean model [1]). However, when α vanishes, a steady-state PDF of the extension no longer exists if $L \to \infty$. This behavior is interpreted as the coil-stretch transition [43]. Finally, if Wi increases beyond the value of the coil-stretch transition, α becomes negative and the maximum of $P_{\xi,\sigma}(R)$ moves from close to R_0 to close to L [9,50]. The statistics of R shown in Figs. 3 and 4 for different values of Wi agrees very well with the theory. We now compare the FENE and FENE-P models and use the above theoretical predictions to interpret the numerical results.

We noted in Sec. II that the comparison between the FENE and the FENE-P models ought to be done in terms of the conformation tensors $\mathcal{C}$ and $\mathcal{C}^{\mathrm{P}}$ (rather than in terms of R and $\mathcal{C}^{\mathrm{P}}$). Let us denote $\rho(t) = \sqrt{\mathrm{tr}\,\mathcal{C}(t)}$ and $\rho^{\mathrm{P}}(t) = \sqrt{\mathrm{tr}\,\mathcal{C}^{\mathrm{P}}(t)}$. To examine the influence of the Peterlin approximation on the statistics of polymer extension, we calculate ρ from the solution of Eq. (1) and ρ^{P} from Eq. (8). We then compare $P_\sigma(\rho/L)$ and $P_\sigma(\rho^{\mathrm{P}}/L)$ in the steady state for different values of Wi. The plots shown in Figs. 3 and 4 correspond to the coiled state (Wi = 2), the coil-stretch transition (Wi = 7), and the stretched state (Wi = 20).

For small values of Wi, $P_\sigma(\rho/L)$ and $P_\sigma(\rho^{\mathrm{P}}/L)$ do not differ significantly. The reason for this behavior is that for small Wi, the extension of most polymers is near R_0; hence $1 - R^2/L \approx 1$ and the Peterlin approximation holds very well [Fig. 3(a)]. For intermediate and large values of Wi, the differences between $P_\sigma(\rho/L)$ and $P_\sigma(\rho^{\mathrm{P}}/L)$ are, in contrast, considerable. This fact is due to the power-law behavior of the PDF of R for intermediate extensions. At large Wi, the statistics of R is indeed characterized by a broad distribution of extensions around the mean value, and the Peterlin approximation is poor. In particular, we note that in the FENE-P model, large extensions are more probable than in the FENE model to the detriment of small and intermediate extensions [Figs. 3(b) and 3(c)]. This phenomenon is easily explained by noting that in the FENE model, the elastic force keeps R^2 smaller than L^2, whereas in the FENE-P model it only ensures that $\rho^2 < L^2$. Hence the restoring term in Eq. (8) is weaker than that in

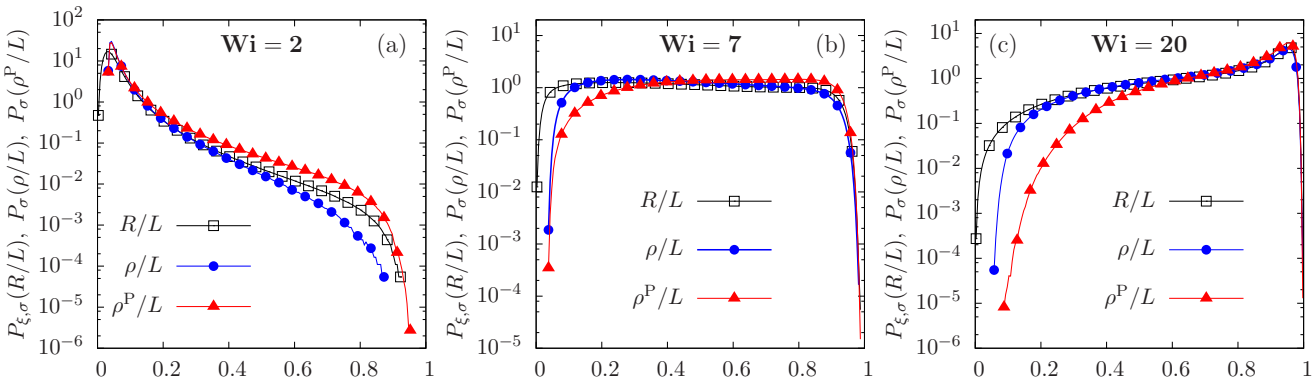

FIG. 4. (Color online) PDF of R/L (black squares), ρ/L (blue circles), and ρ^{P}/L (red triangles) in a semilogarithmic scale for (a) Wi = 2, (b) Wi = 7, and (c) Wi = 20.

Eq. (1) and allows larger extensions. The FENE-P model, therefore, overestimates the average extension of polymers for large values of Wi [Fig. 3(d)]. An analogous behavior has been observed in turbulent channel flows [10,15].

We also note that whereas for large Wi the PDFs of R and ρ are approximately the same [Fig. 3(c)], they are significantly different for intermediate or small Wi [Figs. 3(a) and 3(b)]. This fact can be explained as follows. In the former case, the stretching action of the velocity gradient is very strong compared to the effect of thermal fluctuations, and in most realizations $R \approx \sqrt{\mathrm{tr}\,C}$. In the latter case, the effect of thermal fluctuations cannot be disregarded and the differences in the statistics of R and ρ (see Sec. II) become evident. Furthermore, $P_{\xi,\sigma}(R/L)$ and $P_\sigma(\rho/L)$ mainly differ for small

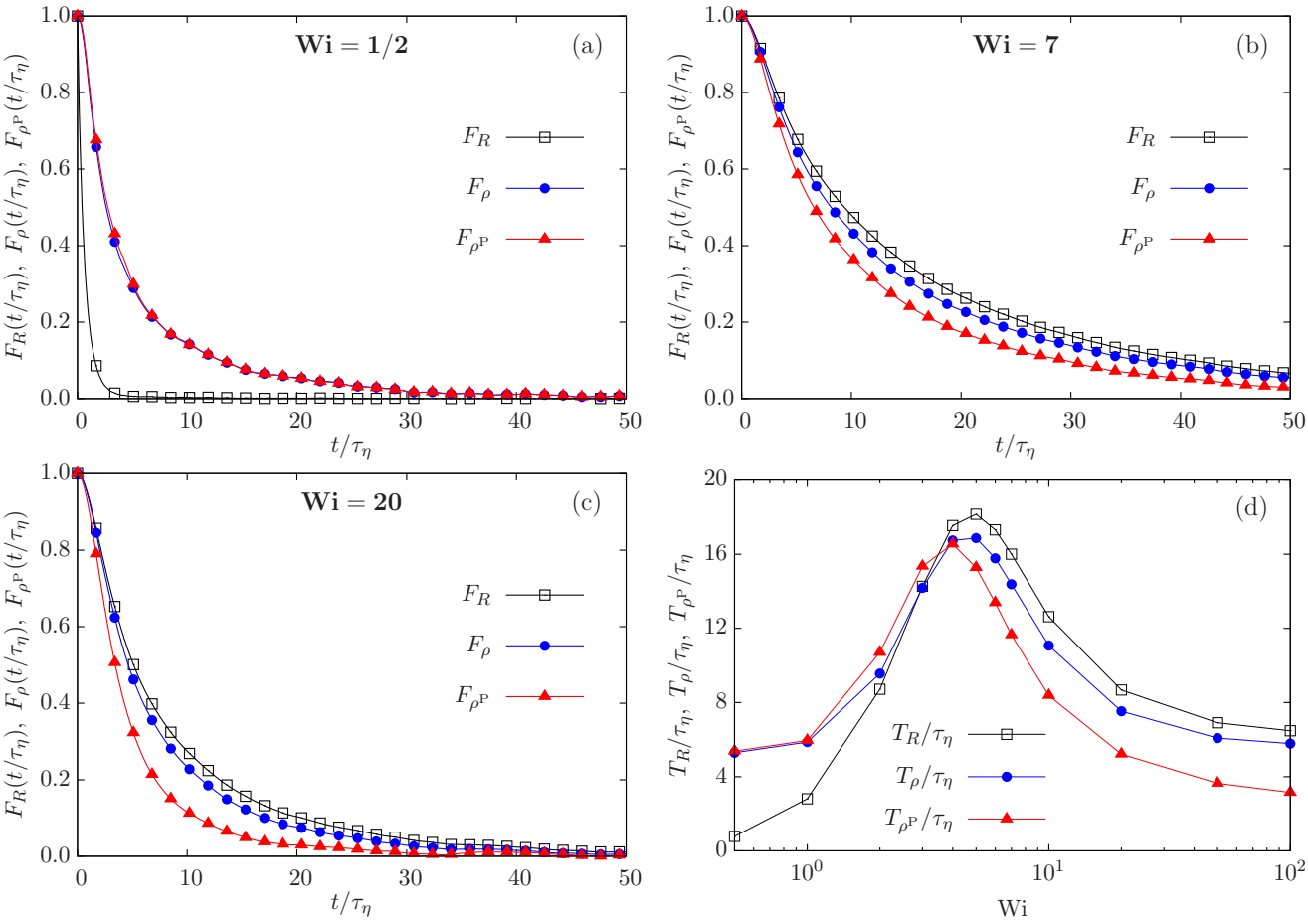

FIG. 5. (Color online) Autocorrelation function of R (black squares), ρ (blue circles), and ρ^{P} (red triangles) for (a) Wi = 0.5, (b) Wi = 7, and (c) Wi = 20. Panel (d) shows the correlation times T_R (black squares), T_ρ (blue circles), and $T_{\rho^{\mathrm{P}}}$ (red triangles) rescaled by τ_η as a function of the Weissenberg number.

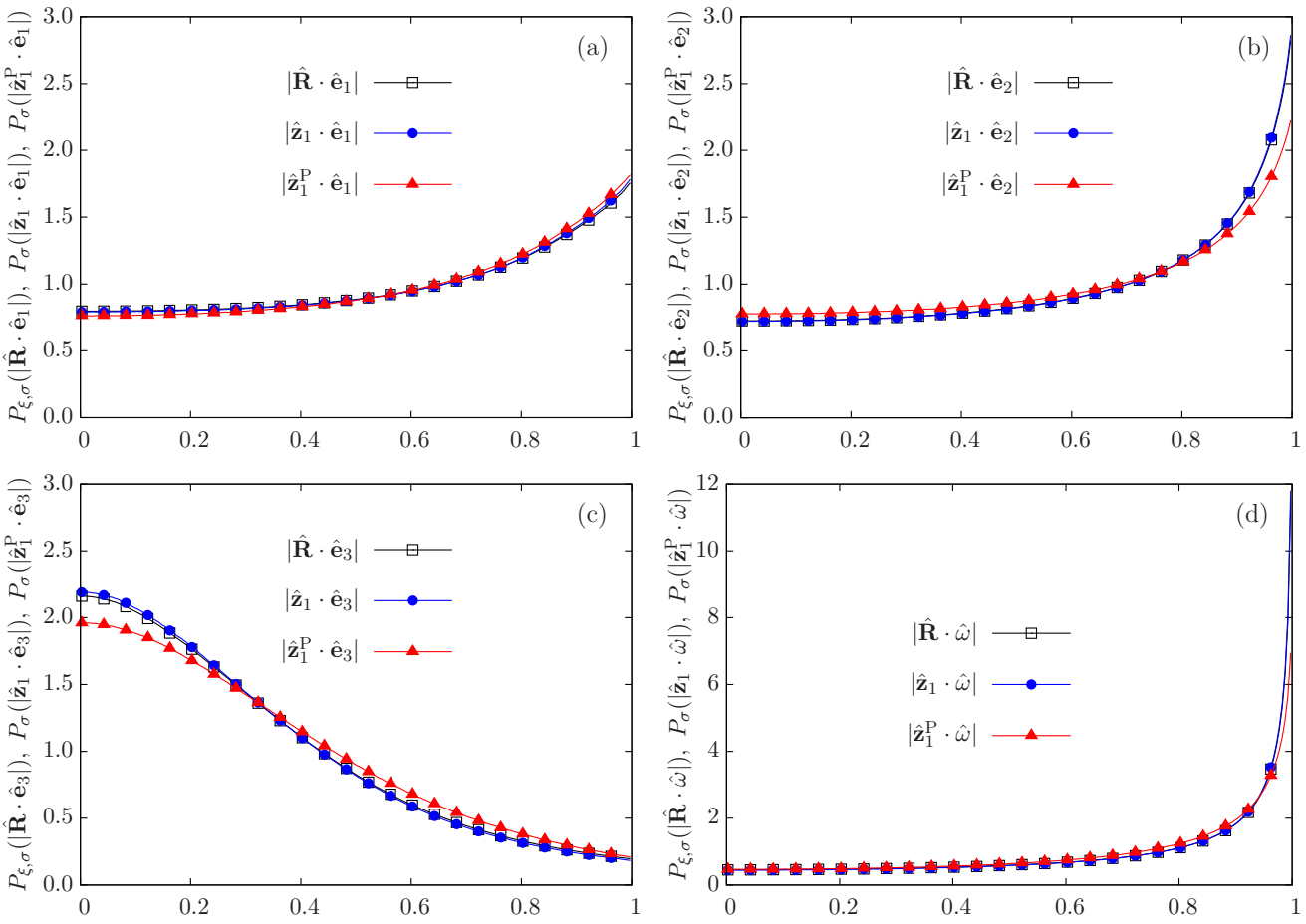

FIG. 6. (Color online) PDF of alignment with (a) $\hat{\boldsymbol{e}}_1$, (b) $\hat{\boldsymbol{e}}_2$, (c) $\hat{\boldsymbol{e}}_3$, and (d) $\hat{\boldsymbol{\omega}}$ for Wi = 20.

and intermediate extensions, because the large extensions are obtained in those realizations in which the velocity gradient is very intense and thermal noise can be neglected. The above results demonstrate that comparing the statistics of $\boldsymbol{R}$ directly with that of $\mathcal{C}^{\mathrm{P}}$ may lead to wrong conclusions; indeed, at small Wi, $P_{\xi,\sigma}(R/L)$ and $P_\sigma(\rho^{\mathrm{P}}/L)$ are clearly different, whereas $P_\sigma(\rho/L)$ and $P_\sigma(\rho^{\mathrm{P}}/L)$ are close.

The autocorrelation function of the extension is approximately exponential both in the FENE and in the FENE-P models. However, $F_{\rho^{\mathrm{P}}}(t)$ is a good approximation of $F_\rho(t)$ only for small Wi [Fig. 5(a)]. In addition, the FENE-P model captures the critical slowing down of polymers near the coil-stretch transition [17,48,49], but for large Wi it underestimates the correlation time of the extension [Fig. 5(d)]. Once again, we note that, for small Wi, a direct comparison between $F_R(t)$ and $F_{\rho^{\mathrm{P}}}(t)$ would lead to wrong conclusions about the effect of the Peterlin closure on the temporal statistics of polymer extension.

C. Statistics of polymer orientation

In a coupled simulation of turbulent drag reduction, the feedback of polymers on the flow is of a tensorial nature; therefore, it depends not only on the extension of polymers but also on their orientation.

In the FENE and FENE-P models, the first eigenvector of $\mathcal{C}$ and of $\mathcal{C}^{\mathrm{P}}$ (denoted as $\hat{\boldsymbol{z}}_1$ and $\hat{\boldsymbol{z}}_1^{\mathrm{P}}$, respectively) gives the direction of the polymer, provided Wi is sufficiently large. The effect of the Peterlin approximation on polymer orientation can then be studied by comparing the statistics of $\hat{\boldsymbol{z}}_1^{\mathrm{P}}$ with that of $\hat{\boldsymbol{z}}_1$.

Figure 6 shows that $\hat{\boldsymbol{z}}_1$ exhibits a moderate alignment with $\hat{\boldsymbol{e}}_2$ and a strong alignment with $\hat{\boldsymbol{\omega}}$. This behavior can be explained as follows. We have already noted that, for intermediate or large values of Wi, thermal fluctuations have a negligible effect on the dynamics of polymers. We therefore expect that the statistics of $\hat{\boldsymbol{z}}_1$ coincides with that of $\hat{\boldsymbol{R}} = \boldsymbol{R}/R$, as is confirmed by the results shown in Fig. 6. If thermal fluctuations are negligible, the evolution of the extension R decouples from that of the orientation $\hat{\boldsymbol{R}}$, which behaves like the orientation vector of a rigid rod and is the solution of the Jeffery equation [51] [see also Fig. 7(b) in Ref. [19]]. Therefore, for large values of Wi, the orientation statistics of $\hat{\boldsymbol{z}}_1$ can be deduced from the dynamics of rigid rods. Pumir and Wilkinson [52] have shown that in isotropic turbulence there is a moderate alignment between rigid rods and $\hat{\boldsymbol{e}}_2$, whereas the alignment of rods with the direction of vorticity is very strong. This phenomenon explains the alignment properties of $\hat{\boldsymbol{z}}_1$ (Fig. 6). Figure 6 also compares the statistics of $\hat{\boldsymbol{z}}_1$ and $\hat{\boldsymbol{z}}_1^{\mathrm{P}}$. The FENE-P model qualitatively reproduces the orientation statistics of the first eigenvector of the

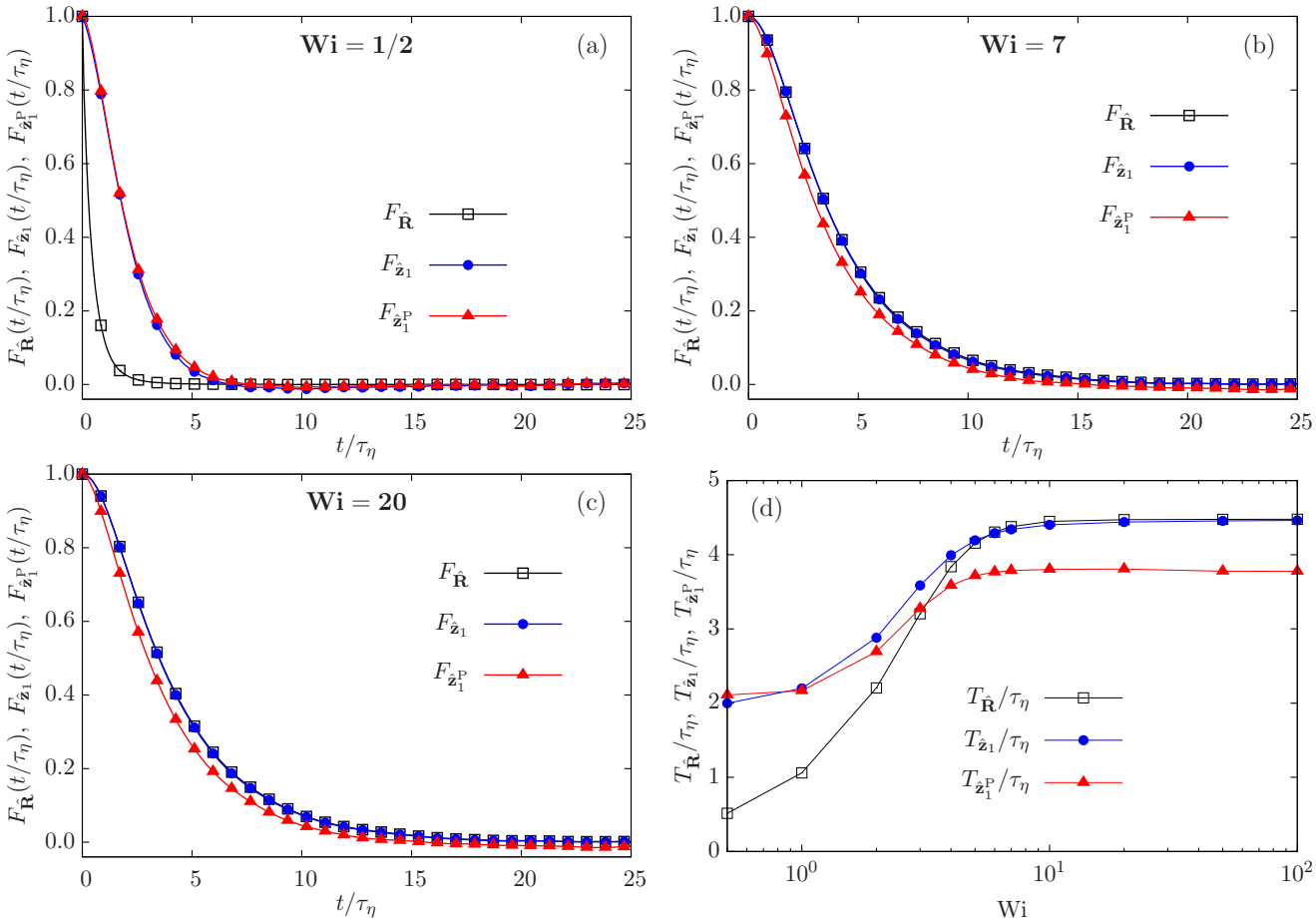

FIG. 7. (Color online) Autocorrelation function of $\hat{\boldsymbol{R}}$ (black squares), $\hat{\boldsymbol{z}}_1$ (blue circles), and $\hat{\boldsymbol{z}}_1^{\mathrm{P}}$ (red triangles) for (a) Wi = 0.5, (b) Wi = 7, and (c) Wi = 20. Panel (d) shows the correlation times $T_{\hat{\boldsymbol{R}}}$ (black squares), $T_{\hat{\boldsymbol{z}}_1}$ (blue circles), and $T_{\hat{\boldsymbol{z}}_1^{\mathrm{P}}}$ (red triangles) rescaled by τ_η as a function of the Weissenberg number.

conformation tensor but underestimates the level of alignment (Fig. 6).

The autocorrelation function of $\hat{\boldsymbol{z}}_1$ decays exponentially [Figs. 7(a)–7(c)], which for large Wi is once again in agreement with the results for the autocorrelation of the orientation of a rod [52]. The correlation time of $\hat{\boldsymbol{z}}_1$ increases for small values of Wi and saturates at large Wi [Fig. 7(d)]. The saturation is due to the fact that at large Wi the statistics of $\hat{\boldsymbol{R}}$ and $\hat{\boldsymbol{z}}_1$ are the same and the evolutions of R and $\hat{\boldsymbol{R}}$ decouple [51], which implies that the statistics of $\hat{\boldsymbol{R}}$ agrees with the orientation statistics of a rod and therefore becomes independent of Wi. The results of the FENE-P model are in agreement with these properties of the FENE model at small Wi, but quantitative discrepancies appear at large Wi [Figs. 7(a) to 7(c)]. In particular, the FENE-P model underestimates the correlation time of polymer orientation [Fig. 7(d)].

V. CONCLUSIONS

Numerical simulations of turbulent flows of polymer solutions use the FENE-P model, which is based on the elastic dumbbell model but requires a closure approximation for the elastic term. We have examined the effect of the Peterlin closure on the steady-state statistics of the extension and the orientation of polymers. The FENE-P model captures the qualitative properties of the statistics, but for large Wi it underestimates the steady-state probability of small extensions and overestimates the probability of large extensions. As a consequence, the Peterlin approximation yields a greater average extension as well as a greater probability that polymers break under the action of a turbulent flow [53]. To quantify this effect, one would need to couple the dynamics of polymers with a fragmentation model connected to the accumulated (or instantaneous) stress along each trajectory and to estimate the relative breaking rate [54]. Since large polymer extensions are more likely in the FENE-P model than in the FENE model, we also expect that the Peterlin approximation yields a stronger feedback of polymers on the flow in two-way coupling simulations of homogeneous isotropic turbulence with polymer additives. A similar argument, however, does not carry over to inhomogeneous flows such as channel flows. In this case, indeed, drag reduction is caused by the strong stretching of polymers in the near-wall region rather than by the dynamics in the bulk of the channel, where the flow is homogeneous and isotropic, and a lower degree of stretching is observed [2,10,12–14,21].

As regards the temporal statistics of the end-to-end separation vector, both the correlation times of the extension

and the orientation of polymers are underestimated by the FENE-P model. The FENE-P model also underestimates the level of alignment of polymers with the eigenvectors of the rate-of-strain tensor and with the direction of vorticity.

It would be interesting to check to what extent these properties of the FENE-P model influence the dynamics of a polymer solution by comparing two-way coupling simulations of the FENE-P model in which the stress tensor is either calculated according to the Peterlin closure or from molecular dynamics.

In this paper, we examined the Peterlin approximation, as this is the main assumption in the construction of a continuum model of polymer solutions. However, it is worth recalling that the FENE-P model is based on the dumbbell model and hence on a very simplified coarse-grained description of a polymer macromolecule. Other approximations may thus impact the performance of the FENE-P model and its comparison with experiments. For instance, even for simple laminar flows, the dumbbell model reproduces the experimental observations only if the maximum extension and the effective bead radius are used as free parameters to fit the experimental data [55,56]. The FENE model also disregards hydrodynamical interactions between the beads of a single dumbbell. However, these hydrodynamical interactions only affect the statistics of small extensions and are negligible at large extensions, where discrepancies between the FENE and FENE-P model become appreciable. Thus, for sufficiently large Wi, we expect the errors due to the absence of bead-bead hydrodynamical interactions to be subleading with respect to those due to the Peterlin closure. Finally, the FENE dumbbell model, which consists of a single oscillation mode, fails to accurately capture the deformation of a polymer after a sudden variation of the strain (see, e.g., Ref. [57]). To fix this limitation of the FENE model, Ghosh *et al.* [58] have derived a dumbbell model in which the maximum extension is adapted to the amplitude of the strain. This model was recently generalized by Gupta [59] to a bead-spring chain model that also describes the internal motions of a polymer molecule.

ACKNOWLEDGMENTS

This work was supported in part by the EU COST Action MP1305 "Flowing Matter" and by a research program of the Foundation for Fundamental Research on Matter (FOM), which is part of the Netherlands Organisation for Scientific Research (NWO). Part of the computations were done at "Mésocentre SIGAMM," Observatoire de la Côte d'Azur, Nice, France. D.V. acknowledges the hospitality of the Department of Physics of the Eindhoven University of Technology, where part of this work was done, and the Indo-French Centre for Applied Mathematics (IFCAM), Bangalore, for financial support.

[1] R. B. Bird, O. Hassager, R. C. Armstrong, and C. F. Curtiss, *Dynamics of Polymeric Liquids* (Wiley, New York, 1987), Vol. 2.
[2] I. Procaccia, V. S. L'Vov, and R. Benzi, Rev. Mod. Phys. **80**, 225 (2008).
[3] C. M. White and M. G. Mungal, Annu. Rev. Fluid Mech. **40**, 235 (2008).
[4] R. Pandit, P. Perlekar, and S. S. Ray, Pramana–J. Phys. **73**, 157 (2009).
[5] R. Benzi, Physica D **239**, 1338 (2010).
[6] M. D. Graham, Phys. Fluids **26**, 101301 (2014).
[7] B. A. Toms, in *Proceedings of the 1st International Congress on Rheology* (North-Holland, Amsterdam, 1949), Vol. 2, pp. 135–141.
[8] A. Gyr and H.-W. Bewersdorff, *Drag Reduction of Turbulent Flows by Additives* (Kluwer Academic, Dordrecht, 1995).
[9] T. Watanabe and T. Gotoh, Phys. Rev. E **81**, 066301 (2010).
[10] V. E. Terrapon, Y. Dubief, P. Moin, and E. S. G. Shaqfeh, in *Proceedings of ASME, ASME/JSME 4th Joint Fluids Engineering Conference (FEDSM2003), Honolulu, HI* (ASME, 2003), pp. 773–780.
[11] H. Massah, K. Kontomaris, W. R. Schowalter, and T. J. Hanratty, Phys. Fluids A **5**, 881 (1993).
[12] P. Ilg, E. De Angelis, I. V. Karlin, C. M. Casciola, and S. Succi, Europhys. Lett. **58**, 616 (2002).
[13] Q. Zhou and R. Akhavan, J. Non-Newtonian Fluid Mech. **109**, 115 (2003).
[14] V. E. Terrapon, Y. Dubief, P. Moin, E. S. G. Shaqfeh, and S. K. Lele, J. Fluid Mech. **504**, 61 (2004).
[15] V. K. Gupta, R. Sureshkumar, and B. Khomami, Phys. Fluids **16**, 1546 (2004).
[16] A. Celani, S. Musacchio, and D. Vincenzi, J. Stat. Phys. **118**, 531 (2005).
[17] A. Celani, A. Puliafito, and D. Vincenzi, Phys. Rev. Lett. **97**, 118301 (2006).
[18] J. Davoudi and J. Schumacher, Phys. Fluids **18**, 025103 (2006).
[19] S. Jin and L. R. Collins, New J. Phys. **9**, 360 (2007).
[20] S. Musacchio and D. Vincenzi, J. Fluid Mech. **670**, 326 (2011).
[21] F. Bagheri, D. Mitra, P. Perlekar, and L. Brandt, Phys. Rev. E **86**, 056314 (2012).
[22] M. Laso and H. C. Öttinger, J. Non-Newtonian Fluid Mech. **47**, 1 (1993).
[23] K. Feigl, M. Laso, and H. C. Öttinger, Macromolecules **28**, 3261 (1995).
[24] M. A. Hulsen, A. P. G. van Heel, and B. H. A. A. van den Brule, J. Non-Newtonian Fluid Mech. **70**, 79 (1997).
[25] T. Peters and J. Schumacher, Phys. Fluids **19**, 065109 (2007).
[26] T. Watanabe and T. Gotoh, J. Fluid Mech. **717**, 535 (2013).
[27] T. Watanabe and T. Gotoh, Phys. Fluids **26**, 035110 (2014).
[28] A. Peterlin, J. Polym. Sci. Pt. B: Polym. Lett. **4**, 287 (1966).
[29] R. B. Bird, P. J. Dotson, and N. L. Johnson, J. Non-Newtonian Fluid Mech. **7**, 213 (1980).
[30] R. Sureshkumar, A. N. Beris, and R. A. Handler, Phys. Fluids **9**, 743 (1997).
[31] E. De Angelis, C. M. Casciola, and R. Piva, Comput. Fluids **31**, 495 (2002).
[32] P. K. Ptasinski, B. J. Boersma, F. T. M. Nieuwstadt, M. A. Hulsen, B. H. A. A. Van den Brule, and J. C. R. Hunt, J. Fluid Mech. **490**, 251 (2003).
[33] Y. Dubief, C. M. White, V. E. Terrapon, E. S. G. Shaqfeh, P. Moin, and S. K. Lele, J. Fluid Mech. **514**, 271 (2004).

[34] P. A. Stone, A. Roy, R. G. Larson, F. Waleffe, and M. D. Graham, Phys. Fluids **16**, 3470 (2004).
[35] A. Robert, T. Vaithianathan, L. R. Collins, and J. G. Brasseur, J. Fluid Mech. **657**, 189 (2010).
[36] E. De Angelis, C. M. Casciola, R. Benzi, and R. Piva, J. Fluid Mech. **531**, 1 (2005).
[37] P. Perlekar, D. Mitra, and R. Pandit, Phys. Rev. Lett. **97**, 264501 (2006).
[38] P. Perlekar, D. Mitra, and R. Pandit, Phys. Rev. E **82**, 066313 (2010).
[39] A. Gupta, P. Perlekar, and R. Pandit, Phys. Rev. E **91**, 033013 (2015).
[40] M. Herrchen and H. C. Öttinger, J. Non-Newtonian Fluid Mech. **68**, 17 (1997).
[41] R. Keunings, J. Non-Newtonian Fluid Mech. **68**, 85 (1997).
[42] H. C. Öttinger, *Stochastic Processes in Polymeric Fluids* (Springer, Berlin Heidelberg, 1996).
[43] E. Balkovsky, A. Fouxon, and V. Lebedev, Phys. Rev. Lett. **84**, 4765 (2000).
[44] E. Calzavarini, M. Cencini, D. Lohse, and F. Toschi, Phys. Rev. Lett. **101**, 084504 (2008).
[45] J. Bec, L. Biferale, A. Lanotte, A. Scagliarini, and F. Toschi, J. Fluid Mech. **645**, 497 (2010).
[46] R. Benzi, L. Biferale, G. Paladin, A. Vulpiani, and M. Vergassola, Phys. Rev. Lett. **67**, 2299 (1991).
[47] J. Bec, L. Biferale, G. Boffetta, M. Cencini, S. Musacchio, and F. Toschi, Phys. Fluids **18**, 091702 (2006).
[48] D. Vincenzi and E. Bodenschatz, J. Phys. A **39**, 10691 (2006).
[49] S. Gerashchenko and V. Steinberg, Phys. Rev. E **78**, 040801 (2008).
[50] M. Martins Afonso and D. Vincenzi, J. Fluid Mech. **540**, 99 (2005).
[51] W. L. Olbricht, J. M. Rallison, and L. G. Leal, J. Non-Newtonian Fluid Mech. **10**, 291 (1982).
[52] A. Pumir and M. Wilkinson, New J. Phys. **13**, 093030 (2011).
[53] J.-L. Thiffeault, Phys. Lett. A **308**, 445 (2003).
[54] M. U. Babler, L. Biferale, and A. S. Lanotte, Phys. Rev. E **85**, 025301(R) (2012).
[55] T. T. Perkins, D. E. Smith, and S. Chu, Science **276**, 2016 (1997).
[56] R. G. Larson, T. T. Perkins, D. E. Smith, and S. Chu, Phys. Rev. E **55**, 1794 (1997).
[57] I. Ghosh, G. H. McKinley, R. A. Brown, and R. C. Armstrong, J. Rheol. **45**, 721 (2001).
[58] I. Ghosh, Y. L. Joo, G. H. McKinley, R. A. Brown, and R. C. Armstrong, J. Rheol. **46**, 1057 (2002).
[59] V. K. Gupta, Rheol. Acta **51**, 51 (2012).

Polymer stretching in the inertial range of turbulence

Adeel Ahmad[1,2] and Dario Vincenzi[1]

[1]*Laboratoire Jean Alexandre Dieudonné, Université Nice Sophia Antipolis, CNRS, UMR 7351, 06100 Nice, France*

[2]*Department of Mathematics, COMSATS Institute of Information Technology, Islamabad, Pakistan*

(Received 4 March 2016; revised manuscript received 18 April 2016; published 11 May 2016)

We study the deformation of flexible polymers whose contour length lies in the inertial range of a homogeneous and isotropic turbulent flow. By using the elastic dumbbell model and a stochastic velocity field with nonsmooth spatial correlations, we obtain the probability density function of the extension as a function of the Weissenberg number and of the scaling exponent of the velocity structure functions. In a spatially rough flow, as in the inertial range of turbulence, the statistics of polymer stretching differs from that observed in laminar flows or in smooth chaotic flows. In particular, the probability distribution of polymer extensions decays as a stretched exponential, and the most probable extension grows as a power law of the Weissenberg number. Furthermore, the ability of the flow to stretch polymers weakens as the flow becomes rougher in space.

DOI: 10.1103/PhysRevE.93.052605

I. INTRODUCTION

One of the main phenomena that characterize the deformation of flexible polymers in a fluid flow is the coil-stretch transition, which consists in an abrupt increase in polymer extension as the intensity of the velocity gradient exceeds a critical value [1–3]. The coil-stretch transition was predicted by de Gennes [4] in the case of a planar extensional flow. The relevant dimensionless parameter for the transition is the Weissenberg number $\mathrm{Wi} = \gamma\tau$, where γ is the amplitude of the velocity gradient and τ is the polymer relaxation time. In an extensional flow, a polymer stays in the equilibrium coiled configuration as long as $\mathrm{Wi} < 1/2$ and unravels almost completely as Wi exceeds $1/2$. Correspondingly, the probability density function (PDF) of polymer extensions consists of a narrow peak that, as Wi exceeds $1/2$, rapidly moves from extensions close to the equilibrium size of the polymer, R_0, to extensions close to its contour length L. In his study of the coil-stretch transition, de Gennes [4] used the elastic dumbbell model, which describes a flexible polymer as two inertialess beads connected by an elastic spring and subjected to thermal fluctuations [5]. In the frame of reference of the center of mass, the configuration of a dumbbell is specified by the separation vector between the beads, $\boldsymbol{R}$, which satisfies the stochastic ordinary differential equation [5]

$$\dot{\boldsymbol{R}} = \boldsymbol{R}\cdot\nabla\boldsymbol{u} - \frac{f(R)}{2\tau}\boldsymbol{R} + \sqrt{\frac{R_0^2}{\tau}}\,\boldsymbol{\eta}(t), \tag{1}$$

where $\boldsymbol{u}$ is the incompressible velocity field, $R = |\boldsymbol{R}|$, $\boldsymbol{\eta}(t)$ is vectorial white noise, $f(R) = 1$ for a Hookean dumbbell and $f(R) = 1/(1 - R^2/L^2)$ for a finitely extensible nonlinear elastic (FENE) dumbbell. Perkins *et al.* [6] have observed the coil-stretch transition in a planar extensional flow by examining the deformation of fluorescently labeled DNA macromolecules.

Lumley [7,8] and subsequently Balkovsky *et al.* [9] have employed the elastic dumbbell model to show that the coil-stretch transition also occurs in chaotic or random flows. This phenomenon has been confirmed experimentally by Steinberg and coworkers [3,10,11] via the direct observation of single-polymer dynamics in chaotic flows generated by elastic instabilities. It has also been studied in numerical simulations of the dumbbell model for randomly fluctuating flows [12,13] and turbulent flows [14–17]. The criterion for the transition is that the Weissenberg number $\mathrm{Wi} = \lambda\tau$ exceeds $1/2$, where λ is the Lyapunov exponent of the flow [9,18]. However, in chaotic flows the statistics of polymer stretching has different properties compared to the laminar case. Indeed, for intermediate extensions ($R_0 \ll R \ll L$), the PDF of R behaves as a power law of the form $R^{-1-\alpha}$. Thus, for a comparable intensity of the velocity gradient, the distribution of the extensions is much broader than in a laminar flow; coiled and stretched polymers coexist in the flow, and the value of Wi determines which configuration is predominant. The exponent α is a decreasing function of Wi; it is positive for $\mathrm{Wi} < 1/2$, equals zero for $\mathrm{Wi} = 1/2$, and is negative for greater values of Wi [9]. Hence, in the Hookean dumbbell model ($L = \infty$), the probability distribution of the extension ceases to be normalizable for $\mathrm{Wi} = 1/2$, and this behavior is interpreted as the sign of the coil-stretch transition in chaotic flows [9]. In the more realistic FENE model, the emergence of the stretched state manifests itself through the fact that the slope of the PDF of intermediate extensions changes from negative to positive, and consequently the maximum of the PDF of R abruptly moves from close to R_0 to close to L [19,20].

The phenomenology described above holds when the correlation time of $\boldsymbol{u}$ is short compared to λ^{-1}. In the opposite regime, the dynamics of the coil-stretch transition is different. The PDF of the extension is bimodal, and the appearance of the stretched state occurs through the drop of the peak at R_0 and the simultaneous rise of a second peak at L as Wi increases [21]. At large values of Wi, the PDF of intermediate extensions behaves as R^{-1} [21].

All the aforementioned studies of the dumbbell model assume that $\boldsymbol{u}$ is spatially smooth in the neighborhood of the polymer and that $\nabla\boldsymbol{u}$ is uniform over the size of the molecule. For sufficiently large Reynolds numbers, the polymer contour length can exceed the viscous scale and polymers can stretch into the inertial range of turbulence, where the flow is spatially rough [22]. The Reynolds number required for polymers to experience inertial-range fluctuations is lower for long biological macromolecules, such as those used in the study of the coil-stretch transition in laminar velocity fields [23]; long fibers can even approach the integral

scale of a turbulent flow [24]. Wiese [25] has studied polymer deformation in a random field with nonsmooth spatial correlations by using renormalization-group techniques. Davoudi and Schumacher [26] have examined the dynamics of dumbbells that can stretch into the inertial range in a numerical simulation of polymer dynamics in a turbulent flow. Here we study this problem analytically by using a stochastic model of inertial-range turbulence. We obtain the PDF of polymer extension as a function of the scaling exponent of the velocity structure functions and show how, in a spatially rough flow, the phenomenology of polymer stretching differs from that observed before in laminar or in smooth chaotic flows.

II. SHORT-CORRELATED RANDOM FLOW

A fully analytical study of the coil-stretch transition in random flows can be performed in the limit in which the correlation time of $\boldsymbol{u}$ is short. This has been achieved in the case of a smooth random flow by using the Batchelor regime of the Kazantsev-Kraichnan model [27,28] to mimic small-scale velocity fluctuations (see Ref. [29] for a review on the application of this model to turbulent transport). The velocity field is Gaussian, statistically homogeneous and stationary, and has zero mean and correlation:

$$\langle u_i(\boldsymbol{x}+\boldsymbol{r},t)u_j(\boldsymbol{x},t')\rangle = D_{ij}(\boldsymbol{r})\delta(t-t'), \tag{2}$$

where the incompressibility of $\boldsymbol{u}$ requires $\sum_i \partial D_{ij}/\partial r_i = 0$. The velocity gradient thus plays the role of a multiplicative noise in Eq. (1). Note that, in virtue of the incompressibility of $\boldsymbol{u}$, whether Eq. (1) is interpreted in the Itô or in the Stratonovich sense is immaterial as far as the statistics of $\boldsymbol{R}$ is concerned [29]. The PDF of the separation vector, $P(\boldsymbol{R})$, indeed satisfies the Fokker-Planck equation [30]:

$$\partial_t P = \left[d_{ij}(\boldsymbol{R}) + \frac{R_0^2}{2\tau}\delta_{ij}\right]\partial_{R_i}\partial_{R_j}P - \frac{1}{2\tau}\partial_{R_i}[f(R)R_iP], \tag{3}$$

where $d_{ij}(\boldsymbol{r}) = D_{ij}(\boldsymbol{0}) - D_{ij}(\boldsymbol{r})$ are the structure functions of the velocity field. If $\boldsymbol{u}$ is smooth and statistically isotropic and invariant under reflections, $d_{ij}(\boldsymbol{r})$ takes the form [29]

$$d_{ij}(\boldsymbol{r}) = D_1 r^2[(d+1)\delta_{ij} - 2\hat{r}_i\hat{r}_j], \tag{4}$$

where $D_1 > 0$ determines the amplitude of the fluctuations of the velocity and d is the dimension of the flow. In this case, the stationary PDF of $\boldsymbol{R}$ only depends on R and can be sought as the long-time solution of the following Fokker-Planck equation in one variable:

$$\partial_T P = -\partial_R[C_1(R)P] + \partial_R^2[C_2(R)P], \tag{5}$$

where $T = t/2\tau, C_1(R) = 2(d+1)\mathrm{Wi}\,R/d - f(R)R + (d-1)R_0^2/R$, and $C_2(R) = 2\mathrm{Wi}\,R^2/d + R_0^2$ [13,19,20,31] (for further details on the notation, see Ref. [32]). Here $\mathrm{Wi} = \lambda\tau$, where $\lambda = D_1 d(d-1)$ is the Lyapunov exponent of the flow [33,34].

As R must be positive, the solution of Eq. (5) must satisfy a reflecting boundary condition at $R = 0$. Thus, in the stationary state the probability current must vanish everywhere, and the stationary solution of Eq. (5) is (e.g., Ref. [35])

$$P_{\mathrm{st}}(R) \propto \exp\left[\int^R d\zeta\, C_1(\zeta)/C_2(\zeta)\right]\Big/ C_2(R). \tag{6}$$

In particular, for the FENE model, the explicit expression of the exponent α that characterizes the power-law behavior of $P_{\mathrm{st}}(R)$ for intermediate extensions is [20]:

$$\alpha = \left(R_0^2/L^2 + 2\mathrm{Wi}/d\right)^{-1} - d. \tag{7}$$

For realistic values of R_0 and L, the ratio R_0^2/L^2 is much smaller than 1; hence $\alpha \approx -d(1 - 1/2\mathrm{Wi})$ and approaches $-d$ as Wi increases.

III. STRETCHING OF POLYMERS IN A SPATIALLY ROUGH FLOW

In a turbulent flow, the assumption that $\boldsymbol{\nabla u}$ is uniform over the size of the polymer is appropriate provided the contour length of the polymer is much smaller than the Kolmogorov dissipation scale ℓ_K (e.g., Ref. [36]). The velocity field can then be Taylor expanded and, to a first approximation, the stretching effect of the flow is entirely given by the velocity gradient [see Eq. (1)]. However, long polymers with $R_0 < \ell_K$ but $L > \ell_K$ may extend beyond the Kolmogorov scale into the inertial range, where $\boldsymbol{u}$ is nonsmooth [36]. Davoudi and Schumacher [26] have considered an elastic dumbbell with maximum length greater than ℓ_K in a turbulent shear flow. The numerical simulations show that the PDF of R reaches a stationary form even for Wi greater than the critical value and for a Hookean force. Indeed, whereas in a smooth flow fluid particles separate exponentially, when the velocity is only Hölder continuous the mean-square separation grows asymptotically in time as t^β with $\beta > 1$ [29]. As a consequence, for extensions $R \gg \ell_K$ the stretching effect of the flow is weaker than the elastic relaxation even for a linear elastic force [26]. These findings are systematized below within the Kazantsev-Kraichnan model.

If R can take values greater than ℓ_K, the full difference between the velocities of the polymer ends must be retained in the dumbbell equation [26,37,38]:

$$\dot{\boldsymbol{R}} = \boldsymbol{u}(\boldsymbol{x}_2,t) - \boldsymbol{u}(\boldsymbol{x}_1,t) - \frac{f(R)}{2\tau}\boldsymbol{R} + \sqrt{\frac{R_0^2}{\tau}}\,\boldsymbol{\eta}(t), \tag{8}$$

where $\boldsymbol{x}_1$ and $\boldsymbol{x}_2$ are the positions of the two beads that compose the dumbbell (the separation vector is defined as $\boldsymbol{R} = \boldsymbol{x}_2 - \boldsymbol{x}_1$). For $r \gg \ell_K$, the tensor $d_{ij}(\boldsymbol{r})$ can be written in such a way as to reproduce the structure functions of a non-smooth velocity field [29]:

$$d_{ij}(\boldsymbol{r}) = a(\xi)D_1\ell_K^{2-\xi}r^\xi[(d-1+\xi)\delta_{ij} - \xi\hat{r}_i\hat{r}_j], \tag{9}$$

where $a(\xi)$ is a positive constant and $\xi/2$ can be interpreted as the Hölder exponent of the velocity field and varies between 0 (white noise) and 1 (smooth flow). The value of ξ corresponding to the inertial-range scaling of a turbulent flow is $\xi = 4/3$ [39]. In this flow, the separation between two fluid particles grows in time according to a generalized Richardson law: $\langle r^\mu\rangle \sim t^{\mu/(2-\xi)}$ [29]. The impact of this property of the flow on the statistics of polymer stretching can be examined by substituting $d_{ij}(\boldsymbol{R})$ from Eq. (9) into Eq. (3) and by setting $f(R) = 1$ and $R_0 = 0$. For $\ell_K \ll R \ll L$, the drift and

diffusion coefficients in Eq. (5) thus take the form

$$C_1(\rho) = \frac{2(d-1+\xi)a(\xi)\mathrm{Wi}}{d}\rho^{\xi-1} - \rho, \tag{10}$$

$$C_2(\rho) = \frac{2a(\xi)\mathrm{Wi}}{d}\rho^{\xi}, \tag{11}$$

with $\rho = R/\ell_K$, and from Eq. (6) the zero-current solution of Eq. (5) is

$$P_{\mathrm{st}}(\rho) \propto \rho^{d-1}\exp\left[-\frac{d\rho^{2-\xi}}{2a(\xi)\mathrm{Wi}(2-\xi)}\right], \quad 1 \ll \rho \ll L/\ell_K. \tag{12}$$

Note that $P_{\mathrm{st}}(\rho)$ has the same form as the instantaneous PDF of the distance between two fluid particles that separate in the inertial range of a turbulent flow [39]. Contrary to the case of a smooth flow, $P_{\mathrm{st}}(\rho)$ is normalizable for all Wi even in the limit $L \to \infty$. Thus, according to the criterion introduced by Balkovsky *et al.* [9], there is not a coil-stretch transition if the maximum length of polymers lies within the inertial range of a turbulent flow. Nevertheless, as Wi increases, polymers can stretch significantly according to the following phenomenology. For $\mathrm{Wi} \lesssim d/2(d-1)$, $P_{\mathrm{st}}(R)$ has a maximum near to R_0, it decays as a power law $R^{-1-\alpha}$ with $\alpha > 0$ for $R_0 \ll R \ll \ell_K$, and decays as a stretched exponential for $R \gg \ell_K$. For $\mathrm{Wi} \gtrsim d/2(d-1)$, the PDF of R increases as a power law for $R_0 \ll R \ll \ell_K$ and behaves as in Eq. (12) for $\ell_K \ll R \ll L$. For all Wi, $P_{\mathrm{st}}(R)$ falls fast to zero near to L. Hence, the peak of $P_{\mathrm{st}}(R)$ is at $R_\star = \ell_K[2(d-1)a(\xi)\mathrm{Wi}/d]^{1/(2-\xi)}$ for the Hookean model and near to the smaller of $R_\star$ and L for the FENE model.

The full PDF of R can be calculated by choosing $d_{ij}(\boldsymbol{r})$ in such a way as to interpolate between the smooth form given in Eq. (4) and the inertial-range behavior discussed in this section. The structure functions of a three-dimensional ($d = 3$), statistically homogeneous, isotropic, and parity invariant velocity field can be written as [40,41]

$$d_{ij}(\boldsymbol{r}) = d_{NN}(r)\delta_{ij} + [d_{LL}(r) - d_{NN}(r)]\hat{r}_i\hat{r}_j, \tag{13}$$

where $d_{LL}(r)$ and $d_{NN}(r)$ are the longitudinal and transverse structure functions, respectively, and can be expressed in terms of the scalar spectrum $E(k)$ as follows [41]:

$$d_{LL}(r) = 4\int_0^\infty \left[\frac{1}{3} + \frac{\cos(kr)}{k^2r^2} - \frac{\sin(kr)}{k^3r^3}\right]E(k)dk, \tag{14}$$

$$d_{NN}(r) = d_{LL}(r) + \frac{r}{2}d'_{LL}(r). \tag{15}$$

The equation for $d_{NN}(r)$ follows from the incompressibility of $\boldsymbol{u}$. In order to obtain structure functions that interpolate between the smooth behavior for $r \ll \ell_K$ and the Hölder behavior with exponent $\xi/2$ for $r \gg \ell_K$, we choose [29]

$$E(k) = ce^{-\ell_k^2k^2}k^{-1-\xi}, \qquad 0 < \xi < 2, \tag{16}$$

where c is a positive constant and has the dimensionality of length$^{2-\xi}$time^{-1}. The above expression assumes that the integral scale of the flow is set to infinity or, in other words, that L is much smaller than this scale. Equation (14) then yields (see formulas 3.952.7, 3.952.8, 9.212.1, in Ref. [42])

$$d_{LL}(r) = c\ell_K^\xi\Gamma\left(-\frac{\xi}{2}-1\right)\left\{\frac{2\ell_K^2}{r^2}\left[{}_1F_1\left(-\frac{\xi}{2}-1;\frac{1}{2};-\frac{r^2}{4\ell_K^2}\right) - {}_1F_1\left(-\frac{\xi}{2}-1;\frac{3}{2};-\frac{r^2}{4\ell_K^2}\right)\right] - \frac{\xi+2}{3}\right\}, \tag{17}$$

where Γ is the Euler gamma function and ${}_1F_1$ is the confluent hypergeometric function of the first kind. The asymptotic expressions of $d_{LL}(r)$ can be obtained by using formulae 13.1.2 and 13.1.5 in Ref. [43]:

$$d_{LL}(r) \sim 2D_1r^2 \qquad (r \ll \ell_K), \tag{18}$$

and

$$d_{LL}(r) \sim 2D_1a(\xi)\ell_K^{2-\xi}r^\xi \qquad (r \gg \ell_K), \tag{19}$$

with

$$D_1 = \frac{c\xi\ell_K^{\xi-2}}{60}|\Gamma(-\xi/2)|, \tag{20}$$

and

$$a(\xi) = 15\frac{2^{1-\xi}\sqrt{\pi}(\xi+4)}{\xi(\xi+2)(\xi+5)\Gamma\left(\frac{\xi+3}{2}\right)}. \tag{21}$$

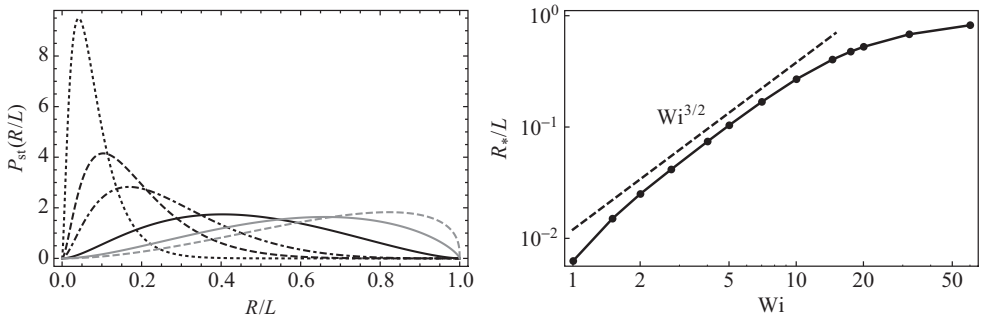

FIG. 1. Left: Stationary PDF of R/L for $R_0 = 0.1$, $\ell_K = 1$, $L = 10^3$, $\xi = 4/3$, and $\mathrm{Wi} = 2.75$ (black dotted line), $\mathrm{Wi} = 5.0$ (black dashed line), $\mathrm{Wi} = 7.0$ (black dot-dashed line), $\mathrm{Wi} = 14.5$ (black solid line), $\mathrm{Wi} = 30$ (gray solid line), $\mathrm{Wi} = 60$ (gray dashed line). The PDF is normalized as follows: $\int_0^\infty P_{\mathrm{st}}(R)dR = 1$. Right: Maximum of the PDF of R rescaled by L as a function of Wi. The dashed line is proportional to $\mathrm{Wi}^{3/2}$.

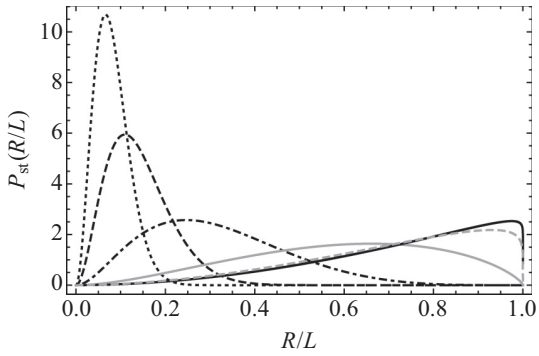

FIG. 2. Stationary PDF of R/L for $R_0 = 0.1$, $\ell_K = 1$, $L = 10^3$, $\mathrm{Wi} = 30$, and $\xi = 1/3$ (black dotted line), $\xi = 2/3$ (black dashed line), $\xi = 1$ (black dot-dashed line), $\xi = 4/3$ (gray solid line), $\xi = 5/3$ (gray dashed line), $\xi = 2$ (black solid line). The gray solid line is the same as described in the caption of Fig. 1. For $\xi = 2$, the stationary PDF of R/L is calculated by using Eq. (4); its explicit form can be found in Ref. [20].

Thus, the structure functions under consideration have the asymptotic behaviors given in Eqs. (4) and (9).

By inserting Eq. (13) into Eq. (3) and by using statistical isotropy, we obtain the following expressions for the drift and diffusion coefficients of the Fokker-Planck equation for $P(R)$ [see Eq. (5)]:

$$C_1(R) = \frac{4\tau d_{LL}(R)}{R} + 2\tau d'_{LL}(R) - Rf(R) + \frac{2R_0^2}{R}, \quad (22)$$

$$C_2(R) = 2\tau d_{LL}(R) + R_0^2. \quad (23)$$

The stationary PDF of R is then calculated by substituting $C_1(R)$ and $C_2(R)$ from Eqs. (22) and (23) into Eq. (6). Figures 1 to 2 illustrate the behavior of the PDF of R/L for different values of Wi and ξ. The equilibrium size and the maximum length of the dumbbell are chosen in such a way as to emphasize the range of extensions $\ell_K \ll R \ll L$, in which the dumbbell experiences spatially rough velocity fluctuations. As Wi increases, the distribution of polymer extensions broadens considerably, and its maximum progressively translates toward larger extensions, until nonlinear elastic effects become important (Fig. 1). Thus, increasing Wi has the effect of stretching polymers beyond ℓ_K, even though fairly large values of Wi are required for the PDF of extensions comparable to L to become appreciable. Moreover, the emergence of the stretched state is gradual as a function of Wi ($R_\star$ only grows as a power law of Wi) and, even for the largest values of Wi, a significant fraction of polymers deforms only in part. Finally, Fig. 2 shows that the ability of the flow to stretch polymers beyond ℓ_K is rather weak for small ξ and strengthens as the spatial regularity of the flow improves. In particular, both the mean and the standard deviation of $P_{st}(R)$ increase with increasing ξ.

IV. CONCLUSIONS

We have studied the statistics of polymer extension in a homogeneous and isotropic turbulent flow in the case in which the contour length of the polymers lies in the inertial range. By using the elastic dumbbell model and a stochastic velocity field with nonsmooth spatial correlations, we have analytically calculated the PDF of polymer extension as a function of the Weissenberg number and of the scaling exponent of the velocity structure functions.

The behavior of $P_{st}(R)$ can be summarized as follows:

$$P_{st}(R) \propto \begin{cases} R^{d-1}, & 0 \le R \ll R_0, \\ R^{-1-\alpha}, & R_0 \ll R \ll \ell_K, \\ R^{d-1} \exp\left(-\frac{b_\xi}{\mathrm{Wi}} \frac{R^{2-\xi}}{\ell_K^{2-\xi}}\right), & \ell_K \ll R \ll L, \end{cases} \quad (24)$$

where α is defined in Eq. (7) and b_ξ is a positive constant. For sufficiently large values of Wi, $P_{st}(R)$ consists of a power-law left tail with an exponent close to $d-1$ and a stretched exponential right tail, which falls fast to zero near to L. The PDF of R is very broad; hence, polymers with very different end-to-end extensions coexist in the solution.

Our study shows that even a spatially rough random flow can stretch polymers. However, the way the stretched state emerges is different from that found in laminar flows and in smooth random flows ($L < \ell_K$). In particular, for a smooth random flow with short correlation time, $P_{st}(R)$ displays a power-law behavior for $R_0 \ll R \ll L$ with a slope that changes from negative to positive as Wi increases [9]. Hence, when Wi exceeds a critical value, the maximum of $P_{st}(R)$ abruptly moves from near to R_0 to near to L [20]. If the contour length of polymers exceeds the dissipation scale of a turbulent flow, increasing the Weissenberg number results in a gradual translation of the maximum of $P_{st}(R)$ from R_0 to $R_\star \propto \ell_K \mathrm{Wi}^{1/(2-\xi)}$, until nonlinear elastic effects dominate the dynamics. Contrary to the case $L < \ell_K$, the emergence of the stretched state is therefore not abrupt and there is not a coil-stretch transition. Moreover, compared to the case $L < \ell_K$, much larger values of Wi are required to obtain comparable fractional extensions if $L > \ell_K$. The stretching effect of the flow also weakens as the flow becomes rougher in space.

The scale $R_\star$ can be identified with Lumley's scale in the theory of turbulent drag reduction [8,26]. The scale $R_\star$ is such that the eddy turnover time associated with $R_\star$ is comparable to the polymer relaxation time τ. At scales smaller than $R_\star$, the stretching effect of the flow dominates the elastic relaxation, whereas the latter is stronger than the former at larger scales.

Our study can be generalized to the case of dumbbells whose maximum extension exceeds the integral scale ℓ_0 of a turbulent flow. By definition of integral scale, the velocity field is indeed spatially uncorrelated at scales greater than ℓ_0. Hence, the behavior of the structure functions for $r \gg \ell_0$ can be captured by setting $\xi = 0$ in Eq. (9). From Eq. (12), the PDF of R for $\ell_0 \ll R \ll L$ is therefore of the form $P_{st}(R) \propto R^{d-1} \exp[-b_0 R^2/\ell_0^2 \mathrm{Wi}]$ with $b_0 > 0$, which indicates that the probability of polymer extension decreases very rapidly for $R \gtrsim \ell_0 \mathrm{Wi}^{1/2}$.

It was shown in Refs. [13,20,30] that in a smooth random flow the coil-stretch transition is characterized by a critical slowing down of polymer dynamics. The time required for the distribution of polymer extension to reach equilibrium indeed shows a peak near to the coil-stretch transition. This behavior is due to the large breadth of the PDF of R for values of Wi near

to the critical one. It would be interesting to study whether or not this phenomenon also persists when polymers can extend into the inertial range. In view of the breadth of the PDFs shown in Figs. 1 and 2, we expect that an analogous peak of the equilibriation time will be associated with the emergence of the stretched state. However, the peak will be much broader than for a smooth flow, because for polymers longer than ℓ_K the emergence of the stretched state is slower as a function of Wi. A second interesting question concerns the effects of a potential preferential sampling of the flow [37,38], which is not present when the correlation time of the velocity field vanishes [44].

ACKNOWLEDGMENTS

The authors thank S. Musacchio for useful suggestions. The work of A.A. was supported by the Erasmus Mundus External Cooperation Window action from EACEA. D.V. acknowledges the support of the EU COST Action MP 1305 "Flowing Matter."

[1] E. S. G. Shaqfeh, The dynamics of single-molecule DNA in flow, J. Non-Newtonian Fluid Mech. **130**, 1 (2005).
[2] R. G. Larson, The rheology of dilute solutions of flexible polymers: Progress and problems, J. Rheol. **49**, 1 (2005).
[3] Y. Liu and V. Steinberg, Single polymer dynamics in a random flow, Macromol. Symp. **337**, 34 (2014).
[4] P. G. de Gennes, Coil-stretch transition of dilute flexible polymer under ultrahigh velocity gradients, J. Chem. Phys. **60**, 5030 (1974).
[5] R. B. Bird, O. Hassager, R. C. Armstrong, and C. F. Curtiss, *Dynamics of Polymeric Liquids*, Vol. 2 (Wiley, New York, 1987).
[6] T. T. Perkins, D. E. Smith, and S. Chu, Single polymer dynamics in an elongational flow, Science **276**, 2016 (1997).
[7] J. L. Lumley, On the solution of equations describing small scale deformation, in *Symposia Mathematica* (Istituto Nazionale di Alta Matematica, Bologna, 1972), vol. 9, pp. 315–334.
[8] J. L. Lumley, Drag reduction in turbulent flow by polymer additives, J. Polymer Sci. Macromol. Rev. **7**, 263 (1973).
[9] E. Balkovsky, A. Fouxon, and V. Lebedev, Turbulent Dynamics of Polymer Solutions, Phys. Rev. Lett. **84**, 4765 (2000).
[10] S. Gerashchenko, C. Chevallard, and V. Steinberg, Single-polymer dynamics: Coil-stretch transition in a random flow, Europhys. Lett. **71**, 221 (2005).
[11] Y. Liu and V. Steinberg, Stretching of polymer in a random flow: Effect of a shear rate, Europhys. Lett. **90**, 44005 (2010).
[12] A. B. Mosler and E. S. G. Shaqfeh, The conformation change of model polymers in stochastic flow fields: Flow through fixed beds, Phys. Fluids **9**, 1222 (1997).
[13] A. Celani, A. Puliafito, and D. Vincenzi, Dynamical Slowdown of Polymers in Laminar and Random Flows, Phys. Rev. Lett. **97**, 118301 (2006).
[14] V. E. Terrapon, Y. Dubief, P. Moin, E. S. G. Shaqfeh, and S. K. Lele, Simulated polymer stretch in a turbulent flow using Brownian dynamics, J. Fluid Mech. **504**, 61 (2004).
[15] T. Watanabe and T. Gotoh, Coil-stretch transition in an ensemble of polymers in isotropic turbulence, Phys. Rev. E **81**, 066301 (2010).
[16] F. Bagheri, D. Mitra, P. Perlekar, and L. Brandt, Statistics of polymer extensions in turbulent channel flow, Phys. Rev. E **86**, 056314 (2012).
[17] D. Vincenzi, P. Perlekar, L. Biferale, and F. Toschi, Impact of the Peterlin approximation on polymer dynamics in turbulent flows, Phys. Rev. E **92**, 053004 (2015).
[18] Balkovsky *et al.* [9] define the polymer relaxation time in such a way that the critical value of Wi is 1. Here we conform with the definition of Wi commonly used in the literature on the coil-stretch transition in laminar flows.
[19] J.-L. Thiffeault, Finite extension of polymers in turbulent flow, Phys. Lett. A **308**, 445 (2003).
[20] M. Martins Afonso and D. Vincenzi, Nonlinear elastic polymers in random flow, J. Fluid Mech. **540**, 99 (2005).
[21] S. Musacchio and D. Vincenzi, Deformation of a flexible polymer in a random flow with long correlation time, J. Fluid Mech. **670**, 326 (2011).
[22] A. M. Crawford, N. Mordant, H. Xu, and E. Bodenschatz, Fluid acceleration in the bulk of turbulent dilute polymer solutions, New J. Phys. **10**, 123015 (2008).
[23] C. M. Schroeder, H. P. Babcock, E. S. G. Shaqfeh, and S. Chu, Observation of polymer conformation hysteresis in extensional flow, Science **301**, 1515 (2003).
[24] C. Brouzet, G. Verhille, and P. L. Gal, Flexible Fiber in a Turbulent Flow: A Macroscopic Polymer, Phys. Rev. Lett. **112**, 074501 (2014).
[25] K. J. Wiese, The passive polymer problem, J. Stat. Phys. **101**, 843 (2000).
[26] J. Davoudi and J. Schumacher, Stretching of polymers around the Kolmogorov scale in a turbulent shear flow, Phys. Fluids **18**, 025103 (2006).
[27] A. P. Kazantsev, Enhancement of a magnetic field by a conducting fluid, Sov. Phys. JETP **26**, 1031 (1968).
[28] R. H. Kraichnan, Small-scale structure of a scalar field convected by turbulence, Phys. Fluids **11**, 945 (1968).
[29] G. Falkovich, K. Gawędzki, and M. Vergassola, Particles and fields in turbulence, Rev. Mod. Phys. **73**, 913 (2001).
[30] A. Celani, S. Musacchio, and D. Vincenzi, Polymer transport in random flow, J. Stat. Phys. **118**, 531 (2005).
[31] M. Chertkov, Polymer Stretching by Turbulence, Phys. Rev. Lett. **84**, 4761 (2000).
[32] Note that here τ is half the relaxation time used in Refs. [9,19,20,30,31]; hence, the same holds for the Weissenberg number. In addition, the vector $f(R)\boldsymbol{R}$ is denoted as $\boldsymbol{F}(\boldsymbol{R})$ in Ref. [20].
[33] Y. Le Jan, Exposants de Lyapunov pour les mouvements browniens isotropes, C. R. Acad. Sci. Paris Ser. I **299**, 949 (1984).
[34] Y. Le Jan, On isotropic Brownian motions, Z. Wahrscheinlichkeitstheor. verw. Gebiete **70**, 609 (1985).
[35] H. Risken, *The Fokker-Planck Equation: Methods of Solution and Applications* (Springer, Berlin/Heidelberg/New York, 1989).
[36] U. Frisch, *Turbulence: The Legacy of A. N. Kolmogorov* (Cambridge University Press, Cambridge, England, 1995).

[37] M. De Lucia, A. Mazzino, and A. Vulpiani, Dumb-bell model for polymer transport in laminar flows, Europhys. Lett. **60**, 181 (2002).

[38] M. F. Piva and S. Gabanelli, A single dumbbell falling under gravity in a cellular flow field, J. Phys. A: Math. Gen. **36**, 4291 (2003).

[39] K. Gawędzki and M. Vergassola, Phase transition in the passive scalar advection, Physica D **138**, 63 (2000).

[40] H. P. Robertson, The invariant theory of isotropic turbulence, Math. Proc. Cambridge Phil. Soc. **36**, 209 (1940).

[41] A. S. Monin and A. M. Yaglom, *Statistical Fluid Mechanics* (Dover, Mineola, New York, 1975), Vol. 2.

[42] I. S. Gradshteyn and I. M. Ryzhik, *Table of Integrals, Series, and Products* (Academic Press, New York, 1980).

[43] M. Abramowitz and I. A. Stegun, *Handbook of Mathematical Functions* (Dover, New York, 1965).

[44] J. Bec, M. Cencini, and R. Hillerbrand, Clustering of heavy particles in random self-similar flow, Phys. Rev. E **75**, 025301(R) (2007).

PHYSICAL REVIEW E **94**, 020501(R) (2016)

Bead-rod-spring models in random flows

Emmanuel Lance Christopher VI Medillo Plan,[1] Aamir Ali,[1,2] and Dario Vincenzi[1]
[1]*Laboratoire Jean Alexandre Dieudonné, Université Nice Sophia Antipolis, CNRS, 06108 Nice, France*
[2]*Department of Mathematics, COMSATS Institute of Information Technology, Attock 43600, Pakistan*
(Received 9 May 2016; published 3 August 2016)

Bead-rod-spring models are the foundation of the kinetic theory of polymer solutions. We derive the diffusion equation for the probability density function of the configuration of a general bead-rod-spring model in short-correlated Gaussian random flows. Under isotropic conditions, we solve this equation analytically for the elastic rhombus model introduced by Curtiss, Bird, and Hassager [Adv. Chem. Phys. **35**, 31 (1976)].

DOI: 10.1103/PhysRevE.94.020501

The study of polymer solutions generally requires a coarse-grained description of a polymer molecule. A successful and well-established approach consists in using bead-rod-spring models, where a polymer is described as a sequence of beads connected by rigid or elastic links [1–4]. By selecting the number of beads and the nature of the links, it is possible to build flexible, semiflexible, or rigid molecules with various internal structures. Bead-rod-spring models play a central role across several fields, including rheology, non-Newtonian fluid mechanics, chemical physics, and soft matter [1,5]. Analytical solutions of these models represent an essential step towards the derivation of constitutive equations and hence the prediction of the non-Newtonian properties of polymeric fluids [1–3,6]. However, in spite of their conceptual simplicity, the internal dynamics of bead-rod-spring models may be exceedingly complex. For this reason bead-rod-spring models have been solved analytically only in simplified settings. In the case of laminar flows, analytical results are restricted to linear velocity fields with elementary time dependence, namely steady, start-up, or oscillatory extensional and shear flows [1–3]. In the case of randomly fluctuating flows, exact solutions are only available for dumbbells, which are simply composed of two beads and a single elastic or rigid link [7–17]. Nevertheless, in recent years there has been a growing interest in the Lagrangian dynamics of complex-shaped objects in turbulent flows, such as elastic polymers [18,19], triaxial ellipsoids [20], flexible fibers [21], crosses and jacks [22], isotropic helicoids and four-bead particles [23], and chiral dipoles [24]. It is therefore important to advance the analytical tools needed for the study of this problem. Here we first derive the diffusion equation for the probability distribution of the configuration of a general bead-rod-spring polymer in a Gaussian random flow with short correlation time. Short-correlated stochastic fields have been widely employed in the theoretical study of turbulent flows and have yielded fundamental results on passive-scalar mixing and the turbulent dynamo [25]; moreover, they have been used to predict the coil-stretch transition of polymers in turbulent flows [9] and the associated critical slowdown [14]. By using the aforementioned diffusion equation, we then analytically calculate the stationary configuration of the elastic rhombus model in an isotropic random flow. The rhombus model was introduced by Curtiss, Bird, and Hassager [26] and is a prototype of a finitely extensible multibead polymer that includes both elastic and rigid internal links.

We start by briefly recalling the diffusion equation for the probability density function (PDF) of the configuration of a bead-rod-spring polymer following Refs. [1,3]. Consider N spherical beads with mass m_μ, $\mu = 1,\ldots,N$. Let $\boldsymbol{x}_\mu$ denote the position vector of the μth bead with respect to a space-fixed coordinate system. The position of the center of mass of the polymer is $\boldsymbol{x}_c = \sum_\mu m_\mu \boldsymbol{x}_\mu / \sum_\mu m_\mu$, and the position vector of the μth bead referred to the center of mass is $\boldsymbol{r}_\mu = \boldsymbol{x}_\mu - \boldsymbol{x}_c$. The polymer is immersed in a Newtonian fluid, whose motion is described by the incompressible velocity field $\boldsymbol{u}(\boldsymbol{x},t)$. The velocity gradient, $\boldsymbol{\kappa} = \nabla \boldsymbol{u}$, $\kappa^{ij} = \partial u^i/\partial x^j$, is assumed to be uniform over the length of the polymer. If the flow is turbulent, this assumption means that the size of the polymer is much smaller than the viscous-dissipation scale. The force of the flow on bead μ is given by Stokes's law with drag coefficient ζ_μ; the inertia of the beads is disregarded. Furthermore, the concentration of the solution is sufficiently small for polymer-polymer hydrodynamic interactions to be negligible, and the flow is unperturbed by the presence of polymers.

Assume that the beads are subject to D' rigidity constraints. Then, the number of degrees of freedom of the polymer in the frame of reference of the center of mass is $D = d(N-1) - D'$, where d is the dimension of the flow. It is therefore convenient to specify the configuration of the polymer in terms of D coordinates $\boldsymbol{q} = (q^1,\ldots,q^D)$, which describe its degrees of freedom. The statistics of the coordinates $\boldsymbol{q}$ is given by the PDF $\psi(\boldsymbol{q};t)$.

We define the tensors $\boldsymbol{\zeta}_{\mu\nu}$ implicitly from the equation $\sum_\nu \boldsymbol{\zeta}_{\mu\nu}\cdot(\zeta_\nu^{-1}\delta_{\nu\mu'}\mathsf{I} + \boldsymbol{\Omega}_{\nu\mu'}) = \delta_{\mu\mu'}\mathsf{I}$, where $\delta_{\mu\mu'}$ is the Kronecker δ, I is the identity matrix, and the tensors $\boldsymbol{\Omega}_{\nu\mu}$ describe the hydrodynamic interactions between the μth and the νth bead (in the simplest approximation $\boldsymbol{\Omega}_{\mu\nu}$ is the Oseen tensor). Define also the tensors $\mathsf{Z} = \sum_{\mu\nu}\boldsymbol{\zeta}_{\mu\nu}$, $\boldsymbol{\Lambda}_\nu = \mathsf{Z}^{-1}\cdot\sum_\mu \boldsymbol{\zeta}_{\mu\nu}$, and $\widetilde{\boldsymbol{\zeta}}_{\mu\nu} = \boldsymbol{\zeta}_{\mu\nu} - \boldsymbol{\Lambda}_\mu^{\mathrm{T}}\cdot\mathsf{Z}\cdot\boldsymbol{\Lambda}_\nu$. Finally, $\boldsymbol{f}_{\mu\nu}$ is the force exerted by the νth bead over the μth one through the springs and f_μ is the external force on bead μ (which is assumed to be independent of $\boldsymbol{x}_c$). Then, $\psi(\boldsymbol{q};t)$ satisfies the diffusion equation [1,3] (summation over repeated indices is understood throughout):

$$\frac{\partial\psi}{\partial t} = -\frac{\partial}{\partial q^i}\left(\widetilde{\mathsf{G}}^{ij}\left\{[\mathsf{M}^{jkl}\kappa^{kl}(t) + F^j + \mathfrak{F}^j]\psi - KT\sqrt{h}\frac{\partial}{\partial q^j}\left(\frac{\psi}{\sqrt{h}}\right)\right\}\right), \tag{1}$$

where K is the Boltzmann constant, T is temperature,

$$\mathsf{M}^{jkl} = r_\nu^l\frac{\partial r_\mu^m}{\partial q^j}\widetilde{\zeta}_{\mu\nu}^{mk}, \quad F^j = \sum_\nu f_{\mu\nu}^k\frac{\partial r_\mu^k}{\partial q^j}, \quad \mathfrak{F}^j = \mathsf{f}_\mu^k\frac{\partial r_\mu^k}{\partial q^j}, \tag{2}$$

$h = \det(\mathsf{H})$, and $\widetilde{\mathsf{G}} = \widetilde{\mathsf{H}}^{-1}$ with

$$\mathsf{H}^{ij} = m_\mu \frac{\partial r_\mu^k}{\partial q^i}\frac{\partial r_\mu^k}{\partial q^j}, \qquad \widetilde{\mathsf{H}}^{ij} = \widetilde{\zeta}_{\mu\nu}^{kl}\frac{\partial r_\mu^k}{\partial q^i}\frac{\partial r_\nu^l}{\partial q^j}. \tag{3}$$

The stationary solution of Eq. (1) can be calculated exactly when hydrodynamic bead-bead interactions are negligible ($\boldsymbol{\Omega}_{\mu\nu} = 0$ for all $\mu,\nu = 1,\ldots,N$) or equilibrium averaged ($\boldsymbol{\Omega}_{\mu\nu}$ is replaced with its average value at equilibrium) and the velocity gradient is time independent and symmetric ($\boldsymbol{\kappa} = \boldsymbol{\kappa}^{\mathrm{T}}$) [1,26]. For other flows, Bird *et al.* [1] note that the analytical solution of Eq. (1) is in general a formidable problem.

Let us consider the case in which the velocity gradient fluctuates randomly in time, as in turbulent flows. Assume that $\boldsymbol{\kappa}(t)$ is a δ-correlated-in-time $(d\times d)$-dimensional Gaussian stochastic process with zero mean and correlation: $\langle \kappa^{kl}(t)\kappa^{mn}(t')\rangle = \mathsf{K}^{klmn}\delta(t-t')$, where the specific form of the tensor K depends on the statistical symmetries of the flow. Equation (1) is now stochastic and describes the evolution of $\psi(\boldsymbol{q};t)$ for a given realization of the flow; $\boldsymbol{\kappa}(t)$ is a multiplicative noise and is interpreted in the Stratonovich sense. Under this assumption on the velocity gradient, the stochastic differential equation associated with Eq. (1) is (see Ref. [28])

$$dq^i = A^i\,dt + \mathsf{B}^{ij}\circ dW^j(t) + \mathsf{C}^{ikl}\circ d\Gamma^{kl}(t), \tag{4}$$

where $\boldsymbol{W}(t)$ is D-dimensional Brownian motion and $\boldsymbol{\Gamma}(t)$ is such that $\boldsymbol{\kappa}(t) = d\boldsymbol{\Gamma}(t)/dt$, i.e., $\boldsymbol{\Gamma}(t)$ is a Gaussian process with $\langle\Gamma^{kl}(t)\rangle = 0$ and $\langle\Gamma^{kl}(t)\Gamma^{mn}(t')\rangle = \mathsf{K}^{klmn}\min(t,t')$ [27]. The symbol $\circ$ indicates that the stochastic differential equation is interpreted in the Stratonovich sense. The coefficients are

$$A^i = \widetilde{\mathsf{G}}^{ij}(F^j + \mathfrak{F}^j) + KT\frac{\beta^{ia}}{\sqrt{h}}\frac{\partial}{\partial q^j}(\sqrt{h}\,\beta^{ja}), \tag{5}$$

$$\mathsf{B}^{ij} = \sqrt{2KT}\beta^{ij}, \quad \mathsf{C}^{ikl} = \widetilde{\mathsf{G}}^{ij}\mathsf{M}^{jkl}. \tag{6}$$

In the above equations, $\boldsymbol{\beta}$ is such that $\boldsymbol{\beta}\boldsymbol{\beta}^{\mathrm{T}} = \widetilde{\mathsf{G}}$ (it is assumed that $\widetilde{\mathsf{G}}$ is positive definite—this condition is easily verified when the masses and the drag coefficients are the same for all beads). The Itô form of Eq. (4) is (see Appendix A):

$$dq^i = \left(A^i + \frac{1}{2}\mathsf{B}^{ja}\frac{\partial \mathsf{B}^{ia}}{\partial q^j} + \frac{1}{2}\mathsf{K}^{klmn}\mathsf{C}^{jmn}\frac{\partial \mathsf{C}^{ikl}}{\partial q^j}\right)dt + \mathsf{B}^{ij}\,dW^j(t) + \mathsf{C}^{ikl}\,d\Gamma^{kl}(t). \tag{7}$$

We denote by $p(\boldsymbol{q};t)$ the PDF of the configuration of the polymer with respect to the realizations both of the velocity gradient and of thermal noise. The diffusion equation corresponding to Eq. (7) is (see Appendix A):

$$\frac{\partial p}{\partial t} = -\frac{\partial}{\partial q^i}\left[\left(A^i + \frac{1}{2}\mathsf{B}^{ja}\frac{\partial \mathsf{B}^{ia}}{\partial q^j} + \frac{1}{2}\mathsf{K}^{klmn}\mathsf{C}^{jmn}\frac{\partial \mathsf{C}^{ikl}}{\partial q^j}\right)p\right] + KT\frac{\partial^2}{\partial q^i\partial q^j}(\widetilde{\mathsf{G}}^{ij}p) + \frac{\mathsf{K}^{klmn}}{2}\frac{\partial^2}{\partial q^i\partial q^j}(\mathsf{C}^{ikl}\mathsf{C}^{jmn}p). \tag{8}$$

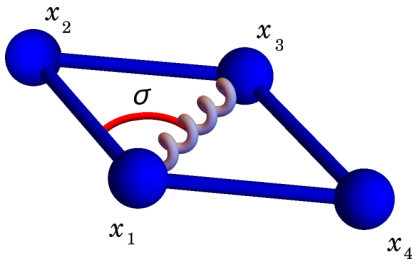

FIG. 1. The elastic plane rhombus.

Rearranging the terms in Eq. (8), we obtain

$$\frac{\partial p}{\partial t} = \frac{\partial}{\partial q^i}\left\{\frac{1}{2}\mathsf{K}^{klmn}\widetilde{\mathsf{G}}^{ia}\mathsf{M}^{akl}\frac{\partial}{\partial q^j}(\widetilde{\mathsf{G}}^{jb}\mathsf{M}^{bmn}p) + \widetilde{\mathsf{G}}^{ij}\left[-(F^j+\mathfrak{F}^j)p + KT\sqrt{h}\frac{\partial}{\partial q^j}\left(\frac{p}{\sqrt{h}}\right)\right]\right\}. \tag{9}$$

Equation (9) determines the evolution of the PDF of the configuration of a general bead-rod-spring model in a short-correlated Gaussian flow. Note that Eq. (9) can also be derived by applying Gaussian integration by parts [29] to Eq. (1).

We now consider a bead-rod-spring model for which the stationary solution of Eq. (9) can be calculated exactly. The elastic plane rhombus model was introduced by Curtiss, Bird, and Hassager [26]. It describes a finitely extensible polymer and consists of four coplanar identical beads connected by four rods and an elastic spring between two opposing beads (Fig. 1). The angle $0 \leqslant \sigma \leqslant \pi/2$ between the spring and one of the rods describes the deformation of the rhombus. The spring is at rest if the rods are perpendicular to each other. If $\sigma \neq \pi/4$, the spring stretches or compresses the rhombus back to its equilibrium; the force that it exerts on the beads is given by the harmonic potential $\phi(\sigma) = A(\sqrt{2}\cos\sigma - 1)^2/2$. Let $m_\mu = m, \zeta_\mu = \zeta$ for all $\mu = 1,\ldots,4$ and ℓ be the length of the rods. In addition, hydrodynamical bead-bead interactions are disregarded ($\boldsymbol{\Omega}_{\mu\nu} = 0$), and no external forces act on the polymer ($\mathfrak{f}_\mu = 0$). Under these assumptions, we have $\boldsymbol{\zeta}_{\mu\nu} = \zeta\delta_{\mu\nu}\mathsf{I}, \boldsymbol{\mathfrak{F}} = 0$, and

$$\mathsf{M}^{jkl} = \zeta r_\mu^l\frac{\partial r_\mu^k}{\partial q^j}, \quad F^j = -\frac{\partial\phi}{\partial q^j}, \quad \widetilde{\mathsf{H}}^{ij} = \zeta\frac{\partial r_\mu^k}{\partial q^i}\frac{\partial r_\mu^k}{\partial q^j}. \tag{10}$$

The contribution of the rhombic particles to the viscoelastic properties of a solution, such as the normal stress coefficient and the viscosity, have been calculated exactly [26]. In particular, the addition of n rhombuses increases the viscosity by $3n\zeta\ell^2$. This result also holds for other variants of the rhombus model, namely the freely jointed and the rigid models. The normal stress coefficient of the polymer solution, by contrast, varies according to the flexibility of the rhombus. A fully elastic rhombus model has been used to investigate the motion of deformable active particles [30]. The rhombus model could also be used to examine how deformability influences the alignment and orientation statistics of microscopic particles in turbulent flows [31].

If the random flow is incompressible and statistically invariant under rotations and reflections, the components of K take

the form $\mathsf{K}^{ijkl} = 2\lambda[(d+1)\delta^{ik}\delta^{jl} - \delta^{ij}\delta^{kl} - \delta^{il}\delta^{jk}]/[d(d-1)]$, where λ is the maximum Lyapunov exponent of the flow [25]. Denoting $\mathsf{G} = \zeta\widetilde{\mathsf{G}}$, we write Eq. (8) as a Fokker–Planck equation [28]:

$$\frac{\partial p}{\partial t} = -\frac{\partial}{\partial q^i}(V^i p) + \frac{1}{2}\frac{\partial^2}{\partial q^i \partial q^j}(D^{ij} p), \tag{11}$$

where the drift and diffusion coefficients are

$$V^i = \frac{1}{2}\mathsf{K}^{klmn}\mathsf{G}^{jb} r_\nu^n \frac{\partial r_\nu^m}{\partial q^b}\frac{\partial}{\partial q^j}\left(\mathsf{G}^{ia} r_\mu^l \frac{\partial r_\mu^k}{\partial q^a}\right) - \frac{\mathsf{G}^{ij}}{\zeta}\frac{\partial \phi}{\partial q^j} + \frac{KT}{\zeta\sqrt{h}}\frac{\partial}{\partial q^j}(\mathsf{G}^{ij}\sqrt{h}), \tag{12}$$

and

$$D^{ij} = \mathsf{K}^{klmn}\mathsf{G}^{ia} r_\mu^l \frac{\partial r_\mu^k}{\partial q^a}\mathsf{G}^{jb} r_\nu^n \frac{\partial r_\nu^m}{\partial q^b} + \frac{2\mathsf{G}^{ij} KT}{\zeta}. \tag{13}$$

In the case of a two-dimensional flow ($d = 2$), the rhombus may be described by $\boldsymbol{q} = (\theta, \sigma)$, where θ gives the orientation of $\boldsymbol{x}_3 - \boldsymbol{x}_1$ with respect to the horizontal axis. The vectors $\boldsymbol{r}_\mu$ can be expressed as

$$\boldsymbol{r}_1 = \ell(-\cos\theta\cos\sigma, -\sin\theta\cos\sigma) = -\boldsymbol{r}_3, \tag{14}$$

$$\boldsymbol{r}_2 = \ell(-\sin\theta\sin\sigma, \cos\theta\sin\sigma) = -\boldsymbol{r}_4. \tag{15}$$

We also have $\mathsf{G}^{ij} = \delta_{ij}/2\ell^2$ and $h = 4\ell^2$. After time is rescaled by the characteristic time scale of the restoring potential $\tau_\mathrm{p} = \zeta\ell^2/A$ and Eqs. (14) and (15) are replaced into Eqs. (12) and (13), the drift and diffusion coefficients in Eq. (11) become

$$V^\sigma = -(\sqrt{2} - 2\cos\sigma)\sin\sigma/2, \tag{16}$$

$$D^{\theta\theta} = Z^{-1} + \mathrm{Wi}\,(5 + \cos 4\sigma)/2, \tag{17}$$

$$D^{\sigma\sigma} = Z^{-1} + \mathrm{Wi}\,(1 - \cos 4\sigma)/2, \tag{18}$$

$$V^\theta = D^{\sigma\theta} = D^{\theta\sigma} = 0, \tag{19}$$

where $Z = A/KT$ is the stiffness parameter and the Weissenberg number $\mathrm{Wi} = \lambda\tau_\mathrm{p}$ measures the relative strength of the flow to that of the restoring potential $\phi(\sigma)$. The fact that all the coefficients are independent of θ reflects the isotropy of the flow and implies that the long-time PDF of the configuration is a function of σ alone. Given reflecting boundary conditions at $\sigma = 0$ and $\sigma = \pi/2$, the stationary PDF $p_\mathrm{st}(\sigma)$ can be analytically calculated to be [28]

$$p_\mathrm{st}(\sigma) \propto \frac{1}{D^{\sigma\sigma}}\exp\left(2\int_0^\sigma \frac{V^\sigma(\omega)}{D^{\sigma\sigma}(\omega)}\,d\omega\right). \tag{20}$$

We can evaluate the integral in Eq. (20) by using Eqs. (3.3.23) and (4.6.22) of Ref. [32], whence the explicit form of the PDF of σ is

$$p_\mathrm{st}(\sigma) \propto \frac{1}{D^{\sigma\sigma}}\left|\frac{C_\sigma^2 - C_+^2}{C_\sigma^2 + C_-^2}\right|^{Z/4C_1}\exp\left\{\frac{Z\sqrt{\mathrm{Wi}\,Z}}{2C_1}\times\left[\frac{\mathrm{arctanh}(C_\sigma/C_+)}{C_+} + \frac{\arctan(C_\sigma/C_-)}{C_-}\right]\right\} \tag{21}$$

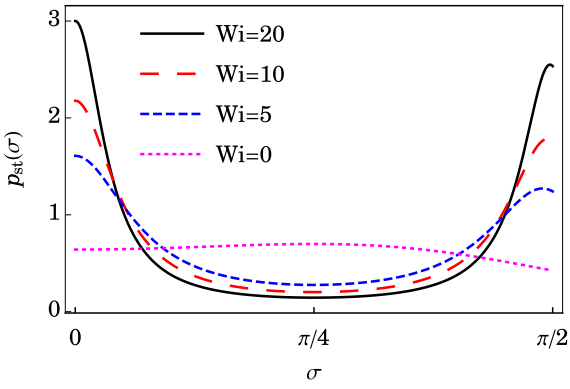

FIG. 2. Stationary PDF $p_\mathrm{st}(\sigma)$ for $d = 2$ and $Z = 1$, normalized such that $\int p_\mathrm{st}(\sigma)\,d\sigma = 1$.

with $C_\sigma = \sqrt{2\mathrm{Wi}\,Z}\cos\sigma$, $C_1 = \sqrt{\mathrm{Wi}\,Z(\mathrm{Wi}\,Z+1)}$, and $C_\pm = \sqrt{C_1 \pm \mathrm{Wi}\,Z}$. Figure 2 illustrates the graph of $p_\mathrm{st}(\sigma)$ for $Z = 1$ and different values of Wi.

The probability of the rhombus being fully stretched ($\sigma = 0$) or fully compressed ($\sigma = \pi/2$) increases with Wi; i.e., the rhombus exhibits an almost rodlike configuration when a very strong flow dominates the dynamics. However, the stretched configuration is favored compared to the compressed one, because the restoring force is weaker for $\sigma = 0$ than for $\sigma = \pi/2$.

In a three-dimensional flow, the number of degrees of freedom of the elastic planar rhombus is $D = 4$. We consider $\boldsymbol{q} = (\alpha, \beta, \gamma, \sigma)$, where the first three coordinates are the Euler angles used to define the configuration of the rhombus in a fixed frame of reference. The details on the definition of the Euler angles, as well as the explicit expressions of G and h, can be found in Refs. [1,26]. Note that our G differs from that of Ref. [26] by a factor of m. The PDF $p(\boldsymbol{q})$ of the configuration again satisfies Eq. (11), where V^i and D^{ij} are given in Appendix B. In view of the isotropy of the flow, we assume that the stationary PDF of the configuration takes the form $p_\mathrm{st}(\boldsymbol{q}) = \tilde{p}(\sigma)\sin\beta\sin 2\sigma$, where the factor $\sin\beta\sin 2\sigma$ is proportional to the Jacobian of the coordinate transformation from $\boldsymbol{r}_\mu$ to $\boldsymbol{q}$. Substituting $p_\mathrm{st}(\boldsymbol{q})$ into Eq. (11) results into a Fokker-Planck equation in the variable σ alone:

$$0 = \frac{\partial p_\mathrm{st}(\boldsymbol{q})}{\partial s} = -\frac{\partial}{\partial\sigma}(V^\sigma p_\mathrm{st}) + \frac{1}{2}\frac{\partial^2}{\partial\sigma^2}(D^{\sigma\sigma} p_\mathrm{st}), \tag{22}$$

where $s = t/\tau_\mathrm{p}$, $V^\sigma = \cot 2\sigma/Z - (\sqrt{2} - 2\cos\sigma)\sin\sigma/2$, and $D^{\sigma\sigma} = Z^{-1} + \mathrm{Wi}\,(1 - \cos 4\sigma)/4$. The partial derivatives with respect to the Euler angles indeed cancel each other. Under reflecting boundary conditions at $\sigma = 0$ and $\sigma = \pi/2$, the solution of Eq. (22) takes the form given in Eq. (20) with modified expressions for V^σ and $D^{\sigma\sigma}$ [28]. Invoking again Eqs. (3.3.23) and (4.6.22) of Ref. [32], we derive the exact form of the stationary PDF of σ in three dimensions:

$$\tilde{p}(\sigma) \propto \frac{1}{D^{\sigma\sigma}\sqrt{\mathrm{Wi}\,Z\sin^2 2\sigma + 2}}\left|\frac{C_\sigma^2 - C_+^2}{C_\sigma^2 + C_-^2}\right|^{Z/4C_1}\times\exp\left\{\frac{Z\sqrt{\mathrm{Wi}\,Z/2}}{2C_1}\left[\frac{\mathrm{arctanh}(C_\sigma/C_+)}{C_+} + \frac{\arctan(C_\sigma/C_-)}{C_-}\right]\right\} \tag{23}$$

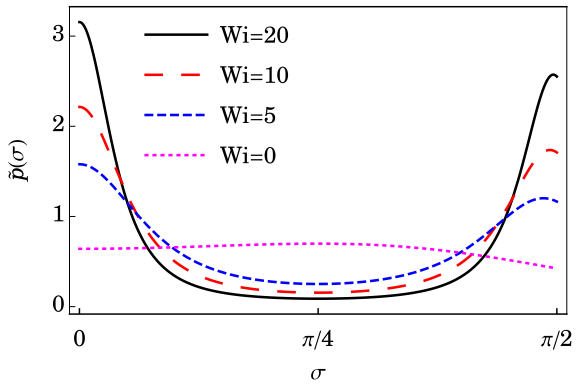

FIG. 3. The function $\tilde{p}(\sigma)$ for $d = 3$ and $Z = 1$, normalized such that $\int \tilde{p}(\sigma) \sin 2\sigma \, d\sigma = 1$.

with $C_\sigma = \sqrt{\mathrm{Wi}\, Z} \cos\sigma$, $C_1 = \sqrt{\mathrm{Wi}\, Z(\mathrm{Wi}\, Z + 2)}/2$, and $C_\pm = \sqrt{C_1 \pm \mathrm{Wi}\, Z/2}$. The graph of $\tilde{p}(\sigma)$ is shown in Fig. 3.

The statistics of the internal angle σ is qualitatively the same for $d = 2$ and $d = 3$ (the curves in Figs. 2 and 3 indeed differ only slightly for the same Wi). This behavior is attributed to the fact that the rhombus can only deform in the plane to which it belongs and cannot undergo three-dimensional deformations, which makes its dynamics weakly sensitive to the dimension of the flow.

Bead-rod-spring models are the foundation of the kinetic theory of polymer solutions. There is a broad literature on the analytic solutions of these models for laminar flows. In the case of fluctuating flows, such as turbulent flows, analytical results are restricted to dumbbells. We have given a general description of bead-rod-spring models in short-correlated random flows. In addition, we have exactly solved the elastic rhombus model under isotropic conditions. To the best of our knowledge, this is the first instance of an exact solution of a multibead model that include both elastic and rigid links and is transported by a randomly fluctuating flow. We hope that the tools developed here will stimulate new studies on the dynamics of complex-shaped particles in turbulent flows. The stretching dynamics of bead-spring chains has also received attention in the context of nonequilibrium statistical mechanics [33]; the probability of work and entropy production have been studied for laminar gradient flows [34–37]. It would be interesting to generalize those studies to the case considered here, where the velocity gradient is a tensorial noise (see, e.g., Ref. [38]).

The authors are grateful to S. S. Ray for useful suggestions. The work of A.A. and E.L.C.M.P. was supported by EACEA through the Erasmus Mundus Mobility with Asia program. E.L.C.M.P. and D.V. acknowledge the support of the EU COST Action MP 1305 "Flowing Matter".

APPENDIX A: DERIVATION OF EQS. (7) AND (8).

The Itô version of Eq. (4) can be derived formally by generalizing the standard transformation rules for stochastic differential equations (see, e.g., Refs. [28,39]) to tensorial Brownian motion. Let us assume that the Itô version is

$$dq^i(t) = \mathfrak{A}^i \, dt + \mathfrak{B}^{ij} \, dW^j(t) + \mathfrak{C}^{ikl} \, d\Gamma^{kl}(t), \tag{A1}$$

where the coefficients $\mathfrak{A},\mathfrak{B},\mathfrak{C}$ are to be determined. We first write Eq. (4) in integral form:

$$q^i(t) = q^i(t_0) + \int_{t_0}^{t} A^i \, dt' + \int_{t_0}^{t} \mathsf{B}^{ia} \circ dW^a(t') + \int_{t_0}^{t} \mathsf{C}^{ikl} \circ d\Gamma^{kl}(t'). \tag{A2}$$

Consider a partition of $[t_0,t]$ into N subintervals $[t_{\tau-1},t_\tau], \tau = 1,\dots,N$. The Stratonovich integrals in Eq. (A2) are, by definition,

$$\int_{t_0}^{t} \mathsf{B}^{ia} \circ dW^a(t') = \lim_{N\to\infty} \sum_{\tau=1}^{N} \mathsf{B}^{ia}\big(\boldsymbol{q}_\tau^{\mathrm{S}}, t_{\tau-1}\big) \Delta W_\tau^a, \tag{A3}$$

$$\int_{t_0}^{t} \mathsf{C}^{ikl} \circ d\Gamma^{kl}(t') = \lim_{N\to\infty} \sum_{\tau=1}^{N} \mathsf{C}^{ikl}\big(\boldsymbol{q}_\tau^{\mathrm{S}}, t_{\tau-1}\big) \Delta \Gamma_\tau^{kl}, \tag{A4}$$

where the limits are understood in the mean square, $\boldsymbol{q}_\tau^{\mathrm{S}} = (\boldsymbol{q}_\tau + \boldsymbol{q}_{\tau-1})/2$, $\boldsymbol{q}_\tau = \boldsymbol{q}(t_\tau)$, $\Delta W_\tau^a = W^a(t_\tau) - W^a(t_{\tau-1})$, and $\Delta\Gamma_\tau^{kl} = \Gamma^{kl}(t_\tau) - \Gamma^{kl}(t_{\tau-1})$. We also introduce the notations $\Delta t_\tau = t_\tau - t_{\tau-1}$ and $\mathsf{X}_\tau^I = \mathsf{X}^I(\boldsymbol{q}_\tau, t_\tau)$ for any tensor X and set of indices I. Define $\Delta\boldsymbol{q}_{\tau-1} = \boldsymbol{q}_\tau - \boldsymbol{q}_{\tau-1}$, whence $\boldsymbol{q}_\tau^{\mathrm{S}} = \boldsymbol{q}_{\tau-1} + \Delta\boldsymbol{q}_{\tau-1}/2$. Expanding the coefficients in Eqs. (A3) and (A4) at $\boldsymbol{q}_{\tau-1}$ yields

$$\mathsf{B}^{ia}\big(\boldsymbol{q}_\tau^{\mathrm{S}}, t_{\tau-1}\big) = \mathsf{B}_{\tau-1}^{ia} + \frac{\Delta q_{\tau-1}^j}{2} \frac{\partial \mathsf{B}_{\tau-1}^{ia}}{\partial q^j} + \text{h.o.t.}, \tag{A5}$$

$$\mathsf{C}^{ikl}\big(\boldsymbol{q}_\tau^{\mathrm{S}}, t_{\tau-1}\big) = \mathsf{C}_{\tau-1}^{ikl} + \frac{\Delta q_{\tau-1}^j}{2} \frac{\partial \mathsf{C}_{\tau-1}^{ikl}}{\partial q^j} + \text{h.o.t.}, \tag{A6}$$

where h.o.t. refers to higher order terms. We now write $\Delta q_{\tau-1}^j$ according to its Itô discretization:

$$\Delta q_{\tau-1}^j = \mathfrak{A}_{\tau-1}^j \Delta t_\tau + \mathfrak{B}_{\tau-1}^{ja} \Delta W_\tau^a + \mathfrak{C}_{\tau-1}^{jmn} \Delta\Gamma_\tau^{mn} + \text{h.o.t.} \tag{A7}$$

After substituting Eqs. (A5), (A6), and (A7) into Eqs. (A3) and (A4) and using the formal rules $\Delta\Gamma^{kl} \times \Delta\Gamma^{mn} = \mathsf{K}^{klmn} \Delta t$, $\Delta W^j \times \Delta W^a = \delta^{ja} \Delta t$, and $\Delta W^j \times \Delta\Gamma^{kl} = 0$ (owing to the independence of the velocity gradient and thermal noise), we can write Eqs. (A3) and (A4) as

$$\int_{t_0}^{t} \mathsf{B}^{ia} \circ dW^a(t') = \lim_{N\to\infty} \sum_{\tau=1}^{N} \left(\mathsf{B}_{\tau-1}^{ia} \, \Delta W_\tau^a + \frac{\mathfrak{B}_{\tau-1}^{ja}}{2} \frac{\partial \mathsf{B}_{\tau-1}^{ia}}{\partial q^j} \, \Delta t \right),$$

$$\int_{t_0}^{t} \mathsf{C}^{ikl} \circ d\Gamma^{kl}(t') = \lim_{N\to\infty} \sum_{\tau=1}^{N} \left(\mathsf{C}_{\tau-1}^{ikl} \, \Delta\Gamma_\tau^{kl} + \frac{1}{2} \mathsf{K}^{klmn} \mathfrak{C}_{\tau-1}^{jmn} \frac{\partial \mathsf{C}_{\tau-1}^{ikl}}{\partial q^j} \Delta t \right).$$

The first terms in the sums yield Itô stochastic integrals, whereas the second terms give ordinary integrals; hence,

$$\int_{t_0}^{t} \mathsf{B}^{ia} \circ dW^a(t') = \int_{t_0}^{t} \mathsf{B}^{ia}\, dW^a(t') + \int_{t_0}^{t} \frac{\mathfrak{B}^{ja}}{2} \frac{\partial \mathsf{B}^{ia}}{\partial q^j}\, dt',$$

$$\int_{t_0}^{t} \mathsf{C}^{ikl} \circ d\Gamma^{kl}(t') = \int_{t_0}^{t} \mathsf{C}^{ikl} d\Gamma^{kl}(t') + \int_{t_0}^{t} \mathsf{K}^{klmn} \mathfrak{C}^{jmn} \frac{\partial \mathsf{C}^{ikl}}{\partial q^j} dt'.$$

Therefore, for Eq. (A1) to be equivalent to Eq. (4), the coefficients must satisfy $\mathfrak{B} = \mathsf{B}$, $\mathfrak{C} = \mathsf{C}$, and

$$\mathfrak{A}^i = A^i + \frac{1}{2}\mathsf{B}^{ja} \frac{\partial \mathsf{B}^{ia}}{\partial q^j} + \frac{1}{2}\mathsf{K}^{klmn}\mathsf{C}^{jmn} \frac{\partial \mathsf{C}^{ikl}}{\partial q^j}.$$

We now derive the diffusion equation (8). Let $f(\boldsymbol{q})$ be a function of $\boldsymbol{q}$. We first generalize Itô's lemma for a tensorial Brownian motion. By expansion, we have

$$f(\boldsymbol{q} + \Delta\boldsymbol{q}) - f(\boldsymbol{q}) = \Delta q^i \frac{\partial f}{\partial q^i} + \frac{\Delta q^i \Delta q^j}{2} \frac{\partial^2 f}{\partial q^i \partial q^j} + \text{h.o.t.}$$

By substituting Δq^i and Δq^j from Eq. (A1) and using the formal rules as above, we obtain

$$\frac{df}{dt} = \left[\mathfrak{A}^i + \mathfrak{B}^{ia} \frac{dW^a(t)}{dt} + \mathfrak{C}^{ikl} \frac{d\Gamma^{kl}(t)}{dt}\right] \frac{\partial f}{\partial q^i} + \frac{1}{2}(\mathfrak{B}^{ia}\mathfrak{B}^{ja} + \mathsf{K}^{klmn}\mathfrak{C}^{ikl}\mathfrak{C}^{jmn}) \frac{\partial^2 f}{\partial q^i \partial q^j}. \quad \text{(A8)}$$

By taking the average over the noises and by using the properties of the Itô integral, we have

$$\left\langle \frac{df}{dt} \right\rangle = \frac{d}{dt}\langle f \rangle = \int f\left(\frac{\partial p}{\partial t}\right) d\boldsymbol{q}, = \int \left[\mathfrak{A}^i \frac{\partial f}{\partial q^i} + \frac{1}{2}(\mathfrak{B}^{ia}\mathfrak{B}^{ja} + \mathsf{K}^{klmn}\mathfrak{C}^{ikl}\mathfrak{C}^{jmn}) \frac{\partial^2 f}{\partial q^i \partial q^j}\right] p\, d\boldsymbol{q}. \quad \text{(A9)}$$

Integrating the right-hand side by parts gives

$$\int f\left(\frac{\partial p}{\partial t}\right) d\boldsymbol{q} = \int f\left[-\frac{\partial}{\partial q^i}(\mathfrak{A}^i p) + \frac{1}{2}\frac{\partial^2}{\partial q^i \partial q^j} \times (\mathfrak{B}^{ia}\mathfrak{B}^{ja} p + \mathsf{K}^{klmn}\mathfrak{C}^{ikl}\mathfrak{C}^{jmn} p)\right] d\boldsymbol{q}. \quad \text{(A10)}$$

Since $f(\boldsymbol{q})$ is arbitrary, the expressions inside the brackets should be equal. This gives Eq. (8) when $\mathfrak{A}, \mathfrak{B}$, and $\mathfrak{C}$ are chosen as above.

APPENDIX B: COEFFICIENTS OF THE DIFFUSION EQUATION

In this Appendix, we give the the drift and diffusion coefficients of Eq. (11) for the three-dimensional elastic rhombus model. After the time variable is rescaled by τ_p, the drift coefficients V^i become

$$\begin{aligned}
V^\alpha &= 2\sin 2\gamma \cot\beta \csc\beta \cot 2\sigma \csc 2\sigma / Z,\\
V^\beta &= \cot\beta \csc^2 2\sigma [(1 + \cos 2\gamma \cos 2\sigma)/Z \\
&\quad + \mathrm{Wi}(1 - \cos 4\sigma)/3],\\
V^\gamma &= -(3 + \cos 2\beta) \csc^2\beta \cot 2\sigma \csc 2\sigma \sin 2\gamma / 2Z,\\
V^\sigma &= \cot 2\sigma / Z - (\sqrt{2} - 2\cos\sigma)\sin\sigma/2.
\end{aligned}$$

The diffusion coefficients D^{ij} are:

$$\begin{aligned}
D^{\alpha\alpha} &= 4\csc 2\beta\, V^\beta,\\
D^{\alpha\beta} &= -\tan\beta\, V^\alpha,\\
D^{\alpha\gamma} &= -2\csc\beta\, V^\beta,\\
D^{\beta\beta} &= (\cos^2\gamma \sec^2\sigma + \sin^2\gamma \csc^2\sigma)/Z + 4\mathrm{Wi}/3,\\
D^{\beta\gamma} &= \sin\beta\, V^\alpha,\\
D^{\gamma\gamma} &= 48\csc^2 2\sigma \{24[4(\cos 2\gamma \cos 2\sigma \cot^2\beta + \csc^2\beta \\
&\quad - \cos 4\sigma) - 3]/Z + \mathrm{Wi}[-3\cos 8\sigma + 12\cos 4\sigma \\
&\quad + 32\csc^2\beta(1 - \cos 4\sigma) - 9]\},\\
D^{\sigma\sigma} &= Z^{-1} + \mathrm{Wi}\,(1 - \cos 4\sigma)/4.
\end{aligned}$$

By symmetry, $D^{\beta\alpha} = D^{\alpha\beta}, D^{\gamma\alpha} = D^{\alpha\gamma}, D^{\gamma\beta} = D^{\beta\gamma}$. All the other coefficients are zero.

[1] R. B. Bird, C. F. Curtiss, R. C. Armstrong, and O. Hassager, *Dynamics of Polymeric Liquids* (John Wiley and Sons, New York, 1977), Vol. 2.
[2] M. Doi and S. F. Edwards, *The Theory of Polymer Dynamics* (Oxford University Press, Oxford, UK, 1988).
[3] H. C. Öttinger, *Stochastic Processes in Polymeric Fluids* (Springer, Berlin, Germany, 1996).
[4] C. Cruz, F. Chinesta, and G. Réigner, Arch. Comput. Methods Eng. **19**, 227 (2012).
[5] R. G. Larson, *The Structure and Rheology of Complex Fluids* (Oxford University Press, Oxford, UK, 1999).
[6] R. G. Larson, J. Rheol. **49**, 1 (2005).
[7] E. S. G. Shaqfeh and D. L. Koch, J. Fluid Mech. **244**, 17 (1992).
[8] M. Chertkov, Phys. Rev. Lett. **84**, 4761 (2000).
[9] E. Balkovsky, A. Fouxon, and V. Lebedev, Phys. Rev. Lett. **84**, 4765 (2000).
[10] J.-L. Thiffeault, Phys. Lett. A **308**, 445 (2003).
[11] A. Celani, S. Musacchio, and D. Vincenzi, J. Stat. Phys. **118**, 531 (2005).
[12] M. Chertkov, I. Kolokolov, V. Lebedev, and K. Turitsyn, J. Fluid Mech. **531**, 251 (2005).
[13] M. Martins Afonso and D. Vincenzi, J. Fluid Mech. **540**, 99 (2005).

[14] A. Celani, A. Puliafito, and D. Vincenzi, Phys. Rev. Lett. **97**, 118301 (2006).
[15] D. Vincenzi, S. Jin, E. Bodenschatz, and L. R. Collins, Phys. Rev. Lett. **98**, 024503 (2007).
[16] K. S. Turitsyn, J. Exp. Theor. Phys. **105**, 655 (2007).
[17] A. Ahmad and D. Vincenzi, Phys. Rev. E **93**, 052605 (2016).
[18] T. Watanabe and T. Gotoh, Phys. Rev. E **81**, 066301 (2010).
[19] Y. Liu and V. Steinberg, Macromol. Symp. **337**, 34 (2014).
[20] L. Chevillard and C. Meneveau, J. Fluid Mech. **737**, 571 (2013).
[21] C. Brouzet, G. Verhille, and P. Le Gal, Phys. Rev. Lett. **112**, 074501 (2014).
[22] G. G. Marcus, S. Parsa, S. Kramel, R. Ni, and G. A. Voth, New J. Phys. **16**, 102001 (2014).
[23] K. Gustavsson and L. Biferale, Proceedings of the 15th European Turbulence Conference (25–28 August, Delft, 2015), No. 103 (unpublished), http://www.etc15.nl/proceedings/proceedings/documents/103.pdf.
[24] S. Kramel, S. Tympel, F. Toschi, and G. A. Voth, arXiv:1602.07413 (unpublished).
[25] G. Falkovich, K. Gawędzki, and M. Vergassola, Rev. Mod. Phys. **73**, 913 (2001).
[26] C. F. Curtiss, R. B. Bird, and O. Hassager, in *Advances in Chemical Physics*, Vol. 35, edited by I. Prigogine and S. A. Rice (John Wiley & Sons, NJ, 1976), pp. 31–117.
[27] Equation (4) may also be written as $dq^i = A^i dt + \mathsf{Q}^{ij} \circ d\eta^j(t)$, where $\boldsymbol{\eta}$ is D-dimensional Brownian motion and $(\mathsf{Q}\mathsf{Q}^\top)^{ij} = \mathsf{B}^{ia}\mathsf{B}^{ja} + \mathsf{K}^{klmn}\mathsf{C}^{ikl}\mathsf{C}^{jmn}$. The thermal and velocity fluctuations would thus be merged into a single noise and the prefactor Q^{ij} would contain the information on the correlations of the random medium.
[28] C. W. Gardiner, *Handbook of Stochastic Methods* (Springer, Berlin, Germany, 1985).
[29] U. Frisch, *Turbulence: The Legacy of A. N. Kolmogorov* (Cambridge University Press, Cambridge, UK, 1995).
[30] N. Küchler, H. Löwen, and A. M. Menzel, Phys. Rev. E **93**, 022610 (2016).
[31] S. Parsa, E. Calzavarini, F. Toschi, and G. A. Voth, Phys. Rev. Lett. **109**, 134501 (2012).
[32] M. Abramowitz and I. A. Stegun, *Handbook of Mathematical Functions* (National Bureau of Standards, U.S. Government Printing Office, Washington, DC, 1964).
[33] A. Dhar, Phys. Rev. E **71**, 036126 (2005).
[34] K. Turitsyn, M. Chertkov, V. Y. Chernyak, and A. Puliafito, Phys. Rev. Lett. **98**, 180603 (2007).
[35] R. Sharma and B. J. Cherayil, Phys. Rev. E **83**, 041805 (2011).
[36] F. Latinwo, K.-W. Hsiao, and C. M. Schroeder, J. Chem. Phys. **141**, 174903 (2014).
[37] M. Vucelja, K. S. Turitsyn, and M. Chertkov, Phys. Rev. E **91**, 022123 (2015).
[38] R. Chetrite and K. Gawędzki, Commun. Math. Phys. **282**, 469 (2008).
[39] P. E. Kloeden and E. Platen, *Numerical Solutions of Stochastic Differential Equations* (Springer, Berlin, Germany, 1999).

Preferential Sampling of Elastic Chains in Turbulent Flows

Jason R. Picardo,[1,*] Dario Vincenzi,[2,†] Nairita Pal,[3,‡] and Samriddhi Sankar Ray[1,§]

[1] *International Centre for Theoretical Sciences, Tata Institute of Fundamental Research, Bangalore 560089, India*
[2] *Université Côte d'Azur, CNRS, LJAD, Nice 06100, France*
[3] *Center for Nonlinear Studies, Los Alamos National Laboratory, Los Alamos, NM 87545, U.S.A.*

A string of tracers, interacting elastically, in a turbulent flow is shown to have a dramatically different behaviour when compared to the non-interacting case. In particular, such an elastic chain shows strong preferential sampling of the turbulent flow unlike the usual tracer limit: an elastic chain is trapped in the vortical regions and not the straining ones. The degree of preferential sampling and its dependence on the elasticity of the chain is quantified via the Okubo-Weiss parameter. The effect of modifying the deformability of the chain, via the number of links that form it, is also examined.

PACS numbers: 47.27.Gs, 05.20.Jj

The development of Lagrangian techniques, in experiments and theory, have lead to major advances in our understanding of the complexity of turbulent flows, especially at small scales [1–3]. What makes this possible is the use of tracer particles which uniformly sample the flow and hence access the complete phase space in which the dynamics resides. This feature of tracers depends, crucially, on the assumption that the particles remain *inertia-less* and *point-like*. When some of these assumptions are relaxed, it may lead to dissipative particle dynamics and preferential sampling of the structures in a flow [4–10]. This is, for instance, the case for heavy, inertial particles, which show small-scale clustering and concentrate away from vortical regions. Various phenomena can influence the properties of inertial clustering in turbulence, such as gravity [11, 12], turbophoresis [13, 14], or the non-Newtonian nature of the fluid [15]. Preferential sampling in turbulent flows may also emerge as a result of the motility of particles, as in the case of gyrotactic [16], interacting [17], or jumping [18] micro-swimmers.

We now propose a novel mechanism for preferential sampling in turbulent flows which is induced by extensibility. A simple model of an extensible object which retains enough internal structure is a chain of tracers with an elastic coupling between the nearest neighbours. We show, remarkably, that turning on such elastic interactions amongst tracers leads to very different dynamics: unlike the case of non-interacting tracers, an elastic chain preferentially samples vortical regions of the flow. We perform a systematic study of this phenomenon and quantify, via the Okubo-Weiss parameter, the level of preferential sampling and its dependence on the elasticity and deformability of the chain.

Harmonic chains have been at the heart of several important problems in the areas of equilibrium and non-equilibrium statistical physics. These have ranged from problems in crystalline to amorphous transitions [19], electrical and thermal transport both in and out-of-equilibrium [20], as well as understanding structural properties of disordered and random systems [21]. Given the ubiquity and usefulness of the elastic chain, it is surprising that the effect of a turbulent medium on *long* chains has not been studied as extensively as in other areas of non-equilibrium statistical physics.

There is another reason why this study is important. The last decade or more has seen tremendous advances in our understanding of heavy inertial particles and their dynamics. These were helped primarily by the pioneering results on the issue of preferential concentration, which plays a dominant role in every aspect of turbulent transport. In contrast, similar studies of extended objects such as fibers are recent [22–25], even though they are just as important and common place in nature and industry. However, the effect of elasticity, which is intrinsic to extensible objects (just as inertia is to finite-sized particles), in determining their dynamics in a turbulent flow is an open question. In this paper, we settle this question through a model which is amenable to detailed numerical simulations.

We consider a chain of N_b identical beads, with negligible inertia, connected through (phantom) elastic links with its nearest left and right neighbours; the two end beads are free. If $\boldsymbol{x}_1, \ldots, \boldsymbol{x}_{N_\mathrm{b}}$ denote the positions of the beads, the position of the center of mass of the chain is $\boldsymbol{X}_c = (\boldsymbol{x}_1 + \cdots + \boldsymbol{x}_{N_\mathrm{b}})/N_\mathrm{b}$, and $\boldsymbol{r}_i = \boldsymbol{x}_{i+1} - \boldsymbol{x}_i$ $(i = 1, \ldots, N_\mathrm{b} - 1)$ are the vector displacements between the i-th and $(i+1)$-th bead. Then the equations of motion for the chain in a velocity field $\boldsymbol{u}(\boldsymbol{x}, t)$ are:

$$\dot{\boldsymbol{X}}_c = \frac{1}{N_\mathrm{b}} \left[\sum_{i=1}^{N_\mathrm{b}} \boldsymbol{u}(\boldsymbol{x}_i, t) + \sqrt{\frac{r_0^2}{2\tau}} \sum_{i=1}^{N_\mathrm{b}} \boldsymbol{\xi}_i(t) \right] \tag{1a}$$

$$\dot{\boldsymbol{r}}_j = \boldsymbol{u}(\boldsymbol{x}_{j+1}, t) - \boldsymbol{u}(\boldsymbol{x}_j, t) + \sqrt{\frac{r_0^2}{2\tau}} \left[\boldsymbol{\xi}_{j+1}(t) - \boldsymbol{\xi}_j(t) \right] - \frac{1}{4\tau} (2 f_j \boldsymbol{r}_j - f_{j+1} \boldsymbol{r}_{j+1} - f_{j-1} \boldsymbol{r}_{j-1}) \tag{1b}$$

with $f_j = (1 - |\boldsymbol{r}_j|^2 / r_\mathrm{m}^2)^{-1}$ and $j = 1, .., N_\mathrm{b} - 1$. The nonlinear elastic links are characterised by their relaxation time τ and maximum length r_m, which, in turn, determines the maximum or contour chain length $L_\mathrm{m} = N_\mathrm{L} r_\mathrm{m}$ ($N_\mathrm{L} = N_\mathrm{b} - 1$ is the number of links). Thus, at any given instant in time, the length of the

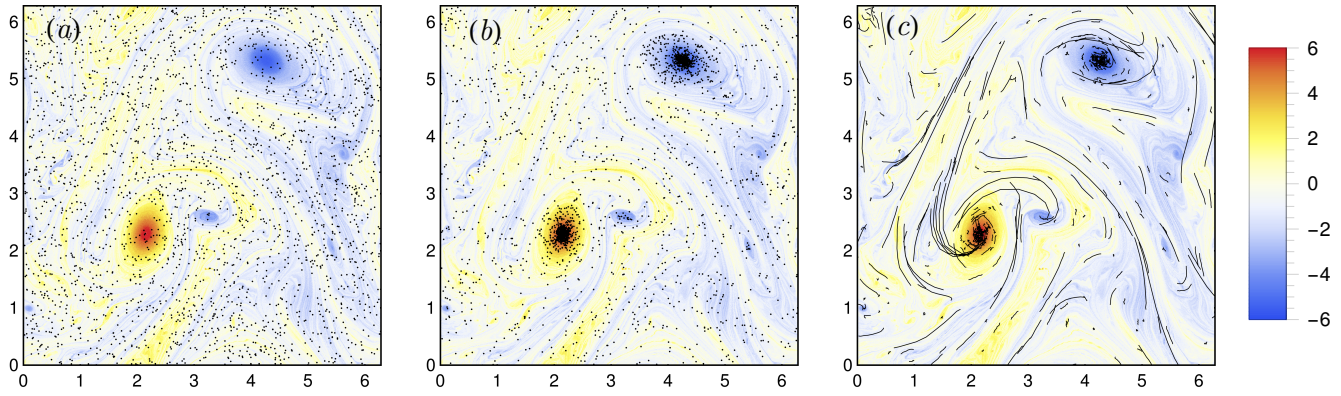

FIG. 1. Representative snapshots showing the positions of a subset of chains ($N_{\rm L} = 9$ and $L_{\rm m} = 4$) overlaid on the vorticity field of the carrier turbulent flow (with $\ell_f = 2$ and $t_f = 2.3$). Panels (a) and (b) show the centers of mass of the chains for $Wi = 0.04$ and $Wi = 0.9$ respectively. Panel (c) shows entire chains for $Wi = 0.9$. Parameter values: $\nu = 10^{-6}$, $\mu = 10^{-2}$, and $F_0 = 0.2$.

chain $R \equiv \sum_j^{N_{\rm L}} r_j < L_{\rm m}$. The thermal fluctuations on each bead are modelled by independent white noises $\boldsymbol{\xi}_i(t)$ ($i = 1, \ldots, N_{\rm b}$), whose amplitude r_0 sets the equilibrium length of the chain in the absence of flow. Although the effect of thermal fluctuations on the motion of the center of mass is negligible in a turbulent flow, their effect on the separation vectors is essential: thermal fluctuations prevent the chain from collapsing into a point-like particle and hence a tracer. Finally, inter-bead hydrodynamic interactions are ignored.

When the separations between the beads are small enough for the velocity differences to be approximated as $\boldsymbol{u}(\boldsymbol{x}_{j+1}, t) - \boldsymbol{u}(\boldsymbol{x}_j, t) \approx \nabla \boldsymbol{u}(t) \cdot \boldsymbol{r}_j$, Eqs. (1) reduce to one of the most common bead-spring models in polymer physics, namely the Rouse model with FENE (finitely extensible nonlinear elastic) springs [26, 27]. Such a model is thus appropriate when the carrier flow is linear in space; in a turbulent flow this requires the size of the links to be smaller than the viscous scale at all times [28–31]. By considering the full velocity difference between adjacent beads, Eqs. (1) generalize the usual bead-spring models and describe an elastic chain that may extend into the inertial range of turbulence or even beyond the integral scale (see Refs. [32–35] for an analogous generalization of the dumbbell ($N_{\rm b} = 2$) model).

What is the effect of a turbulent velocity field $\boldsymbol{u}$ on the motion of such chains? To answer this, we solve, by using a pseudo-spectral method with a 2/3 de-aliasing rule, the two-dimensional Navier-Stokes equation on a square grid with 1024^2 collocation points and 2π periodic boundary conditions. We drive the system to a homogeneous and isotropic, turbulent, statistically steady state through an external, deterministic force $f = -F_0 k_f \cos(k_f x)$ (F_0 is the amplitude and k_f the energy-injection scale in Fourier space, which sets the typical size of the vortices $\ell_f = 2\pi k_f^{-1}$). Forcing at small wavenumbers ensures that the vortices are fairly large: this allows us to clearly illustrate the issues of preferential sampling which are central to this work. We use a small Ekmann-friction coefficient μ (in addition to a coefficient of kinematic viscosity ν) to prevent pile-up of energy at the large scales due to inverse cascade. Consequently the turbulent flow is in the direct-cascade regime. The definition of ℓ_f also allows us to characterise the stretching ability of the flow in terms of the dimension-less Weissenberg number $Wi = \tau/t_f$, where $t_f = \ell_f/\sqrt{2E}$ is the turnover time scale of the large vortices (E is the mean kinetic energy of the flow).

The temporal evolution of the chain (Eqs. (1)) is done by a second-order Runge-Kutta scheme, augmented by a rejection algorithm [27] to avoid numerical instabilities due to the divergence of the nonlinear force for $|\boldsymbol{r}_j|$ approaching $r_{\rm m}$. A bilinear scheme is used to interpolate, from the Eulerian grid, the fluid velocity at the typically off-grid positions of the beads [36, 37]. In order to observe the regime of preferential sampling, we choose parameters for the chain which ensure that its equilibrium length in a quiescent flow is similar to the enstrophy dissipation scale, while $\ell_f < L_{\rm m} < 2\pi$.

This model of an elastic chain in a turbulent flow is the ideal setting, theoretically and numerically, to investigate the natural interplay between the relative importance of Lagrangian (uniform) mixing and the elasticity of the links. It is this competing effect that leads to a surprising preferential sampling of the flow by the chain, hitherto not observed.

To illustrate this phenomenon, we begin by randomly seeding 5×10^4 chains into the flow and study their evolution in time for different Wi. (We evolve a large number of chains simultaneously for the purpose of visualizing their sampling behaviour and for obtaining good statistics of the chain dynamics; we do not describe the collective motion of an ensemble of chains, which would interact with each other hydrodynamically or by direct

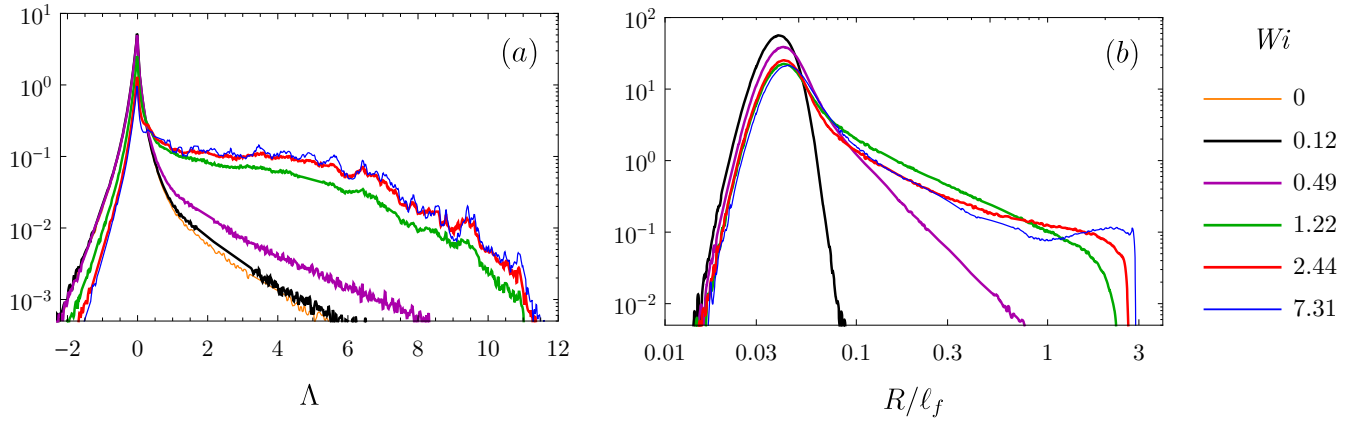

FIG. 2. Lagrangian pdfs of (a) the Okubo-Wiess parameter Λ and (b) the scaled lengths of the chains R/ℓ_f for different values of Wi. Parameter values: $\ell_f = 1.25, t_f = 1.35, L_m = 3.75, N_L = 9$, $\nu = 10^{-6}$, $\mu = 10^{-2}$, and $F_0 = 0.2$.

contact.) In Fig. 1 we show the center-of-mass positions at an instant of time overlaid on the vorticity field of the turbulent flow for $Wi = 0.04$ and $Wi = 0.9$. It is immediately apparent that for the case of small elasticity the chains behave like tracers and distribute evenly (Fig. 1(a)). However, for larger Wi there is a preferential sampling of the vortical regions (Fig. 1(b)).

Figure 1(c) demonstrates the coupling between the translational and the extensional dynamics of the chain by showing a snapshot in which the entire chains, and not just the centers of mass, are overlaid on the vorticity field. This figure emphasises the strong correlation between the positions of elongated chains with regions of low vorticity, where the straining flow stretches out the chains. In contrast, the chains that encounter vortices tend to curl up and contract to a much smaller size. These strikingly different phenomena are best seen in a video of the time evolution of the chains [38]. All of this suggests the following picture: a stretched chain is more likely to leave straining zones and coil up in vortical regions.

The above observations can be quantified via a Lagrangian approach by measuring the statistics of the extension R and the Okubo-Weiss parameter Λ along the trajectories of the centers of mass of the chains. We recall that $\Lambda = (\omega^2 - \sigma^2)/4\langle\omega^2\rangle$, where ω is the vorticity and σ is the strain rate, is the discriminant of the characteristic equation for $\nabla \boldsymbol{u}$ and is here rescaled with the mean enstrophy. The sign of Λ uniquely determines the local flow geometry: For positive Λ, the flow is vortical; for negative Λ it is extensional [36, 39]. Values of Λ near zero correspond to either a weak amplitude of $\nabla \boldsymbol{u}$ or to a shearing flow, which has comparable amounts of vorticity and straining.

In Fig. 2 we show the Lagrangian probability distribution function (pdf) of (a) Λ and (b) R for different values of Wi. The Λ distribution for tracers ($Wi = 0$) is also shown for comparison (its positive skewness is a consequence of the strongest velocity gradients occurring in intense vortical zones [40–42]). We find strong quantitative evidence that increasing elasticity leads to a chain preferentially sampling vortical regions of the flow (Fig. 2(a)). This is accompanied by an increase in the probability of highly stretched configurations (Fig. 2(b)).

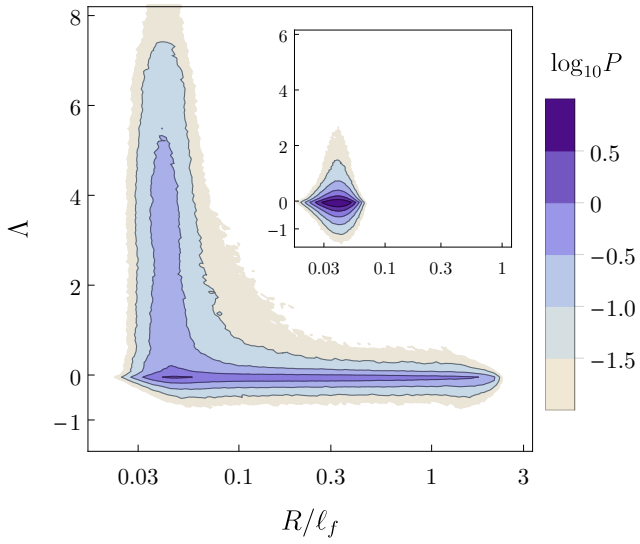

FIG. 3. Joint pdf of Λ sampled by the centers of mass of the chains and R/ℓ_f for $Wi = 1.22$ and (inset) $Wi = 0.12$.

The key to understanding the phenomenon of preferential sampling lies in the correlation between the translational and the extensional dynamics of a chain. This is quantified through the joint pdf $P(R, \Lambda)$, which shows that when its center of mass is in vortical regions, a chain is in a contracted state (Fig. 3). The velocity terms in Eq. (1a) can therefore be Taylor-expanded about $\boldsymbol{X}_c(t)$, and Eq. (1a) reduces to the equation of motion of a tracer. Thence, the center of mass follows the flow and remains trapped in the vortex. Contrastingly, away from vortical

regions, i.e., in straining or shearing regions, an extensible chain is highly stretched (Fig. 3). As time proceeds, a large-Wi chain stretches to lengths so long that eventually it is unable to follow the rapidly evolving straining zones. On departing from these zones, such a chain is likely to encounter a vortex and begin to coil up (seen clearly in the video [38]). The links of the chain that enter the vortex shrink and follow the rotational flow, eventually leading to the entrapment of the entire chain within the vortex. A stiff chain (small-Wi), which remains short in straining zones, samples the negative values of Λ more, leading to annular contours (Fig. 3, inset).

The stretching out of a chain in straining zones may thus be seen as a precursor to its entrapment inside vortices. This explains why strong preferential sampling of vortices occurs only when Wi is so large that there is a significant probability for chains to be stretched beyond ℓ_f (see Fig. 2 for $Wi = 0.49, 1.22$). On the other hand, if the maximum length $L_m < \ell_f$, then one would expect this mechanism to fail and the chain to uniformly sample the flow for all Wi. We have confirmed this hypothesis in our simulations but do not show the results for brevity.

The results, so far, suggest a complete picture for the dynamics of an elastic chain in a turbulent flow: A chain with a sufficient degree of elasticity—defined as the ratio of elastic and fluid time scales—preferentially samples the flow. But is this effect truly independent of the characteristic *length* scales present in the system? The short answer is no, and the ability of a chain to preferentially sample the flow is determined by the relative magnitudes of its typical inter-bead separation (which for a fixed value of L_m depends only on N_b) and the characteristic fluid length scale ℓ_f.

For large values of Wi, as we have seen, the typical inter-bead separation approaches L_m/N_L. For the results reported so far, N_b was such that $L_m/N_L \ll \ell_f$. As N_b decreases, however, we will eventually obtain characteristic inter-bead separations of the order of $L_m/N_L > \ell_f$. In this setting, typically, no two neighboring beads will be able to reside in a vortex simultaneously. Hence the mechanism for preferential sampling will fail, and the chain will start sampling the flow uniformly once more. This suggests that, apart from the role of elasticity, the dynamics of a chain for large values of Wi ought to depend on a second dimensionless number $\Phi \equiv L_\mathrm{m}/(N_\mathrm{L}\ell_f)$, such that for $\Phi > 1$ there should be uniform sampling, while for $\Phi < 1$ preferential sampling.

Direct evidence for this is presented in Fig. 4, which shows the mean value of the Okubo-Wiess parameter, $\langle\Lambda\rangle$, as a function of Wi, for different values of Φ. For smaller Φ, there is an increase in $\langle\Lambda\rangle$ that eventually saturates for $Wi \gtrsim 5$. However, for larger values of Φ, $\langle\Lambda\rangle$ increases initially [43]—indicating preferential sampling of the vortical regions of the flow—before decreasing again to reflect uniform sampling (see video [44]). The chain, however, continues to stretch as the elasticity increases

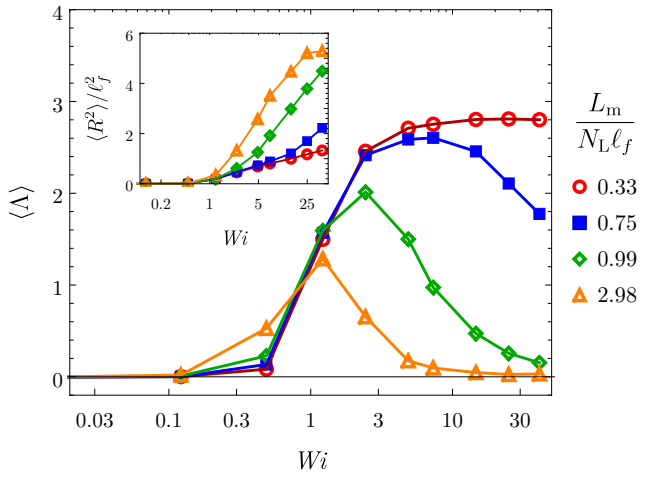

FIG. 4. $\langle\Lambda\rangle$ vs Wi for different values of $\Phi \equiv L_\mathrm{m}/(N_\mathrm{L}\ell_f)$; we use $N_\mathrm{L} = 9$, 4, 2, and 1 (dumbbell), while keeping $L_\mathrm{m} = 3.75$ and $\ell_f = 1.25$ fixed. Inset: The variance of R/ℓ_f vs Wi. The flow parameters are the same as those in Fig. 2.

for all values of Φ, and its mean square extension does not show any non-monotonic behavior (inset of Fig. 4). At large Wi a chain is indeed typically longer for larger values of Φ owing to the reduced level of preferential sampling of vortices and correspondingly lower probability of being in a contracted state.

Figure 4 lends itself to an intuitively appealing picture of the motion of a chain. For a given turbulent flow (characterised by t_f and ℓ_f), whether or not a chain of a given elasticity and maximum length L_m may coil—and hence preferentially sample—depends on the number of links which form the chain. In particular, for a highly extended chain (large Wi), decreasing the number of links limits the ability of the chain to coil up into vortices. This result highlights the importance of *deformability* of extensible chains. In our study, we have considered a freely-jointed chain. However, the bending stiffness of the chain may be modeled by introducing a potential force that is a function of the internal angle between neighboring links and restores them to an anti-parallel configuration [26]. Such stiffness would prevent the chain from coiling up and, therefore, would reduce preferential sampling in a manner analogous to that of increasing Φ in our freely-jointed model.

The elastic chain is a simplified model for various physical systems, which include, *inter alia*, fibers, microtubules, and algae in marine environments. Such systems of course present additional properties that were not taken into account here, such as the inertia and the stiffness of the system, hydrodynamic and excluded-volume interactions between different portions of it, and the modification of the flow generated by the motion of the system. These effects will certainly change quantita-

tive details of the dynamics, but the mechanism at the origin of preferential sampling identified here is of general validity. It indeed relies on a few basic ingredients: the system must be extensible, its equilibrium size should be smaller than ℓ_f and its contour length greater than ℓ_f.

Before we conclude, it is also important to stress that we chose two-dimensional turbulent flows to take advantage of their long-lived vortical structures, which help to convincingly illustrate these new phenomena of preferential sampling; needless to say the mechanism itself is independent of whether the flow is two- or three-dimensional. Finally, we cannot avoid mentioning that the preferential concentration of inertial particles through dissipative dynamics is completely different from the mechanism that we report here. Hence it is tempting to investigate the interplay between the competing effects of inertia and elasticity in future studies of inertial extensible objects in turbulent flows.

We thank Abhishek Dhar, Anupam Kundu, and Rahul Pandit for useful suggestions and discussions. We acknowledge the support of the Indo-French Centre for Applied Mathematics (IFCAM). SSR acknowledges DST (India) project ECR/2015/000361 for financial support. JRP acknowledges travel support from the ICTS Infosys Collaboration grant. The simulations were performed on the ICTS clusters *Mowgli* and *Mario*, as well as the work stations from the project ECR/2015/000361: *Goopy* and *Bagha*.

* jrpicardo@icts.res.in
† dario.vincenzi@unice.fr
‡ nairitap2009@gmail.com
§ samriddhisankarray@gmail.com

[1] P. K. Yeung, Annu. Rev. Fluid Mech. **34**, 115 (2002).
[2] F. Toschi and E. Bodenschatz, Annu. Rev. Fluid Mech. **41**, 375 (2009).
[3] J. P. L. C. Salazar and L. R. Collins, Annu. Rev. Fluid Mech. **41**, 405 (2009).
[4] E. K. Longmire and J. K. Eaton, J. Fluid Mech. **236**, 217 (1992)
[5] J. Bec, Phys. Fluids **15**, 81 (2003); J. Fluid Mech. **528**, 255 (2005).
[6] J. Bec. A. Celani, M. Cencini, and S. Musacchio, Phys. Fluids **17**, 073301 (2005).
[7] J. Chun, D. L. Koch, S. L. Rani, A. Ahluwalia, and L. R. Collins, J. Fluid Mech. **536**, 219 (2005).
[8] J. Bec, L. Biferale, M. Cencini, A. Lanotte, S. Musacchio, and F. Toschi, Phys. Rev. Lett. **98**, 084502 (2007).
[9] R. Monchaux, M. Bourgoin, and A. Cartellier, Int. J. Multiphase Flow **40**, 1 (2012).
[10] K. Gustavsson and B. Mehlig, Adv. Phys. **65**, 1 (2016).
[11] J. Bec, H. Homann, and S. S. Ray, Phys. Rev. Lett. **112**, 184501 (2014).
[12] G. H. Good, P. J Ireland, G. P. Bewley, E. Bodenschatz, L. R. Collins, and Z. Warhaft, J. Fluid Mech. **759**, R3 (2014).
[13] S. Belan, I. Fouxon, and G. Falkovich, Phys. Rev. Lett. **112**, 234502 (2014).
[14] F. De Lillo, M. Cencini, S. Musacchio, and G. Boffetta Phys. Fluids **28**, 035104 (2016).
[15] F. De Lillo, G. Boffetta, S. Musacchio, Phys. Rev. E **85**, 036308 (2012).
[16] W. M. Durham, E. Climent, M. Barry, F. De Lillo, G. Boffetta, M. Cencini, and R. Stocker, Nature Communications **4**, 2148 (2013).
[17] A. Choudhary, D. Venkataraman, and S. S. Ray, Europhys. Lett. **112**, 24005 (2015).
[18] I. Benkeddad, F. G. Schmitt, S. Souissi, F. Toschi and E. Calzavarini, Phys. Rev. E **93**, 043117 (2016).
[19] Z. H. Stachurski, Materials **4**, 1564 (2011); B. Illing, S. Fritschi, H. Kaiser, C. L. Klix, G. Maret, and P. Keim Proc. Nat. Acad. Sci. **114**, 1856 (2017).
[20] A Dhar, Phys. Rev. Lett. **86**, 5882 (2001); S. Lepri, R. Livi, A. Politi, Phys. Rep. **377**, 1 (2003); A Dhar, Adv. Phys. **57**, 457 (2008); A. Kundu, S. Sabhapandit, and A. Dhar, J. Stat. Mech., P03007 (2011).
[21] A. M. Mayes, Macromolecules **27**, 3114 (1994); K. Binder, J. Baschnagel, and W. Paul, Prog. Polymer Sc. **28**, 115 (2003); P. Chaudhuri, S. Karmakar, C. Dasgupta, H. R. Krishnamurthy, and A. K. Sood, Phys. Rev. Lett., **95**, 248301 (2005); T. Sridhar, D. A. Nguyen, R. Prabhakar, and J. R. Prakash, Phys. Rev. Lett. **98**, 167801 (2007).
[22] C. Brouzet, G. Verhille, and P. Le Gal, Phys. Rev. Lett. **112**, 074501 (2014).
[23] G. Verhille and A. Bartoli, Exp. Fluids **57**, 117 (2016).
[24] M. E. Rosti, A. A. Banaci, L. Brandt, and A. Mazzino, Phys. Rev. Lett. **121**, 044501 (2018).
[25] S. Allende, C. Henry, and J. Bec, arXiv:1805.05731
[26] R. B. Bird, C. F. Curtiss, R. C. Armstrong, and O. Hassager, *Dynamics of Polymeric Liquids* (John Wiley and Sons, New York, 1977), Vol. 2
[27] H. C. Öttinger, *Stochastic Processes in Polymeric Fluids* (Springer, Berlin, Germany, 1996).
[28] Q. Zhou and R. Akhavan, J. Non-Newtonian Fluid Mech. **109**, 115 (2003).
[29] V. K. Gupta, R. Sureshkumar, and B. Khomami, Phys. Fluids **16**, 1546 (2004).
[30] J. Jin and L. R. Collins, New J. Phys. **9**, 360 (2007).
[31] T. Watanabe and T. Gotoh, Phys. Rev. E **81**, 066301 (2010).
[32] M. De Lucia, A. Mazzino, and A. Vulpiani, Europhys. Lett. **60**, 181 (2002).
[33] M. F. Piva and S. Gabanelli, J. Phys. A: Math. Gen. **36**, 4291 (2003).
[34] J. Davoudi and J. Schumacher, Phys. Fluids **18**, 025103 (2006).
[35] A. Ahmad and D. Vincenzi, Phys. Rev. E **93**, 052605 (2016).
[36] P. Perlekar, S. S. Ray, D. Mitra, and R. Pandit, Phys. Rev. Lett. **106** 054501 (2011).
[37] M. James and S. S. Ray, Sci. Rep. **7**, 12231 (2017)
[38] `https://youtu.be/etLuK6ovAqk`
[39] A. Okubo, Deep-Sea Res. Oceanogr. Abstr. **17**, 445 (1970); J. Weiss, Physica (Amsterdam) **48D**, 273 (1991).
[40] P. Perlekar and R. Pandit, New J. Phys. **11**, 073003 (2011)
[41] A. Gupta, P. Perlekar, and R. Pandit, Phys. Rev. E **91**, 033013 (2015)

[42] D. Mitra and P. Perlekar, Phys. Rev. Fluids **3**, 044303 (2018)
[43] See also Refs. [32, 33] for dumbbells in cellular flows.
[44] Online movie showing uniform sampling of highly stretched dumbbells: `https://youtu.be/YdFXMFFU1qU`

Annexe D

Flexion

D1. E.L.C. VI M. Plan & D. Vincenzi
Tumbling of a Brownian particle in an extensional flow
Proc. R. Soc. A **472**, 20160226 (2016)

D2. A. Ali, E.L.C. VI M. Plan, S.S. Ray & D. Vincenzi
Semi-flexible particles in isotropic turbulence
Phys. Rev. Fluids **1**, 082402(R) (2016)

PROCEEDINGS A

rspa.royalsocietypublishing.org

Research

Cite this article: Plan ELC VI M, Vincenzi D. 2016 Tumbling of a Brownian particle in an extensional flow. *Proc. R. Soc. A* **472**: 20160226. http://dx.doi.org/10.1098/rspa.2016.0226

Received: 30 March 2016
Accepted: 5 September 2016

Subject Areas:
fluid mechanics, chaos theory

Keywords:
tumbling, extensional flow, trumbbell

Author for correspondence:
Emmanuel Lance Christopher VI Medillo Plan
e-mail: elcplan@unice.fr

Electronic supplementary material is available online at http://dx.doi.org/10.6084/m9.figshare.c.3473661.

THE ROYAL SOCIETY PUBLISHING

Tumbling of a Brownian particle in an extensional flow

Emmanuel Lance Christopher VI Medillo Plan and Dario Vincenzi

Laboratoire J. A. Dieudonné, Université Nice Sophia Antipolis, CNRS, 06108 Nice, France

ELCVIMP, 0000-0003-2268-424X

The phenomenon of tumbling of microscopic objects is commonly associated with shear flows. We address the question of whether tumbling can also occur in stretching-dominated flows. To answer this, we study the dynamics of a semi-flexible trumbbell in a planar extensional velocity field. We show that the trumbbell undergoes a random tumbling-through-folding motion. The probability distribution of long tumbling times is exponential with a time scale exponentially increasing with the Weissenberg number.

1. Introduction

Various microscopic objects, when immersed in a laminar shear flow, perform a tumbling motion in the plane of the shear. These include anisotropic solid particles [1], flexible and semi-flexible polymers [2–4], vesicles [5], bacteria [6], red blood cells [7] (for related numerical studies, e.g. [8–13]). The tumbling dynamics depends on the nature of the object and on its interaction with the fluid: tumbling may occur only within a restricted range of shear rates, and it can be periodic, chaotic or random.

Axisymmetric solid particles and elastic dumbbells are among the simplest objects that tumble in shear flows. In a viscous simple shear flow of a Newtonian fluid, a neutrally buoyant axisymmetric particle spends most of the time aligned with the direction of the flow and periodically reverses its orientation [14,15]. If the axisymmetry of the particle is broken, the tumbling motion may become doubly periodic or even chaotic [1,16,17]. An elastic dumbbell, which consists of two beads joined by a spring, also performs an end-over-end tumbling motion in a shear flow [18–21]. Under the effect of Brownian fluctuations, the reversals occur at random times and are characterized by a transition from the

stretched to the coiled state. The distribution of the time intervals separating two reversals has an exponential tail with a time scale that decreases as a power law of the Weissenberg number (the product of the amplitude of the velocity gradient and the relaxation time of the spring).

Here we address the question of whether tumbling can also exist in stretching-dominated flows and, if so, what the minimal requirements are for a particle to tumble in such flows and how the resulting tumbling motion compares with the analogous motion in a shear flow. The orientational dynamics of an axisymmetric particle or of an elastic dumbbell in a purely extensional velocity field is trivial: such objects indeed simply align with the stretching direction. In order to observe tumbling in an extensional flow, we must consider objects that can bend. The 'trumbbell' is one of the simplest semi-flexible objects: it consists of three beads joined by two rigid connectors and of an elastic hinge at the central bead [22] (see also [23]). Owing to its simplicity, the trumbbell was originally used to study the low-frequency dynamics of stiff macromolecules analytically (e.g. [24,25]). We show that in an extensional flow a trumbbell spends a significant amount of time extended and oriented along the stretching direction of the flow; occasionally, a favourable sequence of Brownian fluctuations make the trumbbell fold, reverse its orientation and unfold. We examine this tumbling-through-folding dynamics in terms of the stable configurations of the trumbbell and of the associated basins of attraction. The properties of the statistics of the tumbling times are explained by using the large deviations theory. In particular, the analysis of the tumbling statistics reveals a fundamental difference between the tumbling motion of a trumbbell in an extensional flow and the tumbling motion of an elastic dumbbell in a simple shear flow. In the former case, indeed, the mean time that separates two reversals grows with the Weissenberg number, and the growth is exponential.

Section 2 describes the trumbell and specifies its configuration in terms of angular variables. Section 3 examines the stationary statistics of the configuration of a trumbbell in a two-dimensional extensional flow. Section 4 analyses the tumbling motion and its statistical properties; analogous results in three dimensions are also presented. Finally, conclusions are drawn in §5.

2. The trumbbell

A trumbbell consists of three identical beads located at $\boldsymbol{x}_\nu$ ($\nu = 1, 2, 3$) and joined by two inertialess rods of length ℓ (figure 1).[1] The internal angle between the rods is denoted by χ; as we distinguish the two configurations obtained by interchanging $\boldsymbol{x}_1$ and $\boldsymbol{x}_3$, χ varies between 0 and 2π. When $\chi = 0, 2\pi$ the trumbbell is folded; when $\chi = \pi$ it is fully extended. A restoring force is imposed so that the trumbbell unfolds towards an equilibrium at $\chi = \pi$. This force is described by the harmonic potential $\phi(\chi) = \mu(\chi - \pi)^2/2$ and models the resistance of the trumbell to bend.

The trumbbell is advected by a linear velocity field $\boldsymbol{u}(\boldsymbol{x}, t)$, in which each bead experiences Stokes' drag with drag coefficient ζ. The fluid is Newtonian. The beads are assumed to be sufficiently small to experience Brownian fluctuations. Furthermore, the inertia of the beads and the hydrodynamic interactions between them are neglected. It is also assumed that the trumbbell does not modify the flow.

The centre of mass of the trumbbell, $\boldsymbol{x}_{\mathrm{CM}} = (\boldsymbol{x}_1 + \boldsymbol{x}_2 + \boldsymbol{x}_3)/3$, moves according to the equation $\dot{\boldsymbol{x}}_{\mathrm{CM}} = \boldsymbol{u}(\boldsymbol{x}_{\mathrm{CM}}, t) + \sqrt{2\zeta k_{\mathrm{B}} T/3}\,\hat{\boldsymbol{\eta}}(t)$, where k_{B} is the Boltzmann constant, T is temperature and $\hat{\boldsymbol{\eta}}(t)$ is white noise (see the appendix). In the reference frame of $\boldsymbol{x}_{\mathrm{CM}}$, the configuration of the trumbbell can be described by $2(d-1)$ angular coordinates $\boldsymbol{q}$, where d is the dimension of the flow [22]. The statistics of the configuration of the trumbbell at a time t is specified by the probability density function (p.d.f.) $\psi(\boldsymbol{q}; t)$, which is normalized as $\int \psi(\boldsymbol{q}; t)\,\mathrm{d}\boldsymbol{q} = 1$ and satisfies the following diffusion equation [22] (see also Bird *et al.* [23] for the derivation):

$$\frac{\partial \psi}{\partial t} = -\frac{\partial}{\partial q^i}\left\{\mathcal{G}^{ij}\left[\left(\kappa^{kl}(t) r_\nu^l \frac{\partial r_\nu^k}{\partial q^j} - \frac{1}{\zeta}\frac{\partial \phi}{\partial q^j}\right)\psi - \frac{k_{\mathrm{B}}T}{\zeta}\sqrt{h}\frac{\partial}{\partial q^j}\left(\frac{\psi}{\sqrt{h}}\right)\right]\right\}, \tag{2.1}$$

[1] Throughout the paper vectors are written in bold; calligraphic letters denote tensors.

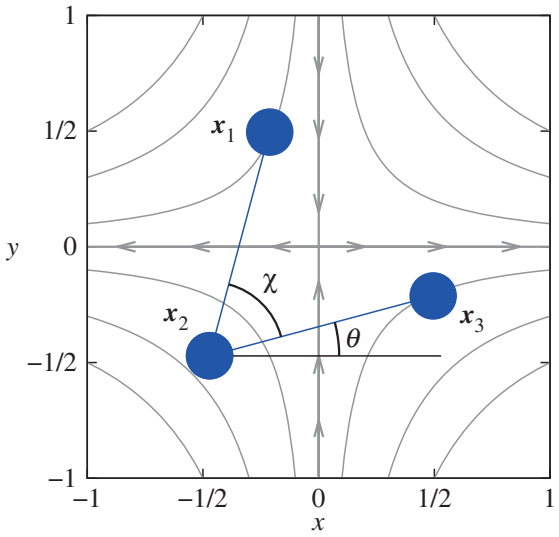

Figure 1. A trumbbell in the frame of reference of its centre of mass. The origin coincides with the centre of mass. The flow is extensional (streamlines shown in grey) with stretching in the x-direction and compression in the y-direction. (Online version in colour.)

where $\kappa^{kl}(t) = \partial^l u^k(t)$ is the velocity gradient evaluated at $\boldsymbol{x}_{\mathrm{CM}}$, $\boldsymbol{r}_\nu = \boldsymbol{x}_\nu - \boldsymbol{x}_{\mathrm{CM}}$ are the separation vectors describing the location of the beads with respect to $\boldsymbol{x}_{\mathrm{CM}}$, $h = \det(\mathcal{H})$ with $\mathcal{H}^{ij} = \sum_{\nu,k}(\partial r_\nu^k/\partial q^i)(\partial r_\nu^k/\partial q^j)$, and $\mathcal{G} = \mathcal{H}^{-1}$. Summation over repeated indices is implied in (2.1). Note that in a linear flow the orientational dynamics of the trumbbell only depends on the velocity gradient, which is spatially uniform (see also the evolution equations for the configuration of the trumbbell in the appendix). The internal configuration of the trumbbell is therefore decoupled from the position of the centre of mass. This implies that the statistics of $\boldsymbol{q}$ is independent of $\boldsymbol{x}_{\mathrm{CM}}$; hence, without any loss of generality, we study the dynamics of the trumbbell in the frame of reference that is translated with the centre of mass.

To simplify the analysis, we assume that the trumbbell is immersed in a thin layer of fluid and we restrict our attention to $d = 2$. The case of a planar three-dimensional flow will be discussed at the end of §4. In two dimensions, we choose $\boldsymbol{q} = (\theta, \chi)$, where $0 \le \theta < 2\pi$ is the angle that the vector $\boldsymbol{x}_3 - \boldsymbol{x}_2$ makes with the x-axis; θ gives the orientation of the trumbbell in the plane. The vectors $\boldsymbol{r}_\nu$ can then be expressed in terms of θ and χ as

$$\boldsymbol{r}_1 = \frac{\ell(2\cos(\theta+\chi) - \cos(\theta), 2\sin(\theta+\chi) - \sin(\theta))}{3},$$

$$\boldsymbol{r}_2 = -\frac{\ell(\cos(\theta+\chi) + \cos(\theta), \sin(\theta+\chi) + \sin(\theta))}{3}$$

and

$$\boldsymbol{r}_3 = \frac{\ell(2\cos(\theta) - \cos(\theta+\chi), 2\sin(\theta) - \sin(\theta+\chi))}{3}.$$

We also have $h = \ell^4(4 - \cos^2\chi)/9$ and

$$\mathcal{G} = \ell^{-2}\begin{pmatrix} \dfrac{6}{4-\cos^2\chi} & -\dfrac{3}{2+\cos\chi} \\ -\dfrac{3}{2+\cos\chi} & \dfrac{6}{2+\cos\chi} \end{pmatrix}.$$

Equation (2.1) can then be rewritten as a Fokker–Planck equation in two variables:

$$\partial_t \psi = -\partial_\theta(V_\theta \psi) - \partial_\chi(V_\chi \psi) + \tfrac{1}{2}\partial_\theta^2(D_{\theta\theta}\psi) + \partial_\theta\partial_\chi(D_{\theta\chi}\psi) + \tfrac{1}{2}\partial_\chi^2(D_{\chi\chi}\psi), \tag{2.2}$$

where

$$D_{\theta\theta} = \frac{12k_BT}{\zeta\ell^2(4-\cos^2\chi)}, \quad D_{\theta\chi} = -\frac{6k_BT}{\zeta\ell^2(2+\cos\chi)}, \quad D_{\chi\chi} = \frac{12k_BT}{\zeta\ell^2(2+\cos\chi)}$$

and

$$\begin{aligned} V_\theta = &-\frac{6k_BT\sin\chi}{\zeta\ell^2(2-\cos\chi)(2+\cos\chi)^2} - \frac{3\mu(\pi-\chi)}{\zeta\ell^2(2+\cos\chi)} \\ &- \frac{1}{4-\cos^2\chi}\{[2\sin\chi\cos^2(\theta+\chi)+\cos\theta(4\sin\theta-\cos\chi\sin(\theta+\chi))]\kappa^{11}(t) \\ &+ [2\cos\chi\sin^2(\theta+\chi)-\sin\theta(2+\cos\chi)\sin(\theta+\chi)+4\sin^2\theta]\kappa^{12}(t) \\ &+ [-2\cos\chi\cos^2(\theta+\chi)+\cos\theta(2+\cos\chi)\cos(\theta+\chi)-4\cos^2\theta]\kappa^{21}(t) \\ &+ [2\cos\theta(\sin(\theta+\chi)-2\sin\theta)+\cos\chi(\sin\theta\cos(\theta+\chi)-\sin(2(\theta+\chi)))]\kappa^{22}(t)\}, \\ V_\chi = &\frac{12k_BT\sin\chi}{\zeta\ell^2(2-\cos\chi)(2+\cos\chi)^2} + \frac{6\mu(\pi-\chi)}{\zeta\ell^2(2+\cos\chi)} + \frac{\sin\chi}{2+\cos\chi}\{[1-2\cos(2\theta+\chi)]\kappa^{11}(t) \\ &- 2\sin(2\theta+\chi)[\kappa^{12}(t)+\kappa^{21}(t)]+[1+2\cos(2\theta+\chi)]\kappa^{22}(t)\}. \end{aligned}$$

The Fokker–Planck equation (2.2) is equivalent to the following system of Itô stochastic differential equations:

$$\left.\begin{aligned} \dot\theta(t) &= V_\theta + \sqrt{D_{\theta\theta}}\xi_\theta(t) \\ \text{and} \quad \dot\chi(t) &= V_\chi + \frac{D_{\theta\chi}}{\sqrt{D_{\theta\theta}}}\xi_\theta(t) + \sqrt{D_{\chi\chi}-\frac{D_{\theta\chi}^2}{D_{\theta\theta}}}\xi_\chi(t), \end{aligned}\right\} \tag{2.3}$$

where $\xi_\theta(t)$ and $\xi_\chi(t)$ are independent white noises. Note that in (2.3), $D_{\chi\chi} - D_{\theta\chi}^2/D_{\theta\theta} = 3k_BT/\zeta\ell^2$.

3. Stationary statistics of the configuration

By rescaling time in system (2.3), it is possible to formulate the equations in terms of two dimensionless parameters: the stiffness parameter $Z = \mu/k_BT$ and the Weissenberg number $Wi = \gamma\zeta\ell^2/\mu$, where γ is the magnitude of the velocity gradient. The former expresses the relative intensity of the restoring force to that of Brownian noise, whereas the latter compares the strengths of the flow and of the restoring force. In addition, we introduce the Péclet number $Pe = \gamma\zeta\ell^2/k_BT = Z\,Wi$, which is the relative intensity of the flow to Brownian noise.

Consider a two-dimensional extensional flow $\boldsymbol{u}(x,y) = \gamma(x,-y), \gamma > 0$, which consists of a stretching direction x and a compressing direction y (figure 1).[2] For this flow, the stationary p.d.f. of θ and χ takes the form $\psi_{st}(\theta,\chi) = N\sqrt{h}\exp[(\Phi-\phi)/(k_BT)]$ with $\Phi = (\zeta/2)\sum\kappa^{ij}r_\nu^i r_\nu^j$ [22]; its explicit expression is

$$\psi_{st}(\theta,\chi) = N\sqrt{4-\cos^2\chi}\exp\left[\frac{Z\,Wi(2\cos\chi-1)\cos(2\theta+\chi)}{3} - \frac{Z(\pi-\chi)^2}{2}\right], \tag{3.1}$$

where N is a normalization constant. The contour plot of $\ln\psi_{st}(\theta,\chi)$ is shown in figure 2*a* for representative values of Z and Wi. It is easily shown that the maxima of $\psi_{st}(\theta,\chi)$ are located at $P_\pi : (\theta = n\pi, \chi = \pi)$, where n is an integer. Hence, the trumbbell spends most of the time in an extended configuration and oriented in the stretching direction of the flow. The peaks at P_π become narrower as Wi increases, showing stronger preference for these configurations (see the marginal p.d.f. of θ, $P(\theta)$ in figure 2*b*). Also note that these peaks are not symmetrically distributed around P_π.

[2]As noted in §2, our study is not restricted to the case in which the centre of mass stays fixed at the stagnation point of the extensional flow, but it is conducted in the frame of reference of the centre of mass and takes advantage of the fact that the statistics of the configuration is independent of x_{CM}.

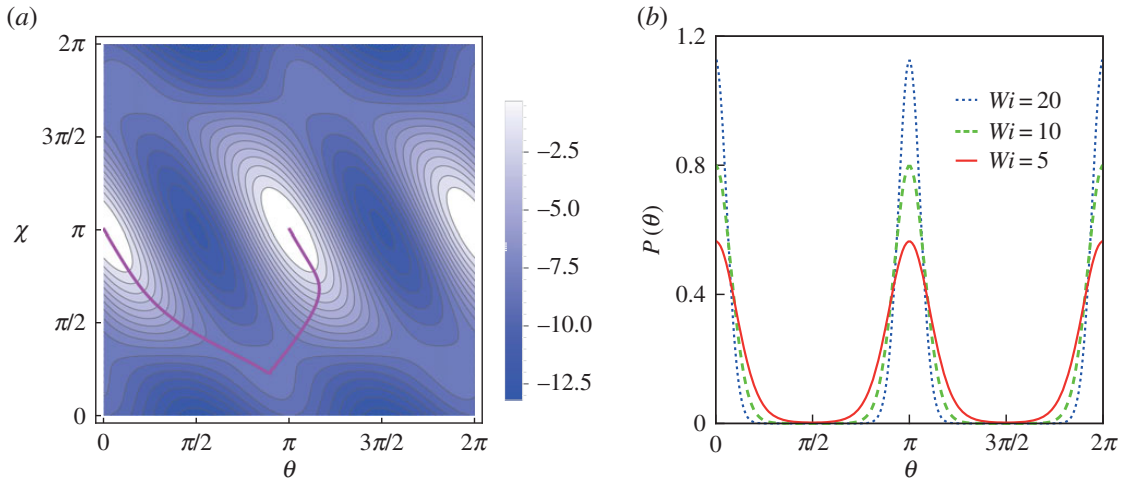

Figure 2. (*a*) Contour plot of $\ln \psi_{st}(\theta, \chi)$ for $Z = 1$ and $Wi = 6$. One minimum energy path (see §4) connecting (π, π) and $(0, \pi)$ is drawn with a solid magenta curve. (*b*) The marginal p.d.f. of θ for $Z = 1$ and $Wi = 5$ (red, solid), $Wi = 10$ (green, dashed) and $Wi = 20$ (blue, dotted). (Online version in colour.)

To understand the behaviour of $\psi_{st}(\theta, \chi)$ when the flow is much stronger than both the restoring force and Brownian noise, we set $\mu = 0$ and $k_B T = 0$ in (2.3), which corresponds to considering the limiting case $Wi = Pe = \infty$. The resulting system is

$$\left.\begin{aligned} \dot{\theta}(t) &= -\frac{\gamma}{2(4-\cos^2\chi)}\left[7\sin(2\theta) + 4\cos(2\theta+\chi)\sin\chi - \sin(2(\theta+\chi))\right] \\ \text{and} \qquad \dot{\chi}(t) &= -\frac{4\gamma}{2+\cos\chi}\left[\sin\chi\cos(2\theta+\chi)\right]. \end{aligned}\right\} \tag{3.2}$$

The linear stability analysis of this system yields two stable configurations, both aligned with the stretching direction of the flow ($\theta = 0, \pi, 2\pi$). The first stable configuration is the extended one P_π and is characterized by two negative eigenvalues: $\lambda_\pi^{(1)} = -4\gamma$ and $\lambda_\pi^{(2)} = -2\gamma$. The second stable configuration is the folded one $P_0 : (\theta = n\pi, \chi = 0, 2\pi)$ with eigenvalues $\lambda_0^{(1)} = -2\gamma$ and $\lambda_0^{(2)} = -4\gamma/3$. As the velocity gradient γ becomes stronger, both configurations become increasingly stable, as the eigenvalues are proportional to γ. However, the ratio of the most negative eigenvalues of the two configurations is $\lambda_\pi^{(1)}/\lambda_0^{(1)} = 2$; hence the extended configuration P_π is more stable than the folded one P_0 for all γ and is expected to dominate the long-time statistics. This fact can be understood by noting that the velocity of a bead is proportional to its distance from the centre of mass, and in the extended configuration P_π, the end beads are further from x_{CM} than they are in the folded configuration P_0.

The presence of the two stable configurations is seen in the vector plot of $(\dot{\theta}, \dot{\chi})$ shown in figure 3*a*. As both $\dot{\theta}$ and $\dot{\chi}$ are proportional to γ (see (3.2)), the geometrical structure of the vector plot does not change with γ. In accordance with the stability analysis of the fixed points of (3.2), the vectors that lie in the neighbourhood of P_π are larger than those in the neighbourhood of P_0. Therefore, the presence of Brownian noise allows an easier escape from the basin of attraction of the folded configuration P_0 than from that of the extended configuration P_π. Conversely, a trumbbell in an extended configuration is more likely to remain in the basin of attraction of this configuration, until there is sufficient noise for it to fold. Also note that the basin of attraction of the points P_π is not symmetrically distributed around them, but there is a preferential direction along which the system is more strongly attracted (figure 3). Consider indeed two configurations with the same value of χ close to π and with θ either slightly less than π or slightly greater than it (figure 4). It is clear that the latter configuration is more strongly attracted to P_π.

In the presence of restoring potential ($Wi < \infty, Pe = \infty$), the fixed points of system (2.3) and their stability can be calculated numerically. Only P_π remain stable fixed points; the

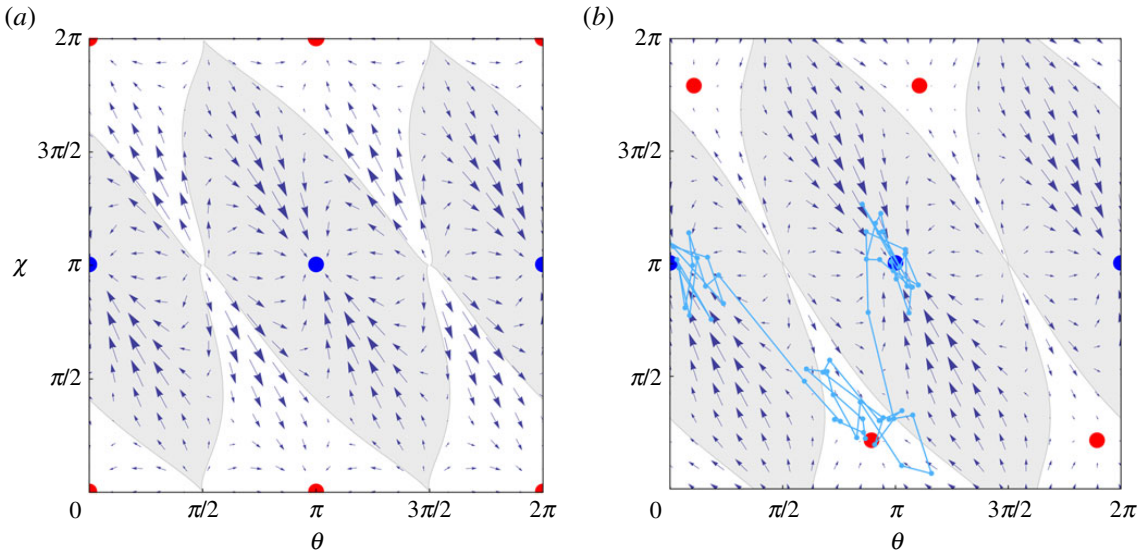

Figure 3. (*a*) Vector plot of $\gamma^{-1}(\dot{\theta}, \dot{\chi})$ for $Wi = Pe = \infty$. The size of the arrows are proportional to the magnitude of the vector $\gamma^{-1}(\dot{\theta}, \dot{\chi})$. The basins of attraction of P_π (blue discs) are in grey; those of P_0 (red discs) are in white. (*b*) Vector plot of $(\dot{\theta}, \dot{\chi})$ for $Z = 1$, $Wi = 6$. The white areas are now the basins of attraction of $P_\star$ (red discs). The light blue curve with markers is a trajectory $(\theta(t), \chi(t))$ corresponding to a tumbling motion from $\theta = \chi = \pi$ to $\theta = 0$, $\chi = \pi$.

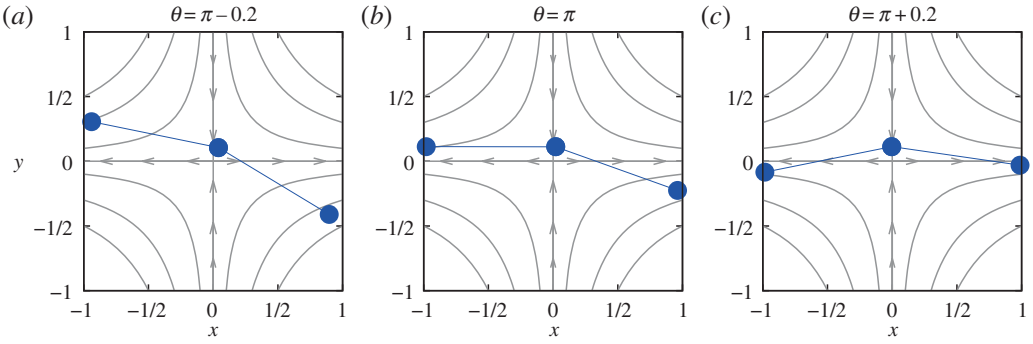

Figure 4. Three configurations near an extended equilibrium configuration for the same value of $\chi = 2.8$. (Online version in colour.)

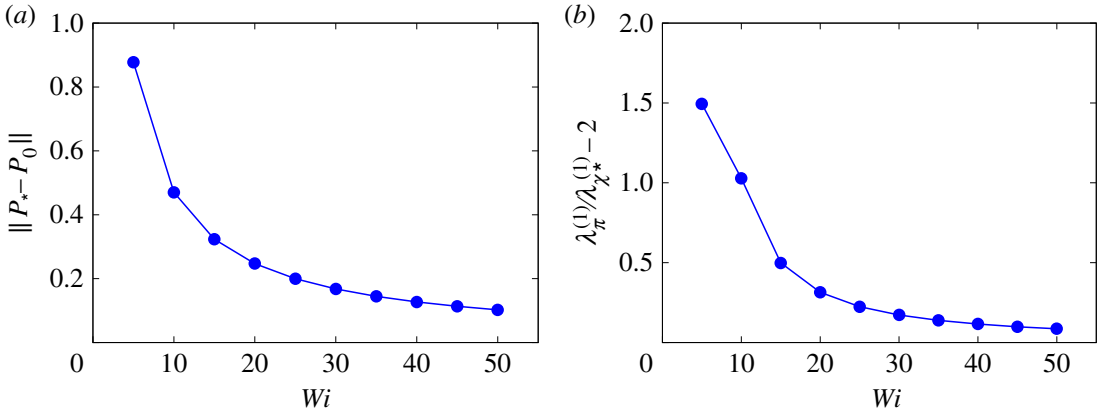

Figure 5. (*a*) Distance of a stable fixed point $P_\star$ from the nearest P_0 for $Pe = \infty$ as a function of Wi. (*b*) Ratio of the most negative eigenvalue of P_π to that of $P_\star$ subtracted by $\lambda_\pi^{(1)}/\lambda_0^{(1)} = 2$. (Online version in colour.)

configurations P_0 are no longer fixed because of the restoring potential. However, if the flow is sufficiently strong ($Wi \gtrsim 4$ for $Z = 1$), there exist stable points $P_\star : (\theta_\star, \chi_\star)$ that approach P_0 as Wi increases (figures 3*b* and 5*a*). Moreover, the points P_π are more stable than $P_\star$ for all γ and as Wi increases, the eigenvalues of P_π and $P_\star$ approach the corresponding eigenvalues of the $Wi = \infty$ case (figure 5*b*). Finally, the basins of attraction of P_π and $P_\star$ have similar structures to those of P_π and P_0 when Wi is infinite (figure 3*b*). These results indicate that the intuition gained from the study of the $Wi = \infty$ case holds true also for $Wi < \infty$. In particular, the stability analysis of the fixed points of the system explains why $\psi_{\mathrm{st}}(\theta, \chi)$ shows high peaks only at the extended configuration P_π and not at the folded configuration. Furthermore, the examination of the basins of attraction of P_π and of the vector field $(\dot{\theta}, \dot{\chi})$ clarifies the shape of these peaks.

4. Tumbling dynamics

For sufficiently large Wi, the trumbbell is trapped in the basin of attraction of one of the extended configuration P_π for a long time. However, Brownian fluctuations may occasionally make it tumble between the aligned configuration ($\theta = 0, 2\pi$) and the anti-aligned one ($\theta = \pi$). To investigate this phenomenon, we have performed numerical simulations of (2.3) by using the Euler–Maruyama scheme with a time step $\mathrm{d}t = 10^{-3}$ [26] (we also performed numerical simulations with smaller time steps, which confirmed the accuracy of our results). The inspection of a representative time series of $\cos\theta(t)$ and $\cos\chi(t)$ confirms the aforementioned tumbling dynamics and shows that these reversals are characterized by partial folding (figure 6). A typical trajectory in the (θ, χ) phase space is shown in figure 3*b*. The trumbbell is initially extended and anti-aligned with the stretching direction. A favourable sequence of Brownian fluctuations makes it exit from the initial basin of attraction and pass through that of the folded configuration. The trumbbell then unfolds towards the extended but aligned configuration. The movie included as the electronic supplementary material further illustrates this tumbling-through-folding motion.

Although the trumbbell always folds (possibly not completely) during a tumbling event, there are instances in which folding does not result into a reversal and the trumbbell rapidly unfolds back into the original configuration (see for instance figure 6 at $t \approx 1.2 \times 10^3$). In order to correctly identify a tumbling event, we shall therefore apply the following criterion. Suppose that at time t_1 the trumbbell is sufficiently extended, i.e.

$$|\cos\theta| > 1 - \epsilon, \quad |\cos(\theta + \chi)| > 1 - \epsilon \quad \text{and} \quad \cos\theta\cos(\theta + \chi) < 0, \tag{4.1}$$

for some small ϵ. We shall say that a tumbling occurs at time t_2 if t_2 is the smallest time after t_1 such that (4.1) is again satisfied and $\cos\theta(t_1)\cos\theta(t_2) < 0$. In our simulations, we set $\epsilon = 0.01$; we have verified that the specific choice of ϵ does not affect the statistical analysis of tumbling, provided the threshold $1 - \epsilon$ is sufficiently close to 1.

The tumbling dynamics described above is not periodic. On the contrary, the time τ separating two tumbling events are distributed randomly. For each different value of Wi, we have collected at least 10^4 tumbling realizations. We find that the p.d.f. of τ has an exponential tail for large $\tau : p(\tau) \propto \exp(-\tau/\tau_0)$ for $\tau \gg \tau_0$. Moreover, τ_0 increases exponentially as a function of Wi (figure 7*a*). Hence, as the flow becomes stronger, it takes a longer time for a tumbling to occur. The configurations P_π indeed become increasingly stable, and larger Brownian fluctuations are required for the system to escape from the basins of attraction of P_π.

The above properties of $p(\tau)$ can be predicted by using the Freidlin–Wentzell large deviations theory [27] (see also [28]). Indeed, for large values of Wi, tumbling in an extensional flow can be regarded as escaping from an attractor of a stochastic dynamical system in the limit of small noise. The p.d.f. of the exit time thus has an exponential tail and the mean exit time increases exponentially as the amplitude of the noise vanishes. The same theory also predicts the tumbling-through-folding phenomenon. Indeed, the most probable transition paths, or minimum energy paths, that connect two adjacent configurations P_π are parallel to the gradient of the pseudo-potential $V = -\ln\psi_{\mathrm{st}}$ [29]. The application of the improved string method to V [30] shows that these minimum energy paths pass through the folded configurations $P_\star$, which are saddle points

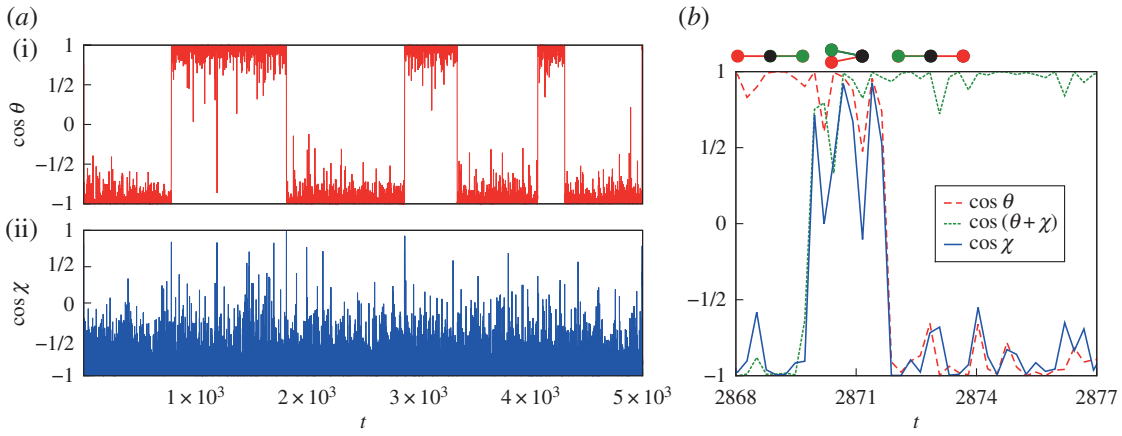

Figure 6. Time series of $\cos\theta(t)$ (*a*, i) and $\cos\chi(t)$ (*a*, ii) for a two-dimensional extensional flow with $Z = 1$, $Wi = 6$. (*b*) Zoom of the time series of $\cos\theta$, $\cos\chi$, $\cos(\theta + \chi)$ over a tumbling event. (Online version in colour.)

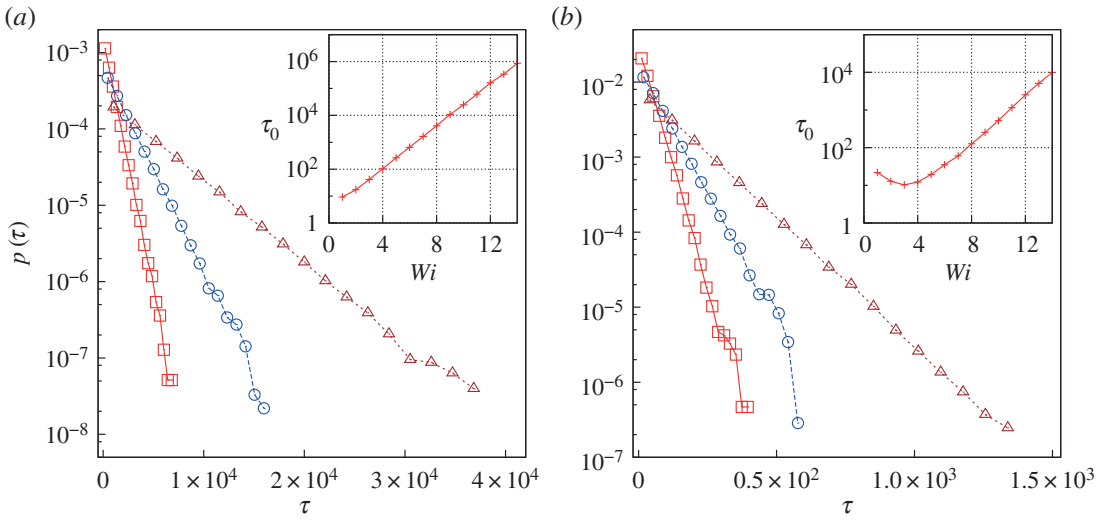

Figure 7. P.d.f.s of the tumbling time in two dimensions (*a*) and three dimensions (*b*) for $Z = 1$ and $Wi = 6$ (red squares), $Wi = 7$ (blue circles) and $Wi = 8$ (brown triangles). The insets show τ_0 as a function of Wi. (Online version in colour.)

of V. By way of illustration, a minimum energy path connecting (π, π) and $(0, \pi)$ is given in figure 3*b*.

The analysis so far considers a two-dimensional velocity field. However, in a realistic planar extensional flow, a trumbbell may move outside the plane of the flow. This situation can be described by considering a three-dimensional velocity field $\boldsymbol{u} = \gamma(x, -y, 0)$. In this case, the trumbbell has four degrees of freedom, which can be described by the internal angle χ and three Euler angles giving the orientation of the particle in space [22,23]. This formulation, however, is not suitable for numerical simulations because of singularities near to the extended configuration (see the form of the tensor $\mathcal{G}$ in [23], p. 618). To circumvent this difficulty, we introduce the vectors $\boldsymbol{\rho}_1 = \boldsymbol{x}_1 - \boldsymbol{x}_2$ and $\boldsymbol{\rho}_3 = \boldsymbol{x}_3 - \boldsymbol{x}_2$, which give the orientation of the rods in the frame of reference of the centre of mass. The system of Stratonovich stochastic differential equations that describes the time evolution of $\boldsymbol{\rho}_1$ and $\boldsymbol{\rho}_3$ is derived in the appendix. This system has been solved by using the Euler–Heun method with $\mathrm{d}t = 10^{-3}$ [26]. When Wi is sufficiently high, the trumbbell is observed to be predominantly in the extended configuration $\chi = \pi$ with the separation vectors aligned or anti-aligned with the stretching direction of the flow. At random times, the trumbbell folds and reverses its orientation, with a dynamics similar to that observed in two dimensions. A time

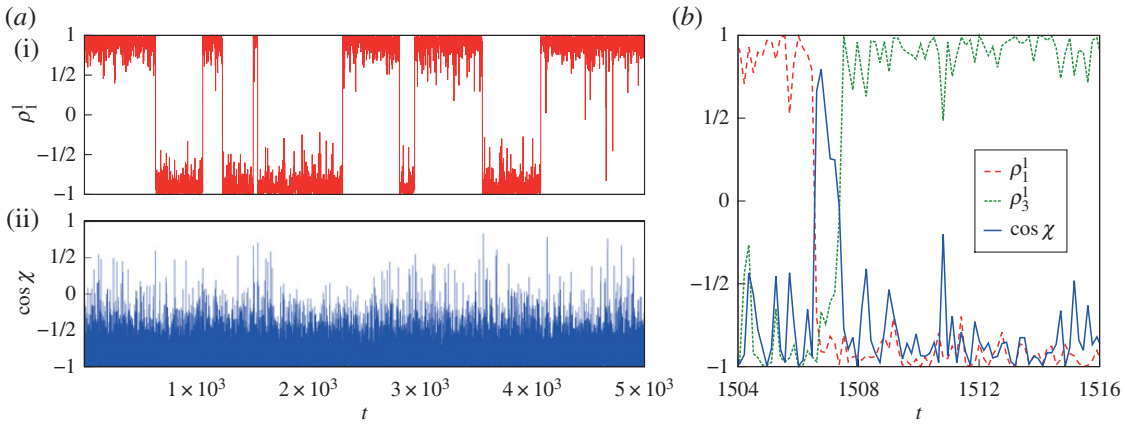

Figure 8. Time series of $\rho_1^1(t)$ (*a*, i) and cos $\chi(t)$ (*a*, ii) for a three-dimensional planar extensional flow with $Z = 1$, $Wi = 10$. (*b*) Zoom of the time series of ρ_1^1, ρ_3^1, cos χ over a tumbling event. (Online version in colour.)

series showing cos χ and the first component of $\boldsymbol{\rho}_1$ is shown in figure 8. The tumbling events can be identified as before by replacing $\cos\theta$, $\cos(\theta + \chi)$ with the first components of $\boldsymbol{\rho}_1$, $\boldsymbol{\rho}_3$, respectively. The p.d.f. of the tumbling time is again exponential for long times with a time scale increasing exponentially with Wi (figure 7*b*). The tumbling statistics, therefore, shows properties similar to those found in a purely two dimensional flow. For the same values of Wi, the mean tumbling time is, however, significantly shorter than in two dimensions. This fact is attributed to the increased dimensionality of the system, which makes it easier for the trumbbell to escape from the aligned or anti-aligned configuration. For the same reason, the asymptotic exponential behaviour of τ_0 is observed at larger Wi compared with the two-dimensional case.

5. Conclusion

The phenomenon of tumbling is commonly associated with shear flows. The simplest objects that perform end-over-end tumbling in a simple shear, namely axisymmetric solid particles and the dumbbell, exhibit a trivial orientational dynamics in an extensional flow and do not tumble. We have shown that, by contrast, a rich dynamics is obtained by considering one of the most elementary semi-flexible objects, namely the trumbbell. The mere consideration of one bending mode indeed yields a random end-over-end tumbling motion with exponentially distributed tumbling times. While it is well known that several microscopic objects tumble in a shear flow, to the best of our knowledge tumbling had not been observed in an extensional flow before. Moreover, we find a fundamental qualitative difference between the tumbling motion in an extensional flow and the analogous motion in a shear flow. In the latter case, the typical tumbling time decreases as a power law of Wi; in the former case, it increases exponentially as Wi increases. This difference is a consequence of the fact that the configurations aligned with the flow are stable in an extensional flow, whereas they are unstable in a shear flow.

We have also shown that, in an extensional flow, a trumbbell reverses its orientation by folding and then extending again in the opposite direction. This dynamics is reminiscent of the buckling instability of a fibre near to a hyperbolic point [31]. Nevertheless, the tumbling motion described here is triggered by Brownian fluctuations that bend the trumbbell, whereas the buckling instability of a fibre results from its internal dynamics and does not necessarily require Brownian fluctuations.

The simplicity of the trumbbell model has allowed us to study its tumbling motion in detail and to relate this phenomenon to the properties of the stable configurations of the trumbbell and to the structure of the corresponding basins of attraction. In our study, we have focused on the most elementary version of the trumbbell model. In particular, we have disregarded hydrodynamic and excluded volume interactions between the beads. If the size of the beads

is sufficiently smaller than their mutual separations, the inclusion of such interactions into the model would somewhat modify the stable folded configuration but not the essential structure of the phase space of the system. Therefore, although a more accurate description of the trumbbell would require taking into account hydrodynamic and excluded volume interactions [32,33], we do not expect these interactions to alter the essential properties of the tumbling dynamics, as long as the size of the beads is small compared with their mutual separations.

Data accessibility. This work does not have any experimental data. The Itô stochastic differential equations that describe the configuration of the trumbbell in two dimensions were solved by using the Euler-Maruyama method with time step $\mathrm{d}t = 10^{-3}$. The Stratonovich stochastic differential equations that describe the configuration of the trumbbell in three dimensions were solved by using the Euler-Heun method with time step $\mathrm{d}t = 10^{-3}$. Numerical simulations with smaller times steps were also performed to confirm the accuracy of the results.

Authors' contributions. E.L.C.M.P. and D.V. conceived the problem and provided the theoretical framework. E.L.C.M.P. conducted the theoretical and numerical analysis and prepared the manuscript. Both authors gave the final approval for publication.

Competing interests. We declare we have no competing interests.

Funding. This work was supported in part by the EU COST Action MP 1305 'Flowing Matter'. E.L.C.M.P. acknowledges the support of EACEA through the Erasmus Mundus Mobility with Asia program.

Acknowledgements. The authors are grateful to A. Ali, F. Delarue, S. Musacchio and S. S. Ray for useful discussions.

Appendix A. Equations of motion of the trumbbell

In this appendix, we derive an alternative formulation of the internal dynamics of the trumbell that is suitable for numerical simulations in three dimensions. In the reference frame of $\boldsymbol{x}_{\mathrm{CM}}$, the configuration of a trumbbell can be described by using the vectors $\boldsymbol{\rho}_1 = \boldsymbol{x}_1 - \boldsymbol{x}_2$ and $\boldsymbol{\rho}_3 = \boldsymbol{x}_3 - \boldsymbol{x}_2$. The position vectors of the beads satisfy

$$m\ddot{\boldsymbol{x}}_\nu = -\zeta[\dot{\boldsymbol{x}}_\nu - \boldsymbol{u}(\boldsymbol{x}_\nu, t)] + \mathbf{t}_\nu + \boldsymbol{f}_\nu + \sqrt{D}\,\boldsymbol{\eta}_\nu(t), \quad \nu = 1,2,3, \tag{A 1}$$

where m is the mass of each bead, $D = 2\zeta k_{\mathrm{B}}T$ and $\boldsymbol{\eta}_\nu(t)$ are independent d-dimensional white noises. The restoring forces $\boldsymbol{f}_\nu$ take the form $\boldsymbol{f}_1 = \mu_\chi(\hat{\boldsymbol{\rho}}_1 \cot\chi - \hat{\boldsymbol{\rho}}_3 \csc\chi)$, $\boldsymbol{f}_3 = \mu_\chi(\hat{\boldsymbol{\rho}}_3 \cot\chi - \hat{\boldsymbol{\rho}}_1 \csc\chi)$ and $\boldsymbol{f}_2 = -(\boldsymbol{f}_1 + \boldsymbol{f}_3)$ with $\mu_\chi = \mu(\pi - \chi)/\ell$ [32]. The tensions $\mathbf{t}_\nu$ keep the distances between the beads constant. The terms on the r.h.s. of (A 1) describe Stokes' drag, the rigidity of the rods, the resistance of the particle to bend and Brownian noise, respectively. Neglecting inertial effects yields

$$\dot{\boldsymbol{x}}_\nu = \boldsymbol{u}(\boldsymbol{x}_\nu, t) + \frac{1}{\zeta}[\mathbf{t}_\nu + \boldsymbol{f}_\nu + \sqrt{D}\,\boldsymbol{\eta}_\nu(t)], \quad \nu = 1,2,3. \tag{A 2}$$

By using the linearity of the velocity field, we obtain

$$\dot{\boldsymbol{x}}_{\mathrm{CM}} = \boldsymbol{u}(\boldsymbol{x}_{\mathrm{CM}}, t) + \sqrt{\frac{D}{3}}\,\hat{\boldsymbol{\eta}}(t), \tag{A 3}$$

where $\hat{\boldsymbol{\eta}}(t)$ is white noise and

$$\left.\begin{aligned} \dot{\boldsymbol{\rho}}_1 &= \boldsymbol{\rho}_1 \cdot \boldsymbol{\nabla}\boldsymbol{u} + \frac{1}{\zeta}(2\mathbf{t}_1 + \mathbf{t}_3) + \frac{1}{\zeta}(2\boldsymbol{f}_1 + \boldsymbol{f}_3) + \Gamma\tilde{\boldsymbol{\eta}}_1 \\ \text{and} \qquad \dot{\boldsymbol{\rho}}_3 &= \boldsymbol{\rho}_3 \cdot \boldsymbol{\nabla}\boldsymbol{u} + \frac{1}{\zeta}(2\mathbf{t}_3 + \mathbf{t}_1) + \frac{1}{\zeta}(2\boldsymbol{f}_3 + \boldsymbol{f}_1) + \Gamma\tilde{\boldsymbol{\eta}}_3, \end{aligned}\right\} \tag{A 4}$$

where $\Gamma = \sqrt{2D}/\zeta$ and $\tilde{\boldsymbol{\eta}}_i = [\boldsymbol{\eta}_i(t) - \boldsymbol{\eta}_2(t)]/\sqrt{2}$ with $\langle\tilde{\boldsymbol{\eta}}_i(t)\rangle = 0$ and $\langle\tilde{\eta}_i^\alpha(t)\tilde{\eta}_i^\beta(t')\rangle = \delta^{\alpha\beta}\delta(t - t')$, $i = 1,3$. We impose the rigidity constraints $\mathrm{d}|\boldsymbol{\rho}_i|^2/\mathrm{d}t = 0$ to obtain

$$\boldsymbol{\rho}_i \circ \dot{\boldsymbol{\rho}}_i = 0, \tag{A 5}$$

where the symbol '$\circ$' indicates that the dot products involving the noise terms are understood in the Stratonovich sense [26]. Equation (A 5) may now be used to calculate the tensions

$$\left.\begin{aligned}\mathbf{t}_1 &= -\zeta c_\chi[2\sigma_1 - \sigma_3\cos\chi - \tilde{\mu}_\chi + 2\Gamma(\hat{\boldsymbol{\rho}}_1\circ\tilde{\boldsymbol{\eta}}_1) - \Gamma\cos\chi(\hat{\boldsymbol{\rho}}_3\circ\tilde{\boldsymbol{\eta}}_3)]\hat{\boldsymbol{\rho}}_1,\\ \mathbf{t}_2 &= -(\mathbf{t}_1+\mathbf{t}_3)\\ \text{and}\qquad \mathbf{t}_3 &= -\zeta c_\chi[2\sigma_3 - \sigma_1\cos\chi - \tilde{\mu}_\chi + 2\Gamma(\hat{\boldsymbol{\rho}}_3\circ\tilde{\boldsymbol{\eta}}_3) - \Gamma\cos\chi(\hat{\boldsymbol{\rho}}_1\circ\tilde{\boldsymbol{\eta}}_1)]\hat{\boldsymbol{\rho}}_3,\end{aligned}\right\} \tag{A 6}$$

where $\sigma_i = \sum_{\alpha,\beta}\ell\hat{\rho}_i^\alpha\partial^\alpha u^\beta\hat{\rho}_i^\beta$ with $\hat{\boldsymbol{\rho}}_i = \boldsymbol{\rho}_i/|\boldsymbol{\rho}_i|$, $c_\chi = (4-\cos^2\chi)^{-1}$ and $\tilde{\mu}_\chi = \zeta^{-1}\mu_\chi\sin\chi(2-\cos\chi)$. By substituting (A 6) into (A 4), we obtain the system

$$\left.\begin{aligned}\dot{\boldsymbol{\rho}}_1 &= \boldsymbol{A}_1 + \mathcal{B}_{11}\circ\tilde{\boldsymbol{\eta}}_1(t) + \mathcal{B}_{13}\circ\tilde{\boldsymbol{\eta}}_3(t)\\ \text{and}\qquad \dot{\boldsymbol{\rho}}_3 &= \boldsymbol{A}_3 + \mathcal{B}_{31}\circ\tilde{\boldsymbol{\eta}}_1(t) + \mathcal{B}_{33}\circ\tilde{\boldsymbol{\eta}}_3(t).\end{aligned}\right\} \tag{A 7}$$

The explicit forms of the vectors $\boldsymbol{A}_1, \boldsymbol{A}_3$ are

$$\boldsymbol{A}_1 = \boldsymbol{\rho}_1\cdot\boldsymbol{\nabla}\boldsymbol{u} - 2c_\chi[2\sigma_1 - \sigma_3\cos\chi - \tilde{\mu}_\chi]\hat{\boldsymbol{\rho}}_1 - c_\chi[2\sigma_3 - \sigma_1\cos\chi - \tilde{\mu}_\chi]\hat{\boldsymbol{\rho}}_3 + \frac{1}{\zeta}(2\boldsymbol{f}_1 + \boldsymbol{f}_3),$$

$$\boldsymbol{A}_3 = \boldsymbol{\rho}_3\cdot\boldsymbol{\nabla}\boldsymbol{u} - 2c_\chi[2\sigma_3 - \sigma_1\cos\chi - \tilde{\mu}_\chi]\hat{\boldsymbol{\rho}}_3 - c_\chi[2\sigma_1 - \sigma_3\cos\chi - \tilde{\mu}_\chi]\hat{\boldsymbol{\rho}}_1 + \frac{1}{\zeta}(2\boldsymbol{f}_3 + \boldsymbol{f}_1)$$

and the matrix-valued coefficients of the noises are

$$\left.\begin{aligned}\mathcal{B}_{11} &= \Gamma[\mathcal{I} + c_\chi(\hat{\boldsymbol{\rho}}_3\cos\chi - 4\hat{\boldsymbol{\rho}}_1)\otimes\hat{\boldsymbol{\rho}}_1],\\ \mathcal{B}_{13} &= 2\Gamma c_\chi(\hat{\boldsymbol{\rho}}_1\cos\chi - \hat{\boldsymbol{\rho}}_3)\otimes\hat{\boldsymbol{\rho}}_3,\\ \mathcal{B}_{31} &= 2\Gamma c_\chi(\hat{\boldsymbol{\rho}}_3\cos\chi - \hat{\boldsymbol{\rho}}_1)\otimes\hat{\boldsymbol{\rho}}_1,\\ \text{and}\qquad \mathcal{B}_{33} &= \Gamma[\mathcal{I} + c_\chi(\hat{\boldsymbol{\rho}}_1\cos\chi - 4\hat{\boldsymbol{\rho}}_3)\otimes\hat{\boldsymbol{\rho}}_3],\end{aligned}\right\}$$

where $\mathcal{I}$ is the identity matrix and $\otimes$ denotes the tensor product. Equations (A 7) can be shown to be statistically equivalent to (2.1). The angle χ can be obtained from $\boldsymbol{\rho}_1\cdot\boldsymbol{\rho}_3 = \ell^2\cos\chi$. The above formulation holds both for $d=2$ and for $d=3$.

References

1. Einarsson J, Mihiretie BM, Laas A, Ankardal S, Angilella JR, Hanstorp D, Mehlig B. 2016 Tumbling of asymmetric microrods in a microchannel flow. *Phys. Fluids* **28**, 013302. (doi:10.1063/1.4938239)
2. Schroeder CM, Teixeira RE, Shaqfeh ESG, Chu S. 2005 Characteristic periodic motion of polymers in shear flow. *Phys. Rev. Lett.* **95**, 018301. (doi:10.1103/PhysRevLett.95.018301)
3. Gerashchenko S, Steinberg V. 2006 Statistics of tumbling of a single polymer molecule in shear flow. *Phys. Revs. Lett.* **96**, 038304. (doi:10.1103/PhysRevLett.96.038304)
4. Harasim M, Wunderlich B, Peleg O, Kröger M, Bausch AR. 2013 Direct observation of the dynamics of semiflexible polymers in shear flow. *Phys. Rev. Lett.* **110**, 108302. (doi:10.1103/PhysRevLett.110.108302)
5. Kantsler C, Steinberg V. 2006 Transition to tumbling and two regimes of tumbling motion of a vesicle in shear flow. *Phys. Rev. Lett.* **96**, 036001. (doi:10.1103/PhysRevLett.96.036001)
6. Kaya T, Koser H. 2009 Characterization of hydrodynamic surface interactions of *Escherichia coli* cell bodies in shear flow. *Phys. Rev. Lett.* **103**, 138103. (doi:10.1103/PhysRevLett.103.138103)
7. Dupire J, Socol M, Viallat A. 2012 Full dynamics of a red blood cell in shear flow. *Proc. Natl Acad. Sci. USA* **109**, 20 808–20 813. (doi:10.1073/pnas.1210236109)
8. Biben T, Misbah C. 2003 Tumbling of vesicles under shear flow within an advected-field approach. *Phys. Rev. E* **67**, 031908. (doi:10.1103/PhysRevE.67.031908)
9. Biben T, Kassner K, Misbah C. 2005 Phase-field approach to three-dimensional vesicle dynamics. *Phys. Rev. E* **72**, 041921. (doi:10.1103/PhysRevE.72.041921)
10. Young YN, Shelley SJ. 2007 Stretch-coil transition and transport of fibers in cellular flows. *Phys. Rev. Lett.* **99**, 058303. (doi:10.1103/PhysRevLett.99.058303)

11. Huang CC, Sutmann G, Gompper G, Winkler RG. 2011 Tumbling of polymers in semidilute solution under shear flow. *Europhys. Lett.* **93**, 54004. (doi:10.1209/0295-5075/93/54004)
12. Walter J, Salsac AV, Barthès-Biesel D. 2011 Ellipsoidal capsules in simple shear flow: prolate versus oblate initial shapes. *J. Fluid Mech.* **676**, 318–347. (doi:10.1017/S0022112011000486)
13. Sinha K, Graham MD. 2015 Dynamics of a single red blood cell in simple shear flow. *Phys. Rev. E* **92**, 042710. (doi:10.1103/PhysRevE.92.042710)
14. Jeffery GB. 1922 The motion of ellipsoidal particles immersed in a viscous fluid. *Proc. R. Soc. Lond. A* **102**, 161–179. (doi:10.1098/rspa.1922.0078)
15. Bretherton FP. 1962 The motion of rigid particles in a shear flow at low Reynolds number. *J. Fluid Mech.* **14**, 284–304. (doi:10.1017/S002211206200124X)
16. Hinch EJ, Leal LG. 1979 Rotation of small non-axisymmetric particles in a simple shear flow. *J. Fluid Mech.* **92**, 591–608. (doi:10.1017/S002211207900077X)
17. Yarin AL, Gottlieb O, Roisman IV. 1997 Chaotic rotation of triaxial ellipsoids in simple shear flow. *J. Fluid Mech.* **340**, 83–100. (doi:10.1017/S0022112097005260)
18. Celani A, Puliafito A, Turitsyn K. 2005 Polymers in linear shear flow: a numerical study. *Europhys. Lett.* **70**, 464–470. (doi:10.1209/epl/i2005-10015-5)
19. Chertkov M, Kolokolov I, Lebedev V, Turitsyn K. 2005 Polymer statistics in a random flow with mean shear. *J. Fluid Mech.* **531**, 251–260. (doi:10.1017/S0022112005003939)
20. Puliafito A, Turitsyn K. 2005 Numerical study of polymer tumbling in linear shear flows. *Phys. D* **211**, 9–22. (doi:10.1016/j.physd.2005.07.016)
21. Turitsyn KS. 2007 Polymer dynamics in chaotic flows with a strong shear component. *J. Expl Theor. Phys.* **105**, 655–664. (doi:10.1134/S1063776107090245)
22. Hassager O. 1974 Kinetic theory and rheology of bead-rod models for macromolecular solutions. *J. Chem. Phys.* **60**, 2111–2124. (doi:10.1063/1.1681321)
23. Bird RB, Curtiss CFC, Armstrong RC, Hassager O. 1987 *Dynamics of polymeric liquids*, vol. II. New York, NY: Wiley.
24. Roitman DB. 1987 The elastic trumbbell model for dynamics of stiff chains. *Lect. Notes Phys.* **293**, 192–207. (doi:10.1007/BFb0032723)
25. Garcia de la Torre J. 1994 Hydrodynamics of segmentally flexible macromolecules. *Eur. Biophys. J.* **23**, 307–322. (doi:10.1007/BF00188655)
26. Kloeden PE, Platen E. 1999 *Numerical solution of stochastic differential equations*. Berlin, Germany: Springer.
27. Freidlin MI, Wentzell AD. 2012 *Random perturbations of dynamical systems*. Berlin, Germany: Springer.
28. Touchette H. 2009 The large deviation approach to statistical mechanics. *Phys. Rep.* **478**, 1–69. (doi:10.1016/j.physrep.2009.05.002)
29. Weinan E, Vanden-Eijnden E. 2010 Transition-path theory and path-finding algorithms for the study of rare events. *Annu. Rev. Phys. Chem.* **61**, 391–420. (doi:10.1146/annurev.physchem.040808.090412)
30. Weinan E, Ren W, Vanden-Eijnden E. 2007 Simplified and improved string method for computing the minimum energy paths in barrier-crossing events. *J. Chem. Phys.* **126**, 164103. (doi:10.1063/1.2720838)
31. Lindner A, Shelley M. 2016 Elastic fibers in flows. In *Fluid–structure interactions in low Reynolds-number flows* (eds C Duprat, H Stone), pp. 168–192. London, UK: Royal Society of Chemistry.
32. Diaz FG, Garcia de la Torre J. 1988 Simulation of the rotational Brownian dynamics of a simple segmentally flexible model: the elastic trumbbell. *J. Chem. Phys.* **88**, 7698–7705. (doi:10.1063/1.454283)
33. Lewis RJ, Allison SA, Eden D, Pecora R. 1988 Brownian dynamics simulations of a three-subunit and a ten-subunit worm-like chain: comparison of results with trumbell theory and with experimental results from DNA. *J. Chem. Phys.* **89**, 2490–2503. (doi:10.1063/1.455043)

PHYSICAL REVIEW FLUIDS **1**, 082402(R) (2016)

Semiflexible particles in isotropic turbulence

Aamir Ali,[1,2] Emmanuel Lance Christopher VI Medillo Plan,[1]
Samriddhi Sankar Ray,[3] and Dario Vincenzi[1]
[1]*Université Côte d'Azur, CNRS, LJAD, 06108 Nice, France*
[2]*Department of Mathematics, COMSATS Intitute of Information Technology, Attock 43600, Pakistan*
[3]*International Center for Theoretical Sciences, Tata Institute of Fundamental Research, Bangalore 560089, India*

(Received 31 July 2016; published 9 December 2016)

The Lagrangian dynamics of semiflexible particles in homogeneous and isotropic turbulent flows is studied by means of analytically solvable stochastic models and direct numerical simulations. The stationary statistics of the bending angle shows a strong dependence on the dimension of the flow. In two-dimensional turbulence, particles are found in either a fully extended or a fully folded configuration; in three dimensions, the predominant configuration is the fully extended one. Such a sensitivity of the bending statistics on the dimensionality of the flow is peculiar to fluctuating flows and is not observed in laminar stretching flows.

DOI: 10.1103/PhysRevFluids.1.082402

The study of hydrodynamic turbulence and turbulent transport has received considerable impulse from the development of experimental, theoretical, and numerical Lagrangian techniques with applications to geophysics, astrophysics, and chemical engineering [1–4]. The translational dynamics of tracer and inertial pointlike particles is, for instance, intimately related to the mixing properties of turbulent flows [5]. In recent years, increasing attention has been drawn to the Lagrangian dynamics of microscopic objects that possess a complex shape or internal degrees of freedom, such as elastic dumbbells (see Ref. [6] and references therein), solid spheroids [7–11] and ellipsoids [12], bead-rod-spring chains [13], crosses and jacks [14], helicoids [15], and chiral dipoles [16].

We study the Lagrangian statistics of yet another internal degree of freedom, i.e., we examine the ability of a turbulent flow to bend a semiflexible particle. As a minimal model, we consider the trumbbell, which consists of three beads connected by two rigid rods and an elastic hinge at the middle [17]. The trumbbell model (also known as the trimer or three-bead two-rod model) was initially introduced in chemical physics to study solutions of stiff macromolecules [17–20]. It also represents the prototypical system for showing that the infinite-stiffness limit of elastic bonds is singular [21]. Here we regard the trumbbell as a simple model that allows us to isolate the bending dynamics of a semiflexible particle from the evolution of other potential degrees of freedom. This approach thus permits us to obtain the probability distribution of the bending angle analytically for laminar and random flows and numerically for fully developed turbulence. We show that the stationary statistics of the bending internal angle depends strongly on the dimension of the flow and on its turbulent character. In a two-dimensional (2D) homogeneous and isotropic incompressible turbulent flow, the distribution of the bending angle is bimodal; the configurations in which the trumbbell is either extended or folded are most probable, with the folded configuration being the most likely for strong turbulence. By contrast, in 3D turbulence, the extended configuration dominates and becomes increasingly probable as the amplitude of the velocity gradient increases. Such a sensitivity of the bending statistics on the flow dimensionality is peculiar to fluctuating flows and is not observed in laminar stretching flows.

A trumbbell consists of three identical beads joined by two inertialess rods of equal length ℓ immersed in a Newtonian fluid (Fig. 1) [17,18]. The drag force acting on the beads is given by the Stokes law with a drag coefficient ζ. An elastic hinge at the middle models the entropic forces that oppose the bending of the trumbbell; the force exerted by the hinge is described by a harmonic

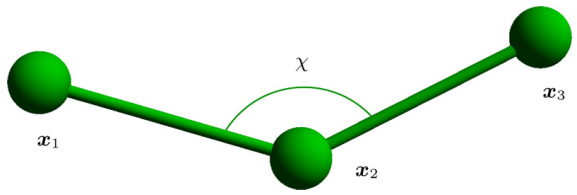

FIG. 1. Trumbbell model.

potential. The size of the trumbbell is sufficiently small for (a) it to experience Brownian fluctuations and (b) the velocity gradient $\nabla \boldsymbol{u}$ to be spatially uniform across the trumbbell. The inertia of the beads and the hydrodynamic interactions between them are disregarded [22,23]. Furthermore, the suspension is dilute; hence, particle-particle hydrodynamic interactions are negligible.

The positions of the beads are denoted by $\boldsymbol{x}_\nu$, $\nu = 1,2,3$. Under the above assumptions, the position of the center of mass $\boldsymbol{x}_c \equiv (\boldsymbol{x}_1 + \boldsymbol{x}_2 + \boldsymbol{x}_3)/3$ evolves like that of a tracer, i.e., $\dot{\boldsymbol{x}}_c(t) = \boldsymbol{u}(\boldsymbol{x}_c(t),t)$. The separation vectors between the beads and $\boldsymbol{x}_c$ are $\boldsymbol{r}_\nu \equiv \boldsymbol{x}_\nu - \boldsymbol{x}_c$. The configuration of the trumbbell in the reference frame of $\boldsymbol{x}_c$ is conveniently described in terms of $2(d-1)$ angular coordinates $\boldsymbol{q}$, where d is the dimension of the fluid [18]. For $d = 2$, $\boldsymbol{q} = (\theta,\chi)$, where $0 \leqslant \theta < 2\pi$ gives the orientation of $\boldsymbol{x}_3 - \boldsymbol{x}_2$ with respect to a fixed frame of reference and $0 \leqslant \chi < \pi$ is the internal angle between $\boldsymbol{x}_1 - \boldsymbol{x}_2$ and $\boldsymbol{x}_3 - \boldsymbol{x}_2$ (Fig. 1). By letting χ vary between 0 and π only, we do not distinguish between the two configurations that are obtained by exchanging $\boldsymbol{x}_1$ and $\boldsymbol{x}_3$. For $d = 3$, $\boldsymbol{q} = (\alpha,\beta,\gamma,\chi)$, where $0 \leqslant \chi < \pi$ is again the internal angle (Fig. 1) and $0 \leqslant \alpha < 2\pi$, $0 \leqslant \beta < \pi$, and $0 \leqslant \gamma < 2\pi$ are the Euler angles that specify the orientation of the orthogonal triad $(\boldsymbol{x}_3 - \boldsymbol{x}_1) \wedge (\boldsymbol{x}_2 - \boldsymbol{x}_c), \boldsymbol{x}_3 - \boldsymbol{x}_1, \boldsymbol{x}_2 - \boldsymbol{x}_c$ with respect to a fixed coordinate system. The relation between $\boldsymbol{r}_\nu$ and $\boldsymbol{q}$ is given in Ref. [24] for $d = 2$ and in Refs. [17,18] for $d = 3$.

The statistics of the configuration of the trumbbell is specified by the probability density function (PDF) $\Psi(\boldsymbol{q};t)$, which is such that $\int \Psi(\boldsymbol{q};t)d\boldsymbol{q} = 1$, and satisfies the following diffusion equation with periodic boundary conditions (summation over repeated indices is understood throughout this paper) [17,18]:

$$\partial_t \Psi = -\partial^i \left\{ \mathcal{G}^{ij} \left[\kappa^{kl}(t) r_\nu^l \left(\partial^j r_\nu^k \right) \Psi - \zeta^{-1} (\partial^j \phi) \Psi - KT \zeta^{-1} \sqrt{h} \partial^j (\Psi/\sqrt{h}) \right] \right\}, \tag{1}$$

where $\partial^i \equiv \partial/\partial q^i$, $\kappa^{ij}(t) = \partial^j u^i(t)$ is the velocity gradient evaluated at $\boldsymbol{x}_c(t)$, ζ is the drag coefficient of the beads, K is the Boltzmann constant, T is temperature, $\phi = \mu(\chi - \chi_\star)^2/2$ with $\chi_\star = \pi$ is the restoring potential, $\mathcal{G} = \mathcal{H}^{-1}$ with $\mathcal{H}^{ij} = \frac{\partial r_\nu^k}{\partial q^i} \frac{\partial r_\nu^k}{\partial q^j}$, and $h = \det(\mathcal{H})$. The explicit expressions of h and $\mathcal{G}$ can be found in Ref. [24] for $d = 2$ and in Ref. [18] for $d = 3$. Note that the stationary PDF of $\boldsymbol{q}$, $\Psi_{\rm st}(\boldsymbol{q})$, takes the form $\Psi_{\rm st}(\boldsymbol{q}) = J\psi_{\rm st}(\boldsymbol{q})$, where J is proportional to the Jacobian of the transformation from the $\boldsymbol{r}_\nu$ to the $\boldsymbol{q}$ coordinates; $J = 1$ for $d = 2$ and $J = \sin\chi \sin\beta$ for $d = 3$.

In the absence of flow gradients ($\boldsymbol{\kappa} = 0$) and the restoring potential ($\mu = 0$), $\Psi_{\rm st}(\boldsymbol{q}) = J\psi_0(\chi)$ with $\psi_0(\chi) \propto \sqrt{4 - \cos^2\chi}$ [17]. Thus, the configuration with the rods being perpendicular ($\chi = \pi/2$) has slightly greater probability than the other configurations, while the folded ($\chi = 0$) and the extended ($\chi = \pi$) configurations are equally probable. The restoring potential breaks this symmetry. For $\mu \neq 0$, $\psi_{\rm st}(\chi) \propto \psi_0(\chi)\exp[-Z(\chi_\star - \chi)^2/2]$ [17], where $Z \equiv \mu/KT$ is a stiffness parameter; the extended configuration is the most probable one and its probability increases as Z increases. Finally, when the trumbbell is introduced in a nonuniform flow ($\boldsymbol{\kappa} \neq 0$) its dynamics results from the interplay between the restoring elastic force and the deformation by the flow.

We first examine the effect of pure stretching on the statistics of the bending angle χ. Consider a 2D extensional flow $\boldsymbol{u} = \sigma(x,-y)$. As $\boldsymbol{\kappa} = \boldsymbol{\kappa}^\top$, the stationary solution of Eq. (1) is known analytically: $\Psi_{\rm st}(\theta,\chi) \propto \sqrt{h}\exp[(\Phi - \phi)/KT]$ with $\Phi = (\zeta/2)\kappa^{ij} r_\nu^i r_\nu^j$ [17]. The statistics of χ varies according to the orientation θ of the trumbbell; however, the average effect of the flow can be understood by considering the marginal stationary PDF of χ: $\hat{\Psi}_{\rm st}(\chi) = J\hat{\psi}_{\rm st}(\chi)$ with $\hat{\psi}_{\rm st}(\chi) \propto \psi_0(\chi)\exp[-Z(\chi_\star - \chi)^2/2]I_0[Z(1 - 2\cos\chi)\mathrm{Wi}/3]$, where I_0 is the modified Bessel function of the first kind of order 0

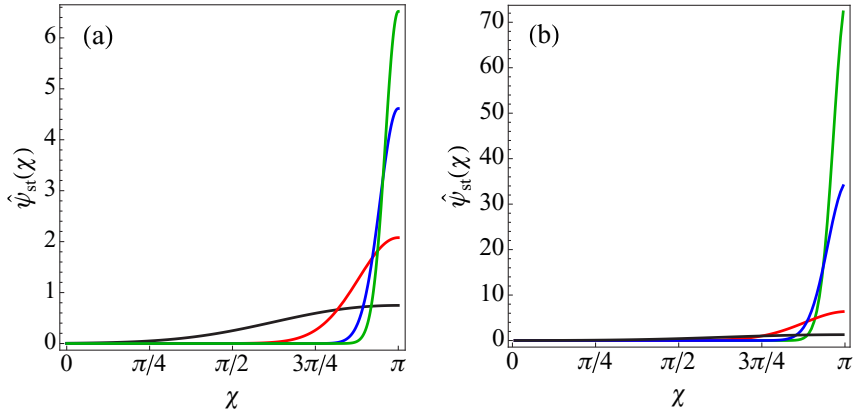

FIG. 2. Extensional flow: $\hat{\psi}_{st}(\chi)$ for (a) $d = 2$ and (b) $d = 3$, $Z = 1$, and $\mathrm{Wi} = 0$ (black line), $\mathrm{Wi} = 10$ (red line), $\mathrm{Wi} = 50$ (blue line), and $\mathrm{Wi} = 100$ (green line).

and the Weissenberg number $\mathrm{Wi} = \sigma\tau$ measures the relative strength of the flow and the restoring potential ($\tau = \zeta\ell^2/\mu$ is the characteristic time scale of the restoring potential). The product of Z and Wi yields the Péclet number $\mathrm{Pe} = \sigma\ell^2\zeta/KT$. On average, the 2D extensional flow favors the $\chi = \pi$ configuration, with this effect becoming stronger as Wi increases [Fig. 2(a)]. A linear stability analysis indeed shows that, when the flow dominates over the restoring potential ($\mathrm{Wi} \gg 1$) and thermal noise is disregarded, both the folded and the extended configurations are stable and their stability improves with increasing Wi, but the latter configuration is more attractive than the former for all Wi [24]. For a 3D uniaxial extensional flow $\boldsymbol{u} = \sigma(x, -y/2, -z/2)$, $\hat{\psi}_{st}(\chi)$ can again be calculated by using $\boldsymbol{\kappa} = \boldsymbol{\kappa}^{\top}$ and is shown in Fig. 2(b). Clearly, $\hat{\psi}_{st}(\chi)$ has a similar shape in two and three dimensions. Nevertheless, an inspection of the temporal dynamics of the trumbbell reveals a strong dependence on the dimension of the flow. To illustrate this point, we consider the situation in which the flow dominates over the restoring force ($\mathrm{Wi} \gg 1$ and $Z = 0$) and study the temporal evolution of $\chi(t)$ as a function of Pe. In particular, it is useful to analyze the average time T_0 it takes for an initially folded trumbbell to exit the interval $(0, \Delta\chi)$; T_0 is shown in Fig. 3 as a function of $\Delta\chi$ and Pe. The exit time T_0 behaves similarly for $d = 2$ and for $d = 3$. For small values of $\Delta\chi$, $T_0 \propto (\Delta\chi)^2$ because the dynamics is dominated by thermal noise, it keeps increasing as a function of $\Delta\chi$ until $\Delta\chi \approx \pi/2$, and it then becomes independent of $\Delta\chi$ because the average time

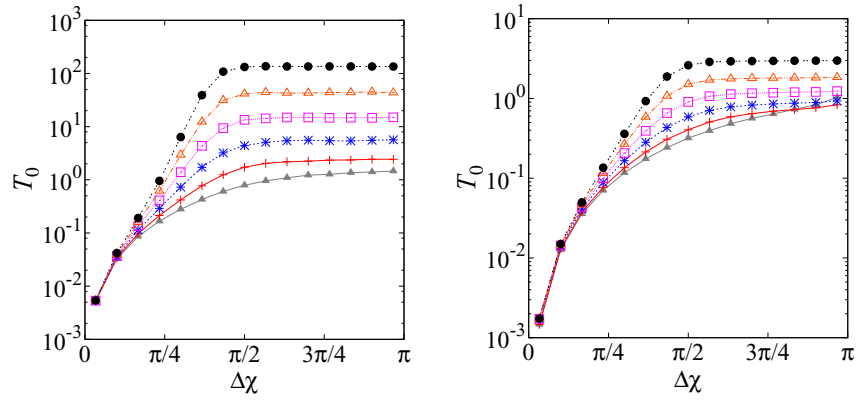

FIG. 3. Extensional flow: T_0 vs $\Delta\chi$ for (a) $d = 2$, $Z = 0$, and (from bottom to top) $\mathrm{Pe} = 4, 8, 12, 16, 20, 24$ and (b) $d = 3$ and the same values of Z and Pe as in (a). Here T_0 is calculated through a Monte Carlo simulation of the stochastic differential equations that govern the Lagrangian dynamics of the trumbbell for $d = 2$ and 3 (see Ref. [24]).

required to completely unfold a trumbbell with $\chi > \pi/2$ is much shorter than the time it takes to unfold an initially folded trumbbell up to $\chi \approx \pi/2$. However, for comparable values of Pe, T_0 is at least one order of magnitude longer in two dimensions than in three. The reason for this difference is geometrical: For $d = 2$ there are two degrees of freedom of the trumbbell, whereas there are four for $d = 3$; hence in the latter case it is easier for thermal noise to move the system away from the folded configuration. Such dependence of the dynamics on the spatial dimension d does not affect the shape of $\hat{\psi}_{\rm st}(\chi)$, because $\boldsymbol{\kappa}$ is constant and the system has the time to evolve to its stationary configuration. However, the flow dimension may impact the stationary statistics of χ in a turbulent flow, since in such a flow $\boldsymbol{\kappa}$ fluctuates.

In order to investigate this point analytically, we consider the Kraichnan random flow [25] in the Batchelor regime. The velocity gradient is a δ-correlated-in-time $(d \times d)$-dimensional Gaussian stochastic process with zero mean and correlation: $\langle \kappa^{ij}(t)\kappa^{kl}(t')\rangle = \mathcal{K}^{ijkl}\delta(t-t')$, where $\mathcal{K}^{ijkl} = 2\lambda[(d+1)\delta^{ik}\delta^{jl} - \delta^{ij}\delta^{kl} - \delta^{il}\delta^{jk}]/d(d-1)$ and λ is the Lyapunov exponent of the flow. The form of the tensor $\mathcal{K}$ ensures that the flow is incompressible and statistically isotropic. Although the assumption of temporal decorrelation is unrealistic, the study of this flow has contributed substantially to the understanding of turbulent transport, because it allows an analytical approach to this problem [1]. Let $P(\boldsymbol{q};t)$ be the PDF of the configuration of the trumbbell with respect to the realizations both of $\boldsymbol{\kappa}(t)$ and of thermal noise [$\int P(\boldsymbol{q};t)d\boldsymbol{q} = 1$]; $P(\boldsymbol{q};t)$ solves the diffusion equation [13]

$$\partial_t P = \partial^i\left\{\tfrac{1}{2}\mathcal{K}^{klmn}\mathcal{G}^{ij}r_\nu^l\left(\partial^j r_\nu^k\right)\partial^a\left[\mathcal{G}^{ab}r_\rho^n\left(\partial^b r_\rho^m\right)P\right] + \mathcal{G}^{ij}\zeta^{-1}[(\partial^j\phi)P + KT\sqrt{h}\partial^j(P/\sqrt{h})]\right\}. \quad (2)$$

Let us first consider the 2D case. By using $\boldsymbol{q} = (\theta,\chi)$ and the corresponding $\mathcal{G}$, we can rewrite Eq. (2) as a Fokker-Planck equation (FPE) in the variables θ and χ. The drift and diffusion coefficients, however, do not depend on θ because of statistical isotropy. Hence the stationary PDF of the configuration is a function of χ alone and is the stationary solution of the following FPE in one variable:

$$\partial_s P = -\partial_\chi(VP) + \tfrac{1}{2}\partial^2_{\chi\chi}(DP), \quad (3)$$

with $s = t/\tau$,

$$V(\chi) = \frac{12\sin\chi}{Z(2-\cos\chi)(2+\cos\chi)^2} + \frac{6(\chi_\star - \chi)}{(2+\cos\chi)} + 2\,\mathrm{Wi}\frac{\sin\chi[5+\cos\chi - 11\cos(2\chi) - \cos(3\chi)]}{(2-\cos\chi)(2+\cos\chi)^3}, \quad (4)$$

and $D(\chi) = 12/Z(2+\cos\chi) + 16\,\mathrm{Wi}\sin^2\chi/(2+\cos\chi)^2$, where now $\mathrm{Wi} = \lambda\tau$. The stationary solution of Eq. (3) that satisfies periodic boundary conditions is [26]

$$P_{\rm st}(\boldsymbol{q}) = Jp_{\rm st}(\chi) \propto \exp\left[2\int_0^\chi d\eta\, V(\eta)/D(\eta)\right]\Big/ D(\chi). \quad (5)$$

The function $p_{\rm st}(\chi)$ is plotted in Fig. 4(a) for different values of Wi. For small Wi, the most probable configuration is the $\chi = \pi$ one, as in the hyperbolic flow. However, as Wi increases, a second peak emerges near $\chi = 0$, while intermediate values of χ become less and less probable. At large Wi, $p_{\rm st}(\chi)$ consists of two narrow peaks, one at $\chi = \pi$ and the other approaching $\chi = 0$, with the latter becoming more and more pronounced with increasing Wi.

In three dimensions, Eq. (2) can be rewritten as a FPE in the variables α,β,γ,χ. Owing to statistical isotropy, $P_{\rm st}(\boldsymbol{q})$ is again the stationary solution of a FPE in the variable χ alone and takes

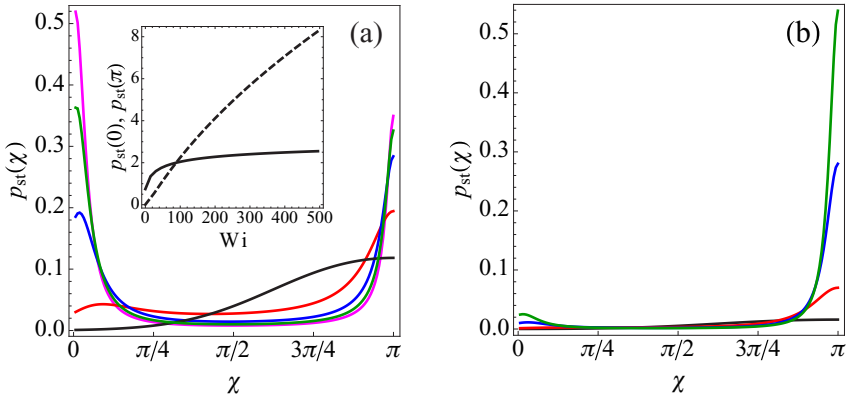

FIG. 4. Batchelor-Kraichnan flow: (a) $p_{st}(\chi)$ for $d = 2$, $Z = 1$, and $\mathrm{Wi} = 0$ (black line), $\mathrm{Wi} = 10$ (red line), $\mathrm{Wi} = 50$ (blue line), $\mathrm{Wi} = 100$ (green line), and $\mathrm{Wi} = 150$ (magenta line). The inset shows the values of $p_{st}(\chi)$ at $\chi = 0$ (dashed line) and $\chi = \pi$ (solid line) vs Wi. (b) $p_{st}(\chi)$ for $d = 3$ and the same values of Z and Wi as in (a).

the form in Eq. (5) with

$$V(\chi) = \frac{3[4 + 13\cos\chi - 4\cos(2\chi) - \cos(3\chi)]}{2Z\sin\chi(2 - \cos\chi)(2 + \cos\chi)^2} + \frac{6(\chi_\star - \chi)}{(2 + \cos\chi)} + \mathrm{Wi}\frac{\sin\chi[63\cos\chi - 15\cos(3\chi) + 296\sin^2\chi]}{12(2 - \cos\chi)(2 + \cos\chi)^3} \tag{6}$$

and $D(\chi) = 12/Z(2 + \cos\chi) + 26\,\mathrm{Wi}\sin^2\chi/3(2 + \cos\chi)^2$. Figure 4(b) shows that a tiny peak at $\chi = 0$ emerges only for very large Wi and the $\chi = \pi$ configuration prevails for all Wi. Thus, the statistics of χ is different in two and three dimensions. In particular, for $d = 3$, the behavior of $p_{st}(\chi)$ is similar to that found for the extensional flow.

The difference in the stationary statistics of χ for $d = 2$ and 3 can again be understood by assuming $\mathrm{Wi} = \infty$ and $Z = 0$ and by considering T_0 and the average time T_π it takes for an initially extended trumbbell ($\chi = \pi$) to exit the interval $(\pi - \Delta\chi, \pi)$ through the left. The ratio T_0/T_π is plotted in Fig. 5 vs $\Delta\chi$ for increasing Pe. For small $\Delta\chi$, $T_0 > T_\pi$ for both $d = 2$ and $d = 3$, because in the folded configuration the end beads have very similar velocities and is therefore difficult for the flow to separate them. However, T_0/T_π is greater for $d = 2$ than for $d = 3$; moreover, it grows fast as a function of Pe for $d = 2$ and is almost independent of Pe for $d = 3$. This is because for $d = 2$ the beads are confined to the plane and is much more difficult for the flow to separate them compared to the 3D case. When $\Delta\chi \approx \pi$, T_0 and T_π are comparable for $d = 2$, whereas $T_0 \ll T_\pi$ for $d = 3$, i.e., in this case the average time required to completely unfold an initially folded trumbbell is much shorter than that required to fold an initially extended one. The reason for this is once again geometrical; it is indeed more difficult to fold two rods whose orientations fluctuate in 3D space than to fold two rods that are confined to the plane. The above discussion explains why, for $d = 2$, $p_{st}(\chi)$ shows a second peak near $\chi = 0$ and this peak dominates for a strong flow, whereas $p_{st}(\chi)$ does not enjoy the same property for $d = 3$.

Are the results obtained so far valid in turbulent flows? To ensure that the qualitative properties of the statistics of χ do not depend on the Gaussianity and temporal decorrelation of the Batchelor-Kraichnan flow, we perform Lagrangian direct numerical simulations of the trumbbell model in 2D and 3D incompressible isotropic turbulence by using a standard pseudospectral method on a 2π-periodic domain. For $d = 2$, our simulation is forced at large scales and uses an air-drag-induced Ekman friction; the choice of the parameters [27,28] yields a Taylor-microscale Reynolds number $\mathrm{Re}_\lambda = 827$, in the nonequilibrium statistically steady state. For $d = 3$, the forcing has a fixed energy input [29,30] and $\mathrm{Re}_\lambda = 121$. We have done other simulations with different Re_λ and forcing scales

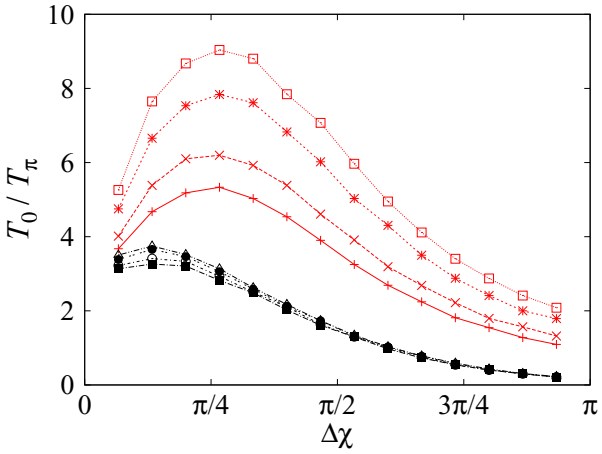

FIG. 5. Batchelor-Kraichnan flow: T_0/T_π vs $\Delta\chi$ for $d = 2$ (red) and $d = 3$ (black), $Z = 0$, and (from bottom to top) Pe $= 30, 50, 100, 150$. Here T_0 and T_π are calculated from a numerical simulation of the Itô stochastic differential equation $\dot{\chi} = V(\chi) + \sqrt{D(\chi)}\,\xi(t)$ for $d = 2$ and of the analogous stochastic differential equation for $\cos\chi$ for $d = 3$ [here $\xi(t)$ is white noise].

that yield results consistent with the ones presented here. The flow is seeded with 10^5 trumbbells in two dimensions and with 10^6 trumbbells in three dimensions, each of whose center of mass evolves as a tracer; the velocity at $\boldsymbol{x}_c$ is evaluated from the Eulerian velocity by using a bilinear-interpolation scheme [27,28]. The statistics of χ is computed from a Lagrangian simulation of the stochastic differential equations for the configuration of the trumbbell [24]. The Weissenberg number is defined as for the random flow, i.e., $\mathrm{Wi} = \lambda\tau$. The numerical results shown in Fig. 6 confirm the predictions based on the Batchelor-Kraichnan flow. In particular, for $d = 2$, the $\chi = \pi$ configuration is favored at small Wi. As Wi increases, the probability of a folded configuration grows significantly and eventually, at extremely large Wi, $p_{\mathrm{st}}(\chi)$ displays strong peaks at $\chi \approx 0$ and $\chi \approx \pi$, with the former peak prevailing over the latter. For $d = 3$, $p_{\mathrm{st}}(\chi)$ has a maximum at $\chi = \pi$, which grows with increasing Wi; a very small peak near $\chi = 0$ only appears for very large Wi.

We have studied the bending statistics of semiflexible particles in laminar and turbulent flows. By using analytical calculations and numerical simulations, we have shown that the stationary distribution of the bending internal angle depends strongly on whether the flow is laminar or

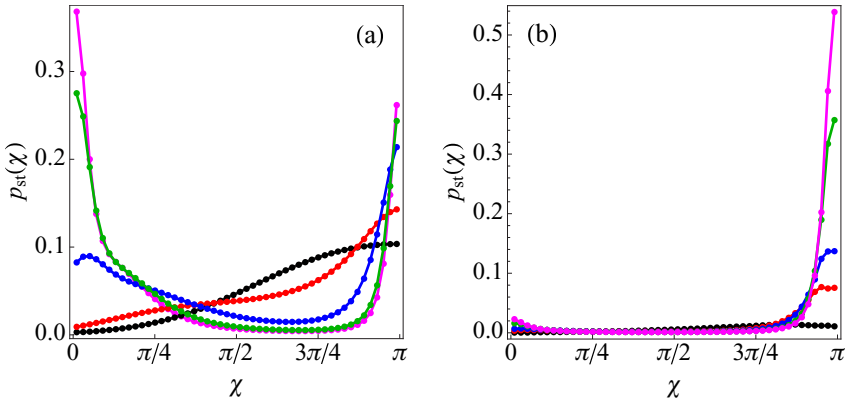

FIG. 6. Homogeneous isotropic turbulence: (a) $p_{\mathrm{st}}(\chi)$ for $d = 2$, $Z = 1$, and $\mathrm{Wi} = 0.04$ (black line), $\mathrm{Wi} = 17.53$ (red line), $\mathrm{Wi} = 45.3$ (blue line), $\mathrm{Wi} = 54$ (green line), and $\mathrm{Wi} = 102$ (magenta line) and (b) $p_{\mathrm{st}}(\chi)$ for $d = 3$, $Z = 1$, and $\mathrm{Wi} = 3.3$ (black line), $\mathrm{Wi} = 26.3$ (red line), $\mathrm{Wi} = 49.3$ (blue line), $\mathrm{Wi} = 131.4$ (green line), and $\mathrm{Wi} = 197.1$ (magenta line).

turbulent and, in the turbulent case, is sensitive to the flow dimensionality. We have interpreted this behavior in terms of the mean exit times from the folded and the extended configurations. These results suggest that the rheology of suspensions of semiflexible particles may also exhibit an analogous strong dependence on the properties of the flow. We hope our work will lead to further experiments directed towards the study of the Lagrangian dynamics of semiflexible particles in turbulent flows and the non-Newtonian properties of turbulent suspensions of such particles.

The work of A.A. and E.L.C.M.P. was supported by EACEA through the Erasmus Mundus Mobility with Asia program. E.L.C.M.P., S.S.R., and D.V. acknowledge the support of the EU COST Action MP1305 "Flowing Matter". S.S.R. and D.V. thank the Indo-French Center for Applied Mathematics for financial support. S.S.R. acknowledges support from the AIRBUS Group Corporate Foundation Chair in Mathematics of Complex Systems established in ICTS-TIFR, the DST (India) Project No. ECR/2015/000361. D.V. would like to thank ICTS-TIFR for the kind hospitality. The direct numerical simulations were done on *Mowgli* at the ICTS-TIFR, Bangalore, India.

[1] G. Falkovich, K. Gawędzki, and M. Vergassola, Particles and fields in fluid turbulence, Rev. Mod. Phys. **73**, 913 (2001).
[2] R. Pandit, P. Perlekar, and S. S. Ray, Statistical properties of turbulence: An overview, Pramana **73**, 157 (2009).
[3] F. Toschi and E. Bodenschatz, Lagrangian properties of particles in turbulence, Annu. Rev. Fluid Mech. **41**, 375 (2009).
[4] J. P. L. C. Salazar and L. R. Collins, Two-particle dispersion in isotropic turbulent flows, Annu. Rev. Fluid Mech. **41**, 405 (2009).
[5] J. Bec, L. Biferale, G. Boffetta, M. Cencini, S. Musacchio, and F. Toschi, Lyapunov exponents of heavy particles in turbulence, Phys. Fluids **18**, 091702 (2006).
[6] S. Musacchio and D. Vincenzi, Deformation of a flexible polymer in a random flow with long correlation time, J. Fluid Mech. **670**, 326 (2011).
[7] A. Pumir and M. Wilkinson, Orientation statistics of small particles in turbulence, New J. Phys. **13**, 093030 (2011).
[8] S. Parsa, E. Calzavarini, F. Toschi, and G. A. Voth, Rotation Rate of Rods in Turbulent Fluid Flow, Phys. Rev. Lett. **109**, 134501 (2012).
[9] D. Vincenzi, Orientation of non-spherical particles in an axisymmetric random flow, J. Fluid Mech. **719**, 465 (2013).
[10] K. Gustavsson, J. Einarsson, and B. Mehlig, Tumbling of Small Axisymmetric Particles in Random and Turbulent Flows, Phys. Rev. Lett. **112**, 014501 (2014).
[11] A. Gupta, D. Vincenzi, and R. Pandit, Elliptical tracers in two-dimensional, homogeneous, isotropic fluid turbulence: The statistics of alignment, rotation, and nematic order, Phys. Rev. E **89**, 021001(R) (2014).
[12] L. Chevillard and C. Meneveau, Orientation dynamics of small, triaxial-ellipsoidal particles in isotropic turbulence, J. Fluid Mech. **737**, 571 (2013).
[13] E. L. C. VI M. Plan, A. Ali, and D. Vincenzi, Bead-rod-spring models in random flows, Phys. Rev. E **94**, 020501(R) (2016).
[14] G. G. Marcus, S. Parsa, S. Kramel, R. Ni, and G. A. Voth, Measurements of the solid-body rotation of anisotropic particles in 3D turbulence, New J. Phys. **16**, 102001 (2014).
[15] K. Gustavsson and L. Biferale, Preferential sampling of helicity by isotropic helicoids, Phys. Rev. Fluids **1**, 054201 (2016).
[16] S. Kramel, G. A. Voth, S. Tympel, and F. Toschi, Preferential Rotation of Chiral Dipoles in Isotropic Turbulence, Phys. Rev. Lett. **117**, 154501 (2016).

[17] O. Hassager, Kinetic theory and rheology of bead-rod models for macromolecular solutions. I. Equilibrium and steady flow properties, J. Chem. Phys. **60**, 2111 (1974); Kinetic theory and rheology of bead-rod models for macromolecular solutions. II. Linear unsteady flow properties, *ibid.* **60**, 4001 (1974).

[18] R. B. Bird, O. Hassager, R. C. Armstrong, and C. F. C. Curtiss, *Dynamics of Polymeric Liquids* (Wiley, New York, 1977), Vol. 2.

[19] D. B. Roitman, The elastic trumbbell model for dynamics of stiff chains, in *Rotational Dynamics of Small and Macromolecules*, Proceedings of a Workshop held at the Zentrum für interdisziplinäre Forschung Universität Bielefeld, Bielefield, edited by Th. Dormfüller and R. Pecora, Lecture Notes in Physics Vol. 293 (Springer, Berlin Heidelberg, 1987), p. 192.

[20] J. Garcia de la Torre, Hydrodynamics of segmentally flexible macromolecules, Eur. Biophys. J. **23**, 307 (1994).

[21] E. J. Hinch, Brownian motion with stiff bonds and rigid constraints, J. Fluid Mech. **271**, 219 (1994).

[22] F. G. Diaz and J. Garcia de la Torre, Simulation of the rotational Brownian dynamics of a simple, segmentally flexible model: The elastic trumbbell, J. Chem. Phys. **88**, 7698 (1988).

[23] R. J. Lewis, S. A. Allison, D. Eden, and R. Pecora, Brownian dynamics simulations of a three-subunit and a ten-subunit worm-like chain: Comparison of results with trumbell theory and with experimental results from DNA, J. Chem. Phys. **89**, 2490 (1988).

[24] E. L. C. VI M. Plan and D. Vincenzi, Tumbling of a Brownian particle in an extensional flow, Proc. R. Soc. London A **472**, 20160226 (2016).

[25] R. H. Kraichnan, Small-scale structure of a scalar field convected by turbulence, Phys. Fluids **11**, 945 (1968).

[26] H. Risken, *The Fokker-Planck Equation* (Springer, Berlin, 1989).

[27] P. Perlekar, S. S. Ray, D. Mitra, and R. Pandit, Persistence Problem in Two-Dimensional Fluid Turbulence, Phys. Rev. Lett. **106**, 054501 (2011).

[28] S. S. Ray, D. Mitra, P. Perlekar, and R. Pandit, Dynamic Multiscaling in Two-Dimensional Fluid Turbulence, Phy. Rev. Lett. **107**, 184503 (2011).

[29] A. G. Lamorgese, D. A. Caughey, and S. B. Pope, Direct numerical simulation of homogeneous turbulence with hyperviscosity, Phys. Fluids **17**, 015106 (2005).

[30] G. Sahoo, P. Perlekar, and R. Pandit, Systematics of the magnetic-Prandtl-number dependence of homogeneous, isotropic magnetohydrodynamic turbulence, New J. Phys. **13**, 013036 (2011).

Annexe E

Rupture

E1. S.S. Ray & D. Vincenzi
"Droplets in isotropic turbulence : deformation and breakup statistics"
J. Fluid Mech. **852**, 313–328 (2018)

J. Fluid Mech. (2018), *vol.* 852, *pp.* 313–328.
doi:10.1017/jfm.2018.453

Droplets in isotropic turbulence: deformation and breakup statistics

Samriddhi Sankar Ray[1] **and Dario Vincenzi**[2,†]

[1]International Centre for Theoretical Sciences, Tata Institute of Fundamental Research, Bangalore 560089, India

[2]Université Côte d'Azur, CNRS, LJAD, 06108 Nice, France

(Received 10 December 2017; revised 23 March 2018; accepted 22 May 2018; first published online 3 August 2018)

The statistics of the deformation and breakup of neutrally buoyant sub-Kolmogorov ellipsoidal drops is investigated via Lagrangian simulations of homogeneous isotropic turbulence. The mean lifetime of a drop is also studied as a function of the initial drop size and the capillary number. A vector model of a drop previously introduced by Olbricht *et al.* (*J. Non-Newtonian Fluid Mech.*, vol. 10, 1982, pp. 291–318) is used to predict the behaviour of the above quantities analytically.

Key words: drops, isotropic turbulence

1. Introduction

The dispersion of drops of one fluid in another fluid that is turbulent and immiscible with the first has numerous applications. Emulsion processing in chemical engineering, for instance, often uses turbulent flow conditions (Walstra 1993; Schuchmann & Schubert 2003), and the design of efficient emulsion apparatus requires a detailed understanding of single-drop dynamics in turbulent flows (Windhab *et al.* 2005).

The theory of Kolmogorov (1949) and Hinze (1955) predicts two different regimes according to whether a drop is larger or smaller, respectively, than the Kolmogorov dissipation scale ℓ_K. In the former case, the dynamics of the drop results from the competition between the inertial hydrodynamic stress, which distorts the drop, and the stress due to surface tension, which restores the drop to its equilibrium configuration. In the latter case, the competition is between surface tension and the viscous stress. The literature on drop dynamics in turbulent flows has largely focused on drops whose size lies in the inertial range. The sub-Kolmogorov regime, albeit difficult to examine both experimentally and numerically, is of practical significance as well. For viscous oils, turbulent emulsification is indeed known to be more efficient in the sub-Kolmogorov regime (Vankova *et al.* 2007). In addition, even if the initial drop sizes are larger than ℓ_K, in high-Reynolds-number flows subsequent breakups can generate sub-Kolmogorov drops at long times (Cristini *et al.* 2003). Another mechanism for the formation of small drops in a turbulent flow was recently reported in Prabhakaran *et al.* (2017): it consists in the nucleation of microdroplets in the

† Email address for correspondence: dario.vincenzi@unice.fr

wake of a large cold drop crossing a supersaturated environment. Drops smaller than ℓ_K were also used as tracers in laboratory experiments with the purpose of examining the statistics of the Lagrangian acceleration in turbulent flows (Ayyalasomayajula, Collins & Warhaft 2008; Ayyalasomayajula, Gylfason & Warhaft 2008).

The deformation and breakup of a drop in a chaotic flow were first studied by Muzzio, Tjahjadi & Ottino (1991) and Tjahjadi & Ottino (1991) by means of a 'journal-bearing' flow generated by the periodic motion of two rotating eccentric cylinders. The fluid trajectories are chaotic in this flow, so a drop becomes highly stretched, folds and eventually breaks. Subsequent breakups of the drop fragments lead to a population of drops with different sizes; various modes of breakup were observed, including capillary-wave instabilities, necking, and end and fold pinching.

Cristini *et al.* (2003) studied the dynamics of a sub-Kolmogorov drop in a numerical simulation of homogeneous and isotropic turbulence at moderate Reynolds number. The trajectory of the centre of mass of the drop was approximated by a fluid trajectory, under the assumption of a small density contrast between the fluids inside and outside the drop. The dynamics of the drop was calculated via a boundary integral approach by using the Stokes equations with appropriate boundary conditions at the drop interface and with a far field given by a linear expansion of the external turbulent flow about the position of the centre of mass. The statistics of drop length, orientation and breakup was studied as a function of the viscosity ratio between the inner and outer fluids and of the capillary number. This latter determines the relative intensity of the viscous and surface-tension forces. It was shown, in particular, that under moderate-deformation conditions drop reorientation is mainly due to the deformation of the drop surface rather than the rotation of the drop by the flow.

For high Reynolds numbers, the direct numerical simulation of sub-Kolmogorov drops is still impractical with the available computational facilities, especially when a very large number of drops needs to be considered in order to resolve the statistical properties of drop dynamics. An alternative approach consists in using simplified models of drops. Biferale, Meneveau & Verzicco (2014) coupled the model of Maffettone & Minale (1998), which describes neutrally buoyant ellipsoidal drops, with a Lagrangian simulation of high-Reynolds-number, homogeneous and isotropic turbulence. The model of Maffettone & Minale (1998) was originally derived for linear flows but can be applied to turbulent flows if the Reynolds number at the scale of the drop is smaller than unity, i.e. the size of the drop is smaller than ℓ_K. This approach allowed the authors to obtain a detailed statistical characterization of drop deformation and orientation. In particular, the statistics of the deformation was related to that of the stretching rates of the flow via an analogy between the model of Maffettone & Minale (1998) and the Oldroyd-B model for flexible polymers (e.g. Bird *et al.* 1987). A critical capillary number for breakup was thus identified for the case in which the viscosities of the fluids inside and outside the drop coincide. Spandan, Lohse & Verzicco (2016) recently applied the model of Maffettone & Minale (1998) to a turbulent Taylor–Couette flow, in order to examine the dependence of drop dynamics on the flow geometry.

The goal of the present study is to further investigate and elucidate the statistical properties of drop deformation and breakup in the sub-Kolmogorov regime. To this end, we follow the approach proposed by Biferale, Meneveau & Verzicco (2014) and use the model of Maffettone & Minale (1998) in combination with Lagrangian simulations of homogeneous and isotropic turbulence. We perform a detailed numerical analysis of the time-dependent and time-integrated probability density functions of drop size as a function of the capillary number, the viscosity

ratio between the inner and outer fluids and the initial drop-size distribution. We also study the breakup rate and the mean lifetime of a drop as a function of the same quantities. The results of the numerical simulations are then derived analytically by means of a vector model of drop originally proposed by Olbricht, Rallison & Leal (1982).

2. Deformation and breakup statistics

The model of Maffettone & Minale (1998) assumes that both the fluid of which the drop is composed and the fluid in which it is immersed are Newtonian. The drop is neutrally buoyant and is transported passively (i.e. it does not affect the surrounding flow), it is ellipsoidal at all times, and its volume is preserved. In addition, the flow about the drop is incompressible and linear. This latter assumption is appropriate for turbulent flows if the size of the drop is smaller than ℓ_K. The volume fraction is very low, so that hydrodynamic interactions between drops are negligible and attention can be directed to the dynamics of a single drop.

The shape and the orientation of the drop are described by a second-rank symmetric positive definite tensor $\boldsymbol{M}$, whose eigenvectors are the semi-axes of the drop and whose eigenvalues $m_1^2 \geqslant m_2^2 \geqslant m_3^2$ yield the squared lengths of the same semi-axes. The centre of mass of the drop evolves as a tracer, while the Lagrangian evolution of $\boldsymbol{M}$ is given by the following equation:

$$\dot{\boldsymbol{M}} = \boldsymbol{G}\boldsymbol{M} + \boldsymbol{M}\boldsymbol{G}^{\top} - \frac{f_1(\mu)}{\tau}[\boldsymbol{M} - g(\boldsymbol{M})\boldsymbol{I}], \tag{2.1}$$

where $\boldsymbol{G} = f_2(\mu)\boldsymbol{S} + \boldsymbol{\Omega}$ is an effective velocity gradient; $\boldsymbol{\Omega} = [\nabla\boldsymbol{u} - (\nabla\boldsymbol{u})^{\top}]/2$ and $\boldsymbol{S} = [\nabla\boldsymbol{u} + (\nabla\boldsymbol{u})^{\top}]/2$ are the vorticity and rate-of-strain tensors evaluated at the centre of mass of the drop, respectively. Note that here $(\nabla\boldsymbol{u})_{ij} = \partial_j u_i$. The coefficients $f_1(\mu)$ and $f_2(\mu)$ depend on the ratio μ of the viscosity of the drop and that of the external fluid and were chosen in such a way as to match theoretical predictions for small capillary numbers (Maffettone & Minale 1998):

$$f_1(\mu) = \frac{40(\mu+1)}{(2\mu+3)(19\mu+16)}, \quad f_2(\mu) = \frac{5}{2\mu+3}. \tag{2.2a,b}$$

Note that $f_2(1) = 1$ and hence, for $\mu = 1$, $\boldsymbol{G} = \nabla\boldsymbol{u}$. The last term in (2.1) describes the capillary relaxation to the spherical shape with a time scale τ. Thanks to an appropriate choice of the function $g(\boldsymbol{M})$, the same term enforces that $\det \boldsymbol{M}$ is constant in time and hence the volume of the drop is preserved. The function $g(\boldsymbol{M})$ has the form $g(\boldsymbol{M}) = 3\mathrm{III}_M/\mathrm{II}_M$, where II_M and III_M are the second and third invariants of $\boldsymbol{M}$, i.e. $\mathrm{II}_M = [(\mathrm{tr}\,\boldsymbol{M})^2 - \mathrm{tr}\,\boldsymbol{M}^2]/2$ and $\mathrm{III}_M = \det \boldsymbol{M}$. Maffettone & Minale (1998) also proposed an improved expression of f_2 that depends on the capillary number and more accurately describes the deformations observed in experiments for large strains and high viscosity ratios. For the sake of simplicity, here we use the coefficients given in (2.2); the improved version of the model of Maffettone & Minale (1998) is discussed in § 4.

This section provides insight into the statistics of drop deformation and breakup in three-dimensional homogeneous isotropic turbulence. We obtain such a turbulent flow by performing direct numerical simulations of the three-dimensional Navier–Stokes equation

$$\partial_t \boldsymbol{u} + \boldsymbol{u}\cdot\nabla\boldsymbol{u} = -\nabla p + \nu\Delta\boldsymbol{u} + \boldsymbol{F} \tag{2.3}$$

for the velocity field $\boldsymbol{u}$ (and pressure p) augmented with the incompressibility condition $\boldsymbol{\nabla \cdot u} = 0$. We use the standard, fully de-aliased pseudo-spectral method on a cubic domain of size 2π with 512^3 collocation points and periodic boundary conditions. By using these boundary conditions, we do not take into account the interaction of the drops with the walls that confine the fluid. The flow is driven to a non-equilibrium steady state by an external force $\boldsymbol{F}$ with a fixed energy input ϵ. Our choice of ϵ and kinematic viscosity ν ensures a Taylor-scale Reynolds number $Re_\lambda \approx 111$.

In order to study the deformation of droplets in a turbulent flow, we seed our turbulent, statistically steady, flow with Lagrangian tracers and follow their trajectories, by using a trilinear-interpolation scheme to obtain the tracer velocity from the Eulerian velocity evaluated from (2.3); such trajectories define the motion of the centre of mass of the droplets. We refer the reader to James & Ray (2017) for a more detailed description of our numerical procedure.

The capillary number is defined as $Ca = \lambda\tau$, where λ is the Lyapunov exponent of the flow. This latter represents the average stretching rate in a turbulent flow and provides a measure of the ability of the flow to deform a drop. We calculate λ by using the fluid velocity gradients along the trajectories and obtain $\lambda \approx 4.22 \approx 0.15\tau_\eta^{-1}$ (where τ_η is the Kolmogorov time scale associated with the flow), consistent with earlier results (Bec *et al.* 2006). (Note that Biferale, Meneveau & Verzicco (2014) defined the capillary number in terms of the root mean square of $\partial_x u_x$ instead of λ. However, this fact only leads to a different proportionality factor in the definition of Ca, since in isotropic turbulence $\sqrt{\langle(\partial_x u_x)^2\rangle} = 1/\sqrt{15}\tau_\eta$ and hence in our case $\sqrt{\langle(\partial_x u_x)^2\rangle} = 1.72\lambda$.)

Equation (2.1) is integrated by using the second-order Adam–Bashforth method with the same time step as for the Navier–Stokes equation. The integration of (2.1) must preserve the positive definite character of $\boldsymbol{M}$. This is achieved by adapting to (2.1) the Cholesky-decomposition method proposed by Vaithianathan & Collins (2003) (see appendix A for details). Unless otherwise stated, the initial condition is $\boldsymbol{M}(0) = \boldsymbol{I}$. As in Biferale, Meneveau & Verzicco (2014), it is assumed that drops break when their aspect ratio $|m_1/m_3|$ exceeds a threshold value α. In view of the fact that we are only interested in the dynamics up to the first breakup and do not consider secondary breakup events, drops are removed from the flow as soon as they break. In the simulations presented below, the initial number of drops $N(0) = 10^6$.

The deformation of a drop is described in terms of the statistics of m_1^2, i.e. the squared length of the semi-major axis. Let $p(m_1^2, t)$ be the probability density function (p.d.f.) of m_1^2 and $\mathcal{P}(m_1^2) \equiv \int_0^\infty p(m_1^2, t)\,\mathrm{d}t$ its time integral. Biferale, Meneveau & Verzicco (2014) showed that $\mathcal{P}(m_1^2)$ behaves as a power law for values of m_1^2 smaller than its maximum value (it is easy to check that the conditions $m_1^2 \geqslant m_2^2 \geqslant m_3^2$, $m_1^2 m_2^2 m_3^2 = 1$ and $|m_1/m_3| \leqslant \alpha$ imply that m_1^2 is bounded and, more precisely, $m_1^2 \leqslant \alpha^{4/3}$). The slope increases as a function of Ca for small Ca and saturates to -1 when Ca exceeds a critical value Ca_c, which for $\mu = 1$ was found to be $Ca_c = f_1(\mu)/2$. Figure 1(*a*) shows that the behaviour of $\mathcal{P}(m_1^2)$ is accurately reproduced in our simulations. The power law is even clearer when the p.d.f of m_1^2/m_3^2 is considered (figure 1*b*).

It should be noted, however, that because of the breakups the total number of drops decays in time. The fraction of drops surviving at time t, $N(t)/N(0) \equiv \int p(m_1^2, t)\,\mathrm{d}m_1^2$, indeed decreases exponentially, the decay rate growing rapidly when Ca exceeds Ca_c (figure 2*a*). Accordingly, the statistics of drop sizes is not stationary and the p.d.f. of m_1^2 varies in time (see figure 2*b*, where the p.d.f.s are translated vertically in

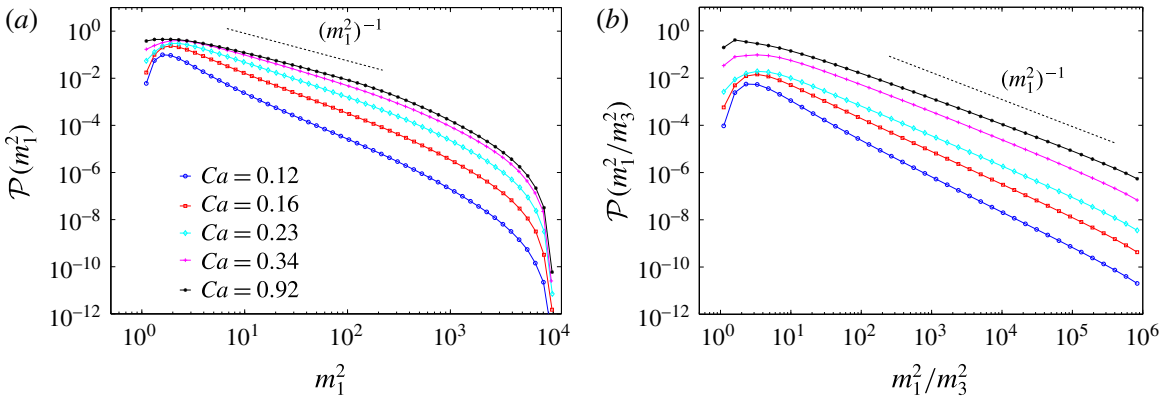

FIGURE 1. (Colour online) Time-integrated p.d.f. of (*a*) the largest eigenvalue of $\boldsymbol{M}$ and (*b*) the ratio of the largest and the smallest eigenvalue of $\boldsymbol{M}$ for $\mu = 1$, $\alpha = 10^3$ and different values of Ca. For this value of μ, $Ca_c = 0.23$ (see § 3). The p.d.f.s are artificially translated in order to render their power-law behaviours more easily visible.

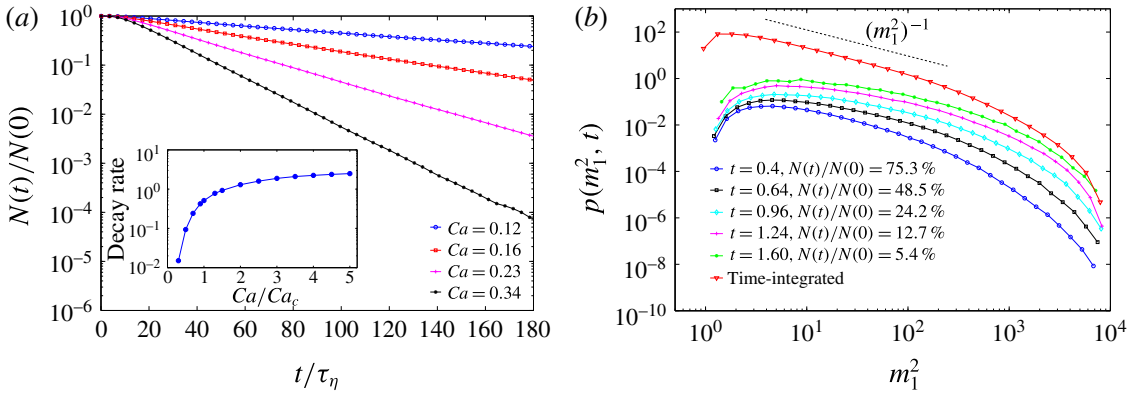

FIGURE 2. (Colour online) (*a*) Fraction of surviving drops as a function of time for $\mu = 1$, $\alpha = 10^3$ and different values of Ca. Time is rescaled by the Kolmogorov time (τ_η) of the flow. The inset shows the exponential decay rate of the fraction of surviving drops versus the capillary number rescaled by its critical value. (*b*) Time-dependent p.d.f. of m_1^2 for $\mu = 1$, $\alpha = 10^3$, $Ca = 1$ and increasing time instants. In the legend, the fraction of drops surviving at time t is also indicated. The red curve is the time-integrated p.d.f. $\mathcal{P}(m_1^2)$ corresponding to the same parameters. For the sake of comparison, the p.d.f.s are translated vertically.

order to facilitate the comparison at different times). At long times $p(m_1^2, t)$ reaches an asymptotic shape, but this does not show any definite power-law behaviour. The power law observed by Biferale, Meneveau & Verzicco (2014) is thus recovered only when the time-integrated p.d.f is considered; indeed the distributions shown in Biferale, Meneveau & Verzicco (2014) were obtained by averaging over both the Lagrangian trajectories and time.

Since the dynamics of drops is not statistically stationary, $\mathcal{P}(m_1^2)$ may depend on the initial shape of drops, namely on the value of the aspect ratio at time $t = 0$. We thus performed simulations in which the initial shape tensor is $\boldsymbol{M}(0) = \mathrm{diag}(\rho_0, 1, \rho_0^{-1})$, where $\rho_0 > 1$ is both the aspect ratio and the largest eigenvalue of $\boldsymbol{M}$ at $t = 0$. Two different behaviours are observed depending on the value of Ca. For small Ca, the shape of $\mathcal{P}(m_1^2)$ is not affected significantly by the value of ρ_0 (not shown). By

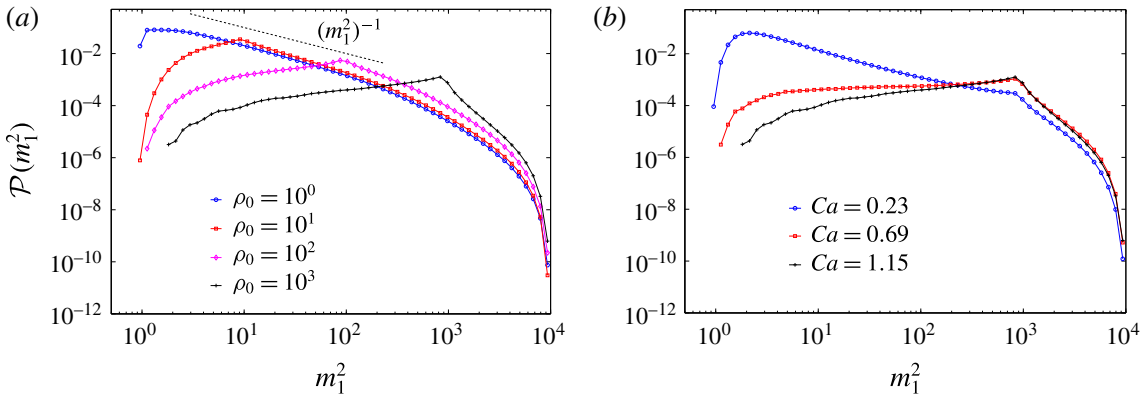

FIGURE 3. (Colour online) (*a*) Time-integrated p.d.f. of the largest eigenvalue of $\boldsymbol{M}$ for $\mu = 1$, $\alpha = 10^3$, $Ca = 1$ and different values of ρ_0. The p.d.f.s are normalized to 1 to facilitate the comparison. The dashed line is proportional to $(m_1^2)^{-1}$. (*b*) Time-integrated p.d.f. of the largest eigenvalue of $\boldsymbol{M}$ for $\mu = 1$, $\rho_0 = 10^3$ and different values of Ca.

contrast, for large Ca, the interval over which $\mathcal{P}(m_1^2) \sim (m_1^2)^{-1}$ shrinks as ρ_0 is increased and the drop volume is kept constant. In this case, indeed, $\mathcal{P}(m_1^2) \sim (m_1^2)^{-1}$ only for $m_1^2 \gg \rho_0$ (figure 3*a*). The $(m_1^2)^{-1}$ behaviour may therefore be difficult to detect when ρ_0 approaches the critical aspect ratio for breakup. In fact, when ρ_0 is sufficiently large a second power law emerges for $m_1^2 \ll \rho_0$ whose slope increases as a function of Ca and can turn from negative to positive at large Ca (figure 3*b*).

The dependence of the deformation and breakup statistics on μ is shown in figure 4. For small values of Ca, the slope of $\mathcal{P}(m_1^2)$ varies with μ and is steeper for larger viscosity ratios (figure 4*a*). It saturates to -1 beyond the critical capillary number, but the transition to the supercritical regime is slower for larger values of μ. These results differ somewhat from those of Biferale, Meneveau & Verzicco (2014). The discrepancy may be explained by considering the time scales associated with the breakup process. Whereas the time-integrated statistics displays a weak dependence on the viscosity ratio, the time scale over which breakup occurs depends strongly on μ, and the breakup process considerably slows down as μ increases (figure 4*b*). For large values of μ, very long Lagrangian trajectories therefore need to be considered in order to compute $\mathcal{P}(m_1^2)$; otherwise small deformations are privileged and the slope of $\mathcal{P}(m_1^2)$ may be steeper than it actually should be. This point is elucidated further in § 3.

Finally, we consider the mean lifetime of a drop, $\overline{T}(\rho_0)$, i.e. the mean time it takes for a drop of initial aspect ratio ρ_0 to break. Two different behaviours are found depending on whether Ca exceeds or not its critical value. The mean lifetime $\overline{T}(\rho_0)$ decreases as a power law of ρ_0 if $Ca < Ca_c$ and logarithmically if $Ca > Ca_c$ (figure 5).

The deformation and breakup statistics presented above is derived analytically in the next section.

3. Analytical predictions

For large deformations, the model of Maffettone & Minale (1998) is statistically equivalent to a vector model proposed by Olbricht, Rallison & Leal (1982). The assumptions on the drop and on the external fluid are essentially the same, and the

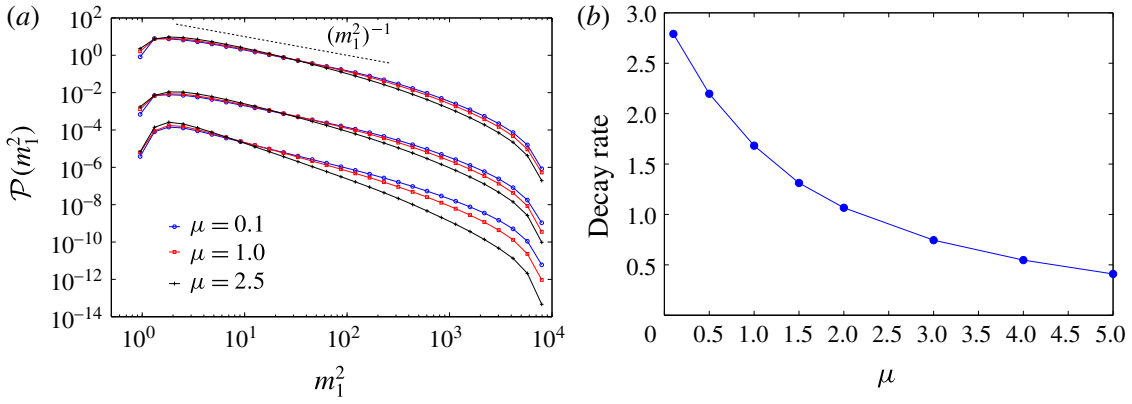

FIGURE 4. (Colour online) (*a*) Time-integrated p.d.f. of the largest eigenvalue of $\boldsymbol{M}$ for (from bottom to top) $Ca = 0.21, 0.32, 0.51$ and different values of μ. The p.d.f.s corresponding to different values of Ca are translated vertically. (*b*) Exponential decay rate of the number of surviving drops as a function of μ for $Ca = 0.6$.

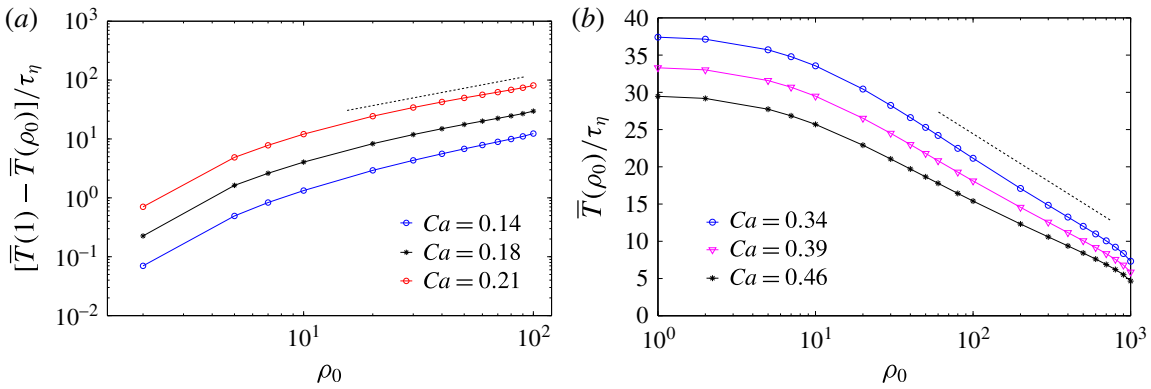

FIGURE 5. (Colour online) Mean lifetime as a function of the initial aspect ratio for (*a*) $\mu = 1$, $\alpha = 10^2$, $Ca < Ca_c$ and (*b*) $\mu = 1$, $\alpha = 10^3$, $Ca > Ca_c$. In (*a*) the $Ca = 0.206$ and $Ca = 0.137$ curves are multiplied by a factor 3 and 1/3, respectively, in order to make the three curves distinguishable.

semi-major axis $\boldsymbol{r}$ of the drop satisfies the equation

$$\dot{\boldsymbol{r}} = \boldsymbol{G}\boldsymbol{r} - \frac{f_1(\mu)}{2\tau}\boldsymbol{r} + \sqrt{\frac{r_{eq}^2 f_1(\mu)}{\tau}}\,\boldsymbol{\xi}(t), \tag{3.1}$$

where r_{eq} is the drop equilibrium size and $\boldsymbol{\xi}(t)$ is white noise describing thermal fluctuations. Although thermal noise does not appear in the original model of Olbricht, Rallison & Leal (1982), it is included in (3.1) in order to regularize the p.d.f. of $\boldsymbol{r}$ at $r = 0$. It is in any case expected to play a minor role when the flow is turbulent or when deformations larger than r_{eq} are considered. In this linear model, the condition for drop breakup is expressed in terms of $r = |\boldsymbol{r}|$, i.e. it is assumed that a drop breaks if r exceeds a threshold size ℓ.

Equation (3.1) is closely related to (2.1). Indeed, from the vector $\boldsymbol{r}$ one can form the second-rank tensor $\boldsymbol{M} = \langle \boldsymbol{r} \otimes \boldsymbol{r} \rangle_\xi$ ($\langle\cdot\rangle_\xi$ denotes the average over the realizations of $\boldsymbol{\xi}(t)$),

which evolves according to the equation (Olbricht, Rallison & Leal 1982)

$$\dot{\boldsymbol{M}} = \boldsymbol{G}\boldsymbol{M} + \boldsymbol{M}\boldsymbol{G}^{\top} - \frac{f_1(\mu)}{\tau}[\boldsymbol{M} - r_{eq}^2\boldsymbol{I}]. \tag{3.2}$$

The only difference between (2.1) and (3.2) is in the coefficient of the identity, which in (2.1) preserves the volume of the drop whereas it does not enjoy this property in (3.2). Notwithstanding, this term is negligible in both models when the drops are sufficiently deformed. Moreover, when r is large $\boldsymbol{M} \approx \boldsymbol{r} \otimes \boldsymbol{r}$, so r^2 is the largest eigenvalue of $\boldsymbol{M}$ and $\boldsymbol{r}$ the associate eigenvector. The statistics of large drop deformations can therefore be deduced from (3.1), and potential discrepancies between the two approaches are only expected for small deformations (see Vincenzi *et al.* (2015) for a more detailed discussion of this point in the $\mu = 1$ case).

Let us introduce the Kubo number $Ku = \lambda\tau_c$, where τ_c is the correlation time of $\boldsymbol{\nabla u}$. In three-dimensional homogeneous and isotropic turbulence $Ku \approx 0.6$ (Girimaji & Pope 1990; Bec *et al.* 2006; Watanabe & Gotoh 2010). However, for $\mu = 1$, it was shown in Musacchio & Vincenzi (2011) that as long as $Ku \lesssim 1$, the p.d.f. of r does not depend upon Ku appreciably. Furthermore, in Biferale, Meneveau & Verzicco (2014) the qualitative features of the statistics of drop deformation were found not to depend significantly on the intermittency of the turbulent flow. To make analytical progress, we therefore study (3.1) under the assumption that $\boldsymbol{\nabla u}$ has a Gaussian statistics and τ_c vanishes. More specifically, we assume that $\boldsymbol{\Omega}$ and $\boldsymbol{S}$ are zero-mean Gaussian processes with correlations $\langle \Omega_{ij}(t)\Omega_{pq}(t')\rangle = (d+2)C(\delta_{ip}\delta_{jq} - \delta_{jp}\delta_{iq})\delta(t-t')$ and $\langle S_{ij}(t)S_{pq}(t')\rangle = dC(\delta_{ip}\delta_{jq} + \delta_{iq}\delta_{jp} - 2\delta_{ij}\delta_{pq}/d)\delta(t-t')$, where d is the spatial dimension of the flow and $C > 0$ determines the amplitude of the fluctuations of $\boldsymbol{\nabla u}$. In this setting, $\boldsymbol{G}(t)$ is a multiplicative noise and is interpreted in the Stratonovich sense (Falkovich, Gawędzki & Vergassola 2001). The form of the correlations ensures that the flow is incompressible and statistically isotropic (e.g. Brunk & Koch 1998). In addition, the Lyapunov exponent of this flow is $\lambda = Cd(d-1)$ (Le Jan 1984, 1985).

Owing to statistical isotropy, at long times the p.d.f. of r, $p(r, t)$, satisfies the Fokker–Planck equation

$$\partial_t p = -\partial_r(D_1 p) + \partial_r^2(D_2 p), \tag{3.3}$$

where time has been rescaled by $2\tau/f_1(\mu)$ (with a slight abuse of notation we continue to denote the rescaled time by t) and

$$D_1(r) = \left[\frac{2(d+1)\gamma(\mu)Ca}{d} - 1\right] r + (d-1)\frac{r_{eq}^2}{r}, \quad D_2(r) = \frac{2\gamma(\mu)Ca}{d}\, r^2 + r_{eq}^2 \tag{3.4a,b}$$

with $\gamma(\mu) = f_2(\mu)/f_1(\mu)$. This equation can be obtained from the $\mu = 1$ case (see Celani, Musacchio & Vincenzi 2005) by noting that the vorticity tensor does not contribute to the time evolution of $p(r, t)$. The assumptions that r is a positive quantity and drops break at $r = \ell$ are implemented by imposing a reflecting boundary condition at $r = 0$ ($D_1 p - \partial_r(D_2 p) = 0$ at $r = 0$) and an absorbing boundary condition at $r = \ell$ ($p(\ell, t) = 0$), respectively.

The form of the coefficients $D_1(r)$ and $D_2(r)$ shows that changing the viscosity ratio merely rescales Ca by a factor of $\gamma(\mu)$. Also note that $\gamma(\mu)$ depends weakly upon μ, since it varies from $\gamma(0) = 2$ to $\gamma(\infty) = 19/8 = 2.375$.

3.1. *Time-integrated distribution of drop sizes*

Equation (3.3) can be used to derive the power-law behaviour of the time-integrated p.d.f $\mathcal{P}(r)$ as well as its dependence on the initial drop-size distribution. From (3.3), $\mathcal{P}(r)$ satisfies

$$-\frac{\mathrm{d}}{\mathrm{d}r}(D_1\mathcal{P}) + \frac{\mathrm{d}^2}{\mathrm{d}r^2}(D_2\mathcal{P}) = -p(r,0), \tag{3.5}$$

with boundary conditions $D_1\mathcal{P} - \partial_r(D_2\mathcal{P}) = 0$ at $r = 0$ and $\mathcal{P}(\ell) = 0$. To obtain (3.5), we have used the fact that in the presence of an absorbing boundary $\lim_{t\to\infty} p(r,t) = 0$ for all r. It is now assumed that $p(r,0) = \delta(r - r_0)$ with $r_0 > r_{eq}$, i.e. a monodisperse initial distribution. Integrating (3.5) from 0 to r and using the reflecting boundary condition at $r = 0$ yields

$$-D_1(r)\mathcal{P}(r) + \frac{\mathrm{d}}{\mathrm{d}r}[D_2(r)\mathcal{P}(r)] = \begin{cases} 0 & \text{if } 0 \leqslant r < r_0, \quad (3.6a) \\ -1 & \text{if } r_0 < r \leqslant \ell. \quad (3.6b) \end{cases}$$

The solution of (3.6) takes the form (Risken 1989)

$$\mathcal{P}(r) \propto \begin{cases} \mathrm{e}^{-\Phi(r)}[\varphi(\ell) - \varphi(r_0)] & \text{if } 0 \leqslant r \leqslant r_0, \\ \mathrm{e}^{-\Phi(r)}[\varphi(\ell) - \varphi(r)] & \text{if } r_0 < r \leqslant \ell, \end{cases} \tag{3.7}$$

with

$$\Phi(r) = \ln D_2(r) - \int_{r_1}^{r} \frac{D_1(\zeta)}{D_2(\zeta)}\,\mathrm{d}\zeta, \quad \varphi(r) = \int_{r_1}^{r} \frac{\mathrm{e}^{\Phi(\zeta)}}{D_2(\zeta)}\,\mathrm{d}\zeta, \tag{3.8a,b}$$

where the specific value of r_1 is irrelevant. To examine the behaviour of $\mathcal{P}(r)$ for $r_{eq} \ll r \ll \ell$, we now insert the limiting forms of $D_1(r)$ and $D_2(r)$ for $r_{eq} \to 0$ into (3.8) and obtain $\mathrm{e}^{\Phi(r)} \sim r^{\beta}$ and $\varphi(r) \sim r^{\beta-1}$ with $\beta = 1 - d + d/2\gamma(\mu)Ca$. Therefore, there exists a critical value of the capillary number, $Ca_c = 1/2\gamma(\mu)$, such that for $Ca < Ca_c$

$$\mathcal{P}(r) \sim \begin{cases} \left(\ell^{\beta-1} - r_0^{\beta-1}\right) r^{-\beta} & \text{if } r_{eq} \ll r \ll r_0, \quad (3.9a) \\ \ell^{\beta-1} r^{-\beta} & \text{if } r_0 \ll r \ll \ell, \quad (3.9b) \end{cases}$$

whereas for $Ca > Ca_c$

$$\mathcal{P}(r) \sim \begin{cases} \left(\ell^{\beta-1} - r_0^{\beta-1}\right) r^{-\beta} & \text{if } r_{eq} \ll r \ll r_0, \quad (3.10a) \\ r^{-1} & \text{if } r_0 \ll r \ll \ell. \quad (3.10b) \end{cases}$$

(The exact form of $\mathcal{P}(r)$ over the entire interval $0 \leqslant r \leqslant \ell$ may be calculated by using the full expressions of $D_1(r)$ and $D_2(r)$ in (3.4) and involves a hypergeometric function; the details, however, are omitted.) Since $\gamma(\mu)$ depends weakly on μ, the same holds true for Ca_c. The above value of Ca_c was also found by Biferale, Meneveau & Verzicco (2014) for more general flows; they applied a criterion based on the statistics of the finite-time Lyapunov exponents of the flow that was previously used to study the deformation of flexible polymers (Balkovsky, Fouxon & Lebedev 2001). Likewise, the prediction of Biferale, Meneveau & Verzicco (2014) for the exponent β in the $Ca < Ca_c$ case reduces to the expression above when $\boldsymbol{\nabla u}$ has the properties considered here.

The scaling of $\mathcal{P}(r^2)$ can be deduced from that of $\mathcal{P}(r)$ by using $\mathcal{P}(r^2) = (1/2)r^{-1}\mathcal{P}(r)$. The above power-law behaviours thus reproduce the numerical results shown in figures 1 and 3 for the time-integrated p.d.f.s of the squared length of the semi-major axis. It should be noted that whereas the power-law behaviour of $\mathcal{P}(r)$ for small r is specific to a monodisperse initial distribution, the large-r power law holds for any $p(r, 0)$ that vanishes beyond a given $r_\star < \ell$. Integrating (3.5) from 0 to $r > r_\star$ indeed yields (3.6*b*) and hence (3.9*b*) or (3.10*b*) depending on the value of Ca. If, by contrast, the initial size of the drops can approach ℓ, in general $\mathcal{P}(r)$ does not display a power-law behaviour.

3.2. *Time-dependent distribution of drop sizes and breakup frequency*

The eigenfunctions of the Fokker–Planck operator that satisfy the reflecting boundary condition at $r = 0$ are of the form $f_\nu(r) = r^{d-1}{}_2F_1(c_\nu^-, c_\nu^+, d/2, -\epsilon r^2)$ (Celani, Musacchio & Vincenzi 2005), where ${}_2F_1$ is the Gauss hypergeometric function with $\epsilon = 2\gamma(\mu)Ca/dr_{eq}^2$ and

$$c_\nu^\pm = \frac{d}{4}\left[\frac{1}{2\gamma(\mu)Ca} + 1\right] \pm \frac{1}{4}\sqrt{d^2\left[\frac{1}{2\gamma(\mu)Ca} - 1\right]^2 - \frac{2d\nu}{\gamma(\mu)Ca}}. \tag{3.11}$$

The absorbing boundary condition $f_\nu(\ell) = 0$ selects a discrete set of acceptable eigenfunctions. The p.d.f. of r can thus be expanded as $p(r, t) = \sum_{n=1}^{\infty} a_n \mathrm{e}^{-\nu_n t} f_{\nu_n}(r)$, and hence

$$p(r, t) \sim \mathrm{e}^{-\nu_1 t} f_{\nu_1}(r) \quad \text{as } t \to \infty. \tag{3.12}$$

This result confirms that at long times $p(r, t)$ approaches an asymptotic shape, but this does not show a power-law behaviour (figure 2*a*). From (3.12), the fraction of drops surviving at time t decays as

$$N(t)/N(0) \equiv \int_0^\ell p(r, t)\,\mathrm{d}r \sim \mathrm{e}^{-\nu_1 t} \quad \text{as } t \to \infty, \tag{3.13}$$

where ν_1 is the smallest solution of the equation $f_{\nu_n}(\ell) = 0$. Figure 6(*a*) shows that the decay rate of the drop number increases rapidly as a function of Ca when Ca exceeds its critical value, whereas it decreases as a function of μ. In addition, although Ca_c depends weakly on μ, the transition to the supercritical regime is much steeper at small μ (see also figure 6(*b*)). These results reproduce the behaviours observed in the numerical simulations (figures 2(*b*) and 4).

3.3. *Mean lifetime of a drop*

The average time it takes for a drop of initial size r_0 to break can be calculated from $\mathcal{P}(r)$ as follows. Consider the transition probability $p(r, t|r_0, 0)$, which is the solution of (3.3) that satisfies the initial condition $p(r, 0|r_0, 0) = \delta(r - r_0)$. Let $T(r_0)$ be the time it takes for the drop to break in a given realization of the flow and of thermal noise, and let $\mathbb{P}(r_0, t)$ be the probability of $T(r_0)$ taking the value t. Note that $\mathbb{P}(r_0, t) = -\partial_t F$, where $F(r_0, t) = \int_t^\infty \mathbb{P}(r_0, s)\,\mathrm{d}s$ is the probability that $T(r_0) \geqslant t$ and can be written as $F(r_0, t) = \int_0^\ell p(r, t|r_0, 0)\,\mathrm{d}r$. Therefore, the average of $T(r_0)$ is (Gardiner 1983)

$$\overline{T}(r_0) = \int_0^\infty t\,\mathbb{P}(r_0, t)\,\mathrm{d}t = -\int_0^\infty t[\partial_t F(r_0, t)]\,\mathrm{d}t = \int_0^\infty F(r_0, t)\,\mathrm{d}t, \tag{3.14}$$

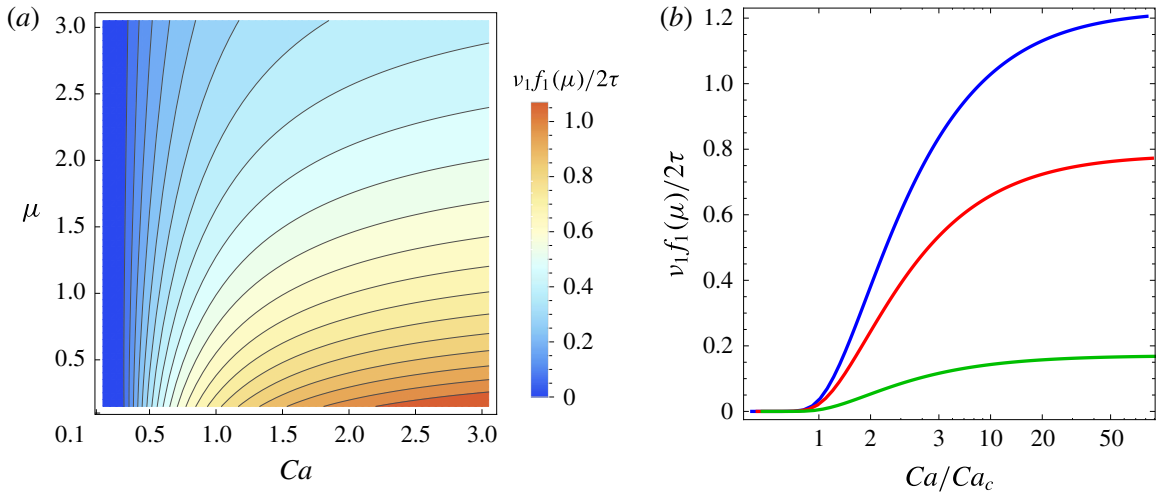

FIGURE 6. (Colour online) Exponential decay rate of the number of drops for $d=3$ and $\ell=10^3$ (*a*) as a function of μ and Ca and (*b*) as a function of the capillary number rescaled by its critical value for fixed $\mu=0.1, 1, 10$ (from top to bottom).

where we used $\lim_{t\to\infty} F(r_0,t)=0$, a consequence of the absorbing boundary condition for $p(r,t|r_0,0)$. By changing the order of integration, we finally obtain

$$\overline{T}(r_0)=\int_0^{\ell}\mathcal{P}(r)\,\mathrm{d}r, \tag{3.15}$$

where $\mathcal{P}(r)$ is the solution of (3.5) corresponding to the initial condition $p(r,0)=\delta(r-r_0)$. Inserting now the asymptotic behaviours (3.9*b*) and (3.10*b*) into (3.15) yields

$$\overline{T}(r_0)\sim\begin{cases}\left(\dfrac{\ell}{r_{eq}}\right)^{\beta-1}-\left(\dfrac{r_0}{r_{eq}}\right)^{\beta-1} & \text{if } Ca<Ca_c,\\ \ln\left(\dfrac{\ell}{r_0}\right) & \text{if } Ca>Ca_c,\end{cases} \tag{3.16}$$

as seen in figure 5.

4. Improved version of the model of Maffettone & Minale (1998)

Maffettone & Minale (1998) proposed a modification of their model that improves the agreement with experimental data for high viscosity ratios and large capillary numbers. In the modified model, the coefficient in front of the strain tensor also depends on Ca, i.e. $f_2(\mu)$ is replaced with

$$\tilde{f}_2(\mu,Ca)=f_2(\mu)+\frac{3(\sigma Ca)^2}{2+6(\sigma Ca)^2}, \tag{4.1}$$

where the coefficient σ accounts for the fact that here Ca is defined in terms of λ (hence in our case $\sigma=1.72$). The above expression still reproduces the theoretical limits, for both small Ca and large μ, as well as the affine deformation of the drop

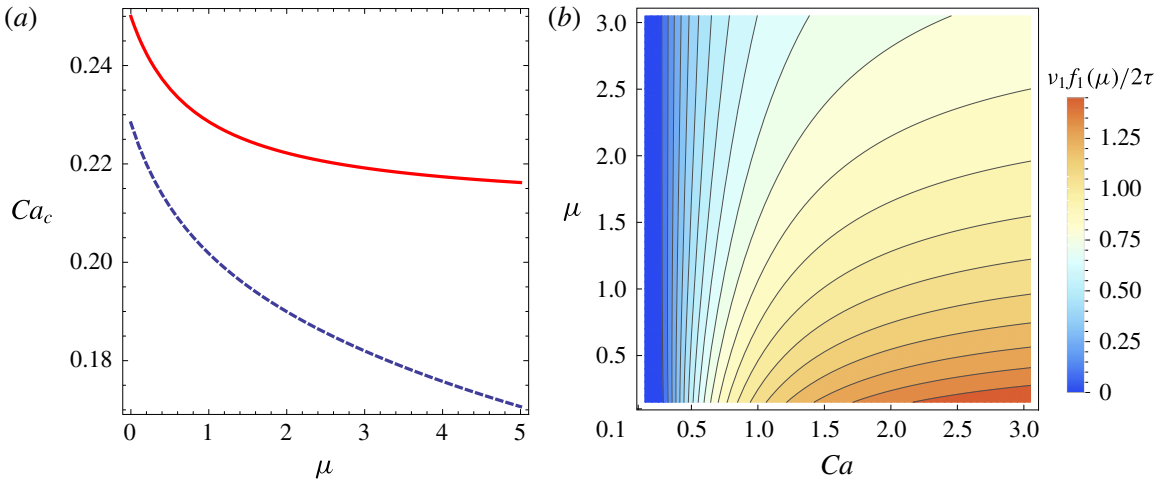

FIGURE 7. (Colour online) (*a*) Dependence of the critical capillary number on the viscosity ratio in the original model (red solid curve) and in the improved model (blue dashed curve). (*b*) Exponential decay rate of the number of drops for $d = 3$ and $\ell = 10^3$ as a function of Ca and μ for the improved model.

when $\mu = 1$ and $Ca \to \infty$. Using $\tilde{f}_2$ instead of f_2 yields significantly more accurate predictions for a pure shear; for an elongational flow, the effect is much weaker (Maffettone & Minale 1998).

It should be noted that the original model and the improved one can be mapped into each other by suitably modifying the viscosity ratio and the capillary relaxation time. The original model with parameters μ, τ is indeed the same as the improved one with parameters μ', τ', where μ' and τ' are the solutions of the system

$$f_1(\mu')/\tau' = f_1(\mu)/\tau, \quad \tilde{f}_2(\mu', \sigma\lambda\tau') = f_2(\mu). \tag{4.2a,b}$$

Therefore, for fixed μ and Ca, the results described in the previous sections also hold for the improved model, provided the parameters are suitably adjusted. The reader should note that such a nonlinear transformation of the parameters leads to a slight variation, quantitatively, of the results without changing the overall picture. It is nonetheless important to examine the effect of the modified coefficient $\tilde{f}_2$ on quantities such as the critical capillary number, the rate of decay of the drop fraction and the exponent β that defines the power-law behaviour of both the p.d.f. of the size and the mean lifetime. This is achieved by replacing $\gamma(\mu)$ in § 3 with $\tilde{\gamma}(\mu, Ca) = \tilde{f}_2(\mu, Ca)/f_1(\mu)$. Thus, the differences between the two versions of the model are mainly due to the fact that $\gamma(\mu)$ varies weakly with μ and is bounded for $\mu \to \infty$, whereas $\tilde{\gamma}(\mu, Ca) \to \infty$ in the same limit. It is shown below that, for a turbulent flow, these differences impact our predictions only marginally.

When the improved model is considered, the critical capillary number is the solution of the cubic equation $\tilde{\gamma}(\mu, Ca_c)Ca_c = 1/2$. It can be checked that the discriminant of this equation is negative for all values of μ and hence there is only one real root. Figure 7(*a*) compares the critical capillary number in the original model and in the improved one. In both cases, Ca_c is a decreasing function of μ. The main difference is that, for $\mu \to \infty$, Ca_c tends to the asymptotic value $4/19 \approx 0.21$ in the original model, whereas it tends to zero in the improved one. Nevertheless, for the values of μ typically found in experiments, Ca_c does not differ considerably in the two models.

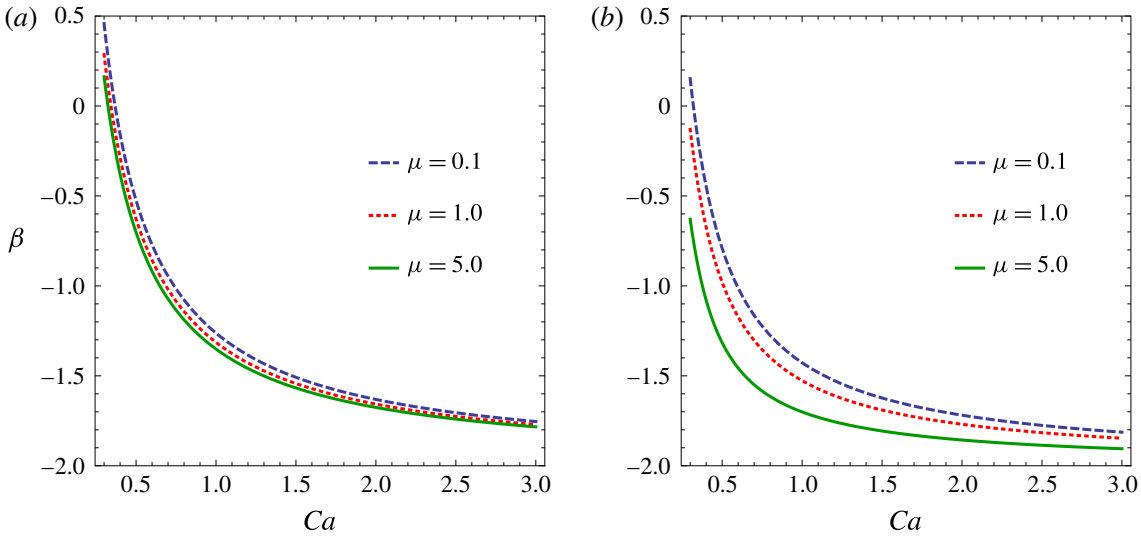

FIGURE 8. (Colour online) Exponent β as a function of the capillary number for $d = 3$ (*a*) in the original model and (*b*) in the improved model.

In the improved model, the rate of decay of the number of drops is slightly greater and decreases less rapidly as a function of μ (compare figures 6*a* and 7*b*). The exponent β takes the form $\beta = 1 - d + d/2\tilde{\gamma}(\mu, Ca)Ca$; it is smaller than in the original model and varies more with μ, as a consequence of the different behaviour of $\tilde{\gamma}(\mu, Ca)$ (figure 8). Both for β and the decay rate, the discrepancies between the two models are, however, small.

In conclusion, despite some quantitative differences, for realistic values of μ and Ca the qualitative behaviour of the model of Maffettone & Minale (1998) in a turbulent flow is largely insensitive to the use of either $f_2(\mu)$ or $\tilde{f}_2(\mu, Ca)$.

5. Conclusions

The Lagrangian dynamics of a sub-Kolmogorov drop in a turbulent flow is determined by the statistics of the velocity gradient. Strong fluctuations of the strain along the trajectory of the drop highly modify the shape and the size of the drop and ultimately break it. We have performed a detailed numerical and analytical study of the deformation and breakup statistics of neutrally buoyant, sub-Kolmogorov, ellipsoidal drops in homogeneous and isotropic turbulence as a function of the capillary number, the viscosity ratio between the inner and outer fluids and the initial drop-size distribution. In particular, we have analytically derived some of the numerical observations reported in Biferale, Meneveau & Verzicco (2014) and have extended the prediction for the critical capillary number to viscosity ratios different from unity. We have also examined further properties of the breakup process, such as the temporal dependence of the number of drops and of the statistics of the size, the role of the initial distribution of the drop sizes and the mean lifetime of a drop.

Our study relies on the model of Maffettone & Minale (1998). Potential extensions concern the impact on the deformation and breakup dynamics of effects that are not taken into account by this model. These include deviations from the ellipsoidal shape, nonlinear deformations near to breakup, large density contrasts between the fluids inside and outside the drop or secondary breakups. More refined models of drop dynamics have indeed been proposed in the literature (e.g. Minale 2010). However,

such models generally depend in a highly nonlinear way on the shape of the drop, and this renders their analytical study very challenging.

It would also be interesting to understand possible intermittency effects for such sub-Kolmogorov-scale droplets (Biferale, Meneveau & Verzicco 2014) (and also studied for larger droplets (Perlekar *et al.* 2012)) and if there are analogues of transparency effects, seen in oscillatory, laminar flows (Milan *et al.* 2018) for droplets in fully developed turbulence.

Finally, Maffettone & Minale (1998) observe that, for $\mu = 1$, their model is closely related to the Oldroyd-B model for solutions of flexible polymers (Bird *et al.* 1987). Likewise, when $\mu = 1$ and hence $\boldsymbol{G} = \boldsymbol{\nabla u}$ the vector model of Olbricht, Rallison & Leal (1982) reduces to the Hookean dumbbell model, which describes the evolution of the end-to-end separation vector of an extensible polymer molecule in the limit in which nonlinear elastic effects are negligible (Bird *et al.* 1987). Therefore, after appropriate redefinition of the parameters, our results also apply to the degradation of polymers in turbulent flows.

Acknowledgements

The authors would like to thank A. Gupta and P. Perlekar for fruitful discussions. They also acknowledge support of the Indo–French Centre for Applied Mathematics (IFCAM) and the EU COST Action MP 1305 'Flowing Matter'. S.S.R. acknowledges support of the DAE and the DST (India) project ECR/2015/000361 and the Fédération Doeblin. Our simulations were performed on the cluster *Mowgli* and the work station *Goopy* at the ICTS-TIFR. D.V. acknowledges the hospitality of the Max Planck Institute for Dynamics and Self-Organization, where part of this work was done.

Appendix A. Cholesky decomposition of the tensor $\boldsymbol{M}$

The Cholesky decomposition of $\boldsymbol{M}$ is $\boldsymbol{M} = \boldsymbol{L}\boldsymbol{L}^{\top}$, where $\boldsymbol{L}$ is a lower triangular matrix. The elements of $\boldsymbol{L}$ satisfy:

$$\dot{L}_{11} = G_{11}L_{11} + G_{12}L_{21} + G_{13}L_{31} + c_\tau\left[\frac{c_g}{L_{11}} - L_{11}\right] \tag{A 1}$$

$$\dot{L}_{21} = G_{21}L_{11} + G_{22}L_{21} + G_{23}L_{31} + G_{12}\frac{L_{22}^2}{L_{11}} + G_{13}\frac{L_{32}L_{22}}{L_{11}} - c_\tau\left[L_{21} + c_g\frac{L_{21}}{L_{11}^2}\right] \tag{A 2}$$

$$\dot{L}_{31} = G_{31}L_{11} + G_{32}L_{21} + G_{33}L_{31} + G_{12}\frac{L_{22}L_{32}}{L_{11}} + G_{13}\frac{L_{32}^2 + L_{33}^2}{L_{11}} - c_\tau\left[L_{31} + c_g\frac{L_{31}}{L_{11}^2}\right] \tag{A 3}$$

$$\dot{L}_{22} = G_{22}L_{22} + G_{23}L_{32} - G_{12}\frac{L_{21}L_{22}}{L_{11}} - G_{13}\frac{L_{32}L_{21}}{L_{11}} + c_\tau\left[-L_{22} + \frac{c_g}{L_{22}} + c_g\frac{L_{21}^2}{L_{11}^2L_{22}}\right] \tag{A 4}$$

$$\dot{L}_{32} = G_{32}L_{22} + G_{33}L_{32} - G_{12}\frac{L_{22}L_{31}}{L_{11}} - G_{13}\frac{L_{31}L_{32}}{L_{11}} + G_{23}\frac{L_{33}^2}{L_{22}} - G_{13}\frac{L_{21}L_{33}^2}{L_{11}L_{22}} + 2c_\tau c_g\frac{L_{21}L_{31}}{L_{11}^2L_{22}} + c_\tau\left[-L_{32} - c_g\frac{L_{32}}{L_{22}^2} - c_g\frac{L_{21}^2L_{32}}{L_{11}^2L_{22}^2}\right] \tag{A 5}$$

$$\dot{L}_{33} = G_{33}L_{33} - G_{13}\frac{L_{31}L_{33}}{L_{11}} - G_{23}\frac{L_{32}L_{33}}{L_{22}} + G_{13}\frac{L_{21}L_{32}L_{33}}{L_{11}L_{22}} - 2c_\tau c_g \frac{L_{21}L_{31}L_{32}}{L_{11}^2 L_{22}L_{33}} + c_\tau\left[-L_{33} + \frac{c_g}{L_{33}} + c_g\frac{L_{31}^2}{L_{11}^2L_{33}} + c_g\frac{L_{32}^2}{L_{22}^2L_{33}} + c_g\frac{L_{21}^2L_{32}^2}{L_{11}^2L_{22}^2L_{33}}\right], \tag{A 6}$$

with $c_\tau = f_1(\mu)/2\tau$ and $c_g = g(\boldsymbol{L}\boldsymbol{L}^\top)$ (the functions f_1 and g are defined after (2.1)). The above equations can be derived by adapting to (2.1) the equations obtained in Vaithianathan & Collins (2003) for a constitutive model of viscoelastic fluid (see also Perlekar, Mitra & Pandit (2006), where a misprint is corrected in the equation for L_{32}). The positivity of L_{ii}, $i = 1, 2, 3$, is enforced by evolving $\ln L_{ii}$ instead of L_{ii} (Vaithianathan & Collins 2003).

REFERENCES

AYYALASOMAYAJULA, S., COLLINS, L. R. & WARHAFT, Z. 2008 Modeling inertial particle acceleration statistics in isotropic turbulence. *Phys. Fluids* **20**, 095104.

AYYALASOMAYAJULA, S., GYLFASON, A. & WARHAFT, Z. 2008 Lagrangian measurements of fluid and inertial particles in decaying grid generated turbulence. In *IUTAM Symposium on Computational Physics and New Perspectives in Turbulence, Nagoya, Japan* (ed. Y. Kaneda), IUTAM Bookseries, vol. IV, pp. 171–175. Springer.

BALKOVSKY, E., FOUXON, A. & LEBEDEV, V. 2001 Turbulence of polymer solutions. *Phys. Rev.* E **64**, 056301.

BEC, J., BIFERALE, L., BOFFETTA, G., CENCINI, M., LANOTTE, A., MUSACCHIO, S. & TOSCHI, F. 2006 Lyapunov exponents of heavy particles in turbulence. *Phys. Fluids* **18**, 091702.

BIFERALE, L., MENEVEAU, C. & VERZICCO, R. 2014 Deformation statistics of sub-Kolmogorov-scale ellipsoidal neutrally buoyant drops in isotropic turbulence. *J. Fluid Mech.* **754**, 184–207.

BIRD, R. B., HASSAGER, O., ARMSTRONG, R. C. & CURTISS, C. F. 1987 *Dynamics of Polymeric Liquids*, vol. II. Wiley.

BRUNK, B. K. & KOCH, D. L. 1997 Hydrodynamic pair diffusion in isotropic random velocity fields with application to turbulent coagulation. *Phys. Fluids* **9**, 2670.

CELANI, A., MUSACCHIO, S. & VINCENZI, D. 2005 Polymer transport in random flow. *J. Stat. Phys.* **118**, 531–554.

CRISTINI, V., BŁAWZDZIEWICZ, J., LOEWENBERG, M. & COLLINS, L. R. 2003 Breakup in stochastic Stokes flows: sub-Kolmogorov drops in isotropic turbulence. *J. Fluid Mech.* **492**, 231–250.

FALKOVICH, G., GAWĘDZKI, K. & VERGASSOLA, M. 2001 Particles and fields in fluid turbulence. *Rev. Mod. Phys.* **73**, 913–975.

GARDINER, C. W. 1983 *Handbook of Stochastic Methods*. Springer.

GIRIMAJI, S. S. & POPE, S. B. 1990 A diffusion model for velocity gradients in turbulence. *Phys. Fluids* A **2**, 242–256.

HINZE, J. O. 1955 Fundamentals of the hydrodynamic mechanism of splitting in dispersion processes. *AIChE J.* **1**, 289–295.

JAMES, M. & RAY, S. S. 2017 Enhanced droplet collision rates and impact velocities in turbulent flows: the effect of polydispersity and transient phases. *Sci. Rep.* **7**, 12231.

KOLMOGOROV, A. N. 1949 On the breakage of drops in a turbulent flow. *Dokl. Akad. Nauk SSSR* **66**, 825–828. For the English translation, see V. M. Tikhomiro (ed.), *Selected Works of A. N. Kolmogorov* (Kluwer Academic Publishers, 1991), pp. 339–343.

LE JAN, Y. 1984 Exposants de Lyapunov pour les mouvements browniens isotropes. *C. R. Acad. Sci. Paris Ser.* I **299**, 947–949.

LE JAN, Y. 1985 On isotropic Brownian motions. *Z. Wahrscheinlichkeitstheor. verw. Gebiete* **70**, 609–620.

MAFFETTONE, P. L. & MINALE, M. 1998 Equation of change for ellipsoidal drops in viscous flow. *J. Non-Newtonian Fluid Mech.* **78**, 227–241.

MILAN, F., SBRAGAGLIA, M., BIFERALE, L. & TOSCHI, F. 2018 Lattice Boltzmann simulations of droplet dynamics in time-dependent flows. *Eur. Phys. J.* E **41**, 6.

MINALE, M. 2010 Models for the deformation of a single ellipsoidal drop: a review. *Rheol. Acta* **49**, 789–806.

MUSACCHIO, S. & VINCENZI, D. 2011 Deformation of a flexible polymer in a random flow with long correlation time. *J. Fluid Mech.* **670**, 326–336.

MUZZIO, F. J., TJAHJADI, M. & OTTINO, J. M. 1991 Self-similar drop-size distributions produced by breakup in chaotic flows. *Phys. Rev. Lett.* **67**, 54–57.

OLBRICHT, W. L., RALLISON, J. M. & LEAL, L. G. 1982 Strong flow criteria based on microstructure deformation. *J. Non-Newtonian Fluid Mech.* **10**, 291–318.

PRABHAKARAN, P., WEISS, S., KREKHOV, A., PUMIR, A. & BODENSCHATZ, E. 2017 Can hail and rain nucleate cloud droplets? *Phys. Rev. Lett.* **119**, 128701.

PERLEKAR, P., BIFERALE, L., SBRAGAGLIA, M. & TOSCHI, F. 2012 Droplet size distribution in homogeneous isotropic turbulence. *Phys. Fluids* **24**, 065101.

PERLEKAR, P., MITRA, D. & PANDIT, R. 2006 Manifestations of drag reduction by polymer additives in decaying, homogeneous, isotropic turbulence. *Phys. Rev. Lett.* **97**, 264501.

RISKEN, H. 1989 *The Fokker–Planck Equation: Methods of Solution and Applications*. Springer.

SCHUCHMANN, H. P. & SCHUBERT, H. 2003 Product design in food industry using the example of emulsification. *Eng. Life Sci.* **3**, 67–76.

SPANDAN, V., LOHSE, D. & VERZICCO, R. 2016 Deformation and orientation statistics of neutrally buoyant sub-Kolmogorov ellipsoidal droplets in turbulent Taylor–Couette flow. *J. Fluid Mech.* **809**, 480–501.

TJAHJADI, M. & OTTINO, J. M. 1991 Stretching and breakup of droplets in chaotic flows. *J. Fluid Mech.* **232**, 191–219.

VAITHIANATHAN, T. & COLLINS, L. R. 2003 Numerical approach to simulating turbulent flow of a viscoelastic polymer solution. *J. Comput. Phys.* **187**, 1–21.

VANKOVA, N., TCHOLAKOVA, S., DENKOV, N. D., IVANOV, I. B., VULCHEV, V. D. & DANNER, T. 2007 Emulsification in turbulent flow. Part 1. Mean and maximum drop diameters in inertial and viscous regimes. *J. Colloid Interface Sci.* **312**, 363–380.

VINCENZI, D., PERLEKAR, P., BIFERALE, L. & TOSCHI, F. 2015 Impact of the Peterlin approximation on polymer dynamics in turbulent flows. *Phys. Rev.* E **92**, 053004.

WALSTRA, P. 1993 Principles of emulsion formation. *Chem. Engng Sci.* **48**, 333–349.

WATANABE, T. & GOTOH, T. 2010 Coil-stretch transition in an ensemble of polymers in isotropic turbulence. *Phys. Rev.* E **81**, 066301.

WINDHAB, E. J., DRESSLER, M., FEIGL, K., FISCHER, P. & MEGIAS-ALGUACIL, D. 2005 Emulsion processing: from single-drop deformation to design of complex processes and products. *Chem. Engng Sci.* **60**, 2101–2113.

Annexe F

Turbulence élastique

F1. S.S. Ray & D. Vincenzi
"Elastic turbulence in a shell model of polymer solution"
Europhys. Lett. **114**, 44001 (2016)

F2. E.L.C. VI M. Plan, A. Gupta, D. Vincenzi & J.D. Gibbon
"Lyapunov dimension of elastic turbulence"
J. Fluid Mech. **822**, R4 (2017)

F3. E.L.C. VI M. Plan, S. Musacchio & D. Vincenzi
"Emergence of chaos in a viscous solution of rods"
Phys. Rev. E **96**, 053108 (2017)

F4. S. Musacchio, M. Cencini, E.L.C. VI. M. Plan & D. Vincenzi
"Enhancement of mixing by rodlike polymers"
Eur. Phys. J. E **41**, 84 (2018)

F5. A. Gupta & D. Vincenzi
"Effect of polymer-stress diffusion in the numerical simulation of elastic turbulence"
`arXiv:1809.09648v1` (2018)

epl A Letters Journal Exploring the Frontiers of Physics

May 2016

EPL, **114** (2016) 44001
doi: 10.1209/0295-5075/114/44001

www.epljournal.org

Elastic turbulence in a shell model of polymer solution

Samriddhi Sankar Ray[1] and Dario Vincenzi[2]

[1] *International Centre for Theoretical Sciences, Tata Institute of Fundamental Research - Bangalore 560089, India*
[2] *Laboratoire J. A. Dieudonné, Université Nice Sophia Antipolis, CNRS, UMR 7351 - Nice 06108, France*

received 5 March 2016; accepted in final form 26 May 2016
published online 15 June 2016

PACS 47.52.+j – Chaos in fluid dynamics
PACS 47.57.Ng – Polymers and polymer solutions

Abstract – We show that, at low inertia and large elasticity, shell models of viscoelastic fluids develop a chaotic behaviour with properties similar to those of elastic turbulence. The low dimensionality of shell models allows us to explore a wide range both in polymer concentration and in Weissenberg number. Our results demonstrate that the physical mechanisms at the origin of elastic turbulence do not rely on the boundary conditions or on the geometry of the mean flow.

Introduction. – Elastic turbulence is a chaotic regime that develops in low-inertia viscoelastic fluids when the elasticity of the fluid exceeds a critical value [1]. It is characterised by power-law velocity spectra (both in time and in space) and by a strong increase of the flow resistance compared to the laminar regime. Elastic turbulence differs from hydrodynamic turbulence in that inertial nonlinearities are irrelevant and the chaotic behaviour of the flow is entirely generated by elastic instabilities. In addition, the spatial spectrum of the velocity decays faster than in hydrodynamics turbulence; thus, the velocity field is smooth in space. Elastic turbulence has important applications, since the possibility of inducing instabilities at low Reynolds numbers allows the generation of mixing flows in microfluidics devices [2,3]. This phenomenon has been used, for instance, to study the deformation of DNA molecules in chaotic flows [4]. Furthermore, elastic turbulence provides a possible explanation of the improvement in oil-displacement efficiency that is observed when polymer solutions are used to flood reservoir rocks [5].

The first experiments on elastic turbulence have used confined flows with curved stream lines [6]. Nonetheless, purely elastic instabilities have been shown to develop also in a viscoelastic version of the Kolmogorov flow, which is periodic and parallel [7,8]. Indeed, elastic turbulence in the viscoelastic Kolmogorov flow exhibits a phenomenology qualitatively similar to that observed in experiments [9,10]. Low-Reynolds-number elastic instabilities have also been predicted for the Poiseuille flow [11] and for the planar Couette flow [12] of a polymer solution at large elasticity. More recently, elastic turbulence has been observed experimentally in a straight microchannel [13,14] and numerically in channels with periodic cylindrical obstacles [15] as well as in a periodic square [16]. These findings indicate that elastic turbulence also develops in simplified flow configurations and that the specific geometry of the system may not play a crucial role in this phenomenon. In this letter, we take a step further in this direction and study elastic turbulence in a shell model of polymer solution.

Hydrodynamical shell models are low-dimensional models that preserve the essential shell-to-shell energy transfer feature of the original partial differential equations in Fourier space. Despite the fact that they are not derived from the principle hydrodynamic equations in any rigorous way, they have played a fundamental role in the study of fluid turbulence since they are numerically tractable [17–20]. Shell models have also achieved remarkable success in problems related to passive-scalar turbulence [21–24], magnetohydrodynamic turbulence [25], rotating turbulence [26], binary fluids [27,28], and fluids with polymer additives [29,30]. Furthermore, the mathematical study of shell models has yielded several rigorous results, whose analogs are still lacking for the three-dimensional Navier-Stokes equations (*e.g.*, refs. [31,32]).

A shell model of polymer solution can be obtained by coupling the evolution of the velocity variables with the evolution of an additional set of variables representing the polymer end-to-end separation field. Shell models of polymer solutions have been successfully applied to the study of drag reduction in forced [29,33,34] and decaying [30] turbulence, two-dimensional turbulence with polymer additives [35], and turbulent thermal convection in viscoelastic fluids [36,37]. Here, we study a shell model of polymer

Table 1: The parameters, defined in the text, for the different sets of our simulations.

Type	ϵ	N	ν	δt	f_0
chaotic for $c = 0$	0.5	15	10^{-1}	10^{-4}	0.01
non-chaotic for $c = 0$	0.3	22	10^{-6}	10^{-4}	0.01

solution in the regime of low inertia and high elasticity. We show that this shell model undergoes a transition from a laminar to a chaotic regime with properties remarkably similar to those of elastic turbulence. Moreover, the use of a low-dimensional model allows us to explore the properties of elastic turbulence over a wide range both in polymer concentration and in Weissenberg number, which would be difficult to cover with direct numerical simulations of constitutive models of viscoelastic fluids.

Shell model of polymer solution. – We consider the shell model of polymer solution introduced by Kalelkar *et al.* [30], which is based on a shell model initially proposed for three-dimensional magnetohydrodynamics [38,39] and reduces to the GOY model [40,41] when polymers are absent. The shell model by Kalelkar *et al.* [30] can be regarded as a reduced, low-dimensional version of the FENE model [42]. It describes the temporal evolution of a set of complex scalar variables v_n and b_n representing the velocity field and the polymer end-to-end separation field, respectively. The variables v_n and b_n evolve according to the following equations [30]:

$$\frac{\mathrm{d}v_n}{\mathrm{d}t} = \Phi_{n,vv} - \nu_s k_n^2 v_n + \frac{\nu_p}{\tau_p} P(b)\Phi_{n,bb} + f_n, \qquad (1)$$

$$\frac{\mathrm{d}b_n}{\mathrm{d}t} = \Phi_{n,vb} + \Phi_{n,bv} - \frac{1}{\tau_p} P(b) b_n - \nu_b k_n^2 b_n. \qquad (2)$$

where $n = 1, \ldots, N$, $k_n = k_0 2^n$, $P(b) = 1/(1 - \sum_n |b_n|^2)$ and $\Phi_{n,vv} = i(a_1 k_n v_{n+1} v_{n+2} + a_2 k_{n-1} v_{n+1} v_{n-1} + a_3 k_{n-2} v_{n-1} v_{n-2})^*$, $\Phi_{n,bb} = -i(a_1 k_n b_{n+1} b_{n+2} + a_2 k_{n-1} b_{n+1} b_{n-1} + a_3 k_{n-2} b_{n-1} b_{n-2})^*$, $\Phi_{n,vb} = i(a_4 k_n v_{n+1} b_{n+2} + a_5 k_{n-1} v_{n-1} b_{n+1} + a_6 k_{n-2} v_{n-1} b_{n-2})^*$, and $\Phi_{n,bv} = -i(a_4 k_n b_{n+1} v_{n+2} + a_5 k_{n-1} b_{n-1} v_{n+1} + a_6 k_{n-2} b_{n-1} v_{n-2})^*$ with $k_0 = 1/16$, $a_1 = 1$, $a_2 = -\epsilon$, $a_3 = -(1-\epsilon)$, $a_4 = 1/6$, $a_5 = 1/3$, $a_6 = -2/3$, and the single free parameter ϵ determines whether or not, in the absence of polymers, the behaviour of the shell model is chaotic. The GOY shell model for fluids indeed shows a chaotic behaviour for $0.33 \lesssim \epsilon \lesssim 0.9$ and a non-chaotic behaviour for $\epsilon \lesssim 0.33$ [43,44]; the standard choice for hydrodynamic turbulence is $\epsilon = 0.5$ [17–20]. As we shall see later, it is useful to study elastic turbulence in both these regimes.

The number of shells that are used is given by N, the coefficient of kinematic viscosity by ν_s, the polymer relaxation time by τ, ν_p is the polymer viscosity parameter, $\nu_b = 10^{-13}\nu_s$ is a damping coefficient to allow for the dissipation term $-\nu_b k_n^2 b_n$ to be added to eq. (2) in order to improve numerical stability [30,33,34], and the forcing f_n drives the system to a non-equilibrium statistically stationary state. In particular we use either a deterministic forcing $f_n = f_0(1+\imath)\delta_{n,2}$ or a white-in-time Gaussian stochastic forcing with amplitude f_0 acting on the $n = 2$ shell. We choose initial conditions of the form $v_n^0 = k_n^{1/2} e^{\imath\phi_n}$ for $n = 1, 2$ and $v_n^0 = k_n^{1/2} e^{-k_n^2} e^{\imath\phi_n}$ for $3 \le n \le N$ and, for the polymer field, $b_n^0 = k_n^{1/2} e^{\imath\theta_n}$ for $1 \le n \le N$. Here ϕ_n and θ_n are random phases uniformly distributed between 0 and 2π. Equations (1) and (2) are solved numerically through a second-order Adams-Bashforth method with a time step δt for all our simulations. The numerical values for the various parameters of our simulations are given in table 1.

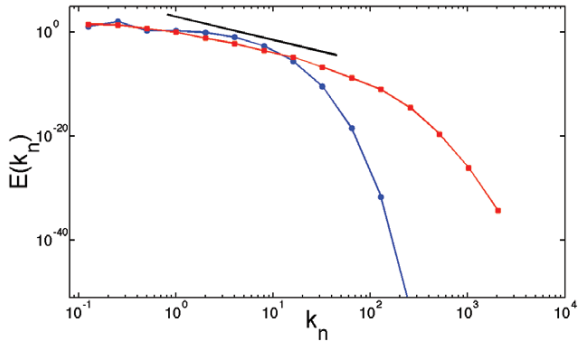

Fig. 1: (Colour online) Log-log plots of the kinetic energy spectrum $E(k)$ *vs.* the wavenumber k for a highly viscous flow with (red, filled squares) and without (blue, filled circles) polymer additives (see text). The curve without the addition of polymers do not show any algebraic scaling. However, the addition of polymers leads to the development of a power-law scaling k^{-4} in the energy spectrum (as indicated by the thick black line). These simulations were done for $\epsilon = 0.5$.

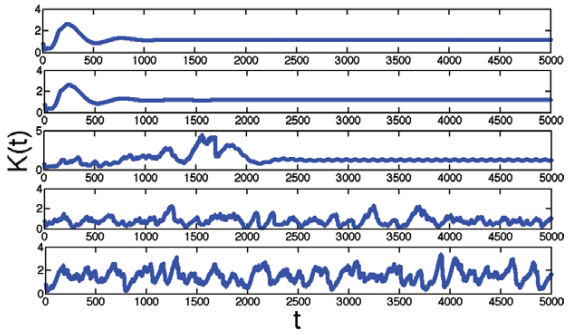

Fig. 2: (Colour online) The kinetic energy *vs.* time, with $\epsilon = 0.5$ for various values of c and Wi. From the uppermost to the lowermost curve the curves correspond to $c = 1.0$, Wi ≈ 0.25; $c = 4.0$, Wi ≈ 0.25; $c = 1.0$, Wi ≈ 25; $c = 4.0$, Wi ≈ 25; and $c = 20.0$, Wi ≈ 25. The top two curves show non-chaotic, laminar behaviour with a transition to periodic dynamics in the middle curve and then fully elastic turbulence in the bottom two.

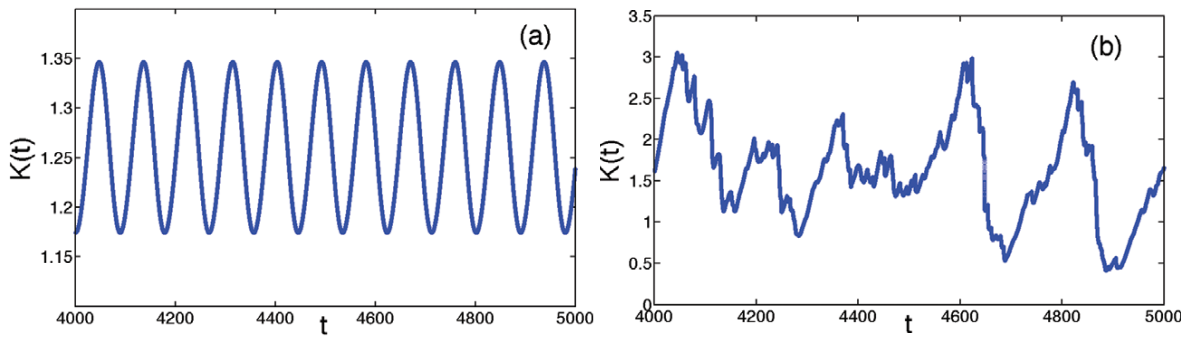

Fig. 3: (Colour online) The kinetic energy *vs.* time, for $\epsilon = 0.5$, at Wi ≈ 25 for (a) $c = 1.0$ and (b) $c = 20.0$ in the time interval where the flow is statistically stationary. We see a clear transition from a periodic behaviour to a fully elastic turbulence regime.

By analogy with continuum models of polymer solutions, we interpret the ratio $c = \nu_p/\nu_s$ as the polymer concentration [30,33,34]. We define the mean dissipation rate of the flow as $\varepsilon = \langle \nu_s \sum_n k_n^2 |v_n|^2 \rangle$; thence we extract the large-scale time $T = (k_1^2 \varepsilon)^{-1/3}$, which allows us to define the Weissenberg number as Wi $= \tau/T$. In our simulations we choose eight different values both of c and of Wi such that $0 \leq c \leq 20$ and $0 \leq$ Wi $\lesssim 25$. The Weissenberg number is varied by varying τ, so that the inertia of the system remains constant and negligible for all Wi.

Elastic-turbulence regime. – In order to understand whether the shell model defined via eqs. (1) and (2) indeed shows the typical features of elastic turbulence, we perform numerical simulations of the shell model with $\epsilon = 0.5$ and a stochastic forcing. The parameters (see table 1) are such that for $c = 0$ the shell model is not turbulent. The time-averaged (in the steady state) kinetic-energy spectrum $E(k_n) = |v_n|^2/k_n$ indeed decreases sharply with the wave number k_n without any apparent power-law scaling (see the blue line with filled circles in fig. 1).

A typical signature for elastic turbulence is the development of a power-law energy spectrum with an exponent smaller than -3 as the Weissenberg number is increased at fixed Reynolds number much smaller than 1 [6,45]. We therefore turn on the polymer field in the shell model ($c \neq 0$), and for sufficiently large c and Wi a power-law scaling emerges. In fig. 1, the energy spectrum for $c = 20$ and Wi $= 25$ is shown (red squares). We see a clear power-law behaviour, namely $E(k_n) \sim k_n^{-4}$, as is indicated by the thick black line. The value of the exponent is close to that found in experiments [6,45] and in numerical simulations [9,10,46,47] and is consistent with the theoretical predictions based on the Oldroyd-B model [48]. The spectrum of the polymer end-to-end separation field does not show a power-law behaviour and is concentrated around small wave numbers, in agreement with direct numerical simulations of elastic turbulence [16]. An analogous behaviour is found with a deterministic forcing. This is accompanied by a corresponding increase of the largest Lyapunov exponent as discussed in detail later. Thus, the shell model reproduces the most obvious signature of elastic turbulence, namely, the emergence of a large-scale chaotic dynamics in a *laminar* flow with the addition of polymers.

A global quantity like the total kinetic energy $K(t) = \sum_n |v_n|^2(t)$ provides further insight into the transition to elastic turbulence; its temporal behaviour with varying Wi and c indeed is an indicator of the changes of dynamical regime which happen in the system [10]. In fig. 2 we show time series of $K(t)$ for various combinations of c and Wi. For cases with very small values of Wi —and independent of the value of c— the total energy quickly saturates to an asymptotic value with no noticeable fluctuations, as is typical for laminar flows (fig. 2, top two panels). However, as Wi increases, even for a small enough value of $c = 1.0$, tiny but regular oscillations are seen in the temporal dynamics of $K(t)$ *vs.* t (fig. 2, middle panel). This behaviour is shown clearly in a zoomed plot in fig. 3(a). Keeping the Weissenberg number fixed, we now increase the concentration (fig. 2, bottom two panels) and see that the total kinetic energy *vs.* time shows increasingly chaotic dynamics with large irregular fluctuations. This behaviour is highlighted in the zoomed-in fig. 3(b). Figures 2 and 3 show that the shell model (which for $c = 0$ is laminar because of our choice of parameters), with increasing effect of polymers characterised by the concentration or the Weissenberg number, undergoes a transition from a laminar phase to one with strong fluctuations through a series of intermediate periodic phases for moderate values of c and Wi. This phenomenon was first observed as a function of Wi in direct numerical simulations of the Oldroyd-B model [42] with periodic Kolmogorov forcing [10] and of the FENE-P model [42] in a cellular flow [16]. The shell model considered here not only reproduces such a transition to chaos through periodic states as the Weissenberg number is increased, but also shows that an analogous transition occurs as a function of polymer concentration. Following ref. [44], in fig. 4 we also show the map $|v_{n+1}|$ *vs.* $|v_n|$, for $n = 2$. The structure of this map for increasing values of c further shows that the elastic-turbulence regime emerges through period doubling.

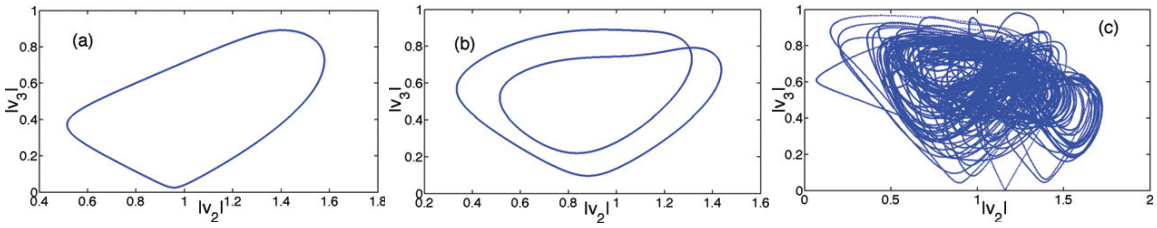

Fig. 4: (Colour online) The map for $|v_3|$ *vs.* $|v_2|$, at fixed Wi $= 25$ and (a) $c = 0.5$ (b) $c = 7.0$ and (c) $c = 20.0$. We see a clear transition from a non-chaotic to a chaotic behaviour for $\epsilon = 0.5$.

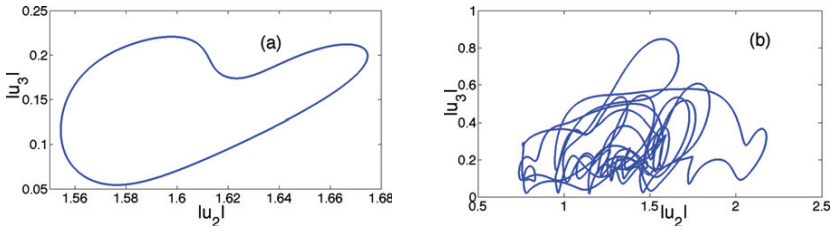

Fig. 5: (Colour online) The map for $|v_3|$ *vs.* $|v_2|$, at fixed Wi $= 5$ and (a) $c = 2.0$ and (b) $c = 10.0$ for $\epsilon = 0.3$. Like in the case for $\epsilon = 0.5$ (fig. 4), we see a similar, clear transition from a non-chaotic to a chaotic behaviour.

The above results confirm that the shell model with polymer additives replicates the global features of elastic turbulence. Given the relative numerical simplicity of shell models, it now behooves us to study in detail the effects of concentration on the small-scale mixing properties of elastic turbulence, which determine the importance of this phenomenon for practical applications. We quantify mixing in elastic turbulence and its dependence on c and Wi by calculating the largest Lyapunov exponent λ of the projection of the shell model on the v_n variables. We recall that for the fluid GOY shell model such calculations show the chaotic–non-chaotic transitions as a function of the single parameter ϵ [43,44]. For this set of calculations we would like to ensure that, in the absence of polymers, the flow is non-chaotic in order to reveal the transition to chaos more clearly. Thus we now study the shell model with $\epsilon = 0.3$ (see table 1), for which $\lambda = 0$ when $c = 0$. In order to check the generality of our conclusions, we use both a deterministic and a stochastic forcing and find our results insensitive to the precise nature of the forcing.

Before we turn our attention to a quantitative measure of the transition to elastic turbulence below, we immediately note, as seen in fig. 5, that the basic feature of transition to chaos, with increasing concentration for a fixed Wi, persists even for the case of $\epsilon = 0.3$. In addition, we also observe the formation of power-law energy spectra with a slope close to that found in the $\epsilon = 0.5$ case.

In fig. 6 we show the Lyapunov exponent rescaled with the polymer relaxation time, $\lambda\tau$, as a function of Wi for different values of c both for deterministic and for stochastic forcing (inset). For small values of $c \lesssim 5$, the rescaled Lyapunov exponent remains close to 0, and hence the system is non-chaotic or *laminar*. For sufficiently large values of $c \gtrsim 5$, we find that beyond a threshold value of the

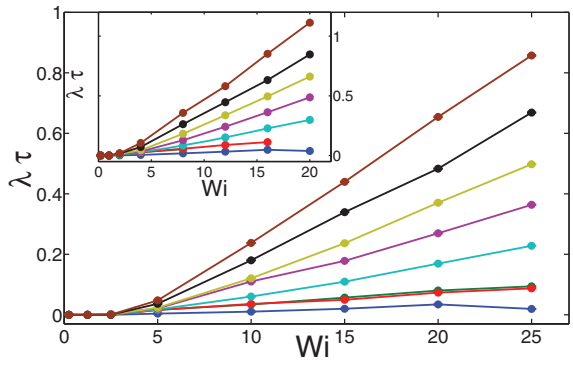

Fig. 6: (Colour online) $\lambda\tau$ *vs.* Wi for $\epsilon = 0.3$ for various values of c and for deterministic and stochastic (inset) forcing. The symbols sizes are proportional to the error bars in our calculations. The concentration varies between 0 and 20 from bottom to top.

Weissenberg number (Wi ≈ 5) the rescaled Lyapunov exponent increases approximately linearly and for the largest value of c, at Wi $\gtrsim 25$, we find $\lambda \approx 1/\tau$. Our findings are in agreement with analogous calculations made in the viscoelastic Kolmogorov flow for a single, fixed value of the elasticity of the flow [9]. It is important to note, though, that the results for the Kolmogorov flow [9] indicates a slightly more dramatic increase of $\lambda\tau$ as a function of the Weissenberg number than seen in the shell model.

We now turn to the behaviour of $\lambda\tau$ as a function of c for different values of Wi, as shown in fig. 7. As before we find that for low Weissenberg numbers, the flow remains non-chaotic even when the polymer concentration increases. Beyond a threshold value of Wi, there is a sharp increase in $\lambda\tau$ when the concentration becomes greater than 5. Thus,

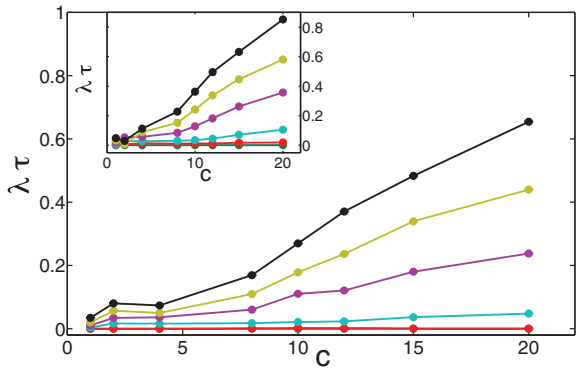

Fig. 7: (Colour online) $\lambda\tau$ *vs.* c for $\epsilon = 0.3$ for various values of Wi and for deterministic and stochastic (inset) forcing. The symbol sizes are proportional to the error bars in our calculations. The Weissenberg number varies from 0 to 25 from bottom to top.

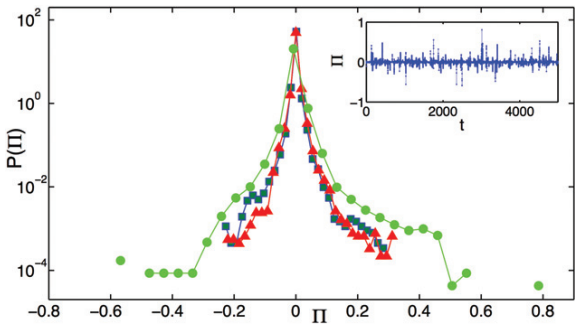

Fig. 8: (Colour online) Probability density function of Π for $\epsilon = 0.3$ at Wi = 5 for concentration values $c = 5.0$ (red triangles), 10.0 (blue squares), and 20.0 (green circles). The inset shows a typical timeseries of Π for $c = 10.0$.

provided Wi is sufficiently large, increasing the concentration has a destabilizing effect comparable to that observed when the Weissenberg number is increased.

Finally, the interaction between the polymers and the flow is described by the energy exchange [34]:

$$\Pi = -\frac{\nu_p P(b)}{\tau}\,\mathrm{Re}\left(\sum_n v_n^* \Phi_{n,bb}\right). \qquad (3)$$

Negative values of Π indicate that energy flows from the velocity variables towards the polymers; positive values of Π correspond to energy transfers in the opposite direction. In turbulent drag reduction, the timeseries of Π is predominantly negative [29,34]. This fact signals that polymers drain energy from the flow and justifies the description of their effect as a scale-dependent effective viscosity [34]. In fig. 8, we show the probability density function of Π in the elastic-turbulence regime of the shell model with $\epsilon = 0.3$ at different concentrations for a fixed value of Wi. We find that Π takes positive and negative values with comparable probabilities, *i.e.* in elastic turbulence there are continuous energy transfers between the flow and the polymers without a definite preferential direction (see also the inset of fig. 8). This result is consistent with the behaviour of the energy-exchange rate in decaying isotropic turbulence with polymer additives, the long-time stage of which has properties in common with elastic turbulence [47].

Conclusions. – We have considered a shell model of viscoelastic fluid that describes the coupled dynamics of the velocity and polymer fields in the flow of a polymer solution. In the regime of large inertia and large elasticity, this model was previously shown to reproduce the main features of turbulent drag reduction. We have studied the regime in which inertial nonlinearities are negligible and have shown that, when the Weissenberg number becomes sufficiently high, the system shows a transition to a chaotic state. A detailed analysis of this chaotic state indicates that the shell model under consideration qualitatively reproduces the transition to elastic turbulence observed in experiments and in numerical simulations. The simplicity of the shell model also allows us to study the elastic-turbulence regime over a wide range of values not only of the Weissenberg number but also of polymer concentration. In particular, we find that, when the concentration is increased while the Weissenberg number is fixed, the emergence of the chaotic regime follows a dynamics analogous to that observed when the Weissenberg number is increased at fixed polymer concentration. Thus the transition to elastic turbulence shows similar features as a function of Wi and of c.

This study enhances our understanding of the transition to elastic turbulence in polymer solutions. The shell model that we have studied mimicks the interactions between the Fourier modes of the velocity field and of the polymer end-to-end separation field in a viscoelastic fluid, but it contains no information on the spatial structure of these fields. The fact that such a model can replicate the main features of elastic turbulence shows that the specific geometrical configuration of the system does not play an essential role in the transition to elastic turbulence and that the physical mechanisms leading to elastic turbulence do not rely on the boundary conditions or the mean flow.

It would be interesting to analyze, through a systematic examination of the parameter space, how the slope of $E(k)$ and the probability density function of Π depend on the concentration and the Weissenberg number.

Finally, low-Reynolds-number instabilities are also found in non-Newtonian fluids that are not viscoelastic, namely in rheopectic fluids [49]. Such instabilities do not rely on phenomena of alignment of the dissolved phase with the flow, because the non-Newtonian nature of the fluid is modelled through a time- and space-dependent viscosity. It is an open question whether the low-Reynolds-number instabilities observed in rheopectic fluids can develop into a chaotic state and how the latter compares with elastic turbulence.

* * *

The authors are grateful to Chirag Kalelkar and Stefano Musacchio for useful discussions. This work was supported in part by the Indo-French Centre for Applied Mathematics (IFCAM) and by the EU COST Action MP 1305 "Flowing Matter". SSR acknowledges support from the AIRBUS Group Corporate Foundation in Mathematics of Complex Systems established at ICTS and the hospitality of the Observatoire de la Côte d'Azur, Nice, France. DV acknowledges the hospitality of ICTS-TIFR, Bangalore, India.

REFERENCES

[1] Groisman A. and Steinberg V., *Nature*, **405** (2000) 53.
[2] Groisman A. and Steinberg V., *Nature*, **410** (2001) 905.
[3] Burghelea T., Segre E., Bar-Joseph I., Groisman A. and Steinberg V., *Phys. Rev. E*, **69** (2004) 066305.
[4] Liu Y. and Steinberg V., *Macromol. Symp.*, **337** (2014) 34.
[5] Mitchell J., Lyons K., Howe A. M. and Clarke A., *Soft Matter*, **12** (2016) 460.
[6] Groisman A. and Steinberg V., *New J. Phys.*, **6** (2004) 29.
[7] Boffetta G., Celani A., Mazzino A., Puliafito A. and Vergassola M., *J. Fluid Mech.*, **523** (2005) 161.
[8] Bistagnino A., Boffetta G., Celani A., Mazzino A., Puliafito A. and Vergassola M., *J. Fluid Mech.*, **590** (2007) 61.
[9] Berti S., Bistagnino A., Boffetta G., Celani A. and Musacchio S., *Phys. Rev. E*, **77** (2008) 055306(R).
[10] Berti S. and Boffetta G., *Phys. Rev. E*, **82** (2010) 036314.
[11] Meulenbroek B., Storm C., Morozov A. N. and van Saarloos W., *J. Non-Newtonian Fluid Mech.*, **116** (2004) 235.
[12] Morozov A. N. and van Saarloos W., *Phys. Rev. Lett.*, **95** (2005) 024501.
[13] Pan L., Morozov A., Wagner C. and Arratia P. E., *Phys. Rev. Lett.*, **110** (2013) 174502.
[14] Bodiguel H., Beaumont J., Machado A., Martinie L., Kellay H. and Colin A., *Phys. Rev. Lett.*, **114** (2015) 028302.
[15] Grilli M., Vázquez-Quesada A. and Elloro M., *Phys. Rev. Lett.*, **110** (2013) 174501.
[16] Gupta A. and Pandit R., arXiv:1602.08153.
[17] Frisch U., *Turbulence: The Legacy of Kolmogorov* (Cambridge University Press, Cambridge) 1995.
[18] Bohr T., Jensen M. H., Paladin G. and Vulpiani A., *Dynamical Systems Approach to Turbulence* (Cambridge University Press, Cambridge) 1998.
[19] Biferale L., *Annu. Rev. Fluid Mech.*, **35** (2003) 441.
[20] Pandit R., Perlekar P. and Ray S. S., *Pramana - J. Phys.*, **73** (2009) 157.
[21] Jensen M. H., Paladin G. and Vulpiani A., *Phys. Rev. A*, **45** (1992) 7214.
[22] Wirth A. and Biferale L., *Phys. Rev. E*, **54** (1996) 4982.
[23] Mitra D. and Pandit R., *Phys. Rev. Lett.*, **95** (2005) 144501.
[24] Ray S. S., Mitra D. and Pandit R., *New J. Phys.*, **10** (2008) 033003.
[25] Plunian F., Stepanov R. and Frick P., *Phys. Rep.*, **523** (2013) 1.
[26] Chakraborty S., Jensen M. H. and Sarker A., *Eur. Phys. J. B*, **73** (2010) 447.
[27] Jensen M. H. and Olesen P., *Physica D*, **111** (1998) 243.
[28] Ray S. S. and Basu A., *Phys. Rev. E*, **84** (2011) 036316.
[29] Benzi R., De Angelis E., Govindarajan R. and Procaccia I., *Phys. Rev. E*, **68** (2003) 016308.
[30] Kalelkar C., Govindarajan R. and Pandit R., *Phys. Rev. E*, **72** (2005) 017301; **83** (2011) 039903(E).
[31] Constantin P., Levant B. and Titi E. S., *Physica D*, **219** (2006) 120.
[32] Flandoli F., *Random Perturbation of PDEs and Fluid Dynamic Models* (Springer-Verlag, Berlin) 2011.
[33] Benzi R., Ching E. S. C., Horesh N. and Procaccia I., *Phys. Rev. Lett.*, **92** (2004) 078302.
[34] Benzi R., Ching E. S. C. and Procaccia I., *Phys. Rev. E*, **70** (2004) 026304.
[35] Benzi R., Horesh N. and Procaccia I., *Europhys. Lett.*, **68** (2004) 310.
[36] Benzi R., Ching E. S. C. and De Angelis E., *Phys. Rev. Lett.*, **104** (2010) 024502.
[37] Benzi R., Ching E. S. C. and Wong C. K., *Phys. Rev. E*, **89** (2014) 053001.
[38] Frick P. and Sokoloff D., *Phys. Rev. E*, **57** (1998) 4155.
[39] Basu A., Sain A., Dhar S. and Pandit R., *Phys. Rev. Lett.*, **81** (1998) 2687.
[40] Gledzer E., *Sov. Phys. Dokl.*, **18** (1973) 216.
[41] Yamada M. and Ohkitani K., *J. Phys. Soc. Jpn.*, **56** (1987) 4210.
[42] Bird R. B., Curtiss C. F., Armstrong R. C. and Hassager O., *Dynamics of Polymeric Fluids*, Vol. **2** (Wiley, New York) 1987.
[43] Biferale L., Lambert A., Lima R. and Paladin G., *Physica D*, **80** (1995) 105.
[44] Kockelkoren J., Okkels F. and Jensen M. H., *J. Stat. Phys.*, **93** (1998) 833.
[45] Burghelea T., Segre E. and Steinberg V., *Phys. Fluids*, **19** (2007) 053104.
[46] Watanabe T. and Gotoh T., *J. Phys.: Conf. Ser.*, **454** (2013) 012007.
[47] Watanabe T. and Gotoh T., *Phys. Fluids*, **26** (2014) 035110.
[48] Fouxon A. and Lebedev V., *Phys. Fluids*, **15** (2007) 2060.
[49] Boi A., Mazzino A. and Pralits J. O., *Phys. Rev. E*, **88** (2013) 033007.

J. Fluid Mech. (2017), *vol.* 822, R4, doi:10.1017/jfm.2017.267

JFM RAPIDS
journals.cambridge.org/rapids

Lyapunov dimension of elastic turbulence

Emmanuel Lance Christopher VI M. Plan[1,†], Anupam Gupta[2], Dario Vincenzi[1] and John D. Gibbon[3]

[1]Université Côte d'Azur, CNRS, LJAD, 06108 Nice, France

[2]FERMaT, Université de Toulouse, CNRS, INPT, INSA, UPS, 31062 Toulouse, France

[3]Department of Mathematics, Imperial College London, London SW7 2AZ, UK

(Received 5 January 2017; revised 4 April 2017; accepted 20 April 2017)

Low-Reynolds-number polymer solutions exhibit a chaotic behaviour known as 'elastic turbulence' when the Weissenberg number exceeds a critical value. The two-dimensional Oldroyd-B model is the simplest constitutive model that reproduces this phenomenon. To make a practical estimate of the resolution scale of the dynamics, one requires the assumption that an attractor of the Oldroyd-B model exists; numerical simulations show that the quantities on which this assumption is based are bounded. We estimate the Lyapunov dimension of this assumed attractor as a function of the Weissenberg number by combining a mathematical analysis of the model with direct numerical simulations.

Key words: nonlinear dynamical systems, viscoelasticity

1. Introduction

One of the most remarkable properties of viscoelastic fluids is the formation of instabilities at very low Reynolds numbers (Larson 1992; Shaqfeh 1996). Such instabilities are of a purely elastic nature; they occur when inertial forces are negligible and elastic forces are strong. In polymer solutions, elastic instabilities eventually lead to a chaotic regime known as elastic turbulence (Groisman & Steinberg 2000). The emergence of this regime is characterized by a fast growth of the Lyapunov exponent of the flow as the polymer elasticity exceeds a critical value (Burghelea, Segre & Steinberg 2004). In addition, the kinetic-energy spatial and temporal spectra have a power-law behaviour, which indicates the presence of a large number of active scales in the flow. The spatial spectrum, however, is steeper than for Newtonian turbulence, i.e. velocity fluctuations are concentrated at small wavenumbers (Groisman & Steinberg 2000; Burghelea, Segre & Steinberg 2007).

Elastic turbulence has important applications in microfluidics in view of the fact that it strongly enhances mixing in devices that, owing to their microscopic size, are

†Email address for correspondence: elcplan@unice.fr

characterized by a low Reynolds number (Groisman & Steinberg 2001). Moreover, the potential use of elastic turbulence in the oil industry has recently emerged as a promising application. Aqueous polymer solutions are indeed used to recover the oil that remains trapped inside the pores of reservoir rocks after an initial water flooding, and elastic turbulence has been proposed as a mechanism to explain the unexpectedly high efficiency of this oil recovery method (Mitchell *et al.* 2016).

The simplest constitutive model of polymer solutions is the Oldroyd-B model (Oldroyd 1950), in which the dissolved polymer phase is described by a symmetric tensor field, termed the polymer-conformation tensor, which represents the moment of inertia of polymers averaged over thermal fluctuations. The Oldroyd-B model is thus a system of partial differential equations (PDEs) that describes the joint evolution of the velocity and the polymer-conformation tensor. In particular, the polymer feedback on the flow is given by a stress term proportional to the conformation tensor. The relevant dimensionless number is the Weissenberg number Wi, i.e. the ratio of the polymer relaxation time and the typical time scale of the flow. The main limitation of this model is that it assumes linear polymer elasticity, which, in extensional flows and in the absence of polymer feedback, can lead to an unbounded growth of the conformation tensor and hence of polymer stresses.

In spite of its simplicity, the model successfully reproduces the main features of elastic turbulence (Fouxon & Lebedev 2003; Berti *et al.* 2008; Berti & Boffetta 2010; Grilli, Vázquez-Quesada & Ellero 2013). In particular, numerical simulations show that elastic turbulence is observed also in two-dimensional settings. It has attracted much attention in the mathematical community over the last two decades, during which analysts have focused on the existence, uniqueness and regularity of solutions (see, e.g., Lei, Masmoudi & Zhou 2010; Barrett & Süli 2011; Constantin & Kliegl 2012; Elgindi & Rousset 2015; Hu & Lin 2016, for some recent studies). To the best of our knowledge, there are few theoretical results on the properties of elastic turbulent solutions.

A mathematical definition of the number of degrees of freedom of a system of PDEs is given by the dimension of its global attractor (Robinson 2001). For the two-dimensional case, the bounds found by Constantin & Kliegl (2012) on the L^2-norms of the vorticity ω and the polymer-conformation tensor $\boldsymbol{\sigma}$, $\|\omega\|_2$ and $\|\boldsymbol{\sigma}\|_2$, are exponential in time (and double exponential for $\|\boldsymbol{\nabla\sigma}\|_2$). Thus, no bounded long-time averages $\langle\cdot\rangle$ have been found to exist, and, therefore, in a strictly rigorous sense, no global attractor is known to exist. Mathematically, we can go no further. However, numerical simulations of elastic turbulence (see § 4) suggest that $\|\omega\|_2$, $\|\boldsymbol{\sigma}\|_2$ and $\|\boldsymbol{\nabla\sigma}\|_2$ are indeed bounded in time for various values of Wi. One practical way of progressing is to work under the following technical assumption with a subsequent strategy.

(i) Given that numerical calculations of $\|\omega\|_2$, $\|\boldsymbol{\sigma}\|_2$ and $\|\boldsymbol{\nabla\sigma}\|_2$ are finite in time, as suggested in § 4, we assume that a global attractor $\mathcal{A}$ exists.

(ii) Based on (i), we estimate the Lyapunov dimension of $\mathcal{A}$, which will use the long-time averages $\langle\|\omega\|_2\rangle$, $\langle\|\boldsymbol{\sigma}\|_2\rangle$ and $\langle\|\boldsymbol{\nabla\sigma}\|_2\rangle$; the numerical bounds found in § 4 for these quantities in terms of Wi are used in our estimates.

A connection between the system dynamics and the attractor dimension is provided by the notion of the Lyapunov exponents via the Kaplan–Yorke formula. For ordinary differential equations (ODEs), the Lyapunov exponents control the exponential growth or contraction of volume elements in phase space, and the Kaplan–Yorke formula expresses the balance between volume growth and contraction realized on the attractor.

The Kaplan–Yorke formula is used to define the Lyapunov dimension of the attractor and is as follows. For Lyapunov exponents $\mu_1 \geqslant \mu_2 \geqslant \cdots \geqslant \mu_n \geqslant \cdots$, the Lyapunov dimension $d_L(\mathcal{A})$ is given by

$$d_L(\mathcal{A}) = N - 1 + \frac{\mu_1 + \cdots + \mu_{N-1}}{-\mu_N}, \tag{1.1}$$

where the number N of μ_n is chosen to satisfy

$$\sum_{n=1}^{N-1} \mu_n \geqslant 0 \quad \text{but} \quad \sum_{n=1}^{N} \mu_n < 0. \tag{1.2a,b}$$

It should be noted that, according to the definition of N, the ratio of exponents in (1.1) satisfies

$$0 \leqslant \frac{\mu_1 + \cdots + \mu_{N-1}}{-\mu_N} < 1. \tag{1.3}$$

In simple terms, the value of N that turns the sign of the sum of the Lyapunov exponents as in (1.2) is the value that bounds above $d_L(\mathcal{A})$ such that

$$N - 1 \leqslant d_L(\mathcal{A}) < N. \tag{1.4}$$

The non-integer Lyapunov dimension $d_L(\mathcal{A})$ generally bounds above the fractal and Hausdorff dimensions $d_F(\mathcal{A})$ and $d_H(\mathcal{A})$. The Kaplan–Yorke formula originated as a phase-space argument for ODEs but has been rigorously applied to global attractors in PDEs by Constantin & Foias (1985) (see also Gibbon & Titi 1997). To use the method for PDEs to find an estimate for $d_L(\mathcal{A})$, it is necessary to extend the idea of the Lyapunov exponents to global Lyapunov exponents via a trace formula for the two-dimensional Oldroyd-B model that is explained in § 3. This uses the methods of Constantin & Foias (1985), Constantin, Foias & Temam (1988), Doering & Gibbon (1991) and, in particular, the L^∞-estimates of Constantin (1987). For a two-dimensional system of side L, the resolution length ℓ_{res} of the smallest feature in the dynamics is connected to $d_L(\mathcal{A})$ by $d_L(\mathcal{A}) \sim (L/\ell_{res})^2$.

2. The Oldroyd-B model for polymer solutions

On the periodic unit square $\Omega = [0,\ 1]^2$, the dimensionless form of the Oldroyd-B model is

$$\partial_t \boldsymbol{u} + \boldsymbol{u} \cdot \nabla \boldsymbol{u} = -\nabla p + Re^{-1} \Delta \boldsymbol{u} + \beta (Wi\, Re)^{-1} \nabla \cdot \boldsymbol{\sigma} + \boldsymbol{F}, \tag{2.1a}$$

$$\partial_t \boldsymbol{\sigma} + \boldsymbol{u} \cdot \nabla \boldsymbol{\sigma} = (\nabla \boldsymbol{u}) \boldsymbol{\sigma} + \boldsymbol{\sigma} (\nabla \boldsymbol{u})^\top - Wi^{-1} (\boldsymbol{\sigma} - \boldsymbol{I}) + Pe^{-1} \Delta \boldsymbol{\sigma}, \tag{2.1b}$$

where $\boldsymbol{u}$ is the incompressible velocity field, $(\nabla u)_{ij} = \partial_j u_i$, $\boldsymbol{\sigma}$ is the polymer-conformation tensor, p is pressure, and where Re, Pe and Wi are the Reynolds, Péclet and Weissenberg numbers respectively. The positive constant β depends on the polymer concentration and equilibrium extension. The forcing $\boldsymbol{F}$ is time-independent, periodic and divergence-free ($\nabla \cdot \boldsymbol{F} = 0$).

The Laplacian term in (2.1*b*) originates from the diffusion of the centre of mass of polymers (El-Kareh & Leal 1989), which ensures the global regularity of the two-dimensional Oldroyd-B model (Constantin & Kliegl 2012) and improves the stability of numerical simulations, even though the values of Pe used in practice are

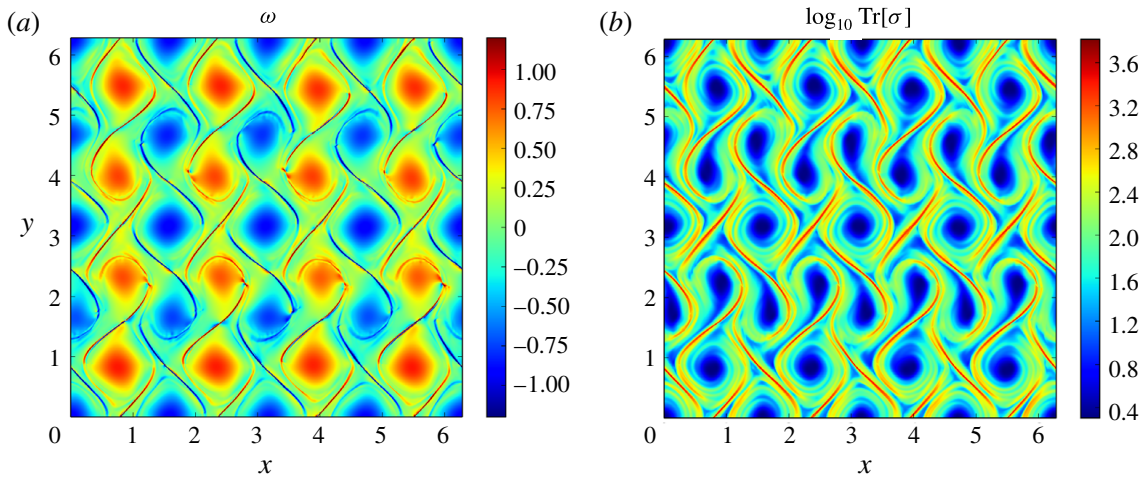

FIGURE 1. Pseudocolour plot of (*a*) ω and (*b*) $\log_{10}\mathrm{Tr}\,\boldsymbol{\sigma}$ for $Re = Re_c/\sqrt{2}$, $Wi = 20$, $\beta = 0.2$ and a cellular forcing with $n = 4$ and $f_0 = 0.16$ (see § 4 for details).

considerably lower than its realistic values (Sureshkumar & Beris 1995; Thomases 2011).

In two dimensions, (2.1) can be rewritten in terms of the scalar vorticity $\omega = \hat{\boldsymbol{z}} \cdot (\boldsymbol{\nabla} \times \boldsymbol{u})$:

$$\partial_t \omega + \boldsymbol{u} \cdot \boldsymbol{\nabla}\omega = Re^{-1}\Delta\omega + \beta(Wi\,Re)^{-1}\,\hat{\boldsymbol{z}} \cdot \boldsymbol{\nabla} \times (\boldsymbol{\nabla} \cdot \boldsymbol{\sigma}) + f, \tag{2.2a}$$

$$\partial_t \boldsymbol{\sigma} + \boldsymbol{u} \cdot \boldsymbol{\nabla}\boldsymbol{\sigma} = (\boldsymbol{\nabla}\boldsymbol{u})\boldsymbol{\sigma} + \boldsymbol{\sigma}(\boldsymbol{\nabla}\boldsymbol{u})^{\top} - Wi^{-1}(\boldsymbol{\sigma} - \boldsymbol{I}) + Pe^{-1}\Delta\boldsymbol{\sigma}, \tag{2.2b}$$

where $f = \hat{\boldsymbol{z}} \cdot (\boldsymbol{\nabla} \times \boldsymbol{F})$ and $\boldsymbol{u} = \boldsymbol{\nabla}^{\perp}\Delta^{-1}\omega$, with $\boldsymbol{\nabla}^{\perp} \equiv (-\partial_y, \partial_x)$. Since $\boldsymbol{F}$ is periodic, the spatial average of ω is zero, and the inverse Laplacian of ω is properly defined. Figure 1 shows snapshots of the ω and $\mathrm{Tr}\,\boldsymbol{\sigma}$ fields from a numerical simulation of (2.2) in the elastic-turbulence regime. It should be noted that $\mathrm{Tr}\,\boldsymbol{\sigma}$ is concentrated over very thin regions, which is associated with large gradients in the polymer-conformation-tensor field.

3. Lyapunov dimension

In the PDE case, the phase space is now infinite-dimensional. We define $\boldsymbol{q} = (\omega, \boldsymbol{\sigma})$ and denote by $\delta\boldsymbol{q} = (\delta\omega, \delta\boldsymbol{\sigma})$ the infinitesimal displacement about $\boldsymbol{q}$; $\delta\boldsymbol{q}$ satisfies the linearized set of equations from (2.2):

$$\delta\dot{\boldsymbol{q}} = \boldsymbol{A}(t)\delta\boldsymbol{q} = \begin{pmatrix} -\boldsymbol{u}\cdot\boldsymbol{\nabla}\delta\omega + \dfrac{1}{Re}\Delta\delta\omega - \delta\boldsymbol{u}\cdot\boldsymbol{\nabla}\omega + \dfrac{\beta}{Wi\,Re}\hat{\boldsymbol{z}}\cdot\boldsymbol{\nabla}\times(\boldsymbol{\nabla}\cdot\delta\boldsymbol{\sigma}) \\ (\boldsymbol{\nabla}\delta\boldsymbol{u})\boldsymbol{\sigma} + \boldsymbol{\sigma}(\boldsymbol{\nabla}\delta\boldsymbol{u})^{\top} - \delta\boldsymbol{u}\cdot\boldsymbol{\nabla}\boldsymbol{\sigma} - \boldsymbol{u}\cdot\boldsymbol{\nabla}\delta\boldsymbol{\sigma} + (\boldsymbol{\nabla}\boldsymbol{u})\delta\boldsymbol{\sigma} + \delta\boldsymbol{\sigma}(\boldsymbol{\nabla}\boldsymbol{u})^{\top} - \dfrac{\delta\boldsymbol{\sigma}}{Wi} + \dfrac{1}{Pe}\Delta\delta\boldsymbol{\sigma} \end{pmatrix}, \tag{3.1}$$

where the explicit form of the operator $\boldsymbol{A}(t)$ is obtained by using $\boldsymbol{u} = \boldsymbol{\nabla}^{\perp}\Delta^{-1}\omega$ to express $\boldsymbol{u}$ and $\delta\boldsymbol{u}$ in terms of ω and $\delta\omega$ respectively. Following Constantin & Foias (1985), we take different sets of initial conditions $\boldsymbol{q}(0) + \delta\boldsymbol{q}_i(0)$ which evolve into $\boldsymbol{q}(t) + \delta\boldsymbol{q}_i(t)$ for $i = 1, \ldots, N$. If they are chosen to be linearly independent, these $\delta\boldsymbol{q}_i$ form an N-volume or parallelepiped of volume $V_N(t) = |\delta\boldsymbol{q}_1 \wedge \delta\boldsymbol{q}_2 \cdots \wedge \delta\boldsymbol{q}_N|$, which

changes along the solution $\boldsymbol{q}(t)$, so we need to find its time evolution. This is given by $\dot{V}_N = V_N \mathrm{Tr}[\boldsymbol{A}\boldsymbol{P}_N]$, which is easily solved to give

$$V_N(t) = V_N(0) \exp\left\{ \int_0^t \mathrm{Tr}[\boldsymbol{A}\boldsymbol{P}_N](\tau)\, \mathrm{d}\tau \right\}, \tag{3.2}$$

where $\boldsymbol{P}_N(t)$ is an L^2-orthogonal projection onto the finite-dimensional subspace span $\{\delta\boldsymbol{q}_1, \delta\boldsymbol{q}_2, \ldots, \delta\boldsymbol{q}_N\}$. In terms of the time average $\langle\cdot\rangle$, the sum of the first N global Lyapunov exponents is taken to be (Constantin & Foias 1985)

$$\sum_{n=1}^{N} \mu_n = \langle \mathrm{Tr}[\boldsymbol{A}\boldsymbol{P}_N] \rangle. \tag{3.3}$$

To estimate the Lyapunov dimension, we wish to find the value of N that turns the sign of $\langle \mathrm{Tr}[\boldsymbol{A}\boldsymbol{P}_N]\rangle$. This value of N bounds above $d_L(\mathcal{A})$ as in (1.4). As we are interested in elastic turbulence, we assume $Pe \gg 1$, $Wi \gg 1$ and $0 < Re < Re_c$, where Re_c is the critical value for the appearance of inertial instabilities. The derivation has been relegated to appendix A. The final result is that the following inequalities are sufficient conditions on N for the growth rate $\langle \mathrm{Tr}[\boldsymbol{A}\boldsymbol{P}_N]\rangle$ to be negative and the N-volume V_N to contract:

$$N > cRe\langle \|\boldsymbol{\sigma}\|_2^3 \rangle^{1/3} (1 + \ln Re + \ln\langle \|\boldsymbol{\sigma}\|_2^3 \rangle^{1/3})^{1/2}, \tag{3.4a}$$

$$N > cRe^{2/3}\langle \|\nabla\boldsymbol{\sigma}\|_2^2 \rangle^{1/3} (1 + \ln Re + \ln\langle \|\nabla\boldsymbol{\sigma}\|_2^2 \rangle^{1/2})^{1/3}, \tag{3.4b}$$

where $\|\cdot\|_2^2 = \int_\Omega |\cdot|^2\, \mathrm{d}\boldsymbol{x}$, $|\boldsymbol{\sigma}|^2 = \sum_{i,j} |\sigma_{ij}|^2$, $|\nabla\boldsymbol{\sigma}|^2 = \sum_{i,j,k} |\partial_k \sigma_{ij}|^2$ and c is regarded as a generic positive dimensionless constant. These conditions depend on estimates for $\langle \|\boldsymbol{\sigma}\|_2^3 \rangle$ and $\langle \|\nabla\boldsymbol{\sigma}\|_2^2 \rangle$. It has been shown in Constantin & Kliegl (2012) that these are exponential in time and thus cannot be used. Instead, we turn to direct numerical simulations to find their behaviour in terms of Wi.

4. Direct numerical simulations of elastic turbulence

To simulate solutions of (2.2), we use the approach described in Gupta, Perlekar & Pandit (2015) and Gupta & Pandit (2017). For the time integration, we use the fourth-order Runge–Kutta scheme with time step $\delta t = 10^{-4}$, while the fourth-order central-finite-difference scheme with 1024^2 collocation points is employed for the spatial derivatives. To accurately resolve the steep gradients of $\boldsymbol{\sigma}$, we apply the Kurganov–Tadmor scheme to the advection term in (2.2*b*) (Kurganov & Tadmor 2000) (see Vaithianathan *et al.* 2006, for the application of this scheme to viscoelastic fluids), which allows us to set $Pe = \infty$ in (2.2). The velocity is calculated from the vorticity via the Poisson equation $\Delta\psi = \omega$, where ψ is the stream function: $\boldsymbol{u} = \nabla^\perp\psi$. The pseudospectral method is used to solve the Poisson equation in Fourier space. The simulations were performed on $[0, 2\pi]^2$ and the solutions were rescaled appropriately.

Three kinds of forcing are considered: a cellular forcing $f = -f_0 n[\cos(nx) + \cos(ny)]$ with $n = 4$, a cellular forcing with $n = 10$ and a Kolmogorov forcing $f = -f_0 n \cos(nx)$ with $n = 8$. In all simulations, $Re = Re_c/\sqrt{2}$, where Re_c is the critical Reynolds number above which inertial instabilities occur. Hence, in the absence of polymers ($\beta = 0$), the stationary vorticity field shows alternating vortices and antivortices for the cellular forcing and a parallel sinusoidal flow for the Kolmogorov forcing. The parameter β is set to $\beta = 0.2$. We checked that in the elastic-turbulence regime, the kinetic-energy

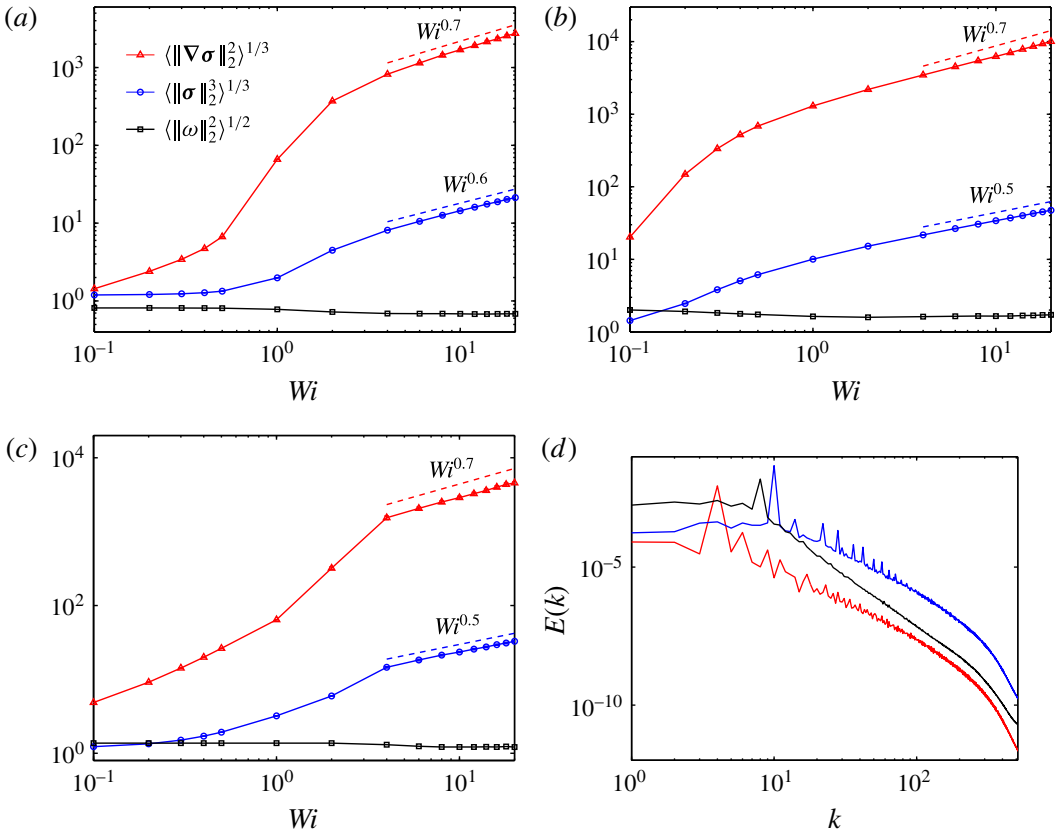

FIGURE 2. Plot of $\langle\|\omega\|_2^2\rangle^{1/2}$ (black squares), $\langle\|\boldsymbol{\sigma}\|_2^3\rangle^{1/3}$ (blue circles) and $\langle\|\nabla\boldsymbol{\sigma}\|_2^2\rangle^{1/3}$ (red triangles) as a function of Wi for $Re = Re_c/\sqrt{2}$, $\beta = 0.2$, and (*a*) cellular forcing with $n = 4$, $f_0 = 0.16$, (*b*) cellular forcing with $n = 10$, $f_0 = 2.50$ and (*c*) Kolmogorov forcing with $n = 8$, $f_0 = 1.28$. (*d*) Kinetic-energy spectrum for $Wi = 20$ for case (*a*) in red, case (*b*) in blue and case (*c*) in black. The spectrum shows a power-law behaviour $E(k) \simeq k^{-a}$ with $a \approx 3.1$ for case (*a*), $a \approx 3.0$ for case (*b*) and $a \approx 3.7$ for case (*c*).

transfer due to the fluid inertia is negligible, so the chaotic dynamics is entirely due to polymer stresses.

The numerical simulations show that $\langle\|\nabla\boldsymbol{\sigma}\|_2^2\rangle^{1/3}$ is greater than $\langle\|\boldsymbol{\sigma}\|_2^3\rangle^{1/3}$, and, at large Wi, $\langle\|\nabla\boldsymbol{\sigma}\|_2^2\rangle^{1/3} \sim Wi^{\alpha}$ with $\alpha \approx 0.7$ for the three different forcings considered here (see figure 2). This result is in agreement with the observation of large gradients in the polymer-conformation field in figure 1 as well as in previous numerical simulations (Berti *et al.* 2008; Berti & Boffetta 2010). It follows that the value of N such that N-volumes contract is determined by inequality (3.4*b*). We conclude that, in the elastic-turbulence regime and under the specified assumptions, the two-dimensional Oldroyd-B model has a finite-dimensional global attractor with Lyapunov dimension

$$d_L(\mathcal{A}) \leqslant \mathcal{N}, \tag{4.1}$$

where $\mathcal{N}$ is the minimum value of N satisfying (3.4*b*). Thus, up to logarithmic corrections,

$$d_L(\mathcal{A}) \lesssim cRe^{2/3}\langle\|\nabla\boldsymbol{\sigma}\|_2^2\rangle^{1/3} \sim CWi^{\alpha}, \tag{4.2}$$

where $\alpha \approx 0.7$ and C depends on Re. We have also performed numerical simulations at smaller values of Re, which indicate that α does not depend on Re. It is worth noting

that since $\|\nabla\boldsymbol{\sigma}\|$ grows with Wi, inequality (3.4) implies that a lower Re requires a higher Wi to obtain the same attractor dimension. This is in agreement with the stability analysis of the Oldroyd-B model, according to which the critical Wi for the appearance of elastic instabilities increases as Re decreases (e.g. Larson 1992; Boffetta *et al.* 2005).

5. Conclusions

Through a mathematical and numerical analysis of the two-dimensional Oldroyd-B model in the elastic-turbulence regime, we have made a practical estimate of the dimension of its (assumed) global attractor, as suggested by numerical simulations. We have also shown that the complexity of the attractor is related to the formation of large gradients in the polymer-conformation field. Although the asymptotic power-law dependence of $d_L(\mathcal{A})$ on Wi was found to be the same for different forcings, further studies are required to confirm the potential universality of the exponent α.

As mentioned in the introduction, the main limitation of the Oldroyd-B model is the absence of a maximum polymer elongation. Other constitutive models of polymer solutions, such as the FENE-P model, overcome this limitation by introducing a nonlinear elastic force that diverges when $\mathrm{Tr}\,\boldsymbol{\sigma}$ approaches the square of the maximum elongation (see Thomases, Shelley & Thiffeault 2011; Gupta & Pandit 2017, for the application of the FENE-P model to the study of elastic turbulence). However, the use of a nonlinear elastic force does not prevent the formation of large gradients in the $\boldsymbol{\sigma}$-field (Thomases, Shelley & Thiffeault 2011). In other words, large values of $\nabla\boldsymbol{\sigma}$ seem to occur independently of the form of the force that describes the elasticity of polymers. Our estimate (4.2) depends on $\|\nabla\boldsymbol{\sigma}\|_2$ rather than $\|\boldsymbol{\sigma}\|_2$. This fact suggests that, albeit based on the Oldroyd-B model, (4.2) may also be relevant to other constitutive models.

Our analysis can be adapted to the Oldroyd-B model coupled with the unsteady Stokes equations, in which the $\boldsymbol{u}\cdot\nabla\boldsymbol{u}$ term is set to zero; the estimates for N given in (3.4) are unchanged. The $Re=0$ case, in which (2.1*a*) is replaced with the Stokes equations (Thomases & Shelley 2009; Thomases *et al.* 2011), would require, by contrast, a separate analysis, because ω would depend on $\boldsymbol{\sigma}$ via a time-independent differential relation and (2.2) would reduce to a dynamical system in the $\boldsymbol{\sigma}$-space only. It would also be interesting to explore whether or not a relation exists between the exponent α in (4.2) and the exponent of the singular structures that emerge near hyperbolic points in the $Re=0$ case (Renardy 2006; Thomases & Shelley 2007).

Elastic turbulence is observed at low Re and high Wi. When both Re and Wi are high, the addition of polymers to a two-dimensional turbulent flow suppresses large-scale velocity fluctuations (Amarouchene & Kellay 2002). This phenomenon is once again correctly reproduced by the Oldroyd-B model (Boffetta, Celani & Musacchio 2003). Our estimate (A 18), which gives a sufficient condition for the contraction of N-volumes, holds for all values of Re. It would be interesting to investigate the implications of this estimate for the attractor dimension in the high-Re regime.

Acknowledgements

The authors would like to acknowledge useful discussions with G. Boffetta, A. Mazzino, S. Musacchio, P. Perlekar and S. S. Ray. The work of E.L.C.M.P. was supported by EACEA through the EMMA program. E.L.C.M.P. and D.V. acknowledge the support of the EU COST Action MP 1305 'Flowing Matter.' The authors also acknowledge the Observatoire de la Côte d'Azur for computing resources.

Appendix A. Derivation of the decay rate of N-dimensional volumes

Here, we show the main steps needed to obtain (3.4). The trace $\mathrm{Tr}[\boldsymbol{A}\boldsymbol{P}_N]$ can be expressed as (e.g. Constantin & Foias 1985; Doering & Gibbon 1995; Robinson 2001)

$$\mathrm{Tr}[\boldsymbol{A}\boldsymbol{P}_N] = \sum_{n=1}^{N} \int_{\Omega} \boldsymbol{\Phi}_n \cdot \boldsymbol{A}\boldsymbol{\Phi}_n \,\mathrm{d}\boldsymbol{x}, \tag{A 1}$$

where $\{\boldsymbol{\Phi}_n\}_{n=1}^{N} = \{(\phi_n^{\omega}, \boldsymbol{\phi}_n^{\sigma})\}_{n=1}^{N}$ is an orthonormal set spanning the subspace generated by the displacements $\{(\delta\omega_n, \delta\boldsymbol{\sigma}_n)\}_{n=1}^{N}$ and where $\{\phi_n^{\omega}\}_{n=1}^{N}$ is such that $\int_{\Omega} \phi_n^{\omega}\phi_m^{\omega}\,\mathrm{d}\boldsymbol{x} = 0$ if $n \neq m$, and $\{\boldsymbol{\phi}_n^{\sigma}\}_{n=1}^{N}$ with $(\boldsymbol{\phi}_n^{\sigma})^{\top} = \boldsymbol{\phi}_n^{\sigma}$ is such that $\int_{\Omega} \boldsymbol{\phi}_n^{\sigma} : \boldsymbol{\phi}_m^{\sigma}\,\mathrm{d}\boldsymbol{x} = 0$ if $n \neq m$. The orthonormality of $\{\boldsymbol{\Phi}_n\}_{n=1}^{N}$ should then be interpreted as follows: $\int_{\Omega} \phi_m^{\omega}\phi_n^{\omega}\,\mathrm{d}\boldsymbol{x} + \int_{\Omega} \boldsymbol{\phi}_m^{\sigma} : \boldsymbol{\phi}_n^{\sigma}\,\mathrm{d}\boldsymbol{x} = \delta_{mn}$, whence

$$\sum_{n=1}^{N} \int_{\Omega} |\boldsymbol{\Phi}_n|^2 \,\mathrm{d}\boldsymbol{x} = \sum_{n=1}^{N} \int_{\Omega} (|\phi_n^{\omega}|^2 + |\boldsymbol{\phi}_n^{\sigma}|^2)\,\mathrm{d}\boldsymbol{x} = N. \tag{A 2}$$

The symbol ':' denotes the inner product between matrices, $\boldsymbol{\sigma} : \boldsymbol{\sigma}' \equiv \mathrm{Tr}[\boldsymbol{\sigma}^{\top}\boldsymbol{\sigma}']$. The following inequality (e.g. Robinson 2001) will also be used when we estimate the norms of $\phi_n^{\omega}, \boldsymbol{\phi}_n^{\sigma}$ or of their gradients:

$$\Theta \equiv \mathrm{Tr}[-\Delta\boldsymbol{P}_N] = -\sum_{n=1}^{N} \int_{\Omega} (\phi_n^{\omega}\Delta\phi_n^{\omega} + \boldsymbol{\phi}_n^{\sigma} : \Delta\boldsymbol{\phi}_n^{\sigma})\,\mathrm{d}\boldsymbol{x} \geqslant cN^2. \tag{A 3}$$

The terms appearing in (A 1) can be explicitly listed as (the terms that follow from $\boldsymbol{u}\cdot\nabla\delta\omega$ and $\boldsymbol{u}\cdot\nabla\delta\boldsymbol{\sigma}$ vanish because of the incompressibility of $\boldsymbol{u}$)

$$\mathrm{Tr}[\boldsymbol{A}\boldsymbol{P}_N] = Re^{-1}\sum_{n=1}^{N} \int_{\Omega} \phi_n^{\omega}\Delta\phi_n^{\omega}\,\mathrm{d}\boldsymbol{x} + Pe^{-1}\sum_{n=1}^{N} \int_{\Omega} \boldsymbol{\phi}_n^{\sigma} : \Delta\boldsymbol{\phi}_n^{\sigma}\,\mathrm{d}\boldsymbol{x}, \tag{A 4a}$$

$$- \sum_{n=1}^{N} \int_{\Omega} \phi_n^{\omega}\boldsymbol{v}_n \cdot \nabla\omega\,\mathrm{d}\boldsymbol{x} - \sum_{n=1}^{N} \int_{\Omega} \boldsymbol{\phi}_n^{\sigma} : (\boldsymbol{v}_n \cdot \nabla\boldsymbol{\sigma})\,\mathrm{d}\boldsymbol{x}, \tag{A 4b}$$

$$+ \beta(Wi\,Re)^{-1}\sum_{n=1}^{N} \int_{\Omega} \phi_n^{\omega}\hat{\boldsymbol{z}} \cdot (\nabla \times \nabla \cdot \boldsymbol{\phi}_n^{\sigma})\,\mathrm{d}\boldsymbol{x} - Wi^{-1}\sum_{n=1}^{N} \int_{\Omega} |\boldsymbol{\phi}_n^{\sigma}|^2\,\mathrm{d}\boldsymbol{x}, \tag{A 4c}$$

$$+ \sum_{n=1}^{N} \int_{\Omega} \boldsymbol{\phi}_n^{\sigma} : [(\nabla\boldsymbol{v}_n)\boldsymbol{\sigma} + \boldsymbol{\sigma}(\nabla\boldsymbol{v}_n)^{\top}]\,\mathrm{d}\boldsymbol{x} + \sum_{n=1}^{N} \int_{\Omega} \boldsymbol{\phi}_n^{\sigma} : [(\nabla\boldsymbol{u})\boldsymbol{\phi}_n^{\sigma} + \boldsymbol{\phi}_n^{\sigma}(\nabla\boldsymbol{u})^{\top}]\,\mathrm{d}\boldsymbol{x}, \tag{A 4d}$$

where $\boldsymbol{v}_n = \nabla^{\perp}\Delta^{-1}\phi_n^{\omega}$. By using (A 3), the Laplacian terms in (A 4a) can be shown to satisfy (under the assumption $Pe > Re$)

$$Re^{-1}\sum_{n=1}^{N} \int_{\Omega} \phi_n^{\omega}\Delta\phi_n^{\omega}\,\mathrm{d}\boldsymbol{x} + Pe^{-1}\sum_{n=1}^{N} \int_{\Omega} \boldsymbol{\phi}_n^{\sigma} : \Delta\boldsymbol{\phi}_n^{\sigma}\,\mathrm{d}\boldsymbol{x} \leqslant -Re^{-1}\Theta. \tag{A 5}$$

We treat the advective terms (A 4b) by using the result of Constantin (1987) and its subsequent use in Doering & Gibbon (1991), i.e. a Cauchy–Schwarz inequality, an L^{∞}

bound for the terms involving $\boldsymbol{v}_n$, and (A 3):

$$\left|\sum_{n=1}^{N}\int_{\Omega}[\phi_n^{\omega}\boldsymbol{v}_n\cdot\boldsymbol{\nabla}\omega+\boldsymbol{\phi}_n^{\sigma}:(\boldsymbol{v}_n\cdot\boldsymbol{\nabla}\boldsymbol{\sigma})]\,\mathrm{d}\boldsymbol{x}\right|\leqslant c\,(1+\ln\Theta)^{1/2}\Theta^{1/4}(\|\boldsymbol{\nabla}\omega\|_2+\|\boldsymbol{\nabla}\boldsymbol{\sigma}\|_2). \tag{A 6}$$

To estimate the feedback term in (A 4*c*), we use integration by parts, the Cauchy–Schwarz inequality, the relations $|\boldsymbol{\nabla}\times(\phi_n^{\omega}\hat{\boldsymbol{z}})|=|\boldsymbol{\nabla}\phi_n^{\omega}|$ and $|\boldsymbol{\nabla}\cdot\boldsymbol{\phi}_n^{\sigma}|^2\leqslant|\boldsymbol{\nabla}\boldsymbol{\phi}_n^{\sigma}|^2$, and (A 3):

$$\left|\sum_{n=1}^{N}\int_{\Omega}\phi_n^{\omega}\hat{\boldsymbol{z}}\cdot(\boldsymbol{\nabla}\times\boldsymbol{\nabla}\cdot\boldsymbol{\phi}_n^{\sigma})\,\mathrm{d}\boldsymbol{x}\right|\leqslant\sum_{n=1}^{N}\int_{\Omega}|\boldsymbol{\nabla}\phi_n^{\omega}||\boldsymbol{\nabla}\boldsymbol{\phi}_n^{\sigma}|\,\mathrm{d}\boldsymbol{x}\leqslant\Theta. \tag{A 7}$$

The second term in (A 4*c*) satisfies

$$Wi^{-1}\sum_{n=1}^{N}\int_{\Omega}|\boldsymbol{\phi}_n^{\sigma}|^2\,\mathrm{d}\boldsymbol{x}=bWi^{-1},\quad 0<b\leqslant N\leqslant c\Theta^{1/2}. \tag{A 8}$$

The stretching term in (A 4*d*) that involves $\boldsymbol{\nabla}\boldsymbol{v}_n$ is first integrated by parts. The Cauchy–Schwarz inequality is then applied twice to obtain

$$\left|\sum_{n=1}^{N}\int_{\Omega}\boldsymbol{\phi}_n^{\sigma}:[(\boldsymbol{\nabla}\boldsymbol{v}_n)\boldsymbol{\sigma}+\boldsymbol{\sigma}(\boldsymbol{\nabla}\boldsymbol{v}_n)^{\top}]\,\mathrm{d}\boldsymbol{x}\right|\leqslant 2\sum_{n=1}^{N}\int_{\Omega}(|\boldsymbol{\phi}_n^{\sigma}||\boldsymbol{\nabla}\boldsymbol{\sigma}||\boldsymbol{v}_n|+|\boldsymbol{\nabla}\boldsymbol{\phi}_n^{\sigma}||\boldsymbol{\sigma}||\boldsymbol{v}_n|)\,\mathrm{d}\boldsymbol{x}. \tag{A 9}$$

We then use the same techniques as employed to get (A 6) and obtain

$$\left|\sum_{n=1}^{N}\int_{\Omega}\boldsymbol{\phi}_n^{\sigma}:[(\boldsymbol{\nabla}\boldsymbol{v}_n)\boldsymbol{\sigma}+\boldsymbol{\sigma}(\boldsymbol{\nabla}\boldsymbol{v}_n)^{\top}]\,\mathrm{d}\boldsymbol{x}\right|\leqslant c(1+\ln\Theta)^{1/2}(\Theta^{1/2}\|\boldsymbol{\sigma}\|_2+\Theta^{1/4}\|\boldsymbol{\nabla}\boldsymbol{\sigma}\|_2). \tag{A 10}$$

The other stretching term in (A 4*d*) is estimated by first applying the Cauchy–Schwarz inequality:

$$\left|\sum_{n=1}^{N}\int_{\Omega}\boldsymbol{\phi}_n^{\sigma}:[(\boldsymbol{\nabla}\boldsymbol{u})\boldsymbol{\phi}_n^{\sigma}+\boldsymbol{\phi}_n^{\sigma}(\boldsymbol{\nabla}\boldsymbol{u})^{\top}]\,\mathrm{d}\boldsymbol{x}\right|\leqslant 2\|\boldsymbol{\nabla}\boldsymbol{u}\|_2\left|\int_{\Omega}\left(\sum_{n=1}^{N}|\boldsymbol{\Phi}_n|^2\right)^2\mathrm{d}\boldsymbol{x}\right|^{1/2}. \tag{A 11}$$

We note that in two dimensions $\|\boldsymbol{\nabla}\boldsymbol{u}\|_2=\|\omega\|_2$, and then use the Lieb–Thirring inequality for the set of orthonormal functions $\{\boldsymbol{\Phi}_n\}_{n=1}^{N}$ (Constantin *et al.* 1988) and (A 3) to obtain

$$\left|\sum_{n=1}^{N}\int_{\Omega}\boldsymbol{\phi}_n^{\sigma}:[(\boldsymbol{\nabla}\boldsymbol{u})\boldsymbol{\phi}_n^{\sigma}+\boldsymbol{\phi}_n^{\sigma}(\boldsymbol{\nabla}\boldsymbol{u})^{\top}]\,\mathrm{d}\boldsymbol{x}\right|\leqslant c\|\omega\|_2\Theta^{1/2}. \tag{A 12}$$

Using (A 5)–(A 8), (A 10) and (A 12), the trace $\mathrm{Tr}[\boldsymbol{AP}_N]$ can now be estimated in terms of Θ as follows:

$$\begin{aligned}\mathrm{Tr}[\boldsymbol{AP}_N]\ \leqslant\ &(\beta Wi^{-1}-1)Re^{-1}\Theta-bWi^{-1}+c(1+\ln\Theta)^{1/2}\Theta^{1/2}\|\boldsymbol{\sigma}\|_2\\&+c(1+\ln\Theta)^{1/2}\Theta^{1/4}(\|\boldsymbol{\nabla}\boldsymbol{\sigma}\|_2+\|\boldsymbol{\nabla}\omega\|_2)+c\|\omega\|_2\Theta^{1/2}.\end{aligned} \tag{A 13}$$

In the third term on the right-hand side of (A 13), it is useful to write $\Theta^{1/2} = \Theta^a \Theta^{1/2-a}$ with $0 < a < 1/2$. Taking the time average of (A 13) and applying the Cauchy–Schwarz and Hölder's inequalities on the time variable, we obtain

$$\begin{aligned}\langle \mathrm{Tr}[\boldsymbol{AP}_N] \rangle \leqslant\ & (\beta Wi^{-1} - 1) Re^{-1} \langle \Theta \rangle - b Wi^{-1} + c \langle \|\omega\|_2^2 \rangle^{1/2} \langle \Theta \rangle^{1/2} \\ & + c \langle (1 + \ln \Theta)^{3/2} \Theta^{3a} \rangle^{1/3} \langle \Theta^{3(1/2-a)} \rangle^{1/3} \langle \|\boldsymbol{\sigma}\|_2^3 \rangle^{1/3} \\ & + c \langle (1 + \ln \Theta) \Theta^{1/2} \rangle^{1/2} (\langle \|\nabla \boldsymbol{\sigma}\|_2^2 \rangle^{1/2} + \langle \|\nabla \omega\|_2^2 \rangle^{1/2}). \end{aligned} \tag{A 14}$$

The bound in (A 14) can be improved by estimating $\langle \|\nabla \omega\|_2^2 \rangle$. We first multiply (2.2*a*) by ω, integrate over space, and take the time average (noting that is necessary to use our assumption that $\|\omega\|_2$ is finite and hence $\langle \partial_t \|\omega\|_2^2 \rangle = 0$):

$$Re^{-1} \langle \|\nabla \omega\|_2^2 \rangle = \left\langle \int_\Omega \omega \hat{\boldsymbol{z}} \cdot \nabla \times \boldsymbol{F} \, \mathrm{d}\boldsymbol{x} \right\rangle + \beta (Wi\, Re)^{-1} \left\langle \int_\Omega \omega \hat{\boldsymbol{z}} \cdot \nabla \times (\nabla \cdot \boldsymbol{\sigma}) \, \mathrm{d}\boldsymbol{x} \right\rangle. \tag{A 15}$$

We then integrate by parts and apply the Cauchy–Schwarz inequality, first in space and then in time, to obtain

$$\langle \|\nabla \omega\|_2^2 \rangle^{1/2} \leqslant Re \|\boldsymbol{F}\|_2 + \beta Wi^{-1} \langle \|\nabla \boldsymbol{\sigma}\|_2^2 \rangle^{1/2}. \tag{A 16}$$

Moreover, Jensen's inequality allows us to express (A 14) as a function of $\langle \Theta \rangle$:

$$\begin{aligned}\langle \mathrm{Tr}[\boldsymbol{AP}_N] \rangle \leqslant\ & (\beta Wi^{-1} - 1) Re^{-1} \langle \Theta \rangle - b Wi^{-1} + c \langle \|\omega\|_2^2 \rangle^{1/2} \langle \Theta \rangle^{1/2} \\ & + c (1 + \ln \langle \Theta \rangle)^{1/2} \langle \Theta \rangle^{1/2} \langle \|\boldsymbol{\sigma}\|_2^3 \rangle^{1/3} + c Re (1 + \ln \langle \Theta \rangle)^{1/2} \langle \Theta \rangle^{1/4} \|\boldsymbol{F}\|_2 \\ & + c (1 + \beta Wi^{-1}) (1 + \ln \langle \Theta \rangle)^{1/2} \langle \Theta \rangle^{1/4} \langle \|\nabla \boldsymbol{\sigma}\|_2^2 \rangle^{1/2}. \end{aligned} \tag{A 17}$$

It should be noted that for this last inequality to hold, a must be such that $\Theta^{3(1/2-a)}$ and $(1 + \ln \Theta)^{3/2} \Theta^{3a}$ are concave functions. The choice $a = 1/5$ guarantees that $\Theta^{3(1/2-a)}$ is concave for all values of Θ and $(1 + \ln \Theta)^{3/2} \Theta^{3a}$ is concave for $\Theta > 5$. This restriction on Θ is justified since $\Theta \geqslant cN^2$ and in elastic turbulence N is large. The trace $\langle \mathrm{Tr}[\boldsymbol{AP}_N] \rangle$ is thus guaranteed to be negative if $\langle \Theta \rangle$ satisfies

$$\begin{aligned}(1 - \beta Wi^{-1}) \langle \Theta \rangle \geqslant\ & c Re \langle \|\omega\|_2^2 \rangle^{1/2} \langle \Theta \rangle^{1/2} + c Re^2 (1 + \ln \langle \Theta \rangle)^{1/2} \langle \Theta \rangle^{1/4} \|\boldsymbol{F}\|_2 \\ & + c Re (1 + \ln \langle \Theta \rangle)^{1/2} \{ \langle \Theta \rangle^{1/2} \langle \|\boldsymbol{\sigma}\|_2^3 \rangle^{1/3} + (1 + \beta Wi^{-1}) \langle \Theta \rangle^{1/4} \langle \|\nabla \boldsymbol{\sigma}\|_2^2 \rangle^{1/2} \}. \end{aligned} \tag{A 18}$$

Under the assumptions that $0 < Re < Re_c$ and $Wi \gg 1$, it is easy to see that $(1 - \beta Wi^{-1}) \langle \Theta \rangle \approx \langle \Theta \rangle$ is greater than each of the terms in the first line of (A 18). As $\|\boldsymbol{F}\|_2$ is independent of Wi, $\langle \Theta \rangle$ dominates the forcing term. In the elastic-turbulence regime of the Oldroyd-B model, the kinetic-energy spectrum decays rapidly as a function of the wavenumber (Berti *et al.* 2008; Berti & Boffetta 2010), and $\|\omega\|_2$ is expected to be small as Wi increases. Therefore, $\langle \Theta \rangle$ also controls the enstrophy term in (A 18) – this is confirmed numerically in figure 2.

The number of significant terms in (A 18) is thus reduced to two. Direct numerical simulations of the Oldroyd-B model show that, in elastic turbulence, $\mathrm{Tr}\,\boldsymbol{\sigma}$ grows as Wi increases and $\boldsymbol{\sigma}$ develops strong gradients (Berti *et al.* 2008; Berti & Boffetta 2010). Therefore, both $\|\boldsymbol{\sigma}\|_2$ and $\|\nabla \boldsymbol{\sigma}\|_2$ are expected to increase with Wi. To analyse the $\boldsymbol{\sigma}$- and $\nabla \boldsymbol{\sigma}$-terms in (A 18), it is useful to note that for any $\mathcal{M}$ independent of $\langle \Theta \rangle^{1/2} \geqslant 4$ and any $0 \leqslant \lambda < 3/2$, the following holds:

$$\langle \Theta \rangle^{1/2} \geqslant c \mathcal{M}^{1/(2-\lambda)} (1 + \ln \mathcal{M})^{1/2(2-\lambda)} \Longrightarrow \langle \Theta \rangle \geqslant c \mathcal{M} \langle \Theta \rangle^{\lambda/2} (1 + \ln \langle \Theta \rangle)^{1/2}, \tag{A 19}$$

which can be proved by generalizing an analogous result by Doering & Gibbon (1991). The inequalities below are thus sufficient conditions for (A 18) to hold:

$$\langle \Theta \rangle^{1/2} > cRe \langle \|\boldsymbol{\sigma}\|_2^3 \rangle^{1/3} (1 + \ln Re + \ln \langle \|\boldsymbol{\sigma}\|_2^3 \rangle^{1/3})^{1/2}, \tag{A 20a}$$

$$\langle \Theta \rangle^{1/2} > cRe^{2/3} \langle \|\nabla \boldsymbol{\sigma}\|_2^2 \rangle^{1/3} (1 + \ln Re + \ln \langle \|\nabla \boldsymbol{\sigma}\|_2^2 \rangle^{1/2})^{1/3}. \tag{A 20b}$$

Since $\Theta \geqslant cN^2$ (see (A 3)), these can be converted into sufficient conditions on N, as in (3.4).

References

Amarouchene, Y. & Kellay, H. 2002 Polymers in 2D turbulence: suppression of large scale fluctuations. *Phys. Rev. Lett.* **89**, 104502.

Barrett, J. W. & Süli, E. 2011 Existence and equilibration of global weak solutions to kinetic models for dilute polymers I. *Math. Models Meth. Appl. Sci.* **21**, 1211–1289.

Berti, S., Bistagnino, A., Boffetta, G., Celani, A. & Musacchio, S. 2008 Two-dimensional elastic turbulence. *Phys. Rev.* E **77**, 055306(R).

Berti, S. & Boffetta, G. 2010 Elastic waves and transition to elastic turbulence in a two-dimensional viscoelastic Kolmogorov flow. *Phys. Rev.* E **82**, 036314.

Boffetta, G., Celani, A., Mazzino, A., Puliafito, A. & Vergassola, M. 2005 The viscoelastic Kolmogorov flow: eddy-viscosity and linear stability. *J. Fluid Mech.* **523**, 161–170.

Boffetta, G., Celani, A. & Musacchio, S. 2003 Two-dimensional turbulence of dilute polymer solutions. *Phys. Rev. Lett.* **91**, 034501.

Burghelea, T., Segre, E. & Steinberg, V. 2004 Statistics of particle pair separations in the elastic turbulent flow of a dilute polymer solution. *Europhys. Lett.* **68**, 529–535.

Burghelea, T., Segre, E. & Steinberg, V. 2007 Elastic turbulence in von Karman swirling flow between two disks. *Phys. Fluids* **19**, 053104.

Constantin, P. 1987 Collective L^∞-estimates for families of functions with orthonormal derivatives. *Indiana Univ. Math. J.* **36**, 603–616.

Constantin, P. & Foias, C. 1985 Global Lyapunov exponents, Kaplan–Yorke formulas and the dimension of the attractors for 2D Navier–Stokes equations. *Commun. Pure Appl. Maths* **38**, 1–27.

Constantin, P., Foias, C. & Temam, R. 1988 On the dimension of the attractors in two-dimensional turbulence. *Physica* D **30**, 284–296.

Constantin, P. & Kliegl, M. 2012 Note on global regularity for two-dimensional Oldroyd-B fluids with diffusive stress. *Arch. Rat. Mech. Anal.* **206**, 725–740.

Doering, C. R. & Gibbon, J. D. 1991 Note on the Constantin–Foias–Temam attractor dimension estimate for two-dimensional turbulence. *Physica* D **48**, 471–480.

Doering, C. R. & Gibbon, J. D. 1995 *Applied Analysis of the Navier–Stokes Equations*. Cambridge University Press.

Elgindi, T. M. & Rousset, F. 2015 Global regularity for some Oldroyd-B type models. *Commun. Pure Appl. Math.* **68**, 2005–2021.

El-Kareh, A. W. & Leal, L. G. 1989 Existence of solutions for all Deborah numbers for a non-Newtonian model modified to include diffusion. *J. Non-Newtonian Fluid Mech.* **33**, 257–287.

Fouxon, A. & Lebedev, V. 2003 Spectra of turbulence in dilute polymer solutions. *Phys. Fluids* **15**, 2060–2072.

Gibbon, J. D. & Titi, E. 1997 Attractor dimension and small length scale estimates for the three-dimensional Navier–Stokes equations. *Nonlinearity* **10**, 109–119.

Grilli, M., Vázquez-Quesada, A. & Ellero, M. 2013 Transition to turbulence and mixing in a viscoelastic fluid flowing inside a channel with a periodic array of cylindrical obstacles. *Phys. Rev. Lett.* **110**, 174501.

Groisman, A. & Steinberg, V. 2000 Elastic turbulence in a polymer solution flow. *Nature* **405**, 53–55.

GROISMAN, A. & STEINBERG, V. 2001 Efficient mixing at low Reynolds numbers using polymer additives. *Nature* **410**, 905–908.

GUPTA, A. & PANDIT, R. 2017 Melting of a non-equilibrium vortex crystal in a fluid film with polymers: elastic versus fluid turbulence. *Phys. Rev.* E **95**, 033119.

GUPTA, A., PERLEKAR, P. & PANDIT, R. 2015 Two-dimensional homogeneous isotropic fluid turbulence with polymer additives. *Phys. Rev.* E **91**, 033013.

HU, X. & LIN, F. 2016 Global solutions of two-dimensional incompressible viscoelastic flows with discontinuous initial data. *Commun. Pure Appl. Maths* **69**, 372–404.

KURGANOV, A. & TADMOR, E. 2000 New high-resolution central schemes for nonlinear conservation laws and convection-diffusion equations. *J. Comput. Phys.* **160**, 241–282.

LARSON, R. G. 1992 Instabilities in viscoelastic flows. *Rheol. Acta* **31**, 213–263.

LEI, Z., MASMOUDI, N. & ZHOU, Y. 2010 Remarks on the blowup criteria for Oldroyd models. *J. Differ. Equ.* **248**, 328–341.

MITCHELL, J., LYONS, K., HOWE, A. M. & CLARKE, A. 2016 Viscoelastic polymer flows and elastic turbulence in three-dimensional porous structures. *Soft Matt.* **12**, 460–468.

OLDROYD, J. G. 1950 On the formulation of rheological equations of state. *Proc. R. Soc. Lond.* A **200**, 523–541.

RENARDY, M. 2006 A comment on smoothness of viscoelastic stresses. *J. Non-Newtonian Fluid Mech.* **138**, 204–205.

ROBINSON, J. C. 2001 *Infinite-dimensional Dynamical Systems*. Cambridge University Press.

SHAQFEH, E. S. G. 1996 Purely elastic instabilities in viscometric flows. *Annu. Rev. Fluid Mech.* **28**, 129–185.

SURESHKUMAR, R. & BERIS, A. N. 1995 Effect of artificial stress diffusivity on the stability of numerical calculations and the flow dynamics of time-dependent viscoelastic flows. *J. Non-Newtonian Fluid Mech.* **60**, 53–80.

THOMASES, B. 2011 An analysis of the effect of stress diffusion on the dynamics of creeping viscoelastic flow. *J. Non-Newtonian Fluid Mech.* **166**, 1221–1228.

THOMASES, B. & SHELLEY, M. 2007 Emergence of singular structures in Oldroyd-B fluids. *Phys. Fluids* **19**, 103103.

THOMASES, B. & SHELLEY, M. 2009 Transition to mixing and oscillations in a Stokesian viscoelastic flow. *Phys. Rev. Lett.* **103**, 094501.

THOMASES, B., SHELLEY, M. & THIFFEAULT, J.-L. 2011 A Stokesian viscoelastic flow: transition to oscillations and mixing. *Physica* D **240**, 1602–1614.

VAITHIANATHAN, T., ROBERT, A., BRASSEUR, J. G. & COLLINS, L. R. 2006 An improved algorithm for simulating three-dimensional, viscoelastic turbulence. *J. Non-Newtonian Fluid Mech.* **140**, 3–22.

Emergence of chaos in a viscous solution of rods

Emmanuel L. C. VI M. Plan, Stefano Musacchio, and Dario Vincenzi
Université Côte d'Azur, CNRS, LJAD, Nice 06108, France
(Received 17 April 2017; published 13 November 2017)

It is shown that the addition of small amounts of microscopic rods in a viscous fluid at low Reynolds number causes a significant increase of the flow resistance. Numerical simulations of the dynamics of the solution reveal that this phenomenon is associated to a transition from laminar to chaotic flow. Polymer stresses give rise to flow instabilities which, in turn, perturb the alignment of the rods. This coupled dynamics results in the activation of a wide range of scales, which enhances the mixing efficiency of viscous flows.

DOI: 10.1103/PhysRevE.96.053108

I. INTRODUCTION

In a laminar flow the dispersion of substances occurs by molecular diffusion, which operates on extremely long time scales. Various strategies have therefore been developed, particularly in microfluidic applications, to accelerate mixing and dispersion at low fluid inertia [1–3]. The available strategies are commonly divided into two classes, passive or active, according to whether the desired effect is obtained through the specific geometry of the flow or through an oscillatory forcing within the fluid [2]. An alternative method for improving the mixing properties of low-Reynolds-number flows was proposed by Groisman and Steinberg [4] and consists in adding elastic polymers to the fluid. If the inertia of the fluid is low but the elasticity of polymers is large enough, elastic stresses give rise to instabilities that ultimately generate a chaotic regime known as "elastic turbulence" [5]. In this regime the velocity field, although remaining smooth in space, becomes chaotic and develops a power-law energy spectrum, which enhances the mixing properties of the flow. While the use of elastic turbulence in microfluidics is now well established [6–10], new potential applications have recently emerged, namely in oil extraction from porous rocks [11].

In this paper we propose a mechanism for generating chaotic flows at low Reynolds numbers that does not rely on elasticity. It is based on the addition of rigid rodlike polymers. In spite of the different microscopic dynamics, elastic- and rigid-polymer solutions exhibit remarkably similar macroscopic behavior at high Reynolds number (see, e.g., Refs. [12–15]). In both cases the turbulent drag is considerably reduced compared to that of the solvent alone. In particular, when either type of polymer is added in sufficiently high concentrations to a turbulent channel flow of a Newtonian fluid, the velocity profile continues to depend logarithmically on the distance from the walls of the channel, but the mean velocity increases to a value known as maximum-drag-reduction asymptote.

Here we demonstrate, by means of numerical simulations of a dilute solution of microscopic rods at low-Re, that the orientational dynamics of rigid polymers is sufficient to originate a chaotic regime similar to elastic turbulence, with increased flow resistance and power-law energy spectra.

II. RHEOLOGICAL MODEL

We consider a dilute solution of inertialess rodlike polymers. The size of the polymers is small enough for the velocity field to be linear at the scale of a polymer. The polymer phase is described by the symmetric unit-trace tensor field $\mathcal{R}_{ij}(\boldsymbol{x},t) = \overline{n_i n_j}$, where $\boldsymbol{n}$ is the orientation of an individual polymer and the average is taken over the polymers contained in a volume element at position $\boldsymbol{x}$ at time t. The coupled evolution of $\mathcal{R}(\boldsymbol{x},t)$ and the incompressible velocity field $\boldsymbol{u}(\boldsymbol{x},t)$ is given by the following equations [16,17] (summation over repeated indices is implied):

$$\partial_t u_i + u_k \partial_k u_i = -\partial_i p + \nu \partial^2 u_i + \partial_k \sigma_{ik} + f_i, \quad \text{(1a)}$$

$$\partial_t \mathcal{R}_{ij} + u_k \partial_k \mathcal{R}_{ij} = (\partial_k u_i)\mathcal{R}_{kj} + \mathcal{R}_{ik}(\partial_k u_j) - 2\mathcal{R}_{ij}(\partial_l u_k)\mathcal{R}_{kl}, \quad \text{(1b)}$$

where $\partial_k = \partial/\partial x_k$, $p(\boldsymbol{x},t)$ is pressure, ν is the kinematic viscosity of the fluid, and $\boldsymbol{f}(\boldsymbol{x},t)$ is the body force which sustains the flow. The polymer stress tensor takes the form $\sigma_{ij} = 6\nu\eta_p \mathcal{R}_{ij}(\partial_l u_k)\mathcal{R}_{kl}$ [16]. The intensity of the polymer feedback on the flow is determined by the parameter η_p, which increases with polymer concentration and whose value is determined by comparing the above constitutive model with experiments (for example, the relation between η_p and the concentration C in weight parts per million (wppm) is $\eta_p = 0.011147C^{1.422}$ for an aqueous solution of xanthan gum [18]). The above expression for the polymer stress tensor is based on a quadratic approximation proposed by Doi and Edwards [16]. More sophisticated closures have been employed in the literature (see, e.g., Ref. [19] and references therein); here we focus on the simplest model of rodlike-polymer solution that may display instabilities at low Reynolds number. In addition, we disregard Brownian rotations to ensure that the chaotic regime arises from the rheological properties of the solution and not from thermal fluctuations.

For large values of the Reynolds number, the system described by Eqs. (1) has been shown to reproduce the main features of drag reduction in turbulent solutions of rodlike polymers [14,17,18,20,21]. Here we study the same system at small values of the Reynolds number. Equations (1) are solved over a two-dimensional 2π-periodic box and $\boldsymbol{f}$ is taken to be the Kolmogorov force $\boldsymbol{f}(\boldsymbol{x}) = (0, F\sin(x/L))$. For $\eta_p = 0$ the flow has the laminar solution $\boldsymbol{u} = (0, U_0\sin(x/L))$ with $U_0 = FL^2/\nu$, which becomes unstable when the Reynolds number $\mathrm{Re} = U_0 L/\nu$ exceeds the critical value $\mathrm{Re}_c = \sqrt{2}$ and eventually turbulent when Re is increased further (e.g., Ref. [22]). Even in the turbulent regime, the mean flow has the sinusoidal form $\langle \boldsymbol{u} \rangle = (0, U\sin(x/L))$, where $\langle \cdot \rangle$ denotes an average over

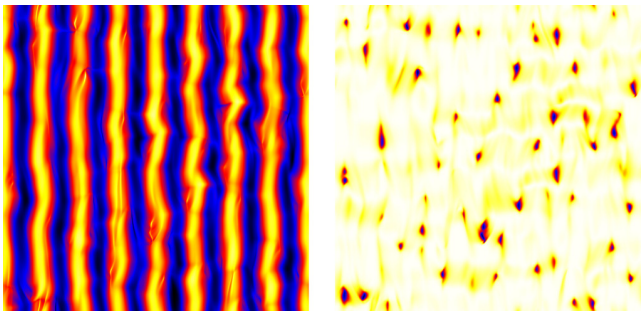

FIG. 1. Left: Snapshot of the vorticity field ω for $\eta_p = 3$ and $L = 1/8$. Black (white) represents negative (positive) vorticity. Right: Snapshot of the component $\mathcal{R}_{11}$. White represents 0, black represents 1.

the variable y and over time. The Kolmogorov force has been previously used in the context of non-Newtonian fluid mechanics to study turbulent drag reduction [23], the formation of low-Re instabilities in viscoelastic [24,25] and rheopectic fluids [26], and elastic turbulence [27,28].

III. NUMERICAL RESULTS

Numerical simulations of Eqs. (1) are performed by using a dealiased pseudospectral method with 1024^2 gridpoints. The time integration uses a fourth-order Runge-Kutta scheme with implicit integration of the linear dissipative terms. The parameters of the simulations are set to keep $\mathrm{Re} = 1$ fixed below Re_c in the absence of polymer feedback ($\eta_p = 0$). The viscosity is set to $\nu = 1$, the length scale of the forcing is either $L = 1/4$ or $L = 1/8$, and its amplitude is $F = \nu^2/L^3$. The feedback coefficient is varied from $\eta_p = 1$ to $\eta_p = 5$ ($\eta_p = 5$ corresponds to a concentration of 73 wppm for an aqueous solution of xanthan gum [18]). The stiffness of the equations increases with η_p, limiting the accessible range of parameters.

Initially the flow is a weak perturbation of the $\eta_p = 0$ stable solution, while the components of $\mathcal{R}$ are randomly distributed. When the feedback of the polymers is absent ($\eta_p = 0$) the initial perturbation decays and the polymers align with the direction of the mean shear flow. Conversely, at large η_p the flow is strongly modified by the presence of the rods. The streamlines wiggle over time and thin filaments appear in the vorticity field $\omega = |\nabla \times \boldsymbol{u}|$ (see Fig. 1, left panel). These filaments correspond to appreciable localized perturbations of the tensor $\mathcal{R}$ away from the laminar fixed point (Fig. 1, right panel) and are due to the rods being unaligned with the shear direction. Notably, we find that the mean flow, obtained by means of long time averages, maintains the sinusoidal form $\langle \boldsymbol{u} \rangle = (0, U \sin(x/L))$ also in the presence of strong polymer feedback (Fig. 2).

The time series of the kinetic energy in Fig. 3 show that, in the case of a low concentration ($\eta_p = 1$), the system repetitively attempts but fails to escape the laminar regime in a quasiperiodic manner. The amount of kinetic energy is initially close to that in the laminar regime. After some time, the solution dissipates a small fraction of kinetic energy but quickly relaxes back towards the laminar regime until it restarts this cyclic pattern. In contrast, for higher concentrations the kinetic energy is significantly reduced and, after an initial

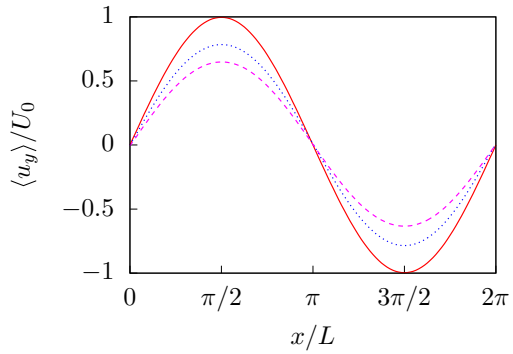

FIG. 2. Mean velocity profiles for $L = 1/8$ and concentrations $\eta_p = 1$ (solid), $\eta_p = 3$ (dotted), and $\eta_p = 5$ (dashed).

transient, fluctuates around a constant value. We have observed that different initial conditions for $\mathcal{R}$ may give rise to longer transients that involve a quasiperiodic sequence of activations and relaxations comparable to that observed for low values of η_p. Nevertheless, the statistically steady state achieved at later times is independent of the peculiar choice of initial conditions.

The reduction of the kinetic energy of the flow at fixed intensity of the external force reveals that the presence of the rods causes an increase in the flow resistance. This effect can be quantified by the ratio of the actual mean power $P = FU/2$ provided by the external force and the power $P_{\mathrm{lam}} = F_0 U/2$ that would be required to sustain a laminar mean flow with the same amplitude U in the absence of polymers. In the latter case, the force required would be $F_0 = \nu U/L^2$ and the corresponding mean power would be $P_{\mathrm{lam}} = F_0 U/2 = \nu U^2/2L^2$. Figure 4 shows the ratio

$$\frac{P}{P_{\mathrm{lam}}} = \frac{F}{F_0} = \frac{FL^2}{\nu U} \tag{2}$$

as a function of η_p and indicates that more power is required to sustain the same mean flow in solutions with higher concentrations.

The analysis of the momentum budget confirms that the increased resistance is due to an increase of the amount of stress due to the polymers. In the steady state the momentum

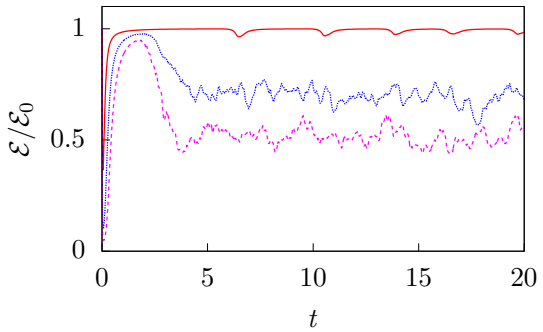

FIG. 3. The kinetic energy $\mathcal{E}$ for $L = 1/8$ and concentrations $\eta_p = 1$ (top, solid), $\eta_p = 3$ (middle, dotted), and $\eta_p = 5$ (bottom, dashed) divided by the kinetic energy $\mathcal{E}_0 = F^2 L^4/2\nu^2$ corresponding to $\eta_p = 0$ and the same value of the force F.

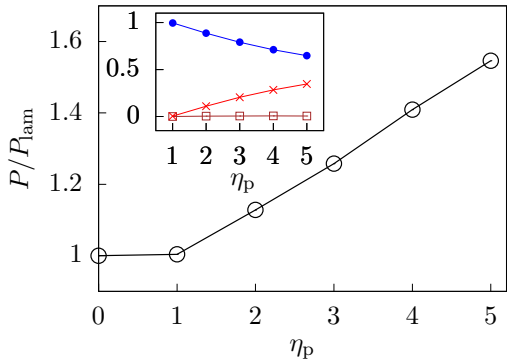

FIG. 4. The normalized mean injected power $P/P_{\rm lam}$ as a function of $\eta_{\rm p}$. Inset: The amplitudes of the stresses Π_r (brown □), Π_ν (blue •), and Π_p (red ×) divided by the amplitude of the total stress $\Pi_{\rm tot}$ for $L = 1/8$ and different values of $\eta_{\rm p}$ (see Table I).

budget can be obtained by averaging Eq. (1a) over y and time:

$$\partial_x \Pi_r = \partial_x(\Pi_\nu + \Pi_p) + f_y, \tag{3}$$

where $\Pi_r = \langle u_x u_y \rangle$, $\Pi_\nu = \nu \partial_x \langle u_y \rangle$, and $\Pi_p = \langle \sigma_{xy} \rangle$ are the Reynolds, viscous, and polymer stress, respectively. Remarkably, we find that these profiles remain sinusoidal as in the $\eta_{\rm p} = 0$ case, namely $\Pi_{\rm r} = -S\cos(x/L)$, $\Pi_\nu = \nu U L^{-1}\cos(x/L)$, and $\Pi_p = \Sigma\cos(x/L)$. Equation (3) then yields the following relation between the amplitudes of the different contributions to the stress:

$$S + \frac{\nu U}{L} + \Sigma = FL. \tag{4}$$

These contributions are reported in Table I and they are shown in the inset of Fig. 4.

The results confirm that the polymer contribution to the total stress increases with $\eta_{\rm p}$, whereas that of the viscous stress decreases. The contribution of the Reynolds stress is extremely small (less than 10^{-2}), which demonstrates that inertial effects remain negligible as $\eta_{\rm p}$ is increased. Figures 3 and 4 also suggest the presence of a threshold concentration for the appearance of fluctuations.

It is interesting to note that the development of a power-law spectrum is observed for values $\eta_{\rm p}$ at which the amplitude of the viscous stress Π_ν is still larger than that of the polymer stress Π_p (see inset of Fig. 4). This is consistent with the results of previous numerical simulations that show that elastic turbulence can start manifesting even for $|\Pi_\nu| < |\Pi_p|$ [27].

TABLE I. Amplitude of the stresses Π_r, Π_ν, and Π_p divided by the amplitude of the total stress $\Pi_{\rm tot} = \Pi_r + \Pi_\nu + \Pi_p$ for different values of $\eta_{\rm p}$ and L.

$\eta_{\rm p}$	L	$\Pi_r/\Pi_{\rm tot}$	$\Pi_\nu/\Pi_{\rm tot}$	$\Pi_p/\Pi_{\rm tot}$
1	1/8	0.001	0.996	0.004
2	1/8	0.004	0.887	0.110
3	1/4	0.005	0.787	0.209
3	1/8	0.005	0.795	0.200
4	1/8	0.007	0.710	0.284
5	1/8	0.006	0.647	0.347

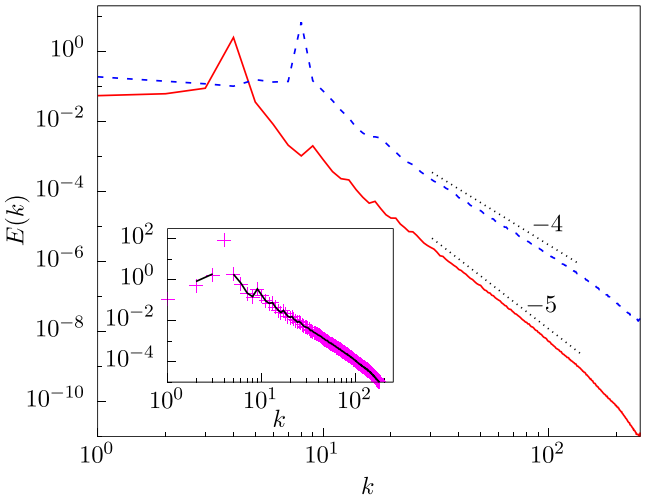

FIG. 5. The kinetic energy spectrum $E(k)$ for $L = 1/4$, $\eta_{\rm p} = 3$ (solid red) and $L = 1/8$, $\eta_{\rm p} = 5$ (dashed blue). The two black dotted segments represent k^{-4} and k^{-5}. Inset: The unsigned kinetic-energy dissipation spectrum $2\nu k^2 E(k)$ (magenta +) and the polymer energy transfer (solid black) for $L = 1/4$ and $\eta_{\rm p} = 3$.

However, experimental studies reported that the elastic and viscous stresses are comparable at the transition to the elastic-turbulence regime [29].

Further insight into the dynamics of the solution is gained by examining the energy balance in wave-number space. For sufficiently large values of $\eta_{\rm p}$, the kinetic-energy spectrum behaves as a power law $E(k) \sim k^{-\alpha}$ (Fig. 5). A wide range of scales is therefore activated, and this results in an enhancement of the mixing properties of the flow. The inspection of the spectrum of polymer energy transfer reveals that the excitation of high modes in the flow is due to the direct injection of energy from the polymers at each wave number (see inset of Fig. 5). This process is balanced scale by scale by the viscous dissipation, whose spectrum $2\nu k^2 E(k)$ coincides with that of the polymer energy transfer. At variance with the classical phenomenology of turbulence, here the energy transfer due to the fluid inertia is negligible.

The spectral exponent α depends both on the concentration and on the scale of the force and lies between 4 and 5. A similar variability of this exponent has been observed in the case of elastic turbulence, in which the exponent α has been shown to depend on the boundary conditions, on the forcing, and on the polymer concentration. For elastic turbulence, the values reported in the literature varies in the range $3 \leqslant \alpha \leqslant 4.6$ [5,27,28,30–34].

IV. CONCLUSIONS

The regime described in this paper has properties comparable to those of elastic turbulence in viscoelastic fluids, namely with the addition of rods the flow resistance is increased and the kinetic-energy spectrum displays a power-law steeper than k^{-3}. In addition, the Reynolds stress and the energy transfer due to the fluid inertia are negligible; hence the emergence of chaos is entirely attributable to polymer stresses. Our study establishes an analogy between the low-Reynolds-number

behavior of rodlike-polymer solutions and that of viscoelastic fluids, similarly to what is observed at high Reynolds number.

These results therefore demonstrate that elasticity is not essential to generate a chaotic behavior at low Reynolds numbers and indicate an alternative mechanism to enhance mixing in microfluidic flows. This mechanism presumably has the advantage of being less affected by the degradation observed in elastic turbulence [35], since there is experimental evidence that the degradation due to large strains is weaker for rodlike polymers than for elastic polymers [36].

We hope that our results will stimulate experimental studies aimed at investigating the phenomenon proposed in this paper. Open questions concern the dependence of the mixing properties of rigid-polymer solutions on the type of force and on the boundary conditions. Additional insight into the dynamics of these polymeric fluids would also come from a stability analysis of system (1), in the spirit of the approach taken for the study of low-Reynolds-number instabilities in viscoelastic [24,25] and rheopectic [26] fluids. The orientation and rotation statistics of microscopic rods in turbulent flows has recently attracted a lot of attention [37–41]. It would be interesting to investigate the dynamics of individual rods in the flow regime studied here as well as the behavior of the suspension when the rod concentration is high and the rods are self-propelled as in active nematics [42–44].

ACKNOWLEDGMENTS

The authors acknowledge the support of the EU COST Action MP 1305 "Flowing Matter." The work of E.L.C. VI M.P. was supported by the Education, Audiovisual, and Culture Executive Agency of the European Commission through the Erasmus Mundus Mobility with Asia program.

[1] J. M. Ottino and S. Wiggins, Phil. Trans. R. Soc. A **362**, 923 (2004).
[2] H. A. Stone, A. D. Stroock, and A. Ajdari, Ann. Rev. Fluid Mech. **36**, 381 (2004).
[3] T. M. Squires and S. R. Quake, Rev. Mod. Phys. **77**, 977 (2005).
[4] A. Groisman and V. Steinberg, Nature **410**, 905 (2001).
[5] A. Groisman and V. Steinberg, Nature **405**, 53 (2000).
[6] T. Burghelea, E. Segre, I. Bar-Joseph, A. Groisman, and V. Steinberg, Phys. Rev. E **69**, 066305 (2004).
[7] Y. Jun and V. Steinberg, Phys. Rev. E **84**, 056325 (2011).
[8] R. J. Poole, B. Budhiraja, A. R. Cain, and P. A. Scott, J. Non-Newtonian Fluid Mech. **177-178**, 15 (2012).
[9] B. Traore, C. Castelain, and T. Burghelea, J. Non-Newtonian Fluid Mech. **223**, 62 (2015).
[10] W. M. Abed, R. D. Whalley, D. J. C. Dennis, and R. J. Poole, J. Non-Newtonian Fluid Mech. **231**, 68 (2016).
[11] A. Clarke, A. M. Howe, J. Mitchell, J. Staniland, and L. A. Hawkes, Soc. Pet. Eng. J. **21**, 0675 (2016).
[12] P. S. Virk, D. C. Sherman, and D. L. Wagger, AIChE J. **43**, 3257 (1997).
[13] J. S. Paschkewitz, Y. Dubief, C. D. Dimitropoulos, and E. S. G. Shaqfeh, J. Fluid Mech. **518**, 281 (2004).
[14] R. Benzi, E. S. C Ching, T. S. Lo, V. S. L'vov, and I. Procaccia, Phys. Rev. E **72**, 016305 (2005).
[15] J. J. J. Gillissen, Phys. Rev. E **78**, 046311 (2008).
[16] M. Doi and S. F. Edwards, *The Theory of Polymer Dynamics* (Oxford University Press, Oxford, 1988).
[17] I. Procaccia, V. S. L'vov, and R. Benzi, Rev. Mod. Phys. **80**, 225 (2008).
[18] Y. Amarouchene, D. Bonn, H. Kellay, T. S. Lo, V. S. L'vov, and I. Procaccia, Phys. Fluids **20**, 065108 (2008).
[19] S. Montgomery-Smith, W. He, D. A. Jack, and D. E. Smith, J. Fluid Mech. **680**, 321 (2011).
[20] E. S. C. Ching, T. S. Lo, and I. Procaccia, Phys. Rev. E **74**, 026301 (2006).
[21] R. Benzi, E. S. C. Ching, E. De Angelis, and I. Procaccia, Phys. Rev. E **77**, 046309 (2008).
[22] S. Musacchio and G. Boffetta, Phys. Rev. E **89**, 023004 (2014).
[23] G. Boffetta, A. Celani, and A. Mazzino, Phys. Rev. E **71**, 036307 (2005).
[24] G. Boffetta, A. Celani, A. Mazzino, A. Puliafito, and M. Vergassola, J. Fluid Mech. **523**, 161 (2005).
[25] A. Bistagnino, G. Boffetta, A. Celani, A. Mazzino, A. Puliafito, and M. Vergassola, J. Fluid Mech. **590**, 61 (2007).
[26] S. Boi, A. Mazzino, and J. O. Pralits, Phys. Rev. E **88**, 033007 (2013).
[27] S. Berti, A. Bistagnino, G. Boffetta, A. Celani, and S. Musacchio, Phys. Rev. E **77**, 055306(R) (2008).
[28] S. Berti and G. Boffetta, Phys. Rev. E **82**, 036314 (2010).
[29] Y. Liu and V. Steinberg, Europhys. Lett. **90**, 44002 (2010).
[30] Y. Jun and V. Steinberg, Phys. Rev. Lett. **102**, 124503 (2009).
[31] T. Watanabe and T. Gotoh, Phys. Fluids **26**, 035110 (2014).
[32] S. S. Ray and D. Vincenzi, Europhys. Lett. **114**, 44001 (2016).
[33] A. Gupta and R. Pandit, Phys. Rev. E **95**, 033119 (2017).
[34] E. L. C. VI M. Plan, A. Gupta, D. Vincenzi, and J. D. Gibbon, J. Fluid Mech. **822**, R4 (2017).
[35] A. Groisman and V. Steinberg, New J. Phys. **6**, 29 (2004).
[36] A. S. Pereira, R. M. Andrade, and E. J. Soares, J. Non-Newtonian Fluid Mech. **202**, 72 (2013).
[37] A. Pumir and M. Wilkinson, New J. Phys. **13**, 093030 (2011).
[38] S. Parsa, E. Calzavarini, F. Toschi, and G. A. Voth, Phys. Rev. Lett. **109**, 134501 (2012).
[39] K. Gustavsson, J. Einarsson, and B. Mehlig, Phys. Rev. Lett. **112**, 014501 (2014).
[40] A. Gupta, D. Vincenzi, and R. Pandit, Phys. Rev. E **89**, 021001(R) (2014).
[41] G. A. Voth and A. Soldati, Ann. Rev. Fluid Mech. **49**, 249 (2017).
[42] M. C. Marchetti, J. F. Joanny, S. Ramaswamy, T. B. Liverpool, J. Prost, M. Rao, and R. Aditi Simha, Rev. Mod. Phys. **85**, 1143 (2013).
[43] S. Zhou, A. Sokolov, O. D. Lavrentovich, and I. S. Aranson, Proc. Natl. Acad. Sci. USA **111**, 1265 (2014).
[44] S. P. Thampi and J. M. Yeomans, Eur. Phys. J. Spec. Top. **225**, 651 (2016).

Eur. Phys. J. E (2018) **41**: 84
DOI 10.1140/epje/i2018-11692-9

THE EUROPEAN PHYSICAL JOURNAL E

Regular Article

Enhancement of mixing by rodlike polymers*

Stefano Musacchio[1,a], Massimo Cencini[2,3], Emmanuel L.C. VI M. Plan[4], and Dario Vincenzi[1]

[1] Université Côte d'Azur, CNRS, LJAD, Nice, France
[2] Istituto dei Sistemi Complessi, CNR, via dei Taurini 19, 00185 Roma, Italy
[3] INFN, Sezione di Roma Tor Vergata, via della Ricerca Scientifica 1, 00133 Roma, Italy
[4] Rudolf Peierls Centre for Theoretical Physics, University of Oxford, Oxford OX1 3PU, UK

Received 4 May 2018
Published online: 11 July 2018

Abstract. We study the mixing of a passive scalar field dispersed in a solution of rodlike polymers in two dimensions, by means of numerical simulations of a rheological model for the polymer solution. The flow is driven by a parallel sinusoidal force (Kolmogorov flow). Although the Reynolds number is lower than the critical value for inertial instabilities, the rotational dynamics of the polymers generates a chaotic flow similar to the so-called elastic-turbulence regime observed in extensible polymer solutions. The temporal decay of the variance of the scalar field and its gradients shows that this chaotic flow strongly enhances mixing.

1 Introduction

The mixing properties of laminar flows are generally poor. In microfluidic applications, where the Reynolds numbers are typically very low, various methods have been developed to enhance the mixing efficiency of the flow. These include the design of grooved walls, the introduction of obstacles, the use of a local forcing, or the addition of *extensible* polymers (*e.g.*, ref. [1]). In this latter case, elastic stresses can generate instabilities at vanishing fluid inertia that in turn lead to a chaotic flow known as elastic turbulence [2,3]. It was shown in ref. [4] that a regime with features similar to those of elastic turbulence can also be obtained via the addition of rigid *rodlike* polymers, *i.e.* polymer stretching is not essential for the generation of a chaotic flow at small Reynolds numbers.

The system considered in ref. [4] is a dilute solution of rodlike polymers driven by a sinusoidal parallel body force (the Kolmogorov force) at a Reynolds number lower than the critical value for inertial hydrodynamic instabilities. A similar setting was used previously to study elastic turbulence induced by extensible polymer solutions [5]. For low rodlike polymer concentrations, the flow is laminar and only displays small deviations from the Newtonian regime. However, when the concentration is increased beyond a critical value, the flow becomes chaotic, the streamlines oscillate and thin vorticity filaments form. An inspection of the snapshots of the vorticity and polymer-orientation fields show that perturbations in the flow are associated with strong deviations of the polymer orientation from the mean-flow direction. The kinetic energy fluctuates around a stationary value lower than that of the laminar case and the mean power required to maintain the mean flow grows with the concentration, which signals a corresponding increase of the kinetic-energy dissipation. In this regime, the Reynolds stress is negligible compared to the polymer and viscous ones. In particular, the polymer stress increases as a function of polymer concentration. Thus, the chaotic dynamics is entirely due to the rotation of polymers, while fluid inertia plays no role. This is further confirmed by the analyis of the kinetic-energy balance in Fourier space. The nonlinear coupling between different Fourier modes due to inertia is indeed negligible; the dynamics of the flow rather results from a scale-by-scale balance between polymer transfer and viscous dissipation. Finally, the kinetic-energy spectrum displays a power law $k^{-\alpha}$ with $\alpha \leqslant 3$, where k is the wave number. A large number of Fourier modes are thus excited, but the energy is concentrated on the large scales and fluctuations decay rapidly with the wave number. It should be noted that the exponent α is not universal, since it depends on polymer concentration and the details of the forcing.

Even though the chaotic regime described above is not generated by polymer stretching, it is similar to elastic turbulence in solutions of extensible polymers. The goal of this paper is to show that the addition of rodlike polymers can be effectively used to enhance mixing at small Reynolds numbers.

* Contribution to the Topical Issue "Flowing Matter, Problems and Applications", edited by Federico Toschi, Ignacio Pagonabarraga Mora, Nuno Araujo, Marcello Sega.

[a] e-mail: stefano.musacchio@unice.fr

2 Passive scalar dispersion in a solution of rodlike polymers

The mixing efficiency of a flow can be quantified by studying its ability to disperse a passive scalar field, such as a colorant injected in the fluid.

We consider a scalar field $\theta(\boldsymbol{x},t)$ with diffusivity D in a two-dimensional solution of rodlike polymers. The dynamics of θ is ruled by the advection-diffusion equation

$$\partial_t\theta + \boldsymbol{u}\cdot\nabla\theta = D\Delta\theta, \tag{1}$$

with $\boldsymbol{u}(\boldsymbol{x},t)$ being the incompressible velocity field of the solution. The polymer phase is described by the unit-trace symmetric tensor field $\mathsf{R}(\boldsymbol{x},t)$, the first eigenvector of which yields the average orientation of polymers in a volume element centred at $\boldsymbol{x}$ at time t. In Doi and Edwards' decoupling approximation the fluid and polymer phases evolve according to the following equations [6]:

$$\begin{aligned}\partial_t\boldsymbol{u} + \boldsymbol{u}\cdot\nabla\boldsymbol{u} &= -\nabla p + (\nu+\nu_p)\Delta\boldsymbol{u} \\ &\quad +6\nu\eta_p\nabla\cdot[(\nabla\boldsymbol{u}:\mathsf{R})\mathsf{R}] + \boldsymbol{f}, \qquad (2)\\ \partial_t\mathsf{R} + \boldsymbol{u}\cdot\nabla\mathsf{R} &= (\nabla\boldsymbol{u})\mathsf{R} + \mathsf{R}(\nabla\boldsymbol{u})^\top \\ &\quad -2(\nabla\boldsymbol{u}:\mathsf{R})\mathsf{R} - 2\alpha(2\mathsf{R}-\mathsf{I}), \qquad (3)\end{aligned}$$

where $(\nabla\boldsymbol{u})_{ij} = \partial u_i/\partial x_j$, p is pressure, ν is the kinematic viscosity of the solvent, I is the identity matrix, and ν_p and α are proportional to the orientational diffusivity of polymers. In numerical simulations a diffusive term $\kappa\Delta\mathsf{R}$ (we used $\kappa = 3\times10^{-3}$) is added to eq. (3) in order to improve stability [7]. The parameter η_p determines the coupling between the polymer phase and the fluid and is an increasing function of the polymer concentration. The values of η_p considered here ($\eta_p \leqslant 5$) correspond to a dilute solution [4,8]. The above polymer model was studied extensively in the turbulent-drag-reduction regime at high Reynolds number [9].

The system is driven by the Kolmogorov force $\boldsymbol{f}(\boldsymbol{x}) = (0, F\sin(Kx))$, where F and K are the amplitude and the wave number of the force, respectively. In the Newtonian case ($\eta_p = 0$), the Navier-Stokes equations admit the laminar solution $\boldsymbol{u}(\boldsymbol{x}) = (0, U_0\sin(Kx))$ with $U_0 = F/\nu K^2$. This solution is stable if the Reynolds number $\mathrm{Re} = U_0/\nu K$ is smaller than the critical value $\mathrm{Re}_c = \sqrt{2}$ (*e.g.*, ref. [10]). In the following, we take $\mathrm{Re} = 1 < \mathrm{Re}_c$ in order to ensure that inertial effects are negligible and that the chaotic regime arises solely from the rotational dynamics of the rodlike polymers.

Equations (1), (2) and (3) are solved on a $2\pi\times 2\pi$-domain periodic in both directions by using a 1/2-dealiased pseudospectral method on a grid with 1024^2 mesh points. Time integration is performed via a fourth-order Runge-Kutta scheme. In the numerical simulations presented below, we use $K = 8$, $F = 512$ and $\nu = 1$. The molecular diffusivity is $D = 10^{-3}$ for most of the simulations reported in sect. 3. The corresponding Péclet number $\mathrm{Pe} = U_0/KD$ is $\mathrm{Pe} = 1000$. For the study of the Péclet number effects we also consider $D = 5\times10^{-4}$ ($\mathrm{Pe} = 2000$) and $D = 2.5\times10^{-4}$ ($\mathrm{Pe} = 4000$). In addition, the orientational diffusion of polymers is disregarded (*i.e.*, we take $\nu_p = 0$ and $\alpha = 0$) for two reasons: 1) it is expected to play a minor role in the chaotic regime and 2) we wish to ensure that the chaotic regime is not triggered by Brownian fluctuations.

In the Newtonian case ($\eta_p = 0$), the dynamics of the velocity field is independent of R and the laminar solution is stable at $\mathrm{Re} = 1$. Therefore we simply integrate eq. (1) with $\boldsymbol{u}(\boldsymbol{x}) = (0, U_0\sin(Kx))$. Conversely, in the non-Newtonian case ($\eta_p > 0$), we performed a preliminary set of simulations by integrating eqs. (2) and (3) with initial condition for the velocity field obtained as a small perturbation of the Newtonian stable flow and with the components of R initially distributed randomly. Once the flow has reached the statistically stationary chaotic regime, we start to integrate the dynamics of the scalar field θ.

The initial condition for the scalar field, $\theta(\boldsymbol{x},0)$, is taken independent of y, so that the initial scalar gradient $\boldsymbol{\nabla}\theta$ is oriented in the x-direction, *i.e.*, perpendicular to the direction of the laminar flow for $\eta_p = 0$. This choice ensures that the mixing in the absence of polymers is solely due to molecular diffusion. Two different initial conditions are considered: A) the monocromatic function $\theta(\boldsymbol{x}) = \cos(Kx)$ and B) the step function $\theta(\boldsymbol{x}) = \mathrm{sign}[\cos(Kx)]$. In both cases we fix $K = 8$, *i.e.*, the same wave number of the base flow. For the former initial condition and in the Newtonian case ($\eta_p = 0$), the exponential decay rate of the scalar variance $\langle\theta^2\rangle(t) \equiv \int\theta^2(\boldsymbol{x},t)\mathrm{d}\boldsymbol{x}$ is known analytically as $\beta_0 = -\mathrm{d}\log[\langle\theta^2\rangle(t)]/\mathrm{d}t = 2DK^2$. The latter initial condition is chosen to mimic the experimental setting in which two differently coloured fluids are injected in a microchannel [3].

3 Mixing enhancement

In fig. 1 we compare the temporal evolution of the scalar field with and without polymers starting from the initial condition B. In the absence of polymers, molecular diffusion simply blurs the borders between the white and black stripes, and even after a long time the scalar field remains essentially unmixed. Conversely, over a comparable time interval the chaotic flow induced by the rodlike polymers mixes the scalar field efficiently.

To quantify the gain in mixing efficiency, we study the temporal behaviour of the variance of the scalar field and of its gradients. As shown in fig. 2, after an initial transient, the decay rate of $\langle\theta^2\rangle$ becomes independent of the specific choice of the initial condition. In the Newtonian case, we recover the analytical prediction $\langle\theta^2\rangle(t) \propto \exp(-\beta_0 t)$. For $\eta_p > 0$, we find that the decay is much faster. The similar decay observed for the cases $\eta_p = 3$ and $\eta_p = 5$ suggests a weak dependence of the decay rate on the concentration of polymers. In ref. [4], it was found that increasing η_p at fixed forcing amplitude F the resulting chaotic flow displays stronger fluctuations, but the amplitude of the mean flow (which remains sinusoidal) is reduced. Likely, the combined effect of the reduction of the mean flow and the growth of the fluctuations, results in a comparable mixing efficiency for the two cases considered here.

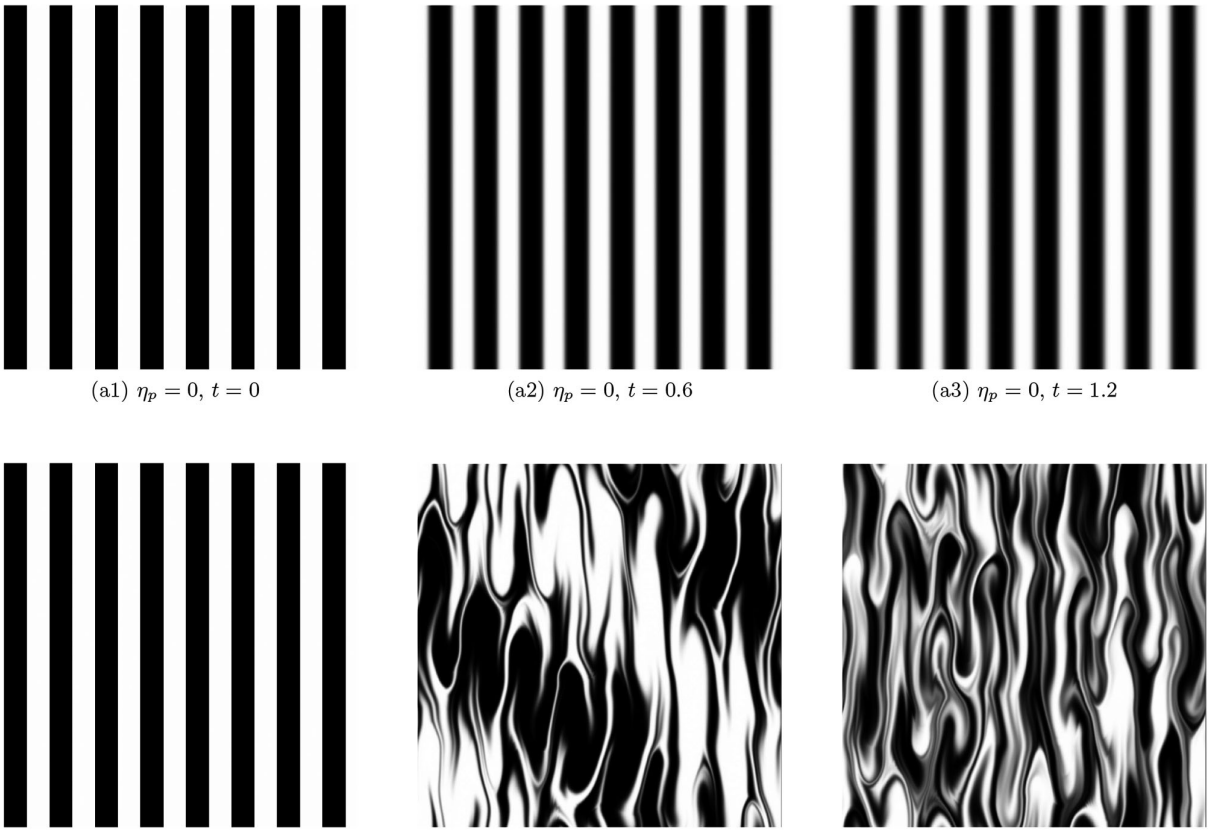

(a1) $\eta_p = 0$, $t = 0$ (a2) $\eta_p = 0$, $t = 0.6$ (a3) $\eta_p = 0$, $t = 1.2$

(b2) $\eta_p = 5$, $t = 0$ (b3) $\eta_p = 5$, $t = 0.6$ (b4) $\eta_p = 5$, $t = 1.2$

Fig. 1. Snapshots of the passive scalar field $\theta(\boldsymbol{x}, t)$ at $t = 0, 0.6, 1.2$ (from left to right) for $\eta_p = 0$ (top) and $\eta_p = 5$ (bottom) and initial condition B. Here Pe = 1000.

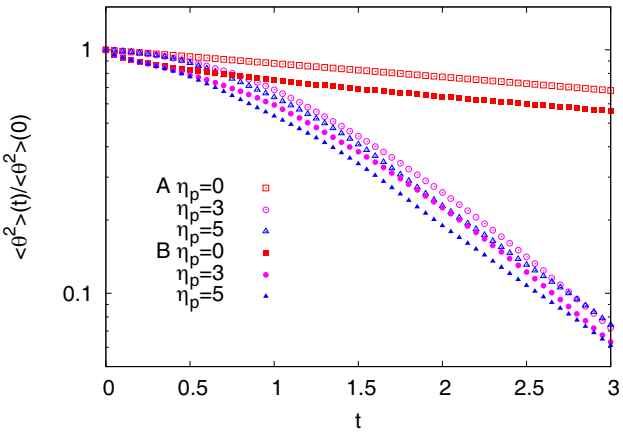

Fig. 2. Temporal decay of the variance $\langle\theta^2\rangle(t)$, normalized with its initial value at $t = 0$, for $\eta_p = 0$ (squares), $\eta_p = 3$ (circles), $\eta_p = 5$ (triangles), and for initial conditions A (empty symbols) and B (filled symbols). Here Pe = 1000.

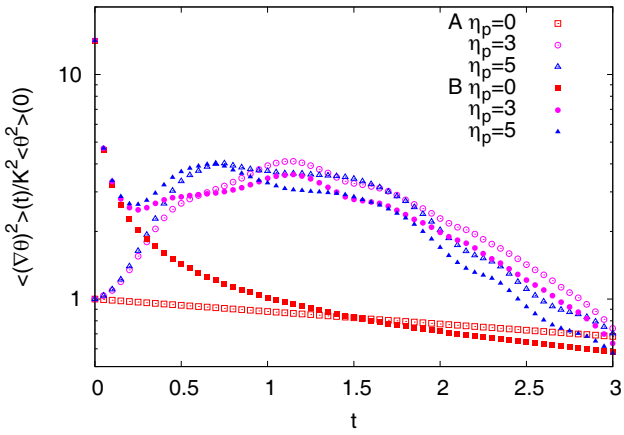

Fig. 3. Temporal evolution of the variance of the scalar gradients, $\langle(\nabla\theta)^2\rangle(t)$, for $\eta_p = 0$ (squares), $\eta_p = 3$ (circles), $\eta_p = 5$ (triangles), and for initial conditions A (empty symbols) and B (filled symbols). Here Pe = 1000.

The time behaviour of $\langle\theta^2\rangle$ is closely related to that of the scalar gradients. In the absence of polymers, $\langle(\nabla\theta)^2\rangle$ asymptotically decays with the same rate as the variance of the field. At short times, however, the decay of $\langle(\nabla\theta)^2\rangle$ depends on the initial condition (fig. 3). In case A, which is monochromatic, the decay is purely exponential from the beginning, whereas in case B the decay is faster, since each Fourier mode k of the scalar field decays with a differ-

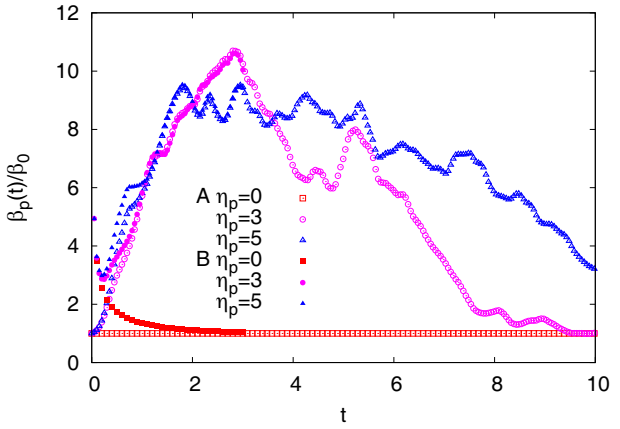

Fig. 4. Instantaneous exponential decay rate $\beta_p(t)$, normalized with $\beta_0 = 2DK^2$, for $\eta_p = 0$ (squares), $\eta_p = 3$ (circles), $\eta_p = 5$ (triangles), and for initial conditions A (empty symbols) and B (filled symbols). Here Pe = 1000.

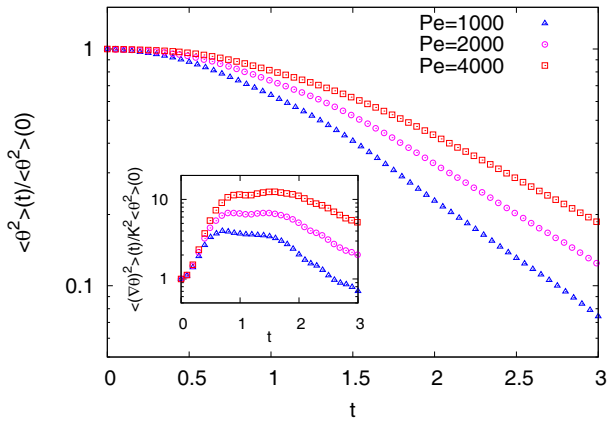

Fig. 5. Temporal evolution of the variance $\langle\theta^2\rangle(t)$ for Pe = 1000 (triangles), Pe = 2000 (circles) and Pe = 4000 (squares). Here $\eta_p = 5$ and the initial condition is monochromatic (case A). Inset: temporal evolution of the variance of the scalar gradients $\langle(\nabla\theta)^2\rangle(t)$.

ent exponential rate $-2Dk^2$. In the presence of polymers and in case A, $\langle(\nabla\theta)^2\rangle$ initially grows because mixing creates thin scalar filaments (the so-called direct cascade of passive scalars); at later times when the gradient scale reaches the diffusive scale we observe a rapid decay, with a rate similar to that of $\langle\theta^2\rangle$, which indicates the increased mixing efficiency of the polymer solution with respect to the Newtonian fluid. Case B is similar to case A, except for an initial transient characterized by the fast diffusive decay of the high Fourier modes of the initial condition.

To accurately measure the asymptotic decay of the scalar variance, it is useful to introduce the instantaneous exponential decay rate

$$\beta_p(t) = -\frac{\mathrm{d}}{\mathrm{d}t}\log\langle\theta^2\rangle = \beta_0\frac{\langle(\nabla\theta)^2\rangle}{K^2\langle\theta^2\rangle}\,. \tag{4}$$

The ratio $\beta_p(t)/\beta_0$ quantifies the increase of the mixing efficiency due to the addition of polymers with respect to molecular diffusion only. As shown in fig. 4, the two initial conditions A and B recover the same values of $\beta_p(t)$ after an initial transient. For $\eta_p = 3$ we observe initially a rapid increase of $\beta_p(t)$, which reaches values much larger than β_0. However, at long times, when the scalar field is almost completely homogeneized, $\beta_p(t)$ reduces and eventually returns close to β_0. For $\eta_p = 5$, after an initial growth similar to the $\eta_p = 3$ case, $\beta_p(t)$ seems to fluctuate around a constant mean value β_* in the time interval $t \in [2, 4]$. At later times $\beta_p(t)$ decreases, but its decay is slower than for $\eta_p = 3$.

We notice that an exponential decay of the passive scalar variance with a constant rate $\beta_p(t)$ implies that $\langle(\nabla\theta)^2\rangle$ must become proportional to $\langle\theta^2\rangle$, meaning that the typical scale of the scalar gradients, defined as $\ell = [\langle\theta^2\rangle/\langle(\nabla\theta)^2\rangle]^{1/2}$, remains constant. For $\eta_p = 5$ we have that the scale separation between the large scale of the base flow $L_u = 2\pi/K$ and ℓ is $L_u/\ell \simeq 3$ for $t \in [2, 4]$.

Theoretical predictions on the asymptotic decay of the scalar field have been derived by exploiting the relation between the statistics of Lagrangian trajectories and the statistics of the passive scalar [11,12]. In particular, it has been shown that for smooth, statistically homogeneous and isotropic flows, in the limit $\mathrm{Pe} \to \infty$ and for large times, the moments of the passive scalar decay exponentially as $\langle|\theta|^n\rangle \propto \exp(-\gamma_n t)$, with γ_n linked to the stretching rate statistics. In our notation β_p corresponds to γ_2. The fact that we observe an exponential decay with constant β_p only for intermediate times could be due to various causes. The mechanism for the exponential decay [11] originates from the chaotic stretching of the passive scalar, which is effective when there is a large scale separation between the typical scale of the flow L_u and the diffusive scale (*i.e.*, in the limit $\mathrm{Pe} \to \infty$). In the following we will show that the asymptotic decrease of $\beta_p(t)$ observed in fig. 4 could be related to the finite values of D required by the numerical simulations. Further, the Kolmogorov flow is neither homogeneous nor isotropic. Moreover, in our case the characteristic large scale of the passive scalar $L_\theta = 2\pi/K$ is equal to that of the base flow L_u. When $L_\theta \sim L_u$ it has been shown that the decay, though still exponential, is dominated by "strange eigenmodes" of the advection-diffusion operator [13], and its connection to the Lagrangian stretching rate becomes more complex [12].

On the basis of the previous observations, we expect that the gain in mixing efficiency due to the addition of polymers should depend on the Péclet number $\mathrm{Pe} = U_0/KD$. Increasing Pe at fixed Re reduces β_0 but increases the generation of smaller scales in the scalar field, thus leading to higher values of $\langle(\nabla\theta)^2\rangle$.

In order to investigate the dependence on Pe, we have compared three simulations with initial condition A at $\eta_p = 5$ and Re = 1 with different diffusivities: $D = 10^{-3}$ (Pe = 1000) $D = 5 \times 10^{-4}$ (Pe = 2000) and $D = 2.5 \times 10^{-4}$ (Pe = 4000). The decay of the variance for the three cases is shown in fig. 5. Although an increase of $\langle(\nabla\theta)^2\rangle$ is observed as a function of Pe at all times (see inset of fig. 5), the decay of $\langle\theta^2\rangle$ is slower at greater Pe because β_0 is reduced. Nevertheless, fig. 6 shows that the gain in the

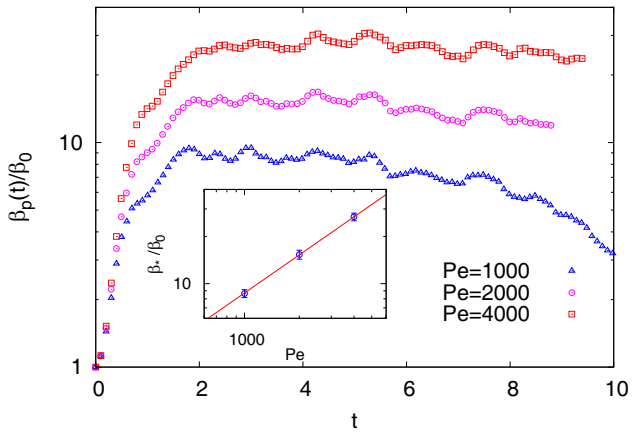

Fig. 6. Instantaneous exponential decay rate $\beta_p(t)$, normalized with $\beta_0 = 2DK^2$, for Pe = 1000 (triangles), Pe = 2000 (circles) and Pe = 4000 (squares). Here $\eta_p = 5$ and the initial condition is monochromatic (case A). Inset: average exponential decay rate β_* as a function of Pe (circles). The line represents the scaling $\mathrm{Pe}^{0.8}$.

mixing efficiency increases with Pe. A power-law fit of β_*, obtained by averaging $\beta_p(t)/\beta_0$ in the interval $2.5 < t < 4$, indicates a growth proportional to $\mathrm{Pe}^{0.8}$. At present we do not have a clear understanding of this power-law dependence. We notice that at increasing Pe, the regime in which $\beta_p(t)$ is almost constant continues for longer times. This suggests that the asympotic decay of $\beta_p(t)$ might be a finite-Pe effect.

4 Conclusions

The addition of rodlike polymers to a low-Reynolds-number Newtonian fluid generates a chaotic flow, similarly to the elastic-turbulence regime observed in extensible polymers solutions. We have shown that this regime strongly enhances the mixing of a passive scalar dispersed in the solution. In particular, the variance of the scalar field and of its gradients decays much faster than in the purely diffusive case. Moreover, we found that this effect increases with the Péclet number. In order to quantify the gain in the mixing efficiency we introduced the instantaneous exponential decay rate $\beta_p(t)$. The rapid initial growth of $\beta_p(t)$ to values much higer than the diffusive decay rate β_0 provides a precise measure of the increased mixing. Our results also show that for high Péclet number and high polymer concentrations, the decay of the scalar variance displays an almost exponential regime, in which $\beta_p(t)$ fluctuates around a constant mean value.

Although our study is conducted in an idealized setting, we hope that it can motivate experimental investigations of the gain in mixing efficiency obtained via the addition of rodlike polymers to a Newtonian fluid at low Reynolds number. In future investigations it would also be interesting to compare the gain in the mixing efficiency obtained with rodlike or extensible polymer solutions at similar concentrations.

The authors acknowledge the support of the EU COST Action MP 1305 "Flowing Matter". MC was partially supported by Université Côte d'Azur through Investissements d'Avenir UCA ref. ANR-15-IDEX-01.

Author contribution statement

All the authors were involved in the preparation of the manuscript. All the authors have read and approved the final manuscript.

References

1. T.M. Squires, S.R. Quake, Rev. Mod. Phys. **77**, 977 (2005).
2. A. Groisman, V. Steinberg, Nature **405**, 53 (2000).
3. A. Groisman, V. Steinberg, Nature **410**, 905 (2001).
4. E.L.C. VI M. Plan, S. Musacchio, D. Vincenzi, Phys. Rev. E **96**, 053108 (2017).
5. S. Berti, A. Bistagnino, G. Boffetta, A. Celani, S. Musacchio, Phys. Rev. E **77**, 055306 (2008).
6. M. Doi, S.F. Edwards, *The Theory of Polymer Dynamics* (Oxford University Press, Oxford, 1988).
7. R. Sureshkumar, A.N. Beris, J. Non-Newton. Fluid Mech. **60**, 53 (1995).
8. Y. Amarouchene, D. Bonn, H. Kellay, T.S. Lo, V.S. L'vov, I. Procaccia, Phys. Fluids **20**, 065108 (2008).
9. I. Procaccia, V.S. L'vov, R. Benzi, Rev. Mod. Phys. **80**, 225 (2008).
10. S. Musacchio, G. Boffetta, Phys. Rev. E **89**, 023004 (2014).
11. E. Balkovsky, A. Fouxon, Phys. Rev. E **60**, 4164 (1999).
12. P.H. Haynes, J. Vanneste, Phys. Fluids **17**, 097103 (2005).
13. J. Sukhatme, R.T. Pierrehumbert, Phys. Rev. E **66**, 056302 (2002).

Effect of polymer-stress diffusion in the numerical simulation of elastic turbulence

Anupam Gupta[1] and Dario Vincenzi[2]

[1]Paulson School of Engineering and Applied Sciences, Harvard University, Cambridge, Massachusetts 02138, USA

[2]Université Côte d'Azur, CNRS, LJAD, 06100 Nice, France

Elastic turbulence is a chaotic regime that emerges in polymer solutions at low Reynolds numbers. A common way to ensure stability in numerical simulations of polymer solutions is to add artificially large polymer-stress diffusion. In order to assess the accuracy of this approach in the elastic-turbulence regime, we compare numerical simulations of the two-dimensional Oldroyd-B model sustained by a cellular force with and without artificial diffusion. We find that artificial diffusion can have a dramatic effect even on the large-scale properties of the flow and we show some of the spurious phenomena that may arise when artificial diffusion is used.

1. Introduction

Polymer solutions can exhibit a chaotic behaviour, even at low Reynolds numbers, as a result of purely elastic instabilities (Groisman and Steinberg 2000, 2004). This regime of polymer solutions, known as elastic turbulence, finds a natural application in microfluidics, where the typical Reynolds numbers are very low and the addition of polymers to the fluid can be employed to accelerate phenomena such as mixing (Groisman and Steinberg 2001), emulsification (Poole et al. 2012) and heat transfer (Traore, Castelain and Burghelea 2015; Abed et al. 2016) or to examine the dynamics of microscopic objects in fluctuating flows (Liu and Steinberg 2014).

The numerical simulation of elastic turbulence is challenging for at least three reasons. The first two are common to the high-Reynolds-number regime of polymer solutions. Indeed, the available constitutive models of viscoelastic fluids are based on rather crude approximations and disregard several, potentially relevant aspects of polymer dynamics (Bird et al. 1987). In addition, a high spatial resolution and advanced numerical schemes are needed to resolve the sharp gradients that form in the polymer-stress field (Jin and Collins 2007; Plan *et al.* 2017). The third reason is specific to elastic turbulence and is the requirement that the time step used for the integration of the Navier–Stokes equations be small; this requirement is a consequence of the high viscosity of the fluid (Press et al. 2007).

Most numerical studies of elastic turbulence have therefore considered simplified flow configurations (e.g. in two dimensions and/or with periodic boundary conditions) and have been restricted to limited ranges of parameters. Notwithstanding, even simple models of viscoelastic fluids in idealized settings have proved successful in capturing the main properties of elastic turbulence. Several experimental observations are reproduced, at least qualitatively, by the Oldroyd-B model, in which only the slowest oscillation mode of the polymer is retained and polymer elasticity is assumed to be linear (Berti *et al.* 2008; Thomases and Shelley 2009; Berti and Boffetta 2010; Thomases, Shelley and

Thiffeault 2011; Grilli, Vázquez-Quesada and Ellero 2013; Plan *et al.* 2017; van Buel, Schaaf and Stark 2018; Garg et al. 2018). Other studies have used the FENE-P model, which improves on the Oldroyd-B one by taking into account the finite extensibility of polymers (Liu and Khomami 2013; Gupta and Pandit 2017), or have taken a Lagrangian approach and have solved the dynamics of a large number of dumbbell-like polymers (Watanabe and Gotoh 2013, 2014). In fact, even a low-dimensional 'shell model' of viscoelastic fluid reproduces elastic turbulence qualitatively (Ray and Vincenzi 2016).

Constitutive models such as the Oldroyd-B and the FENE-P ones consist of a coupled system of partial differential equations for the velocity of the solution and for the polymer stress tensor. This latter is by nature symmetric and positive definite, but numerical errors may lead to the loss of these properties and hence to instabilities (Joseph 1990). A standard way to prevent such instabilities is to include *global* artificial diffusivity in the model, i.e. to add a Laplacian term to the evolution equation for the polymer stress with a space-independent coefficient (Sureshkumar and Beris 1995). Numerical simulations of turbulent polymer solutions that use artificial diffusivity are in qualitative agreement with experiments (e.g. Graham 2014, and references therein). Polymer-stress diffusion in fact has a physical origin, for it results from the diffusion of the centre of mass of polymers due to thermal noise (El-Kareh and Leal 1989). However, the values of diffusivity needed to achieve numerical stability are three to six orders of magnitude greater than those appropriate for real polymers (e.g. Vaithianathan et al. 2006). For this reason, numerical schemes have been proposed that avoid using artificial diffusivity. These include, inter alia, schemes that only employ polymer diffusivity at those locations in the fluid where the polymer stress loses its positive definite character (Min, Yoo and Choi 2001), methods adapted from hyperbolic solvers (Vaithianathan et al. 2006), or schemes based on representations of the polymer stress tensor that guarantee the preservation of its positive definiteness (Vaithianathan and Collins 2003; Fattal and Kupferman 2003; Balci *et al.* 2011). Such numerical schemes have been compared with simulations using artificial diffusivity at high or moderate Reynolds numbers, and quantitative discrepancies have emerged: for instance, the level of drag reduction is diminished by artificial diffusivity, the velocity and polymer-stress fields are significantly smeared, excessive polymer-stress diffusion may lead to relaminarization (Min et al. 2001; Vaithianathan et al. 2006; Sid, Terrapon and Dubief 2018). Thus a consensus seems to have formed that at high or moderate Reynolds numbers alternative methods should be preferred to the use of artificial diffusivity.

At low Reynolds numbers, several studies on elastic turbulence have employed artificial diffusivity (Berti *et al.* 2008; Thomases and Shelley 2009; Berti and Boffetta 2010; Thomases et al. 2011; Liu and Khomami 2013; Garg et al. 2018). It was shown in Thomases (2011) that in viscoelastic creeping flows this has the effect of smoothing the polymer-stress field and keeping it bounded. However, to the best of our knowledge, the effect of artificial diffusivity in the elastic-turbulence regime has not been examined yet. This is the goal of the present study, in which we compare numerical simulations of elastic turbulence with and without artificial diffusivity. As a case study, we consider the Oldroyd-B model with a cellular forcing on a periodic square. Our results demonstrate that in simulations of elastic turbulence artificial diffusivity may have a more dramatic effect than at high Reynolds numbers. Even for relatively small diffusivities, the properties of the velocity field are indeed strongly affected, to such an extent that also the large-scale flow may be misrepresented. In particular, we show that some phenomena observed in previous simulations are due to artificial stress diffusion and are not present when alternative integration methods are used.

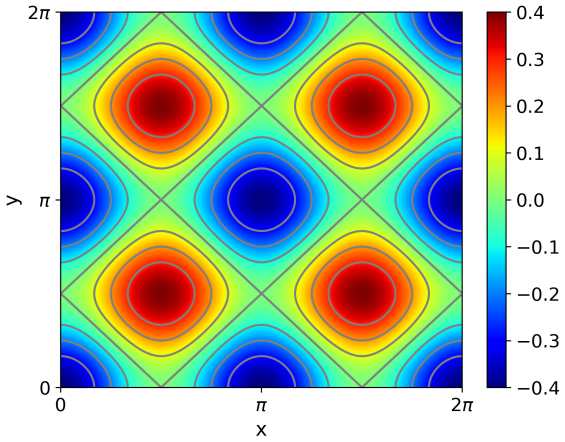

Fig. 1. Vorticity field of the laminar solution of (2.1a) in the absence of polymer feedback, $\omega(\boldsymbol{x}) = -f_0(\cos Kx + \cos Ky)/\nu K$, for $K = 2$, $f_0 = 0.02$ and $\nu = 0.05$.

2. Viscoelastic model

The Oldroyd-B model (Oldroyd 1950) describes the polymer phase by means of a space-time dependent positive-definite symmetric tensor: the polymer conformation tensor $\boldsymbol{C}(\boldsymbol{x}, t)$. In the limit of vanishing inertia, the coupled evolution of $\boldsymbol{C}(\boldsymbol{x}, t)$ and the velocity field $\boldsymbol{u}(\boldsymbol{x}, t)$ that describes the motion of the solution is given by the following equations:

$$\boldsymbol{\nabla} p = \nu \Delta \boldsymbol{u} + \frac{\mu}{\tau} \boldsymbol{\nabla} \cdot \boldsymbol{C} + \boldsymbol{f}, \qquad \boldsymbol{\nabla} \cdot \boldsymbol{u} = 0, \tag{2.1a}$$

$$\partial_t \boldsymbol{C} + \boldsymbol{u} \cdot \boldsymbol{\nabla} \boldsymbol{C} = (\boldsymbol{\nabla} \boldsymbol{u}) \boldsymbol{C} + \boldsymbol{C} (\boldsymbol{\nabla} \boldsymbol{u})^{\top} - \frac{1}{\tau} (\boldsymbol{C} - \boldsymbol{I}), \tag{2.1b}$$

where p is pressure, ν is the kinematic viscosity of the solvent, τ is the polymer relaxation time, the components of the velocity gradient are defined as $(\boldsymbol{\nabla} \boldsymbol{u})_{ij} = \partial u_i / \partial x_j$ and $\boldsymbol{I}$ is the identity matrix. The coupling coefficient μ represents the polymer contribution to the total kinematic viscosity of the solution and is proportional to the concentration of polymers. The body force $\boldsymbol{f}(\boldsymbol{x})$ that sustains the motion of the solution is such that $\boldsymbol{\nabla} \cdot \boldsymbol{f} = 0$. In the above equations, the conformation tensor is rescaled with the polymer mean square equilibrium extension in the absence of flow.

In considering the limit of the Oldroyd-B model for vanishing inertia, we follow Fouxon and Lebedev (2003); Thomases and Shelley (2009); Thomases et al. (2011); Balci *et al.* (2011), who describe the motion of the solution by means of the Stokes equations in lieu of the Navier–Stokes equations. However, as is discussed in § 4, our conclusions on the effect of artificial diffusivity are unchanged if we use the Navier–Stokes equations with a Reynolds number smaller than the critical value for the appearance of inertial instabilities.

Equations (2.1) are studied on the two-dimensional domain $[0, 2\pi]^2$ with periodic boundary conditions. We consider the cellular force:

$$\boldsymbol{f}(\boldsymbol{x}) = f_0(-\sin Ky, \sin Kx), \tag{2.2}$$

where f_0 is the amplitude and K the spatial frequency. In the absence of polymer feedback on the flow (i.e. $\mu = 0$), (2.1a) admits the fixed-point laminar solution: $\boldsymbol{u} = -\boldsymbol{f}/\nu K^2$. The corresponding vorticity field $\omega(\boldsymbol{x}, t)$, where $\omega \hat{\boldsymbol{z}} \equiv \boldsymbol{\nabla} \times \boldsymbol{u}$, is shown in figure 1 and consists of a sequence of vortices of alternate sign separated by lines of pure strain. At time $t = 0$, $\boldsymbol{u}$ is the fixed-point velocity field and $\boldsymbol{C}$ is a random perturbation of the identity matrix. By using the length scale $1/K$ and the amplitude $f_0/\nu K^2$ of the laminar velocity, we

obtain the turnover time $T = \nu K/f_0$. This allows us to define the Weissenberg number $Wi \equiv \tau/T$, which quantifies the ability of the flow to deform polymers.

The reason for choosing the cellular force is twofold. On the one hand, it generates a flow structure in which the straining and vortical regions are clearly separated, similarly to the four-roll mill force considered in Thomases and Shelley (2009) and Thomases et al. (2011)—this feature will turn out useful in highlighting the effect of artificial diffusivity on elastic turbulence. On the other hand, the polymer stress generated by the cellular force is less strong than in the case of the four-roll mill force; thus even in the absence of artificial diffusivity a moderate spatial resolution is sufficient to compute the velocity and polymer-stress fields accurately.

Equation (2.1b) is solved on a regular grid with 1024^2 collocation points by using a fourth-order finite difference scheme for the spatial derivatives and a fourth-order Runge–Kutta scheme with time step $\mathrm{d}t = 2 \times 10^{-3}$ for the temporal integration. We obtain the velocity field by solving the vorticity equation associated with (2.1a) in Fourier space. The parameters of the simulations are $K = 2$, $f_0 = 0.02$, $\mu = 0.01$, $\nu = 0.05$, $\tau = 50$ and yield a Weissenberg number $Wi = 10$. In particular, the ratio μ/ν is comparable to that used in previous simulations of elastic turbulence. Two different methods for stabilizing the numerical integration are compared:

(i) In the first case, we use artificial diffusivity and add the term $\kappa \Delta \boldsymbol{C}$ to the right hand side of (2.1b). We set $\kappa = 5 \times 10^{-5}$, so that the Schmidt number $Sc \equiv \nu/\kappa = 10^3$ is the same as in previous numerical simulations of elastic turbulence (Thomases and Shelley 2009; Thomases et al. 2011; Garg et al. 2018). This value of Sc is much higher than that used in high-Reynolds-number simulations, where typically $Sc = 0.5$ (e.g. Graham 2014), but is nevertheless three orders of magnitude smaller than it would be in reality (Vaithianathan et al. 2006). However, it is not interesting to consider values of Sc much greater than 10^3, because in general they are not sufficient to prevent numerical instabilities;

(ii) In the second case, we use a scheme based on the Kurganov–Tadmor hyperbolic solver (Kurganov and Tadmor 2000). This solver was first generalized to the numerical simulation of polymer solutions by Vaithianathan et al. (2006). At locations where the original finite-difference scheme would yield a too large gradient of C_{ij}, it selects a lower-order scheme that reduces the gradient of C_{ij} thereby preserving the positive definiteness of the conformation tensor. Numerical schemes based on the Kurganov–Tadmor solver have later been employed in studies of both turbulent polymer solutions (e.g. Vaithianathan et al. 2007; Perlekar, Mitra, Pandit 2010; Dallas, Vassilicos and Hewitt 2010; Robert et al. 2010; Valente, da Silva and Pinho 2014; Gupta, Perlekar and Pandit 2015) and elastic turbulence (Gupta and Pandit 2017; Plan *et al.* 2017). Here we follow the approach described in Gupta et al. (2015) (see also Perlekar et al. 2010, for the three-dimensional version), where $\boldsymbol{C}$ is first factorized according to Cholesky (Vaithianathan and Collins 2003; Perlekar, Mitra, Pandit 2006) and then the Kurganov–Tadmor scheme is applied to the evolution equations for the logarithms of the components of the triangular matrix that results from the factorization.

3. Results

In this section, we compare numerical simulations of (2.1) based on the two approaches described in § 2, i.e. using either artificial diffusivity with $Sc = 10^3$ or the Kurganov–Tadmor scheme, for which $Sc = \infty$. As we shall see, the effect of artificial diffusivity is so big that to describe it, it is sufficient to examine the qualitative properties of the flow.

Figure 2 shows the time series of the kinetic energy $e(t) \equiv \frac{1}{2} \int |\boldsymbol{u}(\boldsymbol{x}, t)|^2 \mathrm{d}\boldsymbol{x}$. For $Sc =$

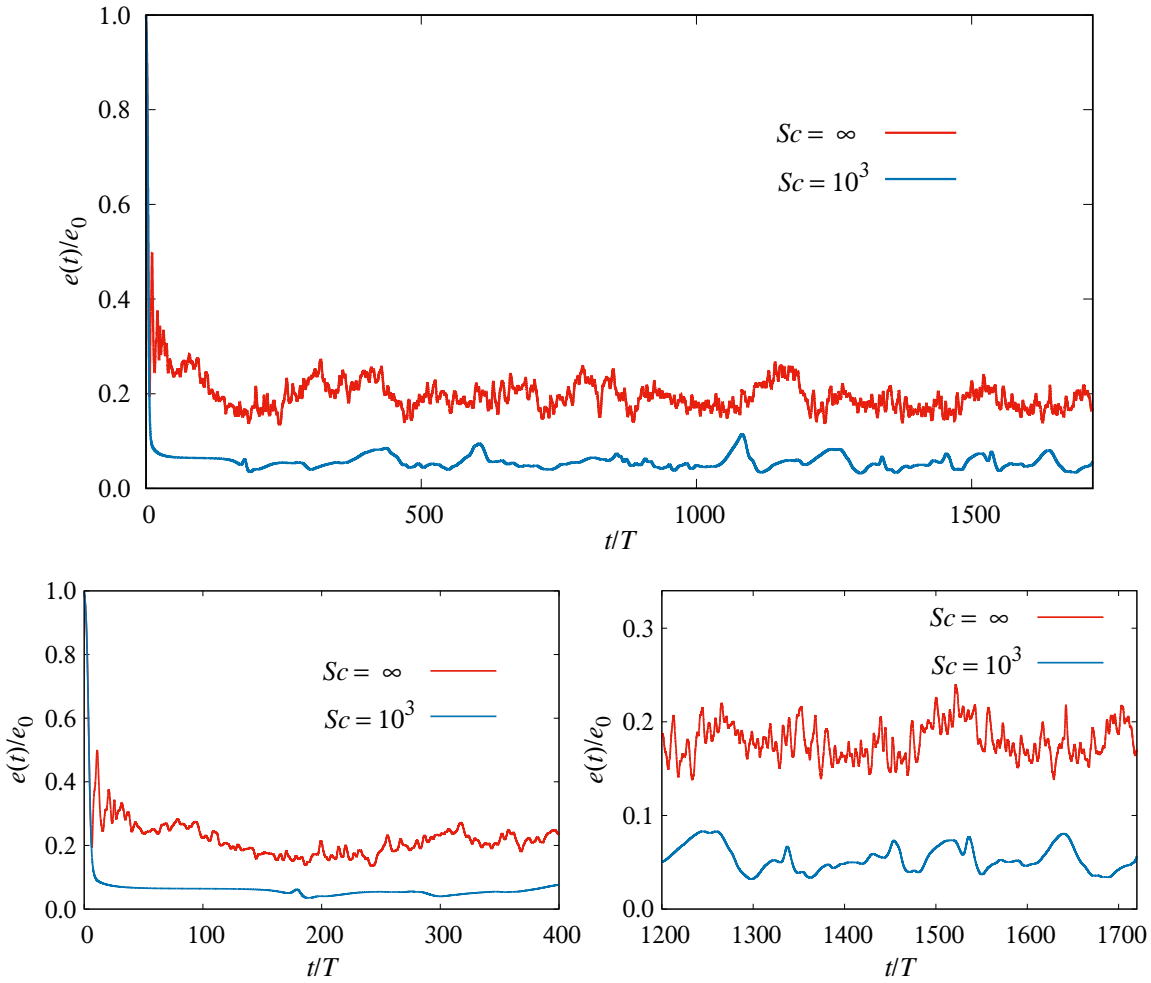

Fig. 2. Top: Time series of the kinetic energy of the polymer solution rescaled by the kinetic energy of the fixed-point laminar flow for $\mu = 0$, i.e. $e_0 \equiv f_0^2/2\nu^2K^4$. Bottom: zooms of the top panel.

10^3, the system remains in an almost frozen state for a long time, after which it becomes chaotic. This behaviour is analogous to that found in Thomases and Shelley (2009) and Thomases et al. (2011) for a four-roll mill force and same value of Sc. For $Sc = \infty$, in contrast, the motion of the solution becomes chaotic much more rapidly and, in the steady state, the kinetic energy fluctuates at a frequency much higher than when artificial diffusivity is present. Moreover, the mean kinetic energy is greater.

The snaphots of the vorticity field also indicate a striking difference between the two integration methods (figures 3 and 4). With artificial diffusivity, once the system starts fluctuating the spatial structure of the flow departs from that which would be imposed by the force (figure 3). Only some of the vortical cells continue to exist, whilst others break down and patches of vorticity contaminate the cellular structure of the base flow. Furthermore, the number and the location of unbroken vortical cells vary in time (see the snapshots at two different times in figure 3). This dynamics is equivalent to the symmetry-breaking transition observed by Thomases and Shelley (2009) and Thomases et al. (2011). Contrastingly, for $Sc = \infty$ the vorticity field displays small-scale fluctuations, but its large-scale structure essentially remains slaved to that of the background force (see figure 4 for a representative snapshot). Large perturbations of the vorticity field are concentrated on thin filaments located in the vicinity of the lines of pure strain which

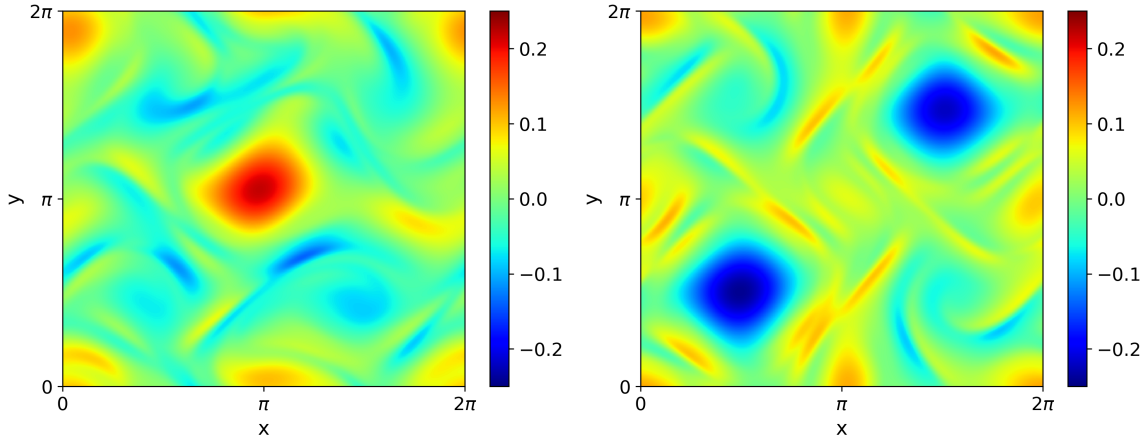

Fig. 3. Snapshot of the vorticity field for $Sc = 10^3$ at $t/T = 620$ (left) and $t/T = 1070$ (right).

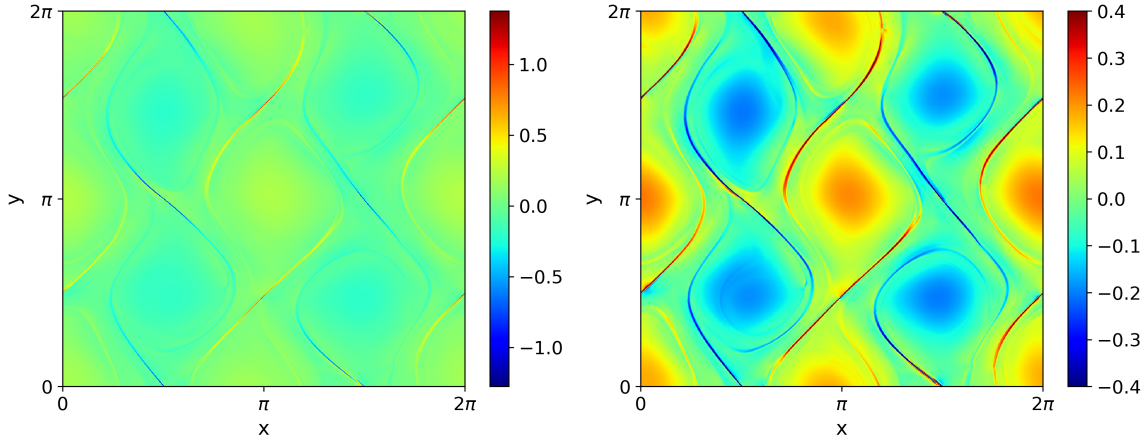

Fig. 4. Left: a representative snapshot of the vorticity field for $Sc = \infty$. Right: the same snapshot as in the left panel but with a rescaled colour bar. The purpose of this rescaling is to show the cellular structure of the flow more clearly.

separate the vortical cells. Thus, the symmetry breaking shown in figure 3 is a spurious effect due to artificial diffusivity.

The snapshots of the trace of $\boldsymbol{C}$ show an analogous strong qualitative difference in the behaviour of the polymer stress (figure 5). The analysis of these snapshots allows us to understand the effect of artificial diffusivity. Rather than the Schmidt number, here the relevant dimensionless parameter is the Péclet number $Pe = f_0/\kappa\nu K^3$, which is the ratio of the time scale associated with polymer-stress diffusion, $(\kappa K^2)^{-1}$, and the time scale at which the polymer stress is convected, T. When $Sc = \infty$, Pe is also infinite and the evolution of the polymer stress is dominated by convection. In this case, highly-stretched polymers—and hence large polymer stresses—are essentially found in strain-dominated regions of the flow, while the polymer stress is weak in vortical regions, where polymers rapidly contract. Thus, in the cellular flow, the vorticity field is strongly affected by polymer stresses at the boundaries of the cells; inside the cells, the external force dominates and imposes the cellular structure. However, when polymer-stress diffusion becomes relevant (i.e. $Sc = 10^3$ and, with our choice of parameters, $Pe = 10^3$), large polymer stresses spread far from the straining lines where they are created and reach the interior of the vortices; this destabilizes the cellular structure and generates the symmetry breaking observed at $Sc = 10^3$.

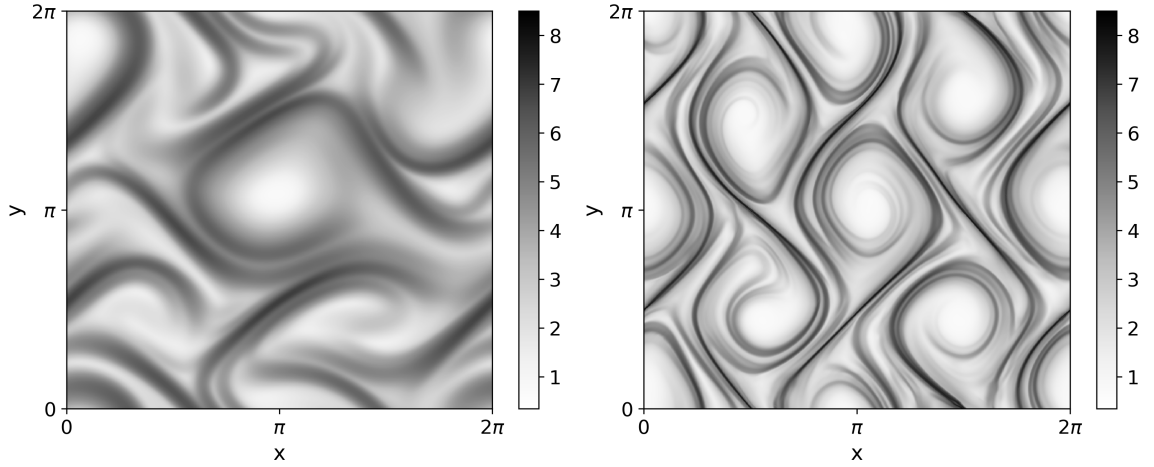

Fig. 5. Snapshots of $\ln(\mathrm{tr}\,\boldsymbol{C})$ for $Sc = 10^3$ and $Sc = \infty$ (right). The snapshots are taken at the same times as in the left panel of figure 3 and in figure 4, respectively.

Figures 3 and 4 also indicate that the vorticity field is much smoother for $Sc = 10^3$ than for $Sc = \infty$. This can be understood by noting that, in elastic turbulence, the small scales of the flow are not activated by a cascade phenomenon but rather by the fluctuations of the polymer feedback at the same scales, and for $Sc = 10^3$ the high-wavenumber fluctuations of the polymer stress are damped by diffusivity. The smoothness of the flow can be quantified by examining the spectrum of the velocity fluctuations, $E(k) \equiv \sum_{k-1/2<k'\leqslant k+1/2} \langle |\hat{\boldsymbol{v}}(\boldsymbol{k}', t)|^2 \rangle_t$, where $\langle \cdot \rangle_t$ denotes the time average over the steady state and $\hat{\boldsymbol{v}}(\boldsymbol{k}, t)$ is the Fourier transform of the velocity field minus its time average. We find again that artificial diffusivity has a strong impact on the flow (figure 6). For $Sc = 10^3$, $E(k)$ decay very rapidly with the wave number, whereas for $Sc = \infty$ it behaves as a power law: $E(k) \propto k^{-2.5}$. Thus, fluctuations are sustained at much smaller scales when $Sc = \infty$. The power law is shallower than those found previously in experiments and numerical simulations with different forcings, in which the exponent varied with the setup but was always smaller than -3 (Groisman and Steinberg 2000, 2004; Berti *et al.* 2008; Ray and Vincenzi 2016; Watanabe and Gotoh 2013, 2014; Gupta and Pandit 2017). A kinetic-energy spectrum steeper than k^{-3} was also predicted by Fouxon and Lebedev (2003). This prediction, however, does not necessarily apply to the case under consideration, because it assumes statistical homogeneity and isotropy and our flow does not enjoy these statistical symmetries. (Note that, for the Kolmogorov force, the same integration scheme used here yields the exponent -3.7 (Plan *et al.* 2017), which agrees with the results of Berti *et al.* (2008); see also Berti and Boffetta (2010) and Garg et al. (2018).)

4. Conclusions

In numerical simulations of constitutive models of polymer solutions the addition of artificial diffusivity is a well-known strategy for overcoming the numerical instabilities generated by the loss of positive definiteness of the polymer stress tensor. We have studied the accuracy of this approach in elastic turbulence by comparing simulations of the two-dimensional Oldroyd-B model sustained by a cellular external force, with and without artificial diffusivity. Our results show that artificial diffusivity has a strong impact on the qualitative spatial and temporal properties of the flow. In particular, with artificial diffusivity the cellular structure imposed by the external force breaks down, as also

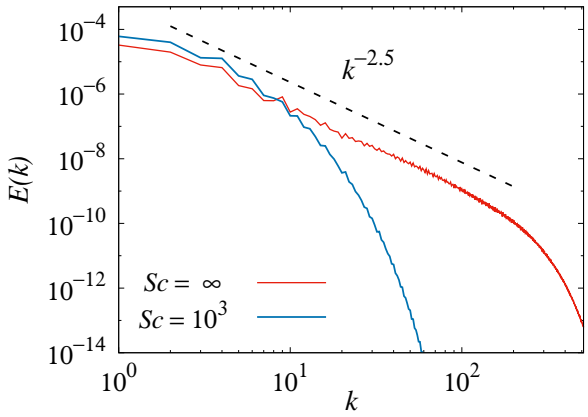

Fig. 6. Kinetic-energy spectrum for $Sc = 10^3$ (blue) and $Sc = \infty$ (red). The dashed line is proportional to the power law $k^{-2.5}$.

found by Thomases and Shelley (2009) and Thomases et al. (2011) for a four-roll mill force and the same value of Sc. Without artificial diffusivity, the flow is mainly perturbed in strain-dominated regions but, albeit chaotic, essentially reproduces the symmetries of the background force.

We have also performed simulations of the FENE-P model in exactly the same setting and found similar results. Thus, the effect of artificial diffusivity is expected to be the same also for other constitutive models of viscoelastic fluids.

As an approach alternative to the use of artificial diffusivity, we have employed an integration scheme based on the Kurganov–Tadmor hyperbolic solver. We believe, however, that our conclusions are independent of the specific scheme we use and hold for any approach that avoids artificial diffusivity or analogous dissipative schemes.

We have described the motion of the fluid by means of the Stokes equations, as in some of the previous studies on elastic turbulence. Other studies have used the Navier–Stokes equations. Thus, we have also performed numerical simulations of (2.1b) coupled with the Navier–Stokes equations with the same cellular force. The Reynolds number $Re = f_0/\nu^2 K^3$ has been set to unity, which is below the critical value for the appearance of inertial instabilities, $Re_c = \sqrt{2}$ (Gotoh and Yamada 1984). The conclusions on the effect of artificial diffusivity are exactly the same as when the Stokes equations are used.

In our study, we specifically selected the cellular force in order to illustrate the impact of artificial diffusivity on numerical simulations of elastic turbulence. This force indeed generates a flow in which the straining and vortical regions are distinct. Hence in the absence of artificial diffusivity the polymer stress is chiefly located at the straining regions, whereas in the presence of diffusivity it spreads outside them. For other external forces that mix strain and vorticity, the effect of artificial diffusivity may be less dramatic. This is the case, for instance, of the Kolmogorov force, which in the absence of polymer feedback and at low Reynolds numbers generates a sinusoidal shear. For the Kolmogorov force, the velocity spectrum indeed behaves as a power law even for $Sc = 10^3$ (Garg et al. 2018), although of course the power law is observed on a smaller range of wave numbers compared to simulations that do not use artificial diffusivity (Plan *et al.* 2017). For the same reasons, for Sc of the order of 10^3, the effect of artificial diffusivity is expected to be stronger in elastic turbulence than at high Reynolds numbers. Indeed, on average, a turbulent flow locally displays comparable amounts of strain and vorticity.

To conclude, in simulations of elastic turbulence, it is preferable to use an integration scheme that does not add artificially large polymer-stress diffusion, because depending

on the spatial structure of the force, this may yield misleading results even for relatively high values of the Schmidt number.

We would like to thank T. Matsumoto for useful discussions. The computations were performed at Centre de Calcul Interactif, Université Nice Sophia Antipolis and Mésocentre SIGAMM, Observatoire de la Côte d'Azur.

Abed, W. M., Whalley, R. D., Dennis, D. J. C. and Poole R. J. 2016 Experimental investigation of the impact of elastic turbulence on heat transfer in a serpentine channel. *J. Non-Newtonian Fluid Mech.* **231**, 68–78.

Balci, N., Thomases, B., Renardy, M. and Doering, C. R. 2011 Symmetric factorization of the conformation tensor in viscoelastic fluid models. *J. Non-Newtonian Fluid Mech.* **166**, 546–553.

Berti, S., Bistagnino, A., Boffetta, G., Celani, A. and Musacchio, S. 2008 Two-dimensional elastic turbulence. *Phys. Rev.* E **77**, 055306(R).

Berti, S. and Boffetta, G. 2010 Elastic waves and transition to elastic turbulence in a two-dimensional viscoelastic Kolmogorov flow. *Phys. Rev.* E **82**, 036314.

Bird, R. B., Hassager, O., Armstrong, R. C. and Curtiss, C. F. 1987 *Dynamics of Polymeric Liquids*, vol. II. Wiley.

van Buel, R., Schaaf, C. and Stark, H. 2018 Elastic turbulence in two-dimensional Taylor-Couette flows. `arXiv:1806.02715`

Dallas, V., Vassilicos, J. C. and Hewitt, G. F. 2010 Strong polymer-turbulence interactions in viscoelastic turbulent channel flow. *Phys. Rev.* E **82**, 066303.

El-Kareh, A. W. and Leal, L. G. 1989 Existence of solutions for all Deborah numbers for a non- Newtonian model modified to include diffusion. *J. Non-Newtonian Fluid Mech.* **33**, 257–287.

Fattal, R. and Kupferman, R. 2004 Constitutive laws for the matrix-logarithm of the conformation tensor. *J. Non-Newtonian Fluid Mech.* **123**, 281–285.

Fouxon, A. and Lebedev, V. 2003 Spectra of turbulence in dilute polymer solutions. *Phys. Fluids* **15**, 2060–2072.

Garg, H., Calzavarini, E., Mompean, G. and Berti, S. 2018 Particle-laden two-dimensional elastic turbulence. `arxiv.org/abs/1804.01441`

Gotoh, K. and Yamada, M. 1984 Instability of a cellular flow. *J. Phys. Soc. Japan* **53**, 3395–3398.

Graham, M. D. 2014 Drag reduction and the dynamics of turbulence in simple and complex fluids. *Phys. Fluids* **26**, 101301.

Groisman, A. and Steinberg, V. 2000 Elastic turbulence in a polymer solution flow. *Nature* **405**, 53–55.

Groisman, A. and Steinberg, V. 2001 Efficient mixing at low Reynolds numbers using polymer additives. *Nature* **410**, 905–908.

Groisman, A. and Steinberg, V. 2004 Elastic turbulence in curvilinear flows of polymer solutions. *New J. Phys.* **6**, 29.

Grilli, M., Vázquez-Quesada, A. and Ellero, M. 2013 Transition to turbulence and mixing in a viscoelastic fluid flowing inside a channel with a periodic array of cylindrical obstacles. *Phys. Rev. Lett.* **110**, 174501.

Gupta, A. and Pandit, R. 2017 Melting of a nonequilibrium vortex crystal in a fluid film with polymers: Elastic versus fluid turbulence. *Phys. Rev.* E **95**, 033119.

Gupta, A., Perlekar, P. and Pandit, R. 2015 Two-dimensional homogeneous isotropic fluid turbulence with polymer additives. *Phys. Rev.* E **91**, 033013.

Jin, S. and Collins, L. R. 2007 Dynamics of dissolved polymer chains in isotropic turbulence. *New J. Phys.* **9**, 360.

Joseph, D. D. 1990 *Fluid dynamics of viscoelastic liquids*. Springer.

Kurganov, A. and Tadmor, E. 2000 New high-resolution central schemes for nonlinear conservation laws and convection-diffusion equations. *J. Comput. Phys.* **160**, 241–282.

Liu N. and Khomami, B. 2013 Elastically induced turbulence in Taylor–Couette flow: direct numerical simulation and mechanistic insight *J. Fluid Mech.* **737**, R4.

Liu, Y. and Steinberg, V. 2014 Single polymer dynamics in a random flow. *Macromol. Symp.* **337**, 34–43.

Min, T., Yoo, J. Y. and Choi, H. 2001 Effect of spatial discretization schemes on numerical solutions of viscoelastic fluid flows. *J. Non-Newtonian Fluid Mech.* **100**, 27–47.

Oldroyd, J. G. 1950 On the formulation of rheological equations of state. *Proc. R. Soc. Lond.* A **200**, 523–541.

Perlekar, P., Mitra, D. and Pandit, R. 2006 Manifestations of drag reduction by polymer additives in decaying, homogeneous, isotropic turbulence. *Phys. Rev. Lett.* **97**, 264501.

Perlekar, P., Mitra, D. and Pandit, R. 2010 Direct numerical simulations of statistically steady, homogeneous, isotropic fluid turbulence with polymer additives. *Phys. Rev.* E **82**, 066313.

Plan, E. L. C. VI M., Gupta, A., Vincenzi, D. and Gibbon, J.D. 2017 Lyapunov dimension of elastic turbulence. *J. Fluid Mech.* **822**, R4.

Poole, R. J., Budhiraja, B., Cain, A. R. and Scott, P. A. 2012 Emulsification using elastic turbulence. *J. Non-Newtonian Fluid Mech.* **177–178**, 15–18.

Press, W. H., Teukolsky, S. A., Vetterling, W. T and Flannery, B. P. 2007 *Numerical recipes: The art of scientific computing*, 3rd edition. Cambridge University.

Ray, S. S. and Vincenzi, D. 2016 Elastic turbulence in a shell model of polymer solution. *Europhys. Lett.* **114**, 44001.

Robert, A., Vaithianathan, T., Collins, L. R. and Brasseur, J. G. 2010 Polymer-laden homogeneous shear-driven turbulent flow: a model for polymer drag reduction. *J. Fluid Mech.* **657**, 189–226.

Sid, S., Terrapon, V. E. and Dubief, Y. 2018 Two-dimensional dynamics of elasto-inertial turbulence and its role in polymer drag reduction. *Phys. Rev. Fluids* **3**, 011301(R).

Sureshkumar, R. and Beris, A. N. 1995 Effect of artificial stress diffusivity on the stability of numerical calculations and the flow dynamics of time-dependent viscoelastic flows. *J. Non-Newtonian Fluid Mech.* **60**, 53–80.

Thomases, B. and Shelley, M. 2009 Transition to mixing and oscillations in a Stokesian viscoelastic flow. *Phys. Rev. Lett.* **103**, 094501.

Thomases, B., Shelley, M. and Thiffeault, J.-L. 2011 A Stokesian viscoelastic flow: Transition to oscillations and mixing. *Physica* D **240**, 1602–1614.

Thomases, B. 2011 An analysis of the effect of stress diffusion on the dynamics of creeping viscoelastic flow. *J. Non-Newtonian Fluid Mech.* **166**, 1221–1228.

Traore, B., Castelain, C. and Burghelea, T. 2015 Efficient heat transfer in a regime of elastic turbulence. *J. Non-Newtonian Fluid Mech.* **223**, 62–76.

Vaithianathan, T. and Collins, L. R. 2003 Numerical approach to simulating turbulent flow of a viscoelastic polymer solution. *J. Comp. Phys.* **187**, 1–21.

Vaithianathan, T., Robert, A., Brasseur, J. G. and Collins, L. R. 2006 An improved algorithm for simulating three-dimensional, viscoelastic turbulence. *J. Non-Newtonian Fluid Mech.* **140**, 3–22.

Vaithianathan, T., Robert, A., Brasseur, J. G. and Collins, L. R. 2007 Polymer mixing in shear-driven turbulence. *J. Fluid Mech.* **585**, 487–497.

Valente P. C., da Silva, C. B. and Pinho, F. T. 2014 The effect of viscoelasticity on the turbulent kinetic energy cascade. *J. Fluid Mech.* **760**, 39–62.

Watanabe, T. and Gotoh, T. 2013 Kinetic energy spectrum of low-Reynolds-number turbulence with polymer additives. *J. Phys. Conf. Ser.* **454**, 012007.

Watanabe, T. and Gotoh, T. 2014 Power-law spectra formed by stretching polymers in decaying isotropic turbulence. *Phys. Fluids* **26**, 035110.